

# COMPRESSIBLE GROUND EFFECT AERODYNAMICS

by  
Graham Doig, M.Eng

A dissertation submitted in fulfillment  
of the requirements for the degree of  
Doctor of Philosophy at the  
University of New South Wales

March 2009



**ORIGINALITY STATEMENT**

'I hereby declare that this submission is my own work and to the best of my knowledge it contains no materials previously published or written by another person, or substantial proportions of material which have been accepted for the award of any other degree or diploma at UNSW or any other educational institution, except where due acknowledgement is made in the thesis. Any contribution made to the research by others, with whom I have worked at UNSW or elsewhere, is explicitly acknowledged in the thesis. I also declare that the intellectual content of this thesis is the product of my own work, except to the extent that assistance from others in the project's design and conception or in style, presentation and linguistic expression is acknowledged.'

Signed .....

Date .....

## *Abstract*

The aerodynamics of bodies in compressible ground effect flowfields from low-subsonic to supersonic Mach numbers have been investigated numerically and experimentally. A study of existing literature indicated that compressible ground effect has been addressed sporadically in various contexts, without being researched in any comprehensive detail. One of the reasons for this is the difficulty involved in performing experiments which accurately simulate the flows in question with regards to ground boundary conditions. To maximise the relevance of the research to appropriate real-world scenarios, multiple bodies were examined within the confines of their own specific flow regimes. These were: an inverted T026 wing in the low-to-medium subsonic regime, a lifting RAE 2822 aerofoil and ONERA M6 wing in the transonic regime, and a NATO military projectile at supersonic Mach numbers.

Two primary aims were pursued. Firstly, experimental issues surrounding compressible ground effect flows were addressed. Potential problems were found in the practice of matching incompressible Computational Fluid Dynamics (CFD) simulations to wind tunnel experiments for the inverted wing at low freestream Mach numbers ( $<0.3$ ), where the inverted wing was found to experience significant compressible effects even at Mach 0.15. The approach of matching full-scale CFD simulations to scale model testing at an identical Reynolds number but higher Mach number was analysed and found to be prone to significant error. An exploration was also conducted of appropriate ways to conduct experimental tests at transonic and supersonic Mach numbers, resulting in the recommendation of a symmetry (image) method as an effective means of approximating a moving ground boundary in a small-scale blowdown wind tunnel. Issues of scale with regards to Reynolds number persisted in the transonic regime, but with careful use of CFD as a complement to experiments, discrepancies were quantified with confidence.

The second primary aim was to use CFD to gain a broader understanding of the ways in which density changes in the flowfield affect the aerodynamic performance of the bodies in question, in particular when a shock wave reflects from the ground plane to interact again with the body or its wake. The numerical approach was extensively verified and validated against existing and new experimental data.

The lifting aerofoil and wing were investigated over a range of mid-to-high subsonic Mach numbers ( $1 > M_\infty > 0.5$ ), ground clearances and angles of incidence. The presence of the ground was found to affect the critical Mach number, and the aerodynamic characteristics of the bodies across all Mach numbers and clearances proved to be highly sensitive to ground proximity, with a step change in any variable often causing a considerable change to the lift, moment and drag coefficients. At the lowest ground clearances in both two and three dimensional studies, the aerodynamic efficiency was generally found to be less than that of unbounded (no ground) flight for shock-dominated flowfields at freestream Mach numbers greater than 0.7.

In the fully-supersonic regime, where shocks tend to be steady and oblique, a supersonic spinning NATO projectile travelling at Mach 2.4 was simulated at several ground clearances. The shocks produced by the body reflected from the ground plane and interacted with the far wake, the near wake, and/or the body itself depending on the ground clearance. The influence of these wave reflections on the three-dimensional flowfield, and their resultant effects on the aerodynamic coefficients, was determined. The normal and drag forces acting on the projectile increased in exponential fashion once the reflections impinged on the projectile body again one or more times (at a height/diameter ground clearance  $h/d < 1$ ). The pitching moment of the projectile changed sign as ground clearance was reduced, adding to the complexity of the trajectory which would ensue.

## *Acknowledgements*

There are many people I would like to mention or thank for a variety of reasons;

My supervisor **Dr. Tracie Barber**, for getting me into this in the first place and helping me get out of it too. Were it not for her amazing ability to find funding, I would have had to donate my body to sleep research at the faculty of medicine... though that actually sounds quite good at the moment. I may have chosen her name at random to contact when I first decided to come to Australia to do my PhD, but now I couldn't imagine having done any of this and much much more without her as my supervisor.

My co-supervisor **Prof. Eddie Leonardi**, who sadly passed away at the end of 2008, and before I could run any of my thesis past him. Apart from everything else he did for Mech. Eng. at UNSW, Eddie helped give me all kinds of opportunities for travel and research that I wouldn't have otherwise had. He always did his best to find a quick moment to talk when it was needed, and provided us all with some catchphrases that will long live on even as he is missed.

My other co-supervisor **Dr. Andrew Neely** at ADFA, who tried his best to show me the wonders of Canberra. His assistance and insight was much valued, even if I did almost have to construct a 300km-long prodding device to get it out of him. Andrew also put me in touch with **Commander (USN) David Myre, D.Sc.**, who was instrumental in organising the transonic wind tunnel tests I was able to do at the US Naval Academy, with generous assistance from the **Royal Aeronautical Society** in the form of a Centennial Scholarship for travel to Annapolis. My research was greatly enriched by the support of these two organisations. Thanks also to those at ADFA who allowed me to become involved in various strands of research being conducted there and always welcomed me during my sporadic visits.

**Mum and Dad** for not asking *too* often how "it's all going" and for quietly keeping me afloat before and after my UNSW scholarship briefly surfaced. And also for being happy that I'm happy here. **Grandpa**, for without his stories about Spitfires and Mustangs and Lancasters and Mosquitos I don't think I ever would've been interested in any of this in the first place; and **Granny**, who sadly won't get to see this, but thankfully I managed by considerable coincidence to see *her* again, just before she died in 2006. I hope they'll all be as proud of my second graduation as they were for my first.

The guys in the **CFD group** who also made a fine band of Wednesday Footballers, especially; **Ian Watson**, **Osama Alshroof**, the interlopers **Julien Berger**, "**Le Dude**" **Vince Galoul**, **Marc Wolf**... **Sam Lor** too, who fixed every computer I broke, and **JP Hwang**, who was also the finest undergrad monkey that any PhD student could hope for. Get your clubs ready! I'm also grateful to **Prof. John Reizes** for far too much food for thought, and **Ian Cassappi** in the workshop for getting those wings made on time.

Most of all of everyone at uni, **Sam Diasinos** and **Chris Beves**, for hallway frisbee, yoghurt time, chocolate time, Tum's Thai, Yeeros, "*lettuce*", many hours of entertaining... ummm "*constructive criticism*" ...of whatever was happening at Mech Eng at the time, and many more hours of learning how to do stuff in Fluent and Catia and Gambit and a million other things. Red curry to L110, Sam? I, 3 times' unbeaten F1 predictor champion, thank you for all these things I'll remember long after everything else.

And **Megan Guhl**, who has just quite rightly told me to go back to work even though it's 1am and I'm only writing this bit. I hope post-thesis life with myself and **Papua the Pig** will more than make up for these stressful months.

## *List of Publications by the author*

**Portions of research presented in or related to this thesis appear in the following published works:**

Journal papers:

**Methods for Investigating Supersonic Ground Effect in a Blowdown Wind Tunnel**

G. Doig, T.J. Barber, E. Leonardi, A.J. Neely, H. Kleine  
*Shock Waves*, 18 (2), 155-159, 2008

**The Onset of Compressibility Effects for an Inverted Aerofoil in Ground Effect**

G. Doig, T.J. Barber, A.J. Neely, E. Leonardi  
*The Aeronautical Journal*, 111 (1126), 797-806, 2007

**Studies of Ground Effect Automotive Aerodynamics**

T.J. Barber, C. Beves, S. Diasinos, G. Doig, E. Leonardi, A.J. Neely  
*Autotechnology*, 2, 2007

Conference papers:

**The Aerodynamics of a Supersonic Projectile in Ground Effect**

G. Doig, H. Kleine, A.J. Neely, T.J. Barber,  
J.P. Purdon, E.M. Appleby, N.R. Mudford, E. Leonardi  
*Proceedings of the 26th International Symposium on Shock Waves, Göttingen, Germany, 2007*

**The Use of Thermochromic Liquid Crystals to Investigate Flowfield Interactions with the Ground around a Supersonic Land Speed Record Vehicle**

G. Doig, A.J. Neely, T.J. Barber, E. Leonardi  
*Proceedings of the 13th International Heat Transfer Conference, Sydney, 2006*

**The Aerodynamics of Aerofoils and Wings in Transonic Ground Effect**

G. Doig, T.J. Barber, A.J. Neely, E. Leonardi  
*Proceedings of the 2008 International Congress of Theoretical and Applied Mechanics, Adelaide, 2008*

## Contents

Abstract	i
Acknowledgements	iii
List of publications by the author	iv
Contents	v
List of figures	ix
Nomenclature	xxv
<b>1 Introduction</b>	<b>1</b>
1.1 Preface	1
1.2 Review of Relevant Research	5
1.3 Thesis Aims and Outline	22
1.3.1 Choice of geometries for investigation	23
1.3.2 Outline	25
<b>2 Numerical Methods</b>	<b>26</b>
2.1 Introduction	26
2.2 Principles of Compressible Fluids and the Navier-Stokes Equations	29
2.2.1 Conservation of mass, momentum and energy	29
2.2.2 Compressible Fluids and associated parameters	30
2.3 Application of the Navier-Stokes Equations to CFD	31
2.3.1 Discretisation	31
2.3.1.1 Spatial Discretisation	33
2.3.1.2 Gradient Evaluation	33
2.3.1.3 Temporal Discretisation	34
2.3.2 Reynolds-Averaged Navier Stokes Modelling	35
2.3.3 Turbulence Modelling	35
2.3.3.1 The Boussinesq Approximation	36
2.3.3.2 The Spalart-Allmaras model	37
2.3.3.3 The Realizable $k-\varepsilon$ model	38
2.3.3.4 The $k-\omega$ SST model	39
2.3.3.5 The $k-k-l-\omega$ model	39
2.3.3.6 Further notes on wall region modelling	40
2.3.4 Pressure-based and density-based solvers	41
2.3.4.1 Coupled vs. Segregated methods	41
2.3.5 Implicit vs. Explicit methods	42
2.3.6 AMG, FAS Multigrid, and Smoothing Techniques	44
2.3.7 Flux splitting	45
2.3.8 Initialization and FMG	45
2.3.9 More on relaxation and stability	46
2.4 Additional Considerations	47
2.4.1 64-bit processing	47
2.4.2 Notes on meshing	47
2.4.3 Residual reduction and convergence	49
2.4.4 Kriging of a vector field	49
2.5 Summary of Solution Procedures	51

<b>3</b>	<b>Experimental Methods</b>	52
3.1	<b>Introduction</b>	52
3.1.1	Determination of suitable approaches	52
3.1.2	Outline of experimental approaches	54
3.2	<b>Supersonic Methods</b>	56
3.2.1	Australian Army Live Arms Proofing Range	56
3.2.1.1	Objective	56
3.2.1.2	Facility	57
3.2.1.3	Apparatus, technique and experimental conditions	57
3.2.1.4	Experimental Error	59
3.2.2	UNSW@ADFA Supersonic Blowdown Wind Tunnel	60
3.2.2.1	Objective	60
3.2.2.2	Facility	60
3.2.2.3	Apparatus, technique and experimental conditions	60
3.2.2.4	Experimental Error	62
3.3	<b>Transonic Wind Tunnel Methods</b>	64
3.3.1	Objective	64
3.3.2	Facility	66
3.3.3	Apparatus, technique and measurement techniques	67
3.3.4	Experimental error	74
3.3.5	Further manufacturing and installation considerations	77
3.4	<b>Summary</b>	78
<b>4</b>	<b>Validation of CFD</b>	80
4.1	<b>Introduction</b>	80
4.2	<b>Subsonic Inverted T026</b>	81
4.2.1	Mesh and boundary considerations	84
4.2.2	Turbulence modelling	86
4.2.3	Further comparison to experimental results (compressible and incompressible)	92
4.3	<b>RAE 2822 Aerofoil</b>	96
4.3.1	RAE 2822 "Case 9"	96
4.3.1.1	Mesh and boundary considerations	99
4.3.1.2	Turbulence modelling	100
4.3.2	RAE 2822 "Case 10"	103
4.4	<b>ONERA M6 Wing</b>	108
4.4.1	Mesh and boundary considerations	111
4.4.2	Turbulence modelling	113
4.5	<b>RAE 2822 Experiments at the US Naval Academy</b>	115
4.5.1	Mesh and boundary considerations	117
4.5.2	Turbulence modelling	121
4.5.2.1	Extent and influence of laminar flow	121
4.5.2.2	Comparison of turbulence models	124
4.5.3	Further experimental comparisons	126
4.5.3.1	Influence of rear sting mount strut	126
4.5.3.2	Quality of two-dimensional flow at the mid-span	127
4.6	<b>Supersonic Projectile</b>	129
4.6.1	Mesh and boundary considerations	131
4.6.2	Turbulence modelling	136

4.7	<b>Additional Aspects</b>	142
4.7.1	Influence of inlet turbulence intensity	142
<b>5</b>	<b>Evaluation of Blowdown Wind Tunnel Methods for Compressible Ground Effect Studies</b>	145
5.1	<b>Introduction</b>	145
5.2	<b>Supersonic Methods</b>	146
5.2.1	Symmetry and elevated ground in schlieren	147
5.2.2	Symmetry and elevated ground in CFD	149
5.2.3	Additional considerations	153
5.2.4	Summary	155
5.3	<b>Transonic Methods</b>	156
5.3.1	Introduction	156
5.3.2	Case 1	157
5.3.3	Case 2	161
5.3.4	Case 3	163
5.3.5	Case 4	167
5.3.6	Further Discussion	170
	5.3.6.1 Other limitations of the elevated ground plane	170
	5.3.6.2 Issues of scale	173
5.4	<b>Summary</b>	174
<b>6</b>	<b>The Onset of Compressibility Effects for an Inverted Wing in Ground Effect</b>	176
6.1	<b>Introduction</b>	176
6.2	<b>Results and discussion</b>	179
6.2.1	Increasing Mach number for a fixed Reynolds number	179
	6.2.1.1 Freeflight reference cases	181
	6.2.1.2 Compressible influence on aerodynamic force coefficients at $h/c=0.179$	182
	6.2.1.3 Resultant pressure coefficient distributions	183
	6.2.1.4 Vortex and wake behaviour	188
	6.2.1.3 Further comments	191
6.2.2	Increasing Mach number and decreasing ground clearance for free-varying a Reynolds number	192
	6.2.2.1 Aerodynamic force and moment coefficients	192
	6.2.2.2 Wing pressure distributions and wake profiles	196
	6.2.2.3 Vortex behaviour	200
6.2.3	Onset of critical Mach effects	200
6.3	<b>Summary</b>	204
<b>7</b>	<b>RAE 2822 Aerofoil in Transonic Ground Effect</b>	
7.1	<b>Introduction</b>	206
7.2	<b>“Case 9” with decreasing ground clearance</b>	207
7.3	<b>Decreasing ground clearance for fixed Mach numbers</b>	213
	7.3.1 2.79° incidence	213
	7.3.2 0° incidence	221
	7.3.3 6° incidence	224
7.4	<b>Increasing Mach number for fixed ground clearances</b>	228

7.4.1	0° incidence	229
7.4.2	2.79° incidence	229
7.4.3	6° incidence	234
7.5	Summary	234
<b>8</b>	<b>ONERA M6 Wing in Transonic Ground Effect</b>	<b>237</b>
8.1	Introduction	237
8.2	“Case 2308” with decreasing ground clearance	239
8.3	Decreasing ground clearance for fixed Mach numbers	247
8.3.1	3.06° incidence	250
8.3.2	0° incidence	255
8.4	Increasing MACH numbers for fixed ground clearances	257
8.4.1	3.06° incidence	257
8.4.2	0° incidence	259
8.5	Isolated case at M=0.95	260
8.6	Summary	262
<b>9</b>	<b>A Supersonic Projectile in Ground Effect</b>	<b>265</b>
9.1	Introduction	265
9.2	Results and discussion	269
9.2.1	Comparisons to live-range experiments	269
9.2.2	The three-dimensional flowfield	273
9.2.3	Forces and moments	280
9.2.4	Projectile and ground pressure distributions	283
9.2.5	Flow in the wake	285
9.3	Summary	293
<b>10</b>	<b>Conclusions</b>	<b>294</b>
10.1	Conclusions	294
10.2	Recommendations for future work	298
	<b>List of References</b>	<b>301</b>
	<b>Appendix A - Selected Publications</b>	

## List of Figures

Fig. 1.1. Examples of compressible ground effect scenarios: a) a rocket sled test facility at supersonic Mach numbers, b) an aerial view of the Thrust SSC land speed record car at Mach 1 highlights the shock wave extent, c) an Ekranoplan capable of Mach 0.45, d) a US Navy Blue Angel display aircraft during a Mach 0.95 pass, e) a modern Formula 1 car with an inverted front wing in close ground proximity, and f) a current-generation Maglev train capable of Mach 0.5.

p.2

Fig. 1.2. Important flow considerations as Mach number is increased.

p.3

Fig. 1.3. a) regular reflection of an oblique shock with a boundary layer b) idealised regular reflection of an oblique shock at an inviscid wall (based on Szwaba *et al.*, 2004)

p.5

Fig. 1.4. a) normal shock/boundary layer interaction with a “ $\lambda$ ” foot, and b) Mach reflection of an oblique shock at an inviscid wall (from Szwaba *et al.*, 2004)

p.5

Fig. 1.5. Schematic of the three-dimensional propagation of the conical shock and inviscid reflection produced by a supersonic store in proximity to a plate, highlighting transition from regular to Mach reflection. (Marconi, 1983)

p.7

Fig. 1.6. Normal (lift) force on the rocket sled wind tunnel model for different rail slipper (and therefore ground clearance) heights with increasing Mach number (Strike and Lucas, 1968)

p.15

Fig. 1.7. An example of the differences between CFD and different wind tunnel methods for predicting  $C_y$  (normal force) and  $Cm_x$  (longitudinal pitching moment) a high-speed train. (Matschke, 1999)

p.19

Fig. 1.8. Comparison of  $C_D$  obtained on train configuration for different experimental ground representations. (Kwon, 2001)

p.19

Fig. 1.9. An aero-levitation electric vehicle (AEV) model in a wind tunnel (left), and predicted lift coefficients for the main wing section at varying height to chord ( $h/c$ ) ground clearances (right), (Moon *et al.*, 2005).

p.20

Fig. 1.10. Bodies used for investigating compressible ground effect in different Mach ranges.

p.23

Fig. 1.11. Flowchart outline of thesis

p.24

Fig. 2.1. A general procedure for the CFD method used in the present investigations

p.32

Fig. 2.2. Schematic of the density-based coupled solution procedure

p.42

Fig. 2.3. Schematic of the pressure-based segregated solution procedure  
p.43

Fig. 2.4. Schematic of the pressure-based coupled solution procedure  
p.43

Fig. 2.5. Pressure gradient-based local mesh adaption: a) original mesh, b) one level of broad gradient refinement, and c) second level of high-gradient shock-specific refinement.  
p.49

Fig. 2.6. An example of a “hanging node” in a locally-refined mesh.  
p.49

Fig. 3.1. Four means of simulating ground effect flows in a wind tunnel: a) the preferred technique of a moving ground, b) boundary layer suction, c) an elevated ground, and d) a symmetry (mirror-image) method.  
p.54

Fig. 3.2. Colour schlieren images of the wedge model used to assess the feasibility of the symmetry method.  
p.55

Fig. 3.3. a) a wind-on image taken as the TLCs activate on the elevated ground plane, and b) a post-processed image of the ‘footprint’ of shocks on the ground around the wedge.  
p.55

Fig. 3.4. Role of supersonic experiments in cooperation with CFD.  
p.57

Fig. 3.5. Schematic of the projectile used for live-range experiments, dimensions in mm.  
p.58

Fig. 3.6. Schlieren stills from the live-range experiments show the unsteady evolution of flow around a bullet entering the ground-proximity regime (Doig *et al*, 2007b).  
p.58

Fig. 3.7. Parameters of importance for the live-range round (left) and the symmetry method wind tunnel model (right), dimensions in mm.  
p.61

Fig. 3.8. The instrumented projectile in the ADFA tunnel with ground plane (Appleby, 2006).  
p.62

Fig. 3.9. Schlieren image of the projectile model with elevated ground plane, highlighting wave produced by the leading edge of the elevated ground.  
p.63

Fig. 3.10. Role of transonic experiments in cooperation with CFD.  
p.65

Fig. 3.11. The US Naval Academy Transonic Blowdown wind tunnel, with test section open. Flow direction is left to right.  
p.65

Fig. 3.12. The elevated ground method setup with endplates.  
p.67

Fig. 3.13. The symmetry method setup with endplates.  
p.67

Fig. 3.14. The wings after the first stage of machining showing (left) the rough first pass to form the 2822 profile and (right) the grooves machined to allow the laying of hypodermic pipe to the tapping locations.  
p.68

Fig. 3.15. The wing in its mould following laying of the hypodermic pipe and subsequent re-profiling with body-filler machined back to the 2822 profile.  
p.68

Fig. 3.16. A schematic of a) wing A with lower surface tappings, b) wing B with upper surface tappings, and c) the elevated ground tapping locations and d) location of the elevated ground plane relative to wing B.  
p.69

Fig. 3.17. An elevated ground setup viewed from upstream, inside the open test section, prior to securing of the vinyl tubing.  
p.71

Fig. 3.18. One of the wings in free flight configuration (no ground plane) prior to sealing of the end plate holes with aluminum tape  
p.71

Fig. 3.19. Wings in symmetry configuration; image shows the support “feet” used to brace the model, and the aluminium tape covering endplate holes.  
p.72

Fig. 3.20. Flow uniformity in the centre of the tunnel along a horizontal plane, using a rake probe for a freestream Mach number of 0.788.  
p.74

Fig. 3.21. Mach number histories for one tunnel run, average  $M_\infty=0.553$  during measurement period.  
p.75

Fig. 3.22. Mach number histories for one tunnel run, average  $M_\infty=0.553$  during measurement period.  
p.75

Fig. 4.1. Notation for an inverted wing in ground effect  
p.83

Fig. 4.2 - an example of the standard mesh for the Tyrell 026 wing with endplate, semi-span model (symmetry) for  $h/c=0.067$ .  
p.83

Fig 4.3. a) coarse, b) standard and c) fine meshes on the symmetry plane and lower wing surface.  
p.85

Fig. 4.4.  $h/c=0.179$  wing surface pressure distributions at  $z=0$  for coarse, standard and fine meshes.  
p.87

Fig. 4.5. Comparisons to experimental lift coefficient for coarse, standard and fine meshes.  
p.87

Fig. 4.6. Comparisons to experimental drag coefficient for coarse, standard and fine meshes.  
p.87

Fig. 4.7  $C_L$  (a),  $C_D$  (b) comparisons to experimental results,  $h/c=0.179$ .  
p.88

Fig. 4.8. Turbulence model comparisons to experimental pressure distributions,  $h/c=0.067$ .  
p.90

Fig. 4.9. Turbulence model comparisons to experimental pressure distributions,  $h/c=0.179$ .  
p.90

Fig. 4.10.  $C_L$ ,  $C_D$  comparisons to experimental result,  $h/c=0.067$   
p.92

Fig. 4.11. Wake profile (a) comparisons to experimental data (Zerihan, 2000) at  $x/c=1.2$  on the symmetry plane, and b) spanwise pressure distributions at  $h/c=0.179$  with CFD overlaid.  
p.92

Fig. 4.12. Lift coefficient vs. ground clearance, compressible and incompressible comparison to experimental values.  
p.93

Fig. 4.13. Drag coefficient vs. ground clearance, compressible and incompressible comparison to experimental values.  
p.93

Fig. 4.14. Compressible and incompressible CFD comparison to experimental pressure distribution,  $h/c=0.179$   
p.94

Fig. 4.15. Compressible and incompressible CFD comparison to experimental pressure distribution,  $h/c=0.067$   
p.94

Fig. 4.16. Domain extent for RAE 2822 'Case 9' simulations.  
p.97

Fig. 4.17. General mesh layout for RAE 2822 simulations, with (right) detail for the near-wall region at the leading and trailing edges.  
p.97

Fig. 4.18. Predicted pressure distributions for different meshes.  
p.98

Fig. 4.19. Predicted lift coefficients for different meshes.  
p.98

Fig. 4.20. Predicted drag coefficients for different meshes.  
p.98

Fig. 4.21. Resolution of density contours at the shock within the mesh for increasingly-refined node-spacing; a) coarse mesh, b) standard mesh, c) standard mesh first adaption, d) standard mesh with a second adaption.  
p.99

- Fig. 4.22. Predicted lift coefficients for two turbulence models with and without forced transition at  $0.03c$ .  
p.101
- Fig. 4.23. Predicted pressure distributions for different turbulence models.  
p.102
- Fig. 4.24. Predicted lift coefficients for different turbulence models.  
p.102
- Fig. 4.25. Predicted lift coefficients for different turbulence models.  
p.102
- Fig. 4.26. RAE 2822 'Case 10' pressure distribution on symmetry (semi-span) plane, averaged over 2 shock oscillation cycles.  
p.104
- Fig. 4.27. RAE 2822 'Case 10' lift coefficient and chordwise shock position on the symmetry (semi-span) plane with respect to time.  
p.104
- Fig. 4.28. (opposite page) Pressure distributions over the course of one shock oscillation cycle, compared to experimental results.  
p.105
- Fig. 4.29 (above) Contours of density for the time steps depicted in figure 4.28.  
p.106
- Fig. 4.30. Parameters and 7 spanwise locations of chordwise tappings for the ONERA M6 wing.  
p.108
- Fig. 4.31. Domain extent for ONERA M6 cases.  
p.109
- Fig. 4.32. General meshing approach applied to the M6 wing, with leading and trailing edge detail (right).  
p.110
- Fig. 4.33. Contours of density on the upper surface of the M6 for increasing mesh resolution; i) coarse mesh, ii) standard mesh, iii) fine mesh, and iv) standard mesh with local shock-adaption.  
p.110
- Fig. 4.34. Chordwise pressure distributions at the 7 tapping stations on the M6 for the coarse, standard and fine meshes.  
p.112
- Fig. 4.35. Chordwise pressure distributions at the 7 tapping stations on the M6, showing effect of increasing mesh resolution.  
p.114
- Fig. 4.36. USNA test section dimensions for CFD, with (inset) example mesh for a case with the elevated ground plane.  
p.116
- Fig. 4.37. USNA Cases 2 (a), 3 (b) and 4 (c), showing contours of density on the wing, endplate and symmetry ground plane, as well as areas of supersonic flow (blue).  
p.116

- Fig. 4.38. Pressure distribution at the mid-span symmetry plane, USNA Case 1, standard and fine meshes.  
p.120
- Fig. 4.39. Time-averaged pressure distribution at the mid-span symmetry plane, USNA Case 4, standard and fine meshes.  
p.120
- Fig. 4.40. Contours of skin friction for the lower wing surface, USNA Case 0.  
p.122
- Fig. 4.41. Pressure distribution at the mid-span symmetry plane, USNA Case 0, free transition and fully turbulent CFD.  
p.122
- Fig. 4.42. Time-averaged pressure distributions at the mid-span symmetry plane, USNA Case 4, free transition and fully turbulent CFD.  
p.123
- Fig. 4.43. Pressure distributions for USNA Case 1, turbulence model comparisons.  
p.124
- Fig. 4.44. Pressure distributions for USNA Case 2, turbulence model comparisons.  
p.124
- Fig. 4.45. Pressure distributions for USNA Case 4, turbulence model comparisons.  
p.125
- Fig. 4.46. Geometry for CFD cases involving the rear support strut.  
p.127
- Fig. 4.47. Pressure distributions for USNA Case 3, comparison between runs with and without the rear support strut  
p.127
- Fig. 4.48. Spanwise pressure distributions at  $x/c=0.167$  for cases 1 (steady state) and 4 (time-averaged transient).  
p.128
- Fig. 4.49. Areas of separated flow for Case 1 (with ground plane). Note separation also present at the elevated ground leading edge and at the ground/endplate junction under the wing.  
p.128
- Fig. 4.50. Coordinate reference frame  
p.130
- Fig. 4.51. Schlieren photograph with annotated flowfield characteristics for the projectile in free flight conditions.  
p.130
- Fig. 4.52. Bullet surface mesh and example quarter-domain for live-range freeflight comparisons  
p.132
- Fig. 4.53. Mesh on z-symmetry, projectile, volume slice, and 'ground' plane (after shock-adaptation) for half model, no-sting simulations of wind tunnel symmetry method.  
p.132

Fig. 4.54. Contours of density as mesh is adapted for non-spinning (symmetry) bullet at  $h/d=0.42$ ; a) coarse ( $2.18 \times 10^6$  cells), b) standard ( $4.91 \times 10^6$  cells), c) fine ( $6.43 \times 10^6$ ), d) standard with shock adaption ( $6.64 \times 10^6$ )

p.133

Fig. 4.55. Pressure coefficients over the bullet on  $0^\circ$  and  $180^\circ$  planes as mesh is refined.

p.136

Fig. 4.56. Example of beneficial shock adaption for the case of  $h/d=0.42$ , illustrated by contours of density.

p.137

Fig. 4.57.  $CN_A$  and  $CD_A$  coefficients as half-model (symmetry) mesh is refined; a) coarse b) standard c) fine, d) standard with shock adaption, e) fine with shock adaption.

p.137

Fig. 4.58. Turbulence model comparisons for pressure coefficient distribution around the wind tunnel model for the  $0^\circ/180^\circ$  plane.

p.138

Fig. 4.59. CFD to wind tunnel model comparison for shock stand-off distance and location of re-establishment of supersonic flow.

p.140

Fig. 4.60. Numerical schlieren comparison to an instantaneous schlieren image from time-resolved live-range footage of the freeflight (no ground) case.

p.140

Fig. 4.61. Influence of inlet turbulence intensity on the shock for the NATO projectile at  $h/c=0.5$ , standard mesh; a) 1%, b) 0.05%.

p.141

Fig. 4.62. Influence of inlet turbulence intensity on the shock for RAE 2822 Case 9, standard mesh, zoomed to the shock location on the upper surface; a) 1% intensity, b) 0.1%.

p.141

Fig. 5.1. Schematic of the elevated ground and symmetry methods as applied to the Mach 2.4 projectile.

p.146

Fig. 5.2. Colour schlieren of elevated ground test,  $\sim h/d=0.5$  (inset, shock/boundary layer interaction detail), (Doig *et al*, 2008).

p.147

Fig. 5.3. Colour schlieren of symmetry method test,  $\sim h/d=0.52$  (inset, crossing shock interaction detail). (Doig *et al*, 2008).

p.147

Fig. 5.4. Simple representation of regular shock reflection from a wall with a boundary layer. (Henderson, 1967)

p.148

Fig. 5.5. Representation of shock/boundary layer interaction with boundary layer separation (S) and reattachment (R), (Delery, 1985).

p.149

**Fig. 5.6.** Numerical schlieren comparisons at  $h/c = 0.5$  of a) symmetry and elevated ground methods, and b) symmetry method and a moving ground.  
p.150

**Fig. 5.7.** Comparisons of projectile pressure distributions at  $h/c=0.5$  for an elevated ground, symmetry ground plane and moving ground (inset; the unclipped pressure distribution)  
p.151

**Fig. 5.8.** Comparisons of ground pressure distributions at  $h/c=0.5$  for an elevated ground, symmetry ground plane and moving ground.  
p.151

**Fig. 5.9.** Comparisons of ground pressure distributions at  $h/c=0.2$  for an elevated ground, symmetry ground plane and moving ground.  
p.152

**Fig. 5.10.** An iso-surface of  $M=2.39$  shows how weak waves from the leading edge affect the flow “seen” by the projectile.  
p.154

**Fig. 5.11.** Conventional shadowgraph images of three-dimensional flows: (a) wedge angle = 20, (b) 28, (c) 35 (Skews, 2000)  
p.154

**Fig. 5.12.** Schematic of the elevated ground and symmetry methods as applied to the RAE2822 aerofoil.  
p.156

**Fig. 5.13.** Time-averaged CFD of 2822 USNA Case 1 comparisons; Mach number distributions at the mid-span symmetry plane for the elevated ground and symmetry methods.  
p.157

**Fig. 5.14.** Time-averaged pressure distribution at the mid-span symmetry plane for 2822 USNA Case 1; comparisons of experimental symmetry and elevated ground methods to CFD.  
p.158

**Fig. 5.15.** Time-averaged pressure distribution at the mid-span symmetry plane for 2822 USNA Case 2; comparisons of experimental symmetry and elevated ground methods to CFD.  
p.159

**Fig. 5.16.** Instantaneous CFD of 2822 USNA Case 2 (half-model with mid-span symmetry plane) with the elevated ground plane, showing contours of density and areas of supersonic flow (blue).  
p.160

**Fig. 5.17.** Instantaneous CFD of 2822 USNA Case 2 with the elevated ground plane, contours of Mach number at the mid-span symmetry plane.  
p.160

**Fig. 5.18.** Instantaneous CFD of 2822 USNA Case 2 (half-model with mid-span symmetry plane) with the symmetry ground plane, showing contours of density and areas of supersonic flow (blue).  
p.160

**Fig. 5.19.** Instantaneous CFD of 2822 USNA Case 2 with the symmetry plane, contours of Mach number at the mid-span symmetry plane.  
p.160

**Fig. 5.20.** Time-averaged CFD of 2822 USNA Case 3 (half-model with mid-span symmetry plane) with the elevated ground plane, showing contours of density and areas of supersonic flow (blue).

p.162

**Fig. 5.21.** Time-averaged CFD of 2822 USNA Case 3 with the elevated ground plane, contours of Mach number at the mid-span symmetry plane.

p.162

**Fig. 5.22.** Time-averaged CFD of 2822 USNA Case 3 (half-model with mid-span symmetry plane) with the symmetry ground plane, showing contours of density and areas of supersonic flow (blue).

p.162

**Fig. 5.23.** Time-averaged 2822 USNA Case 3 with the symmetry plane, contours of Mach number at the mid-span symmetry plane.

p.162

**Fig. 5.24.** Time-averaged pressure distribution at the mid-span symmetry plane for 2822 USNA Case 3; comparisons of experimental symmetry and elevated ground methods to CFD.

p.163

**Fig. 5.25.** Time-averaged pressure distribution at the mid-span symmetry plane on the ground plane, for 2822 USNA Case 3; comparisons of experimental elevated ground methods to CFD of symmetry, elevated ground and moving ground cases.

p.164

**Fig. 5.26.** Instantaneous CFD of 2822 USNA Case 4 (half-model with mid-span symmetry plane) with the elevated ground plane, showing contours of density and areas of supersonic flow (blue).

p.166

**Fig. 5.27.** Instantaneous CFD of 2822 USNA Case 4 with the elevated ground plane, contours of Mach number at the mid-span symmetry plane.

p.166

**Fig. 5.28.** Instantaneous CFD of 2822 USNA Case 4 (half-model with mid-span symmetry plane) with the symmetry ground plane, showing contours of density and areas of supersonic flow (blue).

p.166

**Fig. 5.29.** Instantaneous 2822 USNA Case 4 with the symmetry plane, contours of Mach number at the mid-span symmetry plane.

p.166

**Fig. 5.30.** Time-averaged pressure distribution at the mid-span symmetry plane for 2822 USNA Case 4; comparisons of experimental symmetry and elevated ground methods to CFD.

p.167

**Fig. 5.31.** Time-averaged pressure distribution at the mid-span symmetry plane on the ground plane, for 2822 USNA Case 4; comparisons of experimental elevated ground methods to CFD of symmetry, elevated ground and moving ground cases.

p.168

**Fig. 5.32.** Instantaneous CFD of 2822 USNA Case 4 at the mid-span symmetry plane showing contours of Mach number for a) the elevated ground plane/lower surface shock interaction, and b) the same case with a moving ground.

p.169

Fig. 5.33. Contours of Mach number around the elevated ground at the test section mid-span symmetry plane for  $M_\infty=0.8$ .  
p.171

Fig. 5.34. USNA 2822 Case 2 pressure distributions at the semi-span symmetry plane; CFD comparisons of experiment conducted and one at a higher Re.  
p.172

Fig. 5.35. USNA 2822 Case 3 pressure distributions at the semi-span symmetry plane; CFD comparisons of experiment conducted and one at a higher Re.  
p.172

Fig. 6.1 - a 50% scale model open-wheel racing car in a moving ground wind tunnel.  
p.177

Fig. 6.2. Notation for an inverted wing in ground effect  
p.178

Fig. 6.3. Freeflight  $C_D$  for increasing  $M_\infty$ , constant Re  $0.459 \times 10^6$ .  
p.180

Fig. 6.4. Freeflight  $C_L$  for increasing  $M_\infty$ , constant Re  $0.459 \times 10^6$ .  
p.180

Fig. 6.5. Freeflight  $C_p$  for increasing  $M_\infty$ , constant Re  $0.459 \times 10^6$ .  
p.180

Fig. 6.6.  $C_D$  for increasing  $M_\infty$ , constant Re  $0.459 \times 10^6$ ,  $h/c=0.179$ .  
p.182

Fig. 6.7.  $C_L$  for increasing  $M_\infty$ , constant Re  $0.459 \times 10^6$ ,  $h/c=0.179$ .  
p.182

Fig. 6.8. Compressible and incompressible pressure coefficients, full-scale.  
p.184

Fig. 6.9. Compressible and incompressible pressure coefficients, 50% scale.  
p.184

Fig. 6.10. Compressible and incompressible pressure coefficients, 25% scale.  
p.185

Fig. 6.11. Compressible pressure coefficients at 50% and 25% scale compared to full-scale incompressible result,  $Re=0.459 \times 10^6$ .  
p.185

Fig. 6.12. Streamlines and x-velocity contours around a) full-scale wing at  $M=0.0882$ , b) 50% scale wing at  $M=0.1764$ , and c) 25% scale wing at  $M=0.3528$ .  
p.186

Fig. 6.13. Density variations around the wing at the symmetry plane for the three Reynolds-scaled cases.  
p.186

**Fig. 6.14.** Line-contours of  $x$ -direction wall shear stress overlaid upon colour contours of density on wing lower surface, 25% scale wing  
p.186

**Fig. 6.15.** Streamlines around the trailing edge at  $z = 0$  for i) 50% scale and ii) 25% scale cases.  
p.188

**Fig. 6.16.** Location of slices used to extract both wake profiles and vortex cores.  
p.189

**Fig. 6.17.** Lower vortex core path in the  $x$ - $y$  plane, and (inset) illustration of upper and lower endplate vortices  
p.189

**Fig. 6.18.** Lower vortex core path in the  $x$ - $z$  plane.  
p.190

**Fig. 6.19.** Streamwise velocity wake profiles at  $2c$  from the leading edge.  
p.190

**Fig. 6.20.** Streamwise velocity wake profiles at  $1.2c$  from the leading edge.  
p.191

**Fig. 6.21.** Incompressible and compressible drag coefficients for decreasing ground clearance and increasing Mach number  
p.193

**Fig. 6.22.** Incompressible and compressible lift coefficients for decreasing ground clearance and increasing Mach number  
p.193

**Fig. 6.23.** Incompressible and compressible velocity streamlines around the wing at  $z = 0$ ,  $h/c=0.313$ , for a)  $M_\infty=0.15$ , and b)  $M_\infty=0.25$   
p.194

**Fig. 6.24.** Incompressible and compressible velocity streamlines around the wing at  $z = 0$ ,  $h/c=0.179$ , for a)  $M_\infty=0.15$ , and b)  $M_\infty=0.25$   
p.196

**Fig. 6.25.** Incompressible and compressible velocity streamlines around the wing at  $z = 0$ ,  $h/c=0.067$ , for a)  $M=0.15$ , and b)  $M=0.25$   
p.197

**Fig. 6.26.** Incompressible and compressible velocity streamlines around the wing at  $z = 0$ ,  $h/c=0.067$   
p.198

**Fig. 6.27.** Vortex core paths in the  $x$ - $y$  orientation.  
p.199

**Fig. 6.28.** Vortex core paths in the  $x$ - $z$  orientation.  
p.201

**Fig. 6.29.** Compressible (orange) and incompressible (blue) streamlines for  $M_\infty=0.25$ .  
p.201

**Fig. 6.30.**  $M_\infty=0.4$ ,  $h/c=0.313$ ; compressible and incompressible pressure distributions at the semi-span.  
p.201

**Fig. 6.31.**  $M_\infty=0.4$ ,  $h/c=0.179$ ; compressible and incompressible pressure distributions at the semi-span, and (inset) region of supersonic flow under the wing.  
p.202

**Fig. 7.1.** Pressure distribution for decreasing ground clearance at “Case 9” conditions  
p.208

**Fig. 7.2.** Dividing streamlines at “Case 9” conditions: freeflight overlaid on  $h/c=0.1$  case.  
p.208

**Fig. 7.3.** Contours of density and regions of supersonic flow around the aerofoil at Case 9 conditions as ground clearance is reduced from  $h/c=1$  to 0.1.  
p.209

**Fig. 7.4.** Lift and drag coefficients at Case 9 conditions as ground clearance is reduced from  $h/c=1$  to 0.1.  
p.210

**Fig. 7.5.** Pitching moment coefficient at Case 9 conditions as ground clearance is reduced from  $h/c=1$  to 0.1.  
p.211

**Fig. 7.6.** (previous page and above) Lift and drag coefficients for  $0^\circ$ ,  $2.79^\circ$  and  $6^\circ$ , with decreasing ground clearance for a)  $M_\infty=0.5$ , b) 0.6, c) 0.7, d) 0.8 and e) 0.9.  
p. 214

**Fig. 7.7.** (previous and above) Contours of Mach number and (inset detail) numerical schlieren for cases at  $M_\infty=0.9$ ,  $\alpha=2.79^\circ$ , as ground clearance is reduced from a) freeflight, to b)  $h/c=1$ , c)  $h/c=0.5$ , d)  $h/c=0.25$  and e),  $h/c=0.1$ .  
p.218

**Fig. 7.8.** Pitching moment coefficients at  $\alpha=2.79^\circ$ , as ground clearance is reduced.  
p.221

**Fig. 7.9.** Contours of density through one cycle of lower shock oscillation at  $M_\infty=0.6$ ,  $\alpha=0^\circ$ ,  $h/c=0.1$ .  
p.223

**Fig. 7.10.** Pressure distributions at  $M_\infty=0.6$ ,  $\alpha=0^\circ$ , as ground clearance is reduced.  
p.223

**Fig. 7.11.** Pressure distribution for decreasing ground clearance to incidence,  $M_\infty=0.6$ .  
p.225

**Fig. 7.12.** (previous and above) Contours of Mach number for cases at  $M=0.9$ ,  $\alpha=6^\circ$ , as ground clearance is reduced from a) freeflight, to b)  $h/c=1$ , c)  $h/c=0.5$ , d)  $h/c=0.25$  and e),  $h/c=0.1$ .  
p.226

**Fig. 7.13.** (previous page and above) Lift and drag coefficients for  $0^\circ$ ,  $2.79^\circ$  and  $6^\circ$ , with decreasing ground clearance for a)  $M_\infty=0.5$ , b) 0.6, c) 0.7, d) 0.8 and e) 0.9.  
p.230

**Fig. 7.14.** Pitching moment coefficients at  $\alpha=2.79^\circ$ , as Mach number increases.  
p.232

Fig. 7.15. Aerodynamic efficiency,  $L/D$ , at  $2.79^\circ$  for different ground clearances as Mach number is increased.

p.233

Fig. 7.16. Aerodynamic efficiency,  $L/D$ , at  $6^\circ$  for different ground clearances as Mach number is increased.

p.233

Fig. 8.1. Contours of density on the wing, symmetry and ground planes, with regions of supersonic flow (blue) as indicated for ground clearances of a) freeflight (no ground), b)  $h/c=1$ , c)  $h/c=0.25$ , and d)  $h/c=0.1$ .

p.238

Fig. 8.2. Chordwise pressure distributions at the 7 tapping stations on the M6, showing the effect of decreasing ground clearance.

p.240

Fig. 8.3. Contours of pressure coefficient with ground clearances of a)  $h/c=1$ , b)  $h/c=0.25$ , and c)  $h/c=0.1$ , at an incidence of  $3.06^\circ$  and  $M_\infty=0.7$ .

p.242

Fig. 8.4. Density contours over the upper (left) and lower (right) surfaces of the wing at a)  $h/c=1$ , b)  $h/c=0.25$ , and c)  $h/c=0.1$ .

p.243

Fig. 8.5. Lift and drag coefficient distributions for "Case 2308" conditions with decreasing ground clearance.

p.244

Fig. 8.6. Wing tip vortex core paths in the  $z$ -direction (measured from the wing root), for freeflight,  $h/c=1$  and  $h/c=0.25$  cases.

p.246

Fig. 8.7. Wing tip vortex core paths in the  $y$ -direction, for freeflight,  $h/c=1$  and  $h/c=0.25$  cases.

p.246

Fig. 8.8. Contours of vorticity on a plane  $0.5c$  downstream of the wingtip for a)  $h/c=1$  and b)  $h/c=0.25$ .

p.247

Fig. 8.9. (previous page and above) Lift and drag coefficients for  $0^\circ$ , and  $3.06^\circ$ , with decreasing ground clearance for a)  $M_\infty=0.5$ , b) 0.6, c) 0.7, d) 0.8 and e) 0.9.

p.249

Fig. 8.10. Contours of pressure coefficient with ground clearances of a)  $h/c=1$ , b)  $h/c=0.25$ , and c)  $h/c=0.1$ , at an incidence of  $3.06^\circ$  and  $M_\infty=0.7$ .

p.251

Fig. 8.11. Wing tip vortex core paths in the  $z$ -direction (measured from the wing root), for  $h/c=1, 0.25$  and  $0.1$ .

p.252

Fig. 8.12. Wing tip vortex core paths in the  $y$ -direction (measured from the wing tip trailing edge), for  $h/c=1, 0.25$  and  $0.1$ .

p.252

Fig. 8.13. Contours of density on the wing, symmetry and ground planes, with regions of

supersonic flow (blue) as indicated for  $M_\infty=0.8$  and ground clearances of a) freeflight (no ground, b)  $h/c=1$ , c)  $h/c=0.25$ , and d)  $h/c=0.1$ .  
p.254

**Fig. 8.14.** Contours of Mach number and streamlines at  $z/b=0.65$  (station 3) for a)  $h/c=1$  and b)  $h/c=0.1$  at  $M_\infty=0.9$ .  
p.256

**Fig. 8.15.** Contours of Mach number and streamlines at  $z/b=0.9$  (station 5) for a)  $h/c=1$  and b)  $h/c=0.1$  at  $M_\infty=0.9$ .  
p.256

**Fig. 8.16.** (previous page and above) Lift and drag coefficients for  $0^\circ$ ,  $3.06^\circ$ , with increasing Mach number, for a) freeflight, b)  $h/c=1$ , c)  $h/c=0.25$ , and d)  $h/c=0.1$ .  
p.258

**Fig. 8.17.** Aerodynamic efficiency,  $L/D$ , at  $3.06^\circ$  for different ground clearances as Mach number is increased.  
p.260

**Fig. 8.18.** a qualitative comparison between shock structures at  $M_\infty=0.95$  for CFD of the M6 wing ( $h/c=1$ , symmetry zone also shown) and an F/A-18 Hornet at approximately  $h/c=2$  and  $M_\infty=0.93$  (photo: Matt Niesen).  
p.261

**Fig. 9.1.** Interpretations of observed shock reflection interaction scenarios, as categorised into three types.  
p.266

**Fig. 9.2.** Instantaneous schlieren images from time-resolved live-range footage with numerical schlieren comparisons showing good agreement with regards to shock angles and wake disturbances.  
p.268

**Fig. 9.3.** Instantaneous vs. time-averaged schlieren images from the live-range experiments.  
p.270

**Fig. 9.4.** Time-averaged (over  $5 \times 10^{-5}$ s) schlieren images from the live-range video footage (top) for  $h/d=1.31$  with CFD contours of density overlaid (bottom).  
p.271

**Fig. 9.5.** Time-averaged (over  $5 \times 10^{-5}$ s) schlieren images from the live-range video footage (top) for  $h/d=0.75$ , with CFD contours of density overlaid (bottom).  
p.271

**Fig. 9.6.** Non-dimensionalised contours of density for ground clearances  $h/d$  of; a) 1.77, b) 1, c) 0.75, d) 0.5, e) 0.365 and f) 0.2.  
p.272

**Fig. 9.7.** Slice locations from projectile nose; 1) 1.49d, 2) 2.37d, 3) 3.25d, 4) 3.68d (1mm downstream of the base) 5) 4.30d, 6) 5.88d, 7) 7.63d, 8) 9.39d, 9) 11.14d.  
p.273

**Fig. 9.8.** Density contours on the symmetry and ground planes for live-range projectile at  $h/d=1$   
p.274

**Fig. 9.9.** Contours of density to illustrate three-dimensional propagation and interactions of

shock and expansion waves around the projectile at  $h/d=0.5$ , for slice locations described in figure 9.7 (not slice 4).  
p.275

**Fig. 9.10.** Density contours on the symmetry and ground planes for live-range projectile at  $h/d=0.5$   
p.276

**Fig. 9.11.** Contours of density to illustrate three-dimensional propagation and interactions of shock and expansion waves around the projectile at  $h/d=0.5$ , for slice locations from figure 9.7: from projectile nose; 1) 1.49d, 2) 2.37d, 3) 3.25d, 4) 3.68d, 5) 4.30d, 6) 5.88d, 7) 7.63d, 8) 9.39d, 9) 11.14d  
p.277

**Fig. 9.12.** Cross-sectional shock shape and isobars for a Sears-Haak body,  $M_\infty=3$  (Marconi, 1983)  
p.280

**Fig. 9.13.** Changes to force coefficients for spinning live-range projectile as ground clearance is reduced  
p.281

**Fig. 9.14.** Changes to moment coefficients for spinning live-range projectile as ground clearance is reduced  
p.281

**Fig. 9.15.** Projectile pressure distribution on the  $0^\circ/180^\circ$  (symmetry) plane for a ground clearance of  $h/d=0.2$ .  
p.284

**Fig. 9.16.** Projectile pressure distribution on the  $0^\circ/180^\circ$  (symmetry) plane for a ground clearance of  $h/d=0.365$ .  
p.284

**Fig. 9.17.** Projectile pressure distribution on the  $0^\circ/180^\circ$  (symmetry) plane for a ground clearance of  $h/d=0.42$ .  
p.284

**Fig. 9.18.** Projectile pressure distribution on the  $0^\circ/180^\circ$  (symmetry) plane for a ground clearance of  $h/d=0.5$ .  
p.284

**Fig. 9.19.** Ground pressure coefficient distributions for type A and type B cases.  
p.286

**Fig. 9.20.** Ground pressure coefficient distributions for type C cases.  
p.286

**Fig. 9.21.** Wake profiles at  $x/d=1$  (from base)  
p.287

**Fig. 9.22.** Wake profiles at  $x/d=5$  (from base)  
p.287

**Fig. 9.23.** Streamlines in the near wake region highlighting the influence of ground clearance on recirculation cells.  
p.289

**Fig. 9.24.** Paths of the two trailing vortices from the spinning projectile at  $h/d=0.5$ , in the xy plane, as compared to the path of vortices from the non-spinning projectile.  
p.290

**Fig. 9.25.** Paths of the two trailing vortices from the spinning projectile at  $h/d=0.5$ , in the xz plane, as compared to the path of vortices from the non-spinning projectile.  
p.290

**Fig. 9.26.** Streamlines released from a plane 1mm from the base of the spinning projectile.  
p.292

### List of Tables

**Table 2.1** Overview of Simulation Settings  
p.48

**Table 3.1.** Experimental parameters  
p.58

**Table 4.2** - 'Case 10' aerodynamic coefficient comparisons  
p.98

**Table 4.3.** Cases used for validation  
p.109

**Table 4.4.** Effect of variations in domain extent for a quarter projectile model  
p.125

**Table 5.1.** Cases used to compare experimental methods  
p.148

**Table 6.1.** List of Mach numbers and related parameters  
p.169

**Table 7.2.** List of simulations conducted, which cases were run as transient and which featured areas of supersonic flow around the wing.  
p.202

**Table 7.1.** List of Mach numbers and related parameters  
p.203

**Table 8.1.** List of Mach numbers and equivalent mean-chord-based Reynolds numbers  
p.235

**Table 8.2.** List of simulations conducted, which cases were run as transient and which featured areas of supersonic flow around the wing.  
p.236

**Table 9.1.** CFD cases for live-range comparisons  
p.253

## Nomenclature

$\infty$	freestream value (usually in subscript form)
b	wing semi-span
c	wing chord
$C_D$	drag coefficient
$C_{DA}$	drag coefficient non-dimensionalised with a reference frontal area ( $m^2$ )
$C_L$	lift coefficient
$C_{LA}$	lift coefficient non-dimensionalised with a reference frontal area ( $m^2$ )
$C_p$	static pressure coefficient
$C_{ZS}$	side force coefficient non-dimensionalised with a reference projected side area ( $m^2$ )
$C_m$	moment coefficient
d	projectile diameter
D	drag
h	height of object from the ground measured from the point closest to the ground plane
I	turbulence intensity
k	turbulent kinetic energy
L	lift
l	characteristic length
M	Mach number
m	moment
N	normal force
P	pressure
t	time
U, V, W	mean velocity component in x, y, z directions respectively
u, v, w	velocities in the x, y, z directions respectively
$y^+$	y plus value

## Greek Symbols

$\alpha$	angle of incidence
$\varepsilon$	turbulent dissipation rate
$\mu$	viscosity
$\rho$	density of fluid
$\omega$	specific dissipation rate (relating to turbulence), rotational velocity

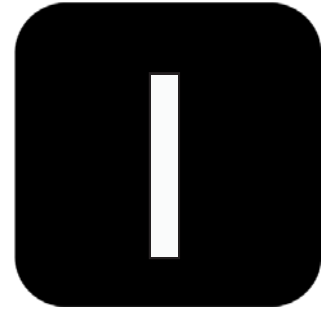
Some further nomenclature that only appears in formulae presented in Chapter 2 is defined in the text accompanying the equations.

## Acronyms

ADFA	Australian Defence Force Academy
AEV	Aero-levitation electric vehicle
AGARD	Advisory Group for Aerospace Research and Development
AIAA	American Institute of Aeronautics and Astronautics
AR	Aspect ratio
C.G.	Centre of Gravity
CFD	Computational Fluid Dynamics
DES	Direct Eddy Simulation
LES	Large Eddy Simulation
NACA	National Advisory Committee for Aeronautics
NASA	National Aeronautics and Space Administration
NATO	North Atlantic Treaty Organisation
ONERA	Office National d'Etudes et Recherches Aérospatiale
RAE	Royal Aircraft Establishment
RANS	Reynolds-averaged Navier-Stokes
RNG	Renormalised Group
SA	Spalart-Allmaras
SSC	supersonic car

SST	Shear-stress transport
TLC	Thermochromic Liquid Crystal
UNSA	United States Naval Academy
UNSW	University of New South Wales
VTOL	Vertical take-off and landing
WIG	Wing in Ground Effect

# Chapter: Introduction

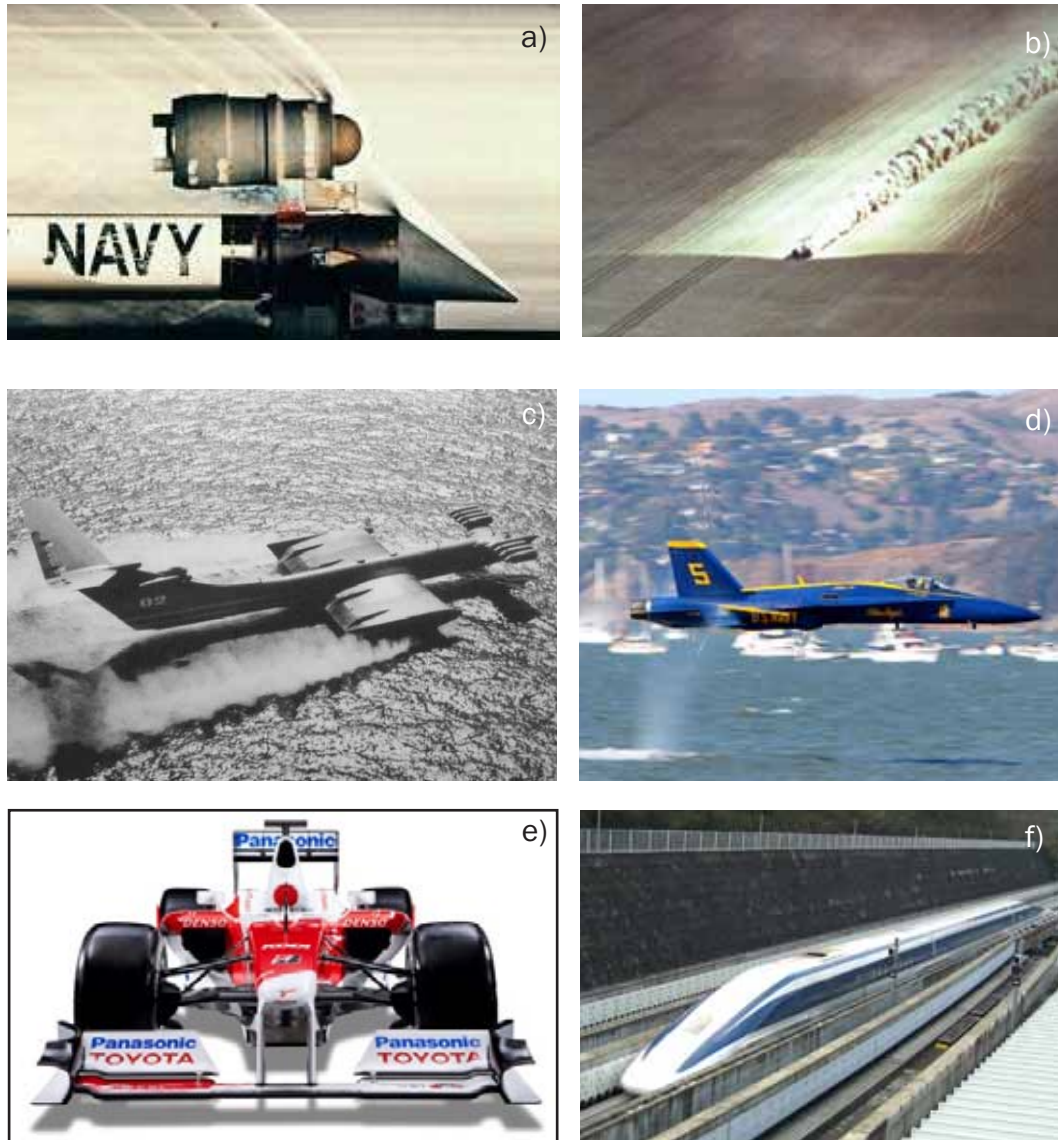


*The topic of compressible ground effect aerodynamics is introduced, and a brief overview of the present research is given. By means of a literature review, it is shown that the topic has not been extensively studied to date, particularly with regards to transonic or supersonic aeronautical applications. Difficulties associated with performing satisfactory experiments with regards to the representation of the ground are also identified. There follows a more detailed statement on the aims of the thesis, along with a summary of the subsequent chapters.*

## 1.1 Preface

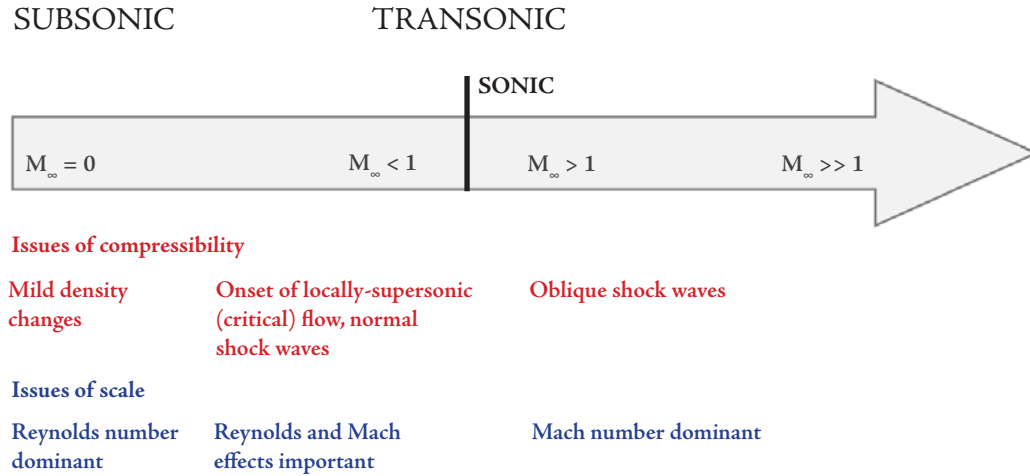
As an object passes through a compressible fluid such as air, the aerodynamics of the body are affected by density changes around it. This influence is enhanced by proximity to a ground plane, in particular when the flow becomes locally supersonic. Traditionally, aeronautical ground effect research (excluding study of vertical take-off and landing (VTOL)) has concentrated on the properties of wings in incompressible flows. Applications have included aircraft in landing or takeoff modes, aircraft designed specifically to fly in ground effect, or in the case of inverted wings, high-performance racing vehicles. In these cases, proximity to the ground serves to enhance the lift (or downforce) performance of the wing, and often the aerodynamic efficiency (lift/drag,  $L/D$ ) as well.

The compressibility of flow in such scenarios has usually been neglected to facilitate ease of theoretical or numerical modelling, based on a generally-accepted notion that compressibility



Examples of compressible ground effect scenarios: a) a rocket sled test facility at supersonic Mach numbers (photo: U.S. Navy), b) an aerial view of the Thrust SSC land speed record car at Mach 1 highlights the shock wave extent (photo: Richard Meredith-Hardy), c) an Ekranoplan capable of Mach 0.45 (photo: Van Opstal), d) a US Navy Blue Angel display aircraft during a Mach 0.95 pass (photo: Matt Niesen), e) a modern Formula 1 car with an inverted front wing in close ground proximity (photo: Panasonic Toyota Racing), and f) a current-generation Maglev train capable of Mach 0.5 (photo: Yosemite/Wikimedia).

effects are essentially unimportant for freestream Mach numbers of less than 0.3 (Anderson, 2001). Particularly for the case of a racing cars, the extreme proximity of the front wing to the ground and the high negative lift characteristics of the section can result in local Mach numbers between two or three times the freestream value, and it has been noted that compressible effects may well be prevalent but remain unaddressed in the public domain (Zhang *et al.*, 2006). In Katz's otherwise comprehensive review of the



Important flow considerations as Mach number is increased.

aerodynamics of racing cars (Katz, 2006), the single mention of compressibility comes in a brief passage about the Mach 0.85 Blue Flame rocket car.

At higher subsonic Mach numbers ( $0.3 < M_\infty < 0.5$ ), compressibility of the flow is an important and acknowledged parameter for vehicles such as high speed trains (i.e. the Shinkansen in Japan or the French TGV), the large wing-in-ground-effect (WIG) Ekranoplans of Cold War-era Russia, or wheel-driven land speed record cars. If one cannot treat the flow as incompressible, the numerical modelling becomes more complex, but more pressingly the speed of the freestream flows makes controlled aerodynamic testing in a wind tunnel a more difficult matter. Some of these issues are outlined in figure 1.2, which also shows the progression of flow from subsonic to supersonic conditions. Note that in the context of this thesis, the term “transonic” is applied to flowfields which feature areas of local supersonic flow.

The correct ground boundary condition for all ground effect testing in a wind tunnel is a moving ground, conventionally achieved by having a belt travelling at the freestream flow velocity. For larger tunnels and models it is often approximated more crudely with an elevated ground plane, which produces a boundary layer which, though undesirable, can be minimised with a combination of suction and blowing. In the earliest days of ground effect research, it was also shown analytically that a symmetry (or mirror-image) method can be a good approximation for the flowfield (Weiselsberger, 1922). It has since been shown that at small ground clearances this can produce inaccurate data

(Barber *et al.*, 1999 and 2002, Sowdon and Hori, 1996), as will be discussed in the following section. A boundary layer will form on a moving ground due to the pressure field influence of the body being examined, and therefore slip walls or symmetry planes can never fully capture the physics of the correct condition.

For testing at transonic and supersonic speeds, for cases such as low-flying military aircraft, jet or rocket land speed record cars, or future magnetic-levitation launch vehicles, the issue of ground representation is critical. It dictates the nature of the interaction between the ground and compression or expansion waves produced by the body in question. Military facilities such as rocket sleds can be used (Ayres, 1996), but these are expensive and access can be severely restricted. The use of an elevated ground has been proposed (Torda and Uzgiris, 1970), but can produce unacceptable interference, particularly if the model is small in relation to the ground boundary layer. Indeed, such issues of scale make the use of any specific ground apparatus a considerable problem (though scale issues are certainly not a problem unique to ground effect studies). With a lack of acceptable and inexpensive wind tunnel testing techniques, increasing emphasis is being placed on the use of computational fluid dynamics (CFD) as the primary or sole design tool, particularly for private, unconventional vehicles such as land speed record cars (Goldberg *et al.*, 2006, Lock, 2006). The use of CFD (with conventional Reynolds-Averaged Navier-Stokes (RANS) modelling), with its persistent difficulties in modelling turbulent structures and boundary layer transition as well as the multi-scale complexities of shock wave interactions and reflections in ground effect, is an endeavour which ought to involve careful experimental validation. For these reasons, the development of a suitable wind tunnel method is vital, and as such is addressed in this thesis, which features an important synergy between CFD and experimental work.

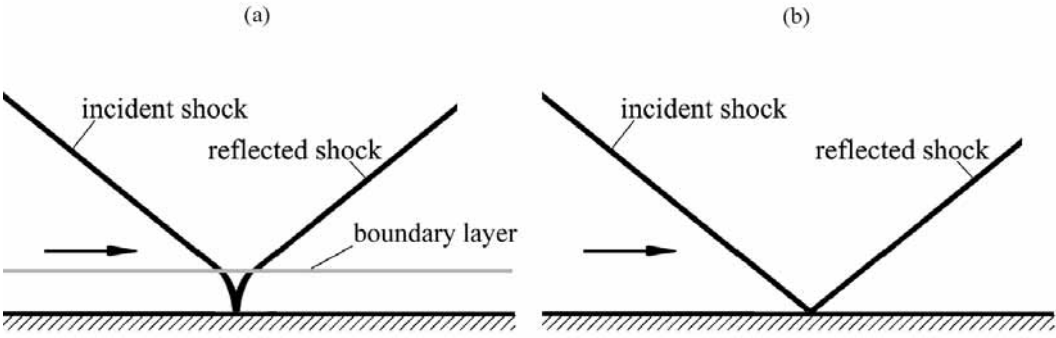
A much-improved understanding of the aerodynamic influence of compressible ground effects and of shock/ground interaction would be timely, particularly given renewed interest in high-speed subsonic (freestream Mach number,  $M_\infty \geq 0.4$ ) WIG aircraft (Rozhdestvensky, 1997), as well as magnetic-levitation space vehicle launch systems (Powell *et al.*, 2008) and high speed rail (Schetz, 2001).

# I.2 Review of Relevant Research

Ernst Mach pioneered studies of shock reflection phenomena, publishing a paper on the planar shock-wave reflections over straight wedges (Mach, 1878). He presented two possible wave configurations: a regular reflection, and an alternate configuration that was later named Mach reflection.

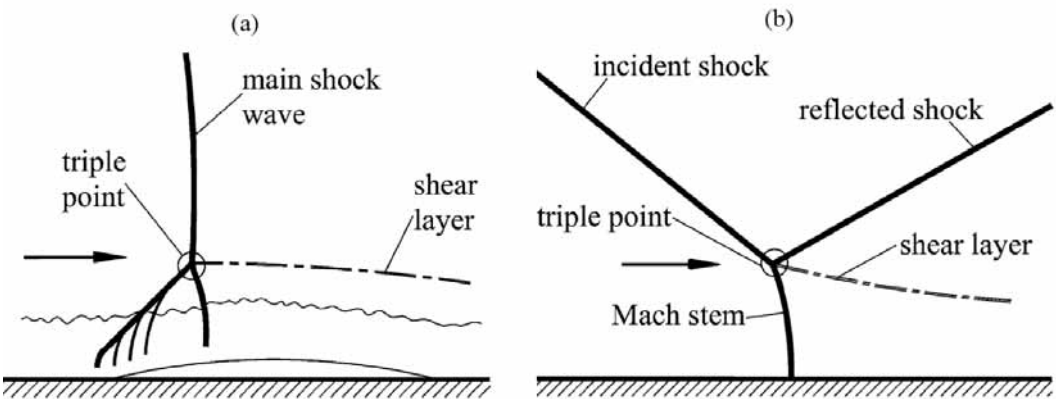
Figures 1.3 and 1.4 show basic schematics of the normal and oblique configurations of most interest. The work in this thesis considers flowfields in which both inviscid (or nominally inviscid) and viscous reflections occur, and thus consideration of several reflection possibilities is important. The normal shock with a lambda ( $\lambda$ ) foot boundary layer interaction is a common occurrence in transonic flows involving wing sections,

1.3  
FIG



a) Regular reflection of an oblique shock with a boundary layer, and b) idealised regular reflection of an oblique shock at an inviscid wall (based on Szwaba *et al.*, 2004)

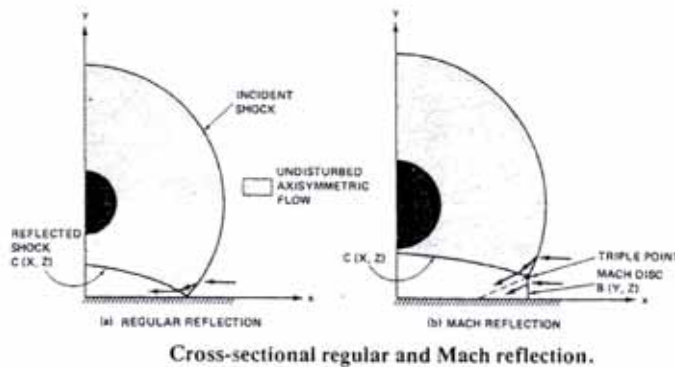
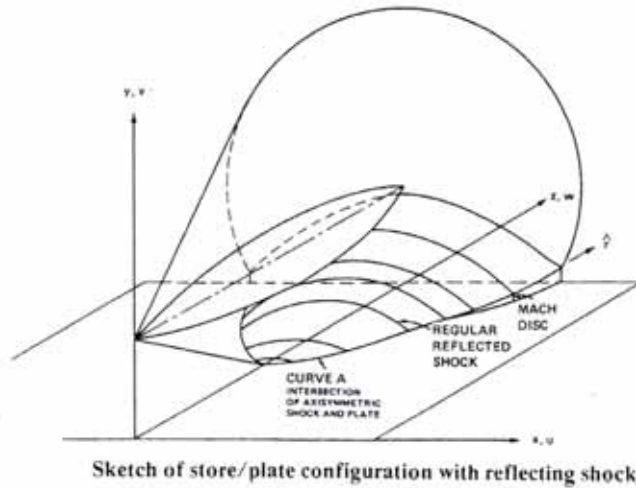
1.4  
FIG



a) Normal shock/boundary layer interaction with a " $\lambda$ " foot, and b) Mach reflection of an oblique shock at an inviscid wall (from Szwaba *et al.*, 2004)

whereas the oblique reflections are often studied more fundamentally outside of a direct aeronautical context. Figure 1.3a) shows regular reflection of an oblique shock wave in a fully supersonic flowfield, where a boundary layer is present on the reflecting surface. Within the boundary layer, the shock and its reflection curve in a refraction to normal at the wall - without a boundary layer (b), in the simplest case, the reflection angle is the same as that of the incident wave. Figure 1.4b) shows a scenario in which the Mach number is such that a normal Mach stem forms between the incident shock and the ground, and a so-called “triple point” exists at the location where the stem meets the incident and reflected wave. Typically, a shear layer forms behind the triple point. The Mach number and shock angles at which the transition from regular to Mach reflection occurs has been the subject of much debate and research. Figure 1.4a) shows a typical transonic shock boundary layer interaction, where the foot of the normal shock provokes some separation of the boundary layer and the “lambda” structure forms to reset the flow direction to normal after the disruption of the separation bubble. Behind the shock structure the flow is subsonic, and the main shock is often referred to as the terminating shock. Such waves are prone to oscillation on the surface over a range of high subsonic freestream Mach numbers, which in an aeronautical context is referred to as buffet.

At the transonic and supersonic Mach numbers considered later in this thesis, the formation and reflection from the ground of normal and oblique shock waves is often highly analogous to several other distinct fields of aerodynamic research, most notably: wind tunnel wall interference, where the effect is exclusively undesirable and well-studied (Goethert, 1961), and studies of external stores on aircraft, which have in the past been investigated as simple supersonic streamlined bodies next to a solid surface (Marconi, 1983). In the latter case, when examining the transition from regular to Mach reflection of a reflected wave from a store as shown in figure 1.5, the assumption of inviscid flow was deemed to be a minor inconvenience. Ironically this actually serves to more closely approximate the moving ground interactions seen for the supersonic projectile in ground effect study (in chapters 3, 4 and 9) of the present work than would have been the case if a fully viscous simulation were feasible at the time. Generally, more recent studies of



Schematic of the three-dimensional propagation of the conical shock and inviscid reflection produced by a supersonic store in proximity to a plate, highlighting transition from regular to Mach reflection. (Marconi, 1983)

stores consider cavities, on-wing configurations and other fully-viscous setups that are far less analogous to the present study.

Hornung (1986) states: “the subject of shock reflection is so complicated that it is necessary to introduce it at some length”, and in this spirit the reader of the present work is assumed to be familiar with the basic aspects of shock waves, and is directed to comprehensive reviews of shock reflection available in literature for discussions which do the topic justice (Hornung, 1986; Henderson, 1968; Ben-Dor, 1992, 2005). Further discussion of relevant and related material (such as studies involving crossing shock waves) is limited to appropriate points in the forthcoming chapters; for now it is sufficient to discuss ground effect literature and examine how the present research fits in with existing work in that field. The following section therefore deals with inverted and lifting wings in ground effect at low subsonic Mach numbers, studies of fast vehicles (trains, WIG aircraft and land speed record cars) at compressible Mach numbers, and the means of experimental testing that have been used for all applications.

.....

Between World War I and World War II, research was conducted into anomalies in aircraft handling in close proximity to the ground, particularly during takeoff and landing, by several researchers (among them; Raymond, 1921, Reid, 1928, Pistolesi, 1937 and Weiselsberger, 1922). Much of the research conducted into lifting wings in ground effect in the recent era has been conducted with regards to potential application to WIG vehicles.

The principal effect of the ground is to move the stagnation point downwards as the wing experiences a reduction in velocity and an increase in pressure on the lower surface, accompanied by an increase in local velocity at the upper surface suction peak near the leading edge (Barber, 2000; Ahmed and Sharma, 2004). This increases the lift of the wing, and, depending on the geometry, can have a relatively small effect on drag. Therefore, the overall efficiency ( $L/D$ ) of the wing can be greatly increased as ground clearance is decreased.

As analytical studies, calculations have been made using boundary element methods which consider subsonic and supersonic compressible flow over aerofoils in ground effect (Dragos, 1989, Dragos and Dinu, 1995), but the formulation can only be generally applied to thin aerofoils. Despite this, results were presented for a (relatively thick) NACA 4412 aerofoil at  $0^\circ$  incidence, indicating that for a freestream Mach number of 0.5, the compressible case predicts  $C_L$  as being 12% higher for ground clearances greater than a height-to-chord ratio ( $h/c$ ) of 0.5, below which the compressible  $C_L$  increasingly agrees with the incompressible prediction. No discussion was offered as to why this occurs and the method does not facilitate a detailed examination of the flowfield.

Other numerical studies have highlighted the difference between stationary, slip wall, symmetry and moving ground boundaries for a lifting NACA 4412 aerofoil in ground effect (Barber *et al.*, 1999). The symmetry method was seen to produce near-identical results to a moving ground simulation up until very low ground clearances ( $h/c < 0.05$ ), at which point a recirculation ahead of the wing at the ground plane produced

inaccurate results. An analogy was drawn between this observed effect and a vortex pair in a potential flow. The symmetry method did, however, correctly predict a slight lift-loss at the lowest clearances, as was observed for the moving ground cases. The CFD was conducted at a freestream Mach number of 0.32 with the flow treated as incompressible, although at this Mach number and at such low ground clearances, one would expect compressible effects to be present.

The symmetry method is not commonly used experimentally, although the method was implemented for studies by NASA in the 1960's (Fink and Lastering, 1961). It was asserted that tests with a symmetry wing setup, with endplates and far from wall interference, had previously produced results which agreed well with data for wings actually moving over a ground, though no citation is given. The Reynolds number was stated as  $0.49 \times 10^6$ , but the freestream Mach number was not stated. Wind tunnel experiments with NACA 4-series aerofoils have also been conducted firstly with a fixed ground plane (Ahmed and Sharma, 2004), where the boundary layer was found to merge with that of the aerofoil to distort results at low clearances, and subsequently with a moving ground. The latter study also examined the low clearance lift-loss at small angles of incidence, as previously observed by others (Barber, 2000), and discussed the importance of the geometry of the curvature of the lower surface in producing this lower surface suction effect. However, these studies were conducted at Reynolds numbers of  $3 \times 10^5$ , equating to freestream velocities of  $30 \text{ms}^{-1}$  ( $M_\infty < 0.1$ )

In an extensive review of WIG aircraft aerodynamics and technology, Rozhdestvensky (2006) categorically affirms "it can be stated that little is still known with regard to GE (ground effect) at high subsonic Mach numbers". Brief test studies (Maskalik *et al.*, 1998) indicate that increased aerodynamic efficiency may be possible for a high aspect ratio wing in ground effect at high subsonic Mach numbers, but some simple analytical treatments suggest the opposite (Rozhdestvensky, 2006). However, the effect of the formation of shock waves either on the wing upper surface, or between the wing and the ground, have not been considered.

.....

The front wing of an open-wheel racing car such as a Formula 1 car is responsible for producing as much as 25-30% of the total downforce, or negative lift, of the vehicle (Agathangelou and Gascoyne, 1998; Dominy, 1992), and affects the aerodynamic performance of downstream bodywork (Zhang and Zerihan, 2003). Dominy, in 1992, described the way in which the negative lift produced by a wing varied with decreasing ground clearance: the increase in suction on the wing was reported as being a function of the increase in the constraint of the flow between the wing and ground, creating a venturi-like effect.

In the last 20 years or so many investigations into inverted wings in ground effect both in wind tunnels and, increasingly, computationally, have been conducted; prior to this there was little available literature directly on the subject (Zhang *et al.*, 2006) despite the ubiquitous use of such devices in motorsport. The first computational investigations involved panel method codes, used in the mid 1980's to generate results with a symmetry ground boundary (Katz, 1985), and later a moving ground boundary (Katz, 1986). Viscous effects were neglected, and results reported a continual increase in negative lift with decreasing ground clearance.

It has since been shown that viscous effects are an important factor with regards to separation, as well as force predictions. Furthermore, subsequent studies identified a distinct limit to the ground clearance at which negative lift would continue to be enhanced by ground proximity - beyond this the "lift loss" phenomena was observed (Zerihan, 2000; Ranzenbach and Barlow, 1994, 1995, 1996, 1997), whereby the negative lift produced would drop off at the most extreme ground proximity. Zerihan (2001), using a T026 inverted wing at various ground clearances and incidences in a wind tunnel with a moving ground ( $Re\ 4.5 \times 10^5$ ), determined this to be a function of the tendency of the flow around the wing to separate more readily, rather than the "merging" of the boundary layers described by others (Ranzenbach and Barlow, 1994; 1995; 1996; 1997). Furthermore, it was determined (Zhang *et al.*, 2002) that the vortex formed under the

wing close to the endplate of the T026 section would “burst” at ground clearances less than approximately 10% of the chord, influencing the lift and drag considerably at these clearances.

This series of investigations by Zhang and Zerihan (2000; 2001; 2002; 2003), and others since (Mahon and Zhang, 2005, 2006), represent the most comprehensive experimental results yet presented for an inverted wing. They involve pressure, force and wake measurements for single and double element wings, at different incidences and ground clearances, for tripped and free boundary layer transition. They therefore have proven useful in the present research for validation purposes, as described in chapter 3 along with discussion of experimental limitations.

Subsequent CFD studies based on the experiments of Zerihan have been conducted, using a variety of turbulence models (Mahon, 2005; 2006), where RANS modelling with two-equation Realizable  $k-\varepsilon$  and  $k-\omega$  SST models was shown to provide excellent predictions of the experimental surface pressure and wake measurements. However, the studies were conducted as two-dimensional, thus neglecting the endplate effects and vortex behaviour. Predating this work, CFD on the original experiments was also conducted (Zerihan, 2000), using RANS and both the one-equation Spalart-Allmaras turbulence model, and the two-equation  $k-\omega$  model. It was known that the flow at the wing semi-span in the experiments was nominally two-dimensional, and two-dimensional CFD on the aerofoil section did provide good agreement, more so with the  $k-\omega$  model.

Interestingly, this original CFD (Zerihan, 2000) utilised a compressible flow solver, CFL3D. However, no mention of actual compressible effects was presented, nor any discussion of possible limitations of using a compressible solver at relatively low Mach numbers (0.088). Compressible solvers can be inadequate at very low Mach numbers, suffering both inefficiency and inaccuracy (Keshtiban *et al.*, 2004), due to the large difference in time scales associated with convection and the propagation of disturbances (Li and Glowinski, 1996).

Experimentally, Ranzenbach and Barlow conducted a series of studies

(Ranzenbach and Barlow, 1994; 1995; 1996; 1997), initially using a NACA 0015 section, at a Reynolds number of  $1.5 \times 10^6$ , with an elevated ground plane in the wind tunnel. They matched results to two-dimensional RANS CFD with a moving ground. They observed the lift-loss phenomenon as well, but initially attributed it to the incorrect ground boundary representation in the wind tunnel. The CFD featured the same reversal of the trend, albeit at a lower height and in a more pronounced fashion, and thus a conclusion was drawn that the elevated ground was not the specific cause of the phenomena, but was distorting the results relating to it. The wind tunnel tests were conducted at a freestream Mach number of 0.13 ( $45 \text{ms}^{-1}$ ), which the authors explicitly state was chosen so as to avoid “introducing significant compressibility effects in the accelerated region”, though the possible extent of such effects was not assessed or speculated upon.

The earliest three-dimensional studies of an inverted wing in ground effect (finite span with an endplate) used an elevated ground plane to approximate the correct ground representation, at a Reynolds number of  $0.7\text{-}1.3 \times 10^6$  (Jasinski and Selig, 1998). At  $h/c < 0.2$ , the ground boundary layer was observed to separate, thus limiting the usefulness of results and re-enforcing the importance of correct ground boundary representation.

Computational studies of three-dimensional wing and endplate configurations have been conducted as computing power has grown exponentially in the last two decades. Such a study by Shew and Wyman considered a three-dimensional optimised Selig 1223 section at a Reynolds number of  $2 \times 10^6$ , which equated to a freestream Mach number of 0.23. The simulations were run as incompressible, though if peak local velocities of two to three times the freestream velocity, as reported by other researchers (Mahon, 2005; Doig, 2007) are present around the suction surface, then the peak Mach number at the lowest clearances examined could have been in excess of 0.5. Due to this, density changes around the wing would have been significant.

.....

Thus far we have seen that while the aerodynamics of wings in ground effect have been studied extensively, the issue of compressibility has been only briefly mentioned or

neglected altogether by most researchers, as the freestream Mach numbers have generally been less than 0.25. Researchers studying racing car aerodynamics have identified compressible effects as a likely source of influence on aerodynamic performance in this range, though no formal studies have been made to date (Zhang *et al.*, 2006). At mid-subsonic through transonic Mach numbers, research in other areas of ground transport has addressed compressibility effects as a necessity. Designers of land speed record cars and high speed trains have recognised the need for accurate numerical simulations and useful experimental testing. Studies at compressible Mach numbers using CFD and wind tunnel experiments together are well-established and validated in the aerospace industry for freeflight applications, but in ground effect there is considerably less literature available, and there is an increasing reliance on CFD as the sole design tool.

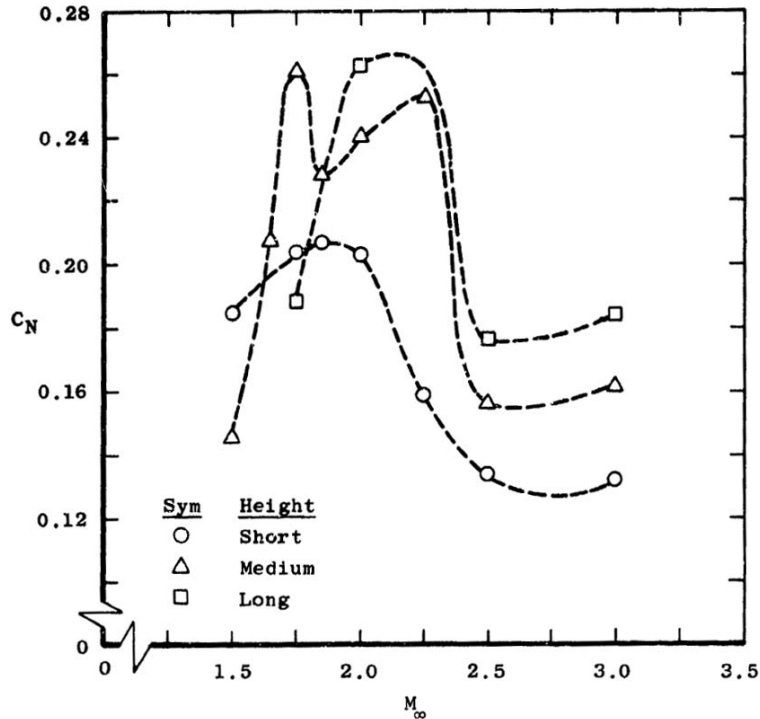
The design of the JCB Dieselmax, the vehicle which currently holds the world land speed record for a diesel-powered car (at approximately Mach 0.47), was examined and refined purely with CFD (Lock, 2007). While the report rightly identifies difficulties in wind tunnel testing for a vehicle up to the Mach 0.5 region, in that such a moving ground does not currently exist and Reynolds number matching is problematic for scale models, the decision to rely purely on RANS CFD was a surprising one. The FLUENT solver was used in segregated mode, with the coupled solver reported as featuring poor numerical stability. Although the simulations conducted were fully viscous, using the Realizable  $k-\epsilon$  turbulence model, the mesh featured only unstructured tetrahedral cells at the surface, which would have led to a poor boundary layer representation (as evidenced by anomalous “tiger-stripe” contours on the body surface in figures) and misleading results for skin friction drag. A tetrahedral mesh of 10 million cells was used for a half-car model, and was compared to a polyhedral mesh of 2 million cells converted directly from the tetrahedral mesh. A difference of 8% in lift and drag was reported between the two meshes and, as observed in the report, there was no way to determine which approach was more accurate in the absence of any wind tunnel data. Therefore while parametric comparisons of models may have provided useful information, the reported lift and drag values obtained, on one mesh and with one turbulence model, may well have

been discrepant with the actual performance of the vehicle.

The proposed “American Challenger” rocket-powered land speed record vehicle, currently under construction, has similarly been studied using CFD without any accompanying wind tunnel programme. The car is designed to go supersonic, and thus will need to traverse the subsonic and transonic ranges as well. The initial study (Goldberg *et al.*, 2006) looked at a half-model with a symmetry plane. The use of anisotropic hexahedral cells in the near-wall region would have resulted in better predictions of the drag components of the vehicle with the Realizable  $k$ - $\epsilon$  turbulence model, but the lack of adequate grid resolution in regions of shock waves would not necessarily produce adequate full flowfield representations of shock waves and their reflections from the moving ground plane. The total cell count was  $8 \times 10^6$  for the symmetry model. The vehicle features wing sections in ground effect as struts to connect outlying rear wheels with the cylindrical main body, and bi-convex and diamond aerofoil sections were examined. It was reported that shock-induced force oscillations were significant at Mach 0.8 with the diamond section, and were present but lessened for the bi-convex profile. From Mach 0.6 to 0.8, complete lift force reversal was observed for the full vehicle in certain configurations (negative to positive lift), as was a reversal of the pitching moment sign (positive to negative). Subsequent modifications to the vehicle based on the initial study resulted in a more stable configuration (Oberoi *et al.*, 2006). Investigations were also made into directional stability (Oberoi *et al.*, 2007).

Predating the modern era of CFD, the Blue Flame land speed record car was developed with a 1/25th scale model in a transonic wind tunnel with a 12” by 12” test section featuring perforated walls (Torda and Uzgiris, 1970). Initially, wings as rear struts similar to those just described for the American Challenger, were proposed, but were removed for the actual vehicle after wind tunnel tests showed “adverse influence” on the pitching moment. It was noted that shock reflections caused a build up of high pressure beneath the vehicle, leading to a tendency for increased lift as Mach number was incremented.

The researchers indicated a consideration of the possible benefits of a symmetry



Normal (lift) force on the rocket sled wind tunnel model for different rail slipper (and therefore ground clearance) heights with increasing Mach number (Strike and Lucas, 1968)

model in the tunnel, but in the end pursued an elevated ground for the test programme. The ground was pressure-tapped to check for flow separation on the ground plane, although no comment is made on the data gathered, presumably implying that separation did not occur. Detail was not given with regards to the design of the leading edge of the elevated ground. Schlieren images indicate that at the rear of the vehicle, in the vicinity of the proposed wings, the boundary layer on the elevated ground occupied approximately 33-50% of the vehicle ground clearance, which would have distorted the pressure and force readings taken. Measurements made on the actual vehicle indicated that the drag predictions of the wind tunnel model were up to 40% higher (Torda and Morel, 1971).

To date the only effective synergy between experiments and CFD for a transonic ground effect vehicle has been the Thrust SSC car, which was the first, and so far only, to set an official supersonic land speed record ( $M=1.0175$ ).

When testing the concept of the Thrust SSC supersonic land speed record car, designers were able to conduct tests using the Pendine Sands rocket sled facility in Wales (Noble, 1998); at supersonic speeds, the most effective means of scale-model testing. The small-scale model was pressure-tapped, as was the ground. The data were never published, but the agreement between experimental results and CFD conducted at the

time was deemed to be excellent (Noble, 1998; Ayres, 1996). However, the CFD, while state-of-the-art in 1992/93, featured a markedly simplified geometry and the fluid was treated as inviscid. Given that the boundary layer on the test model would have been considerable in relation to the model itself, and numerous underbody shock-boundary layer interactions would have occurred, such agreement seems fortuitous in retrospect.

Rocket sled facilities (for transonic, supersonic and hypersonic testing) such as those in figure 1a are generally military property. Studies using rocket sleds are related to non-ground effect applications, and the goal of researchers is to place the test object *out* of ground effect, though the rocket sled itself operates in such conditions. Research related to the design and development of such systems offer greater insight for the current topic. Several studies into the design of the Holloman facility in New Mexico were conducted (Strike and Lucas, 1968; Rhudy and Corce, 1975) during its life as a supersonic facility (it is now primarily a hypersonic facility). Wind tunnel testing was conducted from  $M=1.5$  to 4, with an elevated ground plane. Results were shown to agree well with subsequent tests with the actual rocket sled, although the margin of error stemming from poor repeatability of ground clearance was considerable.

With regards to the data obtained from the wind tunnel tests, it was noted that the normal force and pitching characteristics of the model, which was a 1/12th scale cylinder with a conical nose mounted to a rail above the elevated ground, changed sign with increasing Mach number (before and after  $M_{\infty}=2$ ). Although not specifically noted in the report of Strike and Lucas (1968), this would most likely have been a function of the way in which the shock from the nose was reflecting from the ground plane and interacting again with the model in relation to the centre of gravity. Rather than consistent trends, the normal force acting on the model was observed to increase and decrease considerably across the Mach number range tested, as shown in figure 1.6, indicating complex shock interactions from the simulated rail as well as the elevated ground plane, and downstream influences on the model sting and force balance due to multiple reflected shocks.

One other area of compressible ground effect has received considerable attention in recent years, as high-speed trains and Maglev systems gain prominence. Studies even

at low subsonic Mach numbers are often concerned with the acoustic and dynamic problems of trains passing each other, or the aerodynamic issues associated with the train travelling in a tunnel, where strong compression waves can be generated (Raghunathan *et al.*, 2002). Many computational studies treat the airflow around a train as incompressible (Breur and Durst, 2000), even at Mach numbers in excess of 0.25 (Suzuki, 2004). The study by Suzuki (2004) includes both incompressible and compressible CFD for different cases at different speeds, but no comparison of the influence of this is made in the paper, and results are not presented in a manner which would allow the reader to make such observations.

Because of the intense interest in the compression waves produced in tunnels and between passing trains (to address acoustic and stability concerns), most modern numerical work tends to involve turbulent, unsteady compressible flow (Schetz, 2000). Complex wave reflections occur in tunnels (Raghunathan *et al.*, 2002), although it is difficult to draw a direct parallel to the present research as the influence and geometry of a tunnel is distinctly different, and generally more complex, than for the case of a ground alone. The pressure waves in question are distinct from the strong normal and oblique shock waves which form the focus of much of this thesis. Furthermore, the actual ground effects are seldom the focus of aerodynamic studies, as conventional trains operate at a fixed distance from the ground only. Maglev studies have looked more closely at the effects of varying ground proximity.

All the problems of wind tunnel road vehicle testing are present for experiments on trains, such as scaling issues, ground representation, extent of laminar flow, and so on. However, the additional complication of flow compressibility, as with the land speed record cars, makes Reynolds and Mach scaling extremely difficult, particularly due to the length of the trains. Studies have shown between 10% (Willemsen, 1997) and 30% (Baker and Brokie, 1991) error in the values of drag coefficient obtained with scale wind tunnel models and actual track-tested trains. The latter study also noted up to 10% difference in lift and drag for wind tunnel studies using a moving ground as compared to an elevated ground plane. 1/25th scale-model track testing has been used by some (Pope,

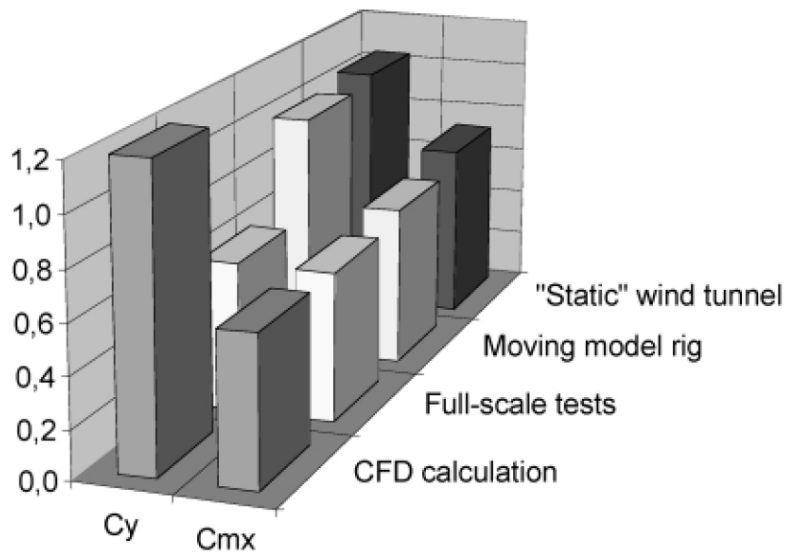
1991) with good success in replicating real-world flows.

Baker and Humphreys (1996), albeit using a very simple model with sharp corners, concluded that results for side-force coefficients in yawed conditions were not particularly dependent on the nature of the wind tunnel ground representation, but lift coefficient was highly dependent on the test conditions and apparatus, and a moving ground with a high Reynolds number was recommended. Studies also indicate that useful data for such bodies should only be used with appropriate levels of atmospheric turbulence if the results are to be applied to real-world designs (Baker and Humphreys, 1991). Some comparison measurements for full-scale and sub-scale models from a moving and static model, compared to RANS CFD using a RNG  $k$ - $\epsilon$  turbulence model, are shown in figure 1.7, highlighting the sensitivity of lift coefficient to modelling and ground representation. Maglev experiments at Mach 0.45, or with passing trains with relative Mach numbers of 0.8, have demonstrated low sensitivity of the vertical forces and rolling moments to sudden increases in Mach number.

Tests have been conducted with a moving track system at the upper ranges of feasible Mach numbers for a moving ground system,  $M_\infty=0.2$  (Tyll et al., 1996). Comparisons between the aerodynamic performance of the model with and without the track (i.e. “without” ground effect) were made, concluding that the inclusion of the track is essential, otherwise normal force coefficient results obtained could be as much as 40% or higher in error. However, considerable interference from the leading edge of the moving belt system and the side of the “track” could have influenced results, and the apparatus was designed using a 3ft diameter open wind tunnel, for use in a 6ft x 6ft square closed test section tunnel, which added considerable uncertainty as to the uniformity and quality of the flow at the ground plane.

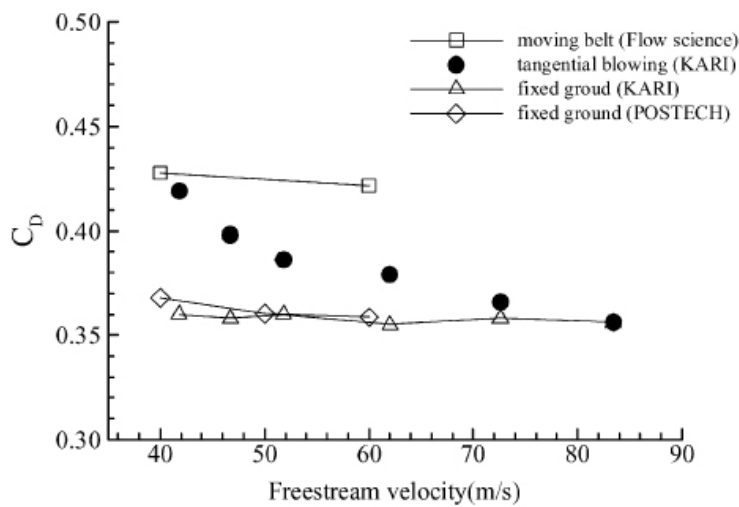
1/20th and 1/25th scale experiments of a train model from Mach 0.1 to 0.25 have also been conducted by others (Kwon et al., 2001), investigating the difference between a stationary ground, a moving ground belt with suction, and a fixed elevated ground plane with tangential boundary layer blowing. Force results were found to be insensitive to Reynolds number in the range  $0.5 \times 10^6$  to  $1.5 \times 10^6$ . The fixed ground experiments were

1.7  
FIG



An example of the differences between CFD and different wind tunnel methods for predicting  $C_y$  (normal force) and  $C_{mx}$  (longitudinal pitching moment) a high-speed train. (Matschke, 1999)

1.8  
FIG

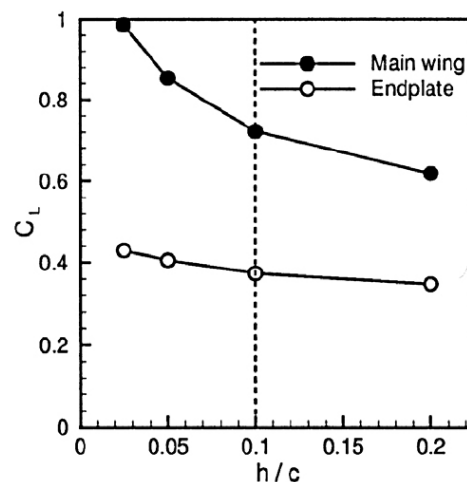


Comparison of  $C_D$  obtained on train configuration for different experimental ground representations. (Kwon, 2001)

found to underpredict drag coefficient by as much as 25% across the Mach number range. At Mach 0.1, the tangential blowing technique produces results close to the moving ground, but the agreement deteriorates with increasing Mach number until the method provides similar underpredictions as the fixed ground method, as shown in figure 1.8.

Finally, an interesting link between high-speed trains and WIG vehicles is

the Korean Aero-levitation Electric Vehicle (AEV), or Japanese Aerotrain (Kohama, 2002), whereby a winged craft, deliberately designed to take advantage of the increased aerodynamic efficiency of wings in ground effect, flies in a ducted guideway. Moon *et al.* (2005) present CFD studies of the design of the main wing section, but do not compare to 1/20th scale wind tunnel studies, which were conducted separately with a fixed ground and boundary layer suction (Kohama *et al.*, 1998), as shown in figure 1.9. The suction was deemed to reduce the displacement thickness caused by the boundary layer by 70% (Han *et al.*, 2005). The CFD was a three-dimensional incompressible study which produced results showing a favourable increase in lift with reducing ground clearance for a wing based on a NACA 4-series aerofoil. The authors state “cruising speed of (an) Aero-levitation Electric Vehicle (AEV) is approximately in the range of 300–400 km/h (or  $M_\infty = 0.24$ – $0.32$ ), and so compressibility effects of the flow are expected to be weak”, though no formal comparison of compressible and incompressible simulations was made, and work later in this thesis shows such an assumption to be flawed. A further study on the vehicle reported by Han *et al.* (2005) state that incompressible CFD was run at  $M_\infty=0.2$ , but only a panel method computation is compared to the experiment, rather than the fully viscous Navier-Stokes simulations also described. The experiments are stated as being run at “same flow conditions as used for the turbulent viscous calculations”, but the tunnel speed is later quoted at  $30\text{ms}^{-1}$ , implying large discrepancies in the Reynolds number and Mach numbers of the simulations compared to the experimental conditions.



An aero-levitation electric vehicle (AEV) model in a wind tunnel (left), and predicted lift coefficients for the main wing section at varying height to chord ( $h/c$ ) ground clearances (right), (Moon *et al.*, 2005).

1.9

FIG

.....

In summary, it has been shown that while much numerical and experimental research has been conducted into inverted and lifting wings (and their respective appropriate vehicles) in ground effect, the flows have been treated as almost-exclusively incompressible in CFD for freestream Mach numbers less than approximately 0.3. The correctness of this approach, particularly when attempting to compare to experimental data, has not been discussed despite acknowledgements of local Mach numbers far in excess of those which could be assumed to be incompressible, particularly for inverted wings.

It has also been shown that a moving ground is the ideal boundary condition for replicating real-world flows, but at mid-subsonic to supersonic speeds, this is simply not feasible. Elevated ground planes have been used at such Mach numbers but with limited success, and no direct comparison has been made between elevated ground, symmetry method and moving ground simulations at mid-to-high Mach numbers, to quantify and examine the extent of the influence of ground representation on the results obtained. Test facilities such as rocket sleds have been shown to be extremely useful, but they are expensive and access to them is extremely limited. The lack of good wind tunnel data with which to validate CFD has been demonstrated to be a pressing concern, given the limitations of commonly-used RANS CFD techniques.

In terms of aerodynamic performance, researchers of land speed record cars with wing components in ground effect have noted large, shock-induced changes to vertical forces and moments with increasing Mach number, but thorough examination of the mechanisms and characteristics of such changes to the flows has not been reported in public literature. More streamlined bodies without stand-alone lifting or downforce-producing surfaces, such as maglev trains, have been shown to be less sensitive to increasing Mach number, though studies have not been conducted at Mach numbers greater than approximately 0.5.

## 1.3 Thesis aims and outline

To maximise the relevance of the research to appropriate real-world scenarios, a range of bodies have been investigated within the confines of their own specific flow regimes; an inverted wing in the low-to-medium subsonic regime, a lifting aerofoil and wing in the transonic regime, and a military projectile in supersonic flow conditions, as shown in figure 1.10. There is little merit in investigating a supersonic projectile in ground effect at low subsonic speeds, nor an inverted wing in ground effect in fully supersonic flow. It is unlikely that either of these bodies would ever be employed to span the full transonic range, either. However, as we have seen from the discussion of literature in the field, different yet related problems present themselves as Mach number increases, all of which are worthy of direct investigation. The primary aims of the thesis are:

- To examine the way in which ground proximity influences the extent of compressibility effects around a wing at subsonic Mach numbers which are traditionally thought of as essentially incompressible, and to assess the relevance of this to current practices of comparison between CFD and wind tunnel experiments.
- To determine, by means of experimentation and CFD comparisons, the most effective way of studying transonic and supersonic ground effect problems in a conventional blowdown wind tunnel, without the need for complex or expensive apparatus.
- To investigate the changes to the aerodynamic characteristics of an aerofoil (two-dimensional) and a wing (three-dimensional) in varying degrees of ground effect as Mach number is increased from mid-subsonic to near-sonic levels.

- To investigate the way in which increasing ground proximity affects the aerodynamic characteristics of a projectile in the fully-supersonic regime..

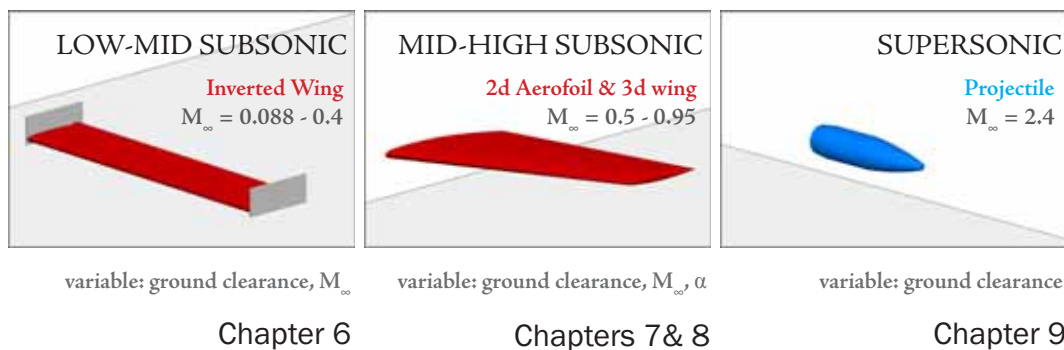
### 1.3.1 Choice of geometries for investigation

The inverted T026 wing with endplate was chosen as it has featured prominently in the major papers on the subject of downforce-producing wings in the last decade (Zerihan and Zhang, 2001; 2002; 2003; Mahon and Zhang, 2005; 2006; Zhang *et al.*, 2006). Extensive experimental results were available in this literature which were necessary for validation purposes, facilitating constructive comparison of technique and results. The wing was held at the ‘reference incidence’ first outlined by Zerihan (2000), and the variables of Mach number, Reynolds number and ground clearance were investigated.

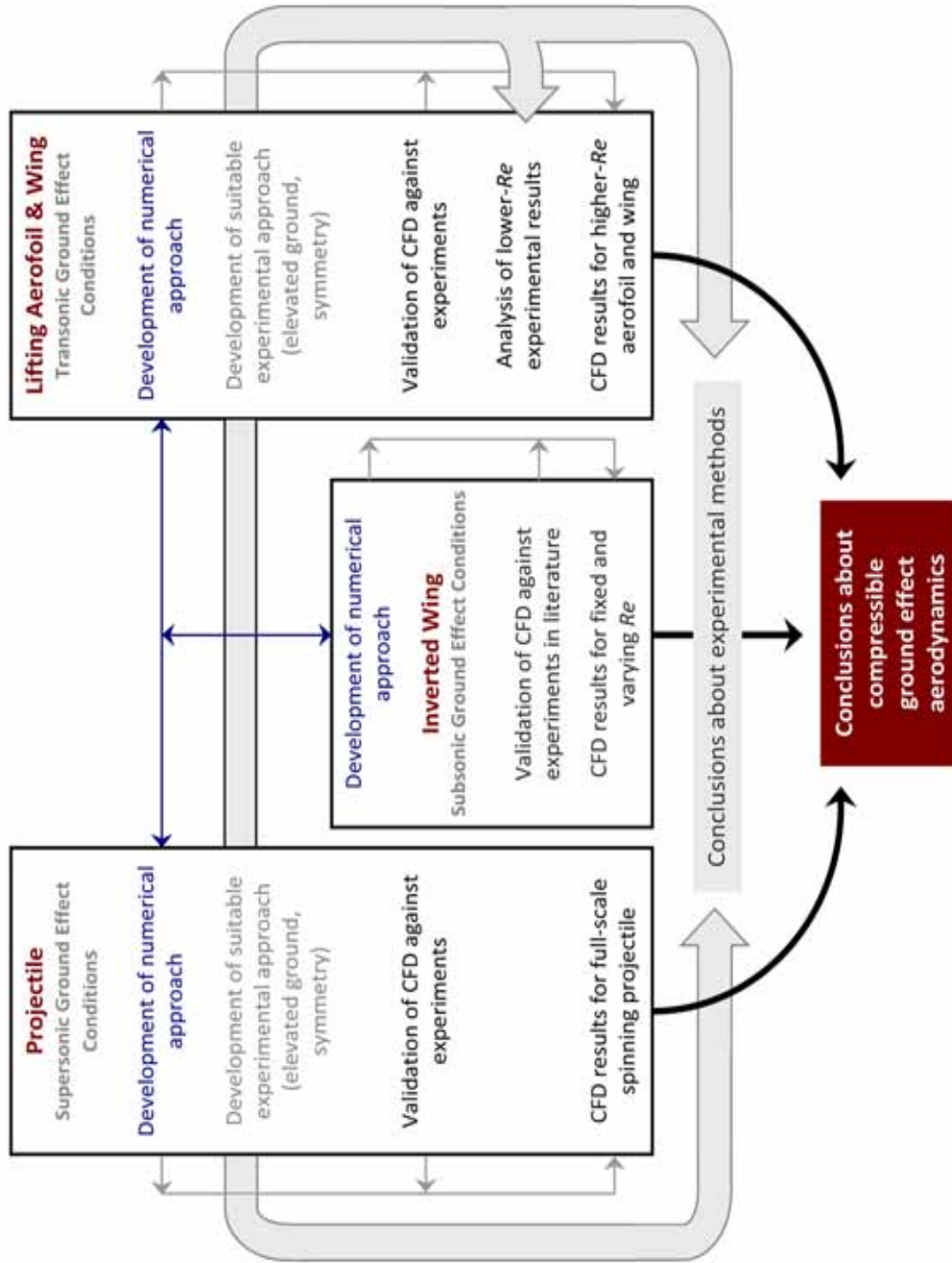
The inclusion of a comprehensive set of experimental results in the AGARD report in the late 1970’s (Cook *et al.*, 1979) which was specifically compiled to provide researchers with a validation database for flows around wings in the transonic region has led the RAE2822 to become one of the most familiar geometries to those studying transonic aerodynamics. Likewise the three-dimensional swept, tapered ONERA M6 wing, represented in the same report (Schmitt and Charpin, 1979). The decision was made to make use of these two bodies not just because of the obvious possibility for validation of the numerical methods employed, but in order to enable the recontextualisation of well-known and relatively simple geometries, such that their changed characteristics when in ground effect would stand in contrast to their familiar “freeflight” traits. The

1.10

FIG



Bodies used for investigating compressible ground effect in different Mach ranges.



Flowchart outline of thesis

transonic studies included the effect of changes in angle of incidence, Mach number, Reynolds number and ground clearance as variables. Although the shape and camber of the body is clearly an important variable, adding these influences to a list which already included Mach number, Reynolds number, ground clearance and angle of attack would have produced a prohibitive amount of data.

Early in the present work, a series of experiments were undertaken by the University of New South Wales at the Australian Defence Force Academy, involving a NATO 5.56mm round fired in close proximity to a ground plane. Given that the tests were the ideal way of studying experimentally the problem about which this thesis was designed, and would thus not only provide an excellent source of validation for the CFD but also provide a vital validation of the wind tunnel methods proposed, it was decided that an investigation of this problem would prove more complete and relevant than a continuation of the wing study into the supersonic regime.

Despite the use of several geometries for different flow regimes, each chapter is far from self-enclosed, as the work described here was not conducted chronologically and as isolated investigations. Rather, the development of numerical and experimental approaches for each chapter concurrently informed those used to produce the results of the others, and so common threads of research and analysis can be seen as developing through the Mach number range from  $M_{\infty}=0.088$  to 2.4. Some similar trends for all the bodies emerged, specific to compressible effects as a consequence of ground proximity, and in this respect the escalation of Mach number is accompanied by an evolution of the consequences of flow compressibility in ground effect scenarios. The flowchart in figure 1.11 outlines the intertwined aspects of the work and provides an overview of the thrust of the research.

### 1.3.2 Outline

*Chapter 2* introduces the numerical method used to produce the CFD results presented throughout the thesis, while *Chapter 3* discusses the experimental approaches used to

investigate transonic and supersonic ground effect, including errors and uncertainties. *Chapter 4* is concerned with the extensive validation of the numerical method against experimental data both from literature and from the experiments described. *Chapter 5* then presents a discussion of experimental and numerical results which allow the comparison of the merits and limitations of the wind tunnel methods proposed for studying supersonic and transonic ground effect problems.

*Chapter 6* is a purely numerical investigation into the onset of compressibility effects for an inverted wing in ground effect, with particular heed paid to the problems of using incompressible CFD to simulate flows which are significantly compressible even at low-subsonic ( $M_\infty < 0.3$ ) Mach numbers. Also discussed are issues of Mach and Reynolds scaling. *Chapter 7* extends the study into the region of mid-to-high subsonic conditions ( $0.9 \geq M_\infty \geq 0.5$ ), with a lifting two-dimensional aerofoil section in varying degrees of ground effect. *Chapter 8* examines a three-dimensional wing for the same Mach number range.

*Chapter 9* examines the aerodynamic characteristics of a small supersonic projectile at Mach 2.4, as ground clearance is reduced. *Chapter 10* summarizes the conclusions made throughout the thesis, and presents recommendations for continued work in the field.

# Chapter: Numerical Methods



*The finite-volume methods employed by FLUENT 6.3 are introduced, including a summary of the Reynolds-averaged Navier-Stokes equations. Discretization schemes and turbulence models used to produce the results in subsequent chapters are described, as well as the solution procedures applied to the problems of each flow regime (subsonic, transonic and supersonic). Numerical issues relating to the meshing are discussed, as well as aspects of post-processing used to generate certain results. Thorough validation and verification of results is presented in chapter 4.*

## 2.1 Introduction

The use of computational fluid dynamics (CFD), and in particular Reynolds-averaged Navier-Stokes (RANS) solvers, is well established in the field of aerodynamics. It can facilitate accurate modelling of often-complex fluid flows, and is becoming increasingly important in the aerodynamic design process as it offers a relatively cost-effective way to refine concepts before they are physically tested in wind tunnels or as prototypes.

As with any computational model, issues of validation and verification are prominent. The American Institute of Aeronautics and Astronautics (AIAA) provides a succinct definition of these terms (AIAA, 1998):

**Verification:** the process of determining that a model implementation accurately represents the developer's conceptual description of the model and the solution to the model.

**Validation:** the process of determining the degree to which a model is an accurate representation of the real world from the perspective of the model.

This chapter concentrates on aspects of verification (i.e. making sure the numerical model is appropriate and robust), as extensive validation comparisons to experimental data for each computational model is contained within Chapter 4, and in other relevant chapters of the thesis. At this point it is also useful to introduce the distinction between uncertainty and error, again defined by the AIAA as:

**Uncertainty:** a potential deficiency in any phase or activity of the modelling process that is due to lack of knowledge.

**Error:** a recognizable deficiency in any phase or activity of modelling and simulation that is not due to lack of knowledge.

This chapter focuses on the probable sources of error in the computational model and the steps taken to minimise their influence.

A commercial finite-volume code, Fluent 6.3, was used to generate all numerical results presented in this thesis. A discussion of the appropriateness of this choice is presented here, with a general description of the numerical formulations used by the code to produce solutions. As several different investigations were conducted for this thesis, across a range of flow regimes, particular emphasis is placed upon the description of solution methodology in each instance. An analysis of the applied turbulence closures is made, with specific reference to their suitability for each problem and the limitations inherent in each approach. A brief description of certain post-processing techniques is also included to better inform the reader with regards to the way in which certain flow features were extracted or are presented in subsequent chapters.

The majority of discourse on the topics of numerical verification with regards to mesh quality (grid convergence), and its influence on the solutions obtained, as well as detailed validation of CFD against experimental results, is contained within the relevant chapters (4-9). This is due to the previously-acknowledged fact that several investigations

have been conducted for considerably different geometries in a range of flow conditions, and thus it better serves the reader to consider these aspects in the immediate context of the investigations on which each main chapter is based.

## 2.2 Principles of Compressible Fluids and the Navier-Stokes equations

### 2.2.1 Conservation of mass, momentum and energy

The Navier-Stokes equations are a set of differential equations describing non-linear viscous fluid motion. As applied to discrete control volumes that define the region of fluid in the finite-volume method, they are defined by the principles of conservation of i) mass, ii) momentum and iii) energy. For reference, these are defined as follows for a three-dimensional, compressible viscous flow:

Conservation of mass (continuity):

$$\frac{\partial \rho}{\partial t} + \nabla \cdot (\rho \bar{u}) = 0 \quad \text{eqn. 2.1}$$

Conservation of momentum:

$$\frac{\partial}{\partial t} (\rho \bar{v}) + \nabla \cdot (\rho \bar{v} \bar{v}) = -\nabla p + \nabla \cdot (\bar{\tau}) + \rho \bar{g} + \bar{F} \quad \text{eqn. 2.2}$$

where the stress tensor is given by:

$$\bar{\tau} = \mu \left[ (\nabla \bar{v} + \nabla \bar{v}^T) - \frac{2}{3} \nabla \cdot \bar{v} I \right] \quad \text{eqn. 2.3}$$

Conservation of energy:

$$\frac{\partial}{\partial t} (\rho E) + \nabla \cdot (\bar{v} (\rho E + p)) = \nabla \cdot \left( k_{\text{eff}} \nabla T - \sum_j h_j \bar{J}_j + (\bar{t}_{\text{eff}} \cdot \bar{v}) \right) + S_h \quad \text{eqn. 2.4}$$

where the non-standard notation is as follows:  $\bar{\tau}$  is the stress tensor,  $\rho \bar{g}$  and  $\bar{F}$  are the gravitational and external body forces respectively, and  $I$  is the unit tensor.  $k_{\text{eff}}$  is the effective conductivity, and  $\bar{J}_j$  is the diffusion flux.

When the flow is considered as incompressible for a purely subsonic aerodynamic flow with no heat transfer, as in some of the simulations in Chapter 6, the energy equation can be neglected.

### 2.2.2 Compressible Fluids and associated parameters

Throughout this thesis, except where explicitly stated, the fluid is air and modelled as an ideal gas, the equation of state being:

$$p = \rho RT \quad \text{eqn. 2.5}$$

where  $T$  is calculated from the energy equation and  $R$  is the specific gas constant, 287  $\text{Jkg}^{-1}\text{K}^{-1}$ .

The isentropic flow relations have been used to describe the flow properties, and these can be neatly summarised in such a form:

$$\frac{p_0}{p} = \left( \frac{\rho_0}{\rho} \right)^\gamma = \left( \frac{T_0}{T} \right)^{\gamma/(\gamma-1)} \quad \text{eqn. 2.6}$$

where it therefore follows that:

$$\frac{T_0}{T} = 1 + \frac{\gamma-1}{2} M^2 \quad \text{eqn. 2.7}$$

$$\frac{p_0}{p} = \left( 1 + \frac{\gamma-1}{2} M^2 \right)^{\gamma/(\gamma-1)} \quad \text{eqn. 2.8}$$

$$\frac{\rho_0}{\rho} = \left( 1 + \frac{\gamma-1}{2} M^2 \right)^{1/(\gamma-1)} \quad \text{eqn. 2.9}$$

The Mach number is itself defined by the equation:

$$M = \frac{u}{a} \quad \text{eqn. 2.10}$$

where the speed of sound,  $a$ , is described by:

$$a = \sqrt{\gamma RT} \quad \text{eqn. 2.11}$$

In all compressible solutions presented in this thesis, a three-coefficient Sutherland viscosity model (Sutherland,1893) was used:

$$\mu = \mu_0 \left( \frac{T}{T_0} \right)^{3/2} \frac{T_0 + S}{T + S} \quad \text{eqn. 2.12}$$

where reference values are;  $T_0$ , reference temperature = 273K,  $\mu_0$ , reference viscosity =  $1.716 \times 10^{-5} \text{ kgm}^{-1}\text{s}^{-1}$  and  $S$ , the Sutherland constant temperature = 110.56K. The freestream density was set appropriately depending on the simulation being run.

## 2.3 Application of the Navier-Stokes Equations to CFD

The general procedure involved in the CFD used to produce all results in this thesis is as outlined in the schematic of figure 2.1. The previous section introduced the principles of conservation of mass, energy and momentum as applied to a fluid, but these equations must be suitably manipulated in order to be solved systematically for a given fluid flow using the finite-volume method around which FLUENT is based. Issues of grid generation and cell quality will be dealt with later; for now we consider the underlying fundamental theorem of the finite-volume method as applied to an arbitrary series of control volumes.

### 2.3.1 Discretisation

The integral form of the equations which govern the model of the fluid can be applied to each control volume, but in order to describe the differences in any given variable between one cell centre and the next, an interpolation is required, which results in the discretised

PRINCIPLES OF CONSERVATION OF MASS,  
MOMENTUM AND ENERGY ESTABLISHED

CHOICE OF A FIXED FINITE CONTROL VOLUME  
TO MODEL THE FLOW

Domain divided into discrete volumes (the mesh).

Integration of the governing equations for individual control volumes to construct algebraic equations for the discrete dependent variables such as velocities, pressure, temperature, and conserved scalars.

DEVELOPMENT OF EQUATIONS IN A FORM SUITABLE  
FOR CFD

Linearization of the discretized equations and subsequent solution of the equation system to yield new values of the variables.

A general procedure for the CFD method used in the present investigations

equation. A general scalar transport equation, for any property, can be discretised to yield an equation that has inbuilt conservation on a control-volume basis, and the resultant linearised system of equations can be written for each cell in the mesh to form a matrix, the solution of which shall be dealt with shortly.

The discretised forms of the integral forms of the continuity, momentum and energy equations therefore underpin the finite-volume approach. For compressible flows featuring discontinuities (shock waves), the finite volume method is characteristically suitable; it is inherently conservative, and thus satisfies the Rankine-Hugoniot “jump” condition (Rankine, 1887) for discontinuities, which itself is an upshot of conservation.

The way in which transported properties are established at each cell face in the domain is highly influential to the ultimate solution, and an appropriate approach is often problem-specific. The method of discretisation has important consequences for, amongst other aspects, the amount of numerical diffusion in the solution, and thus higher order methods are generally preferred.

### 2.3.1.1 Spatial Discretisation

Discrete values of a scalar stored at the cell centres must be interpolated to obtain cell face values. As a balance between accuracy and computational efficiency, a second-order upwinding method was employed to achieve this in producing the results presented in this thesis.

A first order approximation implies that the cell-centre values for any given property hold for the entire cell volume, such that the face quantities are identical to the cell quantities.

The second order method offers a more advanced approach whereby a multidimensional linear reconstruction approach is employed (Barth and Jespersen, 1989). That is, a Taylor series expansion of the cell-centered solutions around the cell centroids is used to achieve higher order accuracy at cell faces. The following expression, for any face value  $\phi_f$ :

$$\phi_{f,SOU} = \phi + \nabla\phi \cdot \vec{r} \quad \text{eqn. 2.13}$$

is used, where  $r$  is the displacement vector from the upstream cell centre to the solution cell centre. The determination of the gradient  $\nabla\phi$  is an important facet of the method.

### 2.3.1.2 Gradient Evaluation

The gradients used to construct scalar values at cell faces and velocity derivatives are calculated in FLUENT using a Green-Gauss theorem. This can either involve a simple cell-centered averaging:

$$\bar{\phi}_f = \frac{\phi_{c0} + \phi_{c1}}{2} \quad \text{eqn. 2.14}$$

or by taking the arithmetic average of the nodal values on a face:

$$\bar{\phi}_f = \frac{1}{N_f} \sum_n^{N_f} \bar{\phi}_n \quad \text{eqn. 2.15}$$

The latter approach is most effective for unstructured meshes (FLUENT, 2006), although it has been applied in all instances to results presented in this thesis for a potentially small gain in accuracy (particularly in the region of shock waves), even though completely hexahedral meshes were used in all instances.

### 2.3.1.3 Temporal Discretisation

Discretisation in both time and space must be undertaken for transient cases. The temporal discretisation formulation requires the integration of each term in the differential equations over a user-specified time step,  $\Delta t$ .

A second order discretisation in time was used for all unsteady calculations in this thesis, as represented by the following expression:

$$\frac{3\phi^{n+1} - 4\phi^n + \phi^{n-1}}{2\Delta t} = F(\phi) \quad \text{eqn. 2.16}$$

An implicit time integration is then used to evaluate  $F(\phi)$  at a future time level:

$$\frac{\phi^{n+1} - \phi^n}{\Delta t} = F(\phi^{n+1}) \quad \text{eqn. 2.17}$$

which can be solved iteratively at each progressive time step.

## 2.3.2 Reynolds-Averaged Navier Stokes Modelling

Reynolds-averaged Navier-Stokes (RANS) modelling is by far the most common form of CFD currently used to examine aerodynamic problems. The notion of the finite volume method has already been introduced, and we now briefly examine how the principles of conservation of mass, momentum and energy can be approximated in an efficient, practical way using the discretised equations.

The approach entails a simplification of the equations such that velocity terms

are time-averaged (though this does not mean that solutions obtained are average results, and therefore the use of RANS modelling to study unsteady problems is not precluded). The exact variable quantities from the Navier Stokes equations are treated as consisting of a mean and a fluctuating component. For the velocity components this can be expressed as:

$$u_i = \bar{u}_i + u'_i \quad \text{eqn. 2.18}$$

or for a scalar quantity:

$$\phi = \bar{\phi} + \phi' \quad \text{eqn. 2.19}$$

Substituting this form of the flow variables into the equations for continuity and momentum yields the Reynolds-averaged Navier Stokes equations:

$$\frac{\partial \rho}{\partial t} + \frac{\partial}{\partial x_i}(\rho u_i) = 0 \quad \text{eqn. 2.20}$$

$$\frac{\partial}{\partial t}(\rho u_i) + \frac{\partial}{\partial x_j}(\rho u_i u_j) = -\frac{\partial p}{\partial x_i} + \frac{\partial}{\partial x_j} \left[ \mu \left( \frac{\partial u_i}{\partial x_j} + \frac{\partial u_j}{\partial x_i} - \frac{2}{3} \delta_{ij} \frac{\partial u_l}{\partial x_l} \right) \right] + \frac{\partial}{\partial x_j} (-\overline{\rho u'_i u'_j}) \quad \text{eqn. 2.21}$$

where the new terms on the right hand side, the Reynolds stresses, represent turbulence in the flow, and these terms cannot easily be solved directly.

In order to solve the equations successfully, a turbulence closure must be used to account for the Reynolds stresses, and the techniques proposed by researchers to achieve this over the last several decades are many and varied. The choice of an appropriate turbulence model for the problem being solved is a pivotal one with repercussions for both the accuracy of the ultimate solution and the time and computational effort expended to obtain it.

### 2.3.3 Turbulence Modelling

Several turbulence models were used to generate the results presented in this thesis.

Each specific problem was examined initially with several models to determine the most effective one for each situation - a necessary level of rigour given that the flow regimes ranged from highly subsonic to transonic and supersonic, each presenting their own unique flow features. The majority of results presented for transonic and supersonic cases utilised the one-equation Spalart-Allmaras (SA) model, while the subsonic studies used a two-equation realizable  $k$ - $\epsilon$  model. The other models tested were the two-equation  $k$ - $\omega$  SST variant and, to examine the effects of free transition in the boundary layer, a four-equation  $k$ - $k$ - $l$ - $\omega$  model was used to generate a handful of results. An overview of these modelling approaches as implemented in the code follows below.

More advanced but much more computationally-expensive approaches such as LES (large-eddy simulation) and DES (detached-eddy simulation) were not considered necessary to accurately describe the flows being examined, and the considerable increase in computing power required would have significantly curtailed the extent of the investigation. A Reynolds-Stress-based turbulence closure, though available, was also not considered for the present work as it requires the solution of 7 extra transport equations which themselves require modelling assumptions for closure. While most applicable to highly-swirling, massively strained flows, it would only be likely to improve solution quality for the rotating supersonic projectile, at a prohibitive cost to computing time and memory requirements. Furthermore, since no experimental data was available for the flow in the wake region where the model was most likely to perform better than the others, there would be no clear way to tell if the model was actually offering an improved result.

### 2.3.3.1 *The Boussinesq Approximation*

The one and two equation turbulence models outlined in this section are all built upon the Boussinesq approximation (Boussinesq, 1877), which relates the Reynolds stresses to the mean velocity gradients as follows:

$$-\overline{\rho u'_i u'_j} = \mu_t \left( \frac{\partial u_i}{\partial x_j} + \frac{\partial u_j}{\partial x_i} \right) - \frac{2}{3} \left( \rho k + \mu_t \frac{\partial u_k}{\partial x_k} \right) \delta_{ij} \quad \text{eqn. 2.22}$$

The overwhelming advantage of this method is the low computational expense incurred by the computation of the turbulent viscosity. In the case of the one equation Spalart-Allmaras model, an additional transport equation for the turbulent viscosity is solved. The k-ε model requires two additional transport equations for the turbulent kinetic energy (k) and the turbulent dissipation rate (ε), and the other two-equation method discussed in this chapter, the k-ω model, solves for the specific dissipation rate (ω) rather than ε.

### 2.3.3.2 The Spalart-Allmaras (SA) model

This relatively simple, versatile one-equation turbulence closure was developed specifically for application to aerospace problems involving wall-bounded flows (Spalart and Allmaras, 1992), and was used to generate the final results discussed in chapters 4, 5, and 7-9. The meshing approach described in section 2.4.2 and Chapter 4 facilitated proper resolution of the boundary layer, enabling the primary form of the SA model to be properly implemented without wall function approximations. Transition to turbulence was not modelled in the original formulation. The transported variable in the SA model is  $\tilde{\nu}$ , and is identical to the turbulent kinematic viscosity except in the near wall region. The transport equation takes the following form:

$$\frac{\partial}{\partial t}(\rho\tilde{\nu}) + \frac{\partial}{\partial x_i}(\rho\tilde{\nu}u_i) = G_\nu + \frac{1}{\sigma_{\tilde{\nu}}} \left[ \frac{\partial}{\partial x_j} \left\{ (\mu + \rho\tilde{\nu}) \frac{\partial \tilde{\nu}}{\partial x_j} \right\} + C_{b2}\rho \left( \frac{\partial \tilde{\nu}}{\partial x_j} \right)^2 \right] - Y_\nu$$

eqn. 2.23

where  $\tilde{\nu}$  is the transported variable,  $G_\nu$  is the production of turbulent viscosity, and  $Y_\nu$  is the destruction of turbulent viscosity in the near-wall region.  $C_{b2}$  and  $\sigma_{\tilde{\nu}}$  are constants.

The model has been extensively validated by others for transonic and supersonic aeronautical flows (Dam, 1999), including a correlation in the original paper (Spalart and Allmaras, 1992) with experimental data for the RAE2822 aerofoil - the same comparison is made in chapter 6 of this thesis. The model has also proven to be effective in determining compressible effects in high-lift, multi-element wing configurations

(Baker *et al.*, 2002).

In modelling the production of turbulence, the original approach of Spalart and Allmaras implies that turbulence only occurs in near-wall regions where vorticity is being generated, and thus may cause difficulties in predicting separated or strongly-recirculating flows. A modification to the model proposed by Dacles-Mariani *et al.* (1995) has been implemented in FLUENT. The alteration consists of an inclusion of both strain and rotation tensors, which benefits the solution by more accurately representing the effects of rotation on turbulence in the flow, which is particularly useful for the solutions involving rotating free shear layers in chapter 4, and those featuring periodically separating and recirculating flow in chapters 6 and 7.

### 2.3.3.3 The Realizable $k$ - $\epsilon$ model

The semi-empirical  $k$ - $\epsilon$  method first proposed by Launder and Spalding (1974) involves transport equations for  $k$  and  $\epsilon$ , the latter of which was obtained from physical reasoning rather than exact formulation. The Realizable version of the  $k$ - $\epsilon$  method (Shih *et al.*, 1995) improves upon the original model by reformulating the turbulent viscosity and incorporating a new transport equation for the dissipation rate which is derived from an exact equation for the transport of mean-square velocity fluctuations.

Via these improvements, the model provides superior performance for separated, recirculating flows and highly-adverse pressure gradients in boundary layer regions, and thus was considered eminently suitable for application to the compressible ground effect problems that comprise this thesis.

The transport equations for the model take the following form:

$$\frac{\partial}{\partial t}(\rho k) + \frac{\partial}{\partial x_j}(\rho k u_j) = \frac{\partial}{\partial x_j} \left[ \left( \mu + \frac{\mu_t}{\sigma_k} \right) \frac{\partial k}{\partial x_j} \right] + G_k + G_b - \rho \epsilon - Y_M \quad \text{eqn. 2.24}$$

and

$$\frac{\partial}{\partial t}(\rho \epsilon) + \frac{\partial}{\partial x_j}(\rho \epsilon u_j) = \frac{\partial}{\partial x_j} \left[ \left( \mu + \frac{\mu_t}{\sigma_\epsilon} \right) \frac{\partial \epsilon}{\partial x_j} \right] + \rho C_1 S \epsilon - \rho C_2 \frac{\epsilon^2}{k + \sqrt{\nu \epsilon}} + C_{1\epsilon} \frac{\epsilon}{k} C_{3\epsilon} G_b \quad \text{eqn. 2.25}$$

$G_k$  represents the generation of turbulence kinetic energy due to the mean velocity gradients, and  $G_b$  is the generation of turbulence kinetic energy due to buoyancy.  $\sigma$  terms are the turbulent Prandtl numbers. Dilatation dissipation is accounted for in the model by introducing an additional term,  $Y_M$  to represent it into the  $k$  equation. This allows an enhanced prediction of the decrease in spreading rate in free shear layers that comes with increasing Mach number, but is ignored entirely in the incompressible formulation.

#### 2.3.3.4 *The $k$ - $\omega$ SST model*

The other two-equation model tested in later chapters in validation efforts, but not ultimately used to produce results in the remainder of the thesis, is the shear-stress-transport (SST) variant of Menter (1994) of the Wilcox  $k$ - $\omega$  model (Wilcox, 2004).

The original  $k$ - $\omega$  model is an empirical formulation which solves transport equations for  $k$  and the specific dissipation rate  $\omega$ , modified for incorporation into FLUENT to better account for compressibility and free shear flows. The principle modifications to this in the SST model are that the standard  $k$ - $\omega$  model as applied in the near-wall region is blended to a high Reynolds number formulation of the  $k$ - $\varepsilon$  model in the outer regions of the boundary layer and the farfield, and the turbulent viscosity formulation is altered to account for the effects of the transport of turbulent shear stress through the fluid.

By virtue of these changes to the model, it is markedly more applicable for adverse pressure gradients and transonic shock waves, and thus was deemed as a viable option for the current work.

#### 2.3.3.5 *The $k$ - $k$ - $l$ - $\omega$ model*

RANS averaging negates the effects of the growth of linear disturbances and it has therefore been difficult to apply to boundary layer transitions where linear and non-linear effects are important. The  $k$ - $k$ - $l$ - $\omega$  model, which is beta-implemented in FLUENT 6.3, was used briefly to estimate the location of natural boundary layer transition for

simulations of the wind tunnel experiments described in chapter 3 and 6. It is a four-equation correlation-based transition model which is based on two transport equations; one for intermittency and one for a transition onset criterion in terms of momentum thickness Reynolds number (Langtry and Menter, 2005).

The model has been well validated against high-lift and supercritical configurations and was thus deemed appropriate for usage in the present context, although no direct experimental comparison of transition locations and behaviour was made.

### 2.3.3.6 Further notes on wall region modelling

The near-wall region can be resolved numerically in a variety of ways with associated variance in the accuracy of the solution in that region. The present investigations make much of predicted values of aerodynamic drag, which are greatly influenced by the behaviour of the boundary layer - with a finer mesh in the wall region, a more complex and realistic model of the boundary layer can be computed. Furthermore, shock/boundary layer interactions are an inherent feature of the flows above the critical Mach number. As a result, enhanced wall modelling has been implemented regardless of the turbulence model used.

The parameter used to define the proximity of the cell centre of the wall-bounded cell to the wall itself is the  $y^+$  value, which is defined as:

$$y^+ = \frac{\rho u_\tau y_p}{\mu} \quad \text{eqn. 2.26}$$

where  $u_\tau$  is the friction velocity and  $y_p$  is the height from the wall at point p.

To capture the viscous-sublayer of the boundary layer as well as the log-law region, a number of cells must be clustered close to all no-slip walls. When the  $y^+$  is less than 5, the cells exist in this viscous-sublayer; meeting such a criteria is a prerequisite for use of the enhanced wall models which can be applied for all the models described above. In order to capture the laminar sublayer, a  $y^+$  of around 1 is most desirable.

For this reason, near-wall meshes for all cases in this thesis, apart from where explicitly stated as otherwise, were designed to produce a  $y^+$  of approximately 1 in wall-bounded flow regions. As the parameter is affected by scale and Mach number, this process was largely trial-and-error until the desired range was achieved.

### 2.3.4 Pressure-based and density-based solvers

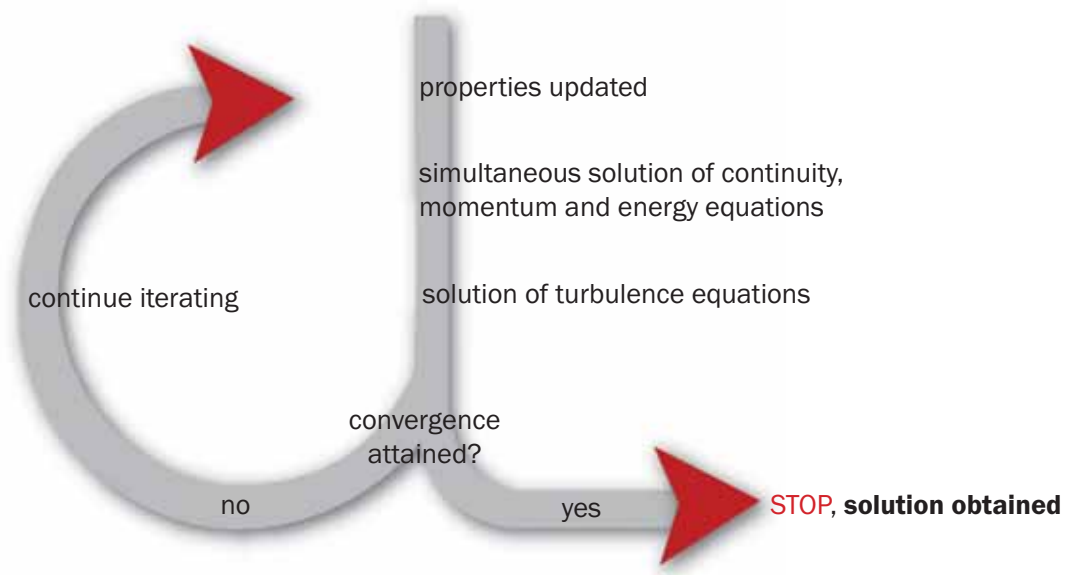
FLUENT offers two solvers; one is a pressure-based solver developed primarily for low-speed incompressible flows, and the other is a density-based formulation developed for high-speed compressible flows. Over time both solvers have been extended to cover a full range of flow conditions while retaining their underlying principles. Both solvers take different approaches to solving the discretised equation set and the merits of these are worth discussion here as both solvers were used to produce results in this thesis: the density-based solver for the fully-supersonic investigation in chapter 4, and the pressure-based solver for all other subsonic and transonic results.

The pressure based solver, which satisfies continuity of the velocity field by solving a pressure equation derived from the continuity and momentum equations, can be used in coupled or segregated form. The density-based solver is a predominantly coupled solver. The solution procedures for each method are summarised in the diagrams of figures 2.2, 2.3 and 2.4.

#### 2.3.4.1 *Coupled vs. Segregated methods*

The pressure-based segregated solver sequentially solves the system of equations, whereas the pressure-based coupled algorithm solves a coupled system of equations comprising the momentum equations and the pressure-based continuity equation. The remaining equations are solved in a decoupled fashion as in the segregated algorithm.

The solution of momentum and continuity equations in a coupled manner, significantly improves the rate of convergence when compared to the segregated algorithm, but increases in RAM are required to store the equation set entirely for each iteration.



Schematic of the density-based coupled solution procedure

Clearly, although the broad approach of iterating step-by-step to a solution is the same for all solver approaches, the means by which that solution is arrived at, and thus the solution itself, is dependent on the method itself and its applicability to the problem being studied. The pressure-based solver solves the linearised equations in “implicit” form, while the density-based solver was used in this thesis in “explicit” form, and it is worth discussing the merits of each approach.

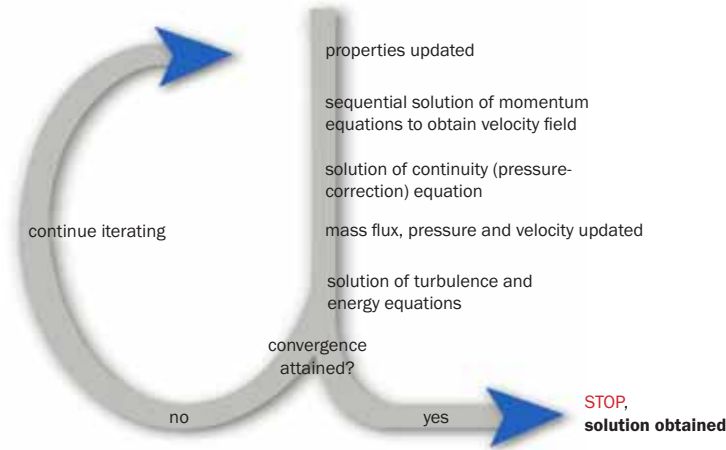
### 2.3.5 Implicit vs. Explicit methods

Two general solution techniques for partial differential equations are commonplace in CFD - implicit and explicit procedures.

An implicit method calculates an unknown value of any variable via a relation that incorporates existing and unknown values from the surrounding cells. As each unknown is therefore bound to appear in more than one equation in the system, they must be solved simultaneously to yield values for the unknowns. This simultaneous solution of the difference equations in the domain therefore involves large matrices. The computational expense required is considerable as a result, and, particularly in the case

2.3

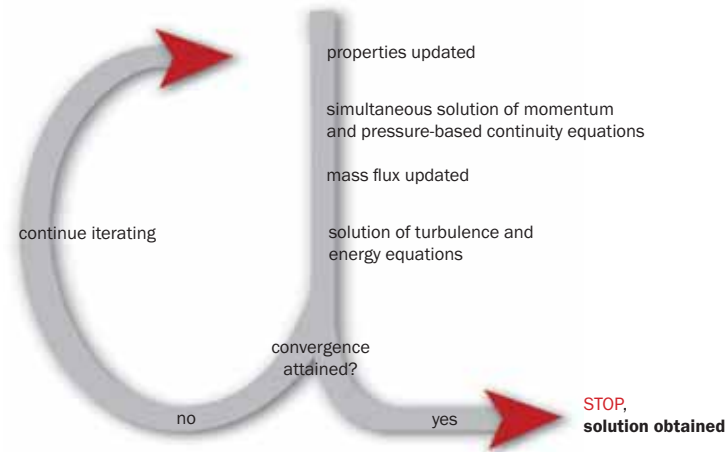
FIG



Schematic of the pressure-based segregated solution procedure

2.4

FIG



Schematic of the pressure-based coupled solution procedure

of time-dependent solutions, the truncation errors for the difference expression of the time derivative can be large. However, most implicit methods are inherently stable in time-marching towards a solution and thus a more rigid progression to a steady-state is possible, with potential time savings as a consequence.

An explicit method evaluates the unknown value of a cell using only existing values, and so each equation in the system can be solved one at a time for the unknowns. It is a less computationally demanding approach but is less stable and as a result, for example, the Courant number may have to be maintained at a relatively low level to avoid divergence, resulting in a longer running time to achieve convergence. This is in part overcome by the use of multigrid techniques as discussed next, and is also less of an issue when using grand-scale parallel processing.

### 2.3.6 AMG, FAS Multigrid, and Smoothing Techniques

The standard solution procedure used in FLUENT to solve the implicit form of the linear equation system involves an algebraic multigrid (AMG) scheme; “algebraic multigrid” in that it solves coarse-level solutions without physically constructing less-fine meshes or evaluating flux or source terms on coarser levels. The crucial disadvantage of this approach is that non-linearities are not sensed, as it were, by the solver until the fine-level stage is evaluated again. This is an important consideration in the context of shock waves, and an alternate approach (full-approximation storage, or FAS) is discussed shortly for the solution of the explicit procedure, which is achieved using a multi-stage (Runge Kutta) solver.

For the solutions obtained using the pressure-based coupled solver (chapters 5, 6 and 7), the AMG method was used. The algorithm uses, by default, a block-method Gauss-Seidel smoothing procedure for solving the system of equations, involving a series of forward and backward sweeps over the unknown variables. To obtain improved convergence rates with the coupled solver, this method was sidelined in favour of an ILU (incomplete upper-lower) smoothing technique. This reconstitutes the solution matrix such that elements can be calculated and stored in memory as the AMG levels are being constructed, and this stage is then followed by a series of sweeps similar to the Gauss-Seidel approach. The method particularly suits the coupled solver, resulting in more robust performance and shorter solution times (FLUENT, 2006).

With the density-based explicit method, the FAS (full approximation storage) multigrid was used to accelerate the solution. Unlike the AMG method, this involves an actual geometric reconstruction of the mesh as coarser levels. Coarse cells are simply formed by combining one with its neighbours, such that 8 original hexahedral cells might become 1 cell on the next coarse level. The accuracy of the final solution is determined only by the fine level mesh and is therefore not affected by the coarse grid discretisation.

The method then solves each iteration on the fine mesh and feeds the solution down to the next, coarser level using the full approximation scheme (Brandt, 1979), and so on as desired. For the present work, 4 coarse levels were used and, despite the

additional solution time required for the procedure, the number of iterations required for convergence was found to be dramatically less than solutions conducted on just the original or only 1 additional coarse level.

### 2.3.7 Flux splitting

The density-based solver used to produce the supersonic projectile results in chapter 4 can be used with either a Roe Flux-Difference Splitting (FDS) (Roe, 1980) method or an advection upstream splitting method (AUSM) to evaluate flux quantities at the cell boundaries.

The AUSM method (originally proposed by Liou and Steffen (1993)) is designed to provide more exact resolution of any shock discontinuities and reduce the susceptibility of the solution to the so-called “Carbuncle Phenomena” which is a shock instability which can disrupt computations of grid-aligned shock waves using upwind discretisation schemes (Dumbser, 2004).

In practice, it was evaluated that the Roe-FDS method provided a swifter and more stable convergence than the AUSM method for, particularly in meshes which were not particularly fine around shock waves (for instance, before local refinement), for a negligibly-different solution.

Thus the Roe-FDS was chosen as the most effective means of flux-splitting for efficiently producing accurate results requiring less-frequent monitoring of the health of the solution.

### 2.3.8 Initialization and FMG

The simulations involving shock waves, and in particular the fully-supersonic cases considered in chapter 4, occasionally proved to be highly unstable in their early stages due to the difficulties of the solver in establishing complex shock reflection patterns in the flowfield.

After considerable experimentation, a satisfactory procedure was settled upon

whereby the flowfield was not initialized simply from freestream conditions, but rather using a full-multigrid (FMG) initialization. This relatively quick procedure makes use of the density-based explicit FAS scheme described above to perform a limited iterative solution procedure on increasingly coarse levels to provide an initialized state that is already a reasonable approximation of the final flowfield, albeit without any turbulent parameters. In this way the initialized state is effectively a first-order inviscid solution.

The subsequent solution-proper was usually considerably more stable in its early stages, allowing significantly higher Courant numbers early in the iterative process, and requiring less under-relaxation of the solution parameters.

### 2.3.9 More on relaxation and stability

In order to obtain stability in the iterative procedure, particularly at the start of solutions featuring one or more shock reflections or boundary layer interactions, some significant relaxation of the flow variables was implemented. This was particularly necessary in the case of the turbulence parameters, most notably of the turbulent viscosity. Later in the solutions, once the flowfield had been well-established, the under-relaxation was alleviated to facilitate swifter convergence. This procedure was determined to have negligible effect on the ultimate solution.

The fully-supersonic cases described in chapter 4, especially those in extremely close proximity and thus featuring multiple shock reflections and boundary-layer interactions with the spinning projectile, were run for a number of first-order cycles until the flowfield settled enough to expedite a second-order continuation to convergence. Again, this procedure was evaluated to impact negligibly on the ultimate solution.

## 2.4 Additional Considerations

### 2.4.1 64-bit processing

Although much early work made use of 32-bit double-precision processing, all the results presented in this thesis were computed in single precision on parallel 64-bit machines. This served to minimize the rounding errors inherent in the iterative process. To use double precision on the 64-bit machines for the size of meshes used for much of the work described here would have required more RAM and computer time than was feasible. A handful of cases run with double precision exhibited slightly more stable convergence behaviour, but did not alter the results to a degree which indicated the additional computational expense was justified (less than 0.02% difference in aerodynamic coefficients and less than 0.1% of chordwise extent in terms of shock locations on a locally-adapted mesh).

### 2.4.2 Notes on meshing

The generation of suitable grids for any CFD problem is often not only immensely time-consuming, but is a crucial influence on the quality of the solution obtained. Much experimentation with unstructured and hybrid meshes was conducted in the early stages of work, with both largely-automated and manual grid generation programs. Only hexahedral-structured, manually-generated grids using GAMBIT 2.4 proved to be consistent, of high-quality, and provided the most robust solution in FLUENT. Therefore only this approach is discussed here.

Structured meshes have the advantage of being largely aligned to the flow in relatively simple aerodynamic problems, as opposed to unstructured elements which can never be aligned to the flow. For problems involving oblique shock waves and reflections, the superiority of this approach in terms of the solution is less clear-cut, but the level of control over the mesh quality is still a powerful factor and the reduced computational expense proved to be valuable given the volume of cases being solved.

For each geometry investigated, body-fitted multiblock grids were generated, with non-conformal spacing in the near wall region (to satisfy  $y^+$  requirements for turbulence modelling, see Chapter 4) and in the farfield (i.e. regions of minimal flow gradients, to keep the overall number of cells down). In this way, truncation errors (the difference between the partial differential equation and the finite equation) were minimized because high aspect ratio cells were only located where they could not exert any undue negative influence on either the solution or its stability, although it is accepted that in some cases, shock waves passing through stretched cells, albeit far from the body of interest, would have been adversely affected.

In order to minimize truncation errors further, outside of the near-wall region the cells were grown slowly to avoid rapid changes in cell volume that would create the potential for unnecessary discretisation errors; in a similar vein, the skew of cells was kept well within acceptable levels ( $<0.7$ ) even in regions of high geometric curvature.

All grids were re-ordered prior to solution with a reverse Cuthill-McKee method (Cuthill and McKee, 1969) to improve the solution efficiency.

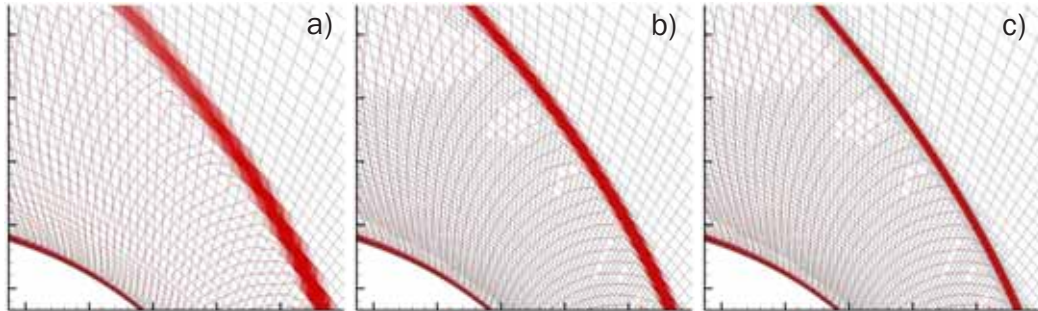
Much more detailed discussion of individual meshes can be found in Chapter 4, including thorough grid convergence studies and discussion of other issues such as geometrical simplifications.

No special shock-fitting techniques were used to obtain the solutions described in this thesis - rather, a simple shock-capturing approach was implemented, due to the large number of cases being run, with shock waves and reflections occurring in regions of the flow not easily-identifiable prior to solution. Mesh density was increased between the objects in question and the ground and in the wake regions, but otherwise the standard modus operandi involved obtaining a converged solution on the initial mesh and then refining the cells locally in the presence of compression or expansion waves in order to best capture shock waves in the flow across as finite a physical distance as possible in the domain.

Typically this involved assessing areas of the highest pressure gradient. Attempts to isolate the shock and expansion waves using density gradients tended to include a high

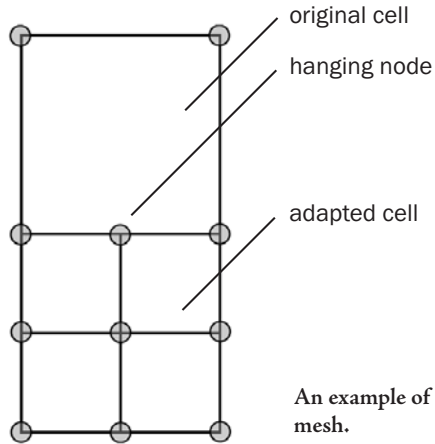
2.5

FIG



2.6

FIG



An example of a “hanging node” in a locally-refined mesh.

Pressure gradient-based local mesh adaption:  
a) original mesh, b) one level of broad gradient refinement, and c) second level of high-gradient shock-specific refinement.

number of cells in the boundary layers, which had already been carefully  $y^+$  matched to the wall models, and thus the pressure gradient method provided a better means to best capture only the waves. Additional refinement in wake or separation regions, when necessary, was performed by simply refining within a geometrical region.

A normalized pressure gradient of above approximately 0.1-0.2 for the subsonic cases and 0.01-0.02 for the supersonic cases was generally a sufficient criteria to increase mesh resolution in the shock regions, although limitations were placed on the supersonic cases (which involved a great number of waves and reflections) in order to avoid the size of the mesh becoming an inordinate strain on the computational resources available.

The process of adapting the mesh in FLUENT on a structured mesh is a simple cell-splitting, such that a two-dimensional quad cell is dissected into 4, or a hexahedral cell is divided into 8 volume cells. This results in “hanging” nodes, as shown in figure 2.6. which trade an increase in truncation errors for a markedly better resolution in the region of shocks, as shown in figure 2.7. A cell-weighted evaluation of properties across the non-conformal interface is performed by FLUENT and, since the hanging nodes

exist in the vicinity of the shock discontinuities, it is not anticipated that this method would introduce errors into the solution of the same order of magnitude as having a poorly-resolved shock wave.

A maximum of two rounds of adaption was implemented, to avoid exacerbating excessive cell volume gradients for little further gain in solution accuracy. All strong shocks were diffused across approximately 3 cells.

### 2.4.3 Residual reduction and convergence

Solutions for the subsonic and transonic cases generally solved in between 1000 and 2000 iterations, depending greatly on the Courant number and relaxation factors used as discussed above. Following shock-adaption of the meshes, another 500 to 1000 iterations was often required. The fully-supersonic cases took between 3000 and 5000 iterations to solve as they were less tolerant of solution acceleration in terms of Courant number due to the sensitivity of the flowfield in the presence of multiple reflecting shock waves.

Convergence was deemed to be obtained not only when the mass and momentum scaled-residual errors ceased to change by more than approximately 0.01% over 1000 iterations (usually at a level of  $\times 10^{-6}$  or  $\times 10^{-7}$  for continuity and  $\times 10^{-9}$  for the velocity parameters) but also when the aerodynamic forces on the body ceased to change by more than 0.01% over 1000 iterations. This level of convergence was found to provide satisfactory stabilisation of the wake and shock characteristics for all fully-steady-state solutions. Further minute adjustments to the shocks with continued iteration was inevitable given the number of waves crossing orthogonally-aligned cells. Detailed analysis of this phenomena was performed for each case and is described in the relevant chapters later in this thesis.

### 2.4.4 Kriging of a vector field

In order to extract the vortex cores for a handful of diagrams in later chapters highlighting the path of vortices in the wake, slices at appropriate coordinates were taken through

the domain. The vector fields obtained were occasionally difficult to analyse, particularly with increasing distance downstream, due to mesh stretching and coarsening. In order to pinpoint the location of the vortex core as accurately as reasonably possible, a 100x100 node grid was overlaid on a approximate 10x10 cell region of the original imported grid. The vector field was then interpolated from the original grid to the new one using a kriging process (Krige, 1951) and the coordinates of the vortex core extracted.

## 2.5 Summary of Solution Procedures

As has been mentioned, different approaches were used to solve for the various flow regimes investigated for this thesis. For clarity and in summary of the major points in this chapter, these methods and procedures are presented in table 2.1. The choice of turbulence models is discussed at length in chapter 4, but is shown here for reference.

Table 2.1. Overview of simulation settings

	Subsonic Inverted Wing	High-subsonic Aerofoil & Wing	Supersonic Projectile
Pressure / Density-based	coupled pressure-based	coupled pressure-based	coupled density-based
Explicit / Implicit form	implicit	implicit	explicit with multigrid
Turbulence Model	realizable k- $\epsilon$	Spalart-Allmaras	Spalart-Allmaras

- General settings:
- fully-hexahedral multi-block meshes,  
locally refined for shock waves.
  - second order upwind discretisation
  - node-based gradient evaluation
  - enhanced wall-region modelling in the boundary layer

Before detailed numerical validation and verification can be demonstrated, the experiments to which the CFD results are compared must be introduced. A description of these now follows in Chapter 3.

# Chapter: Experimental Methods

# 3

*After introducing the elevated ground plane and symmetry methods for high-speed ground effect investigations in blowdown tunnels, the experimental facilities of the U.S. Naval Academy Transonic Wind Tunnel, the University of New South Wales at the Australian Defence Force Academy's Supersonic Wind Tunnel, and the Australian Army's Small Arms Proofing Range are described. Experimental procedures for the tests conducted in each location are outlined, though only the tests in the transonic tunnel were specifically conducted by the author. Experimental error is discussed for each set of tests. An evaluation of the suitability of the methods for the flows under investigation is dealt with in more detail in chapter 5.*

## 3.1 Introduction

### 3.1.1 Determination of suitable approaches

In order to conduct experiments to study the aerodynamics of transonic or supersonic objects in ground effect, particular consideration must be given to the way in which the ground is represented.

As discussed in Chapter 1, for a wind tunnel environment with a fixed model, ideally a moving ground would be used for the greatest physical realism but this is impractical at supersonic speeds. It is arguably more straightforward to move the object through quiescent air using, for example, a rocket-sled testing facility or a ballistic range, but in addition to the enhanced complexity of all diagnostics related to free-flight measurements, these facilities are generally expensive and may also be subject to restricted

military access.

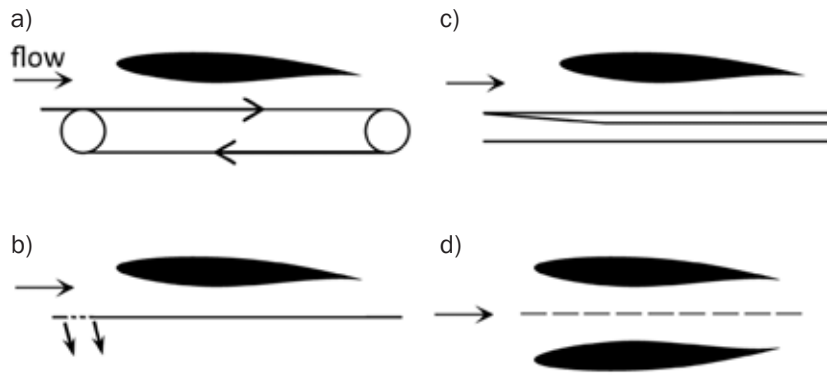
By contrast, supersonic blowdown tunnels are relatively common and accessible, and thus a major aspect of this thesis is the investigation of the applicability of two simple subsonic ground effect modelling techniques to transonic and supersonic applications in such facilities.

In most small university blowdown tunnels, models must be small in size to avoid blockage effects and thus the tunnel wall boundary layers can be substantial in relation to the dimensions of the object of interest, and therefore can influence the flow. In the supersonic tunnel used for the investigations described here, for example, the boundary layer on the test section wall at the location of the model is approximately 5 mm thick at the test conditions described further below, while the model diameter is 14 mm. Simply placing the model near the ground would produce a significant shock-boundary layer interaction which is not present in the true ground effect condition. The flowfield established in the tunnel would therefore fail to properly represent the full-scale case.

Figure 3.1, shows a handful of traditionally-subsonic techniques available to the experimentalist to simulate the ground effect in the case of a stationary model. As already stated, a supersonic moving ground (along the lines of the subsonic version depicted in Fig.3.1a) would be unfeasible, and blowing and suction techniques to remove or minimize the boundary layer (Fig. 3,1b) would be expensive and potentially complex. These techniques would also have the inherent problem of possibly introducing small-scale disturbances into the sensitive flow in the region of interest between the object and the ground, particularly in supersonic flows where various waveforms would be the result.

Precisely because of this lack of simple means for experimental testing, it is tempting to become reliant on CFD. However, dependence on CFD alone to investigate transonic and supersonic flowfields, particularly with regards to ground interactions, does not engender a sufficient level of confidence in the results.

Therefore the two experimental methods examined in more detail for this thesis are the elevated ground plane (Fig. 3.1c), which reduces the extent of, but does not entirely



Four means of simulating ground effect flows in a wind tunnel: a) the preferred technique of a moving ground, b) boundary layer suction, c) an elevated ground, and d) a symmetry (mirror-image) method.

remove, the ground boundary layer, and a symmetry ground condition (Fig. 3,1d), which does not feature a solid boundary. This method is also often used for shock reflection studies (Skews, 2000; Schmisser and Gaitonde, 2001) as discussed further in Chapter 5.

Wind tunnel experiments with these model arrangements, using pressure tappings and schlieren photography, have been carried out and supplemented by numerical simulations of the experiments in order to better quantify the relative merits of each method. The research described in this thesis involves a constructive relationship between experimental testing and CFD; in effect using the CFD to confirm the effectiveness of the experiments and using the experiments to validate the computational approach to the point where it can be used alone to further understanding of the flows investigated. A thorough evaluation of the results pertaining to the merits and limitations of the two approaches can be found in chapter 5 once the numerical model has been proven as capable in chapter 4; this chapter describes the experimental facilities, apparatus and relevant flow conditions, along with a discussion of sources of error.

### 3.1.2 Outline of experimental programmes

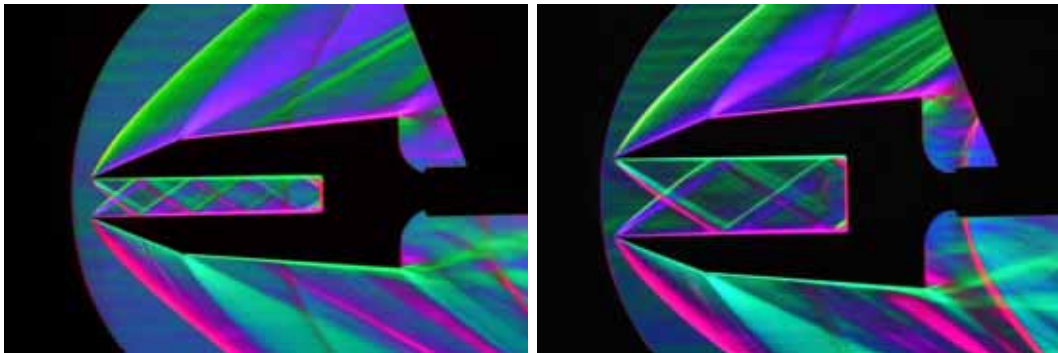
The experiments described here were conducted specifically for, or in association with the present work. Experiments used to validate the inverted wing CFD were taken

directly from literature and are discussed in the following chapter. This chapter describes the transonic and supersonic experiments conducted with regards to their design, implementation and the errors involved. The projectile experiments conducted at the Australian Army's Small Arms Proofing Range were devised and conducted prior to the author's involvement in that particular project, but are described here as the results were used for validation of the CFD presented in chapters 4, 5 and 9, providing a valuable source of corroboration for the experimental results obtained using the symmetry method in the wind tunnel.

The ADFA blowdown wind tunnel experiments for the supersonic projectile were also not conducted by the author, but the design of experiments was based upon preliminary tests using a double wedge symmetry method which *were* designed and tested by the author in the ADFA tunnel. Images from these tests are shown in figure 3.2, along with contemporary experiments in figure 3.3 made using an elevated ground plane to assess the suitability of using thermochromic liquid crystals (TLCs) as a visualisation

3.2

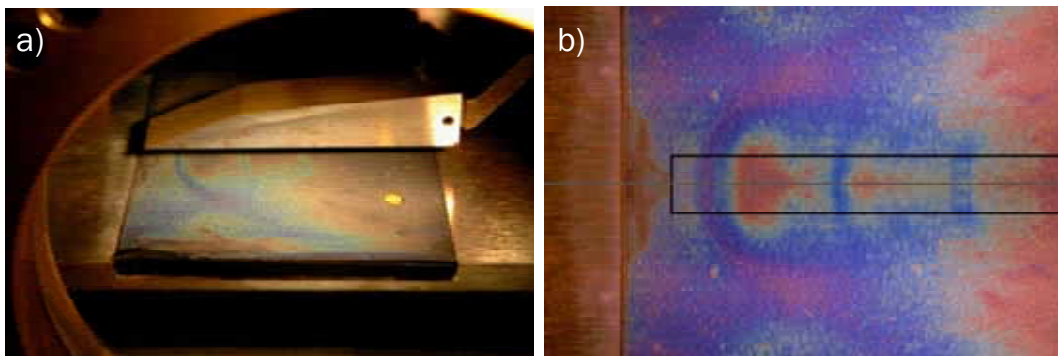
FIG



Colour schlieren images of the wedge model used to assess the feasibility of the symmetry method.

3.3

FIG



a) a wind-on image taken as the TLCs activate on the elevated ground plane, and b) a post-processed image of the 'footprint' of shocks on the ground around the wedge.

tool to observe the “footprint” of shock waves around the body on the ground (Doig *et al.*, 2006). Both the wedge geometry and the TLC paint were not used beyond these early studies, but provided a useful basis for the models and methods subsequently chosen to produce the experimental results in this thesis.

The results obtained from the projectile model tests in the wind tunnel are used here primarily for validation of the CFD approach and the symmetry method itself; the raw experimental results have not been published at the time of writing. The author was responsible entirely for the experimental programme conducted at the U.S. Naval Academy’s transonic blowdown tunnel.

For the purposes of clarity, each set of experiments has been described in standard, comparable sections of: objective; facility; apparatus, techniques and experimental conditions; and assessment of experimental error.

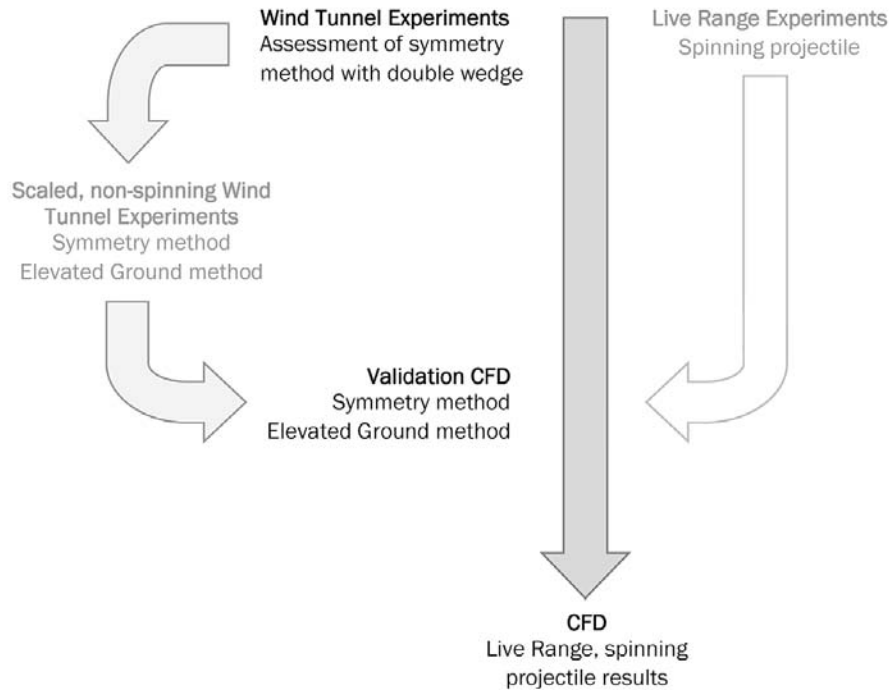
## 3.2 Supersonic Methods

A brief discussion of the supersonic methods is appropriate given their integral part in initiating the study and providing validation for the CFD that comprises the remainder of this thesis. The post-processing and analysis with regards to error and image manipulation is original to this document. Considerably more detail on the experiments can be found in the literature (Doig *et al.*, 2007; Purdon *et al.*, 2006, Purdon, 2006). The way all strands work together is demonstrated in figure 3.4.

### 3.2.1 Australian Army Live Arms Proofing Range

#### 3.2.1.1 Objective

The experiments, devised at the University of New South Wales at the Australian Defence Force Academy (UNSW@ADFA), were intended as a way of using time-resolved schlieren photography to examine the effect of ground proximity on a fully-supersonic projectile as fired from a rifle in controlled circumstances (Purdon, 2006).



**Role of supersonic experiments in cooperation with CFD.**

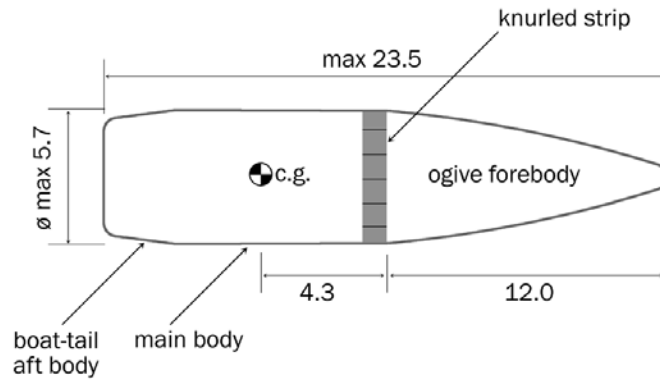
### 3.2.1.2 Facility

The live-range experiments were conducted at the Australian Army Land Equipment Agency’s Small Arms Proofing Range at Maribyrnong, Victoria. An indoor range of 2x2m square was used as a test section, with the projectiles fired at a close range of 25m from the intended location of the ground effect investigation to minimise the effect of gravity on the desired horizontal trajectory.

### 3.2.1.3 Apparatus, technique and experimental conditions

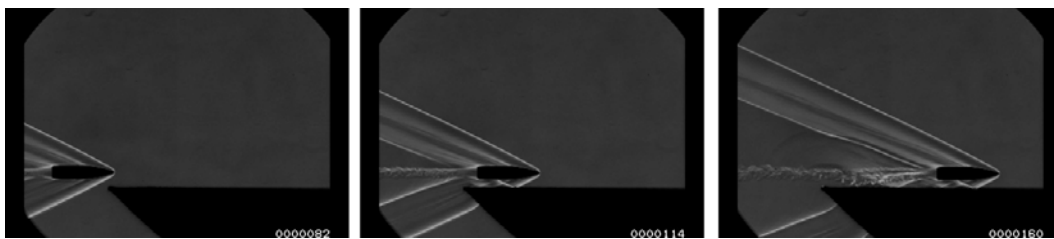
A simple ‘table’ of MDF board was used as the ground plane. A NATO 5.56mm round was fired from an ADI AUSSTEYR A1/A2 rifle at a Mach number of 2.4. Powder loads were adjusted to achieve this, in order that wind tunnel tests using an existing Mach 2.4 liner for the ADFA supersonic blowdown tunnel could be made for subsequent comparison.

The projectile, as shown in the schematic of figure 3.5, is composed of an ogive forebody, a narrow knurled strip to aid in the sealing of the projectile within the cartridge



3.5  
FIG

Schematic of the projectile used for live-range experiments, dimensions in mm.



3.6  
FIG

Schlieren stills from the live-range experiments show the unsteady evolution of flow around a projectile entering the ground-proximity regime (Doig *et al*, 2007b).

case, a near-cylindrical main body which contacts the rifling of the barrel directly on firing, thus inducing spin, and a tapered boat-tail blended to the flat, solid base. Grooved striations of approximately  $7^\circ$  (produced by the barrel rifling) are present on the projectile main body in flight, and the rate of spin of the projectile under the test conditions described was determined from subsequent calculations, based on the barrel geometry and the striations measured on the projectile, to be  $17700\text{rads}^{-1}$  upon leaving the barrel (Purdon, 2006). The Reynolds number for the projectile in flight was determined to be  $1.056 \times 10^6$ .

A variety of ground clearances over a horizontal plate of MDF were observed using time-resolved schlieren from a high-speed video camera (Shimadzu HPV-1). The video was captured at 500,000 frames per second (fps), and some frames from one test, where the field of view includes the leading edge of the MDF, are shown in figure 3.6.

The experimental conditions at the time of testing were such that the ambient density was measured as  $1.026\text{kgm}^{-3}$  and the static pressure in the room was assumed to be  $101300\text{Pa}$ . Time-resolved schlieren video was the only technique used to produce results.

#### 3.2.1.4 Experimental Error

The Mach number of 2.4 had an estimated error range of  $\pm 0.03$  ( $10\text{ms}^{-1}$  on an airspeed of around  $815\text{ms}^{-1}$ ) at ambient conditions, based on test firings which were assessed with high accuracy by Australian Army trajectory-tracking equipment. Subsequent analysis of the schlieren images for a simple correlation between distance, time and speed confirmed the speed of the projectile as  $815\text{ms}^{-1}$  within the experimentally obtained error envelope.

The camera was limited to a maximum of 103 frames for each experiment, and the field of view was limited to  $105 \times 87\text{mm}$ . The resolution of the camera was  $312 \times 260$  pixels. While still images can be compared to show the effects of gravity over the field of view, precise determination of the movement of the projectile is difficult due to the low resolution of the video. An error of around 2 pixels ( $0.07d$ ) is involved in any measurement from the video of ground clearance or movement, which, at the lowest clearances observed in the tests (around  $0.75d$ ), would equate to an envelope of error of just over 9%. This is considerable, but in this instance only applies to CFD cases intended for direct comparison to experimental schlieren.

During the firings, “good” repeatability of ground clearance was defined as  $1d$ . Neither the rifle nor the round are intended for high-accuracy firing (Purdon, 2006). In this instance, good repeatability is not necessarily an issue given that a variety of ground clearances was obtained at any rate, and the schlieren obtained is the only aspect used for validation of the CFD model.

The spin of the projectile was calculated based on the assumption that the projectile instantly reaches the maximum muzzle velocity. Though no approximation of error is quoted in existing literature, but it is unlikely to be a significant value as the striation markings on the projectile are consistent with the quoted value (Purdon, 2006).

The determination of the centre of gravity, which is used to evaluate the pitching characteristics of the projectile in chapter 4, contained significant assumptions - the body was simplified to comprise of an axisymmetric lead cylinder and a steel cone. Therefore the stated value of  $17.2\text{mm}$  from the nose of the projectile (Purdon, 2006) is likely to

contain a fairly high margin of error, but this is difficult to evaluate without more detailed information regarding the projectile, or a physical specimen, and thus is taken as-is.

### 3.2.2 UNSW@ADFA Supersonic Blowdown Wind Tunnel

#### 3.2.2.1 Objective

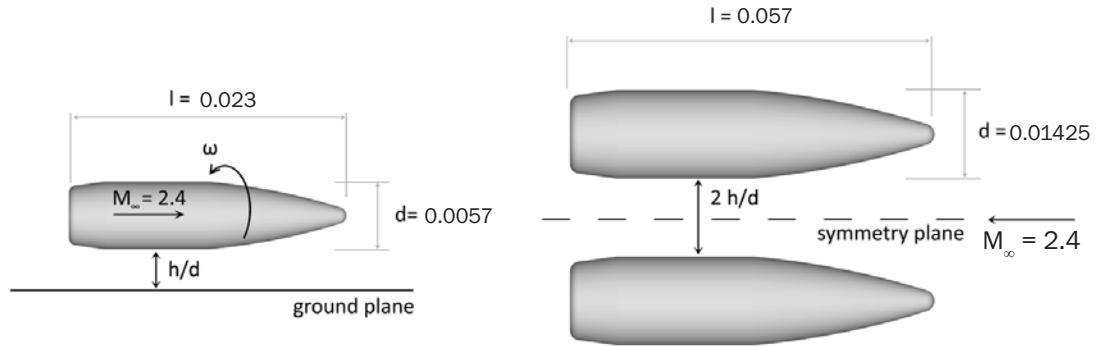
The projectile topic was investigated further in a subsequent UNSW@ADFA undergraduate thesis (Appleby, 2007) which involved blowdown wind tunnel experiments to recreate the flowfield. These used an elevated ground plane and a simplified, scaled model to attempt to attain a general answer as to whether the pressure distribution would change enough to influence the trajectory of the projectile. Experiments conducted later by Kleine (Kleine *et al.*, 2007), with a symmetry method based on that devised by the present author, aimed to more accurately model the live-range scenario. They were performed in the same facility and thus the test program is treated as contiguous.

#### 3.2.2.2 Facility

The working test section of the blowdown tunnel at the School of Aerospace, Civil and Mechanical Engineering was 155mm x 90mm and run times of approximately 20s were possible at Mach numbers 2 and 2.4, for which solid section liners exist. Static pressure on the tunnel wall was measured at a discrete tapping upstream of the test section window, and detailed output on the stagnation conditions was recorded during each run.

#### 3.2.2.3 Apparatus, technique and experimental conditions

The elevated ground plane was a remnant from a set of experiments on another topic (Dillon, 2005). It sat at the approximate vertical centre of the tunnel, with the leading edge some considerable way upstream (69mm, or 1.2 projectile lengths) of the location of the projectile model's leading edge. An instrumented projectile model, with a sting at the base, was placed in proximity to the ground. The model was scaled to be 2.45 times the



Parameters of importance for the live-range round (left) and the symmetry method wind tunnel model (right), dimensions in mm.

Table 3.1. Experimental parameters

	Live-Range	Wind Tunnel
Mach number	2.4	2.35-2.4
Reynolds Number	$1.056 \times 10^6$ (approx.)	$1.31 \times 10^6$ (approx.)
Spin rate	$17700 \text{ rads}^{-1}$	n/a

original size, and eight discrete pressure tappings on the surface of the projectile (6 located axially on one side of the projectile, 2 on the diametrically opposite side) were present, with the model rotating around its axis at  $30^\circ$  intervals to provide detailed circumferential mapping of the pressure distributions. The ground plane was also pressure-tapped in a staggered fashion to provide additional information. A ground clearance of  $h/d = 0.42$  was the only one tested with the instrumented model. The model was grooved with striations at an angle designed to represent the actual ones at the increased scale. The experiments were repeated at a later date in a much more extensive programme, using the symmetry method as the primary technique after an investigation suggested it would provide a greatly enhanced simulation of the live-range scenario (Doig *et al.*, 2008a).

The model was pressure tapped as before, but the striations were removed. Multiple ground clearances were examined, but a clearance of  $h/d = 0.5$  was the only one made available for use in this thesis. Colour schlieren photographs were taken during all the experiments to provide good comparison with the live-range tests.

The Reynolds number of the experiment based on the model length scale was



The instrumented projectile in the ADEFA tunnel with ground plane (Appleby, 2006).

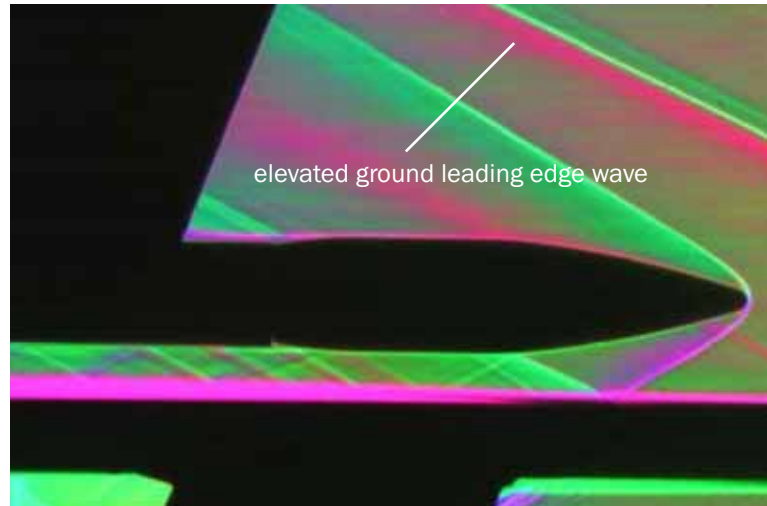
$1.31 \times 10^6$ , which is 1.24 times the live-range Reynolds number, and thus within a reasonable margin of dynamic similarity for a flow regime where similarity in the Mach number is overwhelmingly the most important factor.

#### 3.2.2.5 Experimental Error

The desired Mach number of 2.4 was not precisely reproduced in the wind tunnel, sitting generally 0.01 to 0.04 short across a variety of tests at several ground clearances. However, since the tunnel conditions can be directly reproduced in CFD, such discrepancies were not deemed critical in determining the effectiveness of the numerical method when comparing to experimental results. However, the leading edge of the ground plane split the flow in a region where the test section walls are not quite yet parallel, and thus the Mach number “seen” by the model would not have been quite the value which was determined from the upstream static pressure port. The Reynolds number discrepancy discussed above is not expected to have had any significant effect on the flowfield as compared to the live-range experimental conditions.

An issue with the elevated ground which will be discussed further in Chapter 5 is the wave which originated from the leading edge as highlighted in figure 3.9. It is not known what significance this would have to the flow conditions subsequently seen by the projectile model, but is likely to have been produced by a combination of several factors: the leading edge not being perfectly sharp or uniform due to manufacturing tolerances,

Schlieren image of the projectile model with elevated ground plane, highlighting wave produced by the leading edge of the elevated ground.



the leading edge not being quite aligned with the flow, and the formation of the boundary layer at the leading edge perturbing the flow enough to cause a weak disturbance. However, measurement of the shock angles in the tunnel tests showed excellent agreement ( $<<1^\circ$  difference) with the live-range schlieren, indicating that the Mach number would have been close to the anticipated value.

Repeatability of the experiments proved to be adequate, and is represented as error bars later in this thesis in comparisons to experiments. The sensitivity of the symmetry method to manufacturing and installation considerations, which were not directly quantified, may have factored into the results, but no significant discrepancies were observed or measured. The models featured a sting at the base of the projectile which was designed to avoid interference with the flow around the rest of body, but no formal study of possible interference in the boundary layer over the boat-tail section was made.

## 3.3 Transonic Wind Tunnel Methods

### 3.3.1 Objective

The experimental programme was devised as a transonic equivalent of the supersonic tests, in order to determine if the symmetry method was still an effective approach at high-subsonic conditions, where the size of the boundary layers would be more of a consideration. It was also deemed a vital step in validating the CFD, since the behaviour of the flow in the transonic regime, including the potential for transient shock oscillations and shock-separated flows, would be the most difficult test for the numerical method to reproduce. Furthermore, supersonic bodies must traverse the transonic region, and such Mach numbers are more appropriate for most of the applications discussed throughout this thesis, including other military projectiles.

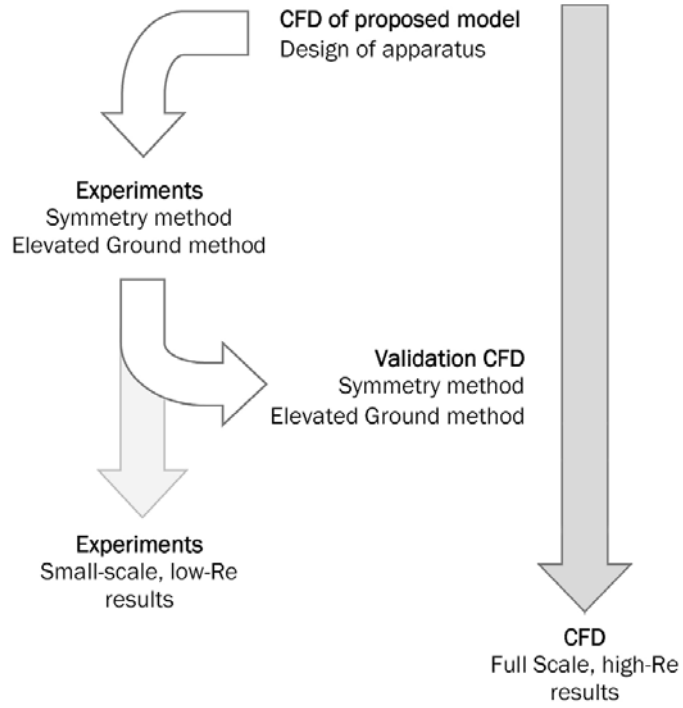
The experiments themselves would also provide data which could be used to provide insight into the consequences of shock formation in ground proximity. As an ancillary benefit, the functionality of the test facility itself could be assessed, it having not been used for research in decades. Initially a wide-ranging programme was envisaged for testing the RAE2822 and M6 wings using a variety of measurement techniques, but unfortunately due to time and financial constraints this was curtailed to simple pressure measurements using an RAE2822, for three variables: ground clearance, angle of attack, and Mach number. Approximately 5 days was devoted to calibration and the solution of minor problems with the model installation and the pressure tapping system, and 5 days to the final test programme.

The aims in summary:

- » Comparison of the elevated ground and symmetry method, in tandem with CFD to evaluate the relative success of each approach.
- » Acquisition of enough data to validate the CFD over a wide range of flow conditions.
- » Use of data to examine transonic ground effect flow at  $Re < 1 \times 10^6$ .

3.10

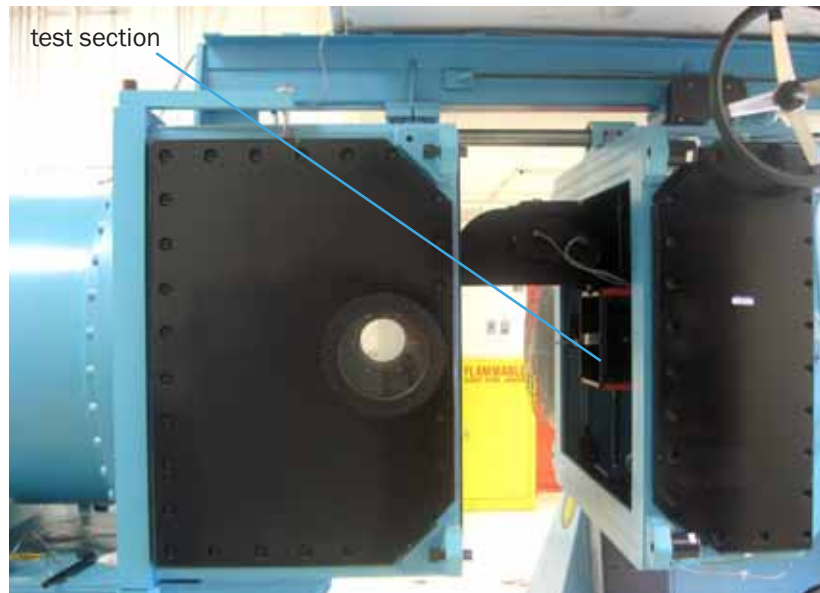
FIG



Role of transonic experiments in cooperation with CFD.

3.11

FIG



The US Naval Academy Transonic Blowdown wind tunnel, with test section open. Flow direction would be left to right.

### 3.3.2 Facility

The transonic wind tunnel of the U.S. Naval Academy in Annapolis, Maryland was damaged by Hurricane Isabel in 2003, yet had not been used extensively prior to this. Subsequent refurbishment of the laboratory led to the eventual restoration and recalibration of the tunnel, to a standard such that the tunnel was deemed to be highly reliable and fully operational for these tests. Nevertheless, the experiments conducted represented the first proper usage of the tunnel in some considerable time, and due to a limited testing campaign a more thorough exploration of the limitations of the tunnel was not possible. The tunnel with test section is shown in figure 3.11.

The tunnel features a test section of cross-sectional area of  $0.0418\text{m}^2$ , with dimensions of  $0.2057 \times 0.2032\text{m}$  (8.1”h, 8”w), and incorporates optional adjustable porous ceiling and floor plates which vent/suck air to/from a plenum chamber of nominally-atmospheric conditions. Mach number is varied as a function of stagnation pressure coupled with the use of a downstream choke; values for both were selected based on the calibration data which had previously allowed a determination of settings designed to produce the greatest proportion of constant desired Mach number flow in the test section. Tests were made with the porous walls partially open, and fully-closed, the latter of which were used for most of the experiments in order to facilitate more reliable CFD modelling of the test conditions with simple boundaries. This is commonly recommended (but seldom implemented) for any code validation of this nature (Aeschliman and Oberkampf, 1998). The porous surfaces can be seen later in figure 3.17.

The roof-mounted sting sits partially in the diffuser section of the tunnel in a region behind the test section, the cross-section of which can be adjusted by increasing or decreasing the angle of the ‘flaps’ which make up the 4 walls there. Again, advice was taken from the calibration figures for flow uniformity, and little experimentation was made with these flap angles.

The turbulent intensity of the flow in the test section (variations in the quality of

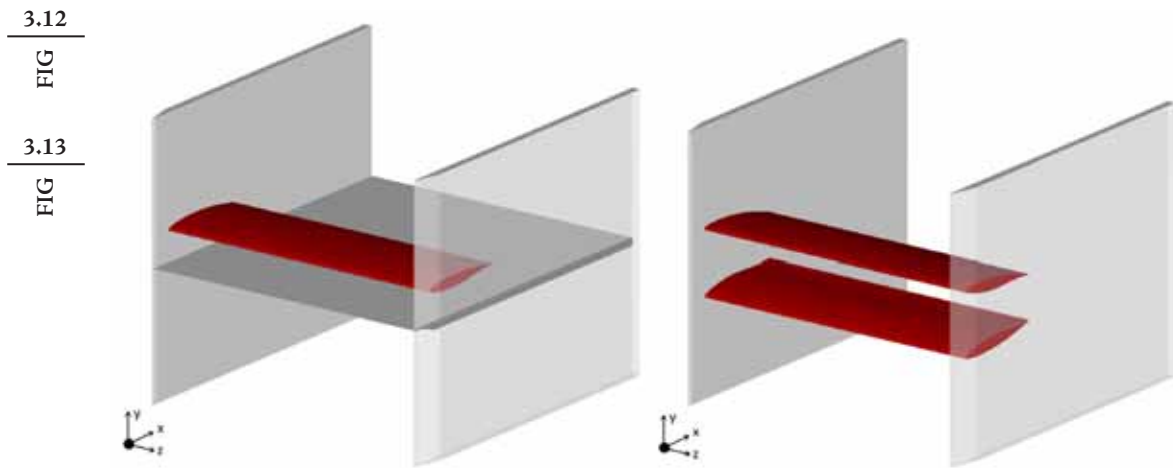
the mean flow during a run) was calculated for the first time during these tests, using the simple equation:

$$I \equiv \frac{u'}{u_{\text{avg}}} = 0.16(\text{Re}_{D_H})^{-1/8} \quad \text{eqn. 3.1}$$

where  $\text{Re}_{D_H}$  is the Reynolds number based on “hydraulic diameter” for pipe flows or characteristic length for the current purposes. An average value of  $I$  of 0.16% was obtained by evaluation of data from runs with the test section empty, at 3 Mach numbers, and was remarkably consistent, with a variation of no more than 0.02% from run to run. At this value, the tunnel was deemed to provide an acceptably low level of turbulence.

### 3.3.3 Apparatus, technique and measurement techniques

The symmetry and ground plane apparatus for the tests are shown schematically in figures 3.12 and 3.13. The wing is an RAE2822 section, the coordinates of which can be found in AGARD (Cook *et al.*, 1979). The chord was nominally 60mm (close to 10% of the scale used in the AGARD experiments), but the trailing edge was purposely blunted after manufacture to ensure a consistent edge, such that the actual chord was 58mm. The span was 180mm as manufactured to give an AR of 3, and once at the Naval Academy this was shortened to 176mm to ensure the side of the wings were flush and



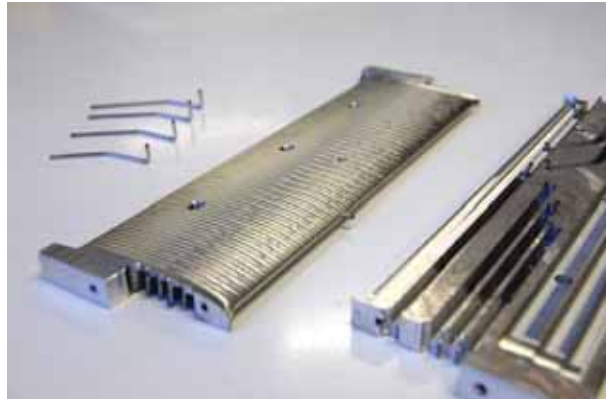
The elevated ground method setup with endplates.

The symmetry method setup with endplates.

3.14

FIG

The wings after the first stage of machining showing (left) the rough first pass to form the 2822 profile and (right) the grooves machined to allow the laying of hypodermic pipe to the tapping locations.



3.15

FIG

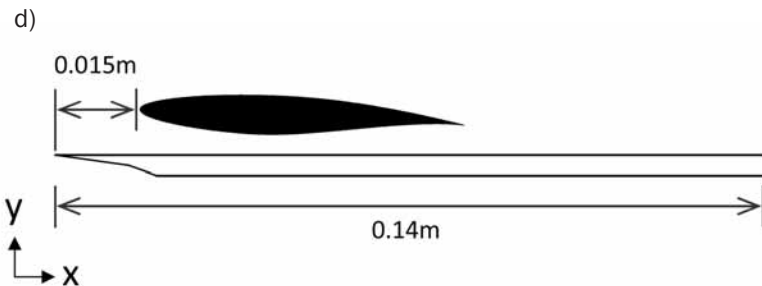
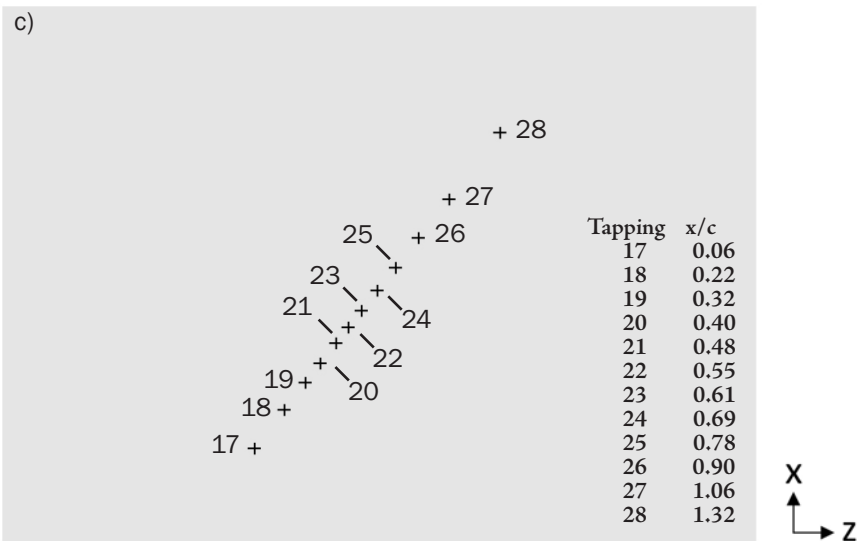
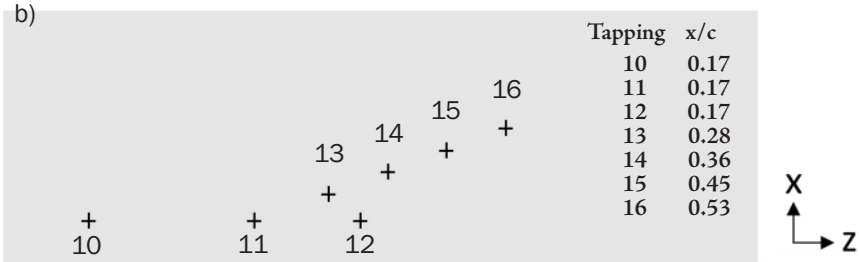
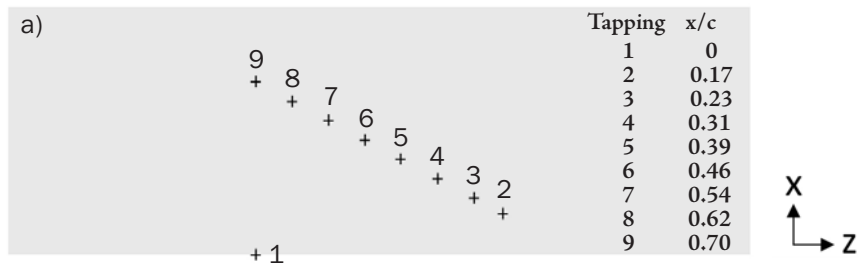
The wing in its mould following laying of the hypodermic pipe and subsequent re-profiling with body-filler machined back to the 2822 profile.



perpendicular with the endplates after it was discovered that the entire assembly was twisting. The modifications eliminated this twist and ensured that the wing/endplate junction was flush.

The wings were machined from aluminium and sanded extensively to ensure a smooth surface. Grooves were cut into the wings to lay hypodermic pipe which then exited the wings at the side, into gaps in the endplates, which were milled from mild steel. These grooves were then filled up with resin body-filler, which was sanded back to be flush with the aluminium surface. Stages in this process can be seen in figures 3.14 and 3.15. The internal diameter of the hypodermic tube was 0.5mm, which was considerable in relation to the dimensions of the wing, but was deemed necessary due to the technique of bending the tube into shape, which with a smaller diameter would be more likely to result in crimping and blockage of the passage.

Due to the very small internal volume of the wings, a decision was made to have a set of tappings for the upper surface on one wing, and separate tappings for the lower surface on another wing. If the apparatus was very close to being symmetric between



A schematic of a) wing A with lower surface tapplings, b) wing B with upper surface tapplings, and c) the elevated ground tapping locations and d) location of the elevated ground plane relative to wing B.

the top and bottom wing, this provided one complete set of upper and lower pressure readings per test.

The transducer bank available at USNA was able to take readings from 16 tappings at any given time, and thus the wings were designed to produce 16 readings in symmetry configuration. The tappings were staggered so as to avoid excessive influence from the wake/wave disturbance of one port to the next, given the relatively large size of each one.

“Wing B” featured 7 tappings on the upper surface, arranged as shown in figure 3.16. Tappings designed for use in producing pressure readings which could be presented in a chordwise fashion were confined to the middle third of the wing, where it was reasoned the flow would be two-dimensional to within a reasonable margin of error. Tappings 1, 2 and 3 were arranged at  $x/c = 0.17$ , with spanwise  $z/b$  locations of 0.10, 0.30, and 0.48. This was aimed at providing a rudimentary way of assessing the two-dimensionality of the flow in the region of the chordwise pressure tappings - this will be discussed further in the coming chapter.

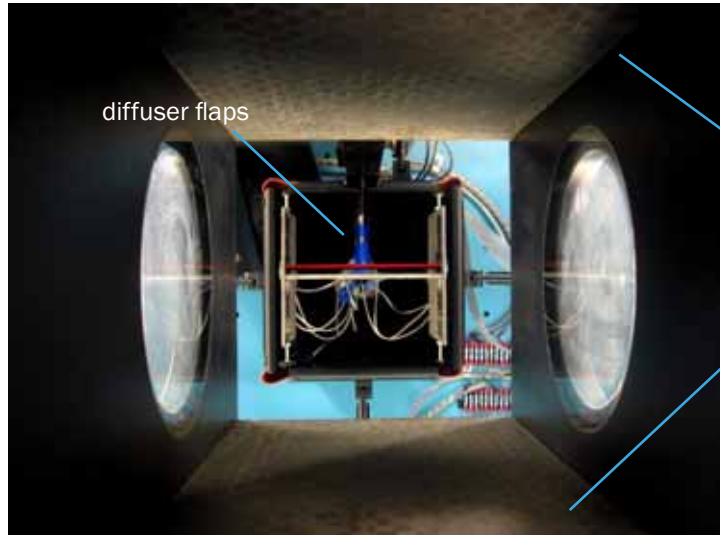
The lower surface of wing A featured a more detailed arrangement of 9 tappings, again in a staggered fashion as shown in figure 3.16a. Given that the expectation, from early CFD on possible configurations, was that a lower-surface shock, produced by close ground proximity, would be produced at  $M_\infty = 0.6$ , the increased emphasis on the lower surface for pressure readings was a reasonable choice in sacrificing greater resolution on the upper surface. A tapping at the leading edge was introduced to provide a stagnation pressure reading, although the size of the port in relation to the leading edge was considerable and would have affected the port or ports downstream.

The elevated ground was tapped at 12 locations, staggered diagonally across the middle 1/3 of the structure as with the wings. Several tappings were located downstream of the wing trailing edge, but otherwise the points were clustered somewhat towards the point at which the wing's maximum thickness would occur and thus where the strongest gradients would likely be observed.

Three coats of paint were applied to the wings (not the ground plane) to smooth

3.17

FIG

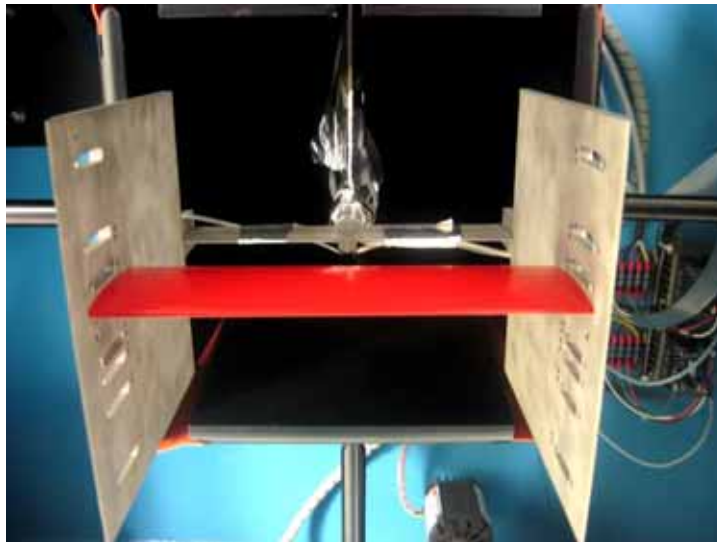


porous ceiling and floor (closed)

An elevated ground setup viewed from upstream, inside the open test section, prior to securing of the vinyl tubing.

3.18

FIG



One of the wings in "free flight" configuration (no ground plane), prior to sealing of the endplate holes with aluminium tape.

any residual deficiencies in the surface quality, with each coat sanded to an acceptable finish again. The wings were measured with digital callipers to check find any variation from the original specifications, as is discussed in section 3.2.3.

The wings, endplates and rear sting mount strut together comprise a test section blockage of 12.1%, which is a considerable amount - the effect of this shall be discussed shortly. This figure is for 2 wings in symmetry configuration, at  $0^\circ$  angle of attack. The blockage is slightly higher (12.8%) for the wings at  $6^\circ$  angle of attack, and slightly lower for the tests involving the ground plane, as the rear sting mount strut is largely 'hidden' from the oncoming flow by the ground plane itself, and the ground plane is 2mm thinner than the wing. Therefore for the tests with the ground plane, the maximum blockage was



Wings in symmetry configuration; image shows the support “feet” used to brace the model, and the aluminium tape covering endplate holes.

9%. With the single wing in the tunnel for gathering “free flight “ data on the wing, the blockage was 6%.

For these “free flight” tests involving one wing, the section was positioned in the lowest-clearance location (i.e. closest to the tunnel centreline), which gave it approximately 2.5c distance from the tunnel roof.

The endplates were introduced because modifications to the tunnel wall were not possible. A means to thread the vinyl tubing attached to the tapping ports on the sides of the wings to the ports at the rear of the test section was required, and could not be allowed to interfere with the flow over the wings. Therefore holes were cut in the endplate for each ground clearance to facilitate this - when not in use, the holes were covered with aluminium tape flush with the rest of the endplate to avoid irregular flow disturbances; this method was qualitatively observed to not present a significant perturbation to the flow. The leading edge of the plates was given a double angle to form a double wedge, to minimize potential separation there, given that the flow was being quite heavily constricted in the gap between the endplates and the walls. The effect of this is discussed in chapter 6 - CFD provided much insight into the effect of the endplates (See Chapter 4), but for now we will concentrate on the experiments alone.

The wings were held in place with one screw close to the leading edge, and a dowel

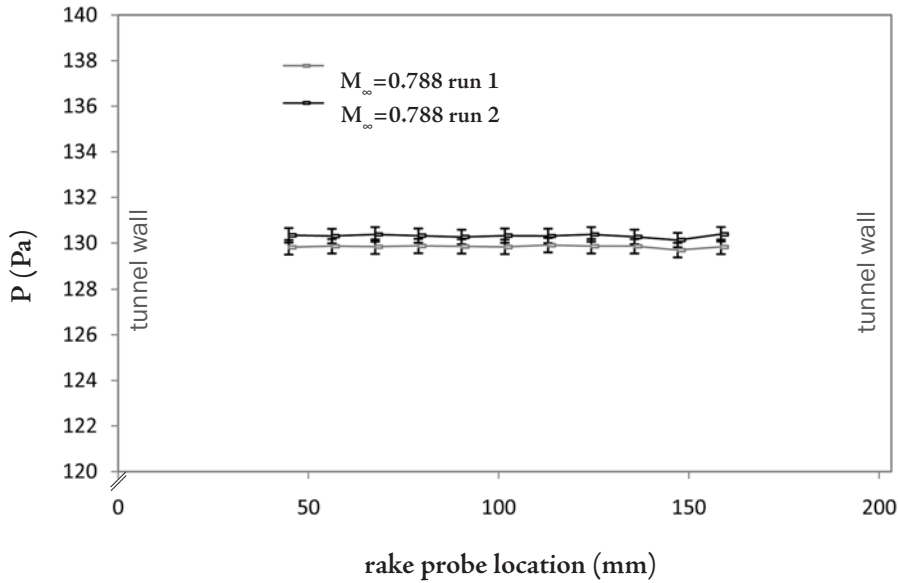
at the trailing edge. Positioning holes were present in the endplates such that 4 ground clearances and 2 angles of attack were possible, though the greatest ground clearance (1.02c) positioned the wings closer to the tunnel roof and floor than to the ground plane, and thus results from tests here were not used for anything other than data-gathering on other wall effects with a single wing.

To minimise the weight of the assembly and to allow the vinyl tubes to ‘hide’ from the freestream flow somewhat, a 3mm pocket was cut into the majority of the outside of the endplates behind the wing location.

The sting itself was found to experience an unacceptably-large deflection in the vertical plane with wind on, and thus in order to brace the assembly against the roof and floor of the tunnel, small support screws were attached to the endplates to act as ‘feet’, with thin rubber ‘boots’ glued on to protect the porous surface from damage. These screws added around 0.05% to the blockage of the tunnel. The bumps created by the taped-down tubes from the pressure taps increased the blockage slightly, but this was not quantified. The support “feet” are shown in figure 3.19.

Atmospheric conditions were noted at the start of each test session (morning and afternoon sessions on each day) and variations were factored in to the determination of all experimental properties calculated subsequently.

The flow properties of the tunnel, including static pressure as measured at a port upstream of the test section windows, were sampled at a rate of 10Hz. These included stagnation pressure and temperature as well as tunnel static pressure. The readings from the static ports on the wings and ground were taken as time-averaged data of 100 samples (10 readings taken for each port simultaneously, with a sequence of 10 sweeps of this procedure) with a calculated standard deviation, rather than raw data. The sample rate was not sufficient to accurately capture the higher frequencies associated with oscillatory shock behaviour, and thus it would be misleading to treat the data obtained as truly representative of transient behaviour. A large standard deviation was indicative in itself of transient behaviour in certain cases, as will be discussed later.



Flow uniformity in the centre of the tunnel along a horizontal plane, using a rake probe for a freestream Mach number of 0.788.

### 3.3.4 Experimental Error

A simple RMS was used to determine error in the calculation of pressure coefficients at each discrete point measurements were taken at, which are presented in this and subsequent chapters. A variety of other sources of error are discussed, but because of insufficient data (due to a lack of either a suitable means for measurement, or the time at the facility to make the necessary tests) these are left out of the error bars with which the results are presented.

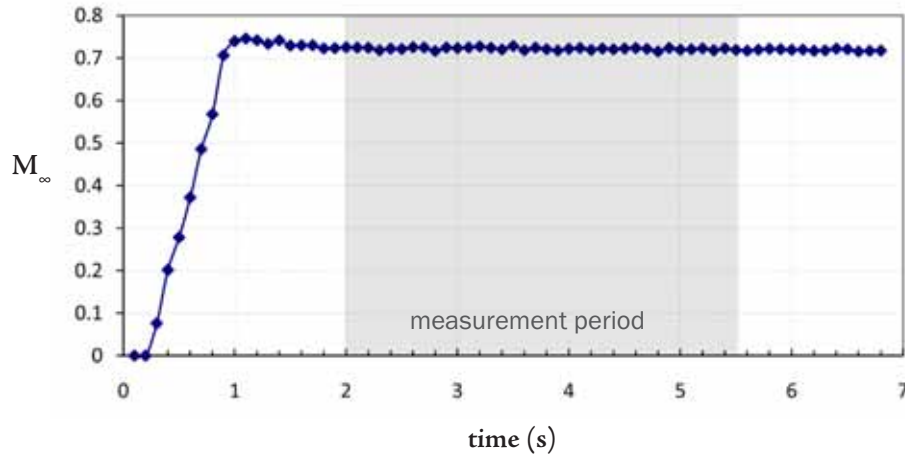
The RMS approach is based on the components of the  $C_p$  equation (assuming unit sensitivity of each term), and takes the general form:

$$x_{rms} = \sqrt{\frac{x_1^2 + x_2^2 + \dots + x_n^2}{n}} \quad \text{eqn. 3.2}$$

for which the standard deviations of the velocity, freestream static pressure, and discrete static pressure measurements were derived from experimental data, and errors implicit in the calculation of freestream density stemmed from established limitations in the instruments used to measure temperature, as well as the known fluctuations in stagnation pressure.

3.21

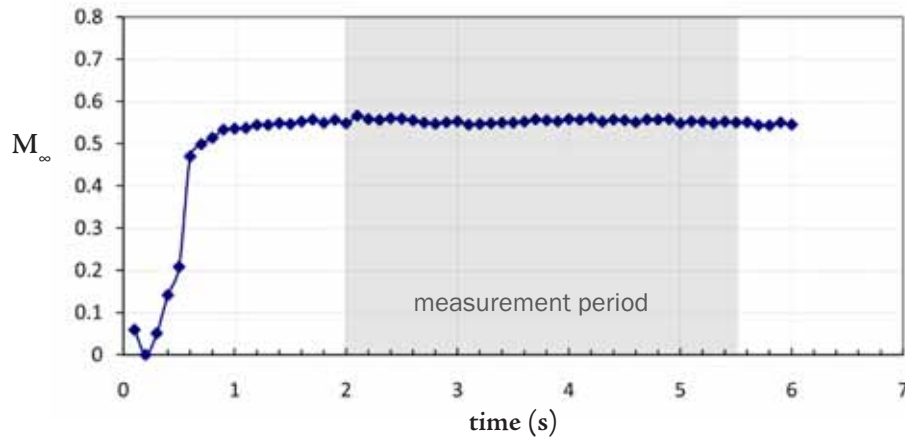
FIG



Mach number histories for one tunnel run, average  $M_\infty=0.553$  during measurement period.

3.22

FIG



Mach number histories for one tunnel run, average  $M_\infty=0.553$  during measurement period.

It is estimated that all other sources of error would be potentially of an order of magnitude less important, following regular calibration procedures, and that cumulative errors due to uncertain measurements being used in isentropic flow relationships to obtain exact values would be similarly lower-order. Repeatability of the experiments proved to be excellent, albeit only assessed for a handful of test cases; the maximum deviation in average Mach number for any desired value was determined to be  $\pm 0.003$  for experiments conducted for several stagnation pressures and atmospheric conditions. Repetition of experiments with separations of more than a few hours was not possible due to time constraints.

Prior to the experiments involving the wing, an 11-probe stagnation pressure

rake was placed in the test section, spanning a vertical or horizontal distance of 125mm. Flow uniformity was tested at Mach numbers of 0.6 and 0.8, although the nature of the rake unfortunately could not provide information in the near-wall regions. A sample result, typical of all those obtained, is shown in figure 3.20 for the rake in horizontal alignment for two runs at a freestream Mach number of 0.788 - the uniformity is very good over the averaged period and the repeatability of the experiments was further shown to be excellent with the trends in readings consistent despite different supply stagnation pressures. The Mach number difference between repeated cases was found to be within the standard deviation of the Mach number within each run.

Fluctuations in the Mach number during two sample runs are shown in figures 3.21 and 3.22, and illustrate the fact that the flow was reasonably steady during the 3.5-4 seconds that were required to take the full set of measurements for each test.

Further uncertainty in the Mach number of the flow seen by the apparatus is introduced by the combination of flap and choke settings which influence the uniformity of flow throughout the test section, as well as the influence of boundary layer growth on the tunnel walls. Calibration documentation for the tunnel was used as a guideline for best-practice when determining the optimum settings for any desired flow condition. From this, a conservative Mach number correction of +0.005 was assumed to account for the increase in Mach number seen at the approximate model location, as opposed to that at the static port upstream of this point. Due to the proximity of the endplates to the tunnel sidewalls, it is appreciated that the extent of the boundary layers here is non-trivial; this influence is discussed later in the context of CFD simulations performed subsequent to the experiments, as detailed measurements at the tunnel walls were not possible at the time.

It is regrettable that boundary layer transition on the wings was not fixed for the experiments, and thus the location at which it occurred across the range of variables tested was not determinable. CFD described in chapter 4 indicates that transition is unlikely to have occurred more than  $0.3c$  from the leading edge, and fully turbulent simulations appear to provide a good comparison. Without further investigation, the

reasons for this remain unclear, although some possibilities arise. The potential for contamination of the transition line on the wing from the endplates is large considering the flow at the endplate inside leading edge was found with CFD to be separated in most cases, and often in a transient state. This, combined with the known fluctuations in the oncoming flow, and the likelihood that the surface finish, even after extensive sanding, was not smooth enough to sustain laminar flow over a large proportion of the wing, suggest that transition was triggered at a forward position on the wing. A fluctuating, non-linear transition line would have consequences for the shock location and behaviour on the wing, as has been observed by others for wings of similar aspect ratios (Sudani *et al.*, 1994). More detailed study using CFD on this aspect can be found in the following chapter, along with a discussion of the two-dimensionality, or otherwise, of the flow in the middle third of the wing where pressure readings were taken.

### 3.2.5 Further Manufacturing and installation considerations

General manufacturing tolerances for all model parts were nominally 0.05mm, however due to the nature of the machining process, extensive sanding of the wings was required and therefore a true tolerance of  $\sim 0.2\text{mm}$  is more likely for the most crucial parts, based on measurements made with digital callipers. This represents 2.5% of the wing thickness, or a little under half a percent of the chord length. This tolerance becomes particularly important at low ground clearances. Additionally, it was known that the wings were not identical in maximum thickness due to one having moved slightly in its reshape mould during machining, and given the sensitivity of the symmetry method to any asymmetry, this cannot be discounted. However, it was not possible to directly quantify this issue at the time of testing.

Once mounted to the sting and placed in the test section, with the “feet” of the assembly in contact with the floor and ceiling of the tunnel, a digital inclinometer was used to ensure that the wing was level (i.e. one “foot” was not sitting lower at one side than the other). This accuracy was to within  $0.1^\circ$ . With the wind on, however, it is unlikely that there would have been no deflection of the model. As has already been noted, there

was considerable travel in the sting which resulted in the “feet” being implemented in the first place. Therefore, whilst vertical travel in the tunnel would be no more than a fraction of a mm due to compression, sideways travel could have occurred to an extent that the alignment of the wing to the flow would have been imperfect. Furthermore this would have the undesirable effect of producing more pronounced endplate effects at one side of the wing than the other. Such deflection was not possible to assess in the limited time available.

Due to the possibility of minor travel with the wind on with respect to angle of attack, given the malleability of the dowels used to secure the rear portion of the wing, a standard error of  $\pm 0.1^\circ$  is estimated. Ground clearance could also be somewhat affected by the minor travel, and is estimated to be 0.1mm in all cases. While these geometric sources of uncertainty are not factored into the error bars presented in the graphs of pressure coefficient, they are almost certainly at least a moderate factor in the occasional discrepancies between the CFD and experimental results, particularly at the lowest ground clearance.

### 3.4 Summary

Two sets of experiments have been described for the Mach 2.4 projectile: a live-range firing, followed by wind tunnel recreations at a larger scale, but for approximately the same Mach number and a similar Reynolds number. The wind tunnel tests used both an elevated ground and symmetry method, to allow comparison between the two approaches as compared to the ideal case of the live-range experiments. Live-range repeatability was found to be poor with respect to ground clearance, but wind tunnel repeatability was acceptable.

For the RAE2822 section in the transonic blowdown tunnel, a full description of apparatus and experimental conditions was provided, along with detailed descriptions of sources of error. Again, a symmetry and elevated ground plane method were used. Repeatability of experiments was found to be excellent with regards to Mach number,

and flow uniformity was satisfactory. The porous roof and ceiling of the tunnel were not used, so as to facilitate a more reliable comparison of CFD to the experiments.

It is unfortunate that the shortfalls of the experimental setup for the transonic tunnel could not be revised for a second campaign, but practical considerations of cost ruled this out. However, as we shall see in the subsequent two chapters, sufficient data was gathered to both validate the CFD and provide insight into the suitability of the methods for investigating real-world problems at scale in the blowdown tunnel.

Now that the experiments have been introduced, it is possible for the numerical methods to be rigorously validated against the test data to ensure that all subsequent CFD can be treated as reliable.

# Chapter: Validation of CFD



*In this chapter the focus is a thorough assessment of the meshes and turbulence models applied to each geometry studied. Low speed (Mach 0.0882) inverted wing results are compared to experimental results in literature, transonic RAE 2822 and ONERA M6 cases are compared to both experimental results in literature and those conducted as described in chapter 3, and the method used to generate the supersonic projectile results is validated against the live-range and wind tunnel results also outlined in chapter 3.*

## 4.1 Introduction

**H**aving arrived at a general numerical approach, as described in Chapter 2, the focus of this chapter concentrates on the problem-specific issues of mesh and turbulence modelling. Each body investigated presented its own unique issues of flow and geometric representation, and thus each is compared in detail to available experimental data from both literature and experiments as described in the previous chapter.

The general procedure was as follows: with a fixed turbulence model, determine the mesh which would best facilitate the most accurate capture of all important flow features within the constraints imposed by computational resources available. Following this, the chosen meshing strategy was used in conjunction with a variety of turbulence models to assess their relative strengths and weaknesses in order to make an informed choice as to the most suitable model for the flow under consideration. Additional aspects

Table 4.1 - Outline of validation cases

	Low-Subsonic	Mid-high Subsonic	RAE 2822 'Case 10'	ONERA M6 Test 2308	RAE 2822 @ USNA	Supersonic
<b>Cases</b>	TO26 Inverted Wing	RAE 2822 'Case 9'	RAE 2822 'Case 10'	ONERA M6 Test 2308	RAE 2822 @ USNA	NATO 5.56mm Projectile
<b>2d/3d</b>	3d	2d	3d	3d	3d	3d
<b>Mach Number</b>	0.0882	0.73	0.75	0.8395	0.5-0.75	2.35-2.4
<b>Reynolds number</b>	$4.59 \times 10^5$	$6.5 \times 10^6$	$6.2 \times 10^6$	$11.72 \times 10^6$	$6-10 \times 10^5$	$1.31 \times 10^6$
<b>Angle of incidence <math>\alpha</math></b>	-3.45°	2.79° (corrected from 3.19)	3.19°	3.06°	0°, 6°	0°
<b>Ground clearance</b>	$h/c=0.067$ to $0.313$	n/a	n/a	n/a	$h/c=0.1$ to $1$	$h/d=0.42, 0.5$
<b>Fidelity of CFD geometry</b>	simplified wind tunnel test section	free-flight 2d model, conditions corrected from wind tunnel data	simplified wind tunnel test section	free-flight model, no corrections from wind tunnel data	wind tunnel test section, with and without simplified sting	wind tunnel test section, with and without simplified sting

of geometric simplifications to the CFD model are also discussed here, as are the more complicated matters of wind tunnel wall interference and its influence on the properties of shocks in the flow. An outline of the cases used for validation is given in table 4.1.

As well as running through the necessary validation required for the presentation of CFD results in subsequent chapters, this chapter also serves to familiarise the reader with the many flowfields that are described and analysed in detail in the remainder of the thesis.

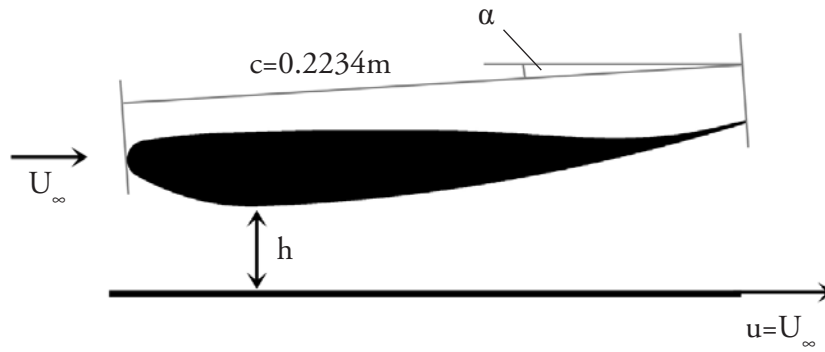
## 4.2 Subsonic Inverted TO26Wing

The coordinates of the aerofoil can be found in Zerihan (2001). It is a modified LS(1)-0413 MOD section, with a constant cross section chord of 223.4mm and a span of 1100mm (75% of the moving ground width), and features a rectangular endplate (250x100x4mm). The aspect ratio of the wing is therefore 4.92, and as such represents a wing approximately 80% of a full-scale Formula 1-style wing. The trailing edge of the main section was blunted to a finite surface of  $0.007c$  thickness.

The closed-circuit wind tunnel used for Zerihan's experiments had an octagonal test section of maximum dimensions 2.1 x 1.7m. An overhead force balance was used to obtain all force results, but little mention is made of quantifying the interference effects of either this setup or the test section walls. The freestream speed of the oncoming air was determined to be  $30\text{ms}^{-1}$ , with the moving ground belt set to the same velocity with an error of  $\pm 0.2\%$ . The chord-based Reynolds number for all experiments, at the conditions described, was in the range of  $0.430\text{-}0.462 \times 10^6$ . In the present CFD, density for all cases was kept at a constant  $1.225\text{kgm}^{-3}$ .

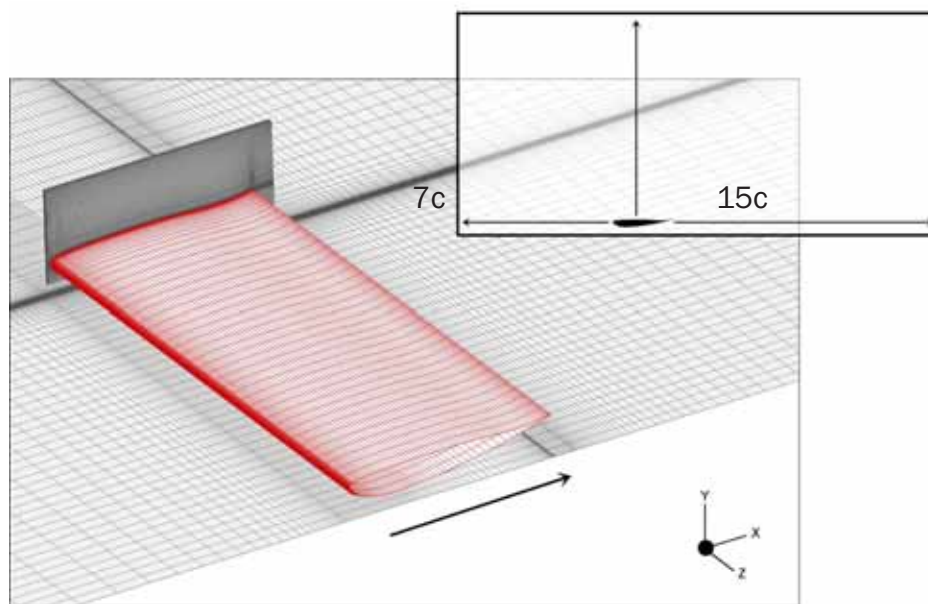
The wing was set at a 'true' reference incidence as described in Zerihan (2001) as equating to  $3.45^\circ$  (anticlockwise, or downwards, rotation from horizontal), with the ground clearance,  $h/c$ , measured from the chordwise point on the wing closest to the ground plane, as shown in the schematic of figure 4.1. Note that for all dimensional and non-dimensional distances quoted in this chapter, the coordinate origin is the leading

4.1  
FIG



Notation for an inverted wing in ground effect

4.2  
FIG



An example of the standard mesh for the Tyrell 026 wing with endplate, semi-span model (symmetry) for  $h/c=0.067$ .

edge point of the wing on the symmetry plane.

Freestream turbulence intensity was determined to be 0.2%, and boundary layer transition on the wing was tripped with a grit strip situated 10% of the chord from the leading edge to assist in the ease of CFD modelling. A full set of results was also obtained for a free-transition case. The flow was found to separate over a non-trivial portion of the wing as it transitioned, although there is no detailed discussion in on the effect of this on the results obtained. Force balance results for drag for the cases involving the transition strip were reportedly not as repeatable as other results (Zerihan, 2000).

Errors in the experimental results were simply calculated as a function of the

standard deviation in repeated tests - additional errors from other sources were not properly quantified. CFD in this study is therefore compared to experiments by treating the stated values as 'correct', in the absence of more reliable error reporting.

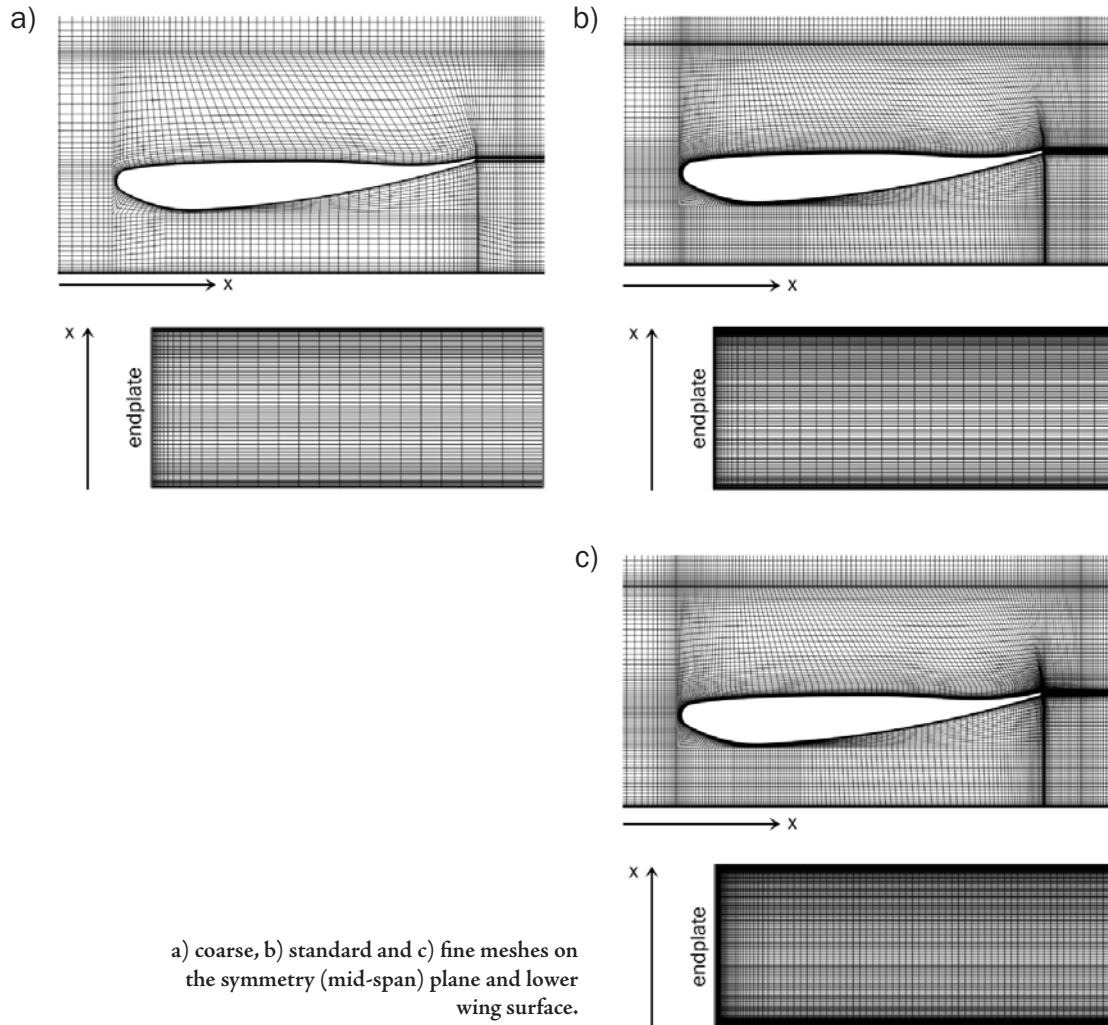
For the present study, comparisons are made to the experimental results for five ground clearances ( $h/c=0.313, 0.179, 0.112, 0.09, \text{ and } 0.067$ ), in terms of pressure distributions and forces (note: for the inverted wing, positive  $C_L$  indicates downforce). Incompressible and compressible cases were run in each instance to compare both modelling approaches.

#### 4.2.1 Mesh and Boundary Considerations

All cases were run as semi-span models with a symmetry plane. The boundaries of the wind tunnel described above were used, although as a rectangular cross-section rather than the octagon used in the actual tunnel. A geometrical description of this feature was not available and, although it would certainly influence the results used in validation comparisons, it does not affect the comparisons which comprise the majority of the study presented in this chapter. Further simplifications for the computational model incorporated a moving ground which spanned the full length and width of the test section.

The sidewall and roof were modelled as simple no-slip walls, and the test section was assumed to extend 7 chord lengths upstream of the leading edge, and 15 chord lengths downstream, as indicated on figure 4.2. For Chapter 6, a "free-flight" configuration was modelled by extending the domain below the wing to equal the space above it, creating a larger-than-life wind tunnel (i.e. the "free-flight" condition was not entirely free of wall effects).

A fully-structured multi-block mesh was generated using 68 volume blocks. Nodes were concentrated in the area around the wing and the endplate, and specifically in the vicinity of the wing and ground boundaries to facilitate enhanced wall modelling. The wall  $y^+$  was between 1 and 2 on the wing when flow was attached, and between 3 and 5 on the endplate and moving ground, for the cases at  $30\text{ms}^{-1}$ . The  $y^+$  reduced accordingly



with higher freestream velocities for the remainder of the simulations.

Coarse, standard and fine meshes, as shown in figure 4.3, were evaluated against the experimental data for  $h/c=0.179$ ,  $U_\infty=30\text{ms}^{-1}$ . Similar meshes were constructed for some other clearances but the results at  $h/c=0.179$  are entirely representative of conclusions made in all cases.

The coarse mesh featured approximately  $2 \times 10^6$  cells, with 130 cells around the wing in the chordwise sense (3 across the blunt trailing edge) and 30 spanwise cells, spaced such that the endplate wall region was adequately resolved. The standard mesh featured 190 cells around the wing (8 across the blunt trailing edge) and 45 spanwise cells, for a total of  $3.1 \times 10^6$  volume cells.

After comparisons showed little difference in surface pressure distributions for these two meshes, the fine mesh was constructed in a largely similar way to the standard

mesh but with a greater cell density in the endplate and wake regions to investigate whether the endplate vortices were being sufficiently resolved (and thus influencing the lift and drag forces obtained); it featured 195 cells around the wing and 80 spanwise cells, with a finer spacing in the wake region to approximately  $2c$  from the trailing edge. The total number of cells was  $7.65 \times 10^6$ .

All the mesh studies used the Realizable  $k$ - $\epsilon$  turbulence model with enhanced wall modelling - the influence of turbulence modelling is discussed in detail in section 4.2.1.3.

Figure 4.4 illustrates the lack of meaningful distinction between all three meshes in terms of surface pressure distributions around the wing at the symmetry plane; the coarse mesh appears to slightly underestimate the extent of the lower surface suction peak at approximately  $x/c=0.18$  but otherwise the plots are near-identical. A similar situation was encountered when comparing spanwise distributions at the quarter chord.

Comparing predicted lift and drag coefficients to the experimental results in figures 4.5 and 4.6 shows that the fine and standard meshes were within close agreement of each other ( $\sim 0.1\%$  difference), but the coarse mesh was overpredicting drag and underpredicting lift by a more noticeable margin. The higher drag is likely to be a consequence of having less cells in the immediate wake and on the blunt trailing edge, leading to a thicker near-wake.

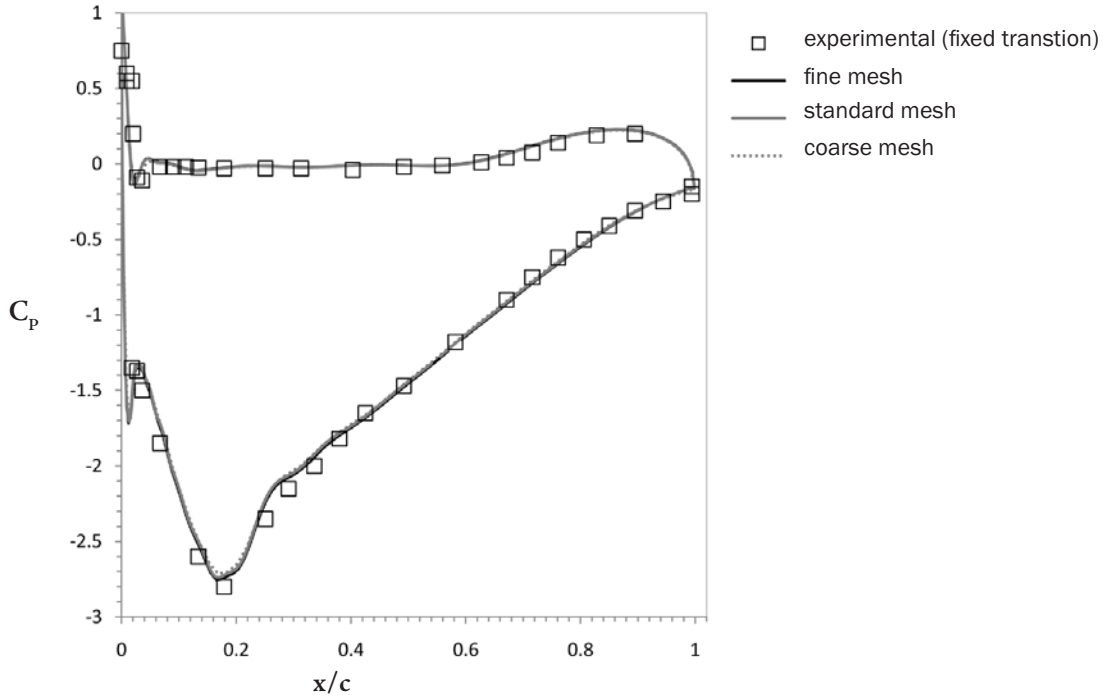
Given the evidence of an acceptably small difference between the results of the standard and fine meshes, the standard mesh was therefore used for all subsequent runs in an effort to limit unnecessary computational expense. Detailed experimental data pertaining to the location of the endplate vortices as they travel downstream was not available and thus a legitimate evaluation of these flow features with respect to mesh and turbulence model considerations cannot be undertaken here.

#### 4.2.2 Turbulence modelling

Three turbulence models in FLUENT 6.3, previously described in Chapter 2, were assessed for their suitability. To recap, these were the vorticity/strain-based Spalart-

4.4

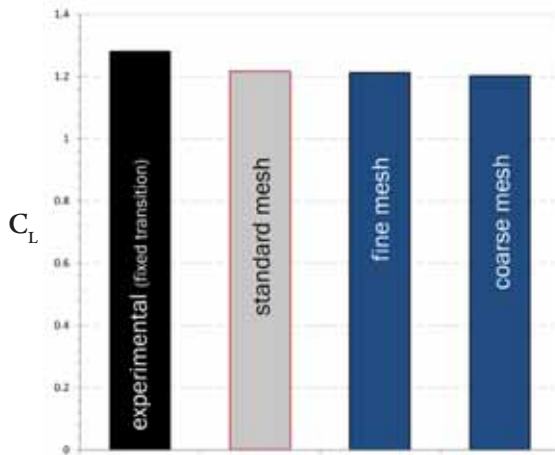
FIG



$h/c=0.179$  wing surface pressure distributions at  $z=0$  for coarse, standard and fine meshes.

4.5

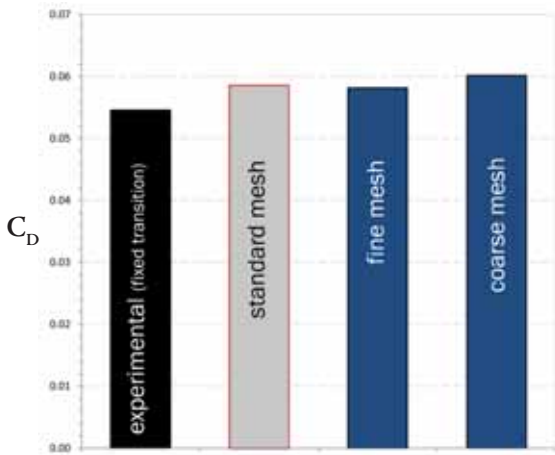
FIG



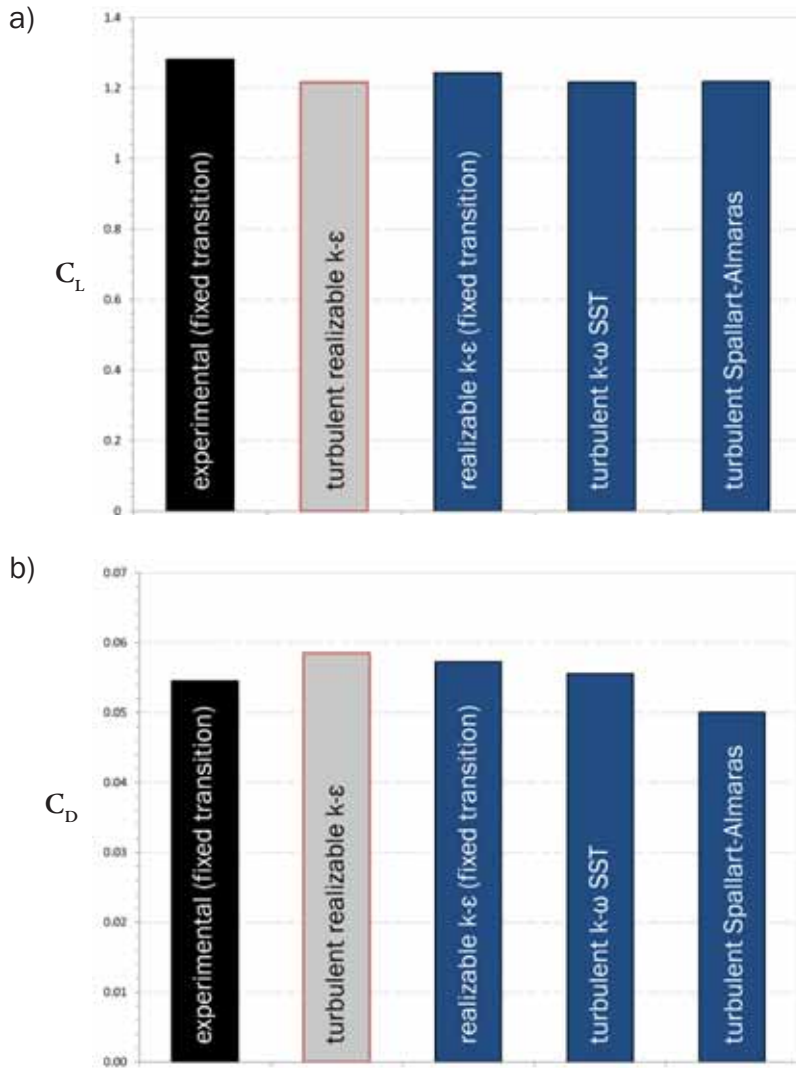
Comparisons to experimental lift coefficient for coarse, standard and fine meshes.

4.6

FIG



Comparisons to experimental drag coefficient for coarse, standard and fine meshes.



$C_L$  (a),  $C_D$  (b) comparisons to experimental results,  $h/c=0.179$ .

Allmaras model, the Realizable k- $\epsilon$  model, and the SST variant of the k- $\omega$  model. Simulations were also made involving a laminar region to 10% of the chord to equate to the transition fixing present in the experiments of Zerihan (2000), but are presented here merely to enforce the reasonable assumption of fully-turbulent flow, particularly at higher Reynolds numbers.

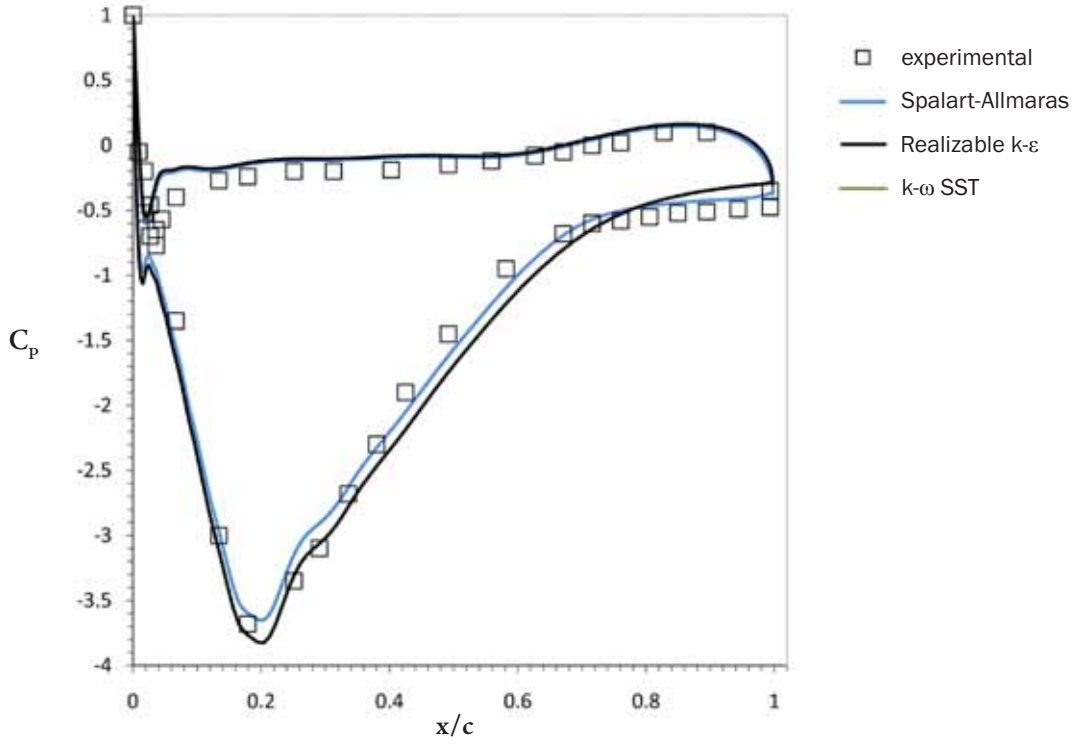
Some validation cases were also run with the k-k-l- $\omega$  model to investigate the possibility of factoring in free transition on the wing, and successful comparisons to the experimental cases (the series which did not feature a transition grit strip) were made. However, the decision was made to assume fully turbulent flow for the remainder of the study, given the lack of experiments at higher Mach and Reynolds number (where

transition would occur earlier) with which to compare to. This also removes the variance of transition location from the list of factors influencing the results, although the extent to which compressibility of the flow affects boundary layer transition would be a worthwhile study in itself.

The majority of turbulence model comparisons were conducted at  $h/c=0.179$  and  $0.067$ , and on the standard mesh while including an assessment of the wall  $y^+$  suitability for the enhanced wall modelling option preferred for each model. It was found that the  $k-\omega$  SST model was fairly sensitive to the  $y^+$  value, leading solutions to become artificially unsteady (due to near-wall instabilities at numerous points on the wing) if the mesh was too fine ( $y^+ < 1$ ). In some cases, it would fail to achieve an acceptable convergence level due to the slightly different wall  $y^+$  scales on the wing, endplate, ground and tunnel walls. While the solution was much more stable with the enhanced wall modelling disabled, this was not deemed to be an effective way to address the problem when good resolution of the boundary layers was obtained with the other models.

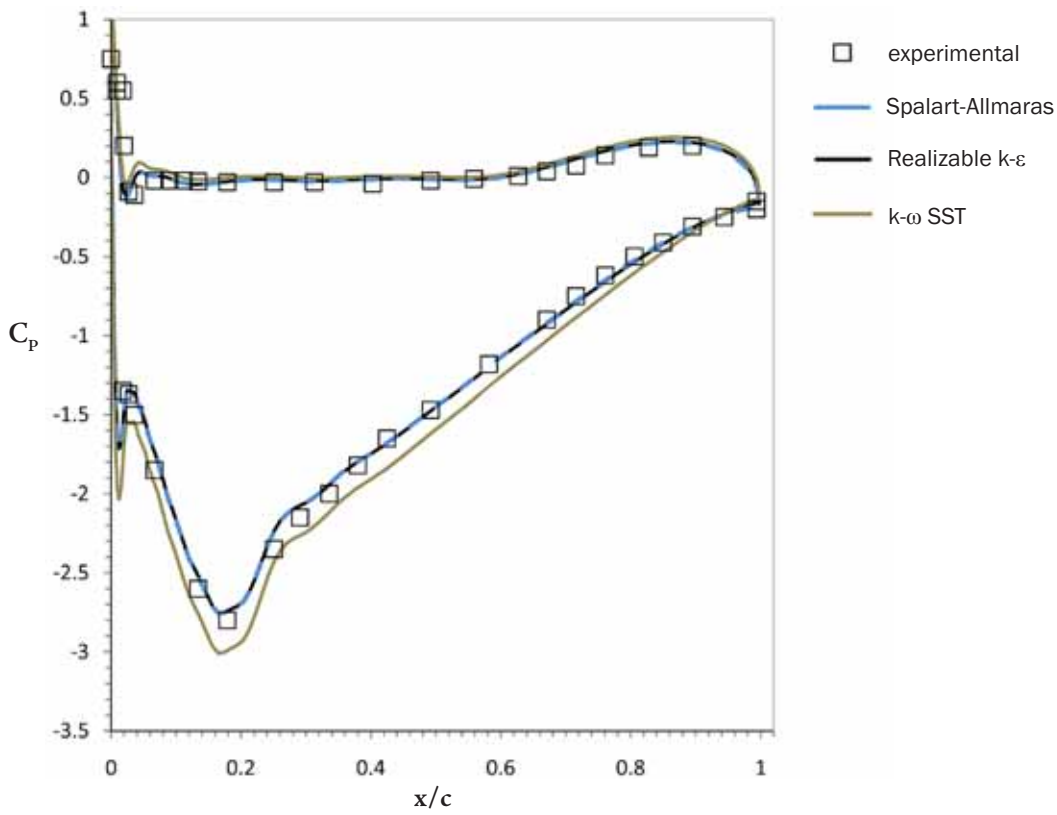
While there is no doubt from literature (Mahon, 2005) that the  $k-\omega$  SST model is extremely capable at accurately modelling the types of flow encountered in this study, it was decided that in this instance the difficulties in ensuring adequate convergence due to the wall  $y^+$  values would require an inordinate amount of time to tailor-mesh each case and then monitor it for signs of volatility during the iterative procedure. This would particularly be the case when the  $y^+$  values would change (generally decreasing) naturally with increasing Mach and Reynolds numbers. Besides these issues, the other two turbulence models assessed provided a closer match to the available experimental data, and thus the main comparisons made were between the Realizable  $k-\epsilon$  and the Spalart-Allmaras models.

Figure 4.7 isolates the  $h/c=0.179$  case as an example of how accurately each model predicted the experimental aerodynamic force coefficient results. All models slightly under-predicted the experimental  $C_L$ , but performed similarly relative to each other. As expected, fixing a laminar zone to 10% of the chord increased the lift coefficient slightly towards the fixed-transition experimental case; the quantitatively small difference



4.8  
FIG

Turbulence model comparisons to experimental pressure distributions,  $h/c=0.067$ .



4.9  
FIG

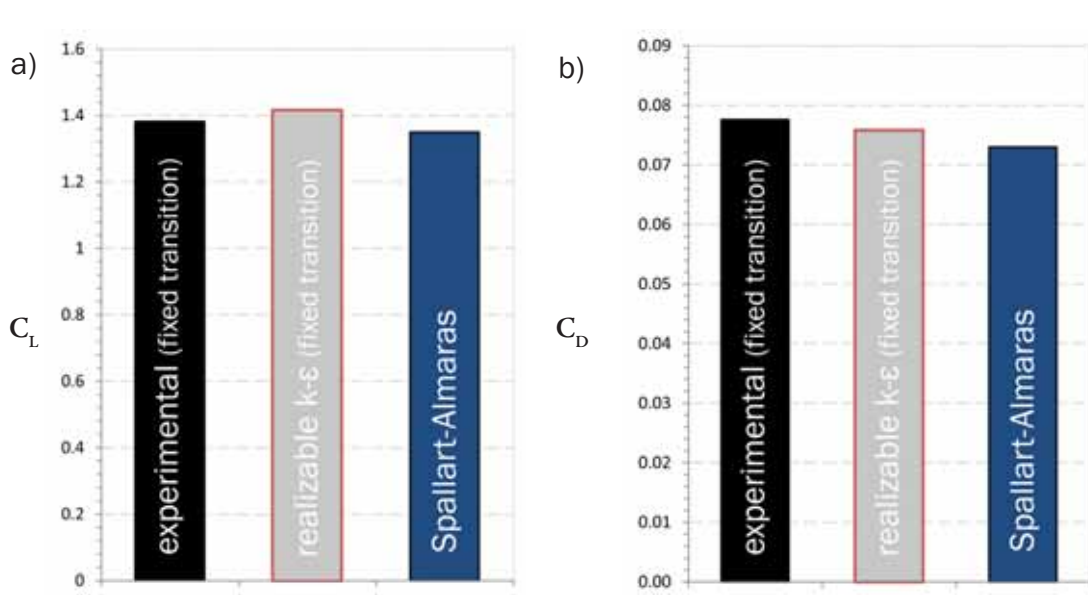
Turbulence model comparisons to experimental pressure distributions,  $h/c=0.179$ .

re-enforcing the choice of fully-turbulent simulations for the main body of the study.

In terms of drag, the turbulent  $k-\omega$  SST model provided the closest comparison to the experimental value, with the Realizable  $k-\varepsilon$  and SA models over-predicting and under-predicting respectively by a similar percentage. Figure 4.8, however, shows that the surface pressure distributions at  $z=0$  on the wing are predicted much more closely (and near-identically) by the Realizable and SA models, whereas the SST model overpredicts the lower surface suction peak. This implies that the discrepancies between the models lies in the prediction of three-dimensional effects, specifically the vortex behaviour.

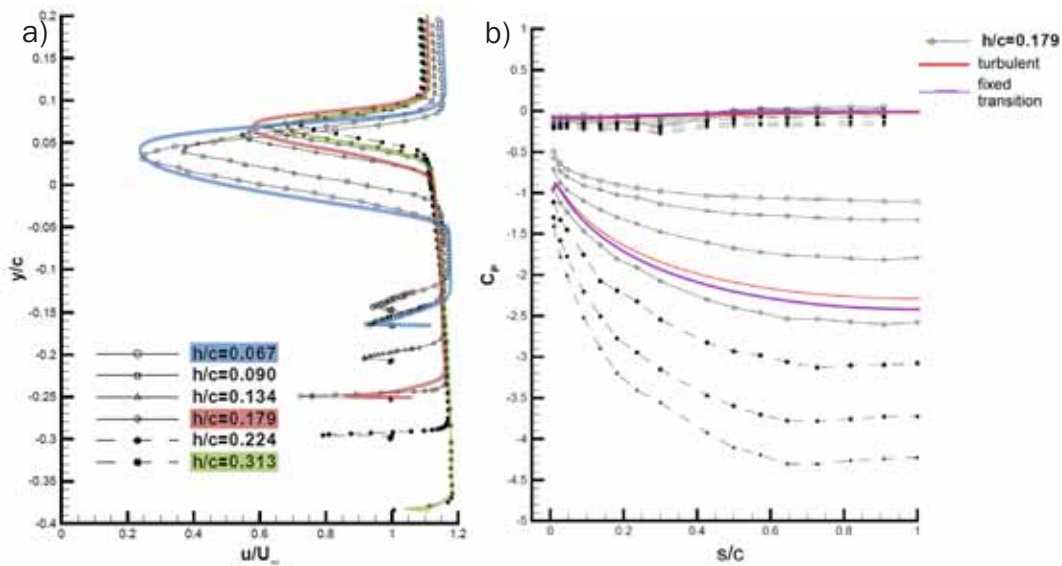
The graph of figure 4.8 depicts the pressure distribution for the  $h/c=0.067$  case, and compares the turbulence models. This ground clearance features a significant separation of the flow on the lower surface near the trailing edge, and is thus a more demanding test of the models' ability. While the Realizable model seems to more accurately resolve the lower-surface suction peak, the SA model provides a closer match to the experimental data in the pressure recovery region across the rest of the chord, and particularly at the trailing edge where the flow is separating. This somewhat contradicts existing literature (Zerihan, 2000; Mahon, 2005), but it must be remembered that the SA variant implemented here is specifically designed to account for free shear layers and recirculating regions and, as with the projectile cases described in Chapter 2, seems likely to provide an improved performance in such scenarios when compared to previous studies using the model which was previously known to significantly over-predict the production of eddy viscosity in such regions (FLUENT, 2006). By contrast, the predicted lift and drag coefficients of the Realizable model are closer to the experimental results, as shown in figure 4.10.

The decision was made to continue with the Realizable  $k-\varepsilon$  model, simply because the core of the rest of the study considers the aerodynamic forces and moments, which were slightly better predicted by the two-equation model. This is a likely consequence of the model's ability to cope with recirculating or free shear layers, whereas the Spalart-Allmaras model can suffer somewhat in this respect (Spalart and Allmaras, 1992; FLUENT, 2006).



4.10  
FIG

$C_L, C_D$  comparisons to experimental result,  $h/c=0.067$



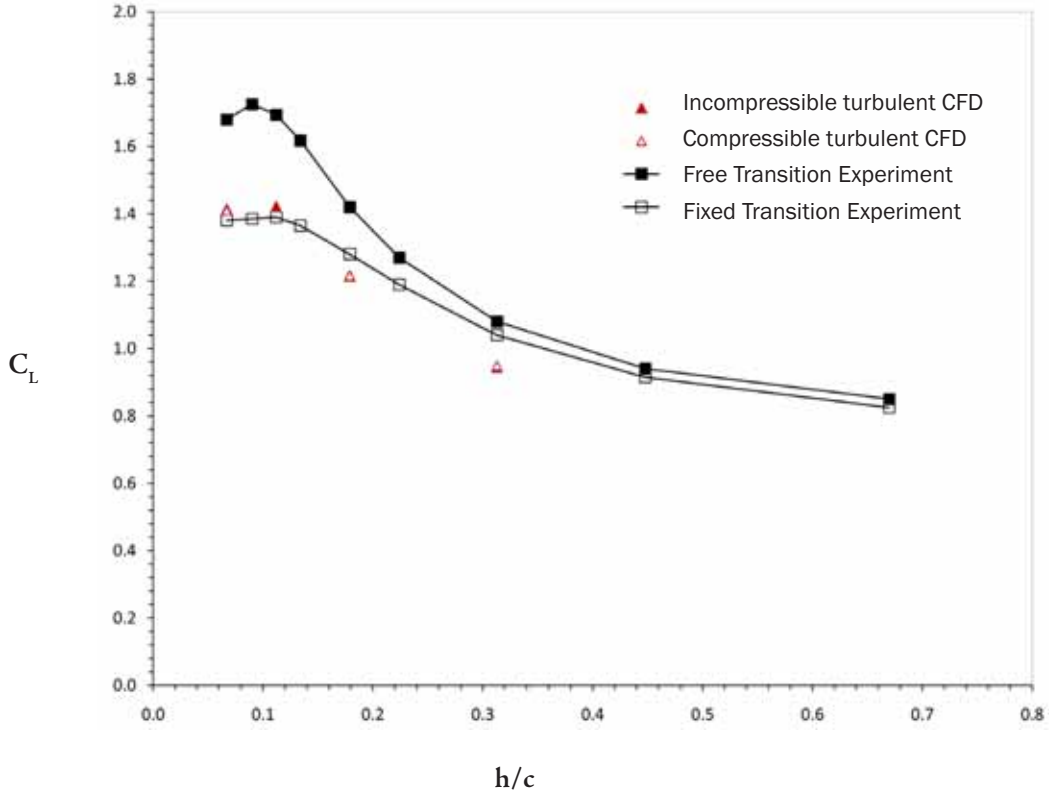
4.11  
FIG

Wake profile (a) comparisons to experimental data (Zerihan, 2000) at  $x/c=1.2$  on the symmetry plane, and b) spanwise pressure distributions at  $h/c=0.179$  with CFD overlaid.

### 4.2.3 Further comparison to experimental results (compressible and incompressible)

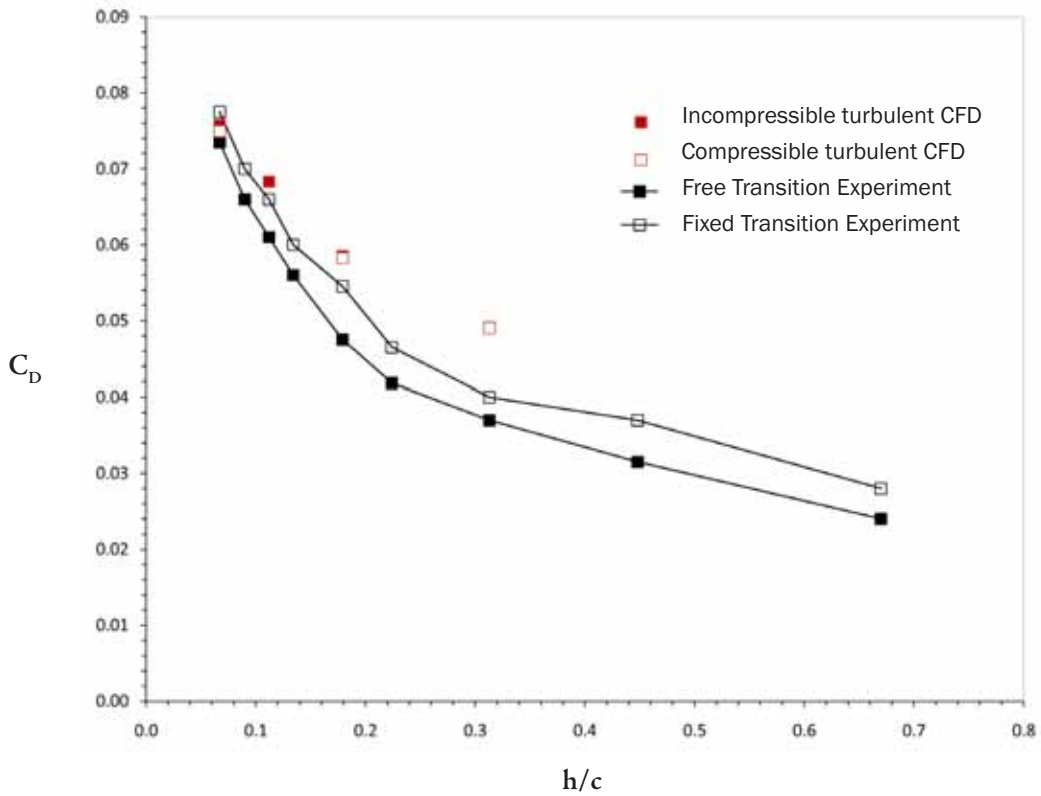
The graphs presented in figure 4.11(a) comprise predicted wake profiles at  $x=1.2c$  (i.e.  $0.2c$  from the trailing edge) overlaid on the original graph (Zerihan, 2000) for the fixed-transition wing at different ground clearances. The CFD shows reasonable agreement at the three clearances tested ( $h/c=0.067, 0.179$  and  $0.313$ ), with a tendency to slightly

4.12  
FIG

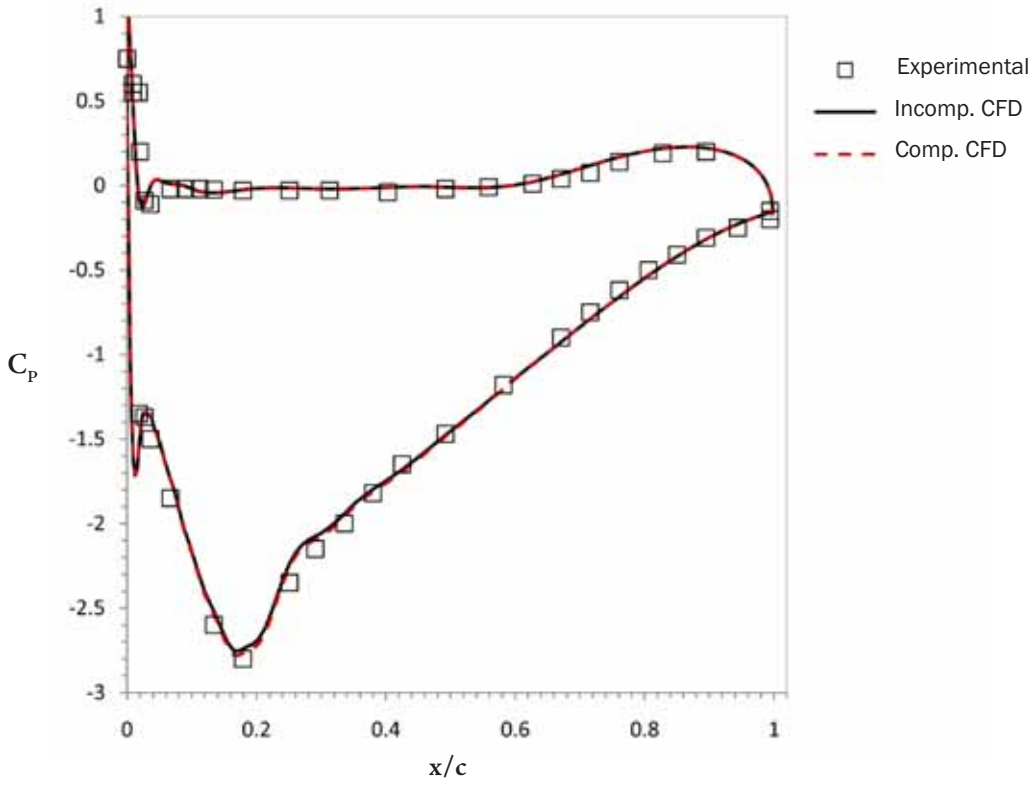


Lift coefficient vs. ground clearance, compressible and incompressible comparison to experimental values.

4.13  
FIG

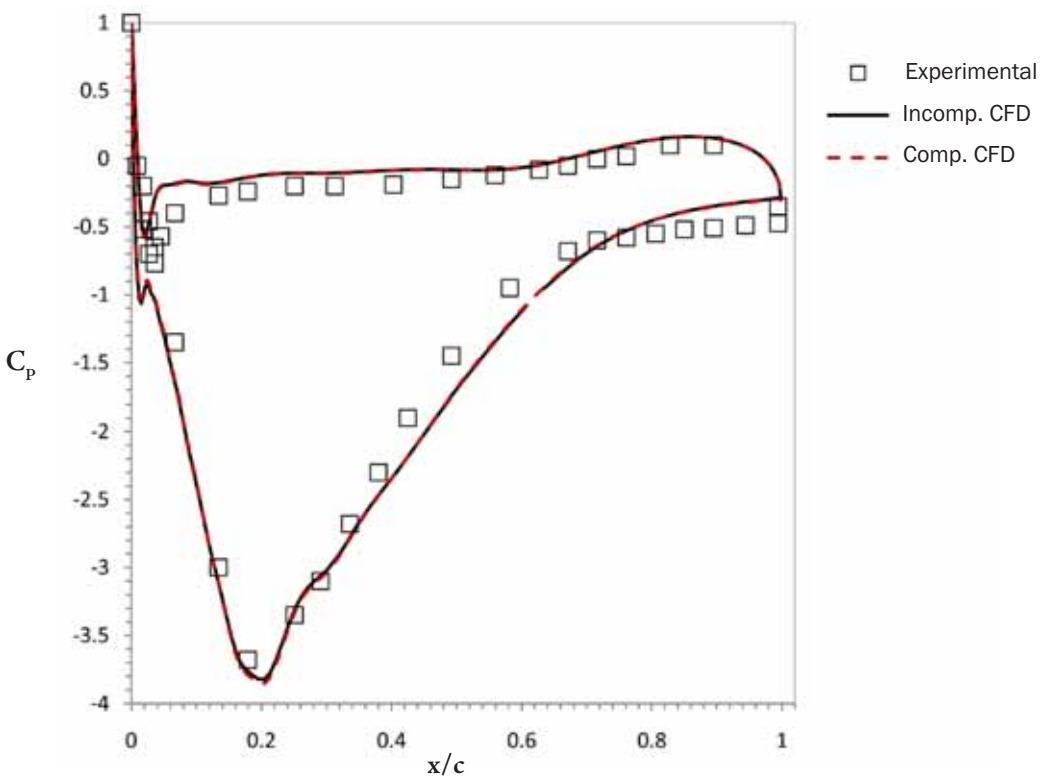


Drag coefficient vs. ground clearance, compressible and incompressible comparison to experimental values.



4.14  
FIG

Compressible and incompressible fully-turbulent CFD comparison to experimental pressure distribution,  $h/c=0.179$



4.15  
FIG

Compressible and incompressible fully-turbulent CFD comparison to experimental pressure distribution,  $h/c=0.067$

overestimate the thickness and maximum velocity deficit. Also shown in figure 4.11(b) are spanwise pressure distributions at the quarter-chord for  $h/c=0.179$ , which exhibit good qualitative agreement. Unfortunately only free-transition results were available for this aspect, and as such both the fully-turbulent and fixed-transition cases computed do not fully match, although the fixed-transition case is somewhat closer as one would expect (transition is estimated to have occurred at beyond 30% of the chord for this  $h/c$ ).

Lift and drag coefficient curves are presented in figure 4.12, which give a clearer indication of how effectively the numerical approach is capturing the important features of the flow as the ground clearance is reduced - the lift-loss phenomena explored in literature (Zerihan, 2000; Zerihan and Zhang, 2003) is fairly well captured between  $h/c=0.112$  and  $0.067$ ; at the higher clearances lift is generally underpredicted. Similar trends are observed for the drag coefficient curve in figure 4.13, although again the overall trend is well replicated.

Reasons for the discrepancies could be numerous. On the experimental side, the error implicit in the determination of ground clearance was estimated to be as high as 5-6% (Zerihan, 2000), and the Reynolds number was found to vary by as much as 7% over the testing programme. At the particularly-sensitive low  $h/c$  values, both these errors would make a significant contribution to the results obtained, on top of the previously-discussed neglect of the influence of the sting and force balance struts. The simplifications made to the numerical model in terms of wind tunnel geometry, as well as the experimental *and* numerical uncertainties surrounding the issue of boundary layer transition, could all contribute to the differences observed.

Critically, however, the trends observed in the experimental results are well-reproduced by the CFD. Furthermore, as the graphs depict, the compressible and incompressible simulations exhibit good similarity, both qualitatively and quantitatively. Indeed, the maximum difference between the incompressible and compressible simulations is approximately 0.5% of  $C_L$  and 0.3% of  $C_D$ , at the lower end of the ground clearance spectrum. These differences, while incorporating a degree of numerical error due to the

compressible scheme being applied to a highly subsonic freestream Mach number of 0.88, seem likely to stem from physical effects. At the lowest clearance of 0.067, the peak local Mach number is 0.19, with a maximum density variance  $\rho/\rho_\infty$  of 2.2% around the semi-span section. Accordingly, in the  $C_p$  distributions presented in figures 4.14 and 4.15 for  $h/c=0.0179$  and 0.067 respectively, the only discernable difference between the compressible and incompressible pressure distributions occurs at the lower surface suction peak: precisely where the maximum Mach number and density variance exists.

## 4.3 RAE 2822 Aerofoil

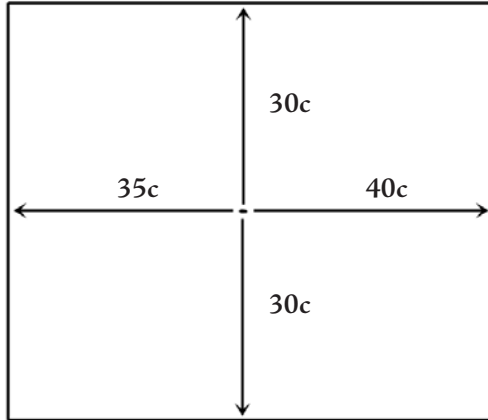
### 4.3.1 RAE 2822 “Case 9”

The “Case 9” of the Advisory Group for Aeronautical Research and Development (AGARD) report (Cook *et al.*, 1979) has been used here to provide a basic evaluation of the two-dimensional transonic capabilities of the numerical approach. The case involves an RAE 2822 section at  $M_\infty=0.73$ ,  $\alpha=2.79^\circ$ , with a strong normal shock wave sitting on the upper surface at approximately  $x/c=0.53$ . The boundary layer behind the shock does not separate and the flowfield is treated as stable and steady-state. A transition trip was located at  $x/c=0.03$ , and the turbulent intensity of the oncoming flow was determined to be 0.1%.

The wind tunnel measurements made by Cook *et al.* (1979) have become a standard benchmark in CFD, despite some fundamental issues. The RAE 2822 section, at an AR of 3 and chord of 0.61m (in conditions yielding a Reynolds number of approximately  $6.5 \times 10^6$ ), was designed to provide two-dimensional flow at the semi-span. It has since been shown that this aspect ratio is not necessarily sufficient to ensure two-dimensional flow (Garbaruk *et al.*, 2003; Sudani *et al.*, 1994), and the results were heavily influenced by the tunnel walls. Slotted walls were used to treat the boundary layers there; not only is little detail given about this in the original report, but this presents a scenario difficult to replicate in CFD.

4.16

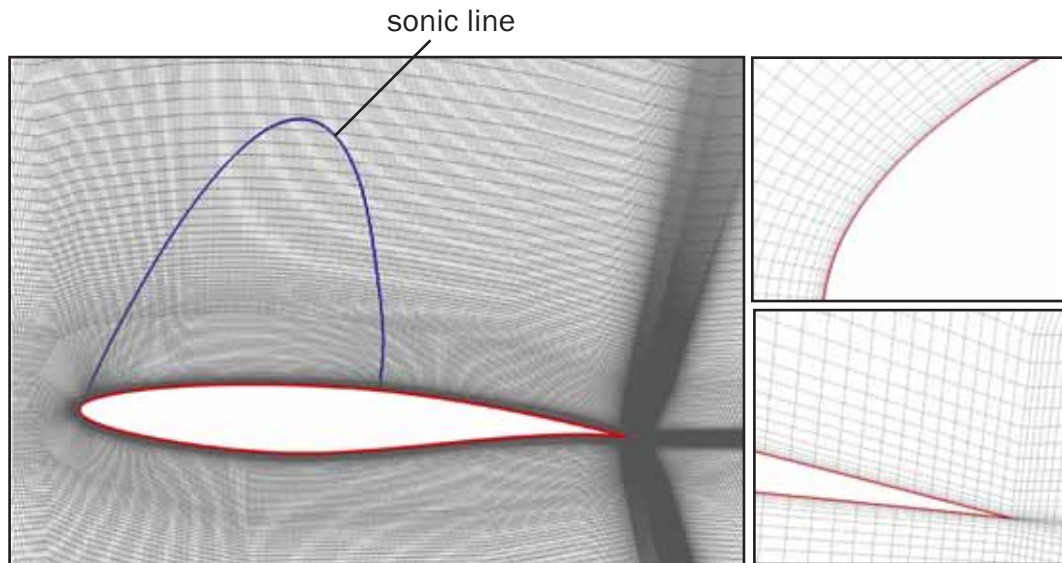
FIG



Domain extent for RAE 2822  
'Case 9' simulations.

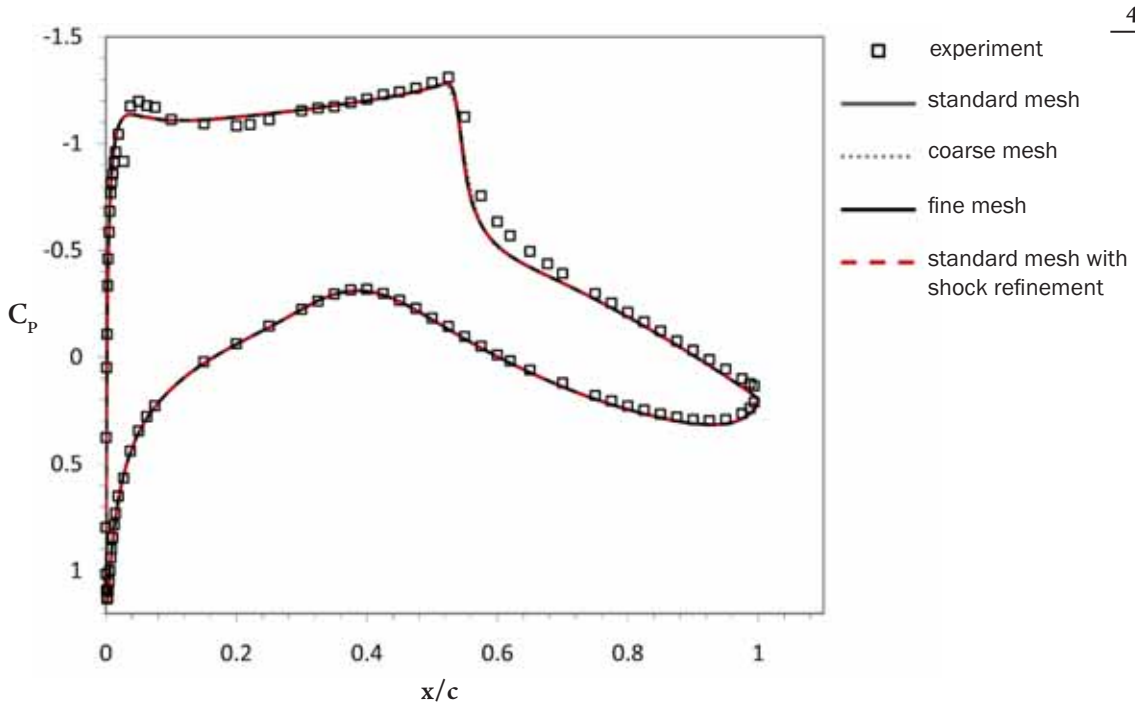
4.17

FIG



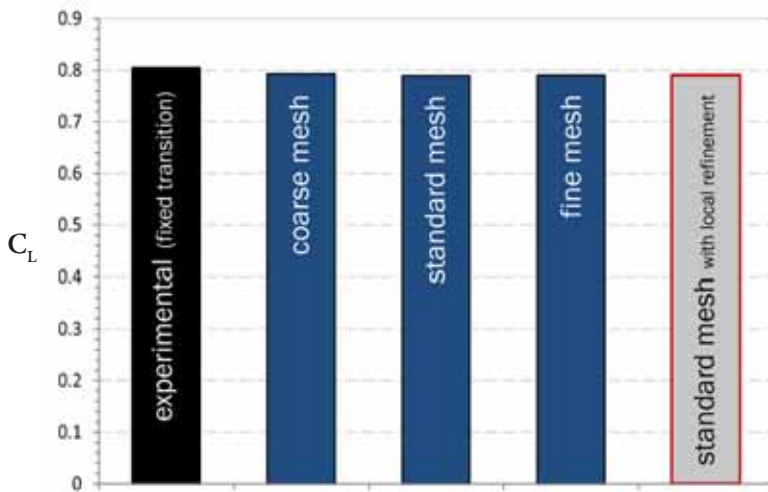
General mesh layout for RAE 2822 simulations, with (right) detail for the near-wall region at the leading and trailing edges.

Due to the wall influence, flow conditions for two-dimensional simulations are routinely corrected, sometimes by fixing the solution values for  $C_L$  and letting the solution find its own freestream conditions, or by adjusting either the Mach number or angle of attack manually to match the experimental pressure distribution. The latter approach has been used here based on the suggestions of Cook *et al.* (1979) - the value of  $\alpha$  used,  $2.79^\circ$ , is considerably altered from the experimental value of  $3.19^\circ$ . The tunnel walls are not considered, and the aerofoil is therefore treated as existing in free-flight.



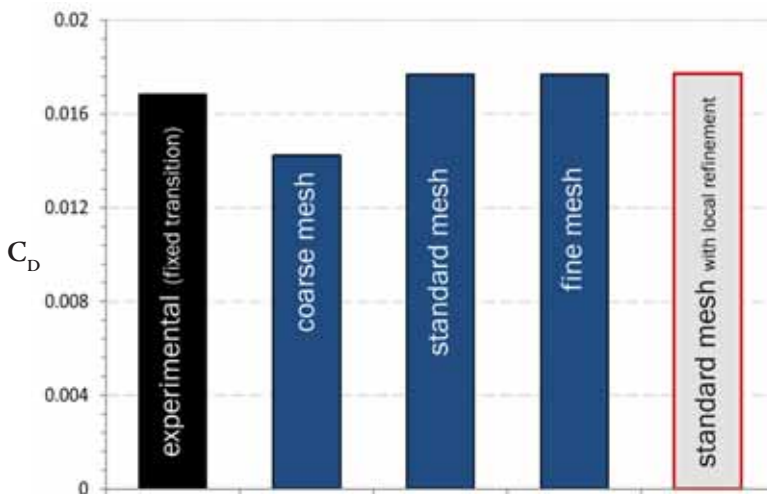
4.18  
FIG

Predicted pressure distributions for different meshes.



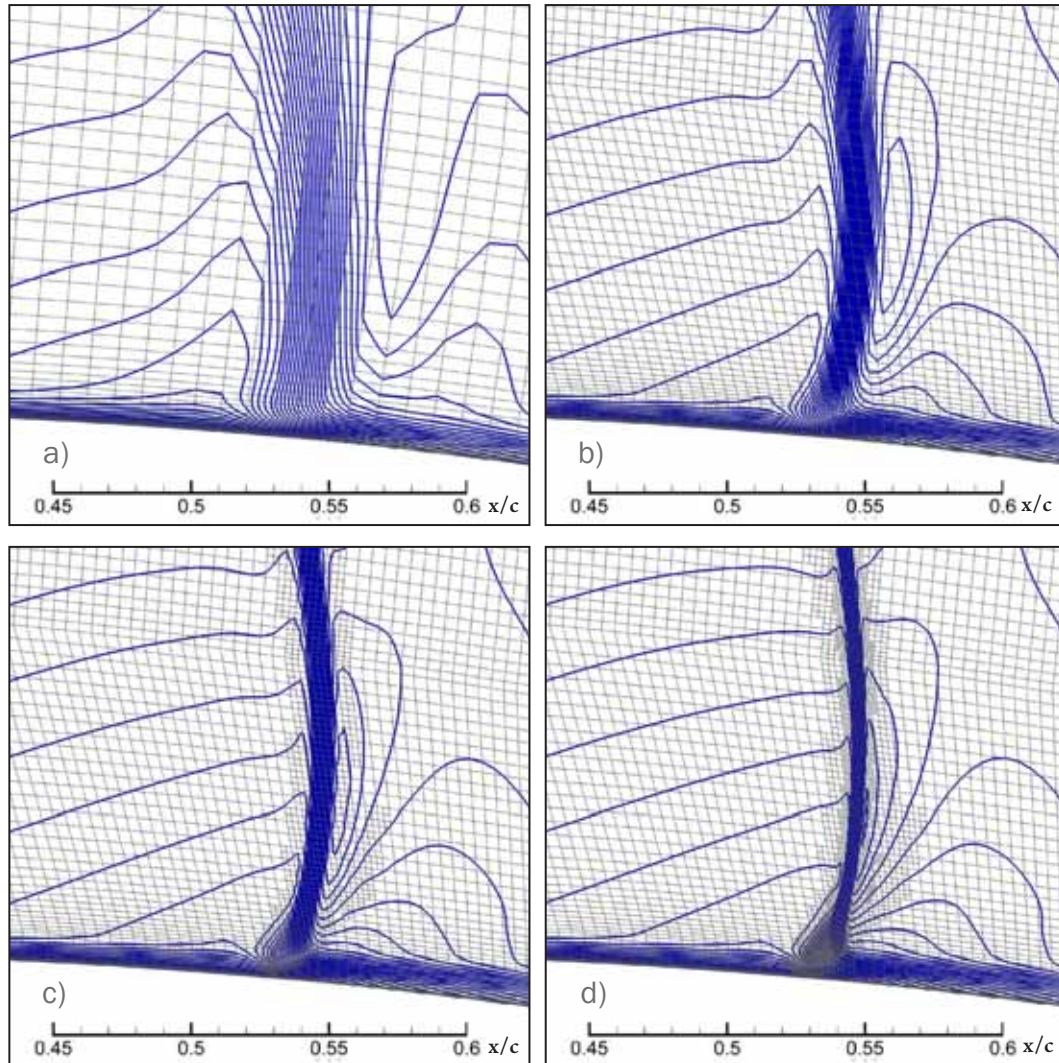
4.19  
FIG

Predicted lift coefficients for different meshes.



4.20  
FIG

Predicted drag coefficients for different meshes.



Resolution of density contours at the shock within the mesh for increasingly-refined node-spacing; a) coarse mesh, b) standard mesh, c) standard mesh first adaption, d) standard mesh with a second adaption.

#### 4.3.1.1 Mesh and Boundary Considerations

The results presented in this section were generated by the Spalart-Allmaras turbulence model, the choice of which is discussed in section 4.3.1.2. All meshes were structured multi-block grids, the general layout of which can be seen in figure 4.17. The appropriate location for the farfield boundaries was examined simply by comparing the results from one simulation with boundaries as shown in figure 4.16, to those with an addition 10 chord lengths in the domain in all directions. The influence of the boundaries on the solution when placed this far from the wings proved to be negligible, resulting in a changed prediction of the aerodynamic coefficients of less than 0.01%.

The initial comparison to the experimental pressure distribution, presented in figure 4.18 as “standard mesh”, shows excellent agreement. In this instance, the laminar zone and trip at  $x/c=0.03$  was not modelled, and the disagreement with experimental data in this region is noted on the suction surface particularly. The shock location is well-predicted, at around  $x/c=0.54$ , and although the shock strength seems slightly overestimated and the pressure recovery somewhat exaggerated in the region immediately behind it, agreement to the trailing edge is generally good.

To obtain a mesh-independent solution, coarse, standard and fine meshes were constructed for evaluation. Local refinement of the mesh at the shock location was also performed. The coarse mesh contained 320 nodes on the wing surface and a total of 130,000 cells. The standard mesh contained 256,000 cells with 545 nodes on the wing. The fine mesh was simply the standard mesh with each cell split into 4, and thus contained a little over 1 million cells.

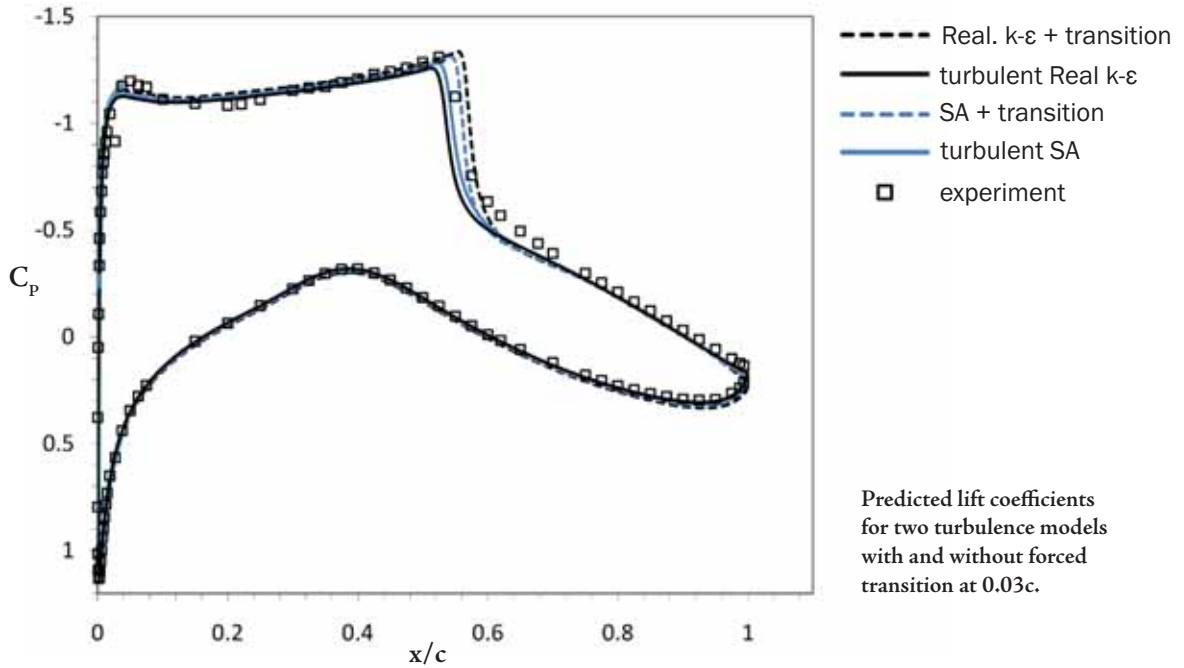
A qualitative assessment of these meshes in the shock region is presented in figure 4.21. Although the mesh resolution does not have a marked influence on the actual location of the shock, the smearing of the contours in the coarse and standard meshes is affected. Local refinement of the mesh around the shock achieves a similar effect as using a mesh that is 4 times as dense, with only a few thousand additional cells, and is thus the preferred method. The pressure distributions presented in figure 4.18 show that even the coarse mesh has largely captured all important aspects of the flow, but the locally-refined mesh provides the sharpest resolution of the shock as illustrated by figure 4.21.

Comparisons to the experimental lift and drag values are presented in figures 4.19 and 4.20. The experimental results do not incorporate a measure of error, but nevertheless the CFD provides a good match, with only the coarse mesh failing to provide adequate drag predictions.

#### 4.3.1.2 *Turbulence Modelling*

As usual, the Spalart-Allmaras,  $k-\varepsilon$  and  $k-\omega$ -SST turbulence models were evaluated for their effectiveness in capturing the flowfield accurately, by comparing to the experimental

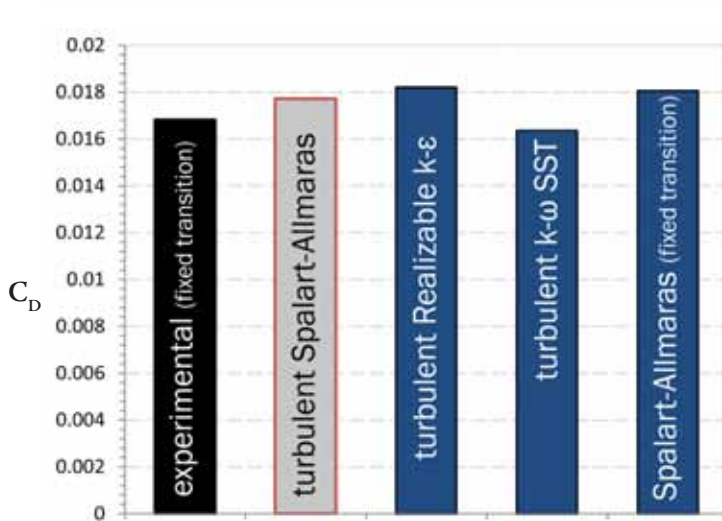
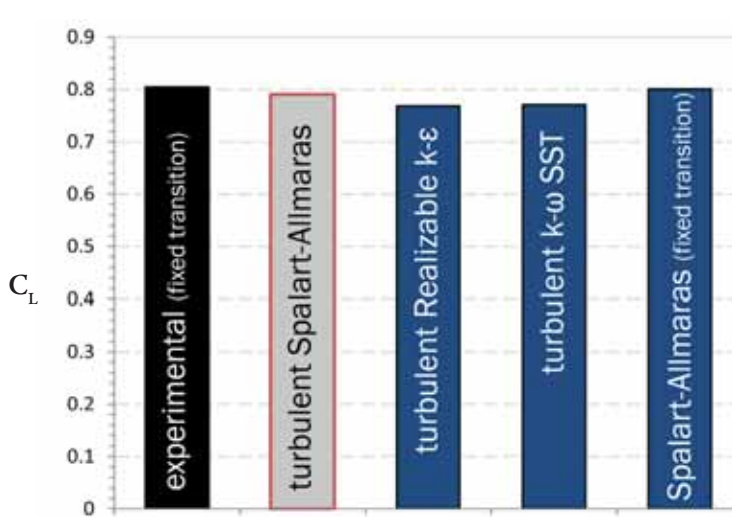
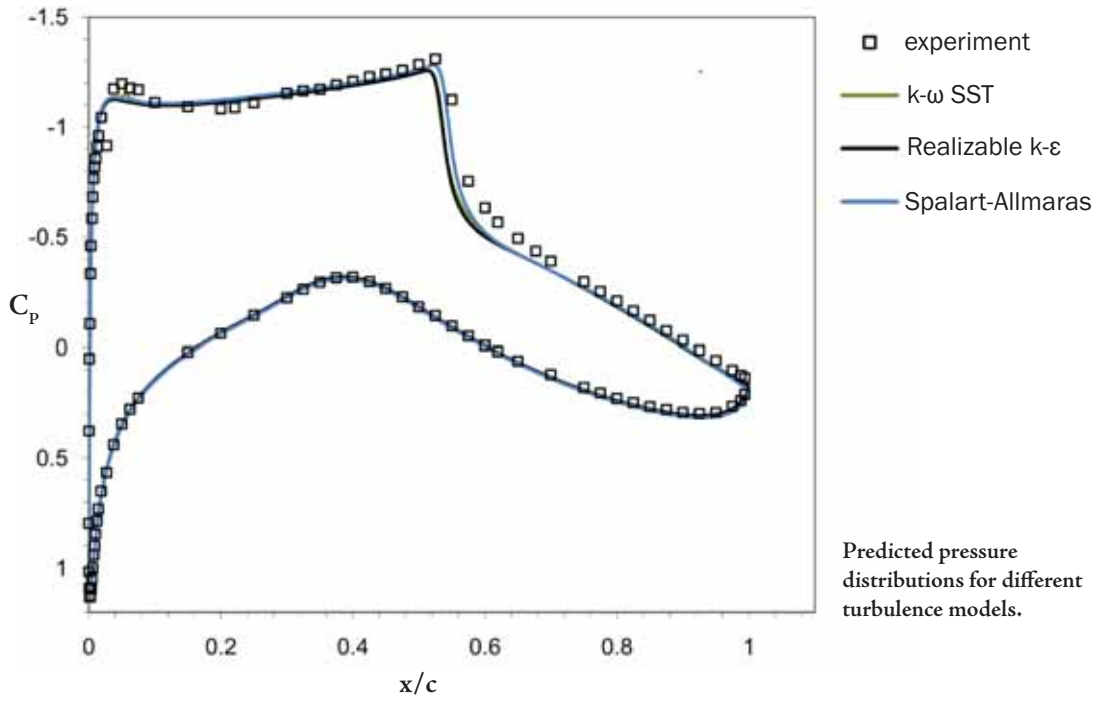
4.22  
FIG



pressure distribution and values of lift and drag coefficient. To justify the fully-turbulent approach, comparisons were made, as shown in figure 4.22, with cases run featuring forced transition from laminar to turbulent flow at  $x/c=0.03$  as per the experiment. The effect on the predicted location of the shock wave is pronounced, though the pressure distribution at the leading edge does not appear to be markedly affected. The SA model appears to slightly over-predict the shock location but across the region around the shock the agreement is improved. The Realizable  $k-\epsilon$  model underpredicts the shock location when fully turbulent, but overpredicts by approximately the same amount when transition is forced, though the agreement behind the shock seems improved.

The shock location moves by about 2% of the chord when transition is incorporated - the results indicate that the model will most accurately reproduce the experiment when this is considered, but a fully-turbulent assumption is generally a good approximation of the flow.

The pressure distributions in figure 4.23 show relatively minor differences between the predictions of the three turbulence models, with the SA model proving to be marginally closer to the experimental readings in the region of the shock. The SA model is also closest in reproducing the experimental lift coefficient, as shown in figure



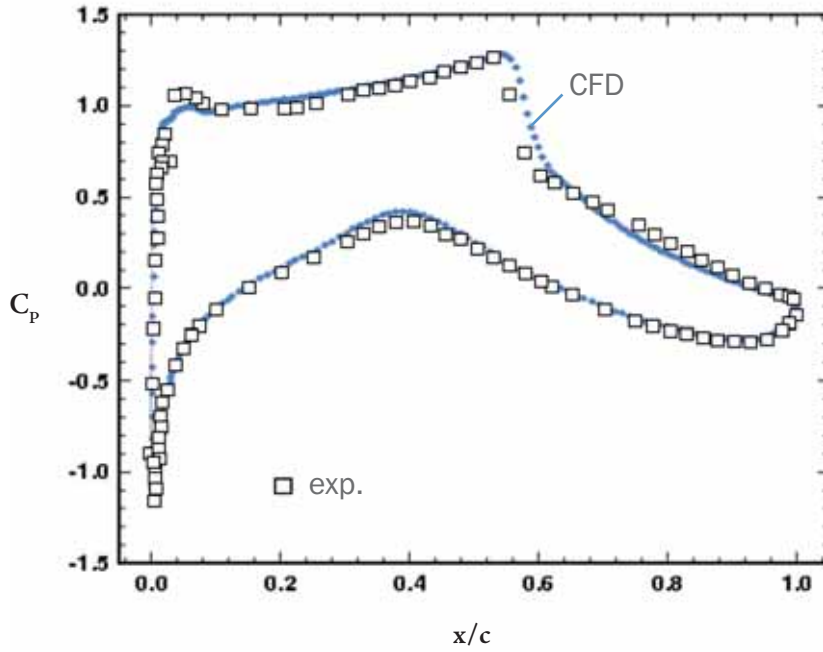
4.24, although the prediction for drag is somewhat less effective. The case involving fixed transition actually features increased drag due to the enhanced strength of the shock wave sitting 1% further downstream on the aerofoil surface. With potentially little to choose between the models other than slightly better pressure and force predictions with the SA model, it was chosen as the most suitable to produce all two-dimensional results for transonic problems.

#### 4.3.2 RAE 2822 'Case 10'

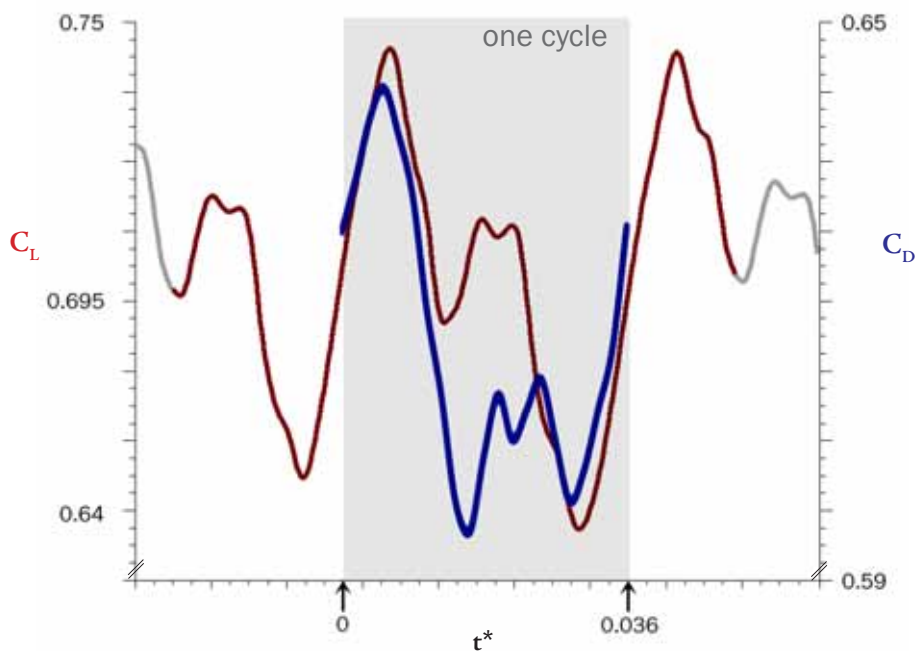
Unlike Case 9, Case 10 from the AGARD report (Cook *et al.*, 1979) features shock-separated flow at a freestream Mach number of only 0.02 higher than that of case 9. This feature has led it to become somewhat notorious in the literature as being a 'difficult' case to validate against, particularly with regards to turbulence modelling, as the shock location and pressure gradient in the suction surface recovery region are systematically over-predicted in virtually all cases reported in the literature. Some have gone as far as to suggest changes to turbulence model (such as the Baldwin-Lomax model, Singh, 2001) specifically to cope with this case (Kalitzin, 1998), while others have conducted simulations across a surprisingly wide range of suggested Mach number or angle of attack corrections (Bartels, 1998, Lien *et al.*, 1998, Wang *et al.* 2000, Elkhoury, 2007).

Garabuck *et al.* (2003) proposed that these problems may not lie with the turbulence models, but rather the geometric representation of the experiments. Attempts to model the full three-dimensional wing in the RAE wind tunnel test section (with and without floor and ceiling, and with and without slotted walls) for steady-state solutions proved ineffective in enhancing the match of CFD to experiment. The study hinted that the test section geometry can neither be treated as having solid walls or having no walls - merely approximating the tunnel in CFD is not any real improvement on the two-dimensional correction method and

When the current author's early simulations of the transonic wind tunnel experiments with an RAE 2822 described in chapter 3 proved to be occasionally unsteady



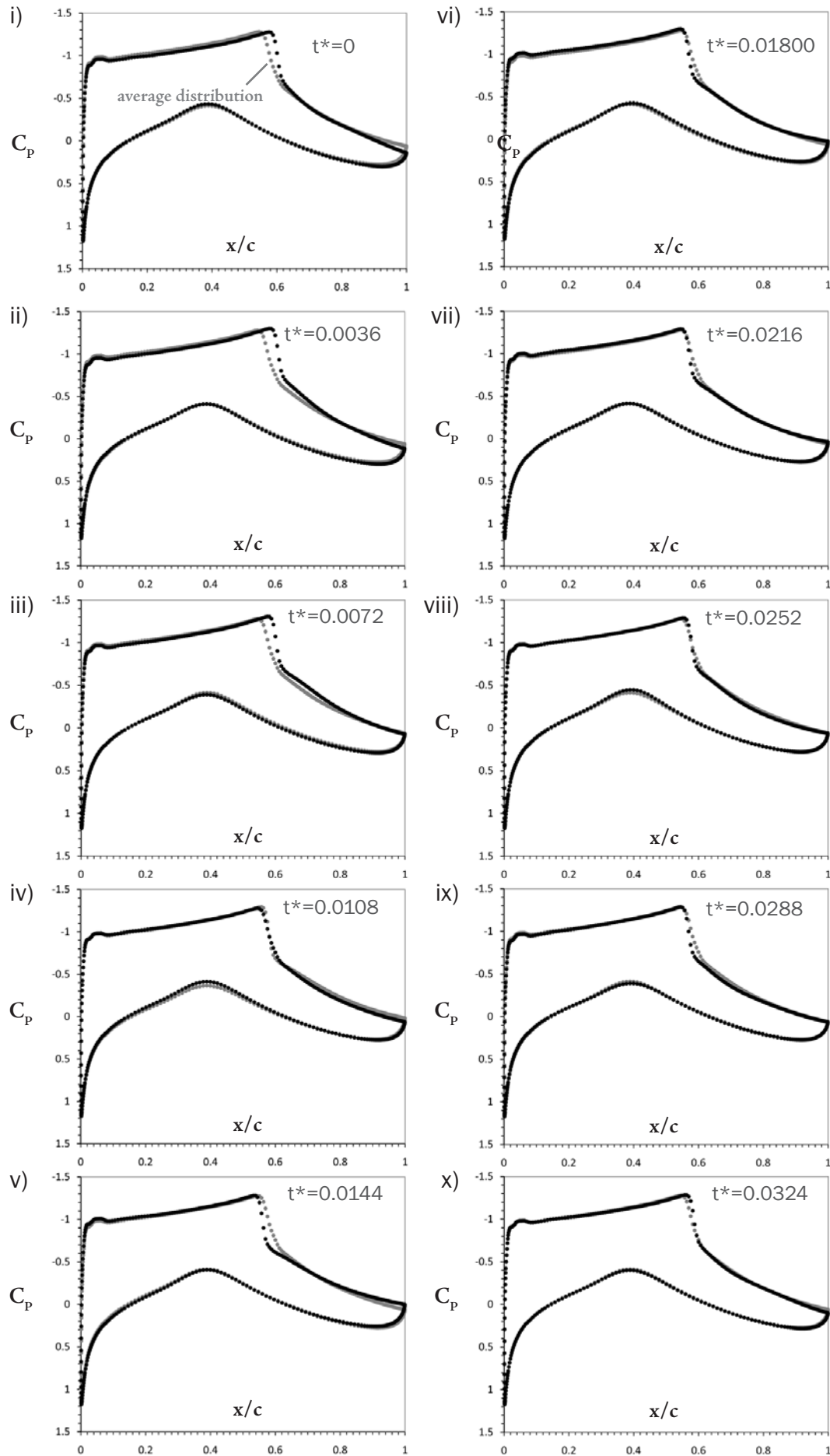
RAE 2822 'Case 10' pressure distribution on symmetry (semi-span) plane, averaged over 2 shock oscillation cycles.



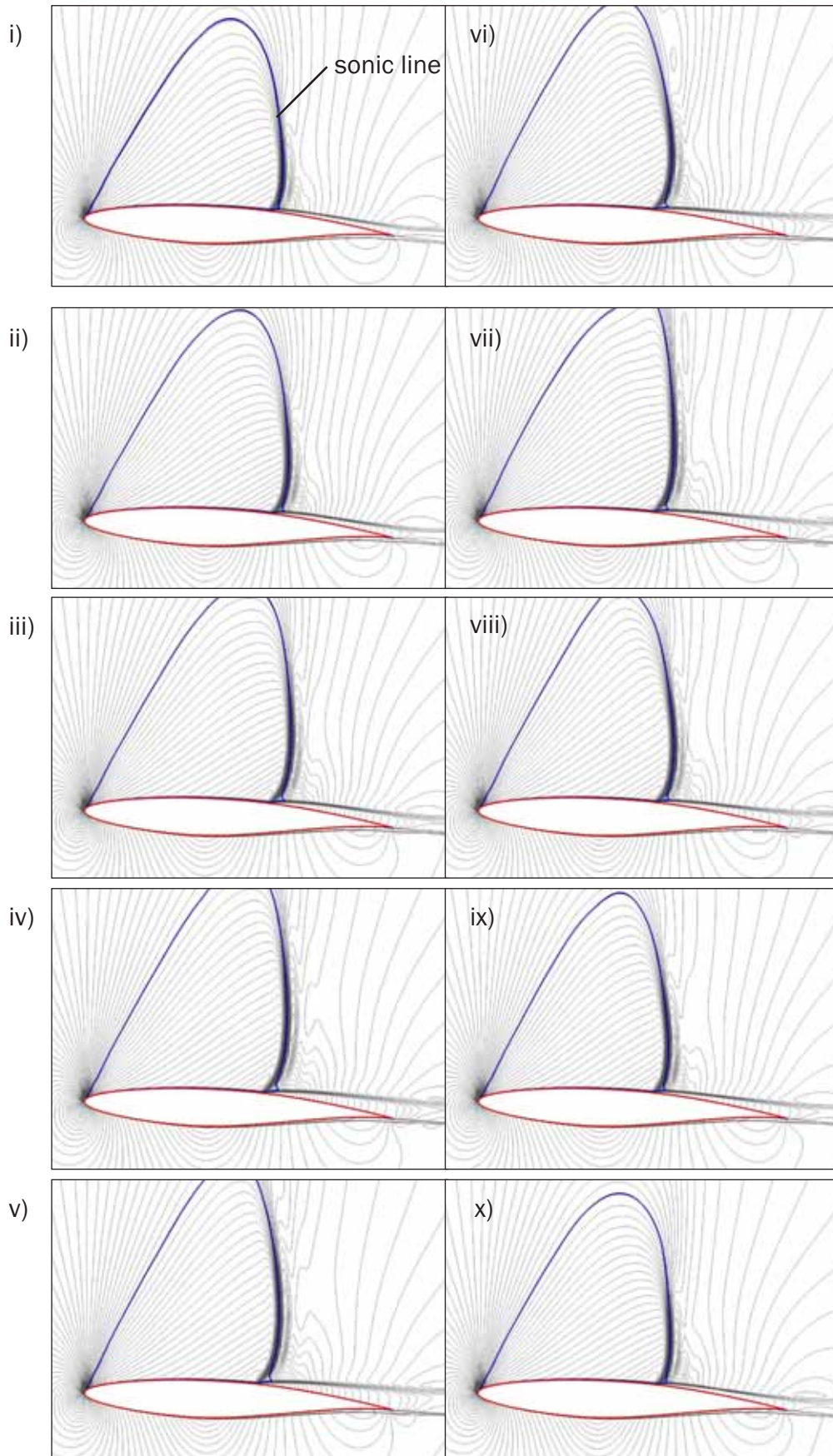
RAE 2822 'Case 10' lift coefficient and chordwise shock position on the symmetry (semi-span) plane with respect to time.

Table 4.2 - 'Case 10' aerodynamic coefficient comparisons

	$C_L$	$C_D$
Experimental	0.7430	0.0242
CFD (transient, time-averaged)	0.7083	0.0181



Pressure distributions over the course of one shock oscillation cycle, compared to experimental results.



Contours of density for the time steps depicted in figure 4.28.

but inherently three-dimensional, an attempt was made to employ the same approach to the AGARD Case 10. This provided an important 'missing link' in the validation cases presented here, as it provided an alternate form of validation for the three-dimensional unsteady work that is presented in the following section, and chapter 5. Given that, as stated earlier, CFD and the transonic experiments were used in unison to effectively validate each other, the successful application of the numerical method to the Case 10 scenario provided a valuable additional level of validation to suggest that later results did not simply match by coincidence resulting from misleading experimental *and* numerical results.

Spalart and Allmaras noted in their original presentation of their turbulence model (1992) that Case 10 simulations tended towards transient behaviour if the mesh was sufficiently fine, but to the best of the author's knowledge a transient three-dimensional simulation of this case has not been published at the time of writing.

A mesh density around the wing equivalent to that used in the Case 9 two-dimensional simulations was used here, with a significantly coarser far-field to reduce the overall number of cells. The test section was modelled as featuring non-slip floor and ceiling walls and slip side walls, which acts as a crude representation of the effect of slotted walls. A time step of 0.0003 seconds was used, based on a brief evaluation of typical unsteady frequencies at Reynolds numbers approximating the  $6.2 \times 10^6$  in this situation.

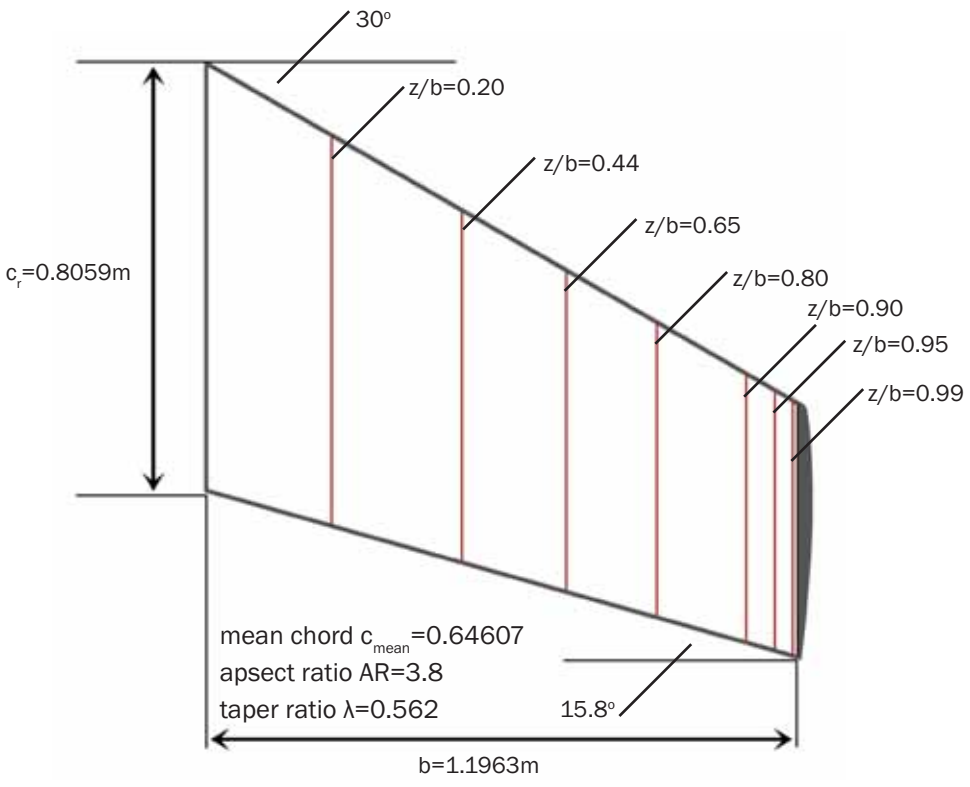
The agreement between CFD and experimental results shown in figure 4.26 is markedly better in the shock region and immediately downstream than results presented in existing literature, and is extremely encouraging. The plot represents an average pressure distribution, constructed with data from each second timestep over 2 periods of regular unsteady flow motion. As can be seen from the lift coefficient plot presented in figure 4.27, the frequency was approximately 29Hz and the motion slightly irregular, perhaps influenced by a secondary frequency created by the side walls. The shock travels over close to 3.5% of the chord over 1 cycle of oscillation, and the motion is very regular. A selection of pressure distributions over 1 period of motion is presented in figure 4.28

and shows the extent to which the  $C_p$  is influenced by the unsteady motion and therefore, inherently, the influence of the wind tunnel test section walls. Table 4.2 shows that while  $C_L$  is closer to the experimental result than is typically obtained in literature (Kral, 1998),  $C_D$  is disappointingly inconsistent with the value obtained in the wind tunnel.

Although more investigation would be required to make a definitive statement, it appears that only full three-dimensional, transient solutions should be used to compare numerical methods to Case 10. The approach of modelling the full test section in as much detail as possible was adopted for all CFD comparisons to the data obtained from experiments in the US Naval Academy's wind tunnel, and seems doubly-justified in light of the Case 10 results.

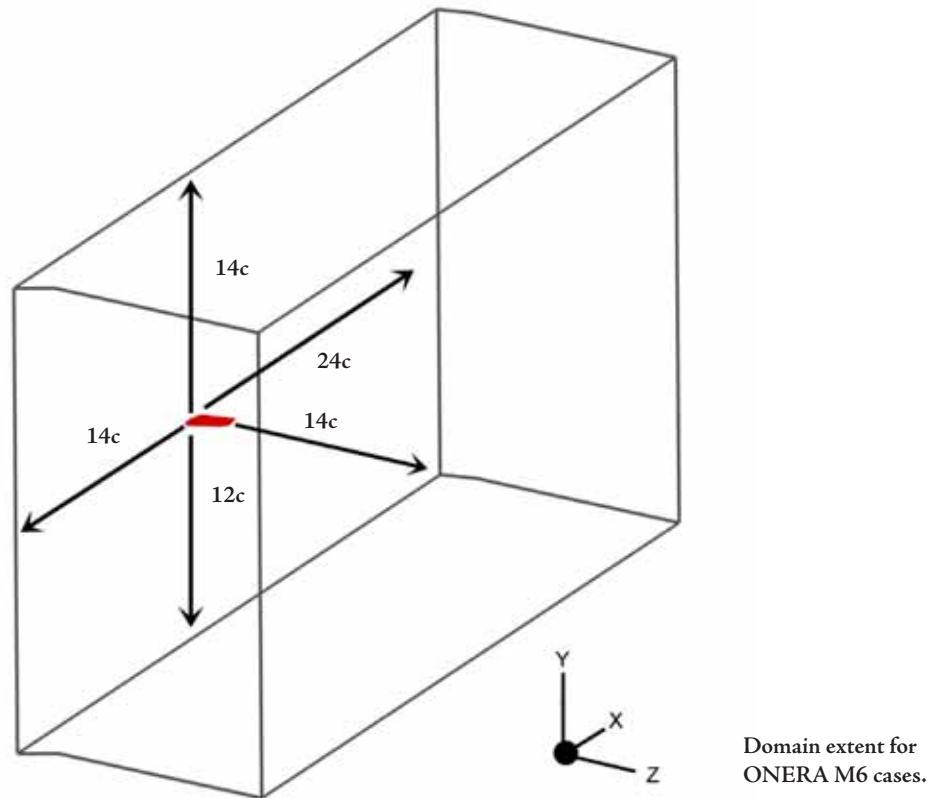
### 4.4 ONERA M6 Wing

The symmetric ONERA M6 semi-span wing used for the experiments presented in the



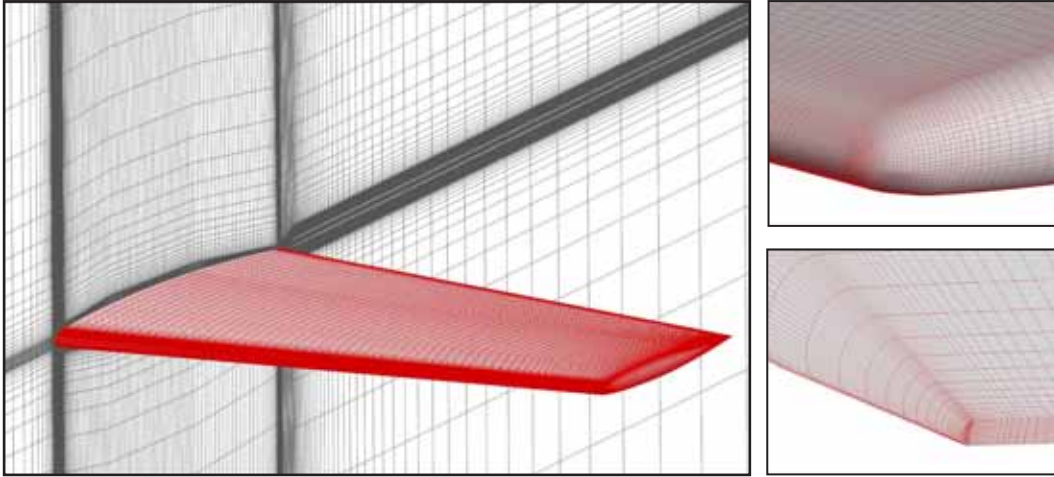
4.30  
FIG

Parameters and 7 spanwise locations of chordwise tapings for the ONERA M6 wing.

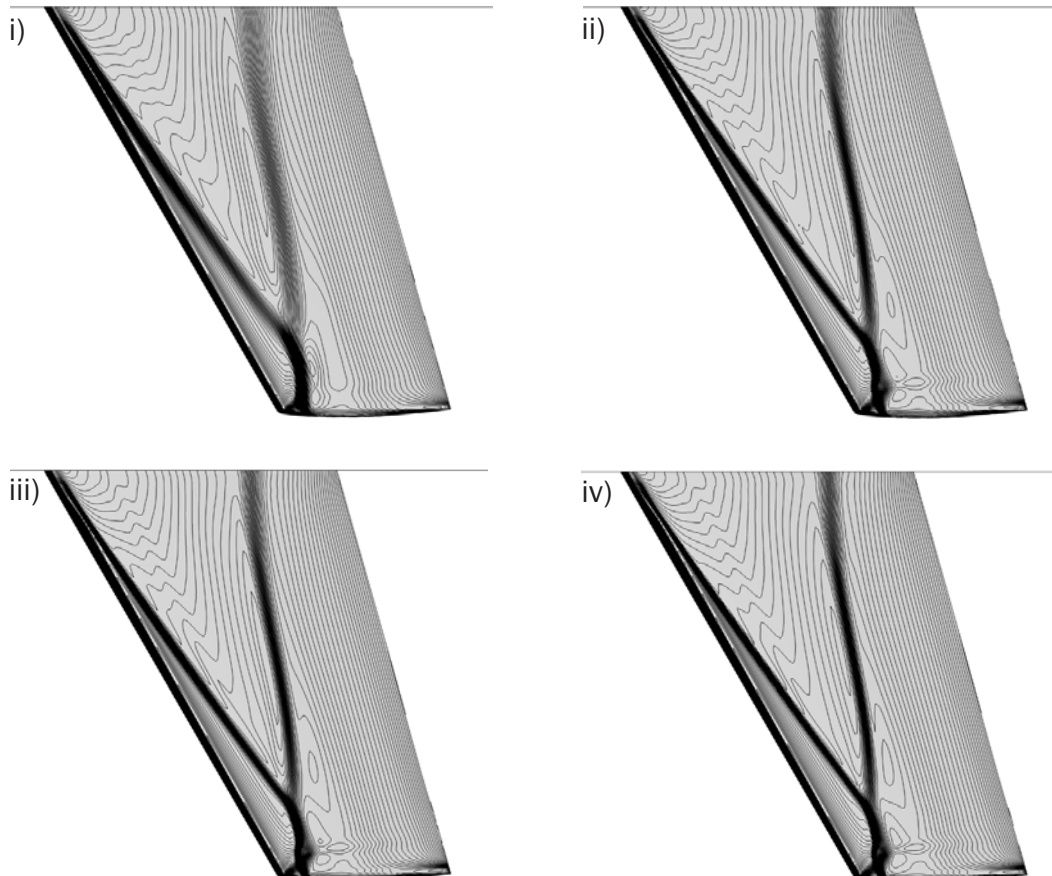


AGARD report (Schmitt and Charpin, 1979) is detailed fully within that publication, but can be summarised as follows: a root chord of 0.8059m, a leading edge taper of  $30^\circ$ , a trailing edge taper of  $15.8^\circ$ , and a span of 1.1963m from root to the tip as it maintains an M6 profile, beyond which it is swept radially to form a symmetric body of revolution. The aspect ratio is 3.8, and the mean chord is 0.64607m. 7 rows of pressure taps were present at  $z/b$  locations of 0.2, 0.44, 0.65, 0.8, 0.9, 0.95 and 0.99 as measured from the root. These parameters are presented for clarity in figure 4.30. A blunt trailing edge of 7mm was present, and was modelled in the CFD described here. A  $y^+$  of less than 1 was not possible over the entire wing, and was closer to 3 towards the wing root - still within the acceptable limits for enhanced wall-modelling. The case in question for this section, 2308, was conducted at a Mach number of 0.8395, an angle of attack of  $3^\circ$ , and a Reynolds number, based on the mean chord, of  $11.72 \times 10^6$ .

The test section dimensions of the continuous ONERA S2MA wind tunnel have been ignored in the validation cases presented here. While this might seem to be a considerable oversight considering the conclusions made in the preceding section, the original report is incomplete with regards to the nature and use of perforated walls.



General meshing approach applied to the M6 wing, with leading and trailing edge detail (right).



Contours of density on the upper surface of the M6 for increasing mesh resolution; i) coarse mesh, ii) standard mesh, iii) fine mesh, and iv) standard mesh with local shock-adaption.

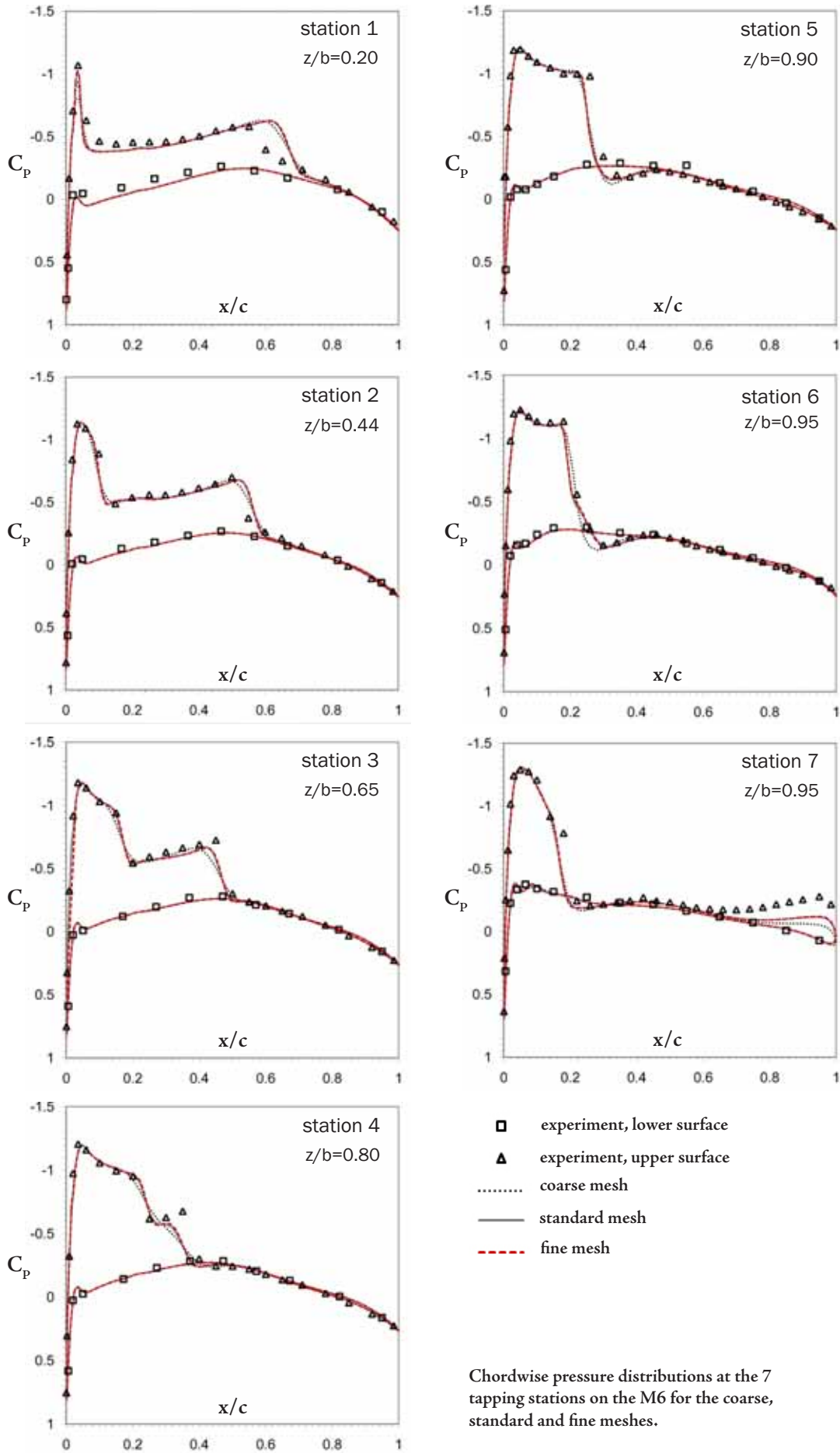
Additionally, as the wing does not span the test section, the flow is able to ‘relax’ around the wing and thus wall effects will be much less pronounced. Attempts by the author to compute the wing in a best-approximation of the test section yielded a worse comparison to experimental results than the “freeflight” cases. This suggests that methods employed by the experimentalists to reduce wall influences were indeed effective, but to the detriment of providing a truly effective test case for CFD. Nevertheless, the practice of simulating the wind tunnel wing as unbounded is normal practice. Investigation of wall effects for the M6 would make for an interesting companion to those described for the RAE 2822 ‘Case 10’, but will not be considered here as the existing comparisons are sufficient. The quoted tunnel turbulent intensity of 0.2% was used for validation cases.

Other important points to note about the experiments include the fact that transition was left to vary freely, and use was made of an endplate at the wing root to minimise wall effects by diverting the tunnel wall boundary layer away from the wing itself. A similar, although somewhat more crude, device was designed by the author for the RAE 2822 experiments in the USNA transonic tunnel, and was found to result in considerable spanwise influence, and thus the M6 experimental results may feature a similar minor disturbance..

#### 4.4.1 Mesh and boundary considerations

The boundaries were located as shown in figure 4.31, much closer to the aerofoil than for the two-dimensional simulations largely to keep the overall size of the mesh down, but as the mesh had to coarsen considerably as a necessity, no significant influence (<0.1% in terms of force coefficients) was observed in the results when the boundaries were extended by a further 5c.

As usual, coarse, standard and fine meshes were constructed along the lines of the general structure depicted in figure 4.32. The coarse mesh consisted of 172 nodes on the wing in the chordwise sense, and 50 spanwise cells clustered somewhat towards the wing tip (~1,500,000 cells in total). The standard mesh featured 195 nodes around the profile in the chordwise sense and 86 spanwise cells, as well as a finer resolution



in the near-wake region ( $\sim 5,100,000$  cells in total). The fine mesh featured 210 nodes around the profile and 100 spanwise cells, and was finer again in the near wake region ( $\sim 6,500,000$  cells in total). All meshes featured 8 cells across the finite trailing edge.

The effect of increasing mesh resolution on the density contours on the upper surface of the wing can be observed in figure 4.33. All meshes predict similar shock locations, but the resolution of the shocks in the vicinity of the wing tip, where the forward and rearward shocks converge, is more clearly defined by the fine mesh and the standard mesh with shock adaption.

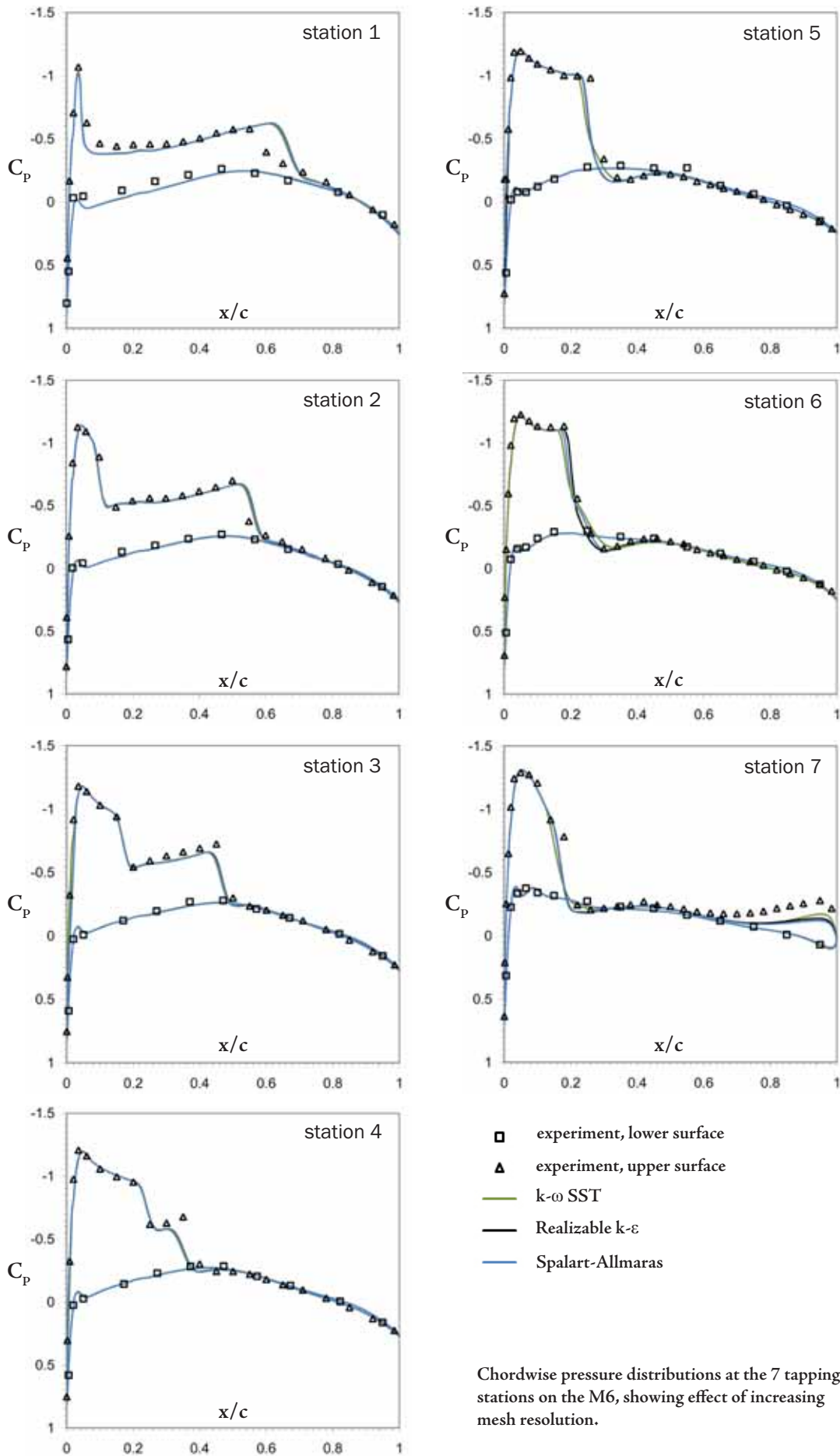
The pressure distributions shown in figure 4.34 highlight the performances of the meshes when compared to the experimental readings. Disagreement on the shock location at station 1 could well be a result of the tunnel wall and endplate effects which are not modelled in the CFD. The experiments indicate two distinct shocks at station 4 - these are represented in the CFD apart from on the coarse mesh. Station 7 is most sensitive to the exact geometry of the wing tip and specifically the mesh resolution at the blunt trailing edge. Agreement here is adequate, but consistent across the meshes tested.

While the coarse mesh provides unsatisfactory capture of the shocks and their locations, the other meshes are relatively consistent. As with the two-dimensional studies, the standard mesh with shock adaption proved to be as acceptable as, if not preferable to, the fine mesh, whilst incorporating just over 500,000 fewer cells even after the local refinement procedure. Thus the standard mesh with refinement was chosen as the method to be applied to all subsequent simulations.

#### 4.4.2 Turbulence modelling

Studies in literature indicate that the presence of the shock close to the leading edge spanning the majority of the wing results in a very short run of laminar flow (Langlois *et al.*, 1998), and thus the flow has been treated as fully turbulent in these simulations.

There is little to choose between the three turbulence models when comparing pressure distributions of the first four stations in figure 4.35. Station 5 shows an



underprediction of the shock location with the  $k-\omega$  SST model, but a better representation of the post-shock recovery region, and a similar situation can be seen at station 6. Here, the Realizable  $k-\epsilon$  model presents the best result in terms of shock location, but the SA model is also close and models the recovery region in superior fashion.

At station 7, none of the models represent the upper surface well towards the trailing edge, though again the consequences of any influence at the root that will have caused a minor disturbance along the wing will be most magnified in the tip region, and thus disagreement here is perhaps to be expected.

It is difficult to see definitively which model is producing the most accurate results, but the SA model captures the shock-induced behaviour at stations 5 and 6 best of all the models, and on balance it was chosen as the preferred model in complement to the two-dimensional study of the previous section.

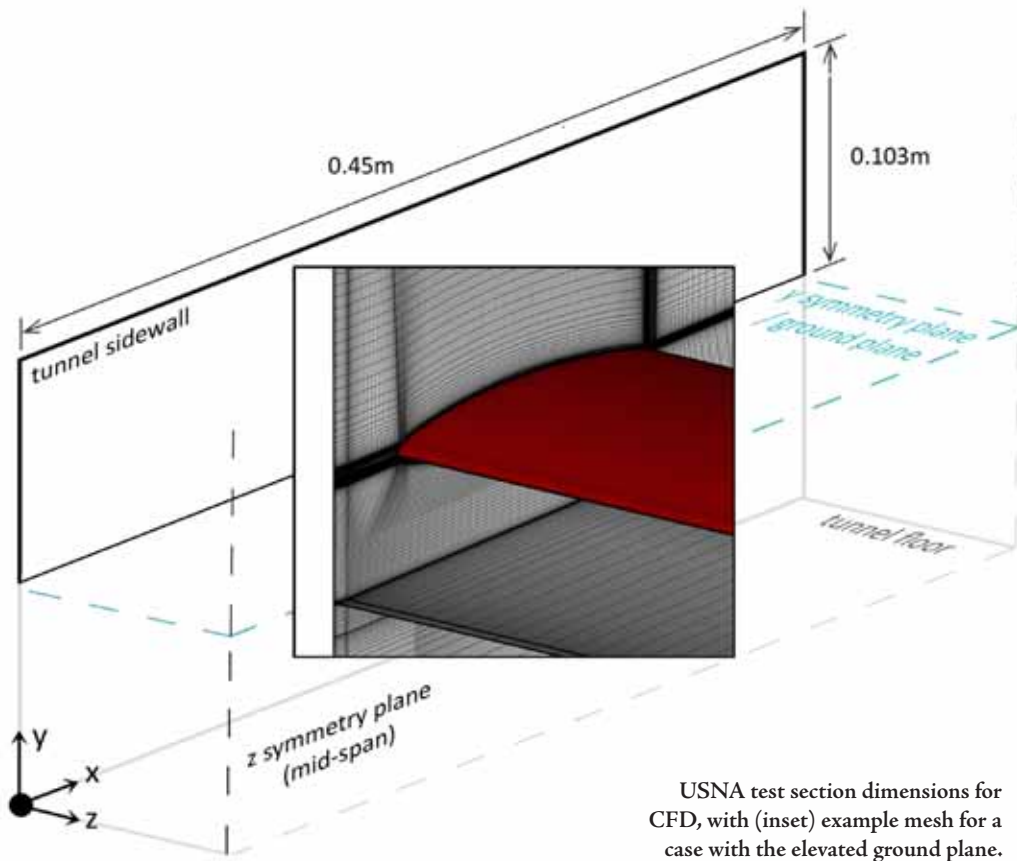
## 4.5 RAE 2822 Experiments at the US Naval Academy

A small number of cases from the USNA test programme have been chosen for presentation in this chapter and the next, as outlined in table 4.3. They have been selected to provide as wide as possible a range of flowfields to necessitate thorough validation, and do not necessarily represent the “best” matches with CFD data obtained from the whole test programme. Rather, they highlight the agreement and limitations of the CFD in a handful of situations of varying complexity. All the results presented here come from symmetry method experiments unless stated otherwise.

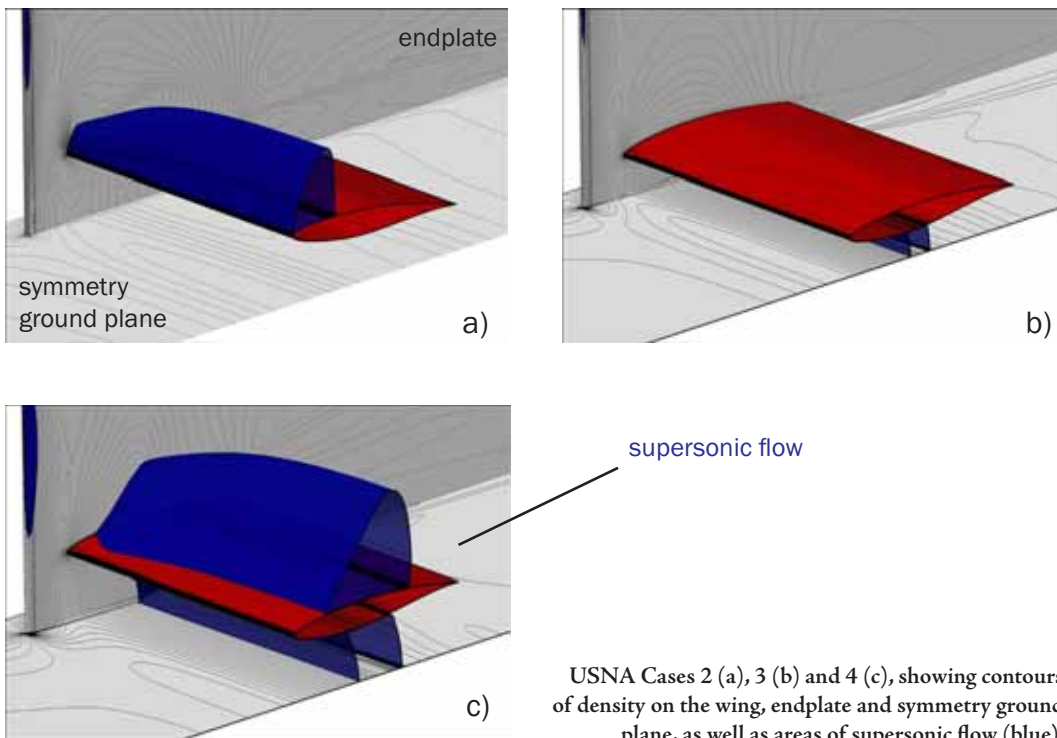
Aspects of the experiments not immediately obvious from the tests themselves are

Table 4.3. Cases used for validation

	$M_\infty$	$\alpha^\circ$	h/c	Comments
2822 USNA Case 0	0.586	0	n/a	<i>“free-flight” (no ground), shock-free, steady flowfield</i>
2822 USNA Case 1	0.531	0	0.128	<i>shock-free, largely-steady flowfield</i>
2822 USNA Case 2	0.629	6	0.232	<i>upper surface shock, unsteady flowfield</i>
2822 USNA Case 3	0.646	0	0.128	<i>lower-surface shock, mild oscillation</i>
2822 USNA Case 4	0.705	0	0.266	<i>upper surface shock almost stationary at symmetry plane, regularly-oscillating lower surface shock</i>



4.36  
FIG



4.37  
FIG

revealed by the CFD, such as the effect of the endplates, the nature of shock oscillations, and the influence of having free boundary layer transition. Experience from the AGARD cases 9 and 10 ensured that there was a sufficient level of confidence in the computational results prior to the present comparisons. This meant that the CFD could be used in this manner, to validate the experimental setup while using the experimental data to further validate the CFD, this time for ground effect cases, without concern that misleading results could come from guesswork or coincidence.

Case 1 features no shock waves in the test section, though the air between the wing and ground is accelerated to near-sonic local conditions ( $M_1=0.97$ ). CFD of these cases was run as transient until a nominally steady-state solution was obtained.

Case 2 presents the wing at an incidence of  $6^\circ$ , promoting a strong shock wave towards the leading edge on the upper surface. CFD was again run as transient - strong separation at the wing/endplate junction was observed, causing large-scale unsteadiness in the flowfield.

Case 3 presents a ground clearance and freestream Mach number sufficient to induce a shock wave on the lower surface only. This wave was found to oscillate regularly across a relatively small portion of the chord (4%), although the motion appears to be influenced as much by the separated flow at the endplate as the wave's own natural tendency for movement.

Case 4 presents the most complex flowfield observed in the tunnel: a mildly-oscillating shock on the upper surface, with an accompanying shock on the lower surface oscillating in a regular, larger-scale motion. Significant supersonic flow is also present around the endplate leading edges on the wing side. Cases featuring areas of supersonic flow are shown in figure 4.37.

#### 4.5.1 Mesh and boundary considerations

At first, the meshes and turbulence models will be examined purely as comparisons against the experimental data obtained, which at this stage was treated as nominally two-dimensional pressure distributions at the wing mid-span. Other three-dimensional

characteristics of the flowfield will be assessed subsequently. All results in this section were generated with the Spalart-Allmaras turbulence model, the selection of which will be discussed in 4.5.2.

The meshing approach from the cases in sections 4.3 and 4.4 established the principles of mesh construction for the wind tunnel cases. Due to the considerable computational expense of running a large number of transient simulations, the meshes were not locally refined at the shock locations.

The general domain and a portion of a sample mesh are presented in figure 4.36. For all cases, the simulations were run with an  $xy$ -symmetry plane at the wing mid-span. For the cases involving the symmetry method, a  $zx$ -plane symmetry plane was used at the imaginary ground plane, and for cases involving the elevated ground, that apparatus was modelled in full. The endplate leading edge angles matched the wind tunnel model, however the pockets milled into them on the side facing the tunnel wall were not included in the CFD geometry, and neither were any approximations of the geometry of the vinyl tubing of the pressure tapings, which ran along the endplate in this region.

The sting mount strut at the rear of the endplates, which also provided sufficient rigidity to the assembly, was included in early simulations to assess its effect on the flowfield and to determine if it was necessary to include it in all CFD cases. We will return to this issue in section 4.5.3.1. The sidewall boundary layer was assumed to begin at the test section inlet - no information on the wall boundary layers was available for input into CFD. Given the relatively small gap between the endplate and the sidewall boundary layer, this assumption may have had ramifications for the extent of separation around the endplate leading edge at higher Mach numbers.

Coarse, standard and fine meshes were developed. The presence of strong unsteady effects in cases 3, 4 and 5 meant that the coarse mesh was not formally assessed, as it would not have had sufficient cell density to resolve the complexity of these cases. The standard mesh featured 374 cells around the wing in the chordwise sense, clustered towards the leading and trailing edges, and 40 spanwise cells, clustered towards the junction with the endplate. The  $y^+$  values for attached flow on the wing, elevated ground

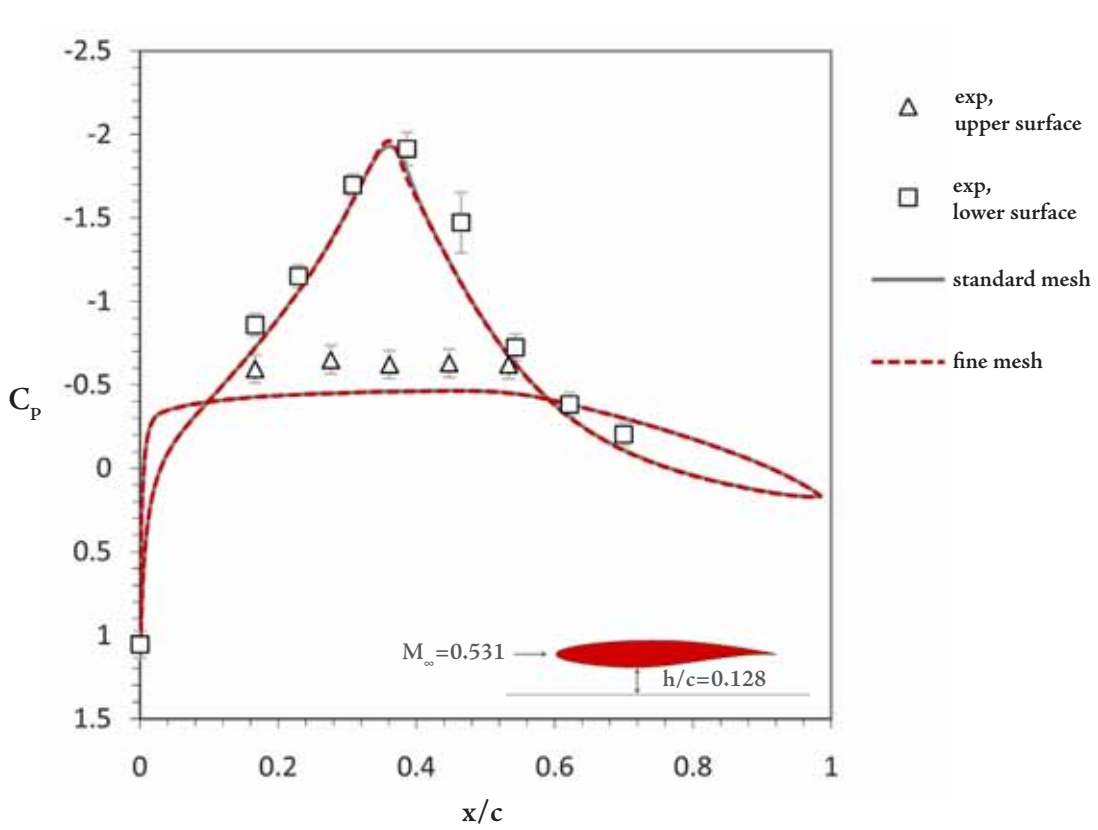
(if used) and endplate varied between 0.1 and 3 depending on the Reynolds number and flow conditions. Values on the tunnel wall, floor and ceiling were between 3 and 5.

A typical symmetry method mesh contained approximately  $3.9 \times 10^6$  to  $4.2 \times 10^6$  cells, depending on the ground clearance. With the elevated ground, the mesh contained approximately  $5.9 \times 10^6$  to  $6.4 \times 10^6$  cells.

The fine mesh featured 55 spanwise cells on the wing, and 568 cells around the wing in the chordwise sense, with the total number of cells in the region of  $7.9 \times 10^6$  to  $8.3 \times 10^6$ . The wake region of the wing was slightly refined, but otherwise the other blocks of the grid were left the same as the standard mesh. A fine mesh was not constructed for the elevated ground tests.

Figure 4.38 shows a comparison between the standard and fine meshes for the shock-free Case 1. The meshes produced almost identical pressure distributions at the mid-span symmetry plane; they both exhibited good agreement with experimental data, though the pressure across the upper surface was overestimated by a consistent amount. The pressure tapping beyond the lower surface suction peak is not well-matched by the CFD. The simulations indicated that the peak local Mach number here was approximately Mach 0.97, such that any minor change to the flow conditions experienced by the wing may have caused a local pocket of supersonic flow to form. It is possible that this is why the experimental pressure recovery is slightly further downstream than that predicted by the CFD, though the experimental distribution indicates lower pressure over the upper surface than that seen in the numerical result, and this implies that more flow was directed over the upper surface in the experiment, such that the attainment of a locally supersonic Mach number on the lower surface would be less likely.

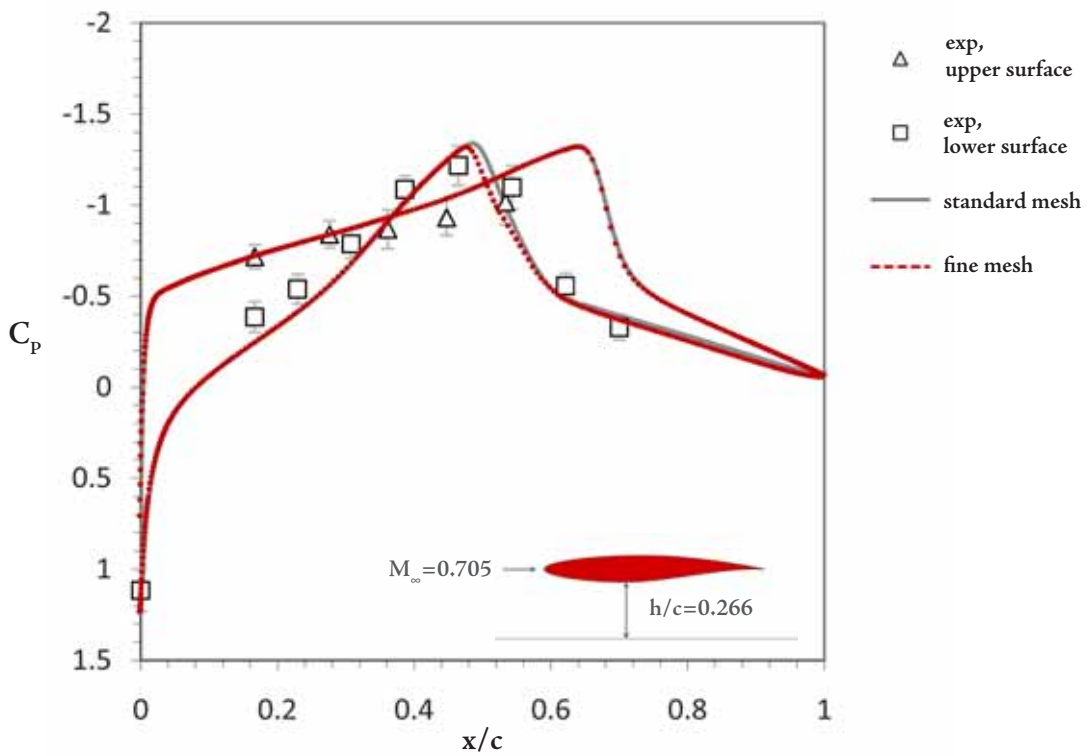
Figure 4.39 shows time-averaged pressure distributions (over 3 oscillation cycles) for the two meshes for Case 4. Again, both meshes match the experimental results satisfactorily, albeit slightly underestimating the upper surface pressure beyond  $x/c=0.4$ , and overestimating the lower surface pressure drop over the forward half of the chord. The lower surface shock wave oscillated considerably, and therefore it is in this region that differences between the two meshes are observed. The standard mesh



4.38

FIG

Pressure distribution at the mid-span symmetry plane, USNA Case 1, standard and fine meshes.



4.39

FIG

Time-averaged pressure distribution at the mid-span symmetry plane, USNA Case 4, standard and fine meshes.

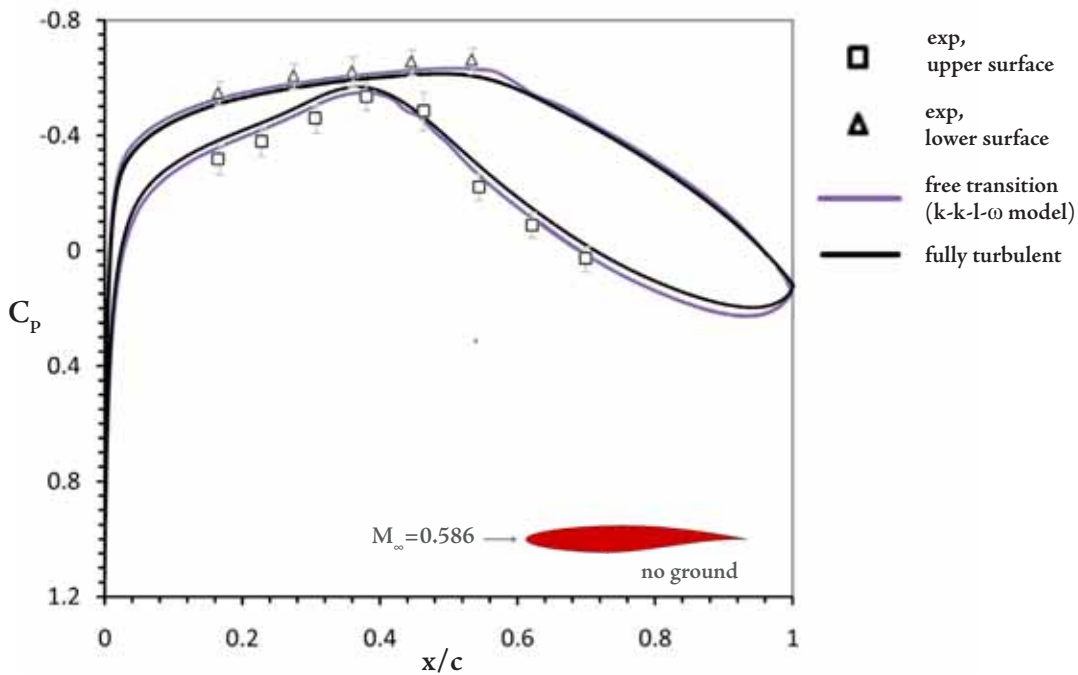
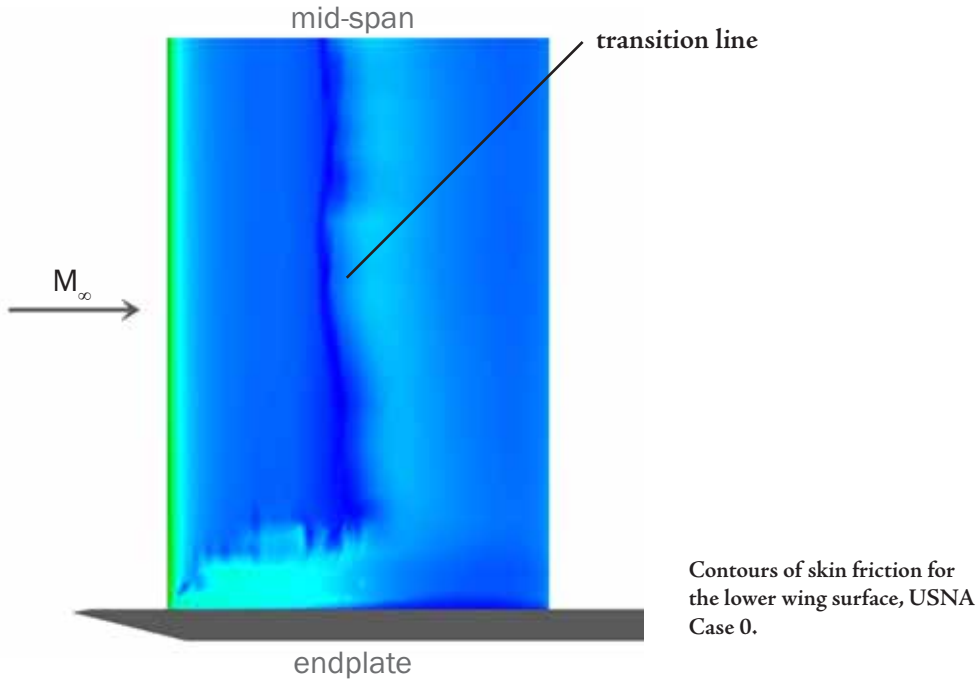
provides a closer match to the experimental readings in this location, which indicates that the higher level of smearing in the shock region as it moved with time may have provided a more fortuitous result than the mesh which physically resolved the waves more effectively. In this respect, it seems that the greater discrepancy between the finer mesh case and the experimental data may be due to modelling deficiencies which may stem more from factors of experimental error. Without the means to effectively pinpoint the source of the discrepancy, the standard mesh was deemed to be of an acceptable quality to produce results within the margin of experimental error, and was used for all subsequent simulations.

## 4.5.2 Turbulence Modelling

### 4.5.2.1 *Extent and influence of laminar flow*

As mentioned in chapter 3, the wings were not equipped with transition strips, and thus free transition occurred at an indeterminate point along the chord. In order to assess the applicability of a fully-turbulent CFD solution in comparison to the experiments, some simulations were run to understand the effect of transition on the results which might be obtained.

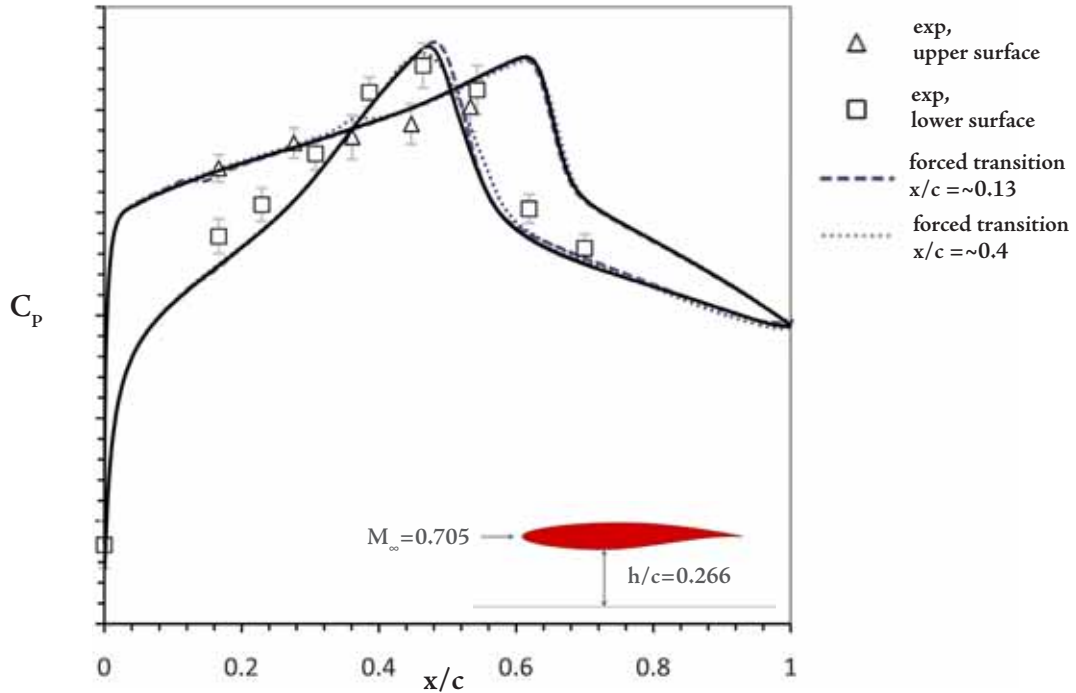
Cases 0 and 5 were selected, presenting the simplest and most complex tunnel flowfields, respectively. Two runs for Case 0 were conducted - one fully turbulent with the Spalart-Allmaras model, and one with the  $k-k-l-\omega$  model, which other researchers have proven as effective for transonic flowfields with free transition (Langtry and Menter, 2005). The contour plot in figure 4.40 suggests that transition would have occurred at  $x/c=0.4$ , with a contamination from the endplate which has only a minor spanwise effect, possibly due to the mesh. The pressure distributions presented in figure 4.41 indicate that this has had a relatively small effect on the overall characteristics of the wing. One must bear in mind, though, that although the geometry of the wind tunnel apparatus was faithfully reproduced and the inlet turbulence characteristics matched, the oncoming flow in the CFD is extremely smooth in time compared to the constantly-fluctuating



Pressure distribution at the mid-span symmetry plane, USNA Case 0, free transition and fully turbulent CFD.

wind tunnel flow. Therefore in the experiment, the transition line would be continually changing, and would have also been affected by the surface roughness of the wing (Sudani *et al.*, 1994). However, based on the pressure distributions of Case 0, it can be surmised that a fully-turbulent simulation is a reasonable approximation of the flowfield.

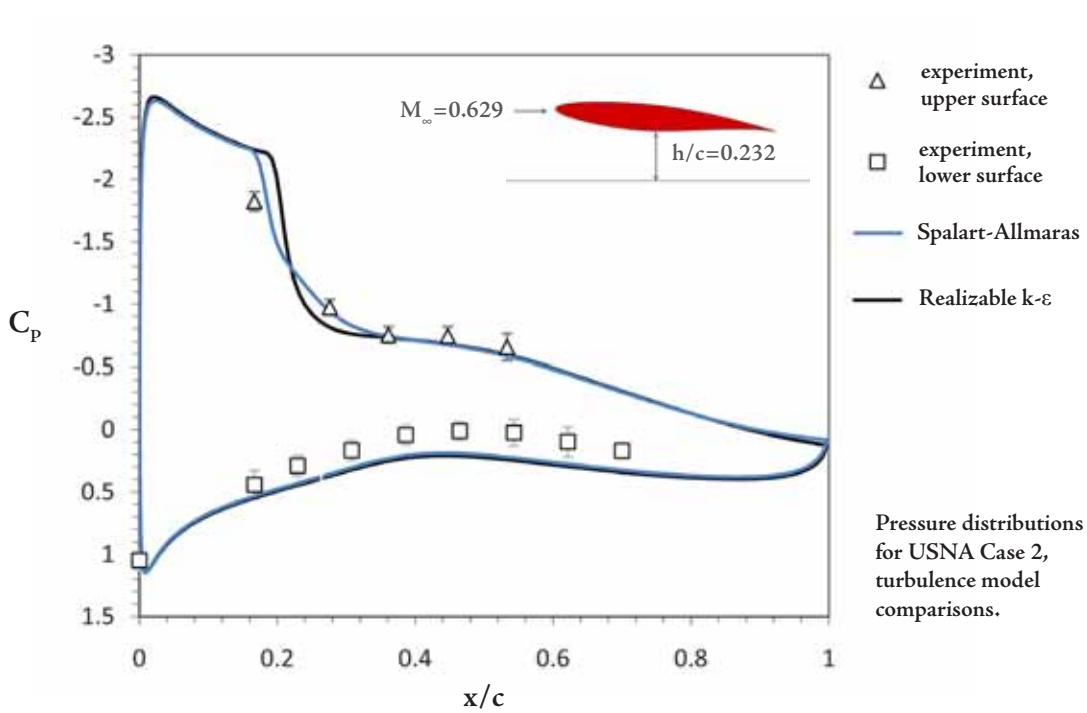
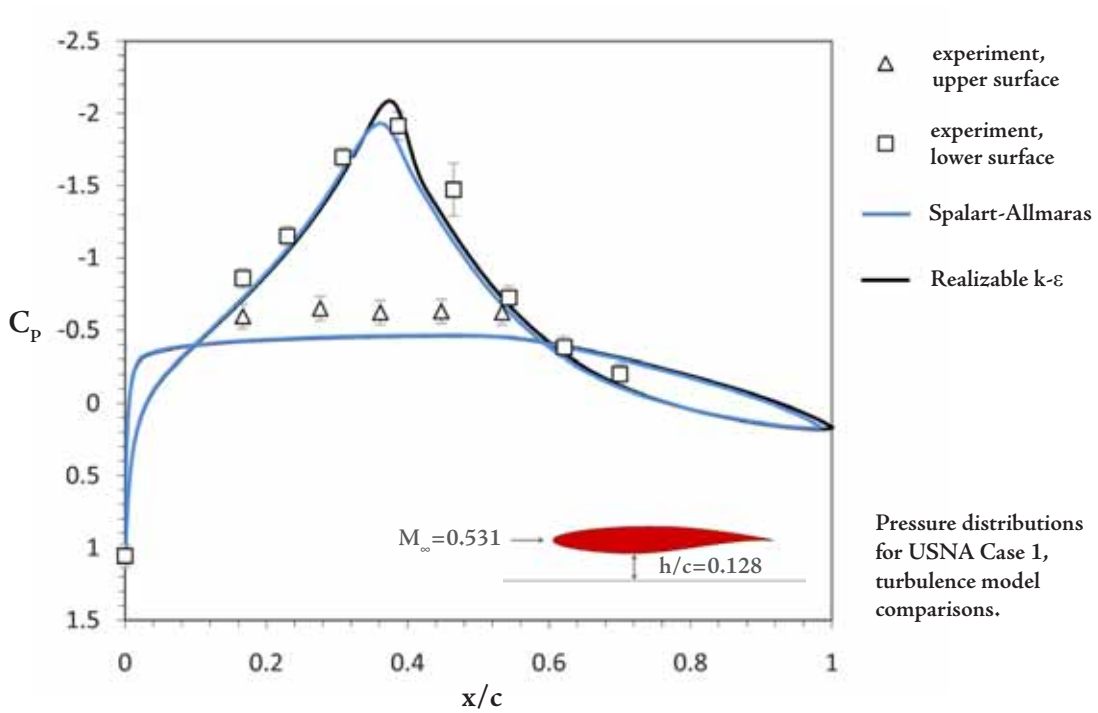
Investigations by Sudani *et al.* (1994) suggest that having transition occur this far back on the wing, particularly when there is an oscillating shock wave, can have a profound



Time-averaged pressure distributions at the mid-span symmetry plane, USNA Case 4, free transition and fully turbulent CFD.

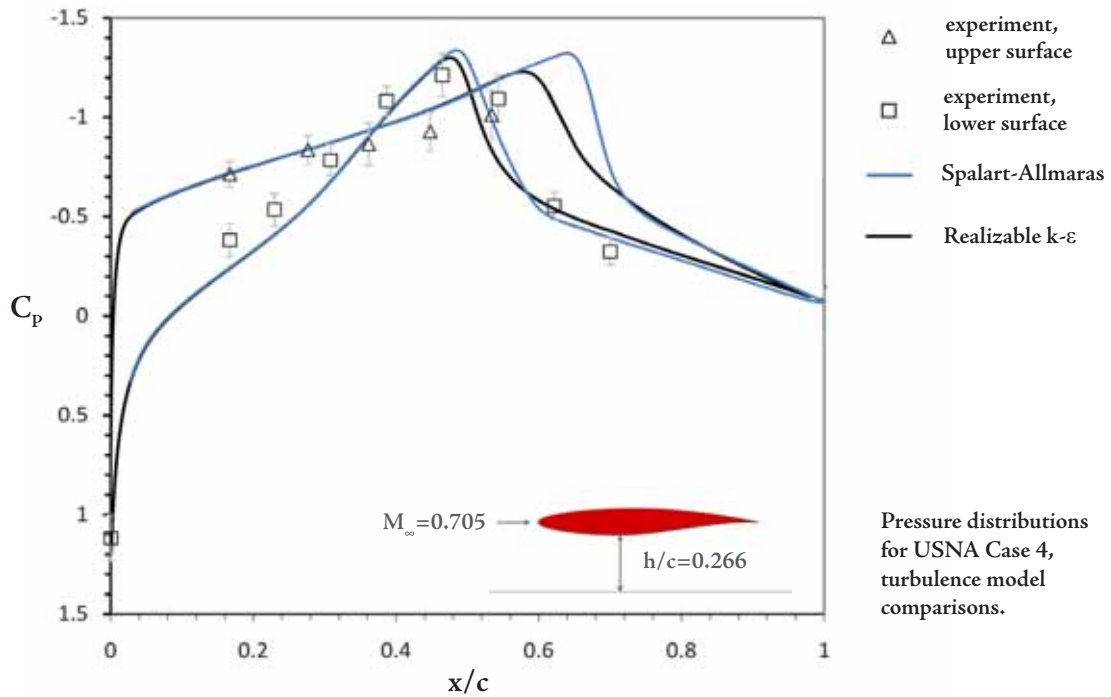
influence on the characteristics of that shock. Therefore three simulations were made with Case 4; with transition numerically tripped at  $x/c=0.13$ , at  $x/c=0.40$ , and fully-turbulent. Time-averaged pressure distributions, representing 3 full cycles of the wing  $C_L$  as the upper and lower shocks oscillated, are presented in figure 4.42 and, encouragingly, present only minor differences despite the large variation in transition. The case with transition at  $x/c=0.4$  is closest to the experimental results, which would indicate that this transition location is closest to that which occurred in the wind tunnel.

Based on these two sets of comparisons, fully turbulent simulations were run for all remaining cases. It would have been difficult to justify using the  $k-k-l-\omega$  model for all simulations - the run times were approximately 50% longer compared to cases using the Spalart-Allmaras model, and the mesh would have had to be finer around the wing and endplate to achieve an acceptable indication of the transition behaviour, thus increasing run times again. Furthermore, the model did not perform with adequate stability in the presence of strongly separated flow. As a result, the Spalart-Allmaras and Realizable  $k-\epsilon$  models were the only ones used for comparison in this study.



#### 4.5.2.2 Comparison of turbulence models

Pressure distributions obtained with the two models are presented for Cases 1, 2 and 5 in figures 4.43, 4.44 and 4.45 respectively. Case 1 comparisons show both models matching the experiment acceptably, both overpredicting the upper surface pressure as with the mesh comparisons, as well as failing to match to the tapping beyond the lower surface pressure peak. That both models and both meshes tested produce this result, one



can say with more confidence that other factors were responsible for the disparity. The Realizable model predicted barely-supersonic, shock-free flow at the suction peak on the lower surface, indicating the sensitivity of the flowfield to modelling choices at critical points on the Mach number scale.

The pressure distributions obtained for Case 2, in figure 4.44, indicate a more severe discrepancy in results. The Spalart-Allmaras model predicts a small region of shock-separated flow on the upper surface from approximately  $x/c=0.165$  to  $0.205$ , whereas the Realizable  $k-\epsilon$  model predicts the shock further back along the chord, and with no significant separation of the flow. The Spalart-Allmaras simulation provides notably better agreement with the experimental results for the two tappings upstream and downstream of the shock, though both models overestimate the lower surface pressure readings.

The clearest difference between the models appears in the Case 4 comparison in figure 4.45. Here, the upper surface shock is significantly more smeared in the time-averaged plot with the Realizable model than with the Spalart-Allmaras model, as a result of a much greater chordwise movement of the shock there, with additional periodic

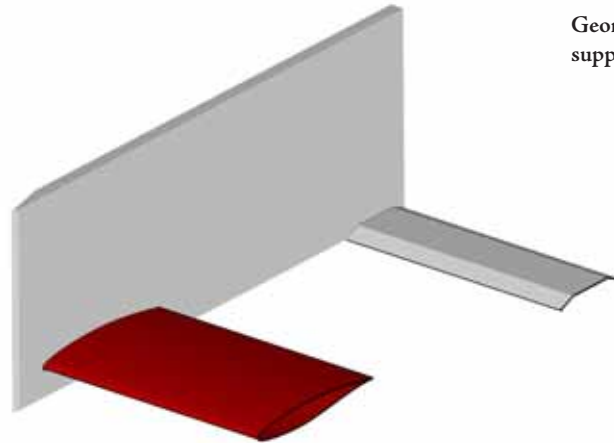
flow separation from the moving shock foot. The lower surface distributions are in closer agreement, although again a greater level of smearing is present in the Realizable plot. Unlike with the upper surface shock, this is due to a greater level of diffusion with the two-equation model, as the extent of shock movement is very similar compared to that of the Spalart-Allmaras simulation. The latter appears to better predict the average shock location more satisfactorily, and provides a better match in the pressure recovery region as a consequence.

On balance, it was decided that the Spalart-Allmaras model was providing a better match to experiments, particularly in the presence of shock waves, and so had been proven to be the most effective model for both the experiments from literature and those conducted for the present research.

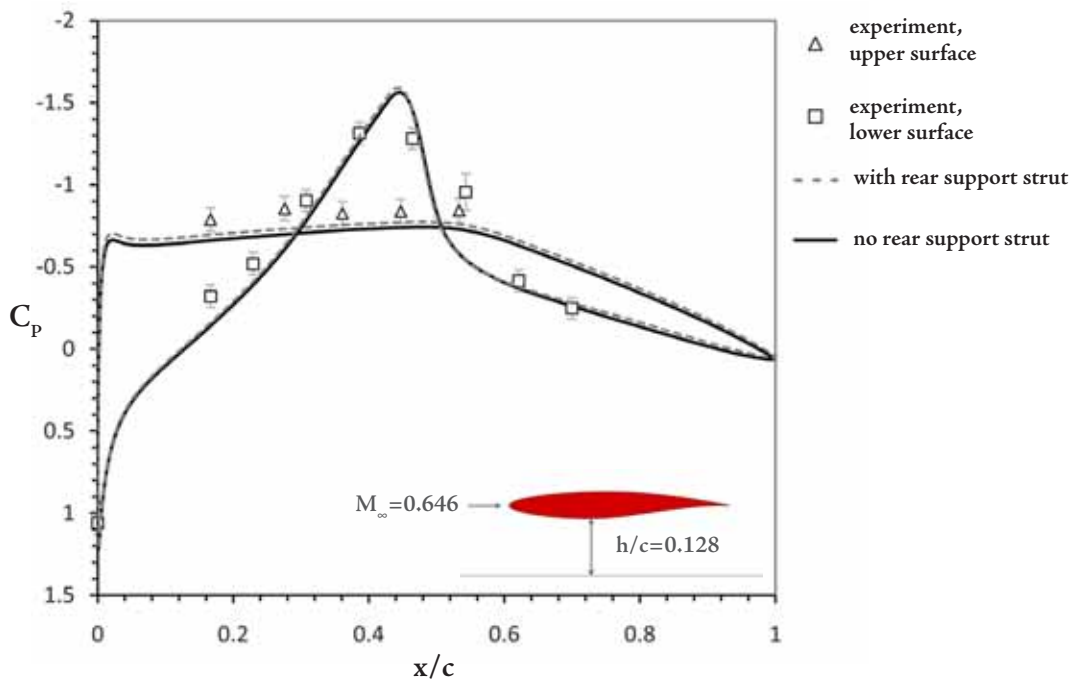
### 4.5.3 Further experimental comparisons

#### 4.5.3.1 Influence of rear sting mount strut

The horizontal strut connecting the two endplates at their rear, as well as mounting the entire assembly onto the sting, was located only  $2.5c$  downstream of the trailing edge, and would therefore influence the flow over the wings to an extent. In order to quantify this, a simulation of Case 3 was run with the strut, in the configuration shown in figure 4.46, to compare to one run without. The time-averaged pressure distributions from these simulations are shown in figure 4.47. Although similar, the plots show that the influence of the strut was to promote a slightly higher flow rate over the upper surface, decreasing the pressure there. This moves the CFD plot closer to the experimental upper surface readings, which had been overpredicting the pressure in this region in all other cases featuring a shock-free upper surface. However, the distribution predicted by the CFD is still barely within the margin of error reported for the upper surface experimental data, and thus the improvement in the match is slight. Neither simulation accurately predicted the experimental value at the lower surface  $x/c=0.543$ , behind the shock wave, which also proved to be poorly-matched in the comparisons to Case 4 presented in this chapter.



Geometry for CFD cases involving the rear support strut.



Pressure distributions for USNA Case 3, comparison between runs with and without the rear support strut

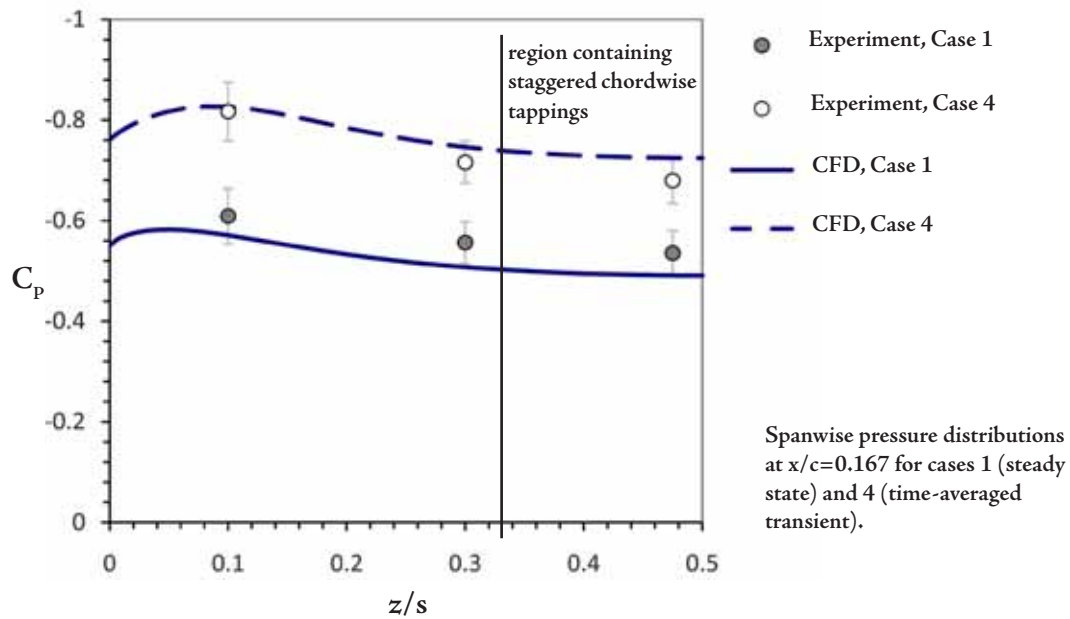
Given the relatively small improvement to the result, but the necessity of having an additional  $3 \times 10^5$  cells required to resolve the flow around the strut in the manner of the standard mesh, the simulations without the strut were deemed to be acceptable and this approach was applied to the results presented throughout this chapter and the next.

#### 4.5.3.2 Quality of two-dimensional flow at the mid-span

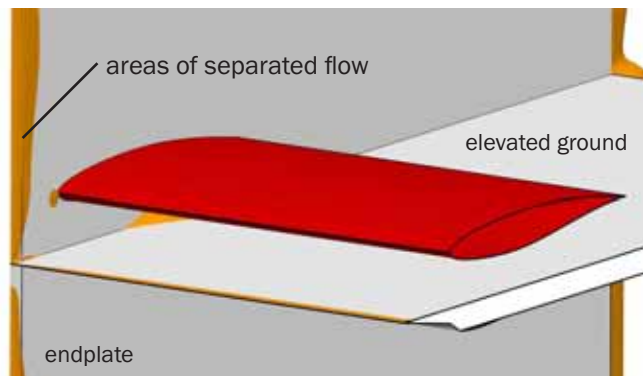
Investigations in literature (Sudani *et al.*, 1994, Barbaruk *et al.*, 2003) indicate that a wing

aspect ratio of 3 is not necessarily sufficient for flows similar to the ones discussed here, particularly in the presence of shock oscillation and uncertain transition behaviour. The influence of spanwise flow is compounded in the present experiments by the flow around the endplate, which was observed in CFD to separate at the leading edge, shown in figure 4.49. As a rudimentary check of the quality of two-dimensional flow at the mid-span, comparisons were made to the three spanwise tappings at a chordwise location of  $x/c=0.167$  for cases 1 and 4.

While the CFD shows good agreement with the experiments in terms of trends and actual values, the simulations indicate that while the flow at the mid-span was marginally two-dimensional, the flow over the central third of the wing, where



4.48  
FIG



4.49  
FIG

Areas of separated flow for Case 1 (with ground plane). Note separation also present at the elevated ground leading edge and at the ground/endplate junction under the wing.

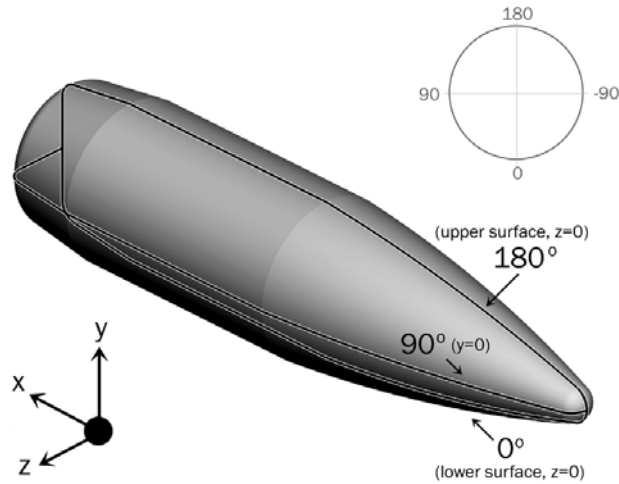
the staggered tappings were located, was not. The variance between  $z/s=0.33$  and  $0.5$  is several percent, and thus while the trends would not be markedly different, the quantitative values would have to be corrected using CFD as guidance if a more accurate two-dimensional plot were to be presented.

This and the other factors already discussed indicates that while the experiments were useful in providing an excellent source of validation of the code for transonic ground effect, the results themselves contain too high a margin of error to be truly useful as stand-alone experimental data for a two-dimensional RAE 2822 in ground effect. The experimental method itself, however, can still be compared directly to numerical simulations which feature a moving ground, and this will be covered in the following chapter.

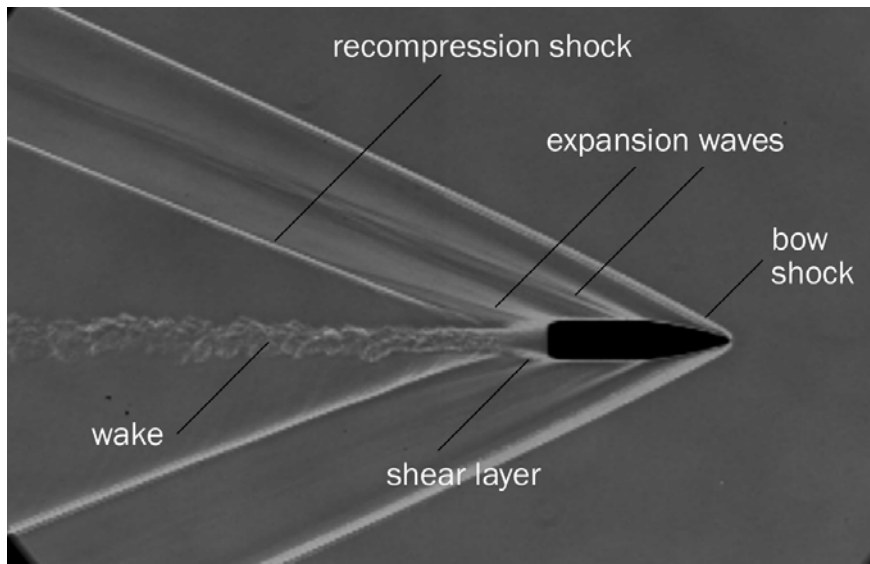
## 4.6 Supersonic Projectile

The utilisation of RANS CFD for the investigation of projectile aerodynamics and flight has become relatively common amongst ballistics researchers, with a particularly large body of work produced by the US Army Research Laboratory's Aberdeen Proving Ground. Both in-house and commercial codes (CFD++; Silton, 2005), Fluent; Catalano and Sturek, 2001) have proven effective at predicting the aerodynamic characteristics of projectiles of varying complexity and dimensions.

With regards to certain meshing and turbulence modelling issues investigated in the present study, these two studies using commercial code are of particular interest. The study involving Fluent (Catalano and Sturek, 2001) examined the effectiveness of turbulence modelling with regards to an axisymmetric wake region only. A five-equation Reynolds Stress model was chosen due to its higher-order properties, although no direct evidence was presented to support its advantage over the much lower order Spalart-Allmaras model. Indeed, all the models tested were reported to perform similarly in terms of streamwise mean velocity in the wake. Mesh convergence studies were made for the wake region but did not address the resolution required to capture shock waves accurately. The more recent study of Silton (2005) 2005), using the CFD++ code for



Coordinate reference frame



Schlieren photograph with annotated flowfield characteristics for the projectile in free flight conditions.

a full three-dimensional spinning projectile, attempted to investigate the influence of geometric simplifications made in the interests of ease of modelling. It was determined that negating the rifling grooves (striations) and other small-scale physical aspects of the body was not markedly detrimental to the prediction of aerodynamic forces and moments, although moments and derivatives directly related to the spinning motion of the projectile were not well predicted by the simplified model. A similar multi-block meshing strategy to the present investigation was used and showed good mesh convergence for grid sizes comparable to the standard meshes described in the following section, though no local

mesh adaption was investigated.

#### 4.6.1 Mesh and boundary considerations

Some salient features of the flowfield around the projectile are shown in figure 4.51, to aid the reader throughout this section prior to the more detailed discussion in Chapter 9.

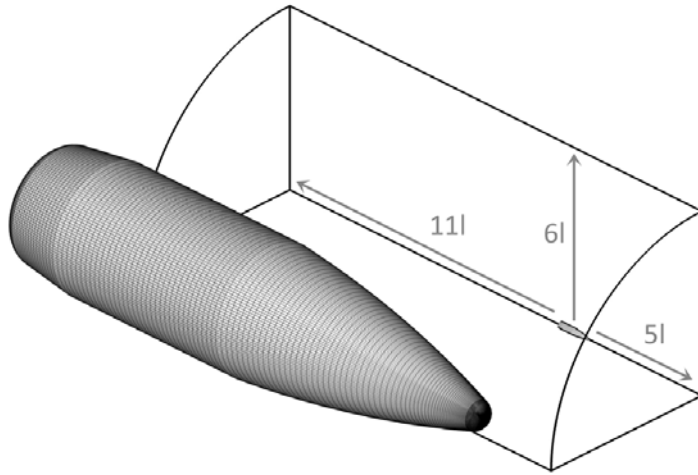
For CFD, the projectile was geometrically simplified by the removal of the knurled strip and rifling striations. This was an aid in mesh creation, as it eliminated the need to have extremely fine mesh in these regions to pick up flow disturbances which are very weak relative to the major waves in the flowfield. It also meant that simulations did not have to be run as a transient cases featuring a dynamic mesh. The simplified approach has been proven as effective at predicting aerodynamic characteristics of a similar projectile (Silton, 2005), though the dynamic derivative and roll damping coefficients are known to be more sensitive to the striations (Silton, 2005; Weinacht *et al.*, 2003]. Since these derivatives and coefficients are not considered in the present study, the assumptions made are justified.

Simulations of the wind tunnel model in the ADFA blowdown tunnel involved a computational domain directly equivalent to the test section (full size cross-section: 155mm x 90mm) as bisected in the  $y$  and  $z$  planes by symmetry boundaries to represent the symmetry ground plane and the vertical centre plane of the apparatus (from the coordinate reference system outlined in figure 4.50, the  $0^\circ/180^\circ$  plane).

The inlet conditions, set at 2.5 model-lengths upstream of the projectile nose, were based on the experimentally-obtained conditions summarised in Chapter 3, and the tunnel sidewall and roof were modelled as no-slip walls. The bow shock reflection from the sidewall, following a strong interaction with the boundary layer there, was found to interact with the sting/wake approximately 4.5 to 5 projectile diameters downstream of the base of the model and thus did not directly influence the flowfield area of interest.

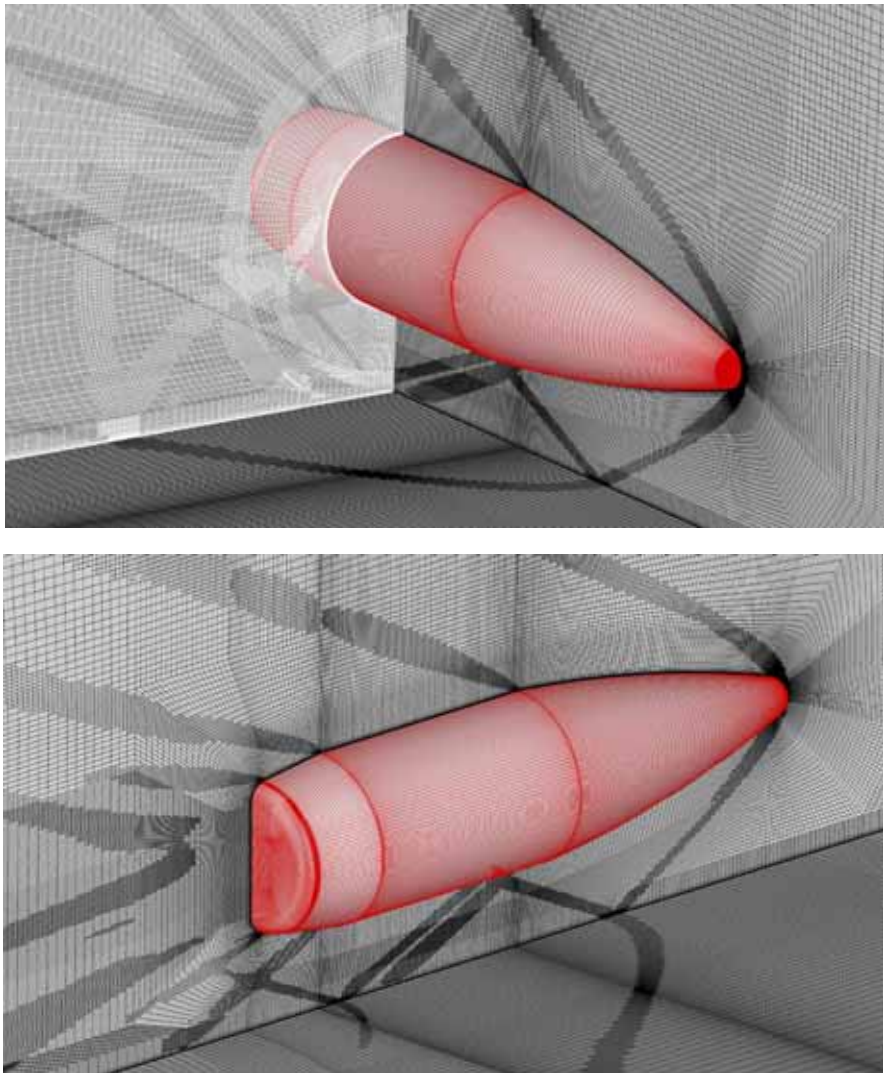
The sting was initially included in the setup. When it was found to have negligible influence on the flow around the projectile apart from at the base region and in the wake,

4.52  
FIG

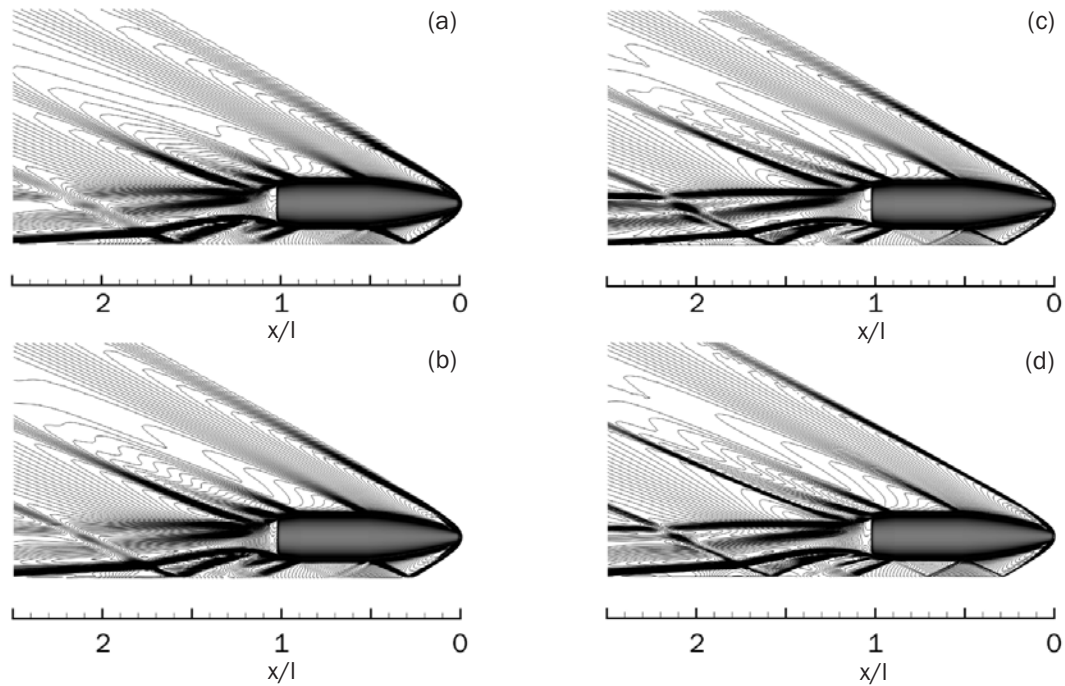


Bullet surface mesh and example quarter-domain for live-range freeflight comparisons

4.53  
FIG



Mesh on z-symmetry, projectile, volume slice, and 'ground' plane (after shock-adaption) for half model, no-sting simulations of wind tunnel symmetry method.



Contours of density as mesh is adapted for non-spinning (symmetry) bullet at  $h/d=0.42$ ; a) coarse ( $2.18 \times 10^6$  cells), b) standard ( $4.91 \times 10^6$  cells), c) fine ( $6.43 \times 10^6$ ), d) standard with shock adaption ( $6.64 \times 10^6$ )

projectiles, and for the wind tunnel model at an  $h/d$  of 0.42 and 0.5. The wind tunnel and live-range meshes were similarly structured, after the general approach depicted in figure 4.53, with the exception of increased resolution at the wind tunnel walls to capture the boundary layers present there. Over both the projectile surface and ground plane for all simulations, the wall  $y^+$  value was between 1 and 2 to facilitate enhanced wall modelling to effectively determine the boundary layer, particularly in regions of shock interaction. The projectile surface mesh featured 160 circumferential cells, and this aspect of the mesh was not altered during the refinement studies.

Detailed presentation of the full range of mesh sensitivity studies is not necessary to convey the outcomes; the case of  $h/d=0.42$  (half model, no spin), in which the bow shock reflects to re-impinge on the projectile body, is representative of the approach applied to all cases. In this and subsequent figures, the levels depicting the contours of density across strong gradients have been exaggerated for clarity in black and white depiction, and thus the shocks appear to be thicker than they are. The resolution of the mesh in the area between the projectile and the ground, in particular, was of interest in

it was removed from subsequent computational models to facilitate clearer comparisons with simulations of the live-range experiments.

Far downstream of the projectile model, an extended portion of test section not present in the actual wind tunnel was introduced to allow the wave reflections to diffuse prior to reaching the pressure-outlet rear boundary. This was done purely to aid the solver; due to the supersonic nature of the flow, no interference from this section or the outlet was observed to affect the flowfield in the area of interest from the projectile to the far wake.

For the live-range experiments, a much larger domain was devised for simulations with both a central symmetry plane at  $z=0$  (for no-spin cases ) as depicted in figure 4.52, and full projectile (spinning). Although the projectile’s rate of spin will begin to decrease immediately upon leaving the barrel, it has been assumed in all simulations to be a constant  $17700\text{rads}^{-1}$  at all stages of motion.

The sensitivity of the results with respect to the farfield boundary locations was examined by benchmarking forces obtained around the projectile in freeflight (quarter model with symmetry) as shown in Table 4.4 for the standard mesh described below. Based on these results, a domain extending 5 projectile lengths upstream of the nose, 11 to the rear from the base, and 6 to the radial boundary was deemed acceptable, although it is acknowledged that all waves have become significantly diffused in the mesh by these boundaries.

Fully-structured multi-block meshes were generated in all cases. Extensive grid-refinement studies were conducted for a quarter bullet (freeflight with symmetry) model, then at several ground clearances for both spinning and non-spinning (half model)

Table 4.4. Effect of variations in domain extent for a quarter projectile model.

(U=upstream l, D=downstream l, R=radial l)	var. in $C_{N_A}$	var. in $C_{D_A}$
3U, 9D, 4R	-2.92%	-7.71%
<b>5U, 11D, 6R</b>		
7U, 11D, 6R	0%	0%
5U, 15D, 6R	0.02%	0.05%
5U, 11D, 8R	0.01%	0.01%

this scenario given the multiple reflections. All results for this stage were generated using the Spalart-Allmaras turbulence model - turbulence modelling is discussed in more detail in section 4.6.2.

Meshes of coarse, standard and finer density were constructed. On the projectile surface and in the nearfield, the mesh resolution increased in broadly exponential fashion. The coarse mesh featured 130 lengthwise cells on the projectile surface, the standard: 255, and the finer, 460. This resulted in overall mesh sizes of  $2.19 \times 10^6$ ,  $4.91 \times 10^6$ , and  $6.53 \times 10^6$  cells respectively. If applied to simulations involving the full spinning projectile, the mesh was exactly doubled in size. The near-field mesh density in the wake and between the projectile and ground increased accordingly with the increases in bullet surface mesh cells.

In order to capture the shock waves more effectively, particularly since they already suffer diffusion by virtue of numerous natural interactions with expansion waves, local mesh adaption in regions of high local density gradient was performed. This was limited to no more than  $3 \times 10^5$  cells per case (increasing the overall number of cells by a maximum  $2.4 \times 10^6$ ). The local adaption was performed on only standard and fine meshes.

The mesh upstream of the projectile, downstream in the wake, and to the radial farfield boundary, was non-conformal, with cells clustered closer to the projectile and growing slowly in volume from there as was seen to an extent in figure 4.53.

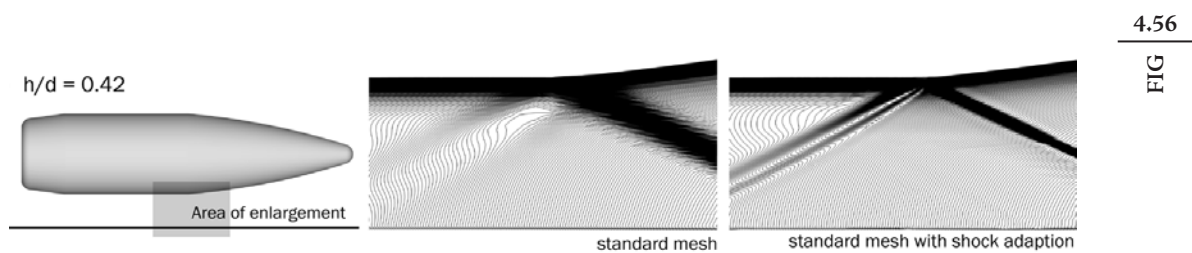
In figure 4.54, one can see the influence of increasing mesh density on the resolution of the shock waves around the projectile. The coarse mesh is able to capture the flowfield relatively well although the waves quickly diffuse into the farfield, and a secondary reflection from the projectile to the ground is very weak and cannot sustain any subsequent reflection. The standard mesh presents an improvement, but the finer mesh shows that flow features in the wake and the multiple reflections between the projectile and the ground require this level of refinement to adequately resolve all the features of interest. Looking at the pressure distributions around the projectile for the  $0^\circ/180^\circ$  plane, in figure 4.55, further evidence of the improvements brought by refining

the mesh can be observed. This ground clearance is unique in that the bow wave reflection impinges at the blend from the ogive to the main body, and thus the reflected shock and an expansion wave exist in very close proximity. The standard and coarse meshes have difficulties in clearly defining the flow in this region, whereas the fine and shock-adapted meshes capture a distinct pressure spike at approximately  $x/l=0.48$ . A visual indication of the beneficial influence of increased mesh density in this region can be seen in fig. 4.56, where the resolution of the shock/boundary layer interaction at the blend to the main body is critical. The base pressure profiles for the finer and adapted meshes are likewise similar, as opposed to the differing distributions predicted by the standard and coarse meshes.

As can be concluded from figure 4.57, the differences between all the meshes in terms of predicted forces are not substantial, with a difference in  $C_{N_A}$  from coarse to finest at a maximum of 2.5%, and  $C_{D_A}$  a maximum of 6%. The difference between fine and shock-adapted standard meshes was modest in terms of drag but significant in terms of lift. Subsequent shock-adaptation of the finer mesh changed both values by less than 0.2%. Therefore the standard mesh with shock adaptation was adopted as the preferred method for capturing the waves as accurately as possible within the limits of available computational resources.

#### 4.6.2 Turbulence modelling

The flow in all simulations was assumed to be fully turbulent. The extent of any laminar flow on the model was not examined or fixed in experiments, however most military



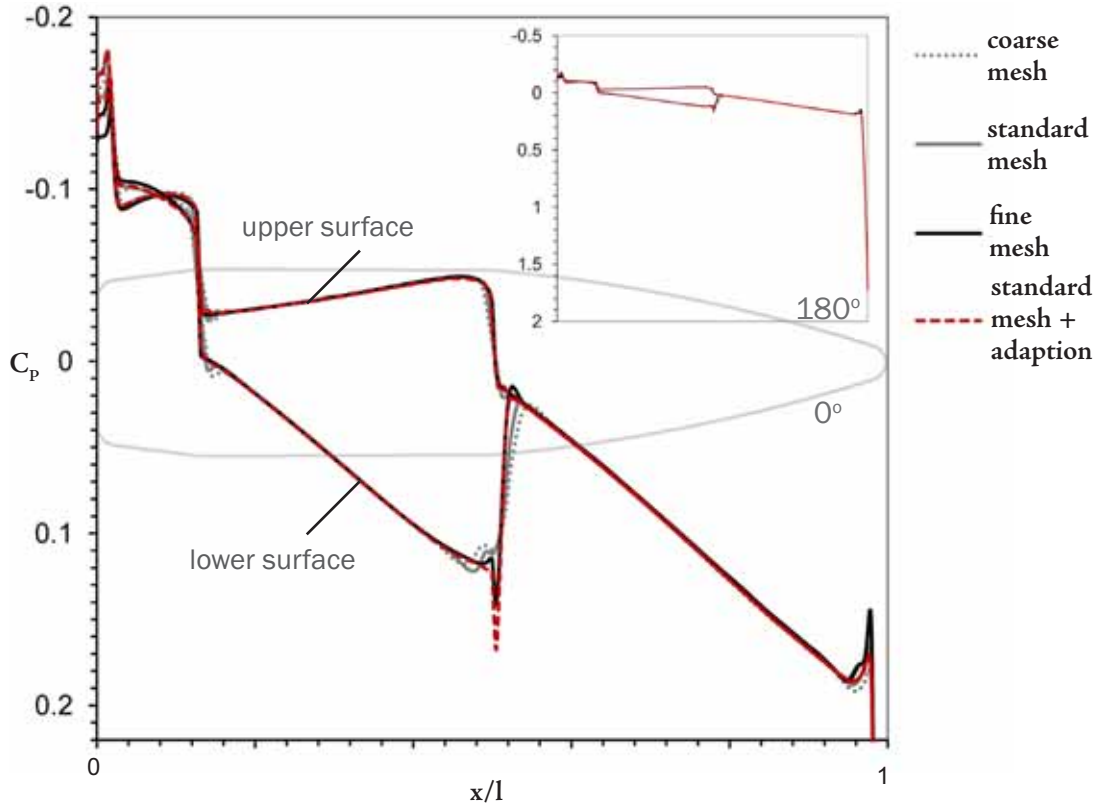
Example of beneficial shock adaption for the case of  $h/d=0.42$ , illustrated by contours of density.

4.56

FIG

4.55

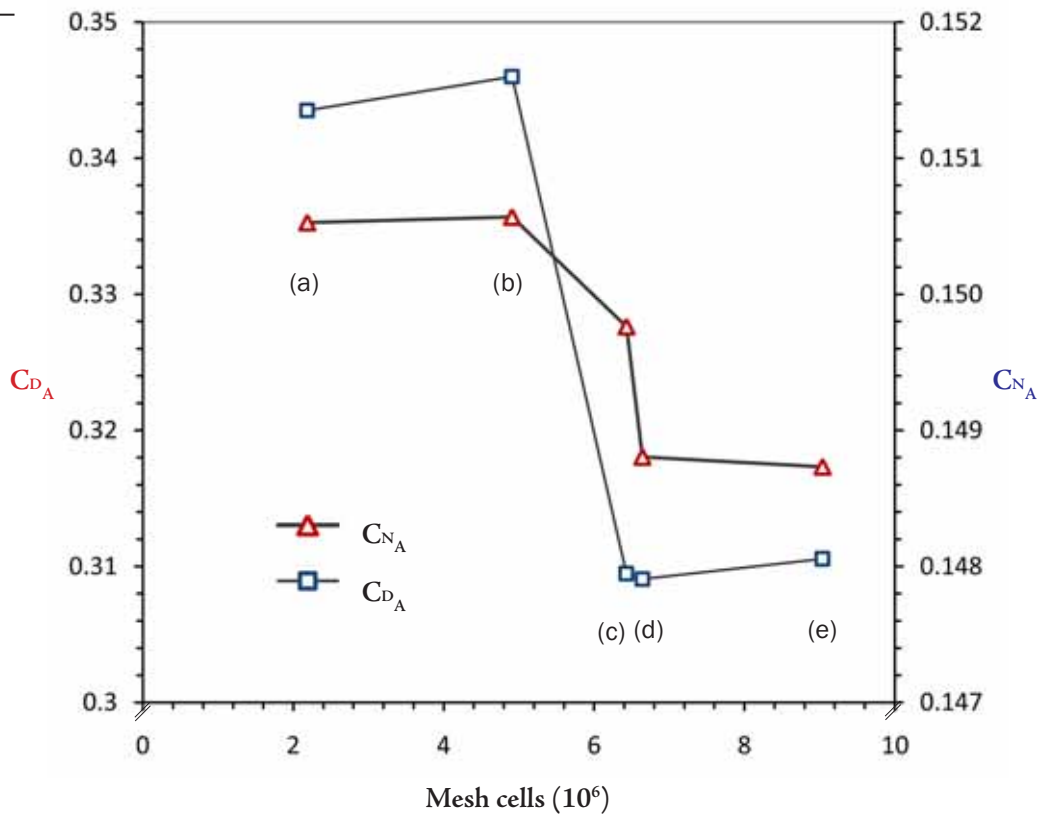
FIG



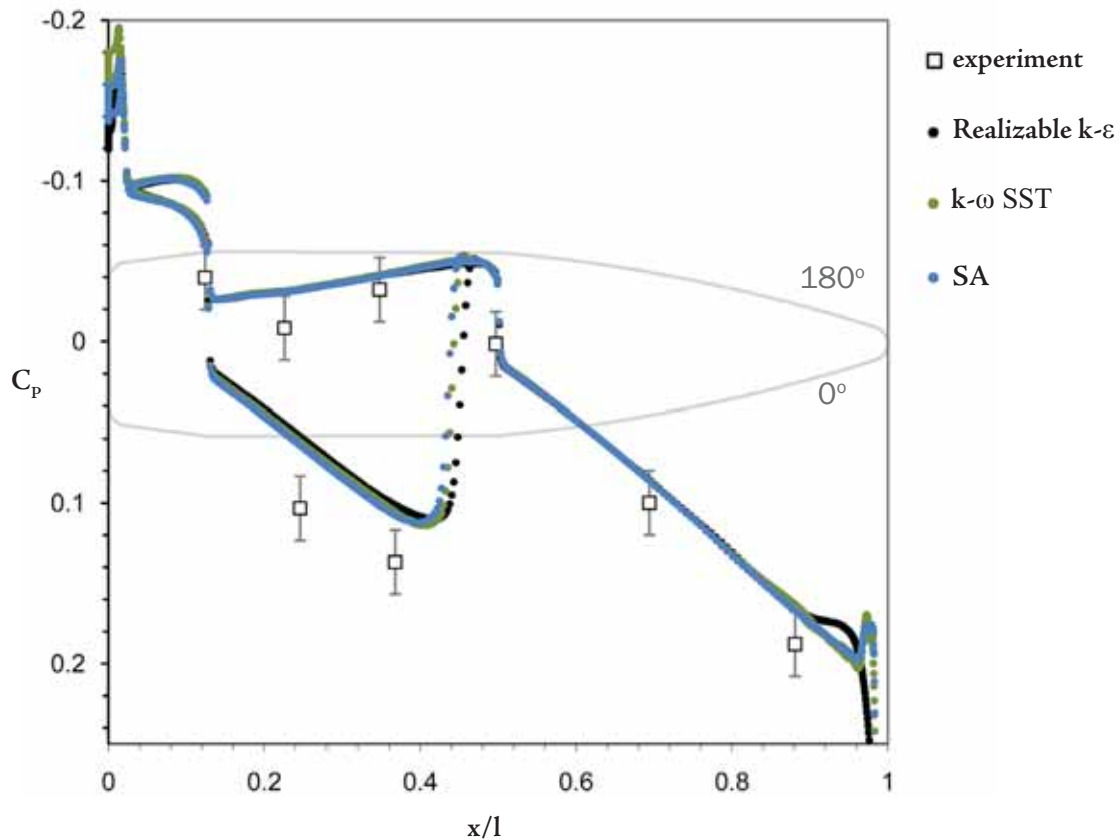
Pressure coefficients over the bullet on 0° and 180° planes as mesh is refined (inset: the unclipped pressure distribution).

4.57

FIG



C<sub>N<sub>A</sub></sub> and C<sub>D<sub>A</sub></sub> coefficients as half-model (symmetry) mesh is refined; a) coarse b) standard c) fine, d) standard with shock adaption, e) fine with shock adaption.



Turbulence model comparisons for pressure coefficient distribution around the wind tunnel model for the 0°/180° plane.

projectiles feature a surface finish that enhances the transition to a turbulent boundary layer (Sturek, 1994) and thus the assumption made with the computational model, in the absence of any special numerical surface treatment, is justified.

Selection of a turbulence model was based purely on the ability of tested models to reproduce the measured surface pressure distributions of the wind tunnel model, given that no quantitative information about the wake or forces was available. The usual three models were selected for this assessment: the Spalart-Allmaras model, the Realizable  $k$ - $\epsilon$  model, and the  $k$ - $\omega$  SST model. It must be remembered that the two-equations models come with the price of varying degrees of additional viscous dissipation across mesh cells, which becomes an extremely important consideration in the presence of multiple shock reflections.

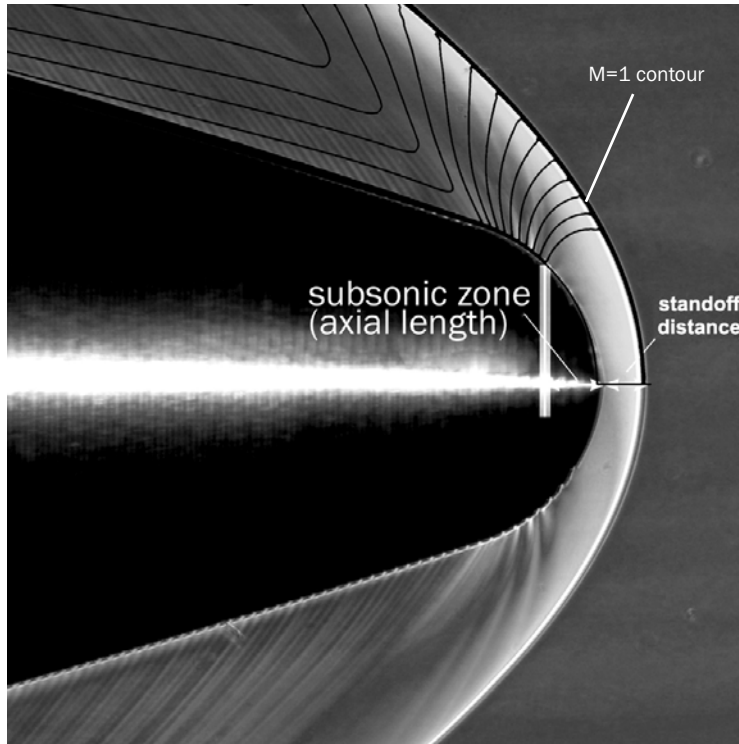
As mentioned in Chapter 3, the error bars reported in figures 4.58 are based on the scatter of results obtained over multiple tests. It is worth noting that in all

comparisons to experimental data, the CFD predictions of pressure distribution are consistently approximately 0.02 to 0.03 higher. This difference exists irrespective of mesh or turbulence model choice. Given that the match between the live-range and wind tunnel CFD is extremely close, despite a Mach number difference of approximately 0.04 and the markedly different atmospheric conditions in these two scenarios, it seems more likely that the offset is an experimental issue. In absolute terms the offset is around 1kPa.

Figure 4.58 shows the  $C_p$  predictions, for the  $0^\circ/180^\circ$  plane, of all 3 models for a wind tunnel test at  $h/d=0.5$ . They all broadly capture the flowfield adequately, with the Realizable  $k-\varepsilon$  predicting an earlier shock impingement on the projectile at approximately  $x/l=0.57$ , as well as a noticeably different pressure distribution towards the rear of the boat-tail section. Of interest is the spike in the pressure distribution close to  $x/l=0.02$ . This would appear to be a mild compression wave at the limit of Mach number and surface curvature which would cause an embedded shock (Rusanov, 1976), and is barely predicted by the Realizable  $k-\varepsilon$ , which produces a much higher stagnation pressure at the projectile tip than the other models. Shock-adaption of the mesh for the Realizable simulations does not extensively change this. Since the compression lies upstream of the first pressure tapping, and all the models predict similar  $C_p$  at that point, it is difficult to determine objectively which model is predicting the flow more accurately. As it is, the only clear basis for making an informed choice is the performance along the  $0^\circ$  plane, where the SA and SST models produce results slightly closer to experimental values. For reasons of reduced viscous dissipation across shock waves and less extensive computational expense, the one-equation model was selected for all subsequent simulations.

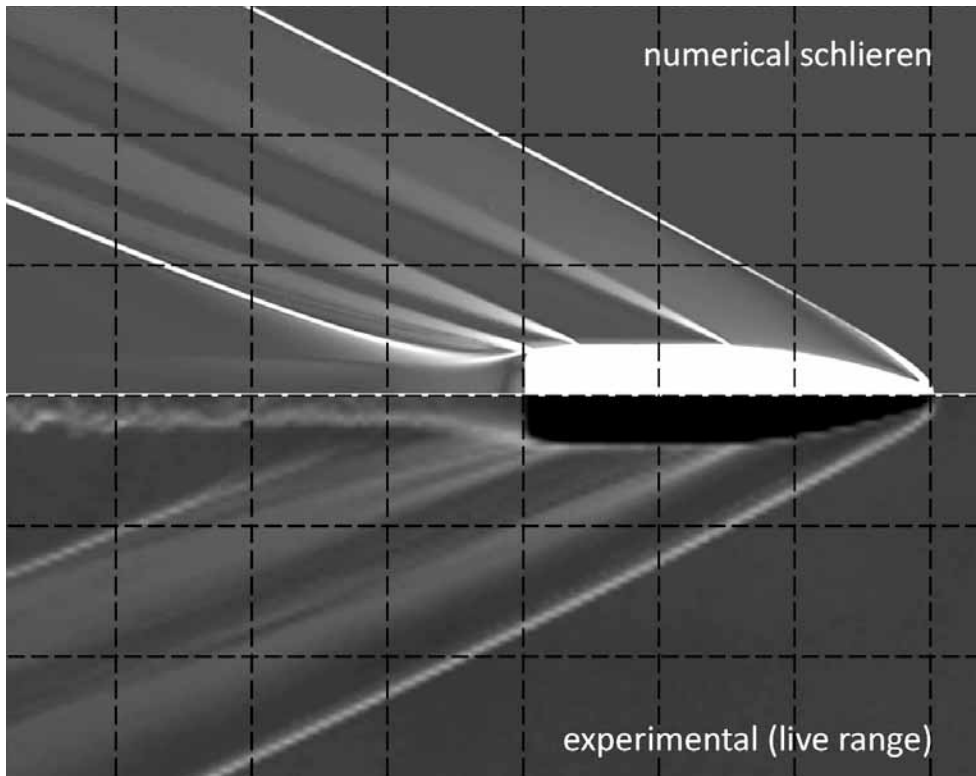
One final useful comparison of the one equation model to available experimental output with this model can be seen in figure 4.59, where the standoff distance of the bow shock observed from a close-up schlieren image is shown, with CFD contours of Mach number overlaid. In this experiment, the bullet surface was etched with a sequence of grooves of 0.2mm depth such that the schlieren would detect a small wave at the first groove location downstream of the point at which the flow became locally supersonic

4.59  
FIG



CFD to wind tunnel model comparison for shock stand-off distance and location of re-establishment of supersonic flow.

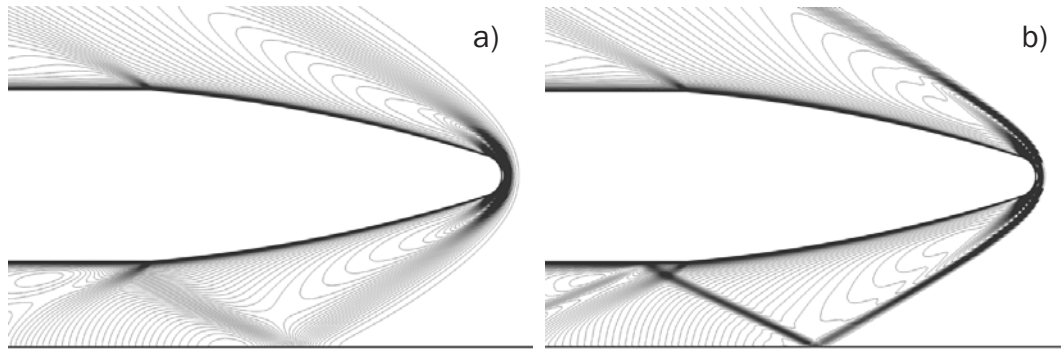
4.60  
FIG



Numerical schlieren comparison to an instantaneous schlieren image from time-resolved live-range footage of the freeflight (no ground) case.

4.61

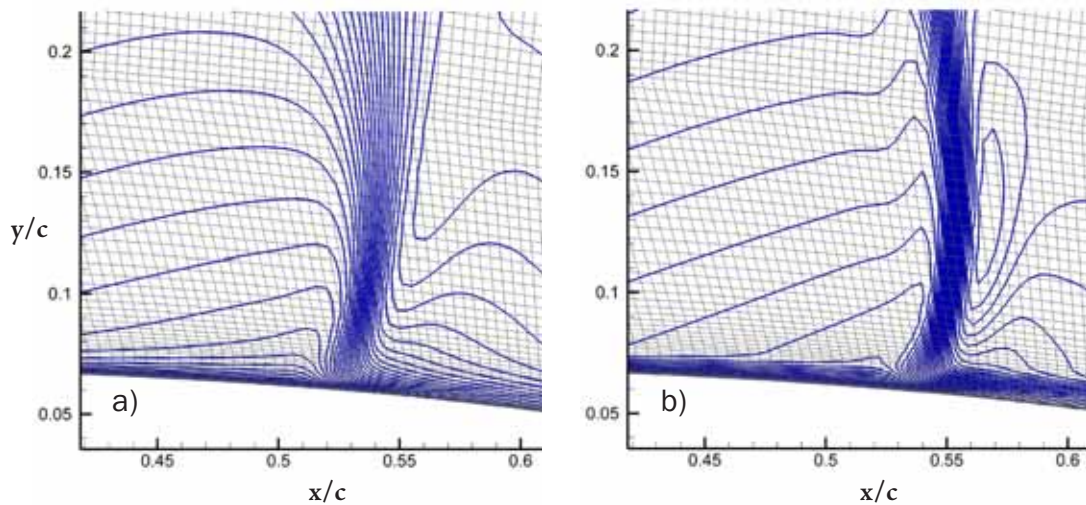
FIG



Influence of inlet turbulence intensity on the shock for the NATO projectile at  $h/c=0.5$ , standard mesh; a) 1%, b) 0.05%.

4.62

FIG



Influence of inlet turbulence intensity on the shock for RAE 2822 Case 9, standard mesh, zoomed to the shock location on the upper surface; a) 1% intensity, b) 0.1%.

again. The bright white along the bullet axis is a reflection of the flash lamp used to illuminate the model. The extent of the subsonic zone around the tip was estimated with considerable accuracy by the CFD, as was the standoff distance of the shock provided the mesh was sufficiently fine (i.e. following shock adaption). A similar comparison to the live-range schlieren is shown in figure 4.60, highlighting good agreement in terms of shock angles and wake thickness - more comparisons are made in chapter 9 in the context of the full investigation of the aerodynamics of the projectile in ground effect.

## 4.7 Additional Aspects

### 4.7.1 Influence of inlet turbulence intensity

The turbulent intensity was known to be 0.2% for the wind tunnel experiments from the AGARD Report (Cook *et al.*, 1979, Schmitt and Charpin, 1979) and was calculated for the USNA Transonic Wind Tunnel experiments conducted by the author at 0.16. These values were retained for calculations performed on the larger-scale RAE 2822.

Values for the projectile wind tunnel experiments were not available, and thus have been taken to be 0.05%. This value allows a significantly enhanced representation of shocks in the flowfield - results are compared in figure 4.61 to those obtained with a turbulent intensity of 1% and show a markedly improved resolution of the shocks on a standard (pre-adaption) mesh. A similar demonstration can be observed for the RAE 2822 normal shock in figure 4.62 - the differences between a turbulent intensity of 0.1% and 2% are highlighted, and the influence on shock location as well as resolution is clear. These results are in strong qualitative agreement with conclusions reported in literature (Gerolymos *et al.*, 2004; Ragunathan and McAdam, 1985), and serve to illustrate the importance of this property on the solution quality of results involving shocks and shock/boundary layer interactions.

## 4.8 Summary

The general numerical approach has been extensively verified and validated and has been proven to be capable of producing reliable results for both free-flight and ground effect cases for each body studied. For the inverted wing at Mach 0.088, comparisons were made between CFD and experiments in literature, and the following conclusions drawn:

- The standard mesh was deemed acceptable ( $\sim 3.1 \times 10^6$  cells) for all simulations, no local refinement was necessary.
- The Realizable k- $\epsilon$  model was chosen as it provided slightly better lift and drag predictions compared to the Spalart-Allmaras model.

- The flow could be reasonably assumed to be fully turbulent for subsequent runs, particularly at higher Mach numbers.

For both the RAE 2822 two-dimensional aerofoil and the ONERA M6 three-dimensional wing at high-subsonic Mach numbers, comparisons were made between CFD and experiments (with no ground effect) in literature (Cook *et al.*, 1979; Schmitt and Charpin, 1979), and the following conclusions drawn:

- The standard mesh was acceptable ( $\sim 0.26 \times 10^6$  cells for the RAE2822,  $\sim 5.1 \times 10^6$  cells for the M6) for all simulations provided that the grid was locally refined in the region of shock waves.
- The Spalart-Allmaras turbulence model proved most accurate for all cases attempted.
- Fully turbulent flow was a satisfactory assumption.
- There still exists a pressing need in the field for a database of transonic experiments as comprehensive as those in the AGARD report, but without wall treatments or other factors which are difficult to incorporate in CFD.

Further mid-to-high Mach number comparisons were made against the data gained from the USNA Transonic Blowdown Wind Tunnel tests:

- Three-dimensional modelling of the test section was essential.
- Given the transient nature of several simulations, local shock-refinement of the mesh was not practical. The standard mesh was acceptable ( $\sim 4 \times 10^6$  cells for symmetry method cases).
- As before, the Spalart-Allmaras turbulence model was the most effective, more so when the flow exhibited unsteady behaviour.
- Fully turbulent flow was a satisfactory assumption, but significant

laminar regions could influence the shock behaviour in some cases.

Finally, some comparisons for the Mach 2.4 projectile were made against wind tunnel data and schlieren images, with the following conclusions:

- Shock-refinement of the meshes on a standard mesh was essential to maintain the waves as they propagated in three-dimensions.
- The Spalart-Allmaras model provided the best comparisons to available data.

It has therefore been demonstrated that the CFD results which form the body of the rest of the thesis provide data which can be treated as reliable in each of the flow regimes examined. Having addressed some of the issues surrounding the validity of the high-subsonic experiments in the US Naval Academy blowdown transonic tunnel, it is now possible to make a direct assessment, using both experimental and numerical results, of the effectiveness of the two experimental methods of ground boundary representation for transonic and supersonic flows: the symmetry method and the elevated ground plane.

# Chapter: Evaluation of Blowdown Wind Tunnel Methods for Compressible Ground Effect Studies

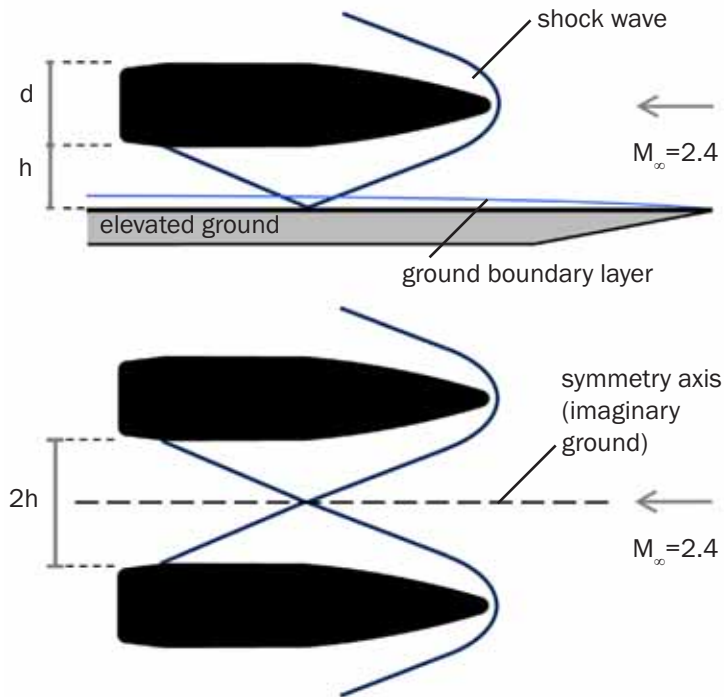


*The symmetry (mirror-image) and elevated ground methods were introduced in chapter 3 as simple means of simulating transonic and supersonic ground effect problems in a small-scale blowdown wind tunnel. Here these two methods are evaluated for the supersonic projectile and the RAE2822 aerofoil at transonic conditions, with experiments and CFD used concurrently to determine the strengths and weaknesses of the techniques. Their relative merits are appraised, and the symmetry method was found to be an excellent approximation of a moving ground. Issues of scale are discussed, particularly for the transonic experiments where Reynolds number cannot be matched to flight conditions.*

## 5.1 Introduction

In the two preceding chapters, the experimental approaches for the supersonic projectile and the high-subsonic RAE2822 have been described along with anticipated sources of error or discrepancy. In this chapter, CFD is used to further examine the limitations of the methods, whilst providing a comprehensive assessment of their ability to produce flowfields as close as possible to those which could be achieved with a moving ground in the wind tunnel.

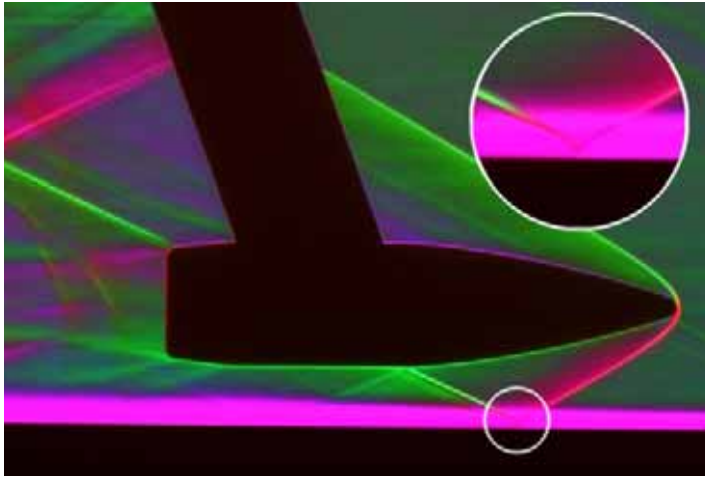
Schematic of the elevated ground and symmetry methods as applied to the Mach 2.4 projectile.



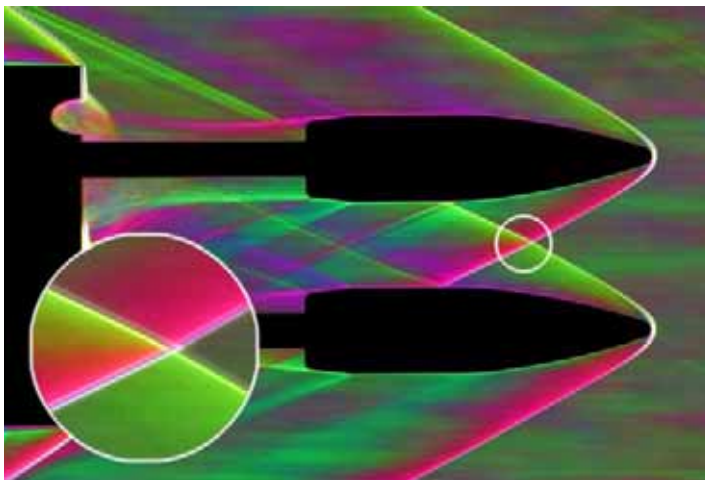
## 5.2 Supersonic Methods

The elevated ground and symmetry methods described in chapter 3 are formally evaluated here. The live-range tests undertaken by ADFA were the ideal means of investigating the problem, but access to the facility was limited and expensive, and thus the scaled wind tunnel model was used for more thorough testing. Unfortunately, wind tunnel results for a ground clearance corresponding to any of the live-range schlieren videos was not available to the author, and thus this section focuses on a comparison of schlieren photographs and CFD results from wind tunnel tests of the elevated ground and symmetry methods at approximately  $h/d = 0.5$ . This is followed by a more detailed investigation of these methods compared to a moving ground using CFD alone. The validation performed in chapter 4 has allowed for sufficient confidence in this approach.

An outline of the symmetry and elevated ground approaches for the projectile is shown in figure 5.1 (not to scale) with a reminder of some relevant parameters.



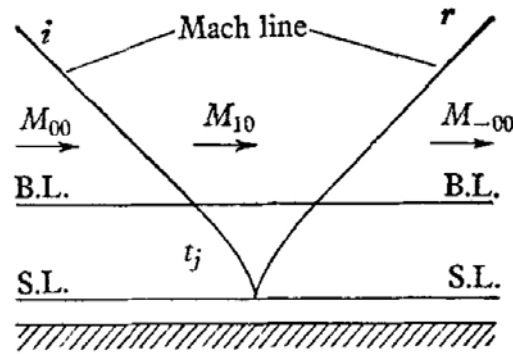
Colour schlieren of elevated ground test,  $\sim h/d=0.5$  (inset, shock/boundary layer interaction detail), (Doig *et al.*, 2008).



Colour schlieren of symmetry method test,  $\sim h/d=0.52$  (inset, crossing shock interaction detail), (Doig *et al.*, 2008).

### 5.2.1 Symmetry and elevated ground in schlieren

Direction-indicating colour schlieren images for both methods are shown in figures 5.2 and 5.3. The boundary layer thickness on the elevated ground plate at the location of the projectile nose is approximately 2.5 mm, or 17% of the projectile model diameter. This boundary layer on the ground plane is significant in relation to the size of the test model, in particular downstream of the impingement of the bow shock generated by the projectile model. Figure 5.2 indicates that at the projectile base the ground boundary layer has increased to approximately 3.8 mm, which corresponds to about 45% of the clearance  $h$  in this flowfield. The image is misleading, however, as what one can effectively see is the boundary layer integrated across the entire test section, including at the windows where the boundary layer will be significantly thicker. Thus the actual boundary layer thickness

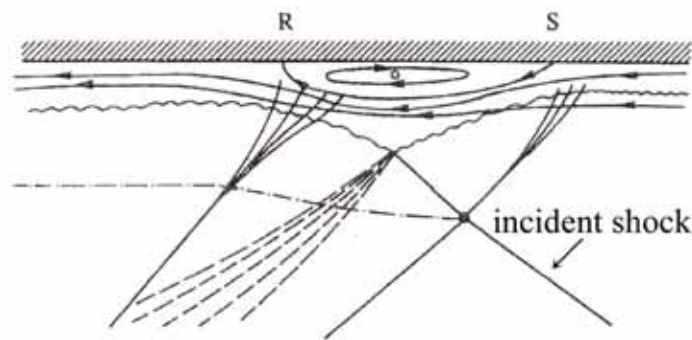


Simple representation of regular shock reflection from a wall with a boundary layer (Henderson, 1967).

under the projectile cannot be determined accurately from these pictures. The only true guide to its extent can be seen in the inset detail of figure 5.2 which shows the shock bending in the boundary layer as it reflects, in keeping with the observations of many in the field of shock/boundary layer reflection such as Henderson (1967), as reproduced in figure 5.4, and Hornung (1986). The visualization clearly shows how the shock is bent upstream when entering the boundary layer, and the reflected shock is also initially curved. Within the boundary layer, the initially oblique shock becomes normal before it disappears in the subsonic part of the boundary layer immediately above the wall. The result is an upstream shift of the impingement point on the projectile which can be directly attributed to the undesirable shock/boundary layer interaction.

From this estimation, the boundary layer height would be between 30-50% less than it appears in the schlieren. The shock pattern under the projectile appears diffused downstream of the first interaction. There is little sign of a second reflection from the ground, as the shock reflecting from the projectile appears to have been absorbed in the boundary layer.

The symmetry method is akin to having an inviscid ground boundary and thus an ideal reflecting surface. A reasonably symmetrical shock reflection pattern extending to the sting mount as shown in figure 5.3 is produced. The aforementioned diffusion of the shock pattern does not occur, and a second reflected shock is seen passing the projectile downstream of the tapered boat tail. The crossing shocks appear to have little influence on each other.



Representation of shock/  
boundary layer interaction with  
boundary layer separation (S) and  
reattachment (R), (Delery, 1985).

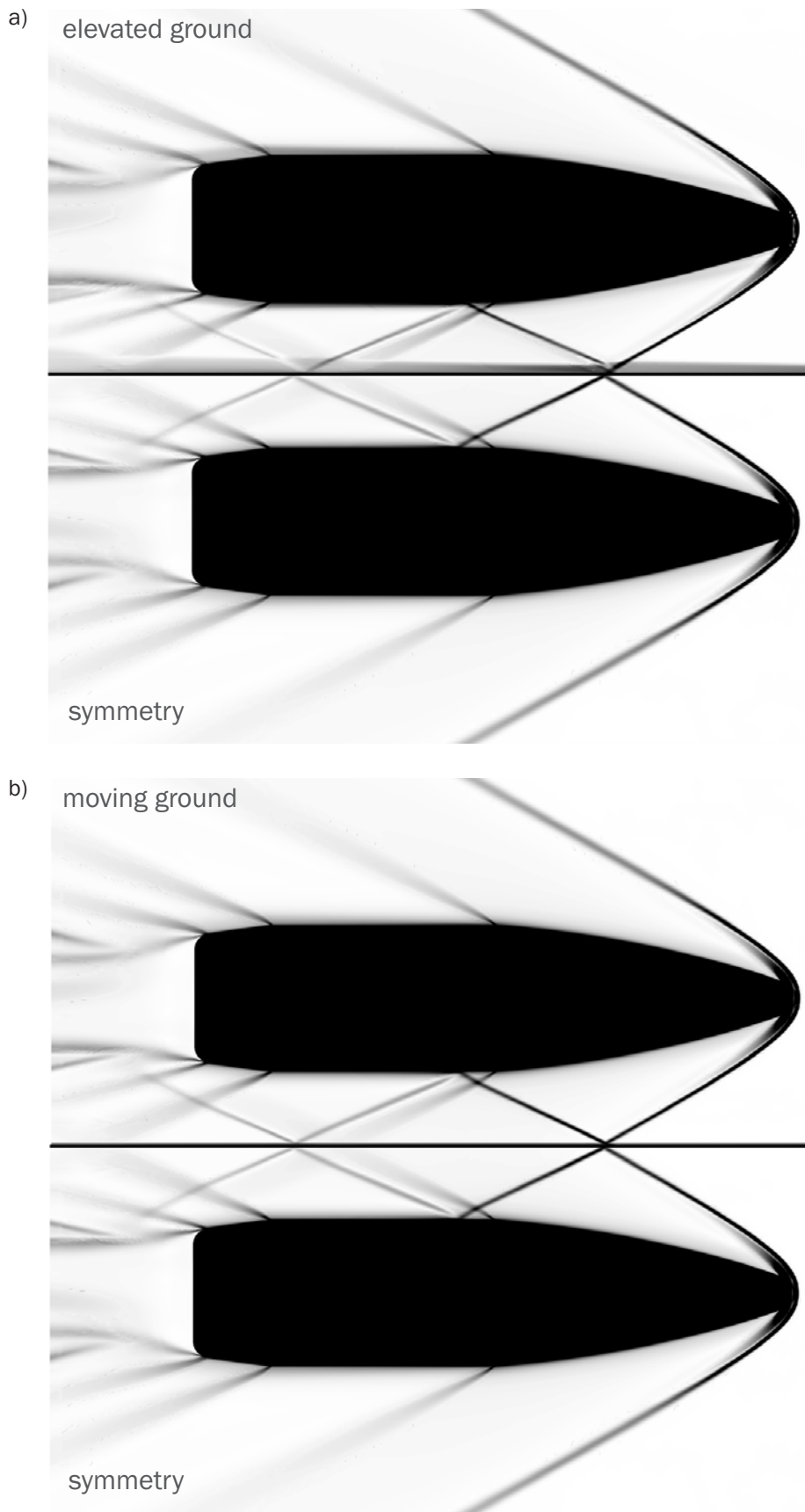
Another feature less prominently seen in the tests with the elevated ground is the double structure of the shock reflecting from the projectile model, which could be indicative of shock-induced separation of the projectile boundary layer of the type shown in the schematic reproduced from Delery (1985) in figure 5.5, whereby separation and reattachment waves form from a single incident shock interacting with a boundary layer. The schlieren was not of sufficient resolution in this area to determine with any certainty if this was indeed the case.

In the tests with the elevated ground plane, the initial shock-boundary layer interaction has modified and shifted the reflected shock so that its subsequent interaction with the projectile model occurs at a different location, and with different shock strength. One consequence of these modifications is that the double structure of the reflected shock is much less pronounced in the elevated ground tests.

In this case, the first reflected shock impinges on the projectile just after the shoulder onto the flat lower surface. One can surmise that if the reflection impingement location should be at a critical point of curvature, for instance, then any small deviation produced by the elevated ground boundary layer interaction could produce markedly different results. The effect is cumulative, as subsequent reflections and interactions become increasingly out of step with the symmetry method locations.

### 5.2.2 Symmetry and elevated ground in CFD

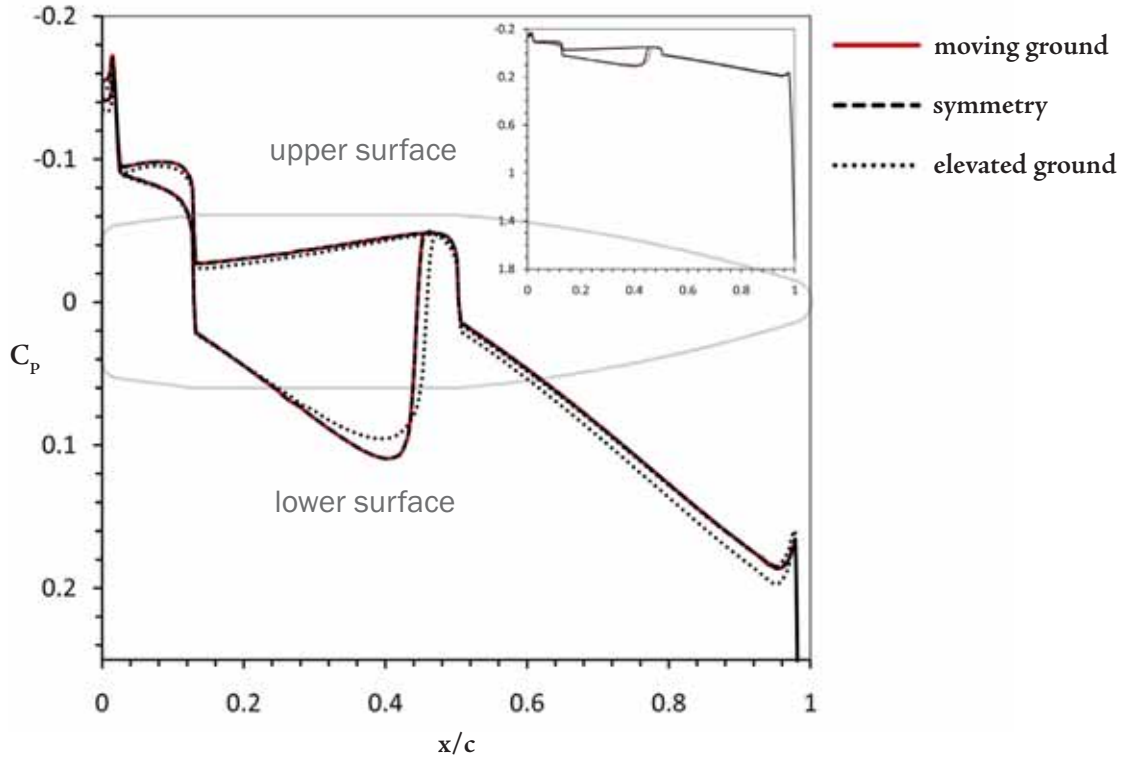
Numerical schlieren of the  $h/d = 0.5$  case is presented in figure 5.6, of comparisons between the symmetry, elevated ground, and moving ground results. Naturally, the



Numerical schlieren comparisons at  $h/c = 0.5$  of a) symmetry and elevated ground methods, and b) symmetry method and a moving ground.

5.7

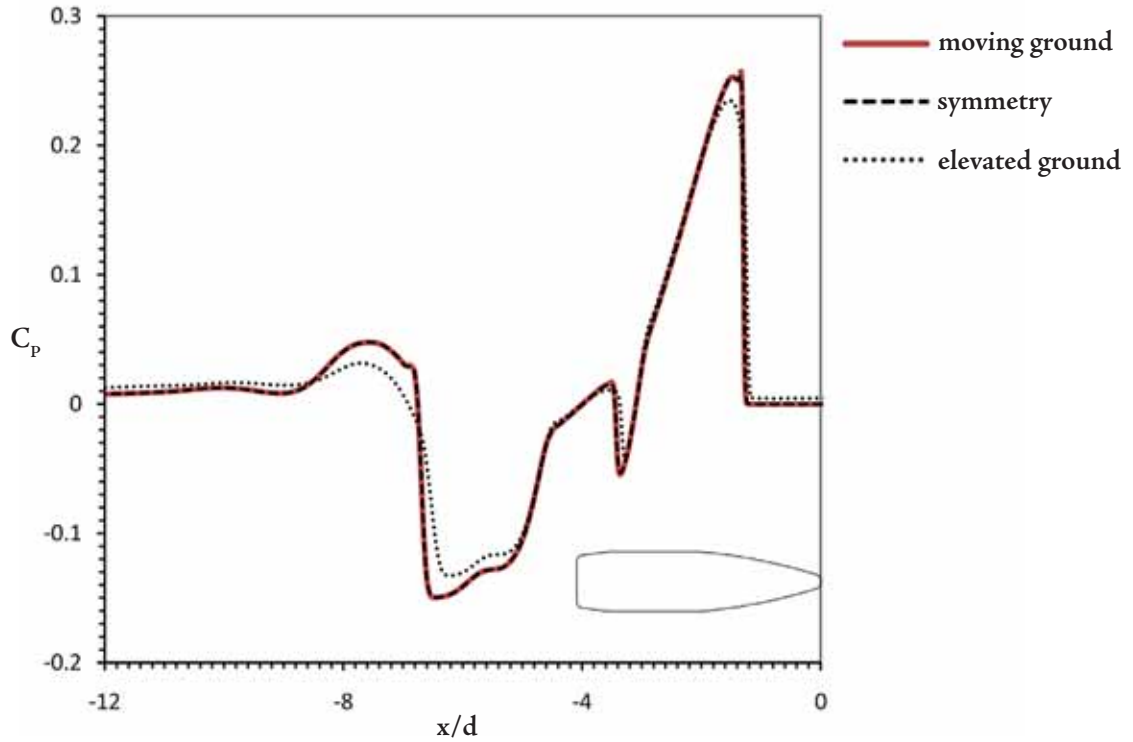
FIG



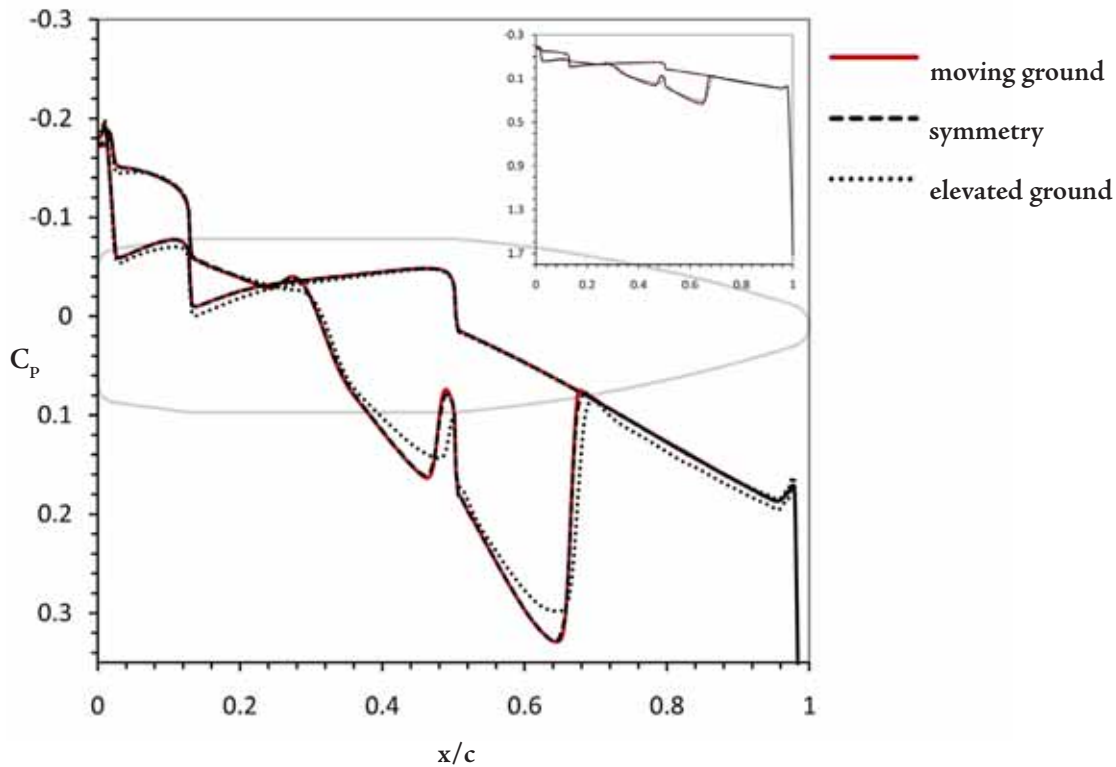
Comparisons of projectile pressure distributions at  $h/c=0.5$  for an elevated ground, symmetry ground plane and moving ground (inset; the unclipped pressure distribution)

5.8

FIG



Comparisons of ground pressure distributions at  $h/c=0.5$  for an elevated ground, symmetry ground plane and moving ground.



Comparisons of ground pressure distributions at  $h/c=0.2$  for an elevated ground, symmetry ground plane and moving ground.

formation of the boundary layer on the elevated ground in CFD is highly dependent on mesh, turbulence model and the assumption of a perfectly-sharp, aligned leading edge. However what is clear is that the boundary layer is, as suspected, considerably smaller than the schlieren would indicate. Its influence on the shock reflections locations is a matter of a few percent, but each interaction visibly thickens the ground boundary layer, particularly downstream of the base of the projectile, where a region of strong expansion promotes rapid growth in boundary layer thickness, which will affect the development of the wake and alter the wake-ground interaction further downstream still.

The symmetry method provides a near-identical match to the moving ground case, and the boundary layer which forms on the moving ground at each interaction is sufficiently thin as to result in very little discernable disruption.

The resulting pressure distributions for this  $h/d = 0.5$  case in the symmetry and moving ground cases are almost exactly the same, while the results for the elevated ground show some clear deviations, as presented in figure 5.7. On the assumption that

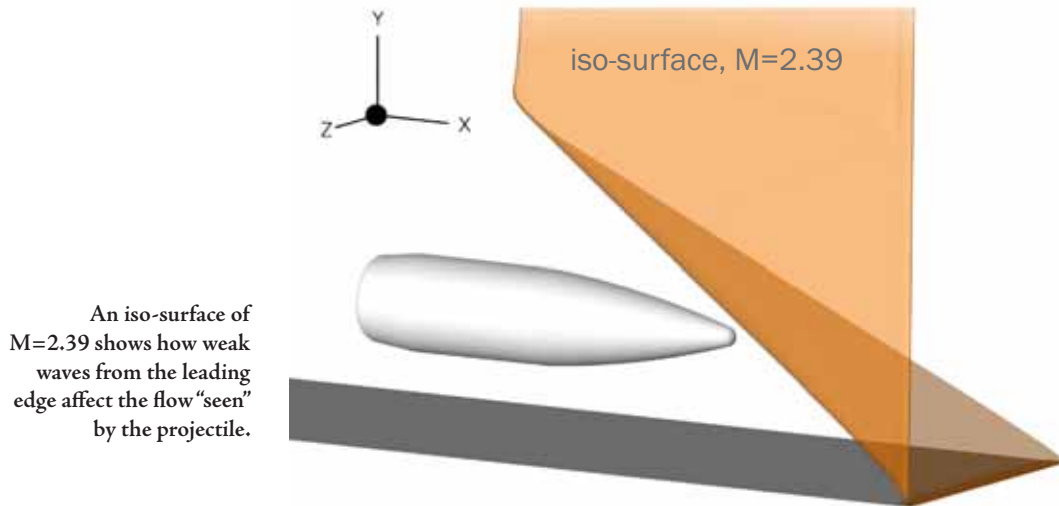
the moving ground simulation represents the ground effect in the most realistic way, the symmetry approach provides results closer to reality and can thus be considered superior to the elevated ground method. The boundary layer on the elevated ground even affects the pressure distribution over the forward section of the projectile before the first shock reflection. It reduces the effective area available for the flow that passes underneath the projectile and thus slows the flow down, which in turn leads to a slightly higher pressure. The discrepancy in the re-impingement location is notable in the graphs.

The ground plane pressure distributions shown in figure 5.8 indicate that the shock reflection locations are indeed similar between the elevated ground and symmetry methods, though the nature of the interaction is starkly different. The effect of the boundary layer is to diffuse or smear the pressure signal, and this effect is cumulative as the flow moves downstream.

At an even lower clearance,  $h/d = 0.2$ , shown in figure 5.9, there is further discrepancy from the elevated ground plane as the second shock reflection impingement occurs 3-4% further upstream, and the third impingement is markedly more diffused still. As before, the symmetry and moving ground results match near-perfectly.

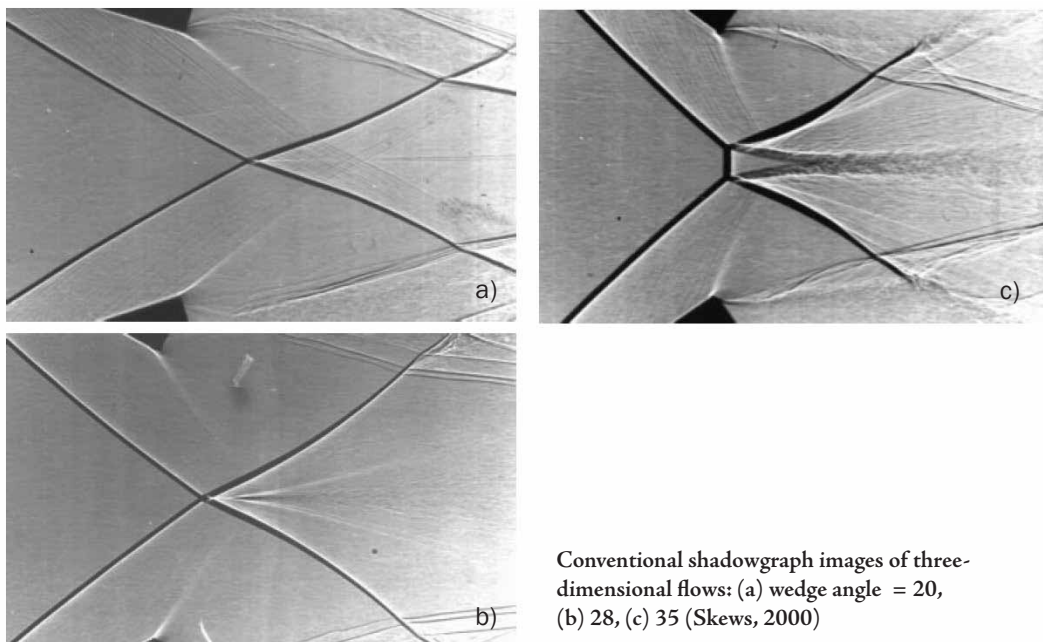
### 5.2.3 Additional considerations

The CFD of the elevated ground has assumed a perfectly-sharp leading edge, aligned with the freestream flow. Even in this case, the boundary layers on the ground plane and the side walls of the wind tunnel produce a corner-flow which, depending on the nature of the tunnel, could have a marked influence on the results obtained. In this case, the influence is minor, but the CFD highlighted an influence that was not obvious from the experiments. Figure 5.10 shows an iso-surface of Mach 2.39, i.e. 0.01 less than the desired freestream. The weak disturbance due to the formation of the ground boundary layer is already enough to influence the flow upstream of the projectile leading edge, and is in effect a much more mild version of the leading edge wave which was observed in the schlieren of figure 3.9 in Chapter 3. The vertical component of the iso-surface is due to the tunnel sidewall. The flow reaching the projectile is approximately Mach 2.385



- reduced from the desired freestream by a large enough margin to influence the shock angles slightly, and the pressure distribution around the projectile.

Although not presented here (as the flowfield becomes confusing to interpret on the page), further iso-surfaces of Mach numbers between 2.35 and 2.39 revealed that waves from the sidewall emanating from the corner flow region would have interacted with the projectile along its body, influencing the experimental readings taken there. If even slightly misaligned with the flow, the elevated ground would begin to behave like a



shock-generator of the type commonly used for fundamental glancing shock/boundary layer interaction studies, which could lead to large-scale three-dimensional effects interfering with the model (Kubota and Stollery, 1982).

If one considers the use of the elevated ground method at lower Mach numbers, where the waves are less oblique, then the model may have to be scaled down in order to avoid any negative influence from the ground plane/tunnel wall junction, but such a solution exaggerates the existing problem of ground boundary layer size in relation to the object being tested. Another consideration is the transition from regular to Mach reflection, which has been extensively studied in crossing shock wave studies. It remains unclear whether the symmetry method would continue to accurately simulate moving ground boundary conditions if the crossing shocks transitioned in a manner similar to that of the shadowgraphs shown in figure 5.11, where the shocks were produced by increasingly-angled wedges.

#### 5.2.4 Summary

The symmetry method produced results (in terms of pressure distribution for all cases examined) closer to that of an ideal moving ground than the elevated ground plane. It would therefore be recommended for all conceivable wind tunnel studies of supersonic ground effect. The presence of any ground boundary layer noticeably distorts the flow downstream of the first shock/ground interaction. It could still be beneficial however, to use the elevated ground method, in particular if the ground plane were extensively instrumented or thermochromic liquid crystals were used (Doig *et al.*, 2006a). This would provide some potentially useful information about the “footprint” of the shocks propagating away from the model which could not be obtained with the symmetry method. There may also be cases in which the modifications of the pressure distribution caused by the boundary layer on the ground plate have a negligible net effect on the resulting aerodynamic forces, but this would have to be verified for each application.

Further study is required to identify any possible shortfalls of the symmetry method for providing adequate results for Mach reflection of the incident shocks.

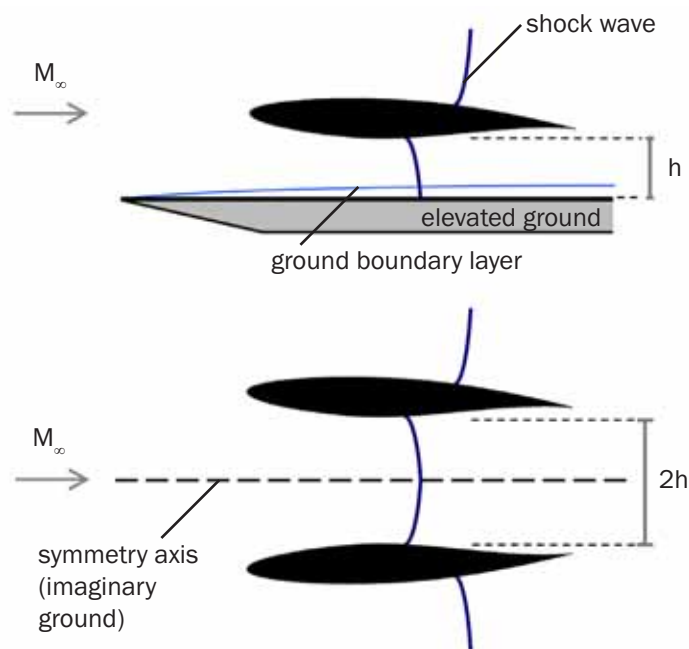
## 5.3 Transonic Methods

### 5.3.1 Introduction

One can intuitively anticipate that the methods applied to the supersonic projectile flows will feature additional considerations when applied to transonic Mach number flows for the RAE2822 section in the USNA blowdown wind tunnel. All apparatus can now influence the upstream flow, and thus the elevated ground now has a significant role to play in the development of the flow that the aerofoil “sees”. The size of the boundary layers is now larger compared to those seen in the supersonic tests, and the presence of strong normal shock waves increases the importance of the shock/ground interaction. In addition, any asymmetry present in the symmetry method apparatus will cause the flow

Table 5.1. Cases used to compare experimental methods

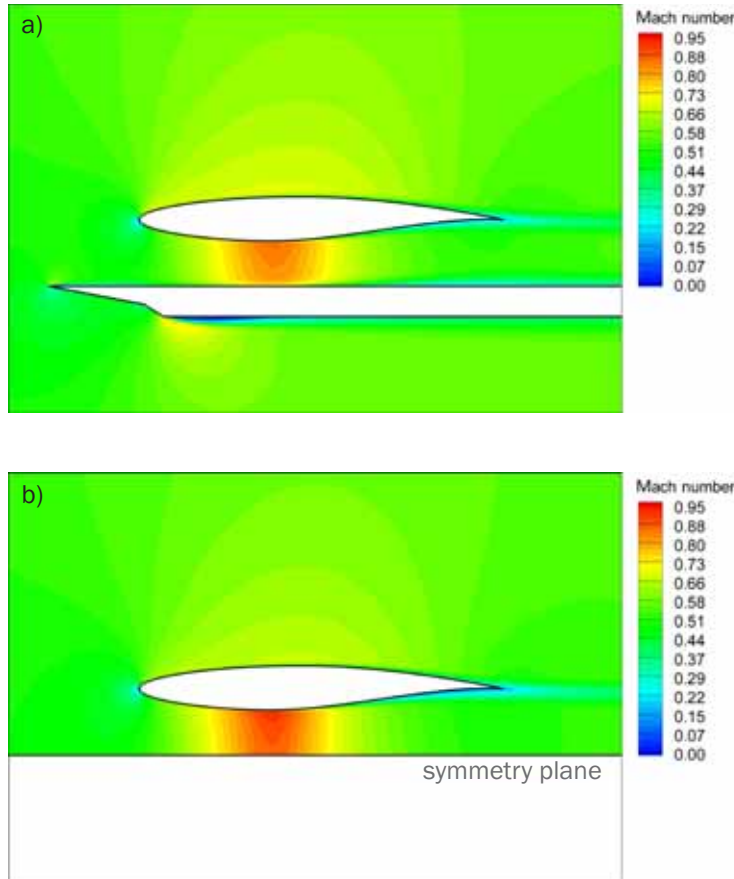
	$M_\infty$	$\alpha^\circ$	$h/c$	Comments
2822 USNA Case1	0.531	0	0.128	<i>shock-free, largely-steady flowfield</i>
2822 USNA Case 2	0.629	6	0.232	<i>upper surface shock, unsteady flowfield</i>
2822 USNA Case 3	0.646	0	0.128	<i>lower-surface shock, mild oscillation</i>
2822 USNA Case 4	0.705	0	0.266	<i>upper surface shock almost stationary at symmetry plane, regularly-oscillating lower surface shock</i>



Schematic of the elevated ground and symmetry methods as applied to the RAE2822 aerofoil.

5.12

FIG



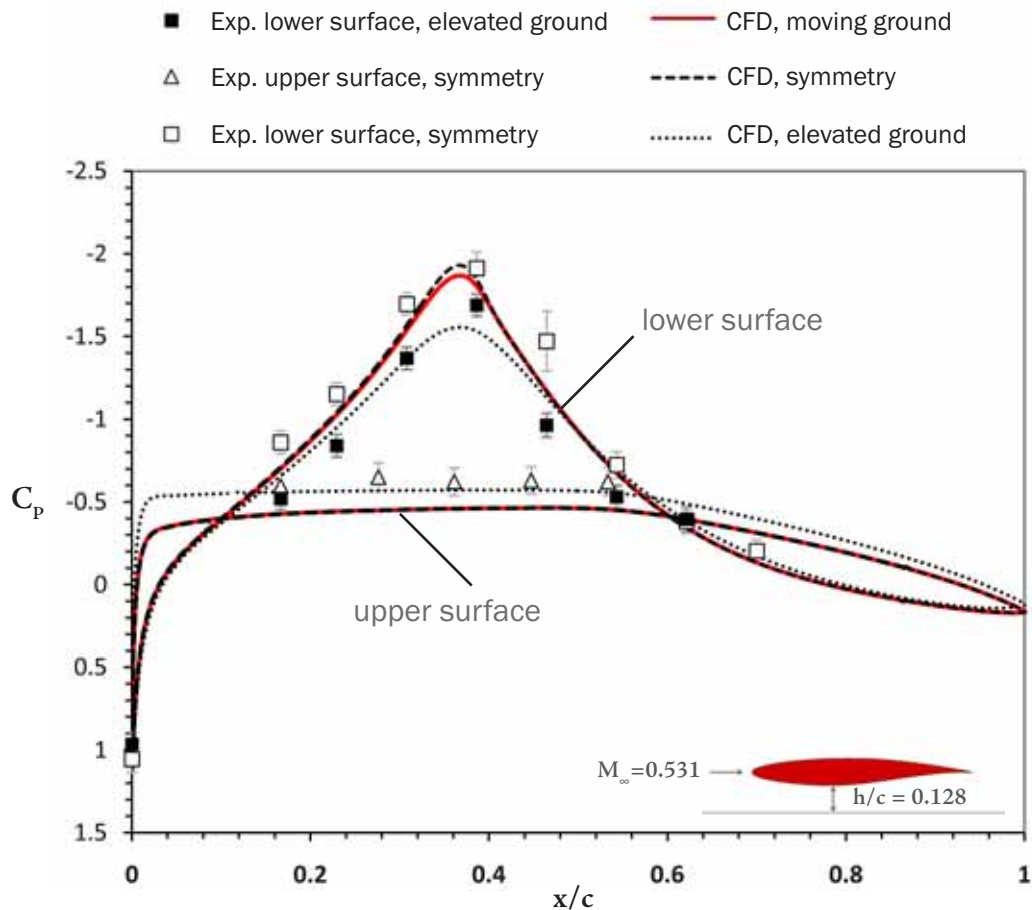
Time-averaged CFD of 2822 USNA Case 1 comparisons; Mach number distributions at the mid-span symmetry plane for the elevated ground and symmetry methods.

to adjust to a state which would provide incorrect flow over the entirety of both wings.

USNA Cases 1 to 4, identical to those discussed in the previous chapter, are presented here as examples of the elevated ground and symmetry approaches, as repeated in table 5.1. The symmetry and elevated ground methods are again summarised in figure 5.12 with relevant characteristics. Experimental sets for symmetry and elevated ground tests were available for all cases, and so the CFD cases were run three times with three boundary conditions: symmetry, elevated ground and moving ground.

### 5.3.2 Case 1

Although the freestream Mach number is only 0.531, CFD of the experimental setups for both elevated ground and symmetry methods reveal that the maximum local Mach number was close to 0.97, meaning that a lower-surface shock was close to formation. Mild unsteadiness in the flow was found in the CFD, due to the presence of the separated flow around the endplate leading edges, but this was damped in the process of running



Time-averaged pressure distribution at the mid-span symmetry plane for 2822 USNA Case 1; comparisons of experimental symmetry and elevated ground methods to CFD.

transient simulations such that a steady-state solution was reached.

Contours of Mach number at the symmetry plane are shown in figure 5.13. The boundary layer which forms on the elevated ground can be observed to compress due to the pressure gradient under the wing, where the flow accelerates to its maximum velocity. The boundary layer's influence on the flow can be seen when compared to the symmetry method, and the images show that the effect of the ground boundary layer is to displace more air over the top of the wing, changing its effective angle of attack, as represented by the upper-surface pressure distribution in figure 5.14.

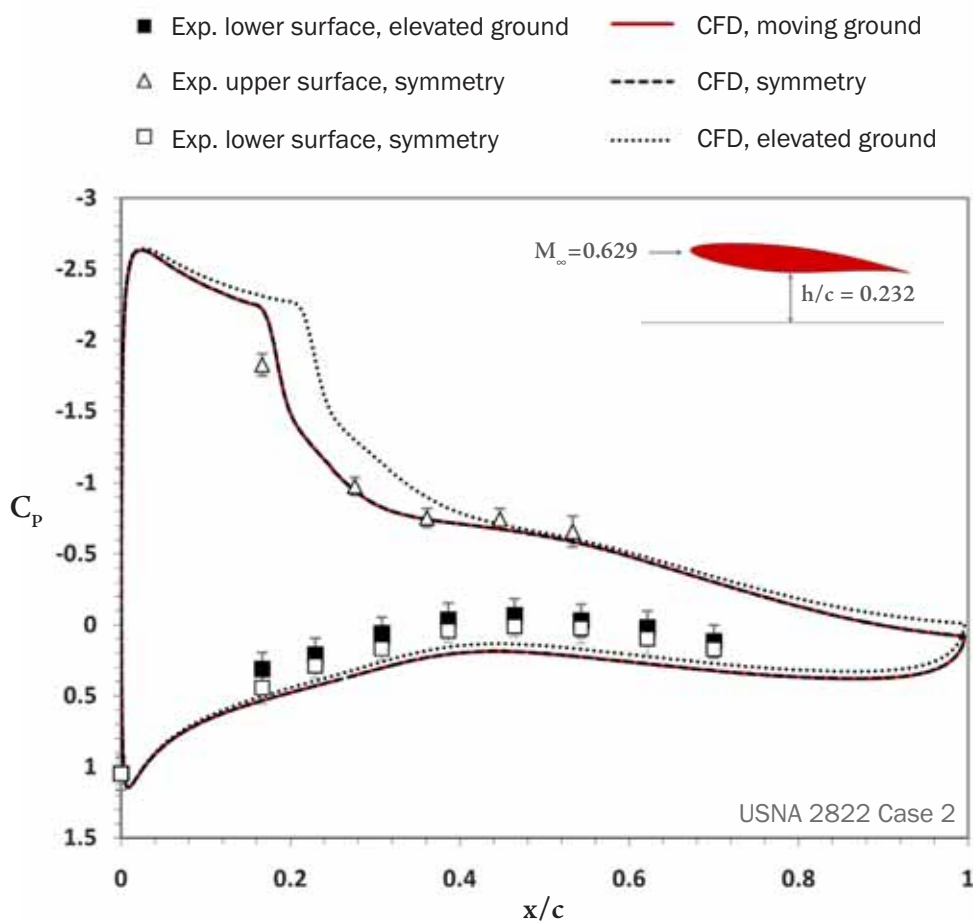
The additional constriction of flow between the wing and the ground caused by the boundary layer is largely offset by this effect, such that the lower surface pressure gradient is reduced, resulting in a lesser suction peak at the point of minimum ground clearance.

Although the CFD of the elevated ground appears to underpredict the suction peak by a  $C_p$  of approximately 0.15, the general agreement for both sets of ground representations is good. The experimental data indicates that around the lower-surface suction peak, the aerofoil over the elevated ground experiences a lesser negative  $C_p$ , with the greatest difference to the symmetry result coming behind the peak itself, suggesting a truncated region of acceleration as seen in the CFD of figure 5.13.

A CFD simulation of the experimental setup which replaced the ground symmetry plane with a moving ground indicated that the symmetry method provided a near-perfect match in terms of the wing pressure distribution, with the symmetry method slightly over-predicting the maximum pressure gradient on the lower surface. This can be attributed to the formation of a thin boundary layer on the moving ground, which produces a similar effect as that which forms on the stationary elevated ground plane, although in this case its significance for the flow around the wing is barely significant.

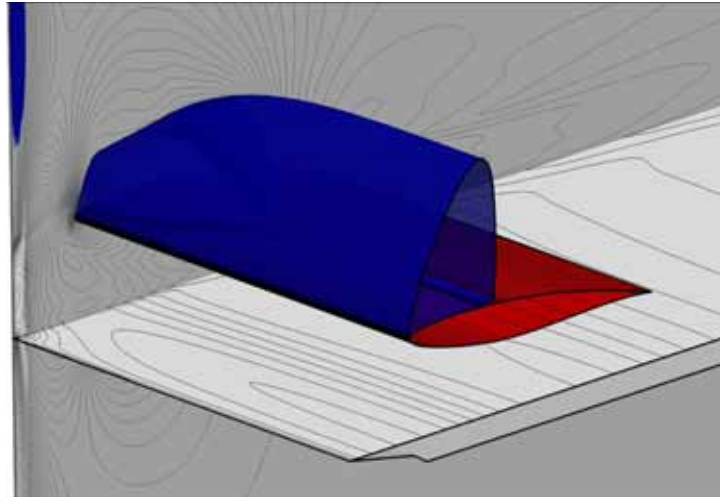
5.15

FIG



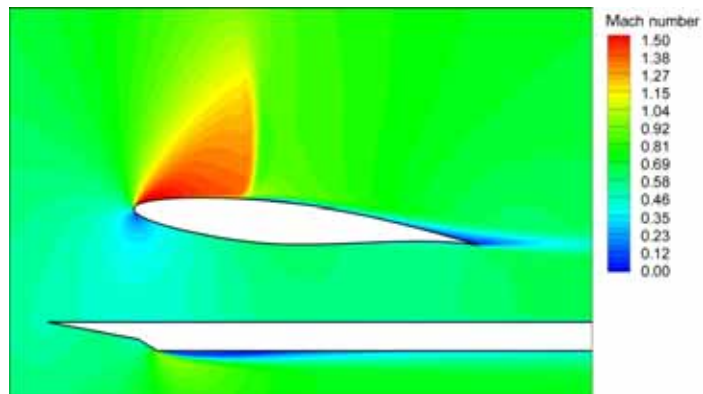
Time-averaged pressure distribution at the mid-span symmetry plane for 2822 USNA Case 2; comparisons of experimental symmetry and elevated ground methods to CFD.

Instantaneous CFD of 2822 USNA Case 2 (half-model with mid-span symmetry plane) with the elevated ground plane, showing contours of density and areas of supersonic flow (blue).



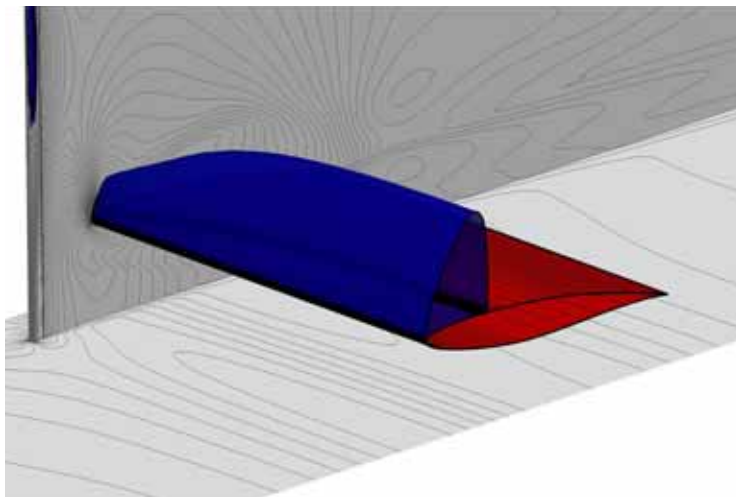
5.16  
FIG

Instantaneous CFD of 2822 USNA Case 2 with the elevated ground plane, contours of Mach number at the mid-span symmetry plane.



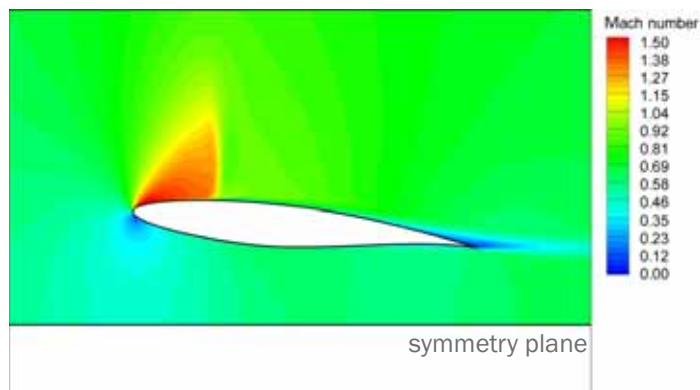
5.17  
FIG

Instantaneous CFD of 2822 USNA Case 2 (half-model with mid-span symmetry plane) with the symmetry ground plane, showing contours of density and areas of supersonic flow (blue).



5.18  
FIG

Instantaneous CFD of 2822 USNA Case 2 with the symmetry plane, contours of Mach number at the mid-span symmetry plane.



5.19  
FIG

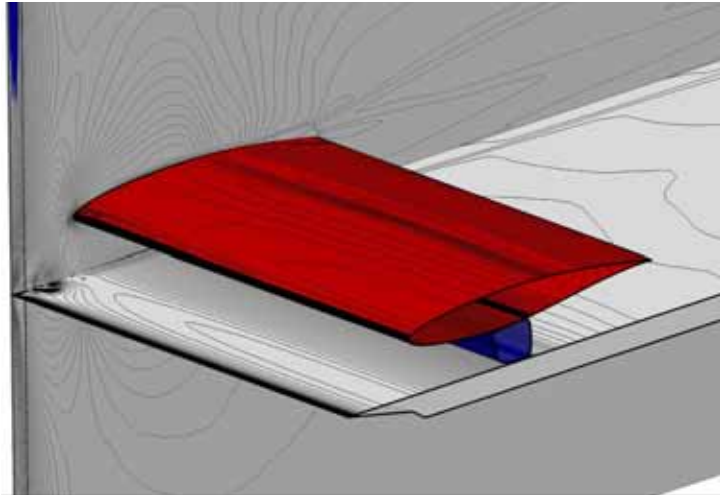
### 5.3.3 Case 2

Case 2 is at a higher angle of incidence, ground clearance and Mach number than case 1, and a strong shock forms at around  $x/c = 0.17$  with the symmetry method, very close to the first pressure tapping on the upper surface. The CFD was again run as transient but this time remained unsteady; a small separation bubble forms at the foot of the lambda shock which caused a mild unsteadiness in attempts to run the simulations as non-transient, but more importantly, large-scale separation was present at the wing/endplate junction. Three-dimensional representations of the flowfields are shown in figures 5.16 and 5.18 for the points in the cycles which produced the maximum lift on the wing, with the regions of supersonic flow highlighted in blue. The two cases are markedly different even from a qualitative point of view, as the extent of separation at the wing/endplate junction is much greater in the elevated ground case, strongly influencing the rest of the flowfield.

The two-dimensional slices of the flowfield taken at the mid-span symmetry plane indicate that, again, the effect of the elevated ground has been to increase the effective angle of attack of the wing, pushing the shock approximately  $0.04c$  further away from the leading edge than the symmetry method shock location, and slightly increasing the peak local Mach number. This causes the shock/boundary layer interaction on the surface to increase in strength, which consequently produces a thicker boundary layer downstream. This is most noticeable at the trailing edge where the upper shear layer is more pronounced, resulting in a stronger, thicker wake, and in three-dimensions it is the underlying cause of the increased separation at the endplate junction.

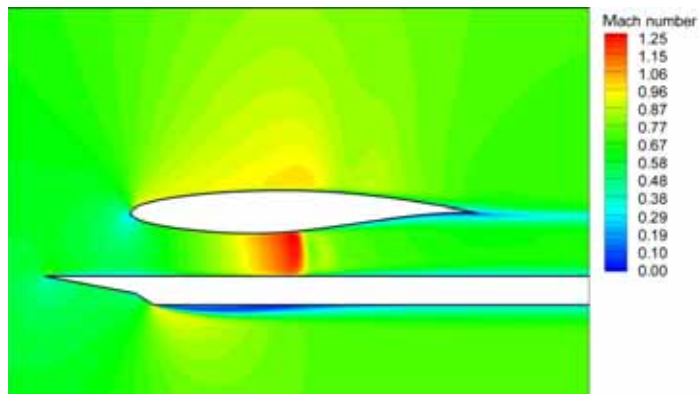
The observations from the CFD are supported by the experimental pressure distributions of figure 5.15, which, as with Case 1, indicate that influence of the elevated ground plane in displacing more flow over the upper surface is to increase the pressure on the lower surface as compared to the symmetry method result. In comparison to the pressure distribution predicted by the use of a moving ground boundary, the symmetry method again proves markedly superior, matching the moving ground case almost precisely. Since the pressure gradient between the wing and the ground is lower than in

Instantaneous CFD of 2822 USNA Case 3 (half-model with mid-span symmetry plane) with the elevated ground plane, showing contours of density and areas of supersonic flow (blue).



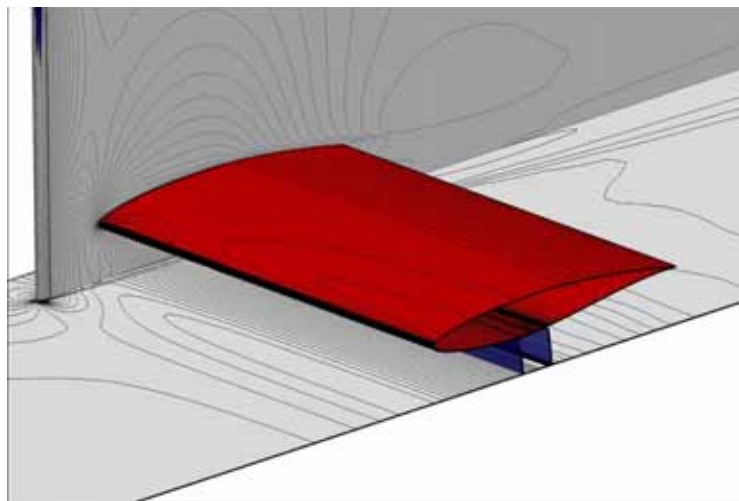
5.20  
FIG

Instantaneous CFD of 2822 USNA Case 3 with the elevated ground plane, contours of Mach number at the mid-span symmetry plane.



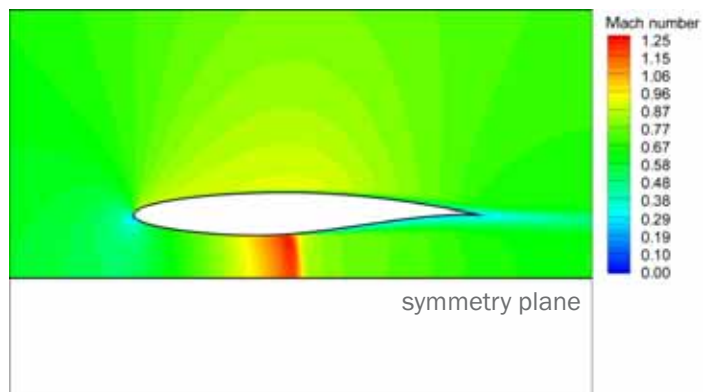
5.21  
FIG

Instantaneous CFD of 2822 USNA Case 3 (half-model with mid-span symmetry plane) with the symmetry ground plane, showing contours of density and areas of supersonic flow (blue).

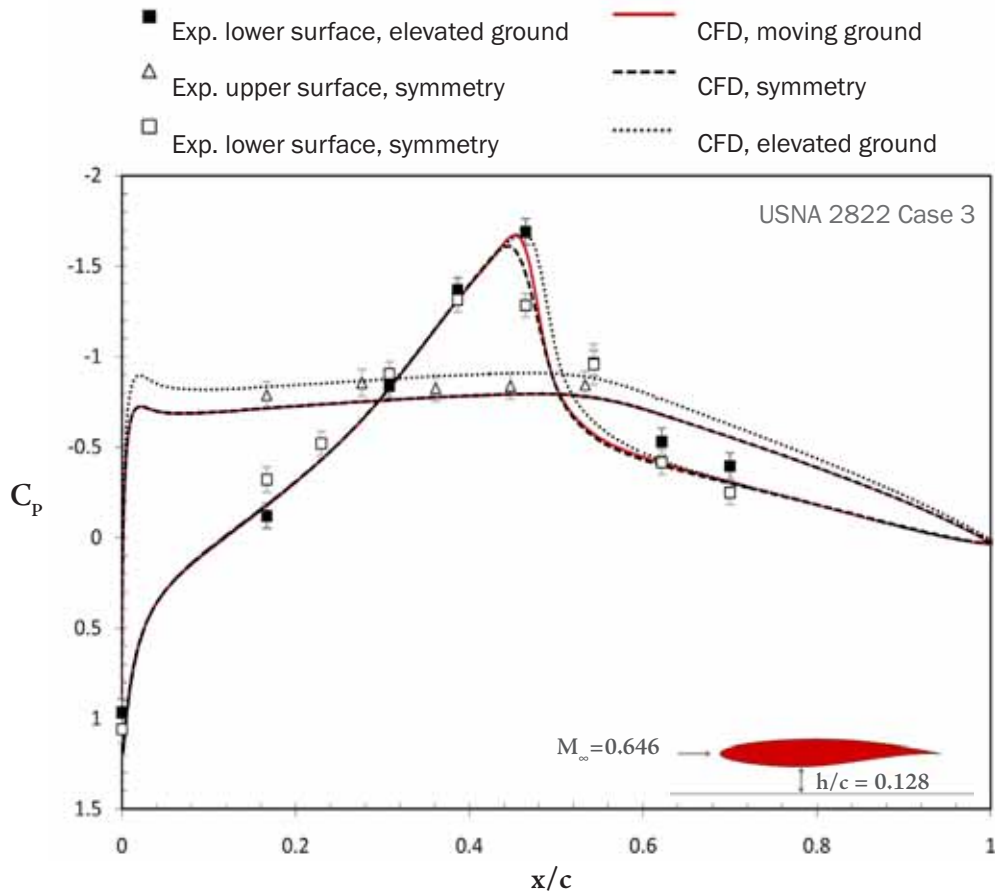


5.22  
FIG

Instantaneous 2822 USNA Case 3 with the symmetry plane, contours of Mach number at the mid-span symmetry plane.



5.23  
FIG

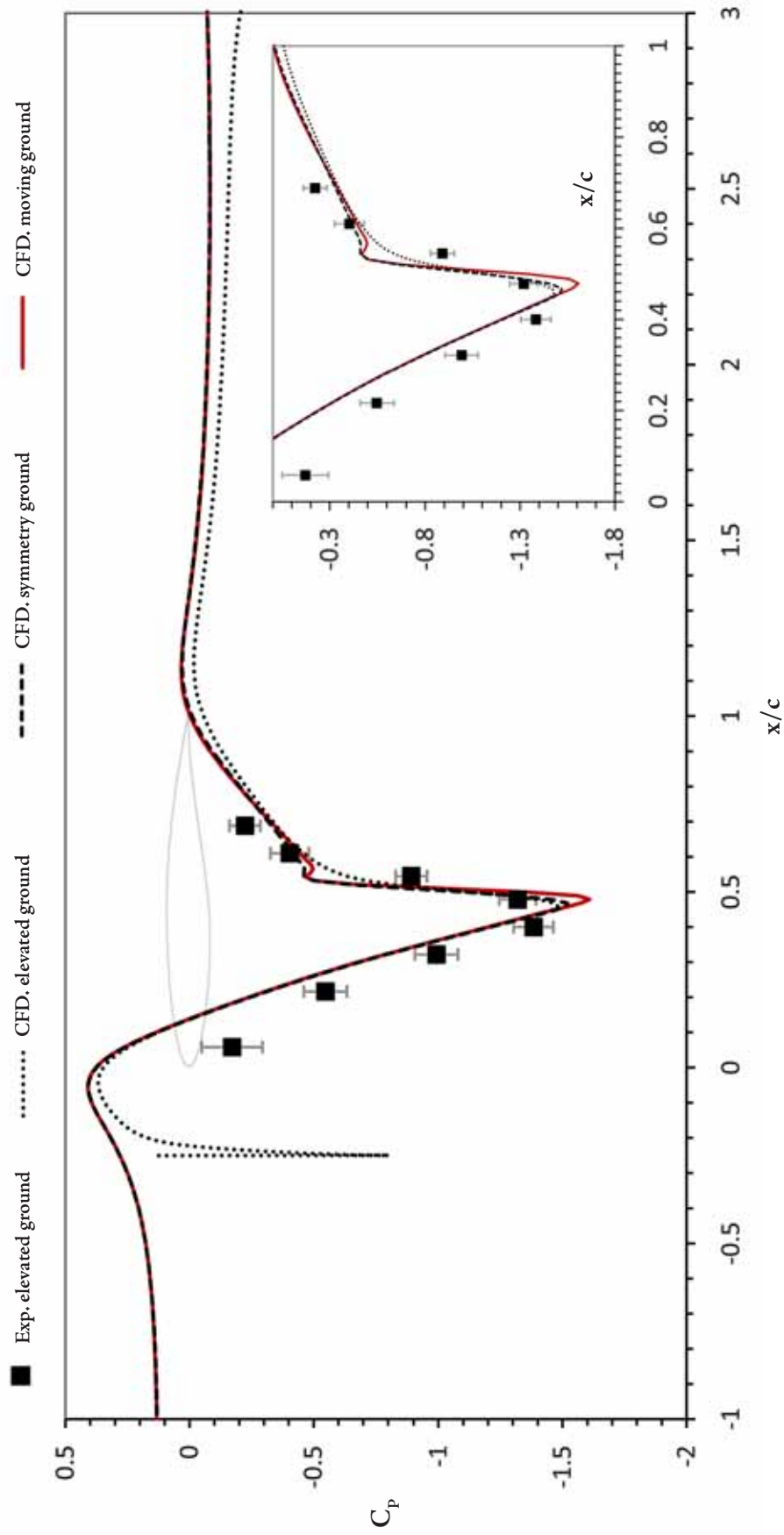


Time-averaged pressure distribution at the mid-span symmetry plane for 2822 USNA Case 3; comparisons of experimental symmetry and elevated ground methods to CFD.

Case 1, as a combination of a higher ground clearance and an increased angle of incidence, any discrepancy that may be caused with the symmetry method being unable to produce a ground boundary layer is not apparent.

### 5.3.4 Case 3

Case 3 presents a strong shock on the lower surface, which oscillates regularly as described in the previous chapter; for now we are only concerned with the time-averaged solution in order to compare to the experimental data. However, for a visual comparison, the three-dimensional CFD plots of figures 5.20 and 5.22 are instantaneous moments in the transient solution which are approximately concurrent in the oscillation cycle for the two different experimental methods at the moment of maximum lift production. Extensive separation at the wing/endplate junction has a large influence on the flow, and is much



Time-averaged pressure distribution at the mid-span symmetry plane on the ground plane, for 2822 USNA Case 3; comparisons of experimental elevated ground methods to CFD of symmetry, elevated ground and moving ground cases.

more pronounced for the elevated ground method.

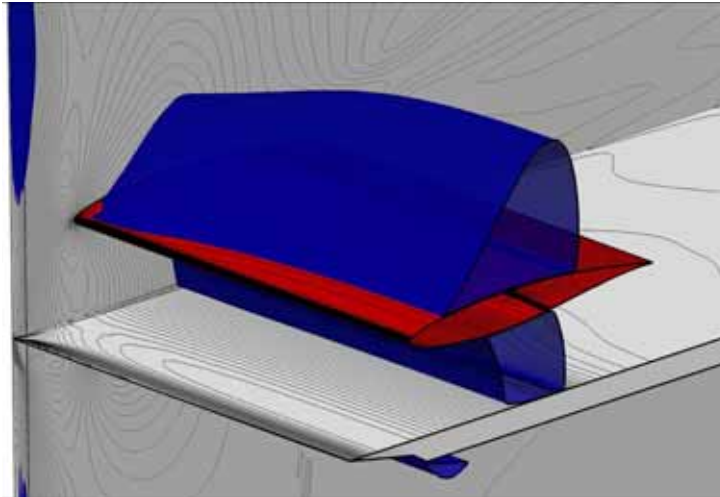
The figures show the shock, which occurs around  $x/c = 0.46$ , behind the point of maximum wing thickness (and thus behind the point of lowest ground clearance), as well as the increasingly-pronounced separation at the endplate, particularly at the root of the elevated ground plate in that case.

The flow over the upper surface in the elevated ground case is, when one compares figures 5.21 and 5.23, an exaggeration of the effect of the ground plate already described for cases 1 and 2. The peak upper surface Mach number is more markedly increased than in the previous two cases, however, and the flow is near-sonic in the elevated ground case. This indicates that at a freestream Mach number slightly higher than that of this particular experiment, an upper surface shock would have formed with the elevated ground where it would not have with the symmetry method.

Unlike in the previous two cases, the flow is also increasingly accelerated in the gap between the wing and the ground, such that the lower surface shock in the elevated ground case is stronger than that observed with the symmetry method, as illustrates in the pressure distributions at the mid-span in figure 5.24. This causes a fairly strong shock/boundary layer interaction on the elevated ground, which immediately thickens the boundary layer there.

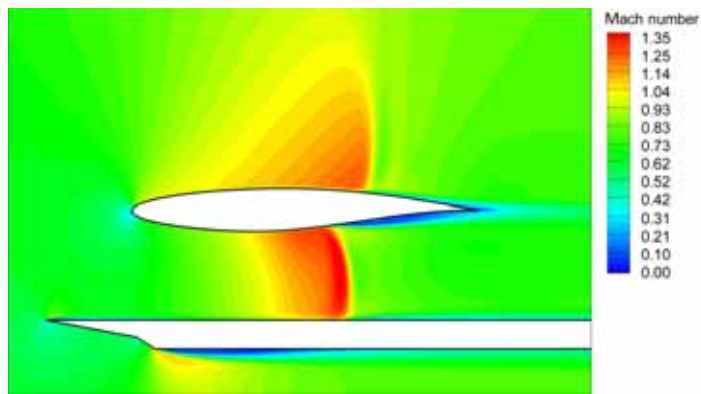
Ground plane pressure distributions are presented in figure 5.25, allowing the character of this interaction to be examined. The symmetry and elevated ground methods show a strong shock presence and accompanying pressure rise at close to  $x/c = 0.5$ , with the elevated ground exhibiting a slightly diffused version of this interaction due to the “cushioning” effect of the boundary layer. The downstream effect of this is such that the elevated ground pressure distribution does not recover to the same extent as the other two, near-identical pressure distributions, and would therefore exert a lingering influence into the wake region. As with Case 1, at an identical ground clearance, the symmetry method does not quite capture the extent of the suction peak, and thus a clear connection between very small ground clearances and increasing discrepancies between the symmetry and moving ground boundary representations emerges.

Instantaneous CFD of 2822 USNA Case 4 (half-model with mid-span symmetry plane) with the elevated ground plane, showing contours of density and areas of supersonic flow (blue).



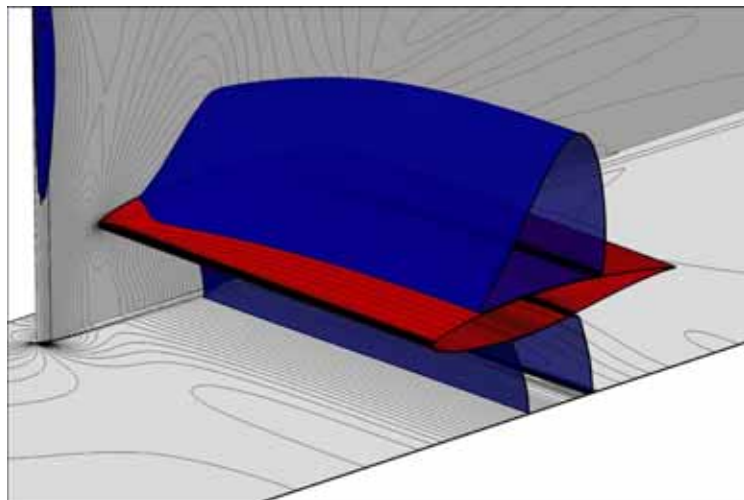
5.26  
FIG

Instantaneous CFD of 2822 USNA Case 4 with the elevated ground plane, contours of Mach number at the mid-span symmetry plane.



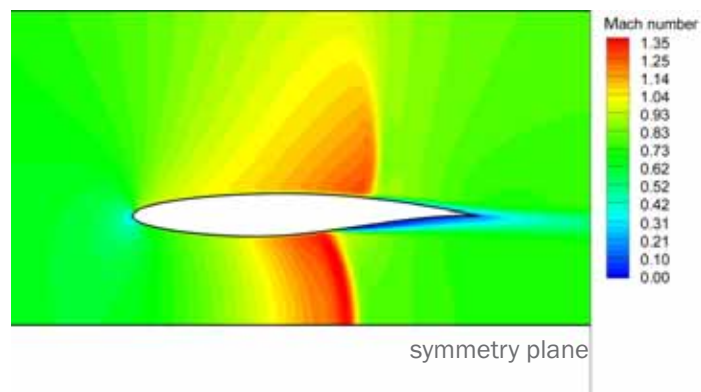
5.27  
FIG

Instantaneous CFD of 2822 USNA Case 4 (half-model with mid-span symmetry plane) with the symmetry ground plane, showing contours of density and areas of supersonic flow (blue).

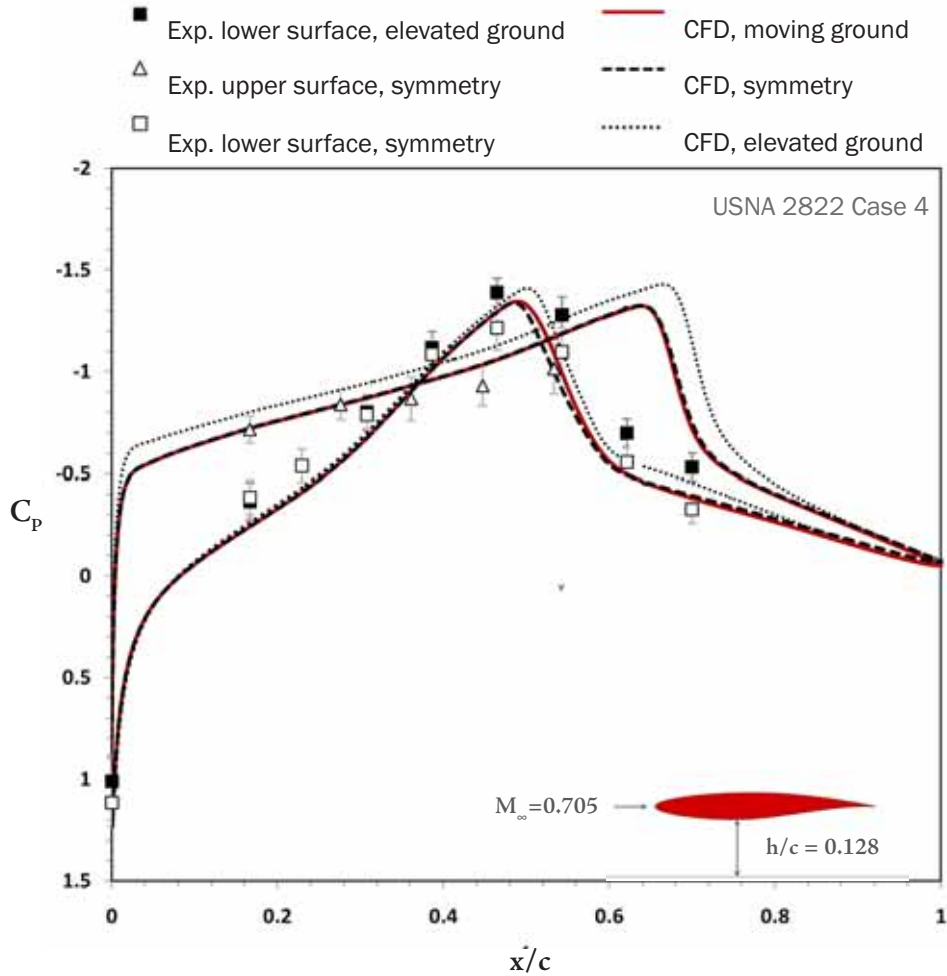


5.28  
FIG

Instantaneous 2822 USNA Case 4 with the symmetry plane, contours of Mach number at the mid-span symmetry plane.



5.29  
FIG

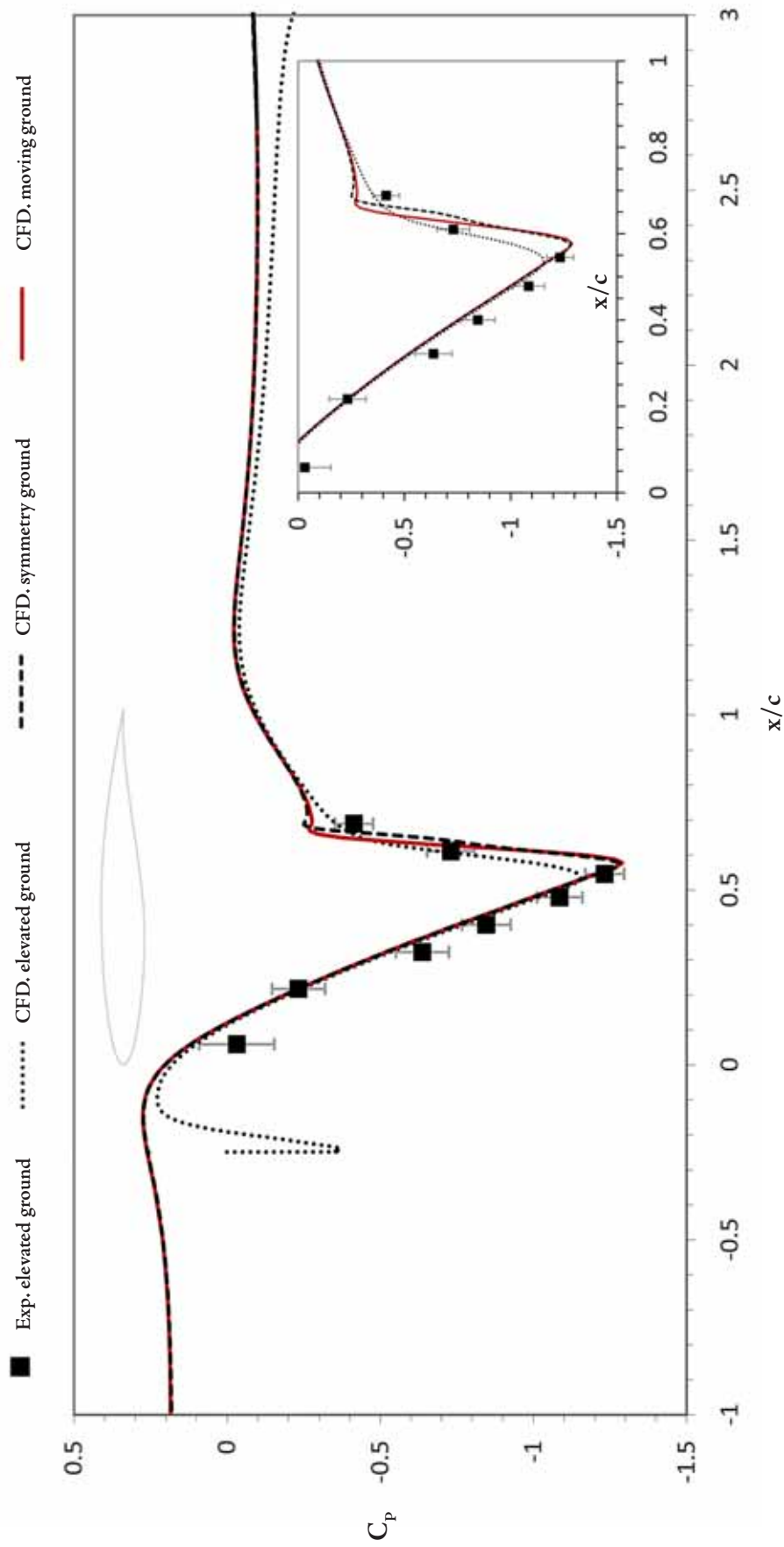


Time-averaged pressure distribution at the mid-span symmetry plane for 2822 USNA Case 4; comparisons of experimental symmetry and elevated ground methods to CFD.

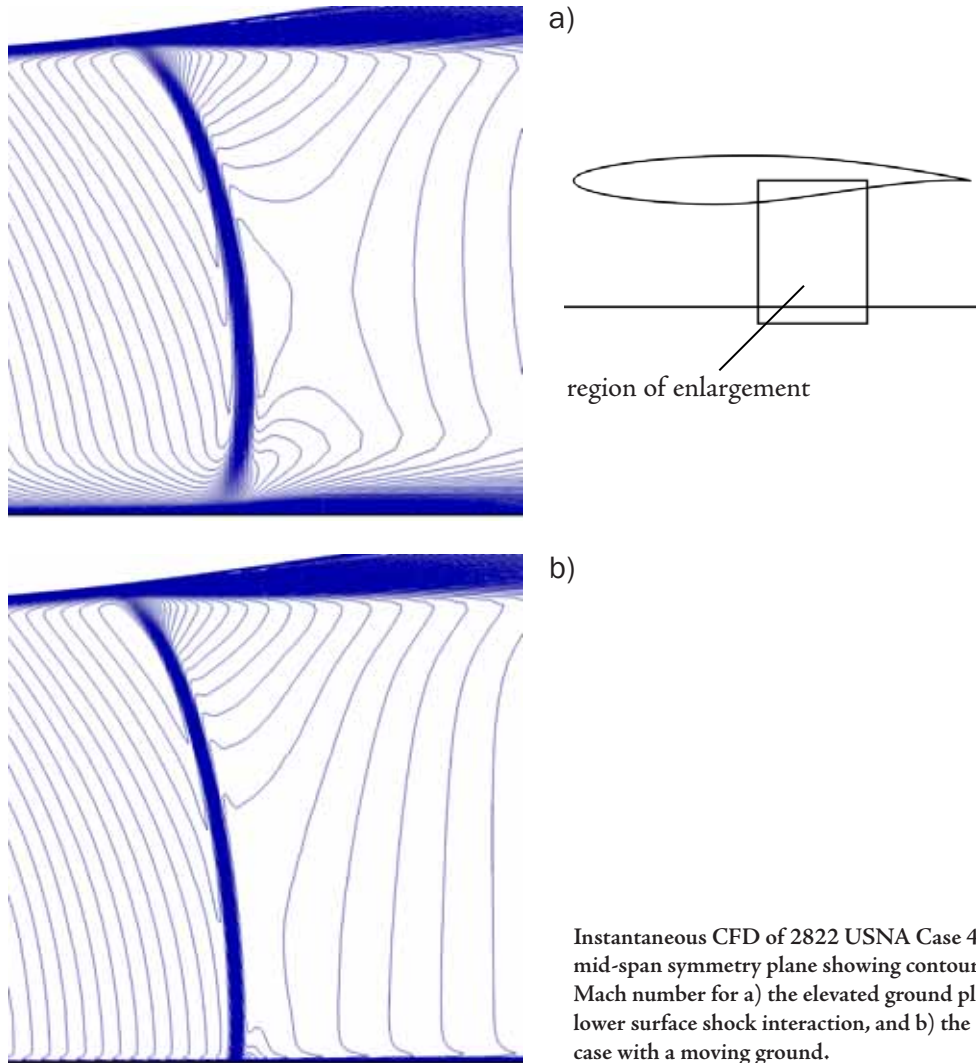
Interestingly, although the elevated ground plate clearly causes a large, unwanted disruption to the flow at the leading edge, the predicted ground pressure distribution in the CFD soon aligns with the symmetry and moving ground distributions. The dominant pressure gradient produced by the actual wing therefore seems to have a useful “settling” effect on the leading edge flow, though the influence of the elevated ground on the upstream flow remains.

### 5.3.5 Case 4

Case 4 was unique in that the flow was not stable at the mid-span, with transverse flow strongly influencing the lower surface shock, which oscillated around an average location of approximately  $x/c = 0.48$  with a dual frequency as discussed in chapter 4. The shock



Time-averaged pressure distribution at the mid-span symmetry plane on the ground plane, for 2822 USNA Case 4; comparisons of experimental elevated ground methods to CFD of symmetry, elevated ground and moving ground cases.



interaction at the wing surface is strong enough to separate the boundary layer in a periodic fashion. The upper surface shock was affected by the lower surface oscillations but moved across a smaller portion of the chord close to  $x/c = 0.7$ .

Although the flowfield was the most complex seen in the experimental programme, the shock interaction with the ground was not as strong as in Case 3. Figures 5.26 and 5.28 show some features of the flowfield in three dimensions, where large areas of supersonic flow can be observed on the upper and lower surfaces. The flow at the wing/endplate junction was separated at the point of shock interaction, heavily influencing the flow to the trailing edge and introducing recurring spanwise disturbances.

As with Case 3, the flow is now accelerated over both the upper and lower surfaces due to the influence of the elevated ground, as compared to the symmetry case. The upper surface shock sits at an average of  $x/c = 0.03$  downstream of the location

from the symmetry tests, and the lower surface shock sits  $x/c = 0.02$  downstream in the same comparison. The lower surface shock in the elevated ground case forms a strong interaction with the ground boundary layer, which thickens markedly downstream of that point.

In figure 5.30, the pressure distribution predicted by the symmetry method now features a slightly reduced suction peak immediately before the lower surface shock as compared to the moving ground case. Again this is attributable to the thin boundary layer which forms on the ground, which now experiences a mild interaction which slightly alters the motion of the shock wave as compared to the symmetry case. Overall, as with all of the other cases, the agreement between the symmetry and moving ground predictions is excellent.

The ground pressure distributions in figure 5.31 show the diffusion of the shock interacting with the boundary layer on the elevated ground. The oscillating motion of the shock is such that the boundary layer at its foot is continually thickening and contracting over time, sending a pulsed signal downstream. It is conceivable, though it does not occur in this case, that the ground boundary layer could separate due to the shock interaction. Clearly, this would produce results in even greater disagreement with the symmetry and moving ground cases. The differences in shock structure and the ground interaction between the elevated ground and the moving ground cases is shown in figure 5.32. Here, it is also useful to observe the extent of the ground boundary layer in the moving ground case which is the source of the minor discrepancy between the moving ground and symmetry cases.

### 5.3.6 Further Discussion

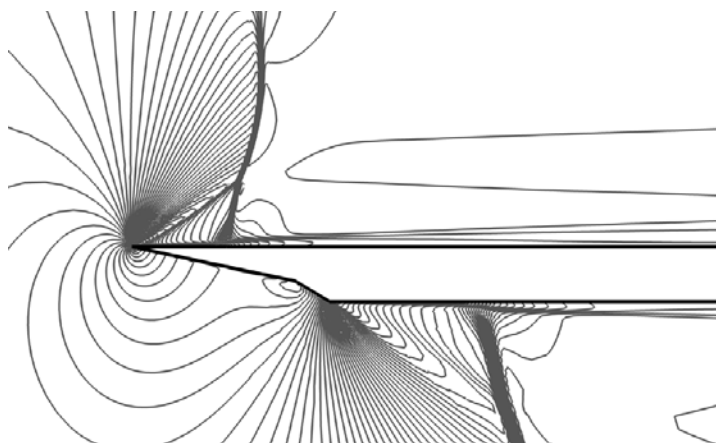
#### 5.3.6.1 *Other limitations of the elevated ground plane*

The onset of supersonic flow around the lower surface of the elevated ground plane for Case 4 points towards a more pressing concern: the emergence of a leading edge shock structure. This occurs at Mach numbers slightly higher than those obtained in the wind

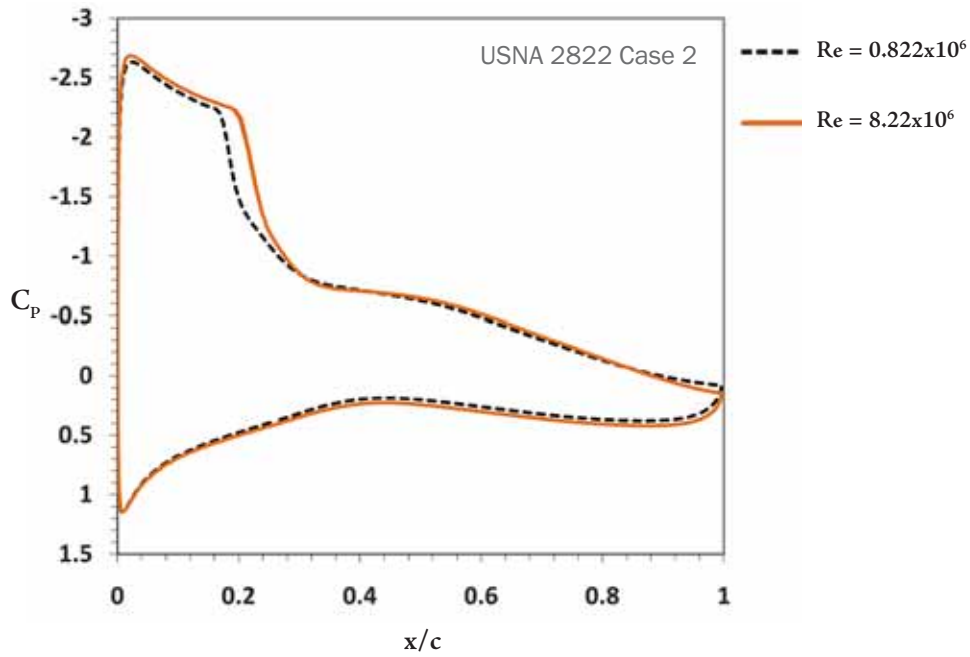
tunnel, but readily attainable from CFD. The plot in figure 5.33 illustrates the way in which a strong, highly-disruptive shock can form close to the leading edge of the ground plane, which would clearly render the downstream flow as an inaccurate representation of the desired oncoming freestream conditions. It occurs because the elevated ground acts much as a wing would - the oncoming flow deflects and accelerates over the upper surface at the leading edge separation bubble to the extent that the flow becomes supersonic well in advance of a supersonic freestream velocity. Furthermore this shock could well physically interact with the wing depending on its placement relative to the ground plane. Therefore, it is clear that the elevated ground cannot be applied at freestream Mach numbers where it has reached its own critical point.

The ground designed as described in chapter 3 had a sharp leading edge - this was acknowledged at the time to be likely to promote flow separation under certain circumstances. One can now appreciate that even a better design of the leading edge, featuring a contour which avoids any separation, has two intrinsic limitations. Firstly it will accelerate the flow at the ground plane to a value which is faster than the freestream, which although beneficial in terms of thinning the boundary layer itself, proves a poor substitute for a moving ground. This is particularly true if the ground clearance of the test model is small, in which case the lower surface could “see” an entirely different oncoming flow than the upper surface. Secondly, introducing significant curvature at the leading edge, even if it is designed to settle the flow downstream to a level which would not significantly disturb the wing, would still result in the emergence of a shock wave at

5.33  
FIG

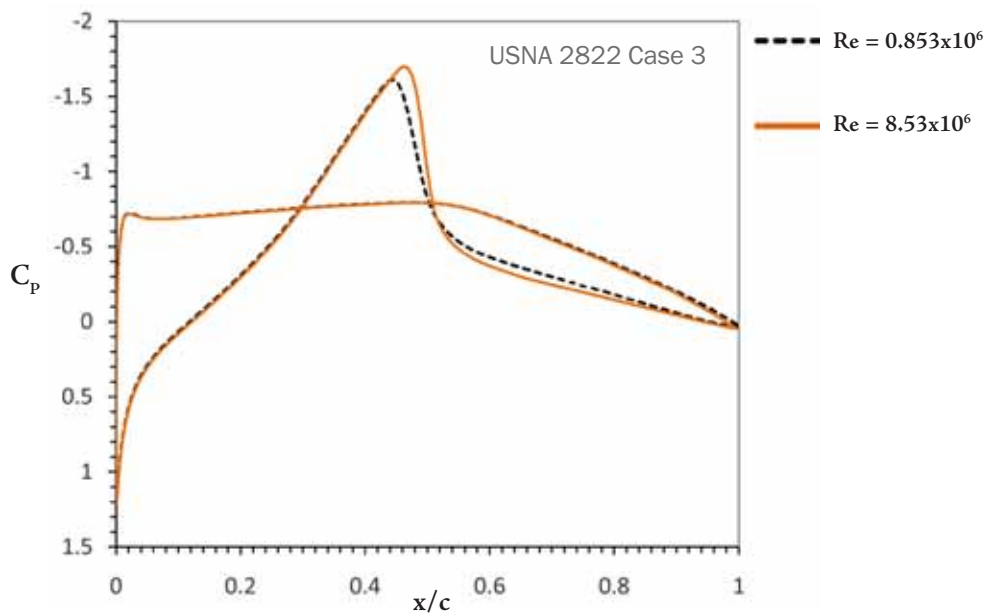


Contours of Mach number around the elevated ground at the test section mid-span symmetry plane for  $M_\infty=0.8$ .



5.34  
FIG

USNA 2822 Case 2 pressure distributions at the semi-span symmetry plane; CFD comparisons of experiment conducted and one at a higher Re.



5.35  
FIG

USNA 2822 Case 3 pressure distributions at the semi-span symmetry plane; CFD comparisons of experiment conducted and one at a higher Re.

a certain critical Mach number. If any form of suction or blowing were to be used to minimise the ground boundary layer, the disturbances introduced into the flowfield by the apparatus, including small shock waves, would prove prohibitively disruptive. The symmetry method suffers from none of these drawbacks.

### 5.3.6.2 *Issues of scale*

It has been shown that the symmetry method provides a superior means of simulating real-world high-subsonic ground effect flows in a wind tunnel, provided the Reynolds number is the same for the real-world case being compared to. The scaling of tests from wind tunnel to actual flight is a long-standing problem in aeronautics (Bushnell, 2006), and, at small-scale, is somewhat enhanced for ground effect problems due to the relatively large influence of the body boundary layer size with regards to the ground clearance. If the elevated ground is used, its boundary layer contributes further to this problem, as we have already seen.

At Reynolds numbers of higher orders of magnitude, the boundary layers are markedly smaller in relation to the body, and thus the effective channel created by the object and the ground is altered. At this stage, if an elevated ground is used and is of sufficient design to provide smooth flow that is as undisturbed at the leading edge and on ground plane as possible, the boundary layer contribution to the size of the gap between object and ground will be reduced to the point at which it will not have such an influence. Thus at this scale a well-designed elevated ground plane may prove preferable for testing, up until the point at which the flow close to the leading edge becomes near-sonic or supersonic.

Assuming the higher Reynolds number is achieved by directly scaling up the model, the symmetry method suffers from a large blockage ratio compared to an elevated ground, which can remain fairly slim as it is scaled up despite having to span the test section. Thus the choice of method for testing may even depend on the size of the test section, at least up until near-sonic freestream Mach numbers where the symmetry method is the only one which could be relied upon. As a brief examination of the applicability of small-scale testing with the symmetry method for flows of a Reynolds number ten times higher than those of the experiments, CFD was re-run with appropriately scaled versions of cases 2 and 3. The pressure distributions obtained as shown in figures 5.32 and 5.33 indicate that in both cases the effect of the increase in scale was to push the shock wave further back along the chord by around  $x/c = 0.03$ . While the general distribution is still similar,

it can be reasoned that certain crucial points in the evolution of the flowfield with respect to increasing Mach number or decreasing ground clearance, such as the determination of the exact critical Mach number, or the onset of buffeting flow, the small-scale tests could provide misleading results. It is important to note that the discrepancies shown in the two brief studies of this section are of an extent in the order of the differences observed in the predictions of different turbulence models in the preceding chapter.

## 5.4 Summary

It has been shown that for all cases examined, in both supersonic and mid-to-high subsonic flow regimes, the symmetry method provides the most effective means of obtaining results as close as possible to those which would be obtained with an ideal moving ground.

The elevated ground provides adequate service in fully supersonic flows, despite the introduction of small disturbances from the leading edge, as the boundary layer remains small. At high subsonic Mach numbers, however, the design of a moving ground is complicated by the need to avoid excessive upstream influence, including separation and even the formation of a shock wave under certain conditions. Although considerably increasing the blockage, the symmetry model provided excellent comparison in CFD to a moving ground across a range of cases for flows with and without shock waves. Increasing the scale of the model as much as possible is preferable, but blockage is a continual, and often limiting, issue. Nevertheless, it has been shown that very small-scale testing is a reasonable approximation of cases at Reynolds numbers ten times higher, and that the magnitude of the scale discrepancy is within the bounds of the differences produced by using different turbulence models in CFD, which is just one source of potential numerical error if no experimental data is available for comparison.

A useful contribution could now be made in this field by an experimental test programme in which the symmetry method could be used to produce detailed datasets specifically designed for CFD validation of compressible ground effect problems. Detailed

information about force, pressure and wake characteristics, gathered in circumstances easily reproducible in numerical methods, would be of considerable benefit to those unable to conduct live range or rocket-sled testing, or even wind tunnel testing at an acceptable scale.

We will return to the RAE 2822 and NATO projectile cases in chapters 7 to 9. The following chapter continues the theme of the importance of using CFD and wind tunnel testing together to improve the understanding of both; in this case, we return to the subsonic range to investigate compressibility effects around an inverted wing in ground effect, and issues which may occur in attempting to match CFD to experiments of different scales, Mach numbers, or Reynolds numbers.

# Chapter: The Onset of Compressibility Effects for an Inverted Wing in Ground Effect



*The flow around a three-dimensional inverted wing with an endplate is assessed at freestream Mach numbers from 0.088 to 0.4. Both fixed and varying Reynolds number cases are evaluated. The numerical method is validated against experimental data in literature; subsequently, CFD alone is used for further investigation. Incompressible and compressible simulations are compared across the Mach number range for four ground clearances. The respective aerodynamic forces and moments obtained, as well as pressure distributions and wake profiles, are considered. The effect of compressibility on the main vortex is also surveyed, as is the critical Mach number and its effect on wing performance.*

## 6.1 Introduction

The effects of compressibility for aerospace applications are generally accepted to manifest themselves in the flowfield at Mach numbers upwards of 0.3 (Anderson, 2001). The study described in this chapter aims to identify the extent to which close proximity to the ground encourages the 'early' onset of compressibility effects around an inverted wing. It specifically utilises a wind tunnel geometry for two reasons; the use of investigations by Zerihan (2000) for validation of the computational



A 50% scale model open-wheel racing car in a moving ground wind tunnel.

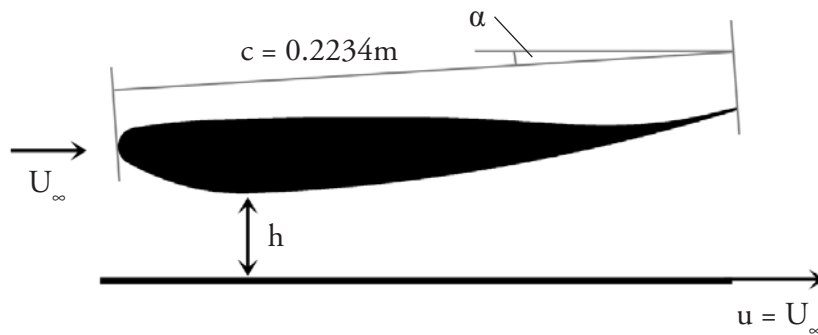
approach for these subsonic simulations, and the applicability of the research to common industry situations where wind tunnel data will be used in comparison with CFD.

The study builds upon early work by the author, involving a purely two-dimensional representation of the problem (Doig *et al.*, 2008) which can be found in Appendix A. The study indicated that at freestream Mach numbers between 0.15 and 0.35, compressible effects became influential to the aerodynamic characteristics of the aerofoil; at ground clearances of  $h/c=0.313$  to 1, incompressible simulations were observed to underpredict the lift and drag coefficients compared to compressible cases, with discrepancies increasing with increasing Mach number, while at lower clearances, the incompressible simulations overpredicted lift and drag coefficients. This was attributed to a movement of the stagnation point forcing more flow over the upper surface, while at the same time separation on the lower surface was more prominent in compressible cases. The critical Mach number at  $h/c=0.179$  and below was determined to exist between 0.35 and 0.4, as a normal shock formed between the aerofoil and ground. Unsteady shock oscillation behaviour was observed, but no experimental data was presented to validate this flow feature.

The three-dimensional approach in this chapter is much more representative of realistic testing conditions, and includes the additional aspect of the endplate, which

induces its own significant changes to the density of the flow around it and strongly influences the vortex behaviour. The endplate serves to minimise flow from the upper to lower surfaces, and therefore improves the efficiency of the wing.

The chapter is split into two sections - a basic assessment of the influence of increasing Mach number for a fixed Reynolds number, and a more thorough investigation of the influence of increasing Mach number with a correspondingly-increasing Reynolds number. An outline of all cases run is in table 6.1. Note: for the inverted wing, positive  $C_L$  indicates downforce.



Notation for an inverted wing in ground effect

6.2  
FIG

Table 6.1. List of Mach numbers and related parameters

Mach Number	Velocity $U_\infty$ ( $\text{ms}^{-1}$ )	Mph	Kmph	Reynolds Number
0.0882	30	67.1	108	$0.459 \times 10^6$
0.15	51.02	113.1	183.7	$0.78 \times 10^6$
0.1764	60	136.2	216	$0.459 \times 10^6$ *
0.2	68.02	152.2	244.9	$1.04 \times 10^6$
0.25	85.03	190.2	306.1	$1.3 \times 10^6$
0.3	102.03	228.2	367.2	$1.56 \times 10^6$
0.3528	120	268.4	432	$0.459 \times 10^6$ **
0.4	136.34	304.9	490.7	$2.085 \times 10^6$

wing geometrically scaled to maintain Re: \* 50% scale, \*\* 25% scale

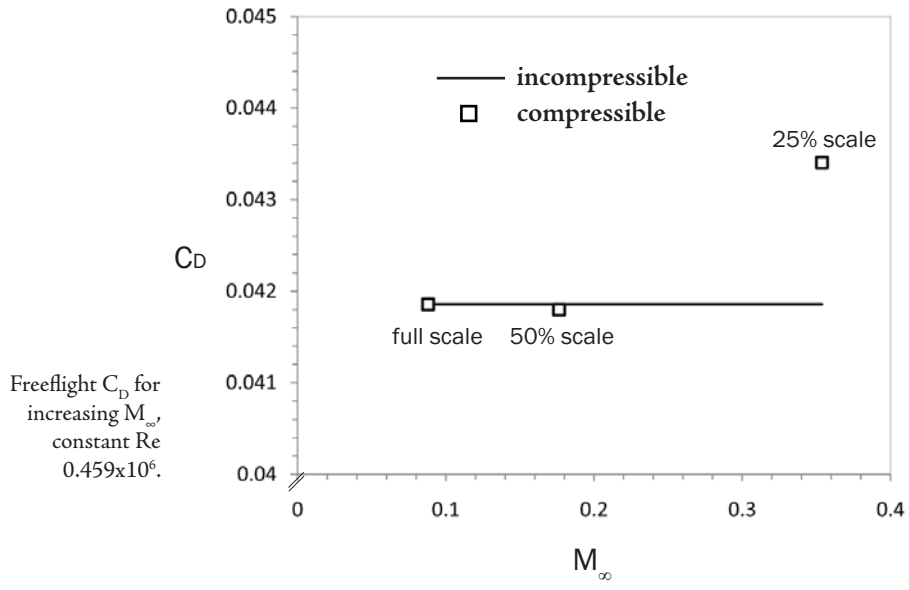
## 6.2 Results and discussion

### 6.2.1 Increasing Mach number for a fixed Reynolds Number

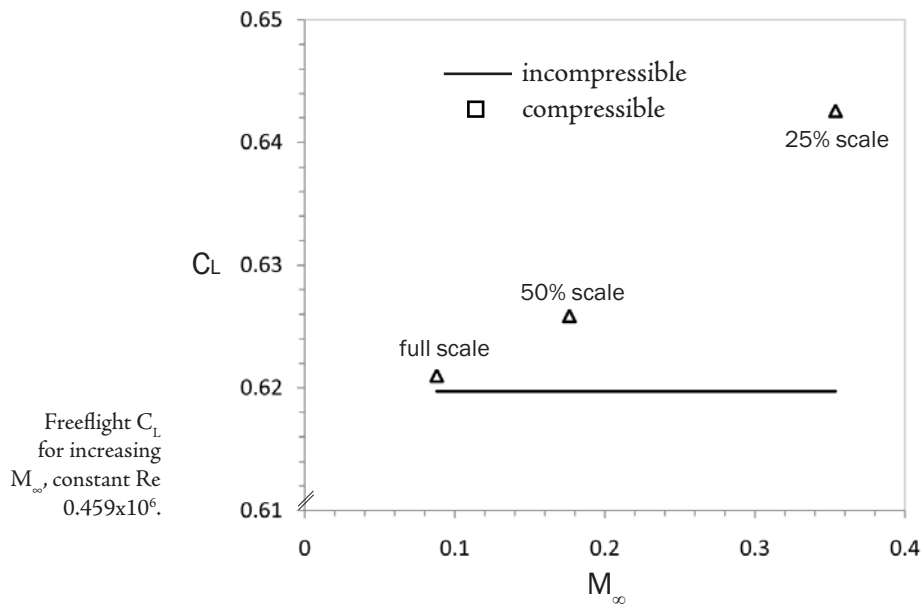
As a prelude to a broader examination of the extent of compressibility effects as they would influence a wing in a real-world scenario (i.e. an increase in Mach number is accompanied by a proportional increase in Reynolds number), it is prudent to consider first the influence of compressibility at a fixed Reynolds number. This facilitates a clearer understanding of how flow compressibility alone can influence the aerodynamic characteristics of the wing, and is relevant to the issue of wind tunnel scaling effects where compressibility may be a significant contributor to CFD/tunnel data comparisons - a 50% scale model is shown in a typical tunnel in figure 6.1.

As mentioned previously, much of the tunnel testing in the motorsport industry is conducted at scale; for instance a 50% model may be examined in a moving ground section at  $50\text{ms}^{-1}$ , as compared to a full-scale CFD model at the same Reynolds number for a freestream velocity of  $25\text{ms}^{-1}$ . This is the proposed standard means of testing in Formula 1 in coming years (essentially to reduce costs). This Mach number discrepancy produces its own compressibility issue as distinct from simply comparing incompressible and compressible CFD for a given flow speed (as constitutes the main thrust of the latter parts of this chapter). While the Reynolds number may be exactly scaled, compressibility effects are non-linear and the difference in Mach number may skew the comparison, particularly when incompressible simulations are used, as is common practice currently in automotive research fields (McBeath, 2006).

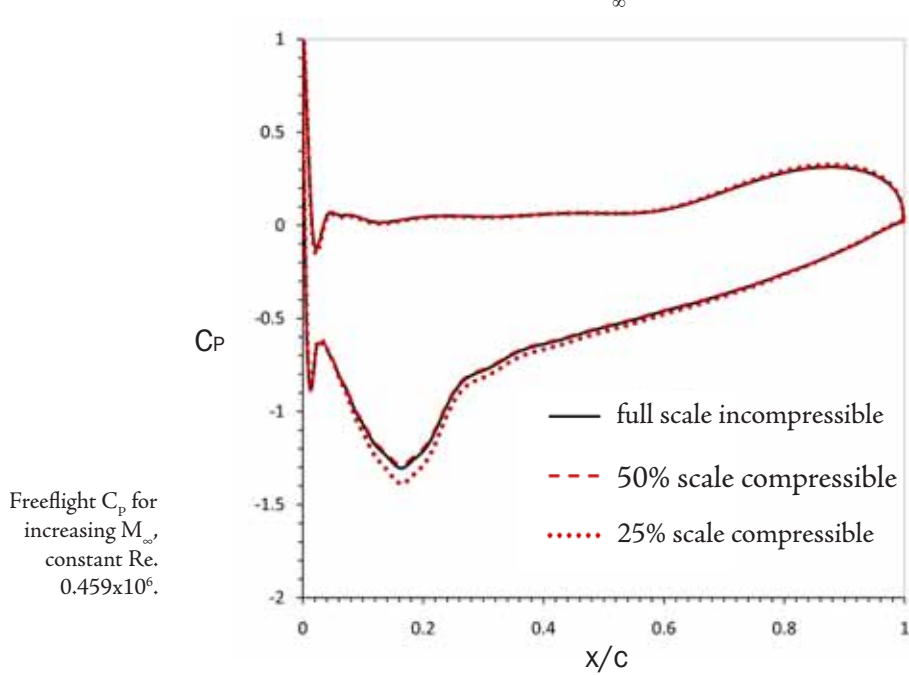
At this stage the wing is held at a constant  $h/c=0.179$  - a clearance low enough to produce a significantly increased peak local Mach number as compared to a freestream case, and representative of a typical wing section ground clearance that might be examined in a wind tunnel test. As outlined in table 6.1, the oncoming flow and ground speed of  $30\text{ms}^{-1}$  ( $M_\infty=0.0882$ ) for the standard-size wing of Zerihan (2000) was Reynolds-scaled for  $Re = 0.459 \times 10^6$  at 50% for a freestream of  $60\text{ms}^{-1}$  ( $M_\infty=0.179$ ), and then again at 25% scale for a freestream of  $120\text{ms}^{-1}$  ( $M_\infty=0.352$ ). The final case corresponds



6.3  
FIG



6.4  
FIG



6.5  
FIG

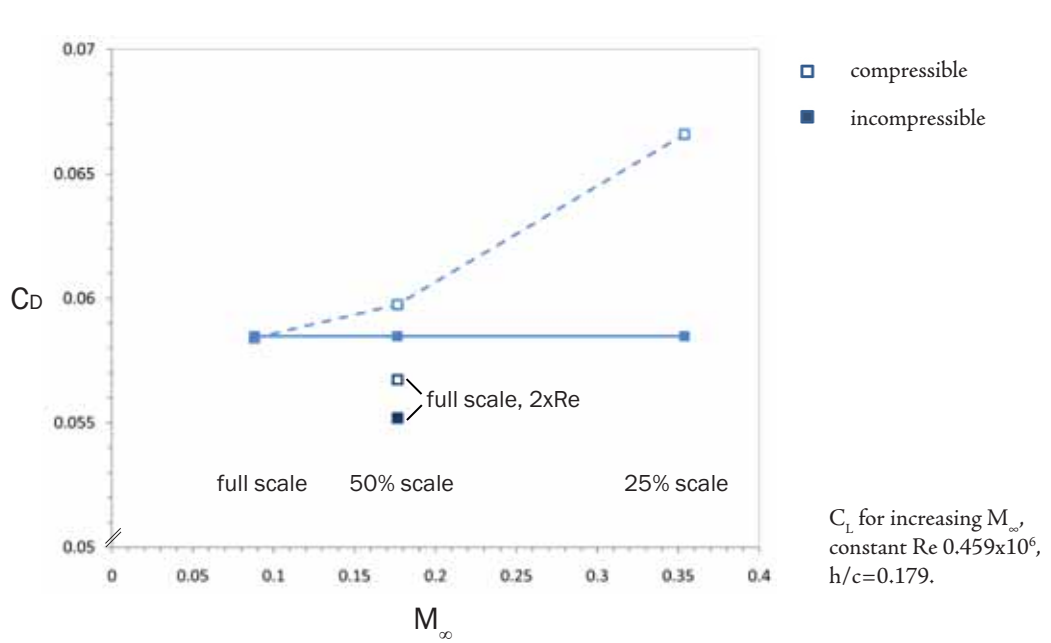
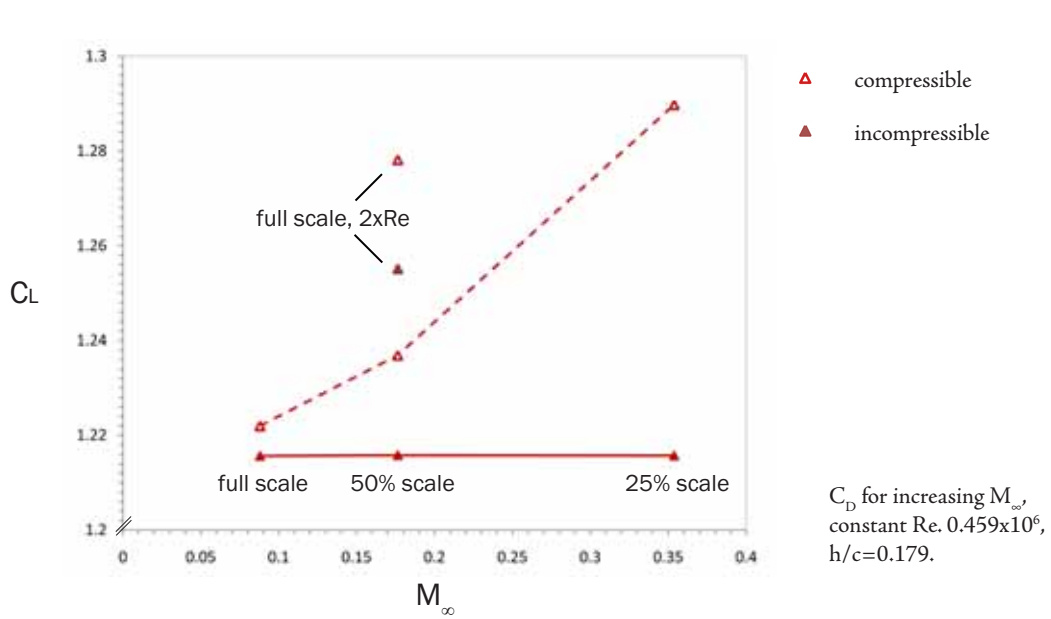
to a freestream velocity close to the wing's critical Mach number in ground effect, as discussed later in section 6.3.3, and thus though Reynolds scaling is preserved, the flow can certainly be expected to behave in a highly compressible fashion.

#### 6.2.1.1 *Freeflight reference cases*

In order to assess the extent to which ground proximity is the underlying cause for differences between incompressible and compressible CFD simulations, the three Reynolds-scaled cases were run for the “freeflight” case.

Figure 6.3 shows that compressible  $C_D$  does not change significantly from  $M_\infty=0.0882$  to  $M_\infty=0.1764$ , and corresponds closely to the incompressible result. At  $M_\infty=0.3528$ , the compressible  $C_D$  is approximately 3.5% greater. The compressible  $C_L$  in figure 6.4 exhibits a small difference even at  $M_\infty=0.0882$ , increasing to around 1% at  $M_\infty=0.1764$  and 3.7% at  $M_\infty=0.3528$ .

If we treat the compressible case as the most physically-realistic representation of the flowfield, resulting in the ‘true’ values of aerodynamic coefficients, it is clear that for a freestream Mach number of 0.3528 the incompressible assumption is no longer particularly appropriate. This is consistent with the fact that the TO26 aerofoil section can be classified as high-lift, and therefore produces a considerable acceleration of the flow around its shape; indeed, the peak local Mach number for this compressible case is 0.547. Even before looking at the ground effect case, it is obvious that the peak local Mach number in the presence of the ground will be considerably higher, and thus the trends observed in freestream will be exaggerated. While the 25% scale model at  $M_\infty=0.3528$  represents a speed of  $120\text{ms}^{-1}$ , which is above that which most large-scale and advanced moving-ground tunnels can achieve, it has been retained for comparison in the subsequent cases as the speed it represents is not far beyond the maximum speed of, for example, an Indycar Series racing car. It is certainly within the range of a vehicle such as a top-fuel dragster or land speed record car, which might be tunnel-tested at scale using a less sophisticated elevated ground plane.



### 6.2.1.2 Compressible influence on aerodynamic force coefficients at $h/c=0.179$

In figures 6.6 and 6.7, the influence of ground proximity on the lift and drag coefficients of the wing by the incompressible simulations is of markedly greater magnitude than in the freeflight cases of figure 6.3 and 6.4. Also included on these graphs for reference are results for a full-scale simulation at  $M_\infty=0.1764$ , such that the difference between Reynolds-scaled and unscaled cases can be assessed.

At  $M_\infty=0.0882$ , the drag predictions are negligibly different, but the incompressible simulation is underpredicting  $C_L$  by around 0.5%. At  $M=0.1764$ , the incompressible simulations underpredict  $C_L$  by 1.7% and  $C_D$  by 2.2%. The non-linearity of compressibility is evident as the trends are extended to  $M_\infty=0.3528$  cases, where lift is underpredicted by 6.1% and drag by 13.9% - a broadly exponential increase in the margin by which the incompressible simulations are underestimating the force coefficients.

Markedly, the results indicate that even at a relatively modest freestream Mach number of approximately 0.25, one would be better served by Mach scaling experiments to compare to incompressible CFD than by maintaining the Reynolds number no matter the freestream velocity. The results suggest that allowing the Reynolds number to increase as a consequence of a Mach number increase while maintaining the original model scale is a more appropriate way to approach the issue, beyond a certain freestream Mach number, than to continue to decrease the model scale while maintaining the same Reynolds number as the full-scale original.

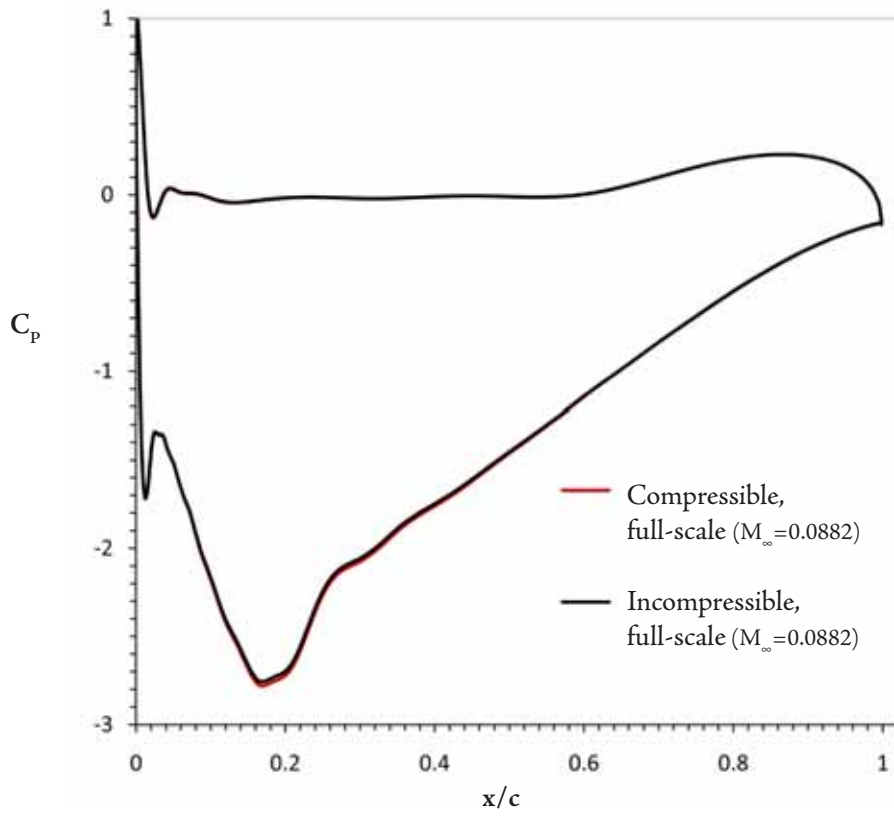
Even before further investigation, it is already clear that the most appropriate way to model the flow, even perhaps at  $M_\infty=0.0882$  and certainly at  $M_\infty=0.1764$ , is to consider the air as compressible.

### 6.2.1.3 Resultant pressure coefficient distributions

To examine in more detail the influence the Mach number and therefore flow compressibility has on the force coefficient results obtained, it is constructive to look to the surface pressure distributions presented in figures 6.8 through 6.10.

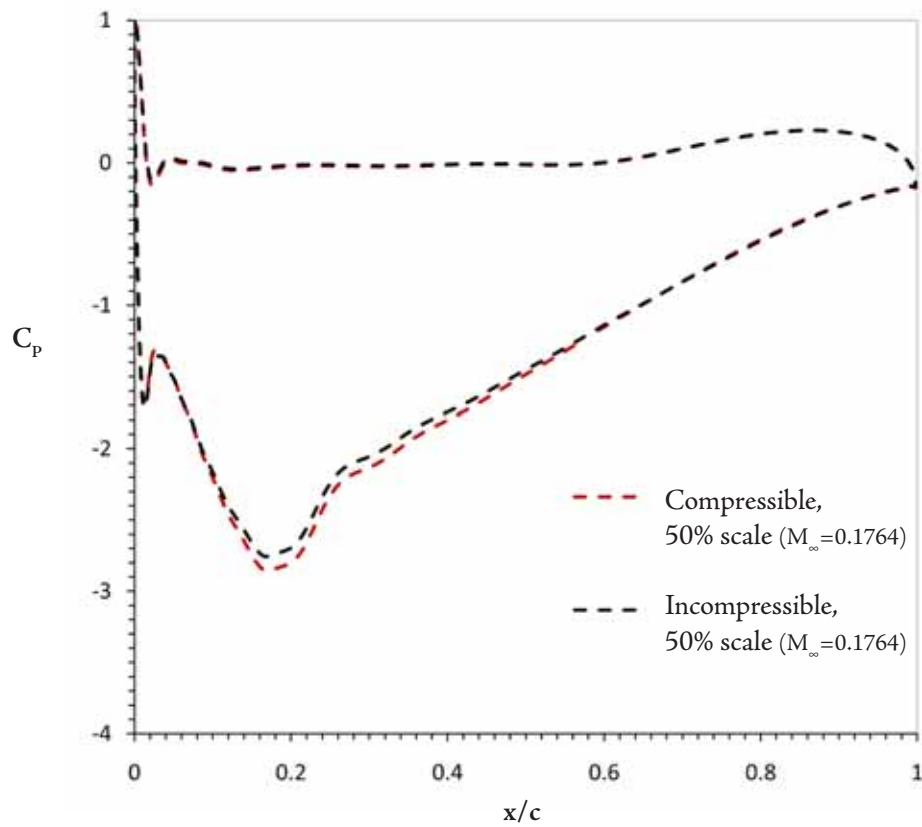
It is clear that the main cause for the differences noted between compressible and incompressible simulations stems from an incompressible underprediction of the suction peak on the lower surface. This is present to a small degree at  $M_\infty=0.0882$ , and is more marked at  $M_\infty=0.1764$ , extending across a longer chordwise stretch of the lower surface.

To this point, the upper-surface pressure distributions are similar. However, for the 25% scale model at  $M_\infty=0.3528$ , the stagnation point has moved slightly such that



Compressible and incompressible pressure coefficients, full-scale.

6.8  
FIG

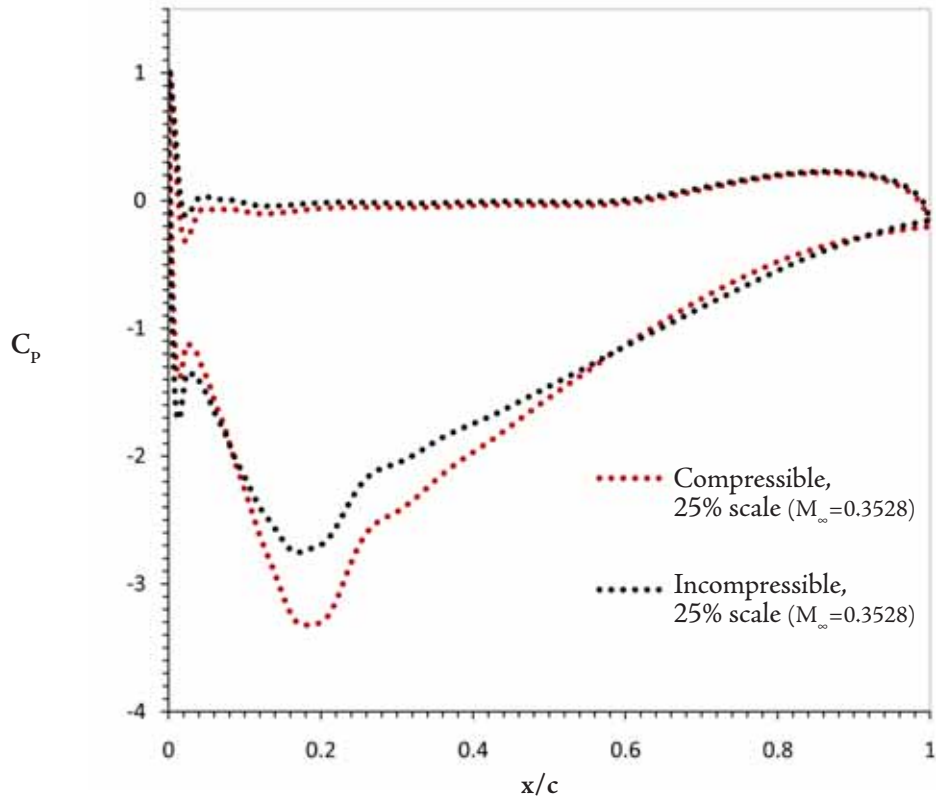


Compressible and incompressible pressure coefficients, 50% scale.

6.9  
FIG

6.10

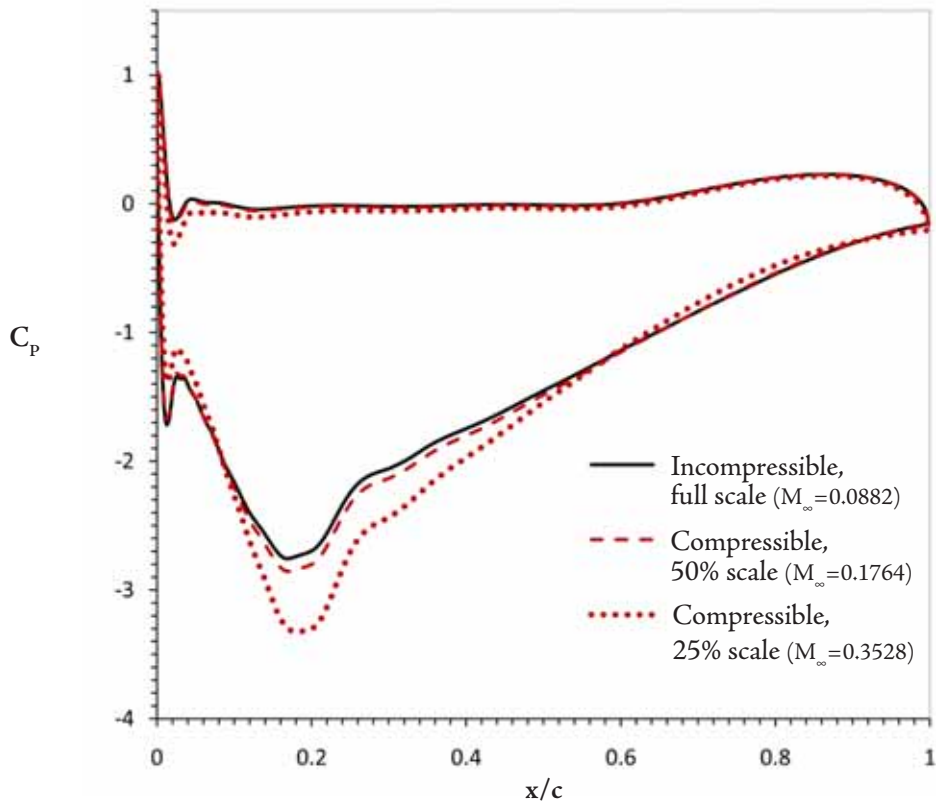
FIG



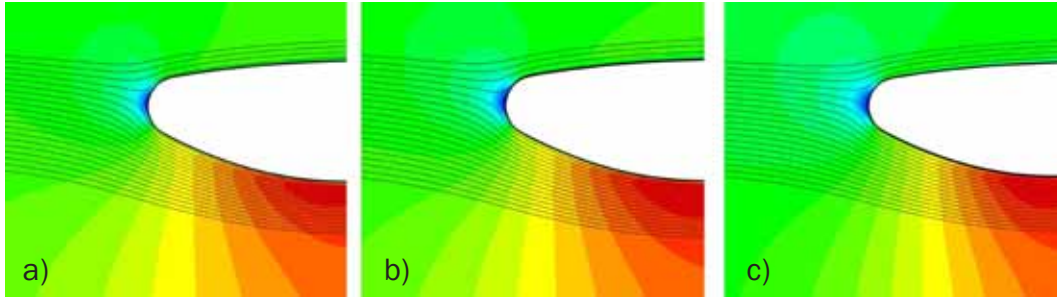
Compressible and incompressible pressure coefficients, 25% scale.

6.11

FIG

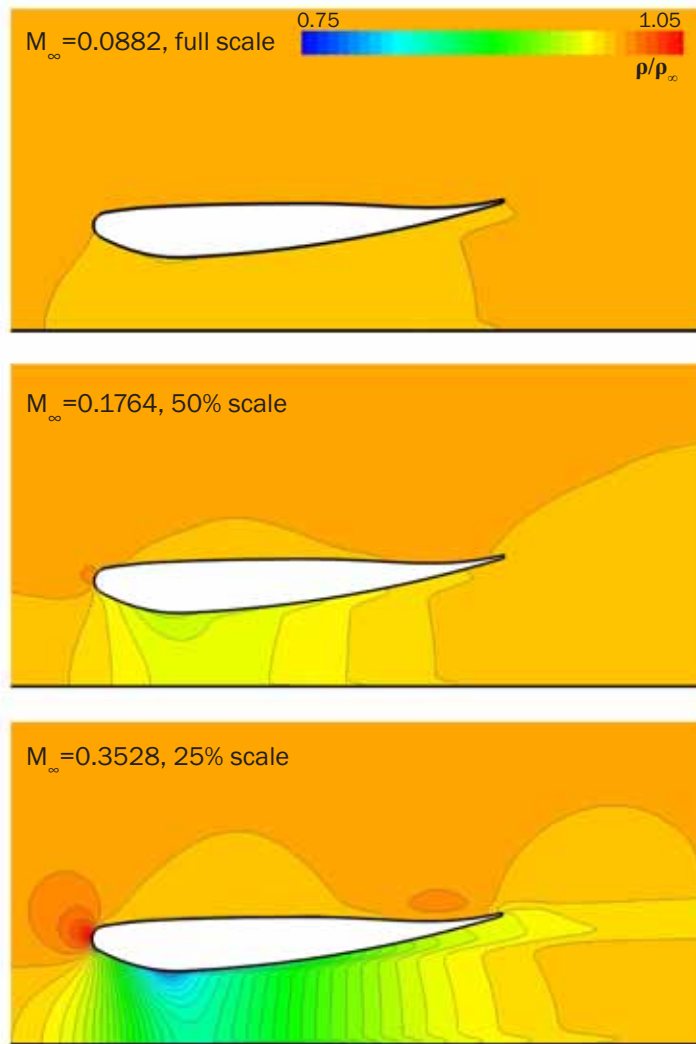


Compressible pressure coefficients at 50% and 25% scale compared to full-scale incompressible result,  $Re=0.459 \times 10^6$ .



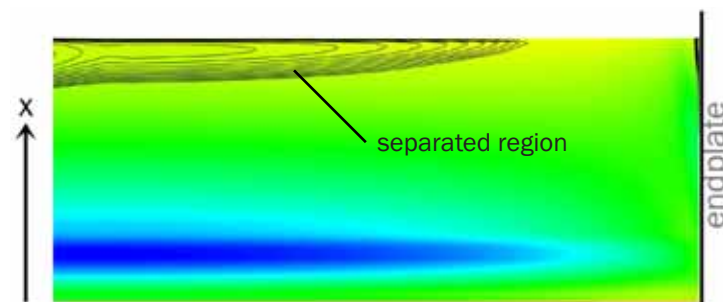
6.12  
FIG

Streamlines and x-velocity contours around a) full-scale wing at  $M=0.0882$ , b) 50% scale wing at  $M=0.1764$ , and c) 25% scale wing at  $M=0.3528$ .



6.13  
FIG

Density variations around the wing at the symmetry plane for the three Reynolds-scaled cases.



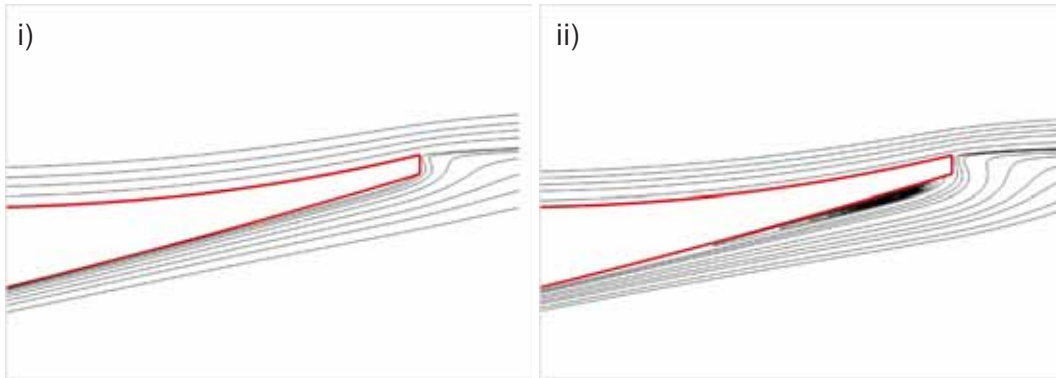
6.14  
FIG

Line-contours of x-direction wall shear stress overlaid upon colour contours of density on wing lower surface, 25% scale wing

the effective angle of attack of the wing is slightly decreased, allowing more flow over the upper surface. This is illustrated by the streamlines in figure 6.12, which also highlight the stronger pressure gradients around the leading section of the wing. The lower-surface suction peak is still significantly underpredicted by the incompressible simulation, and by this stage the extent of the rearwards adverse gradient is now underestimated, due to the changed trailing-edge conditions facilitated by the altered upper-surface  $C_p$  distribution. From the full-scale to half-scale model, the stagnation point moves by less than 1% of the maximum section thickness, but from the full-scale to the quarter-scale geometry, the stagnation point moves downwards by a more significant 2.18% of maximum section thickness.

A direct comparison of the pressure distributions for the three freestream Mach numbers is presented in figure 6.11, and reinforces the way in which Reynolds-scaling can quickly begin to offer erroneous comparisons to simulations or experiments at a lower Mach-number. Naturally, the primary driver for the differences is the ability of the density of the fluid to change as the Mach number is increased, and this is illustrated in figure 6.13. Here, the density variations around the wing relative to the freestream value at the mid-span symmetry plane are clear, with a considerable (close to 6%) variation in density at  $M_\infty=0.1764$ . While at this scale the peak local Mach number less than 1% higher for the compressible simulation, it is enough to slightly alter the pressure gradient, whereas the 25% scale model experiences a significantly higher peak local Mach number (at a maximum of  $\sim 0.79$ ).

Significantly, as shown in figure 6.15 the  $M_\infty=0.3528$  case experiences a notable separation near the trailing edge. Figure 6.14 shows that this separation develops in the centre region of the wing, and remains attached at the endplate. These results appear to indicate that any full-scale body in ground effect which is designed close to the point at which flow separate, could well experience significant flow separation in tunnel tests at a higher Mach number for the same Reynolds number. This would lead to potentially-considerable discrepancies when compared even to compressible full-scale simulations if the Mach number remains mismatched.



Streamlines around the trailing edge at  $z = 0$  for i) 50% scale and ii) 25% scale cases.

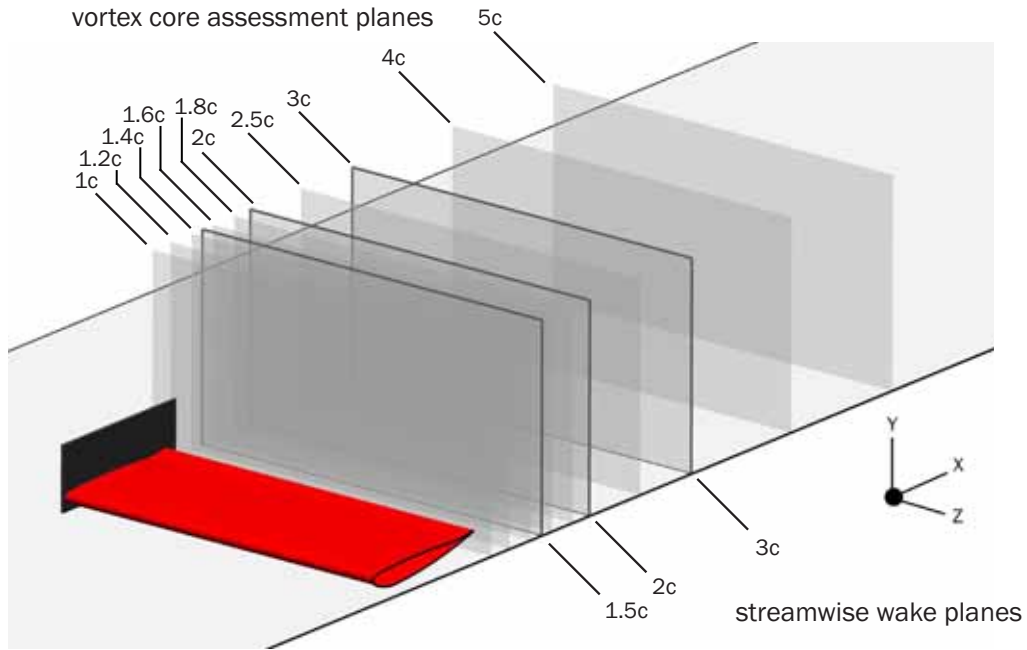
#### 6.2.1.4 Vortex and wake behaviour

A brief comparison of the behaviour of the lower vortex from the wing is presented in figures 6.17 and 6.18, with the vortex path assessed at the planes indicated in figure 6.16, and shows that the path of the vortex remains largely unaffected by the increase in freestream Mach number. The figures show the  $y$  and  $z$  positions of the vortex changing by small increments from case to case, but remaining generally little-affected by the increase in freestream Mach number, though an exaggeration of the general trend is present for the 25% scale case at the highest Mach number, albeit a fairly minor difference until around two chord lengths downstream of the wing trailing edge.

Figures 6.19 and 6.20 present  $u/U_\infty$  wake profiles for all the incompressible and compressible cases compared in this section, at  $1.2c$  and  $2c$  from the leading edge, respectively. The profiles in both instances for all the incompressible cases are almost exactly identical, as one would expect. At full scale and  $30\text{ms}^{-1}$ , the wake profiles for compressible and incompressible cases are similar, with the compressible case predicting a slightly higher peak velocity deficit ( $<0.1\%$  greater) at  $1.2c$  and a more substantial deficit by  $2c$  ( $0.9\%$  greater). Comparing the two 50% scale,  $60\text{ms}^{-1}$  cases, the velocity deficit differences have increased to  $2.5\%$  at  $1.2c$  and  $1.2\%$  at  $2c$ . The compressible centreline of the wake is also situated subtly lower than its incompressible counterpart, as a result of the mild increase in pressure difference caused by the additional acceleration of the compressible flow under the wing.

6.16

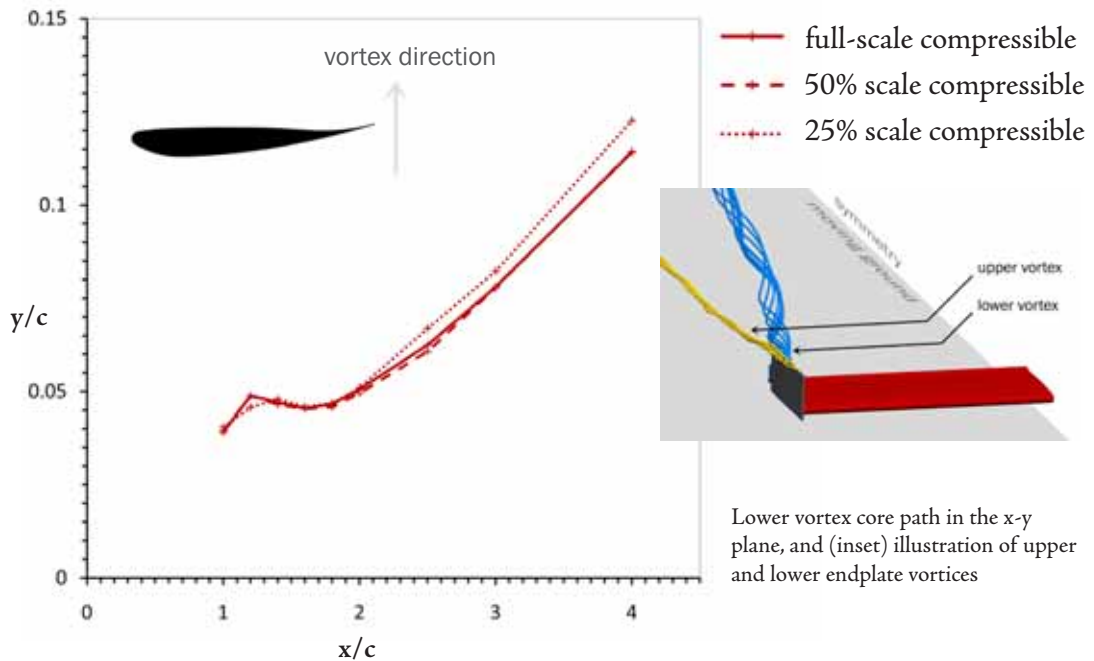
FIG



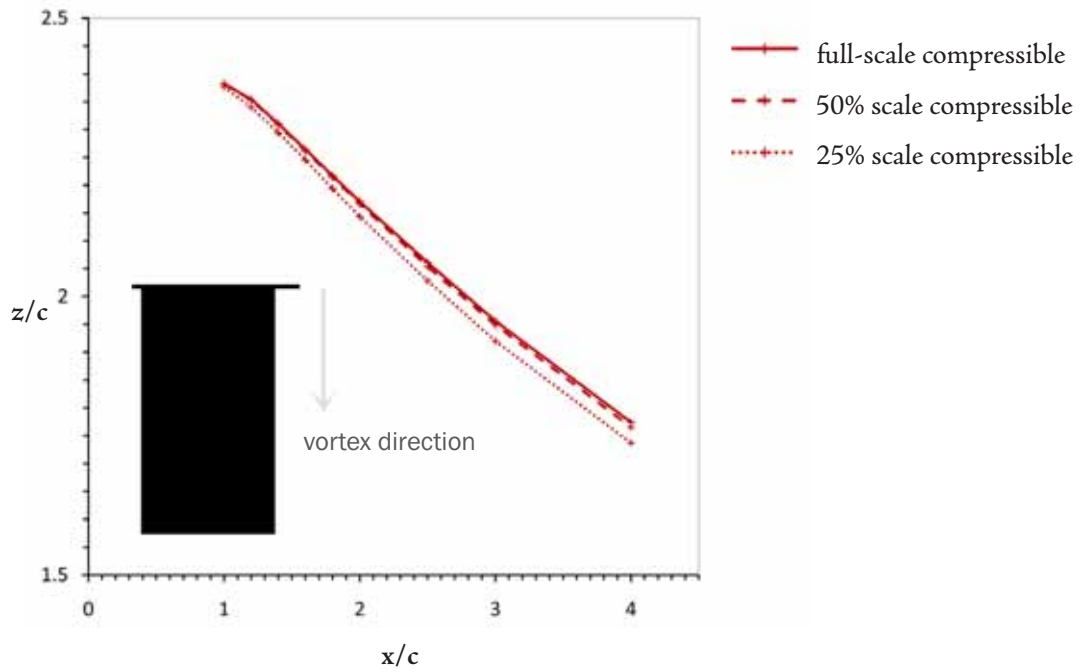
Location of slices used to extract both wake profiles and vortex cores.

6.17

FIG



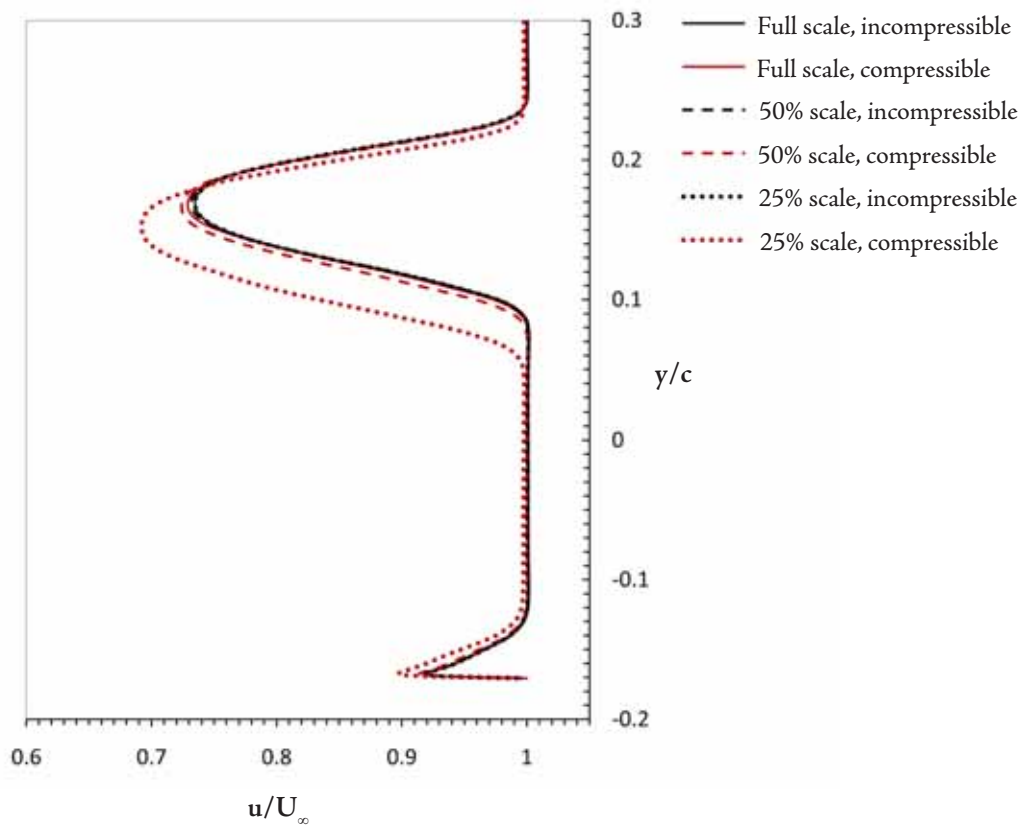
This effect is magnified when the oncoming velocity is increased to  $120\text{ms}^{-1}$  and the scale reduced to 25%. The wake is visibly and distinctly stronger, thicker, and closer to the ground, consistent with the separation observed previously. Thus it is confirmed that the primary cause of the marked increase in predicted drag is the effect on the wake of the increased pressure gradient of the lower surface.



6.18

FIG

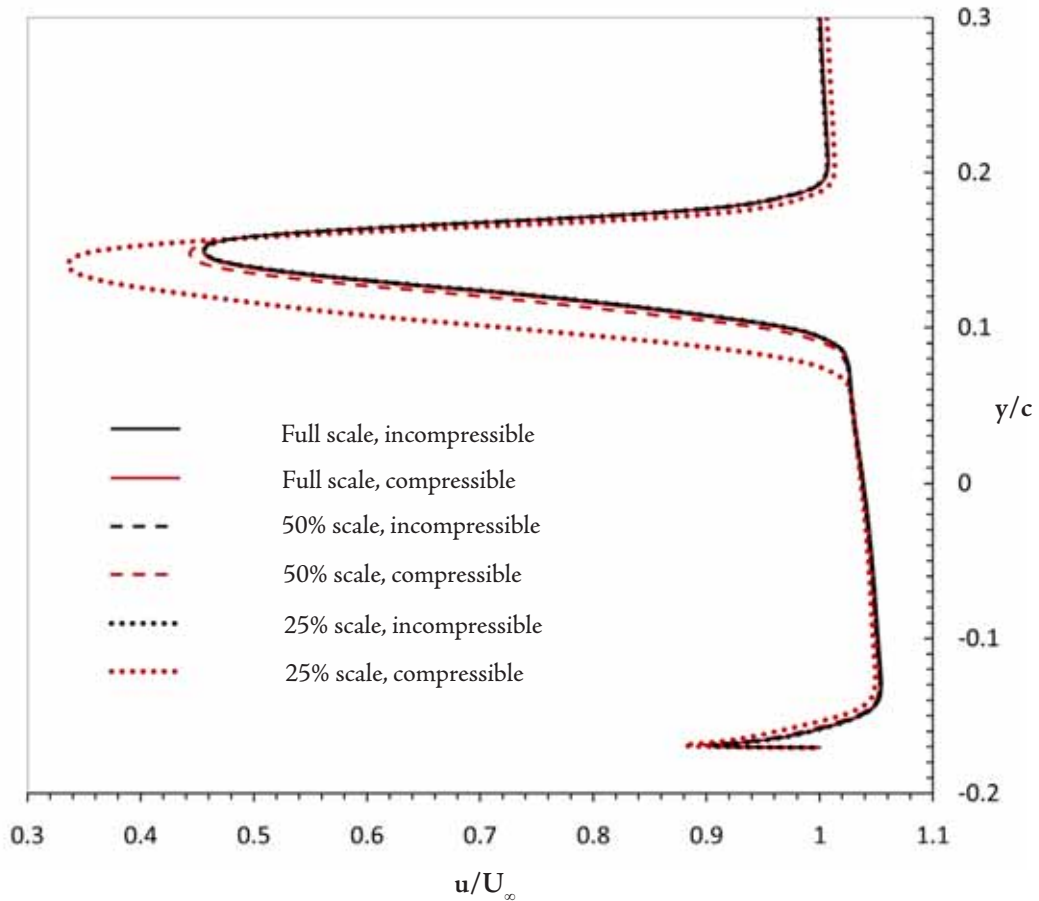
Lower vortex core path in the x-z plane.



6.19

FIG

Streamwise velocity wake profiles at  $2c$  from the leading edge.



Streamwise velocity wake profiles at  $1.2c$  from the leading edge.

Given the minor differences in vortex behaviour but the more substantial discrepancies in the streamwise wake profiles behind the wing on the symmetry plane, the flow reaching any components downstream of the wing (i.e. the wheels, suspension or sidepods of an open-wheel race car) would experience conditions for higher freestream Mach numbers which do not conform closely to those seen at the lowest freestream Mach number.

#### 6.2.1.5 Further comments

Although it is possible that the Reynolds and Mach number scaling effects manifest themselves in different fashions in the flow, leading to a misleading constructive or destructive interference between the two, Mach scaling in most large-scale subsonic tunnels would involve impractical or prohibitively expensive additional equipment to modify the pressure and temperature being delivered to the test section. Therefore this

strand of thought has not been pursued further here. One can conclude from the data presented that the only way to achieve truly effective validation between experiments and CFD for inverted wings even at relatively low Mach numbers is to ensure the computational model matches the experiment as closely as possible; that is, not only should the Reynolds number be matched, but the scale and Mach number should be comparable. Given the considerable influence which compressibility has on the flow even at the lowest end of the range of freestream velocities examined here, unlike for the same wing in free (unbounded) flow or a section which is much less cambered than the TO26, one can already see that running all CFD as compressible is desirable in order to obtain the most accurate simulation results.

The next section explores this notion further in looking more broadly at compressibility effects across a range ground clearances and Mach numbers, and consists of results in which the Reynolds number has been allowed to vary with the Mach number. This corresponds to a more realistic scenario in which a racing car increases its velocity and thus the flow Reynolds number based on the wing chord increases correspondingly.

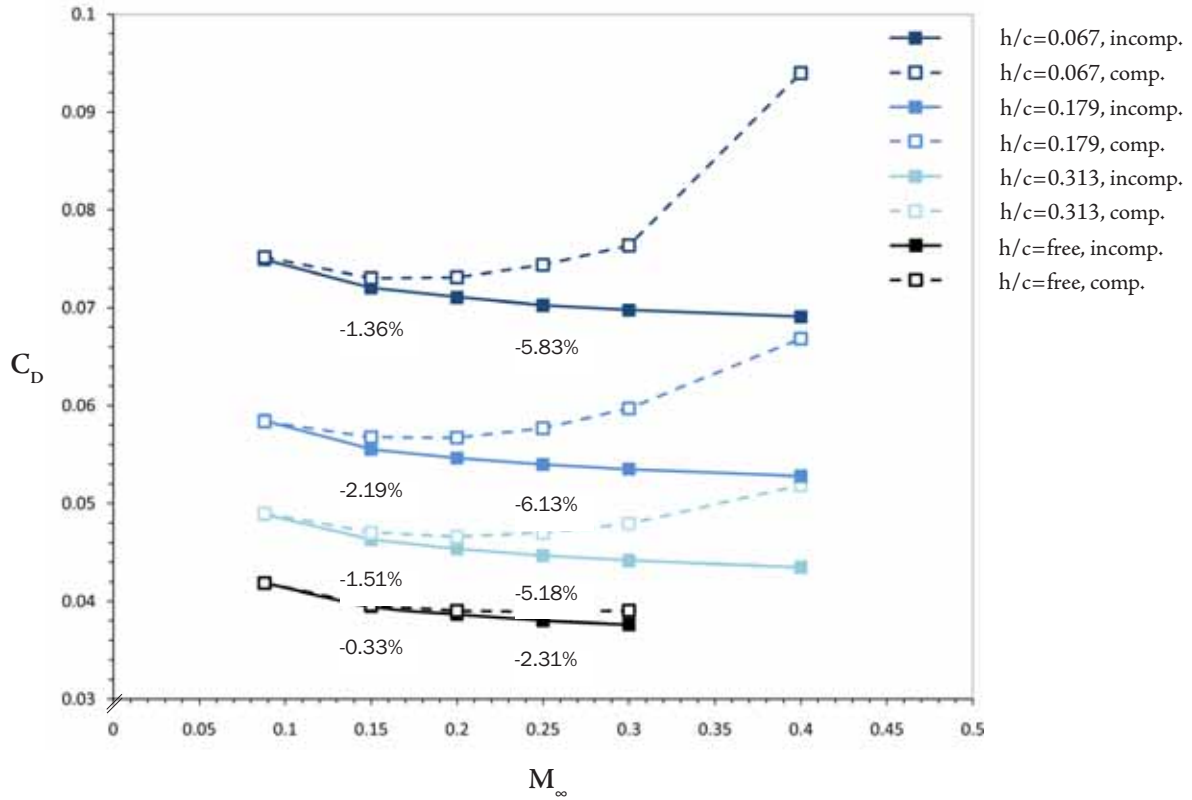
## 6.2.2 Increasing Mach number and decreasing ground clearance for a free-varying Reynolds number

### 6.2.2.1 Aerodynamic force and moment coefficients

Figures 6.21, 6.22 and 6.23 present chord-based drag, lift and pitching moment coefficients, respectively, for the full range of ground clearances examined, across the spectrum of Mach numbers detailed previously in table 6.1 up to 0.4. Subsequent subsections will focus more on  $M_\infty=0.15$  and 0.25, to examine the flow at a freestream at which compressible effects are beginning to become apparent, and one at which an incompressible simulation is wholly inadequate, respectively. Therefore, again treating the compressible cases as representative of the “true” flow, the graphs in figures 6.21, 6.22 and 6.23 are annotated with a percentage incompressible underprediction or overprediction at these two Mach numbers.

6.21

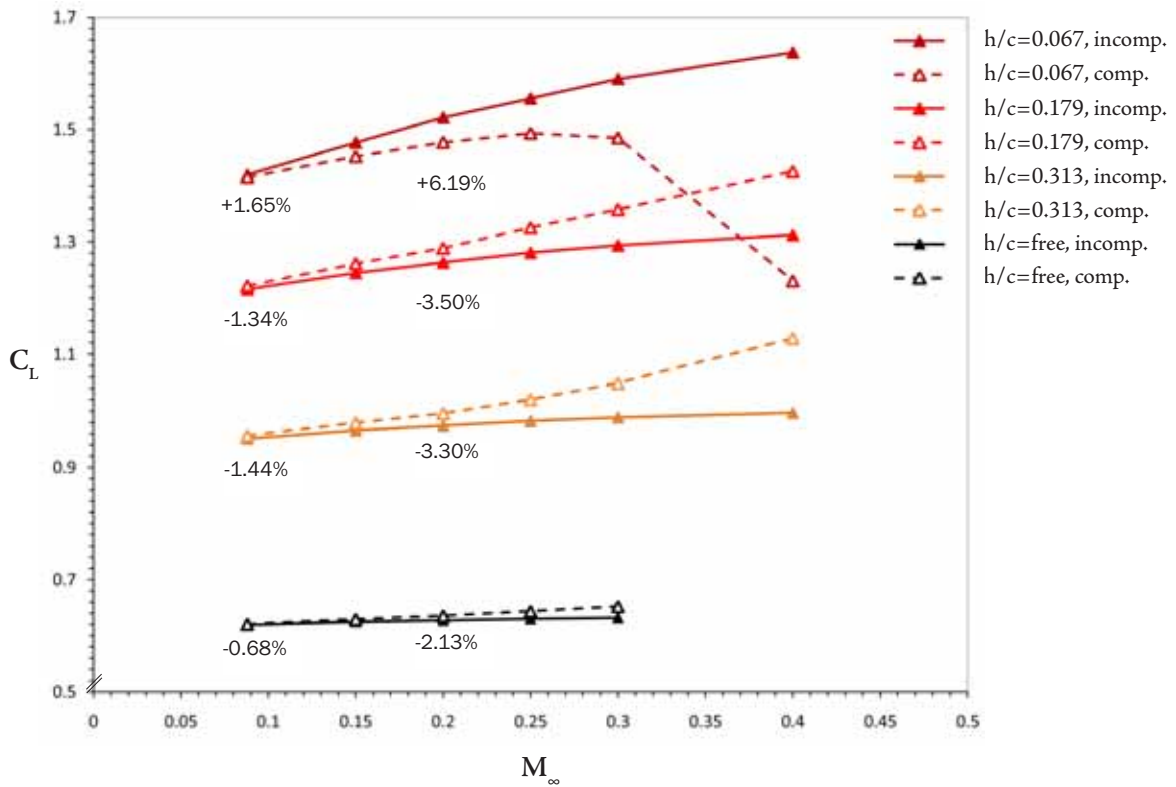
FIG



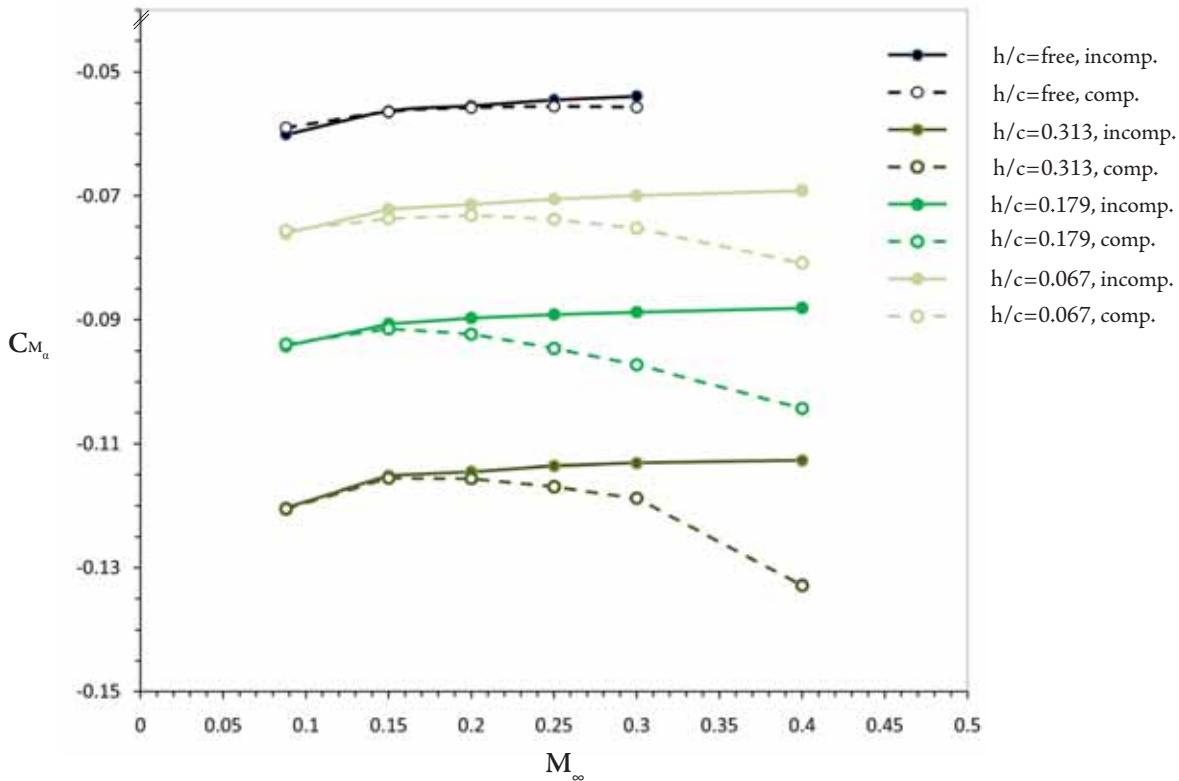
Incompressible and compressible drag coefficients for decreasing ground clearance and increasing Mach number

6.22

FIG



Incompressible and compressible lift coefficients for decreasing ground clearance and increasing Mach number



Incompressible and compressible pitching moment coefficients for decreasing ground clearance and increasing Mach number

$C_D$  reduces with Mach number for all incompressible cases, whereas the compressible  $C_D$  tends to increase with any Mach number increment from a freestream value of 0.15 upwards, regardless of ground clearance. Therefore, drag is increasingly underpredicted by incompressible simulations as the freestream Mach number is raised. The viscous component of the drag is affected, but it is the pressure component of the drag which is the main factor in these increases, including the wake region. This is consistent with the results discussed in the previous section - by allowing the flow to compress in the simulations, the wake proves stronger and thicker than its incompressible counterpart, and an earlier onset of flow separation is encouraged.

In percentage terms, the discrepancies between compressible and incompressible simulations reach their peak for the ground clearance of  $h/c=0.179$ . This can be attributed to the way in which the stagnation point begins to move to such an extent at  $h/c=0.067$  as to force a more significant portion of the oncoming flow over the top of the wing. This reduces the acceleration of flow on the underside, rendering the compressible effect on drag not as prominent as at  $h/c=0.179$ . In absolute terms, the drag at  $h/c=0.067$  is still

greater.

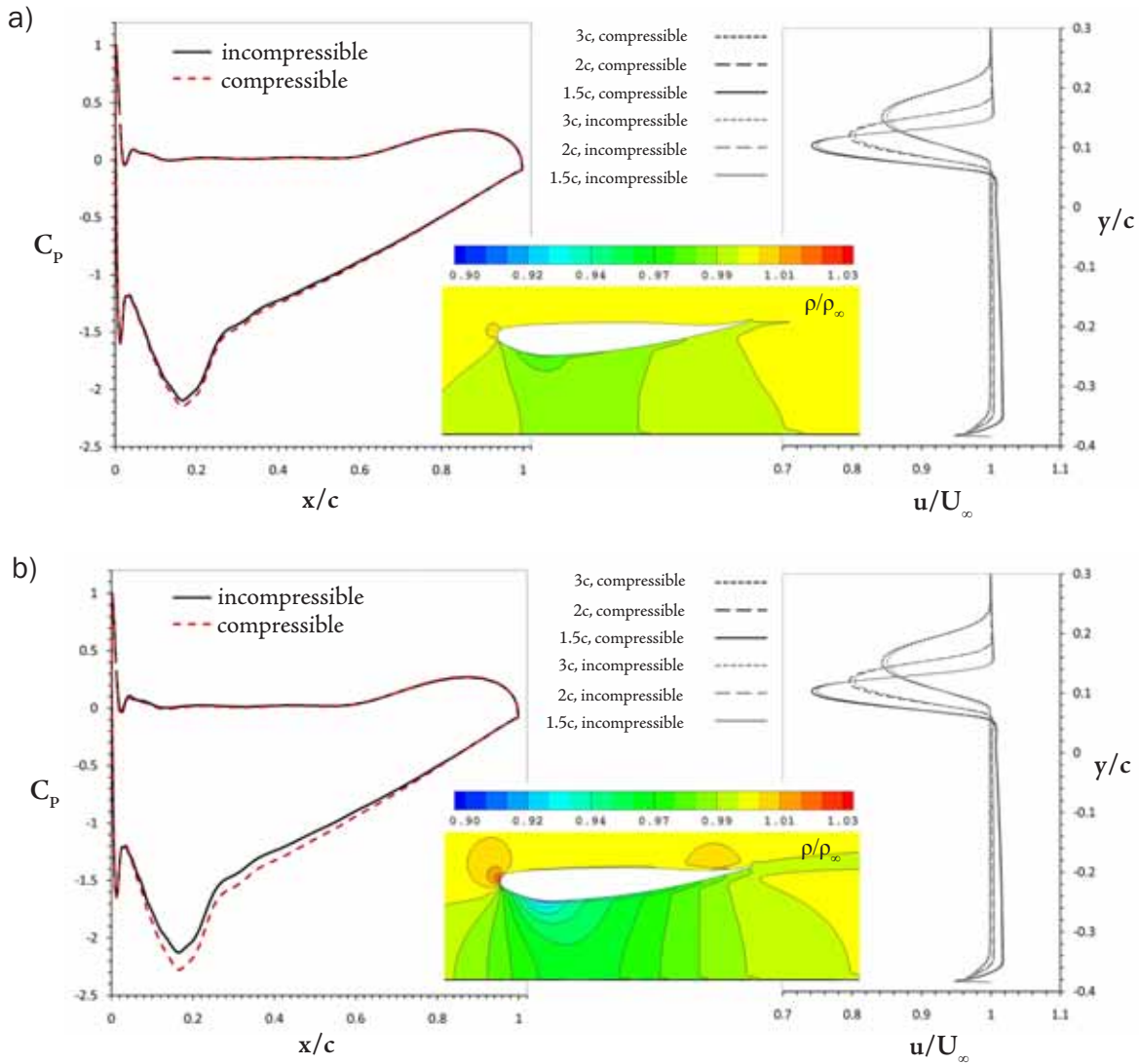
$C_L$  at all ground clearances bar  $h/c=0.067$  is underpredicted by the incompressible CFD, as density dropping around the lower surface increases the local flow velocity and thus lowers the local pressure - at the lowest ground clearance, this trend is reversed for reasons just mentioned, and the incompressible simulations overestimate the lift as freestream Mach number increases. This is consistent with results for two-dimensional simulations (Doig *et al.*, 2008) where the same phenomena occurred at both  $h/c=0.179$  and  $0.067$ ; a slight relaxation of the flow due to three-dimensional effects is the reason that only the  $h/c=0.067$  case is affected in such a manner in the present study.

The reversal of the trend at the lowest clearance removes any possibility of introducing a simple compressible “correction” for incompressible results, and thus provides further compelling evidence that the problem should be treated as a compressible one where possible.

The reason for the sharp drop-off in lift and exponential rise in drag for this lowest clearance at  $M_\infty=0.4$  is explained by the formation of a shockwave between the wing and the ground, spanning a large proportion of the wing and resulting in a large amount of separated flow at the rear of the wing.

While a shockwave is also present at this Mach number for  $h/c=0.179$ , it is not as strong, does not span such a large proportion of the lower surface, and does not separate the flow as significantly - for this reason the lift produced continues to be much greater than the incompressible simulation can predict, due to the greatly increased low pressure around the suction peak.

As density changes around the wing alter the pressure distribution, the pitching characteristics of the wing are also affected, as shown in figure 6.23 - compressible CFD predictions of the extent of  $C_{M_\alpha}$  taken at the quarter-chord tend to be less than those of the incompressible simulations, and as with lift and drag this inclination becomes stronger as ground clearance is reduced. The effect is a consequence of the forward shift of the centre of pressure around the wing.

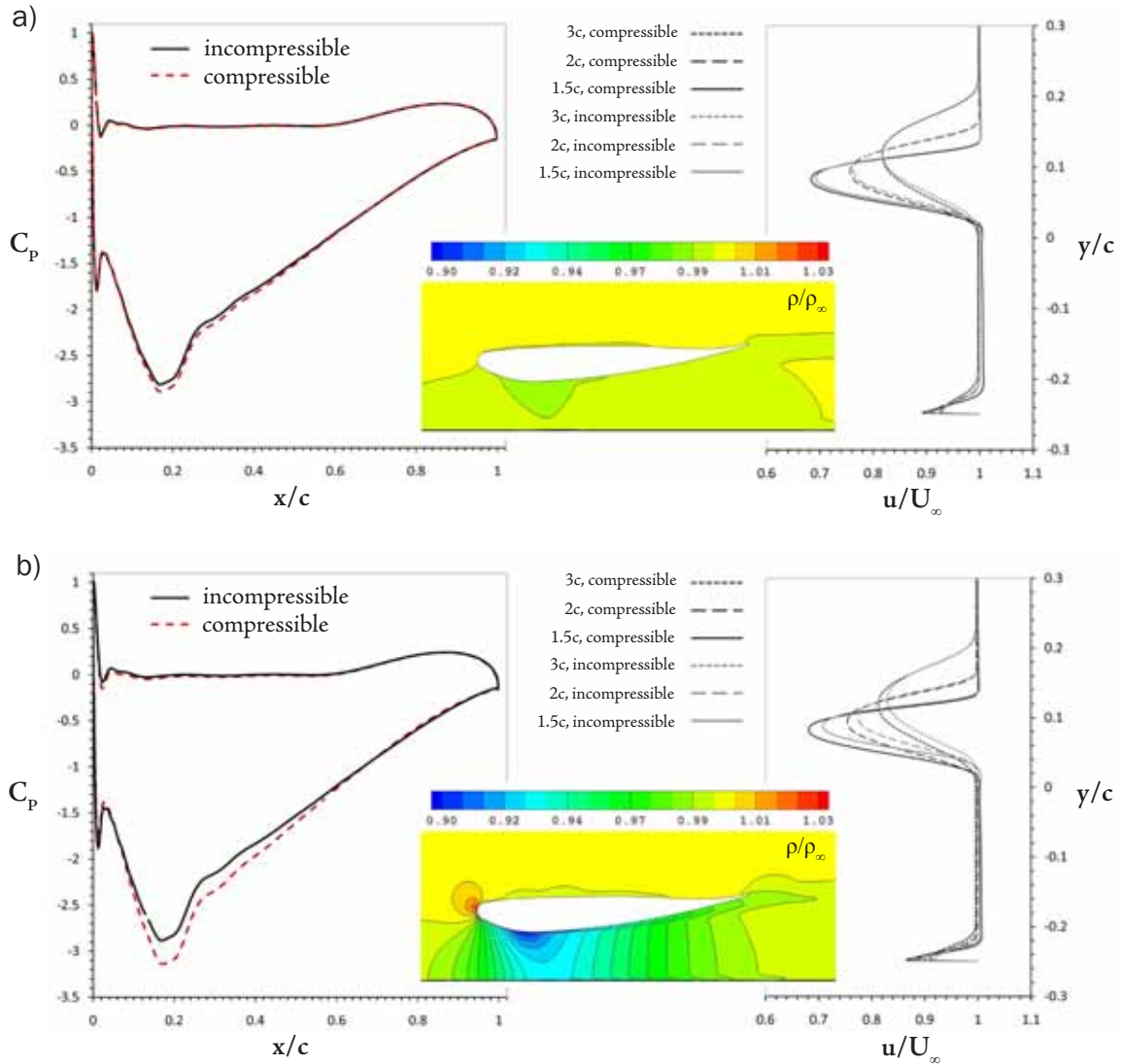


Incompressible and compressible pressure distributions around the wing at  $z = 0$ ,  $h/c = 0.313$ ,  $\rho/\rho_\infty$  contour plots, and wake profiles at 1.5c, 2c and 3c from the leading edge for a)  $M_\infty = 0.15$ , and b)  $M_\infty = 0.25$ .

### 6.2.2.2 Wing pressure distributions and wake profiles

Examining the pressure coefficient distributions on the wing at the symmetry plane allows a clearer understanding of the source of the compressible effects inherent in the aerodynamic force and moment plots.

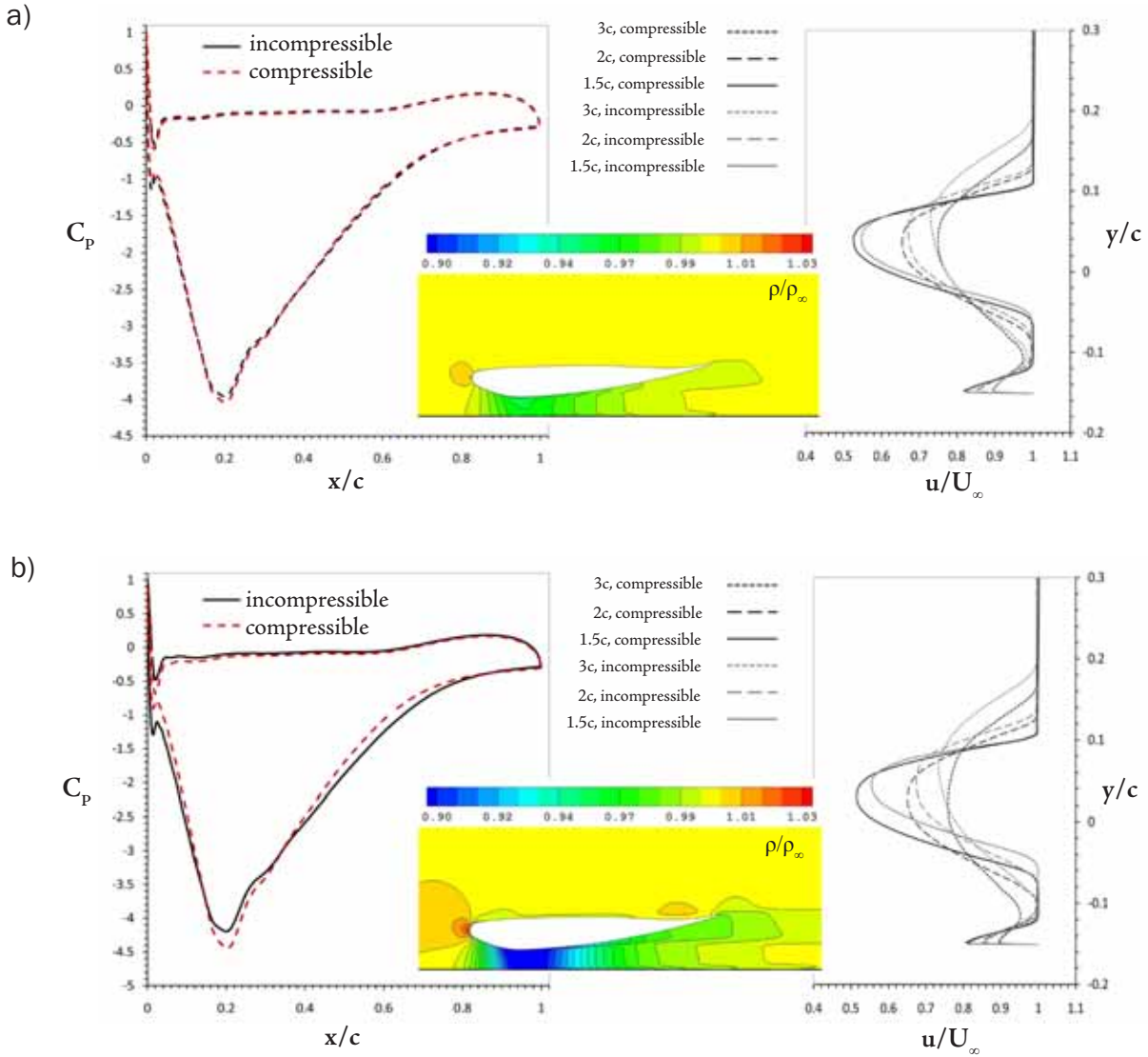
A series of plots for the three ground effect clearances of  $h/c = 0.313$ , 0.179 and 0.067 are presented in figures 6.24, 6.25 and 6.26, and show compressible and incompressible plots of  $C_p$ , wake profiles at  $x/c = 1.5$ , 2 and 3, as well as contour plots



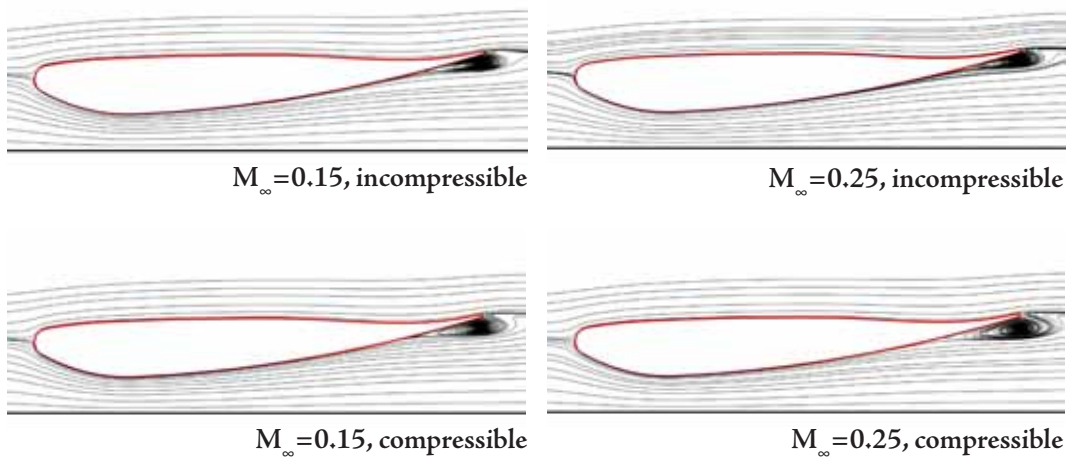
Incompressible and compressible pressure distributions around the wing at  $z = 0$ ,  $h/c=0.179$ ,  $\rho/\rho_\infty$  contour plots, and wake profiles at 1.5c, 2c and 3c from the leading edge for a)  $M_\infty=0.15$ , and b)  $M_\infty=0.25$ .

illustrating the changes in density around the wing facilitating the changes in pressure distributions. In all cases, plots are presented for  $M_\infty=0.15$  and  $0.25$ .

From these figures, the influence of the ground becomes most apparent. In terms of the pressure coefficients, at  $M_\infty=0.15$ , at all clearances there is an incompressible underprediction of the suction peak on the lower surface, which is magnified as ground clearance is reduced. At the lowest  $h/c$ , 0.067, the pressure recovery immediately following the peak is more pronounced in the compressible case, and the pressure distribution at the leading edge has been noticeably affected even on this scale, shifting the stagnation point downwards. This effect is present across the board and is the primary reason for



Incompressible and compressible pressure distributions around the wing at  $z = 0, h/c = 0.067, \rho/\rho_\infty$  contour plots, and wake profiles at 1.5c, 2c and 3c from the leading edge for a)  $M_\infty = 0.15$ , and b)  $M_\infty = 0.25$ .



Incompressible and compressible velocity streamlines around the wing at  $z = 0, h/c = 0.067$

the reversal in the trend of incompressible underprediction of lift which is seen at the other clearances.

At  $M_\infty=0.25$ , the effects on pressure distribution at all clearances are more pronounced, with the leading edge area at  $h/c=0.179$  now affected as well as at  $h/c=0.067$ . The stronger pressure gradient downstream of the suction peak at the lowest clearance is a clear cause of a drop off in effective lift production, and now the upper surface pressure distribution is appreciable, particularly upstream of the quarter-chord.

One can observe the way in which density changes around the wing grow markedly more pronounced as clearance is reduced, as both the peak density drop and the extent of the chord over which the lower-density flow exists is magnified by a reduction in ground clearance. Also apparent is the way in which the narrowing of the channel formed by the wing and the ground appears to amplify the upstream and downstream influence of density changes.

As was noted in section 6.2, the wake regions for compressible cases tended to feature an intensified streamwise velocity deficit when compared to the incompressible cases, and this is observed once again for all the comparison cases at  $M_\infty=0.15$  and  $0.25$ . At  $h/c=0.179$ , the wake is not only thicker and stronger, but deviates from its incompressible path in a downwards direction. This effect is more potent at  $h/c=0.067$ , where the incompressible wake deflects upwards as in the other cases, but the compressible wake deflects downwards from  $x/c = 1.5$  to  $2$ , and then levels off somewhat, and there are indications of an earlier, more significant interaction between the shear layers shed from the wing and the ground. This can be attributed to a larger region of separation towards the trailing edge, as illustrated by the streamlines in figure 6.27.

Figure 6.27 also emphasizes the change in effective angle of attack of the wing caused by the downwards movement of the stagnation point in the compressible cases - despite the decrease in flow passing under the wing, the acceleration of the air due to the lower density still results in the pressure gradient being severe enough to encourage separation over a much more significant section of the wing than in the incompressible simulations.

### 6.2.2.3 Vortex behaviour

As with the cases compared in section 6.2, the location of the vortex cores for the 4 cases at  $h/c=0.179$  for  $M_\infty=0.15$  and  $0.25$  are not markedly different between compressible and incompressible simulations, as shown in figures 6.28 and 6.29. The discernable effect of compressibility is to push the vortex more in the existing direction of travel, i.e. higher in  $Y$  and further inboard in  $Z$ . However, in real terms this is only by a matter of a few millimetres. The streamlines shown in figure 6.30 show qualitative aspects of this movement.

### 6.2.3 Onset of critical Mach effects

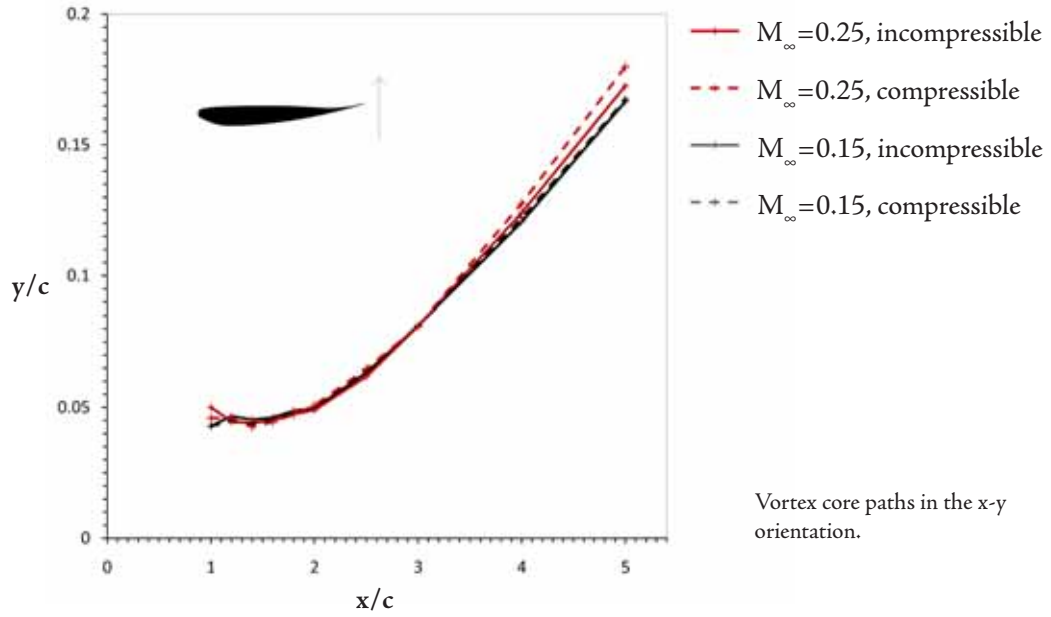
As was stated in the discussion of the aerodynamic coefficients in section 6.2, the cases involving a freestream Mach number of 0.4 incorporate the emergence of a critical flowfield around the wing. At  $h/c=0.313$ , the peak local Mach number is 0.84, but at  $h/c=0.179$  this increases to 1.18, with a shock wave forming approximately 40% of the semi-span inboard from the endplate as seen in the inset of figure 6.31. The shock wave is small and does not interact directly with the ground even at this low clearance, indicating that the critical Mach number has only just been exceeded.

The peak local Mach number at  $h/c=0.067$  is 1.26 and the shock wave interacts with the ground. The region of supersonic flow depicted in the inset of figure 6.31 indicates that the constraint of the ground plane has expanded the region in which  $M_1 > 1$ , and indeed the shock wave now spans a much greater proportion of the wing semi-span.

Unlike in the two-dimensional study of Doig *et al.* (2008), the shock wave did not exhibit any tendency towards movement in a transonic buffeting sense; a mild unsteadiness in the original solution was eliminated by local refinement of the mesh in the area of the shock, suggesting that the instability was mesh-related and thus solved by grid adaptation. It is likely, therefore, that although the flow achieves supersonic Mach numbers along a significant portion of the undersurface, it has not yet reached the buffet

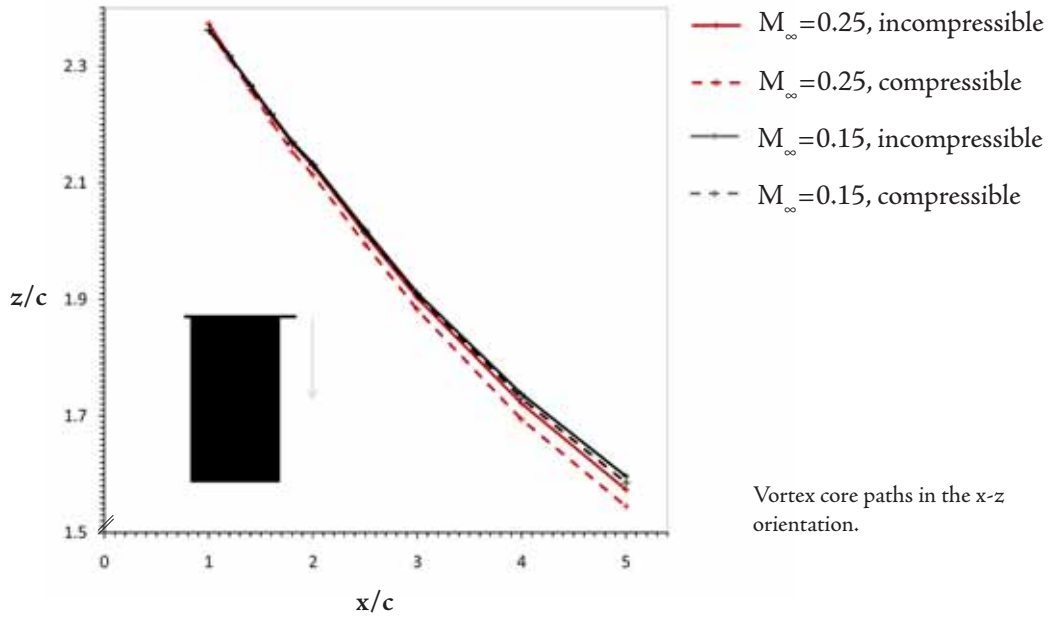
6.28

FIG



6.29

FIG

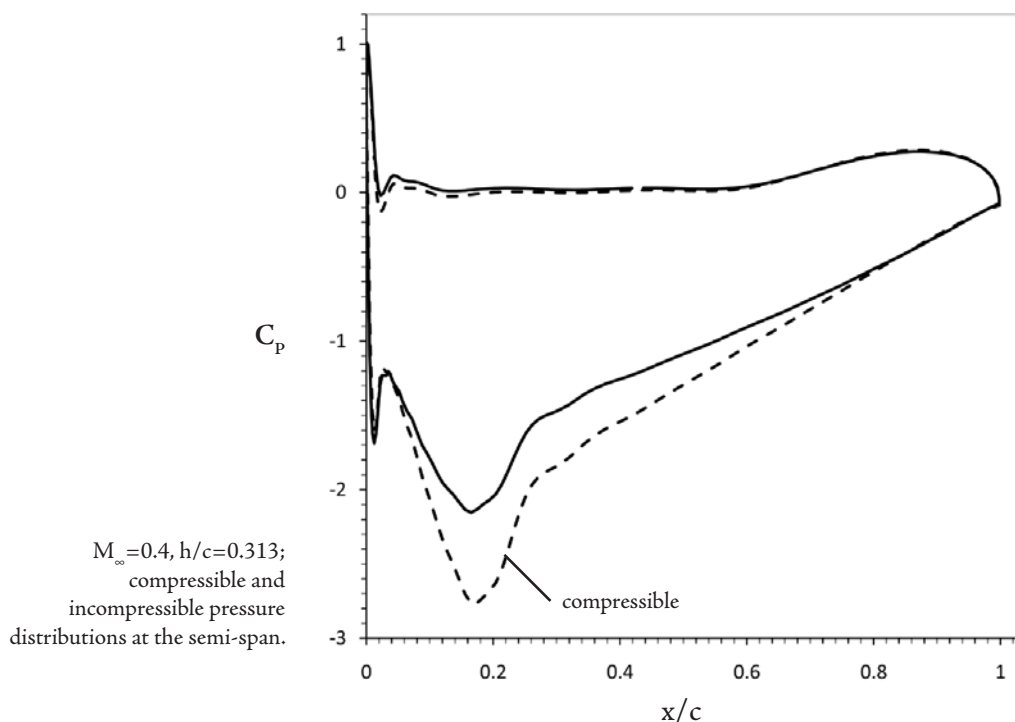


6.30

FIG



Compressible (orange) and incompressible (blue) streamlines for  $M_\infty = 0.25$ .



boundary that was experienced in the two-dimensional study. This is almost certain to be a facet of the three-dimensionality of the present wing, wherein the flow is not completely constrained in the channel between the wing and the ground, but is able to relax laterally and the onset of unsteady shock-oscillations is delayed.

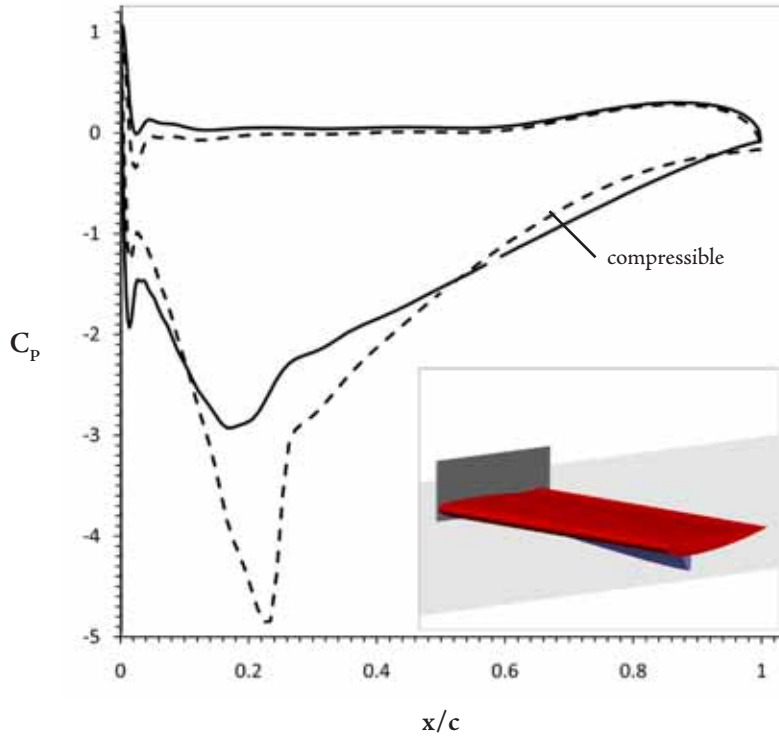
The sensitivity of the wing to ground clearance close to the critical Mach number is evident, in that the wing is only approximately 30mm closer to the ground at  $h/c=0.179$  than at  $h/c=0.313$ , yet a region of supersonic flow has developed.

The pressure distributions shown in figures 6.31, 6.32 and 6.33 for the three ground clearances emphasise the unconditional inappropriateness of an incompressible approach to simulation, even for the fully-subsonic case at  $h/c=0.313$ . The compressible distribution at  $h/c=0.179$  highlights the shock location at  $x/c = 0.24$ , and the very strong pressure gradient to the trailing edge. However, the shock is not strong enough to separate the boundary layer and the flow remains attached to the trailing edge. Extensive separation around the endplate is present.

At  $h/c=0.067$  the shock interacts with the ground, such that the boundary layers on the ground and the wing at approximately  $x/c = 0.29$  are substantially thickened, though unseparated by the shock in both cases. The pressure distributions highlights

6.32

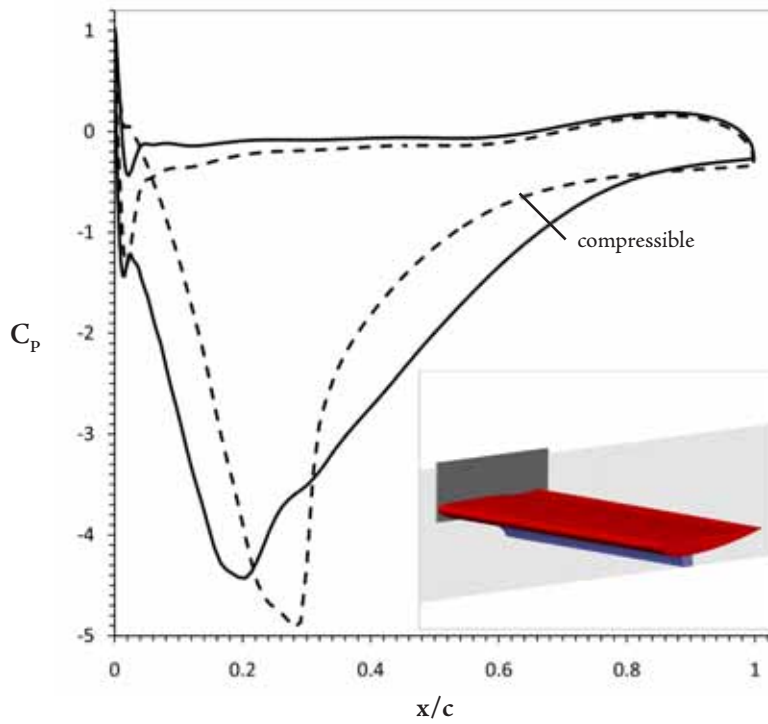
FIG



$M_\infty=0.4, h/c=0.179$ ; compressible and incompressible pressure distributions at the semi-span, and (inset) region of supersonic flow under the wing.

6.33

FIG



$M_\infty=0.4, h/c=0.067$ ; compressible and incompressible pressure distributions at the semispan, and (inset) region of supersonic flow under the wing.

the reason for the drop-off in lift coefficient seen in figure 6.21; not only is a significant portion of the flow now directed over the upper surface of the wing, but the strong adverse gradient from the shock to the trailing edge minimizes the pressure difference between surfaces to destroy a large proportion of the potential of the wing to create downforce.

## 6.3 Summary

A number of conclusions about the flow around an inverted wing in compressible ground effect can be drawn:

- Due to the accelerated flow between the wing and the ground, compressibility effects alter the flowfield to the extent that predicted aerodynamic forces and moments can be affected by several percent, even at a highly-subsonic freestream Mach number of 0.15 or less. These effects become increasingly magnified as Mach number is increased or ground clearance is reduced.
- Compressible effects will markedly affect Reynolds-scaled wind tunnel tests on models which must experience a higher freestream Mach number in order to maintain a Reynolds number consistent with a full scale model in CFD. The discrepancy at 50% scale and a Mach number of 0.1764, compared to a full-scale model at Mach 0.0882, can again be several percent in terms of lift and drag, and the wake behaviour is affected.
- At a point between  $M_\infty=0.2$  and 0.3, it would become more vital to Mach-scale a wind tunnel model than to Reynolds-scale it; an unrealistic proposition. The best approach for validation would be to ensure the CFD model represented the *exact* conditions of tunnel testing, as Mach number effects would ensure that even a compressible full-scale simulation would not be an effective match for a scale wind tunnel model at a higher  $M_\infty$ .

- The behaviour of the lower endplate vortex isn't greatly effected by compressibility, exhibiting only small-scale differences in comparisons between compressible and incompressible simulations.
- The critical Mach number of the wing is exceptionally low at the lower ground clearances of  $h/c=0.179$  and  $0.067$ , lying between  $M_\infty=0.3$  and  $0.4$ .  
The formation of a shock wave between the wing and ground has a highly destructive effect on the level of negative lift produced, and markedly increases the drag.

Having established that supersonic flow can arise in ground effect at a critical freestream Mach number far lower than would be expected were the ground absent, the next two chapters concentrate on flow at freestream  $M_\infty$  from  $0.5$  to  $0.9$ , in a context more appropriate for the higher Mach numbers; that of the lifting RAE2822 aerofoil and ONERA M6 wing.

# Chapter: RAE 2822 Aerofoil in Transonic Ground Effect



*The RAE 2822 aerofoil at “Case 9” conditions is initially placed close to the ground with increasing proximity to provide an examination of the ground’s influence on the aerodynamic characteristics of the section. There follows a parametric study of the aerofoil at five ground clearances, five freestream subsonic Mach numbers (from 0.5 to 0.9) and three modest angles of attack. Forces, moments, and shock wave characteristics are discussed in two contexts - decreasing ground clearance for fixed Mach numbers, and increasing Mach numbers for fixed ground clearances. Reynolds number is left to vary freely with Mach number.*

## 7.1 Introduction

The RAE 2822 aerofoil, used for validation in Chapter 4 and the experiments in Chapter 5, is revisited here for a broad study across several ground clearances (freeflight (no ground), and  $h/c=1, 0.5, 0.25,$  and  $0.1$ ), Mach numbers ( $0.5, 0.6, 0.7, 0.8, 0.9$ ) and angles of attack ( $0^\circ, 2.79^\circ$  and  $6^\circ$ ). At certain flight conditions, a shock forms between the aerofoil and the ground similar to those seen in Chapters 4 and 5 for the transonic wind tunnel tests at the U.S. Naval Academy, and here such an occurrence is studied in more detail alongside the numerous other shock interactions

which emerge across the range of conditions.

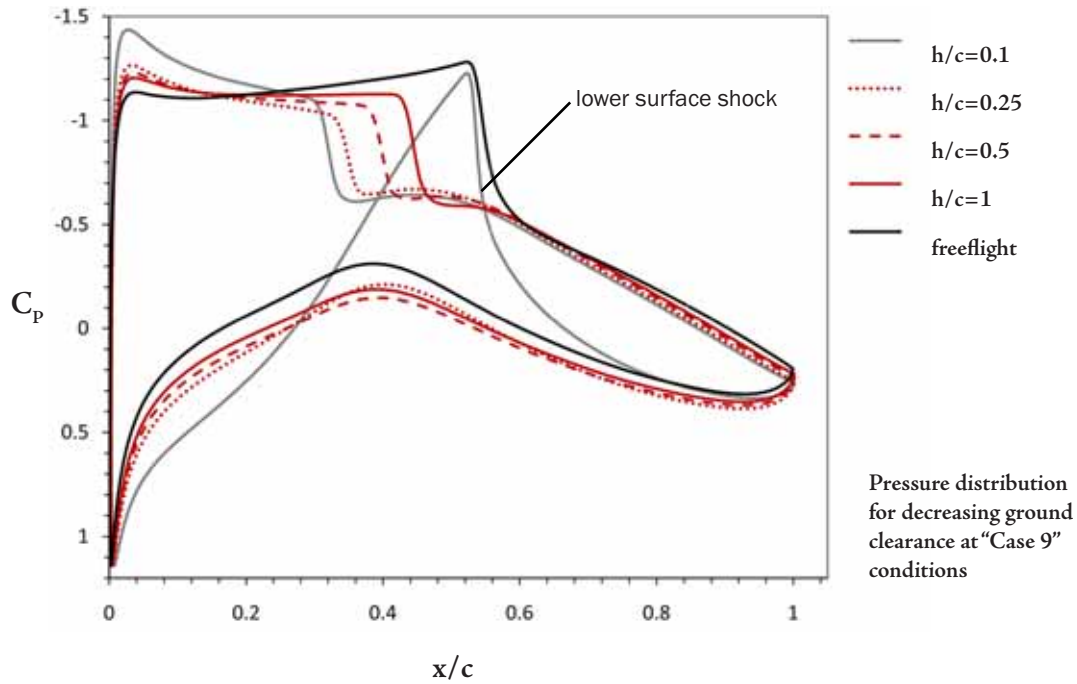
Higher angles of attack would be virtually impossible to achieve while maintaining ground clearance, as the additional lift would pull the body away from the ground and therefore out of ground effect very rapidly. Higher freestream Mach numbers than 0.9 were not examined for the two-dimensional geometry in this case, as the inability of the flow to relax in the third dimension would eventually lead to rather unrealistic detached shock waves at freestream Mach numbers far lower than that which they could be expected to appear at for any real-world body.

Initially results for AGARD “Case 9” conditions (a freestream Mach number of 0.73 and an angle of attack of  $2.79^\circ$ , Cook *et al.*, 1979) are reproduced for the various ground clearances to provide an introductory comparison of cases for increasing proximity to the ground plane. Subsequently the full range of results for all variables are presented in terms of aerodynamic coefficients for two contexts: decreasing ground clearance for a fixed Mach number, and increasing Mach number for a fixed ground clearance.

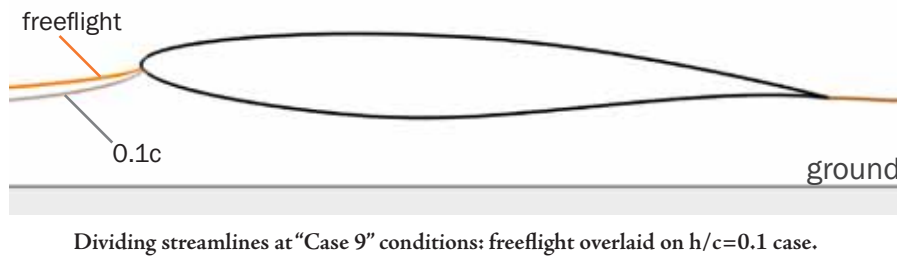
## 7.2 “Case 9” with decreasing ground clearance

Here, the ground clearance is the only variable, to provide a clear indication of the effect on aerodynamic performance of increasing ground proximity as compared to the freeflight condition. The Reynolds number and scale remain the same as in Chapter 4;  $6.2 \times 10^6$  and a chord of 0.61m, respectively.

Figure 7.1 illustrates the way in which the pressure distribution around the aerofoil changes as the ground clearance is reduced in stages. Several points are immediately apparent. Most importantly, the upper surface shock location moves progressively upstream from its freestream location. It also gently reduces in intensity, resulting in a less severe pressure increase across the wave. One of the main reasons for this behaviour seems to be the downward movement of the stagnation point at the leading edge, as shown in figure 7.2, which also increases the strength of the suction peak near the leading edge on the upper surface. This increase in the effective angle of



7.1  
FIG

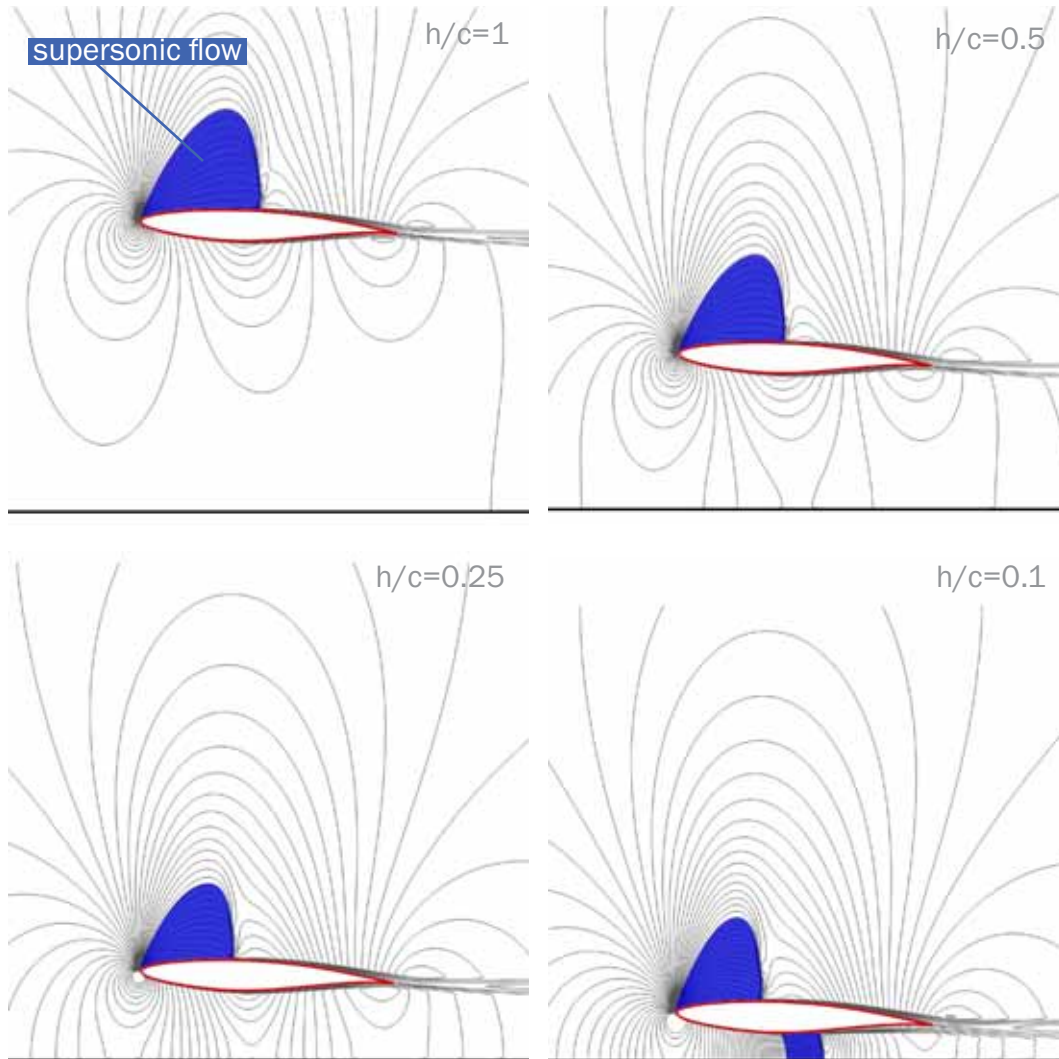


7.2  
FIG

attack draws the shock upstream, and creates a stronger adverse pressure gradient across the forward portion of the upper surface leading to the earlier, weaker shock. The flow remains attached at the foot of the shock.

At the same time, the pressure distribution under the wing is affected as the air which is forced under the wing is increasingly constricted by reducing ground clearance. As more mass is directed over the upper surface, the lower velocity under the wing causes higher pressure in the region between the wing and the ground, particularly near the leading edge as the stagnation point is drawn downwards, and thus the maximum pressure difference between the upper and lower surface is exaggerated with increasing proximity to the ground.

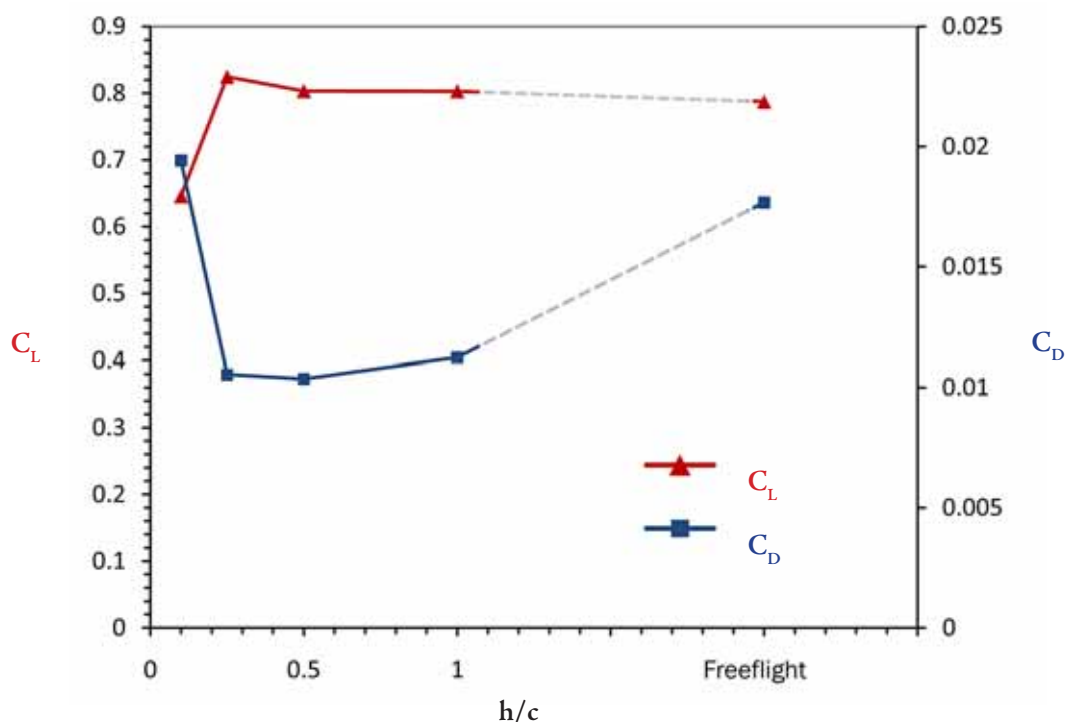
These trends, well-established for wings in ground effect, hold until the lowest ground clearance,  $h/c=0.1$ . Here, as shown clearly in figure 7.3, the flow between the



Contours of density and regions of supersonic flow around the aerofoil at Case 9 conditions as ground clearance is reduced from  $h/c=1$  to 0.1.

aerofoil and the ground has accelerated to supersonic local Mach numbers causing a strong shock wave at approximately  $x/c=0.54$ . Whereas the peak local Mach number on the upper surface occurs close to the leading edge, on the lower surface the local peak of approximately  $M=1.36$  occurs immediately prior to the shock wave and the strength of the shock is such that it separates the flow in a small bubble on the surface. As a result the lower surface boundary layer is considerably thickened to the trailing edge, and results in a much broader wake boundary than at higher clearances.

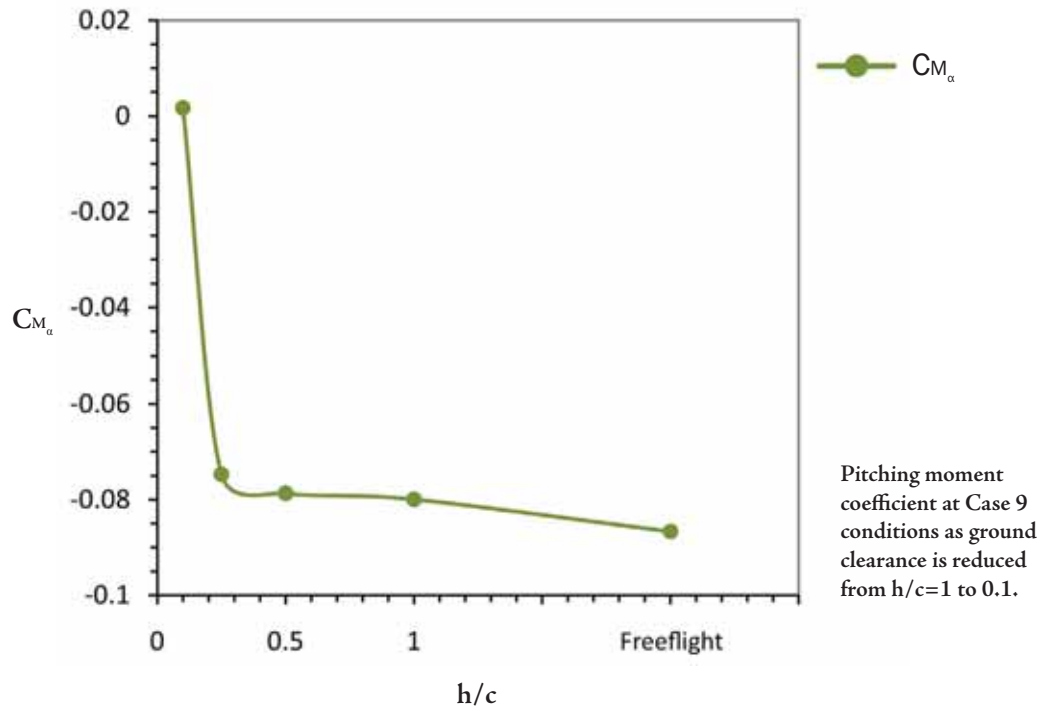
The influence of these effects on the lift and drag coefficients is shown in figure 7.4. Drag decreases with ground clearance until  $h/c=0.1$  is reached. In subsonic cases, aerofoils with attached flow tend to experience a small reduction in pressure drag as



Lift and drag coefficients at Case 9 conditions as ground clearance is reduced from  $h/c=1$  to  $0.1$ .

the suction over the forebody of the wing can have a component which pulls the wing forwards to a small extent. The effect seen in the present cases is related, though the large (>25%) reduction in drag is attributable to a much greater extent to the reduction in the strength of the shock wave, which diminishes the wave drag and also lessens the thickening effect the shock has on the boundary layer (although this latter contribution to overall drag is much smaller). At  $h/c=0.1$ , the drag coefficient increases markedly, due to the emergence of the lower surface shock and the separated flow it produces.

$C_L$  increases slightly from the freestream value, up 2% to  $h/c=0.5$  and peaking at 5% higher at  $h/c=0.25$ . This is due to the increase of effective angle of incidence caused by increasing ground proximity, and the build up of higher pressure already noted between the aerofoil and the ground which increases the maximum suction the section produces. The formation of the lower shock at  $h/c=0.1$  destroys much of this capacity to create lift, as the flow is greatly accelerated under the aerofoil and produces a large amount of low pressure prior to the shock. The relatively high curvature of the lower surface of this particular aerofoil section is a major



contributor to this.

Figure 7.5 illustrates the changes to the aerofoil pitching moment (taken around the aerofoil 1/4 chord) while the flowfields described above are developing. The presence of the ground serves to lessen the magnitude of the nose-down moment by between 10% and 15% at  $h/c=0.5$  and 0.25 respectively, though this trend is not severe until  $h/c=0.1$  is reached, at which point the moment becomes a nose-up pitching tendency, as the lower surface shock forms behind the 1/4 chord point and the strength of the upper surface suction diminishes.

Were the results for “Case 9” in ground effect to hold across a range Mach numbers and angles of attack, the aerodynamics of the aerofoil in the mid-to-high subsonic regime would be fairly predictable. However, as will now be discussed, the flows can be very sensitive to changes in any variable.

The results presented from this point onwards use an aerofoil which is scaled to be 5 times greater than that of the “Case 9” tests, to better approximate real world flight Reynolds numbers. Thus the chord is 3.05m, and the chord-based Reynolds numbers for each Mach number considered are outlined in table 7.1. The case matrix of all simulations is presented in table 7.2, and highlights which cases were run as steady-state, which were

Table 7.2. List of simulations conducted, which cases were run as transient and which featured areas of supersonic flow around the wing.

<b>h/c=∞ (Freeflight)</b>	<b>α=0°</b>	<b>α=2.79°</b>	<b>α=6°</b>
M <sub>∞</sub> =0.5			
0.6			
0.7			
0.8			
0.9			
<b>h/c=1</b>	<b>α=0°</b>	<b>α=2.79°</b>	<b>α=6°</b>
M <sub>∞</sub> =0.5			
0.6			
0.7			
0.8			
0.9			
<b>h/c=0.5</b>	<b>α=0°</b>	<b>α=2.79°</b>	<b>α=6°</b>
M <sub>∞</sub> =0.5			
0.6			
0.7			
0.8			
0.9			
<b>h/c=0.25</b>	<b>α=0°</b>	<b>α=2.79°</b>	<b>α=6°</b>
M <sub>∞</sub> =0.5			
0.6			
0.7			
0.8			
0.9			
<b>h/c=0.1</b>	<b>α=0°</b>	<b>α=2.79°</b>	<b>α=6°</b>
M <sub>∞</sub> =0.5			
0.6			
0.7			
0.8			
0.9			

No supersonic flow	Areas of M <sub>1</sub> >1	Transient~steady state	Transient
--------------------	----------------------------	------------------------	-----------

run as transient but which came to a steady-state with time, and those which featured transient regular oscillatory shock motion. Aerodynamic force coefficients and pressure distributions presented for the latter type are time-averaged over three oscillation cycles in subsequent diagrams. This table also allows the reader to see at a cursory glance which

Table 7.1. List of Mach numbers and related parameters

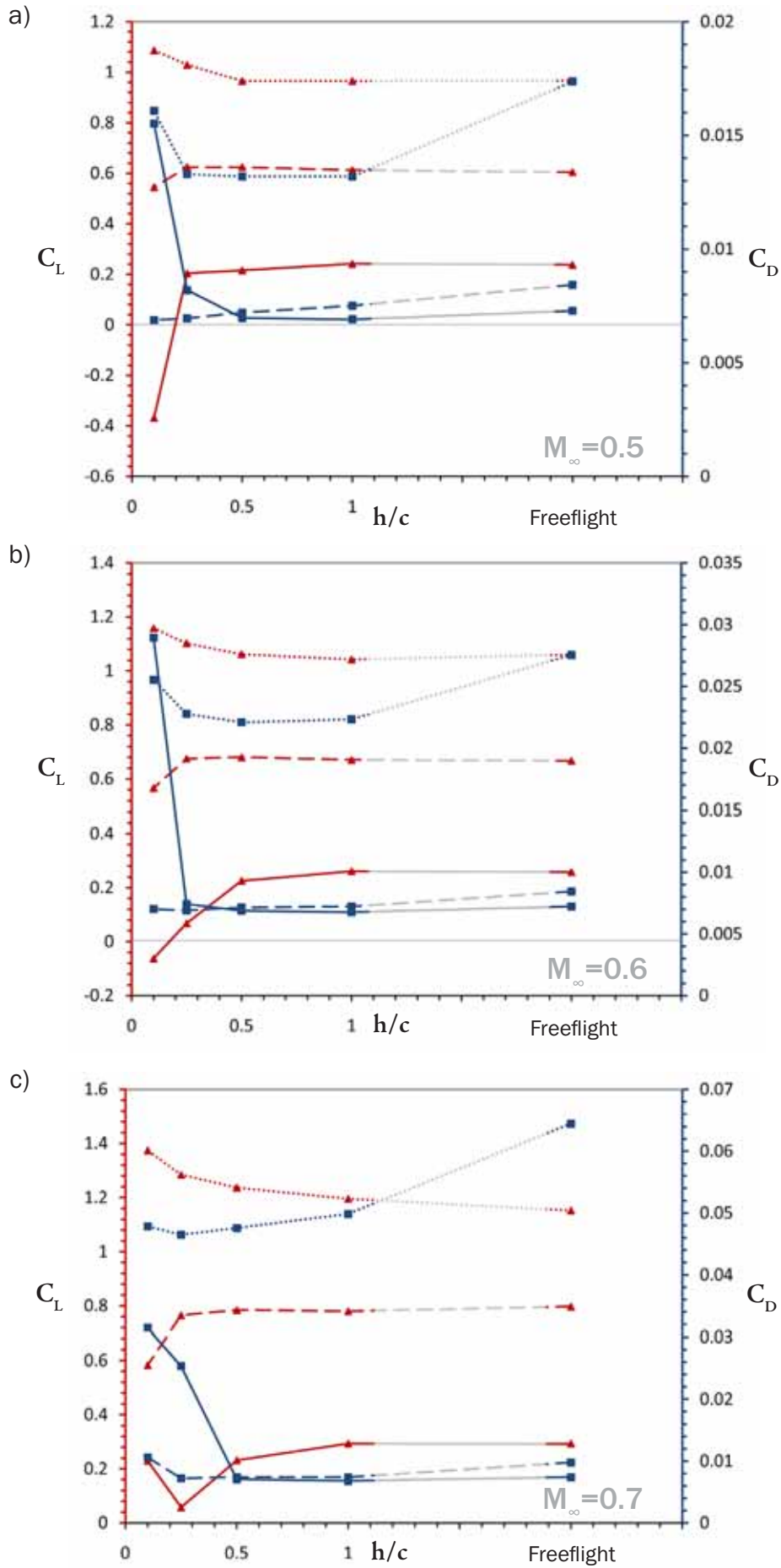
$M_\infty$	$U_\infty$ (ms <sup>-1</sup> )	Reynolds Number
0.5	170.04	35.52x10 <sup>6</sup>
0.6	204.05	42.63x10 <sup>6</sup>
0.7	238.05	49.73x10 <sup>6</sup>
0.8	272.06	56.84x10 <sup>6</sup>
0.9	306.07	63.94x10 <sup>6</sup>

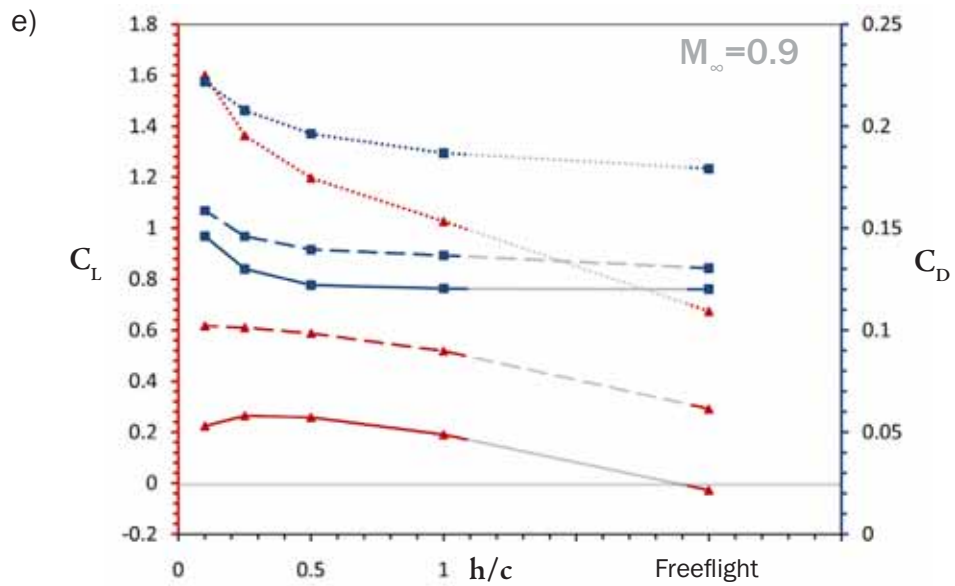
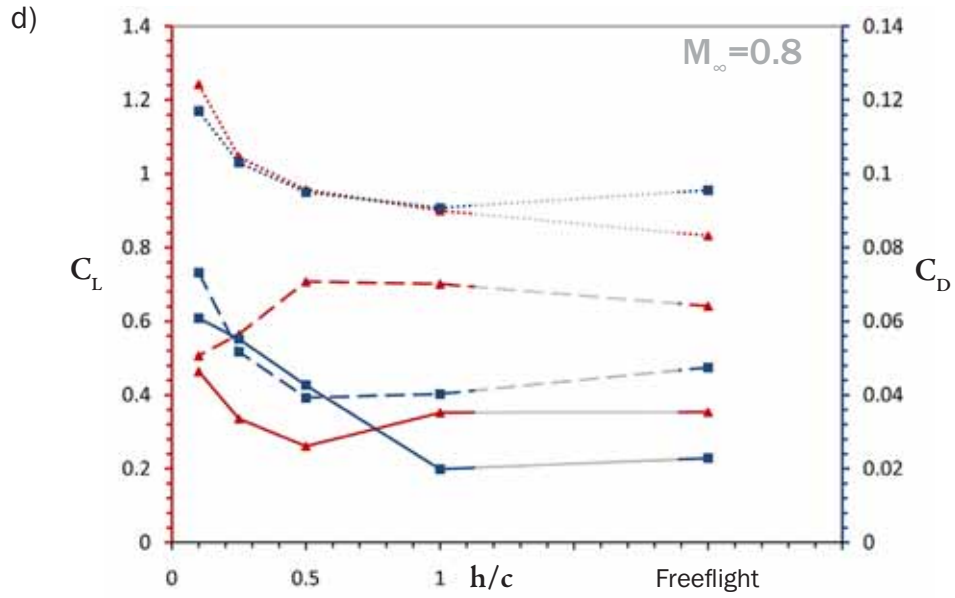
flowfields included areas of supersonic flow, and therefore the reduction of critical Mach number with decreasing ground clearance for certain conditions is revealed. It is also worth noting that there is no clear pattern when it comes to the onset of transient shock behaviour as indicated by the transient cases, and as such the buffet boundary of the aerofoil, at which point the shock begins to exhibit oscillatory behaviour accompanied by periodic separation of flow, is also shown to be highly sensitive to ground clearance. In the following section we focus on the influence of the ground, with results presented for constant Mach numbers and angles of attack. The subsequent section, 7.4, will recast the results in terms of fixed ground clearances and angles of attack for increasing freestream Mach number, more akin to an acceleration for an otherwise constant flight condition.

## 7.3 Decreasing ground clearance for fixed Mach numbers

### 7.3.1 2.79° incidence

Of the three incidences examined in this chapter, 2.79° is most representative of an actual flight condition and is therefore discussed in most detail here. The angle of the section ensures that there is not such a strong acceleration of flow between the aerofoil and ground as at 0°, but it also does not feature the strong tendency for separation on the upper surface as does the aerofoil at 6°. Aerodynamic coefficients are presented in figure 7.6.





- ▲—  $C_L, \alpha=0^\circ$
- -▲- -  $C_L, \alpha=2.79^\circ$
- ...▲...  $C_L, \alpha=6^\circ$
- $C_D, \alpha=0^\circ$
- -■- -  $C_D, \alpha=2.79^\circ$
- ...■...  $C_D, \alpha=6^\circ$

Lift and drag coefficients for  $0^\circ$ ,  $2.79^\circ$  and  $6^\circ$ , with decreasing ground clearance for a)  $M_\infty=0.5$ , b)  $0.6$ , c)  $0.7$ , d)  $0.8$  and e)  $0.9$ .

At  $M_\infty=0.5$ ,  $C_D$  reduces by approximately 20% from freeflight to  $h/c=0.1$ , accompanied by a 14% increase in  $C_L$  from freeflight to  $h/c=0.25$ , after which there is a marked drop at  $h/c=0.1$ . The drag reduction stems from a diminishment of the slight downwash angle of the wake from the trailing edge, as the high pressure region near the trailing edge grows with decreasing clearance, and this also contributes to the overall lift of the section which benefits from a higher effective angle of attack despite the mild changes to the wake angle. The drop in lift at  $h/c=0.1$  stems from a marked local acceleration of the flow around the lower surface through the area of minimum ground clearance, where the peak local Mach number is approximately 13% higher than the equivalent freeflight case. At higher clearances, this increased local Mach number effect is slight.

These trends remain largely unchanged at  $M_\infty=0.6$ , but now the lift-loss at  $h/c=0.1$  is more pronounced. For cases at all the higher clearances,  $C_L$  is higher than at  $M_\infty=0.5$ , and  $C_D$  lower, as the effects described previously are enhanced. In all cases, a small region of shock-free supersonic flow has emerged around the upper surface, close to the leading edge. In freeflight, peak  $M_1$  is 1.03, and at  $h/c=0.1$ ,  $M_1$  is 1.11.

At  $M_\infty=0.7$ , the trends again remain largely unchanged, despite all cases featuring an upper surface shock. Instead of a slight increase in lift, there is a 3% decrease from freeflight to  $h/c=0.25$ , though a drag reduction remains over the same range of ground clearances. We have already seen in the previous section, for the similar “Case 9” conditions, that this is a result of the shock wave reducing in strength as it is drawn forward as the ground is approached. The gain in lift made from an increased effective angle of attack is countered by the shortened run of acceleration prior to the shock, which reduces the amount of low pressure the aerofoil is able to generate there.

At  $h/c=0.1$ , there now exists a lower shock between the aerofoil and ground, and a significant accompanying drag rise is observed, along with a drop in lift due to the intense pressure drop underneath the section which is the culmination of the undersurface acceleration effect which had been building at this ground clearance from  $M_\infty=0.5$ .

By  $M_\infty=0.8$ , both  $h/c=0.1$  and  $0.25$  feature lower shocks, explaining the sudden increase to drag and decrease to lift at these clearances. Further from the ground plane,

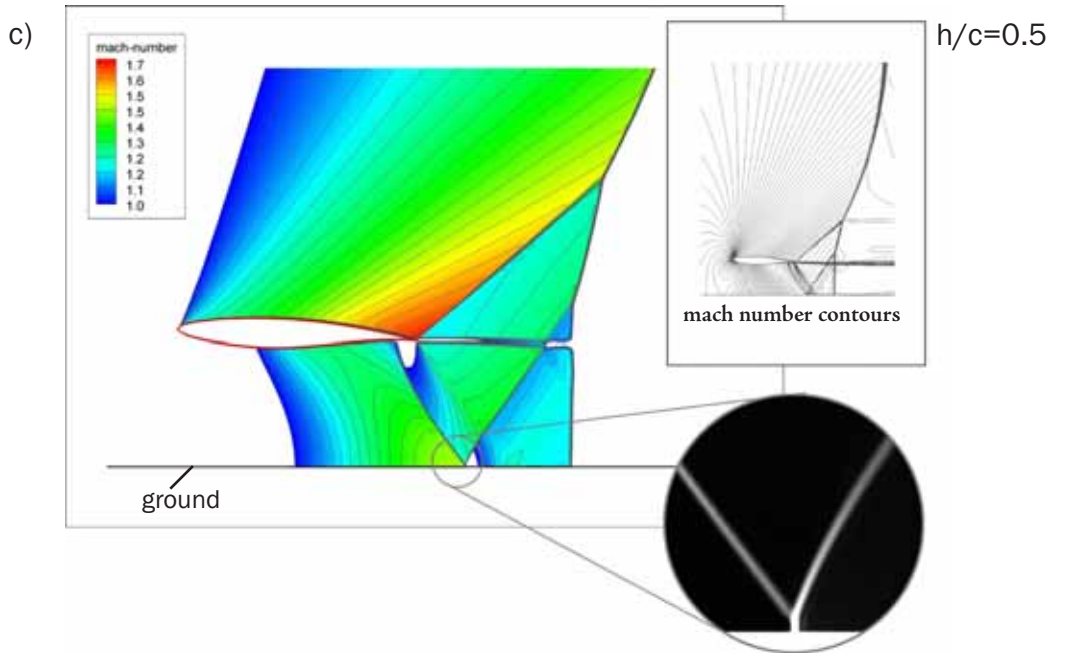
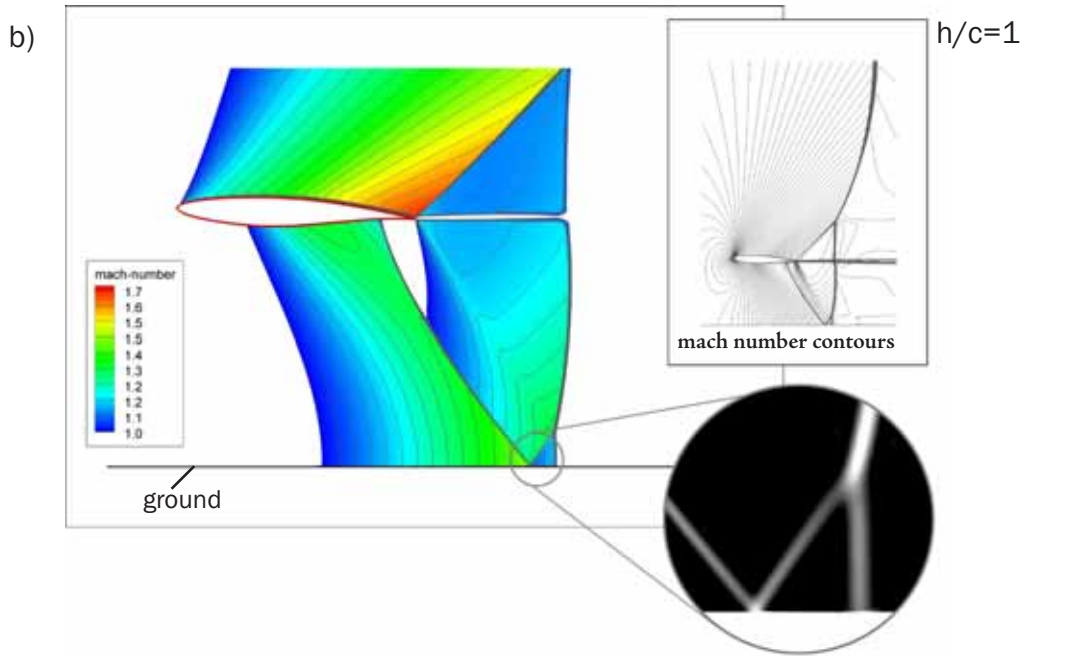
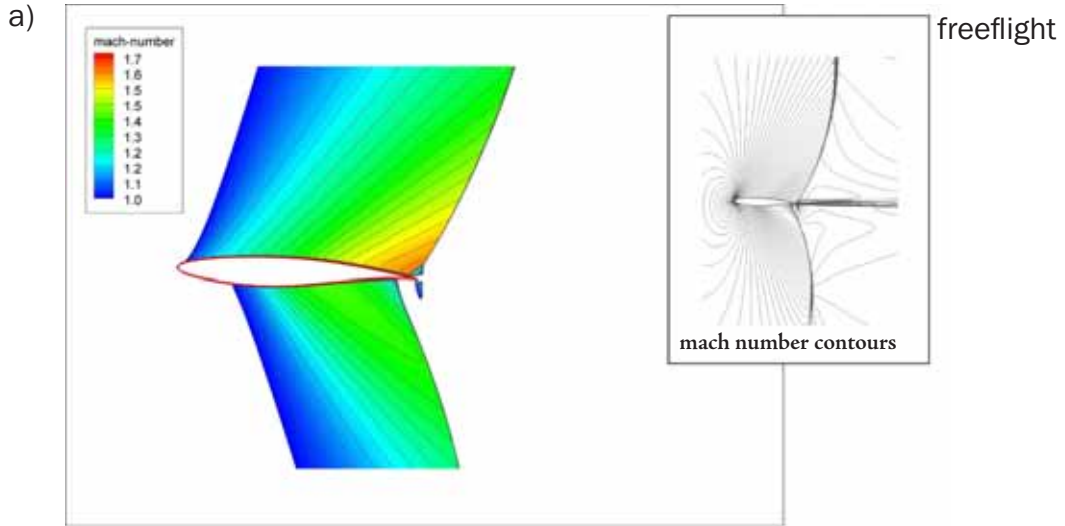
the flow is now detached behind the upper shocks to the trailing edge, and results in a much stronger, thicker wake, and so  $C_D$  has risen an order of magnitude from the  $M_\infty=0.7$  cases. It is clear that the closest ground clearances will affect the critical Mach number of the section; particularly that of the lower surface shock wave, which appears weakly around the aerofoil in freestream at a point close to  $M_\infty=0.8$ , whereas at the closest ground proximity it has been present on the wing since  $M_\infty=0.6$ . At clearances where the lower shock is not present, the efficiency of the wing remains improved by the ground influence.

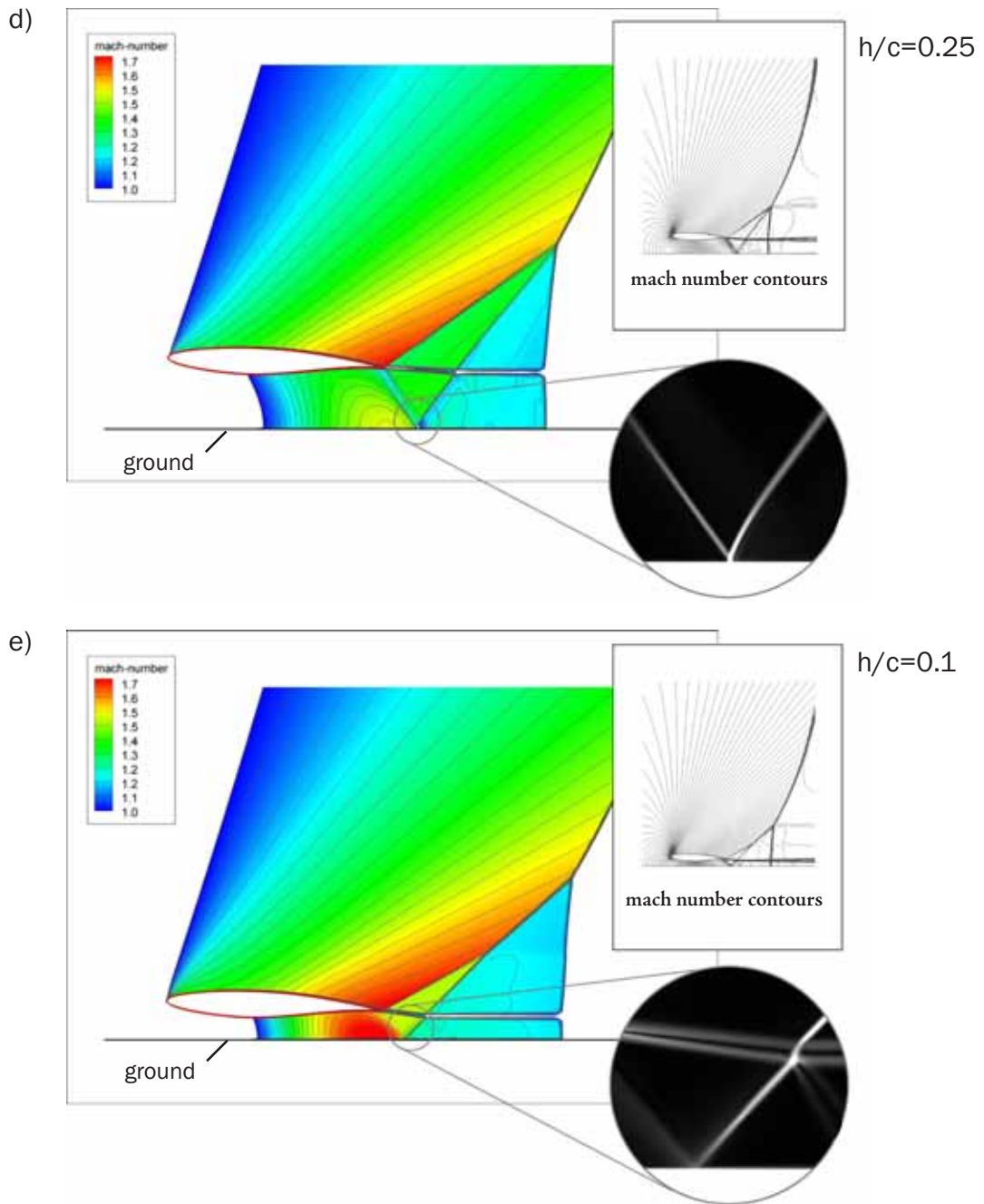
At  $M_\infty=0.9$ , extremely large-scale shock structures exist at the trailing edge, where in freeflight conditions the peak local Mach number is 1.61, resulting in shocks which are highly angled, rather than approximating normal, in the near-field flow. The RAE 2822 section was designed for optimal effectiveness at sub-critical Mach numbers (design condition  $M_\infty=0.66$  at  $\alpha=1.06^\circ$ ), and so at this upper range of the Mach number scale it features very poor performance. Additionally, the two-dimensional nature of these simulations is liable to produce greatly exaggerated shock structures that would be unlikely to exist in three-dimensional cases up until freestream Mach numbers in the immediate vicinity of 1.

Nevertheless, the shock structures produced, particularly at the point of ground reflection, are worthy of closer inspection. In terms of the aerodynamic forces, it is sufficient to observe that the lift and drag trends are now clear and stable, as the both upper and lower shocks sit at the trailing edge in both cases.

Lift coefficient increases with decreasing clearance simply because the acceleration of the upper surface continues to be enhanced by the presence of the ground, and the lower surface shock for the ground effect cases at or below  $h/c=0.5$  does not sit on the aerofoil itself; rather, in the supersonic flowfield, a series of weaker compression waves are generated by the trailing edge contour at  $x/c=0.96$ , and subsequently coalesce into a shock wave away from the aerofoil.

Drag coefficient increases as well with decreasing ground clearance, as the strength of the shocks increase, as does the complexity of their interaction with the wake;





Contours of Mach number and (inset detail) numerical schlieren for cases at  $M_\infty=0.9$ ,  $\alpha=2.79^\circ$ , as ground clearance is reduced from a) freeflight, to b)  $h/c=1$ , c)  $h/c=0.5$ , d)  $h/c=0.25$  and e),  $h/c=0.1$ .

the lower shock reflects from the ground plane and interacts with the free shear layers trailing the aerofoil.

A series of images is shown in figure 7.7 for the  $M_\infty=0.9$  cases, along with numerical schlieren insets detailing the nature of the ground interactions. From freeflight to  $h/c=1$ , the peak local Mach number prior to the upper shock increases from

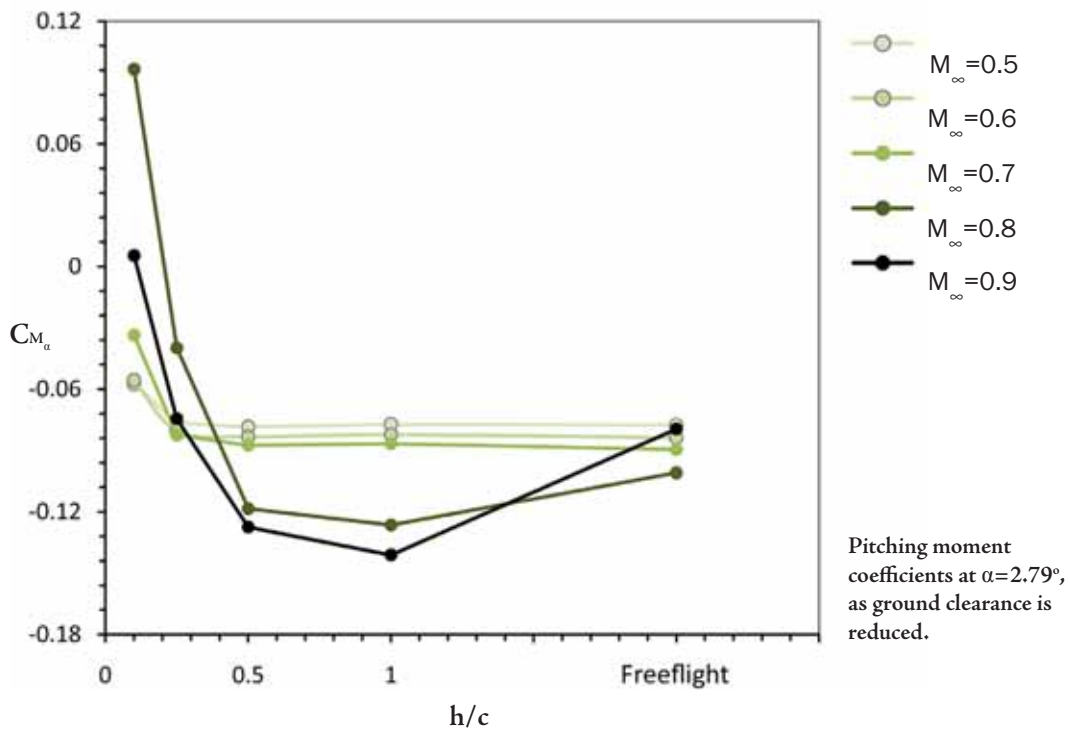
approximately 1.6 to 1.7, increasing the oblique angle of the shock in the wing vicinity. This effect is exaggerated with further proximity to the ground, as the extent of the high-Mach region increases. In all cases this oblique wave is observed to normalise in the far field, many chord lengths' from the aerofoil. At  $h/c=1$ , the lower shock experiences regular reflection, which is followed by a normal recompression stem; these two waves join in forming a large normal recompression approximately  $0.5c$  downstream from the trailing edge, bringing the flowfield back to a subsonic condition.

At  $h/c=0.5$ , the structure is identical, but the extent of it is greatly magnified. The reflection at the ground, which now features its own small Mach stem, is able to pass through the wake before being joined by the normal stem from the ground at close to  $0.65c$  downstream of the trailing edge. The influence on the wake is to thicken it, and align it with the freestream following a mild downwards deflection.

By  $h/c=0.25$  the immediate downwards deflection of the wake is more prominent and the reflected lower wave now passes through the wake and merges with the normal recompression and the upper shock at a quadruple point. The lower wave itself now no longer forms at the aerofoil surface; rather, a series of compression waves are generated which coalesce into a shock at the ground plane.

The same is true of the wave at  $h/c=0.1$ , and the peak local Mach number in the flowfield now occurs at the ground plane immediately prior to the shock reflection. The upper wave now merges with the reflection of the lower wave prior to the normal recompression to subsonic conditions, which occurs  $0.8c$  downstream of the trailing edge. The reflected lower wave straightens the wake to parallel with the freestream, but the numerical schlieren in the inset of figure 7.7e indicates that a weak reflection of the wave from the shear layer also exists, and the wave itself bends significantly in passing through the shear layers. However, its angle in exiting this region is essentially unchanged from that prior to the interaction.

Figure 7.8 presents a plot of pitching moment coefficient, taken around the  $1/4$  chord mark, for  $\alpha=2.79^\circ$ , as ground clearance is reduced and for the five freestream Mach numbers investigated. At  $M_\infty=0.5$  through  $0.7$ , the nose-down moment is fairly constant



with decreasing clearance, until  $h/c=0.1$  is reached, at which point the moment becomes notably less negative, due to the increase in low pressure forming between the aerofoil and the ground, which reaches its peak behind the  $1/4$  chord and therefore contributes a nose-up (positive) component. At  $M_\infty=0.8$ , the negative moment increases in magnitude from freeflight to  $h/c=1$ , after which it becomes exponentially less negative with further reduction in ground clearance, eventually producing an overall nose-up moment at  $h/c=0.1$ , coinciding with the point where the lift coefficient was seen to drop away in figure 7.6.

### 7.3.2 $0^\circ$ incidence

Although not typical of a flight incidence except in momentary pitching, the  $0^\circ$  cases provide the most exaggerated ground effects between the aerofoil and the ground, due to the lower surface curvature.

Returning to figure 7.6a, for  $M_\infty=0.5$ , the lift coefficient is seen to decrease slightly as ground clearance is reduced. This is a direct consequence of the increasing acceleration of the flow between the aerofoil and ground, which is more exaggerated at

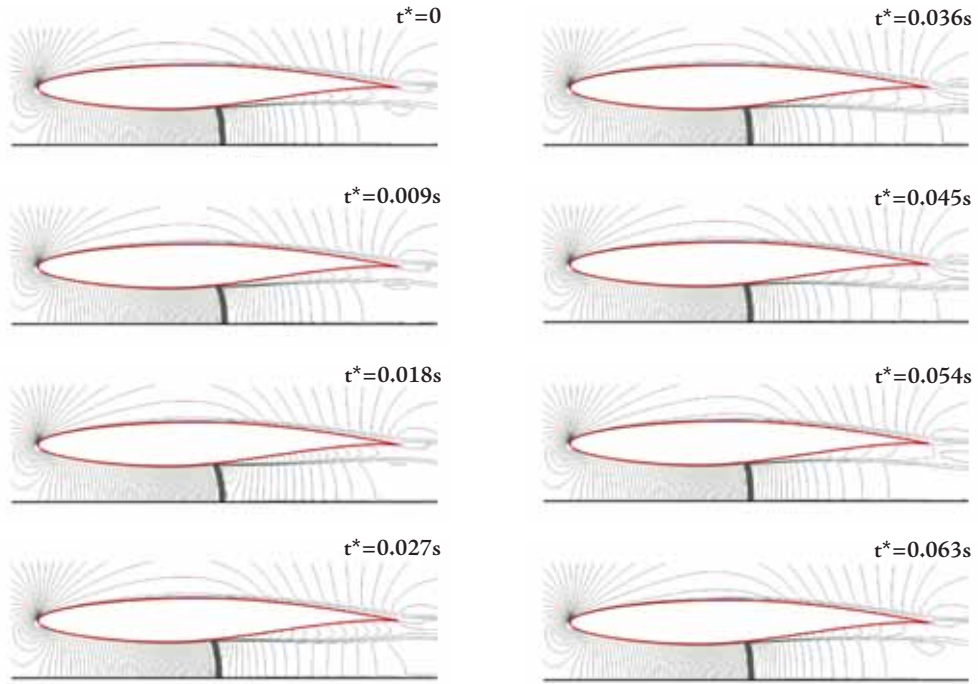
this incidence than at  $2.79^\circ$ , and means that the stagnation point is drawn upwards by a small margin. At  $h/c=0.1$ , the lift coefficient reverses sign, and the section produces a negative  $C_L$  of  $-0.39$ , or roughly  $-200\%$  of the lift produced at  $h/c=0.25$ . The drag coefficient initially reduces by a small margin (1-2%) to  $h/c=0.5$ , after which it increases sharply with further proximity to the ground. At  $h/c=0.25$  this is simply a function of the accelerated flow around the wing causing a slightly thicker wake, but at  $h/c=0.1$  a shock wave has formed on the lower surface. There is no significant separation at the foot of the shock but the wake is markedly thicker as a result of the shock/boundary layer interaction.

For  $M_\infty=0.6$ , in figure 7.6b, the trends are almost identical apart from that the marked drop-off in lift and mild increase in drag at  $h/c=0.25$  (where lift remains positive in sign), as well as  $h/c=0.1$  where the lower surface shock is present (again producing negative lift). At  $h/c=0.25$  this new trend is caused by the increased acceleration of the flow under the wing, where the peak local Mach number now  $0.85$ , as opposed to a peak of  $M_1=0.73$  on the lower surface in the freeflight case. The  $h/c=0.1$  lower surface shock, which has begun oscillating, has now triggered significant periodic boundary layer separation from the shock foot to the trailing edge, and is the cause of the exponential rise in  $C_D$ , close to  $100\%$  higher than at the same clearance at  $M_\infty=0.5$ .

Although other cases feature shock oscillation (noted in table 7.1), this case was the only one to produce mild buffet flow specifically with the lower shock, and therefore has been singled out as a brief example. The density contours in figure 7.9 indicate that the shock movement is limited to a  $0.02c$  portion of the aerofoil, with a low oscillation frequency of  $16\text{Hz}$ . The shock foot periodically separates the boundary layer to the trailing edge.

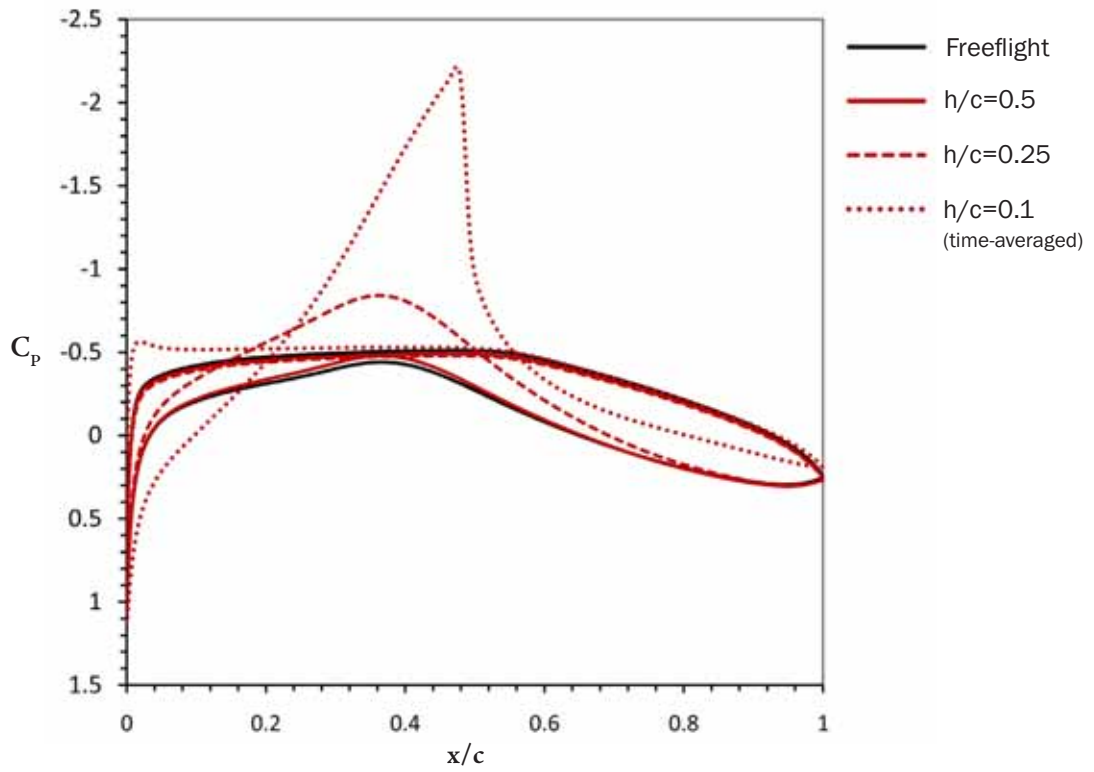
The evolution of the flow with decreasing ground clearance to produce this flowfield is highlighted in figure 7.10. Aerofoil pressure distributions show the relatively mild ground influence at  $h/c=0.5$ , where the distribution is close to that of the freeflight case. At  $h/c=0.25$ , the acceleration of flow in the aerofoil/ground channel lowers the pressure there, while the upper surface distribution remains similar. Then, at  $h/c=0.1$ ,

7.9  
FIG



Contours of density through one cycle of lower shock oscillation at  $M_\infty=0.6$ ,  $\alpha=0^\circ$ ,  $h/c=0.1$ .

7.10  
FIG



Pressure distributions at  $M_\infty=0.6$ ,  $\alpha=0^\circ$ , as ground clearance is reduced.

the shock wave forms, causing a large low pressure spike on the lower surface. With the flow so restricted underneath the aerofoil, the air directed over the upper surface produces a greater suction peak close to the leading edge, though this is more than offset by the negative lift produced by the suction region prior to the shock. This distribution and shock behaviour is reminiscent of the USNA Case 3 discussed in chapters 4 and 5, at a similar ground clearance and Mach number, though in this case the small-scale oscillation remains without the influence of three-dimensional effects from the endplate.

At  $M_\infty=0.7$ , a shock has now formed on the lower surface at  $h/c=0.25$ , and at  $h/c=0.1$  the effective choking of the flow between the aerofoil and ground has forced sufficient air over the upper surface to result in nearsonic conditions there. The lower surface shock was not oscillating, indicating that the increased Mach number lies on the far side of the buffet boundary produced by this wave. The drag rise now begins at  $h/c=0.25$ , though no significant separation exists from that shock.

For  $M_\infty=0.8$ , in figure 7.5b, the marked drag rise now affects  $h/c=0.5$  too; now the flowfield incorporates both an upper and lower surface shock system. At  $h/c=0.1$ , the flowfield is significantly transient once more, as the upper surface shock is now oscillating, with the periodic separation structures at the trailing edge triggering a mild movement in the lower shock as well.  $C_L$  initially drops as ground clearance is reduced from  $h/c=1$  to 0.5, but then increases despite the presence of the shocks. The flow is being forced over the upper surface to an extent that the low pressure there is much extended with decreasing clearance, though it does result in a stronger shock sitting further back on the aerofoil.

At  $M_\infty=0.9$ , extremely large-scale shock structures exist at the trailing edge as in the previous section, although unlike for the  $6^\circ$  cases which follow, they are not different enough from the  $2.79^\circ$  cases, in terms of general characteristics, to warrant a detailed description here.

### 7.3.3 $6^\circ$ incidence

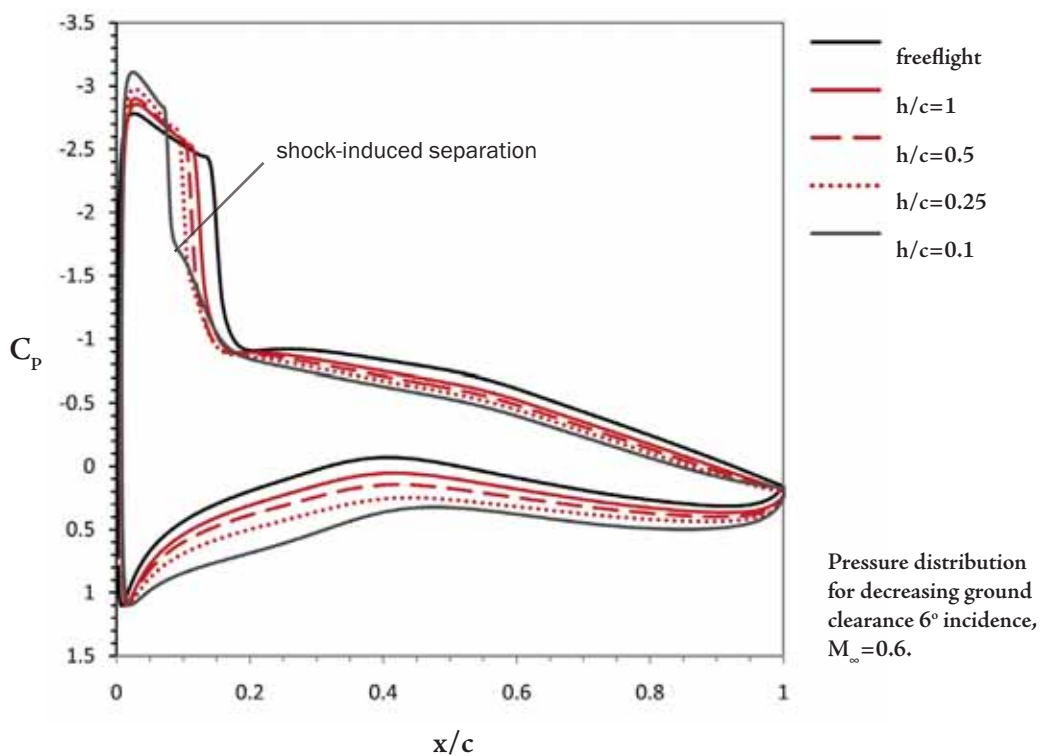
Although the incidence here is high enough to promote large-scale separation on the

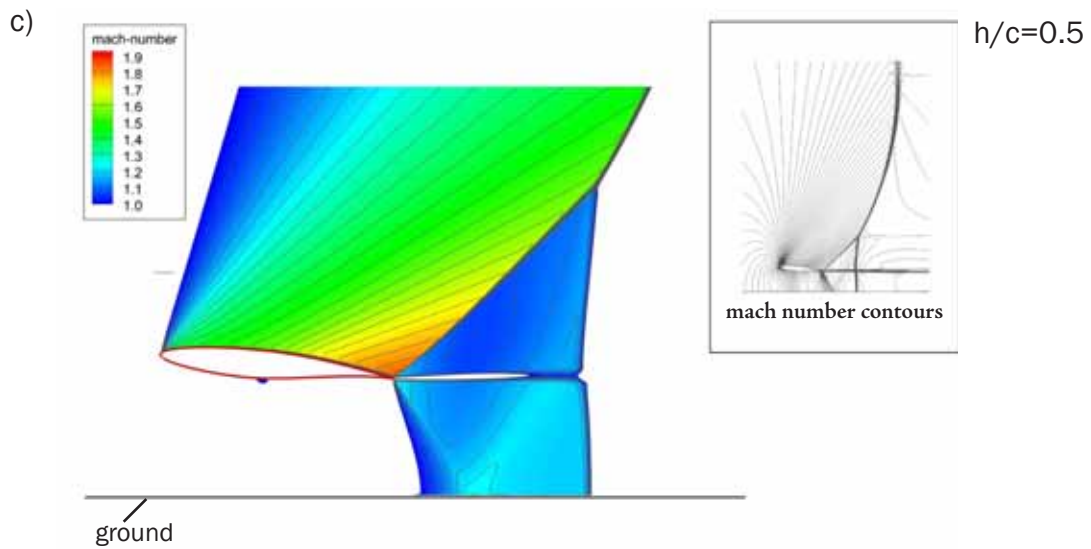
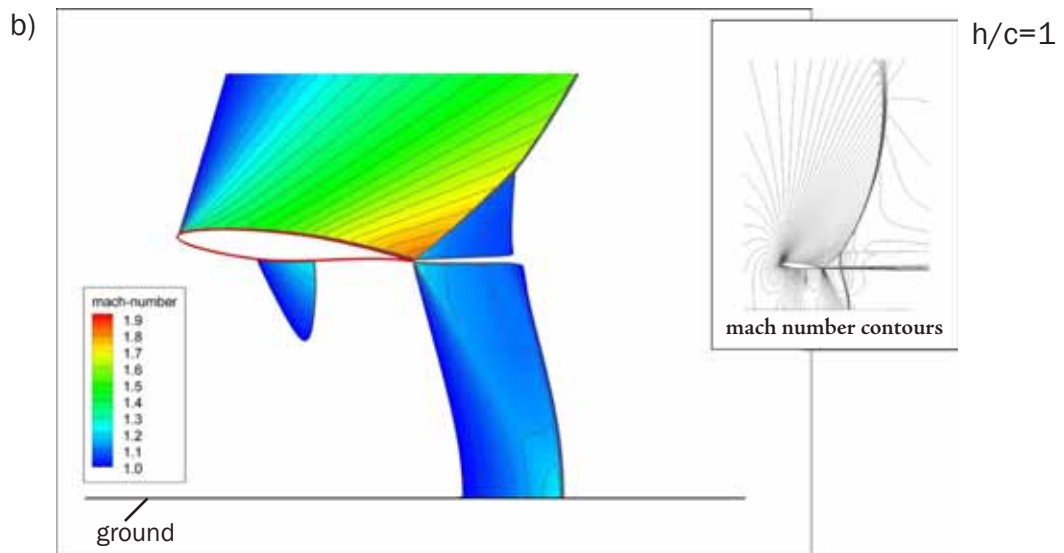
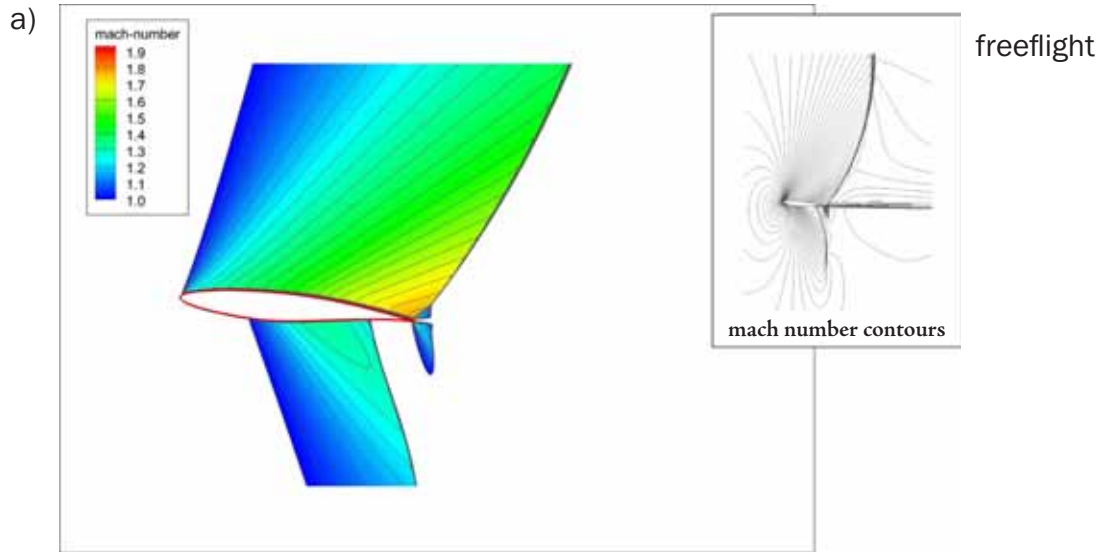
upper surface, the flow between the aerofoil and ground is closer to the “ram” effect that can be achieved at lower incidence for a more flat-bottomed section, as the profile is fairly parallel with the ground from the point of minimum ground clearance to the trailing edge. In this scenario, the region under the aerofoil is almost exclusively a high pressure zone, and features little local acceleration due to curvature.

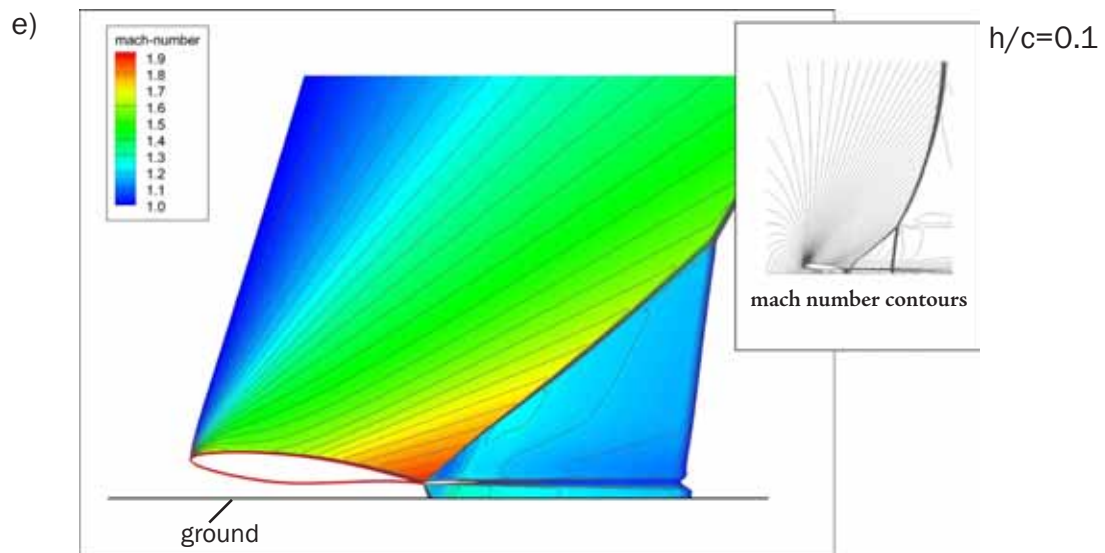
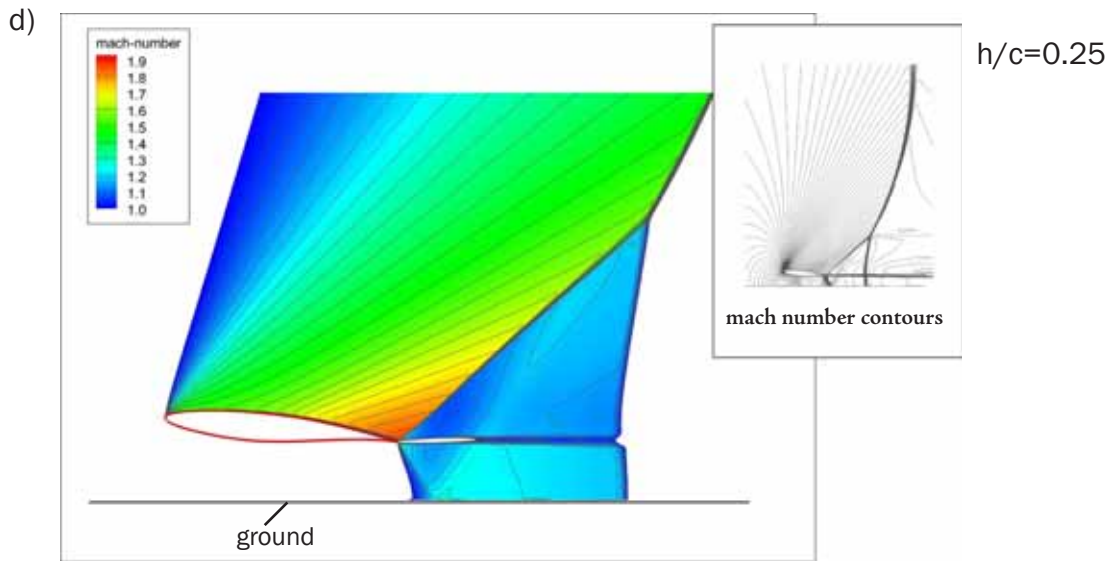
In the absence of lower surface shock waves up until  $M_\infty=0.9$ , most of the observed changes to lift and drag are due to the influence of the ground on the upper surface shock. At  $M_\infty=0.5$  and  $0.6$ ,  $C_L$  only shows distinct improvement at  $h/c=0.25$  and  $0.1$ . Above this clearance, the “ram” effect is not as strong. Prior to  $h/c=0.1$ , the drag reduces by almost 24% in ground effect as compared to the freeflight case, as the shock wave moves even further towards the leading edge, and the thickness of the upper shear layer leaving the aerofoil at the trailing edge is reduced as a result. The downwash angle of the wake is also lessened to a small extent ( $1-2^\circ$  in the immediate vicinity of the trailing edge). At the lowest clearance, lift and drag increase from their levels further from the ground. The drag increase is due to the fact that although the shock is even further forward on the profile as a result of the continued increase to effective angle

7.11

FIG







Contours of Mach number for cases at  $M=0.9$ ,  $\alpha=6^\circ$ , as ground clearance is reduced from a) freelifght, to b)  $h/c=1$ , c)  $h/c=0.5$ , d)  $h/c=0.25$  and e),  $h/c=0.1$ .

of attack, the flow is now significantly separated at the foot of the shock and therefore the boundary layer following reattachment downstream remains thicker and increases the strength of the wake as a result. Pressure coefficients with decreasing clearance for  $M_\infty=0.6$  are shown in figure 7.11 to illustrate these effects.

These trends continue to hold at  $M_\infty=0.7$ , though the drag now increases across the range as separation bubbles at the shock foot are present in all the cases. The influence of the ground to this point appears to be to produce the onset, and subsequent magnification, of separation by virtue of continued increase in the effective angle of attack.

However, the ability of the wing to produce ever-increasing levels of lift as clearance is reduced for a fixed Mach number is not affected. At  $M_\infty=0.8$ , with every case producing large areas of separated flow to the trailing edge, the “ram” effect on the lower surface still results in increasing efficiency as the aerofoil is placed closer to the ground.

At  $M_\infty 0.9$ , lift and drag both increase as ground clearance is reduced. We see an emergence of some of the shock structures discussed in the previous section, though at this incidence the flow is considerably different and warrants closer inspection in figure 7.12. In freeflight, the upper surface shock sits at the trailing edge, forming a lambda-foot with the upper shear layer behind the trailing edge, while a strong shock exists on the lower surface past the point of maximum thickness. After this compression, the lower surface flow accelerates to supersonic again, resulting in a second, much smaller, shock coincident with the stem of the upper shock.

At  $h/c=1$ , the initial lower-surface shock has reduced greatly in magnitude, and the secondary region of supersonic flow is now much expanded, extending to the ground plane and forming a large-scale curved recompression shock. This structure does not change characteristics as clearance is further reduced, though the peak local Mach number prior to the upper shock increases and the final recompression behind the aerofoil exists increasingly downstream of the trailing edge as was seen for the  $2.79^\circ$  case. The elimination of the initial lower surface shock seen at higher clearances greatly increases the ability of the wing to produce lift.

## 7.4 Increasing Mach numbers for fixed ground clearances

For the three incidences examined, data is reconstructed in figure 7.13, for fixed angles of attack and ground clearances as Mach number increases. This is briefly examined here as it is approximately representative of attempting flight at a constant attitude and altitude during long-term acceleration, and therefore provides a different way of interpreting the results. It ignores the intrinsic short-term effects of sudden acceleration, which would

alter the results were this a truly time-dependent increase in freestream Mach number (Roohani and Skews, 2008). Freeflight results are included for comparison.

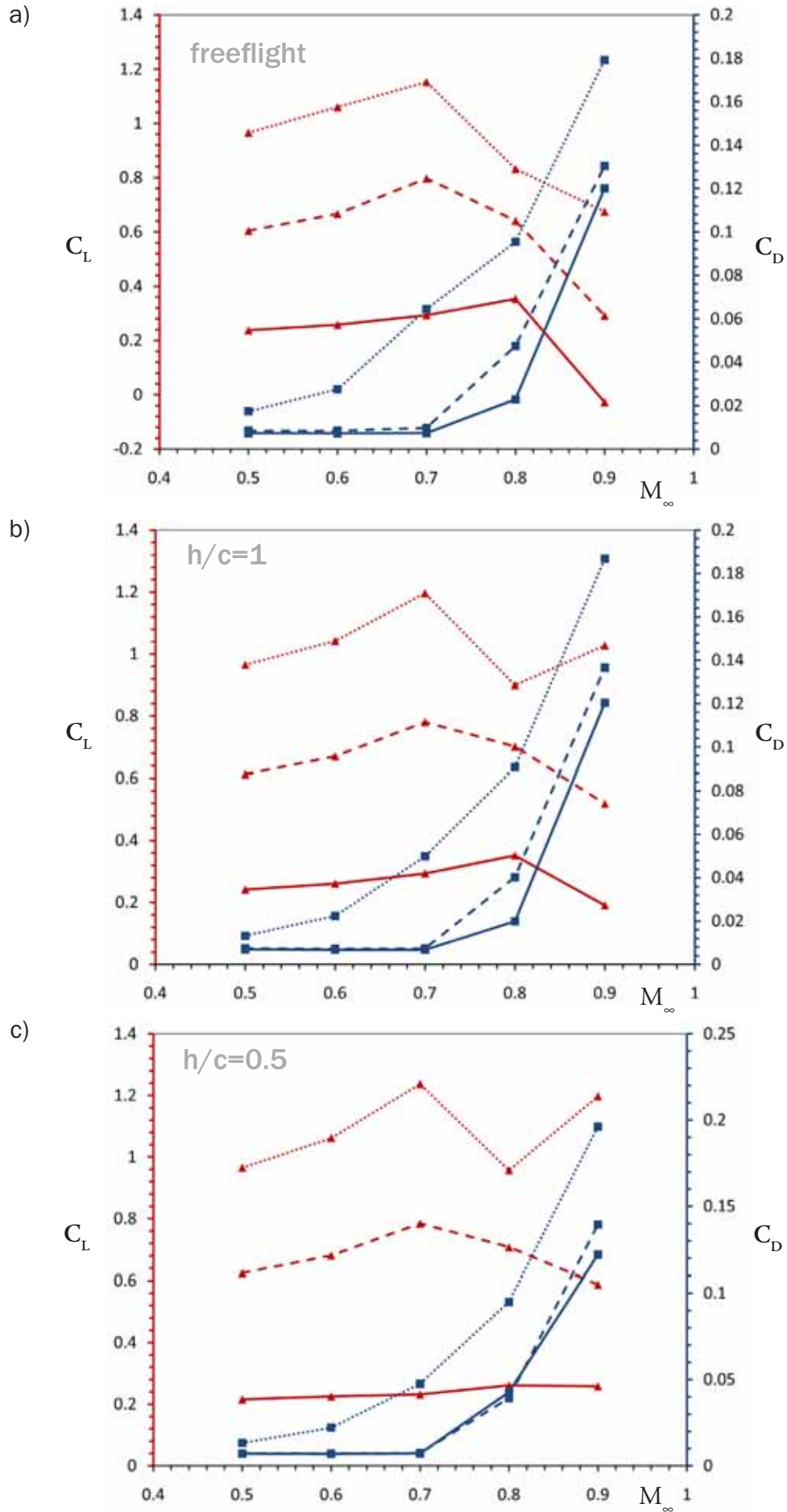
#### 7.4.1 0° incidence

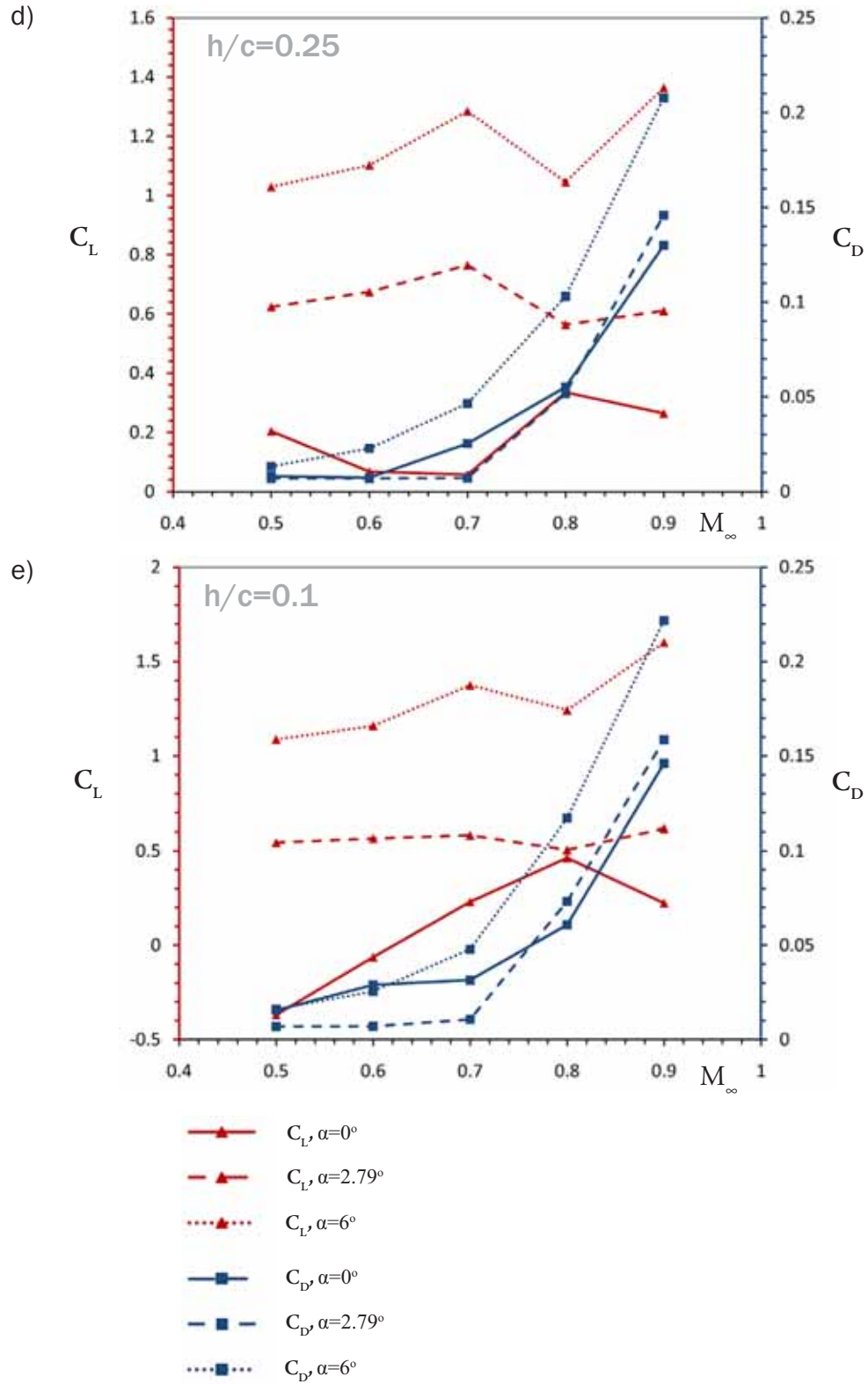
In freeflight, lift and drag coefficients increase with Mach number, until at  $M_\infty=0.9$  lift production drops off. At  $h/c=0.5$ , this drop is eliminated and lift coefficient remains largely constant through the Mach number range, though the drag increases at a greater magnitude. This clearance produces the most stable trends; at  $h/c=0.25$ ,  $C_D$  at first decreases from  $M_\infty 0.5$  to 0.6, then increases to  $M_\infty 0.8$ , then decreases again to  $M_\infty 0.9$ , due to the influence of the formation of the lower surface shock. The transonic drag rise begins between  $M_\infty 0.6$  and  $M_\infty 0.7$  as a result, rather than between  $M_\infty 0.7$  and  $M_\infty 0.8$  at the higher clearances. At  $h/c=0.1$ , as we have already seen, the wing produces negative lift until  $M_\infty 0.7$ , and as the lower surface shock has already formed prior to  $M_\infty 0.5$ , the transonic drag rise has already established itself.

#### 7.4.2 2.79° incidence

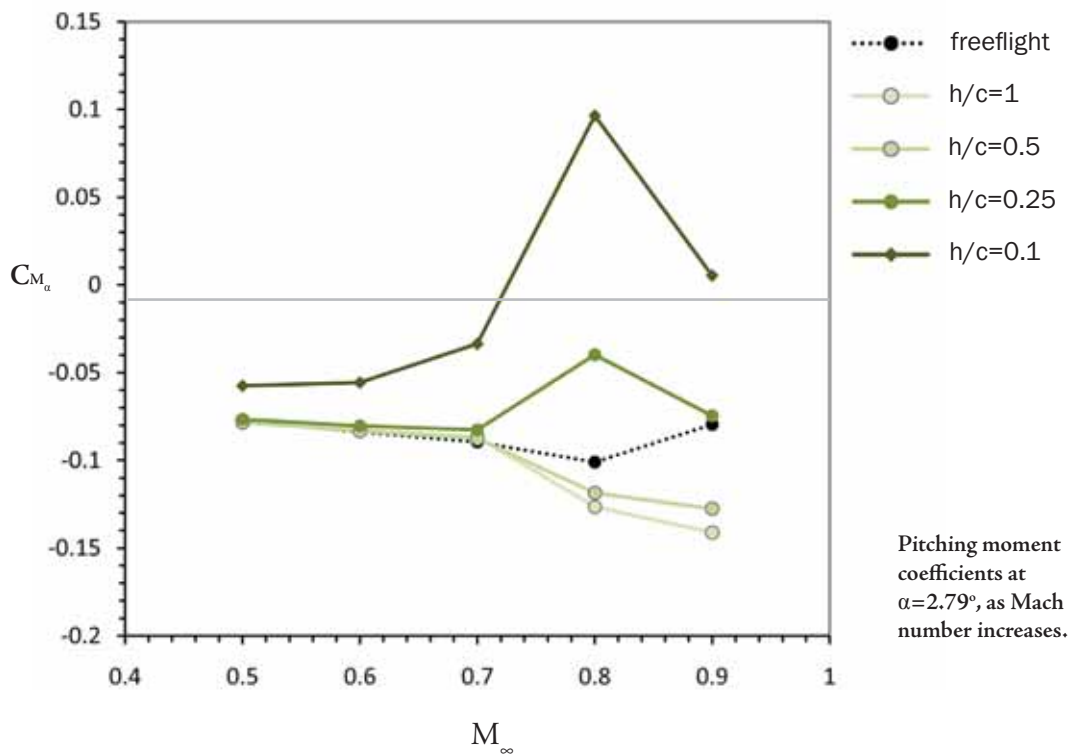
With increased incidence, trends for lift and drag with increasing Mach number remain similar from freeflight to  $h/c=0.5$ , with the flowfields at  $M_\infty 0.7$  representing a peak in the lift coefficient after which it drops off with the additional acceleration under the aerofoil to the point at which the lower shock forms. Drag rises predictably and asymptotically with Mach number for these cases and those at lower ground clearances as well. At  $h/c=0.25$  and 0.1,  $C_L$  still peaks at  $M_\infty 0.7$ , then drops, but makes a partial recovery at  $M_\infty 0.9$ .

Pitching moment coefficient trends for this incidence are presented in figure 7.14, and show a clear distinction between the clearances from freeflight to  $h/c=0.5$ , and those at  $h/c=0.25$  and 0.1. A spike in the  $C_{M_q}$  at  $M_\infty 0.8$  at these latter clearances is due to the marked shift forwards of the peak high pressure region, which now dominates the lower region close to the leading edge, rather than at the point of minimum clearance





Lift and drag coefficients for  $0^\circ$ ,  $2.79^\circ$  and  $6^\circ$ , with decreasing ground clearance for a)  $M_\infty=0.5$ , b)  $0.6$ , c)  $0.7$ , d)  $0.8$  and e)  $0.9$ .



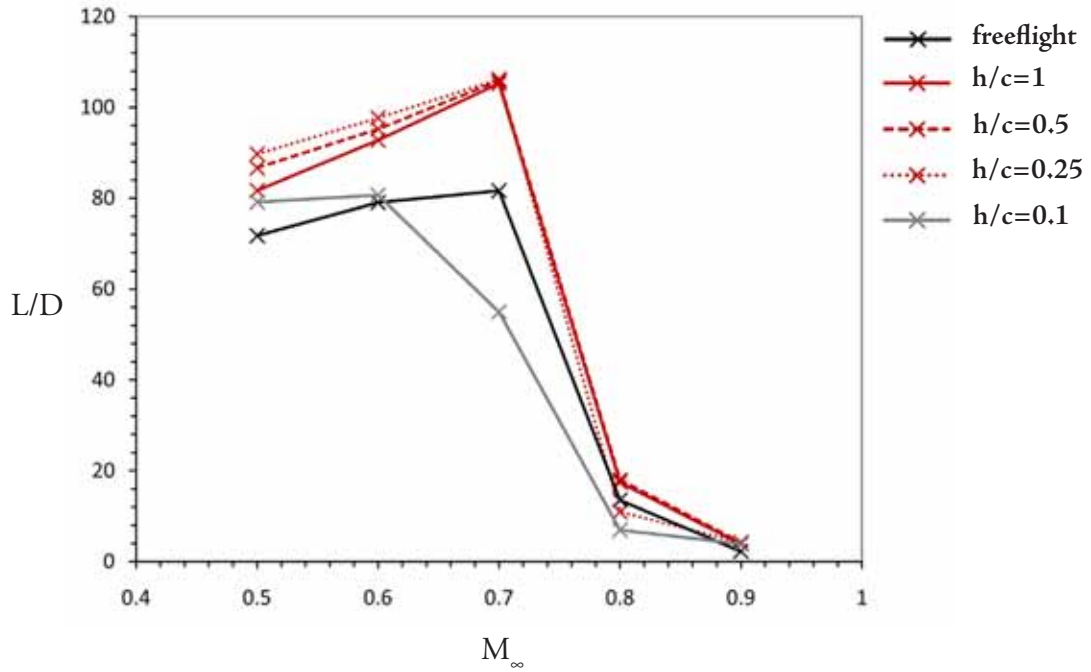
Pitching moment coefficients at  $\alpha=2.79^\circ$ , as Mach number increases.

or the trailing edge where it is produced more naturally around the aerofoil without the constriction of the ground, at higher clearances. Clearly, the trim of an aircraft at low clearances accelerating or decelerating through the Mach number range would be affected. This would occur abruptly in the case of lower shock formation, and would imply a necessity for rapid-response pitch correction to maintain altitude. Alternatively, any sudden change to altitude over the small ground clearance range would have significant effects for stability at a constant flight Mach number.

The aerodynamic efficiency of the aerofoil at the various ground clearances with increasing Mach number is shown in figure 7.15. The lower-surface-shock dominates the flowfield at  $h/c=0.1$  at  $M_\infty 0.6$  onwards, with the immediate result being that it is considerably less efficient to fly at this ground clearance than in freeflight. The clearances of  $h/c=0.25$  represents the best efficiency gains until  $M_\infty 0.8$ , at which point the aerofoil at all clearances features a shock on the lower surface and thus lift drops off as drag increases. The peak efficiency for all clearances bar  $h/c=0.1$  comes at  $M_\infty 0.7$ , beyond which large-scale shock-induced separation destroys the advantages of flying in ground effect.

7.15

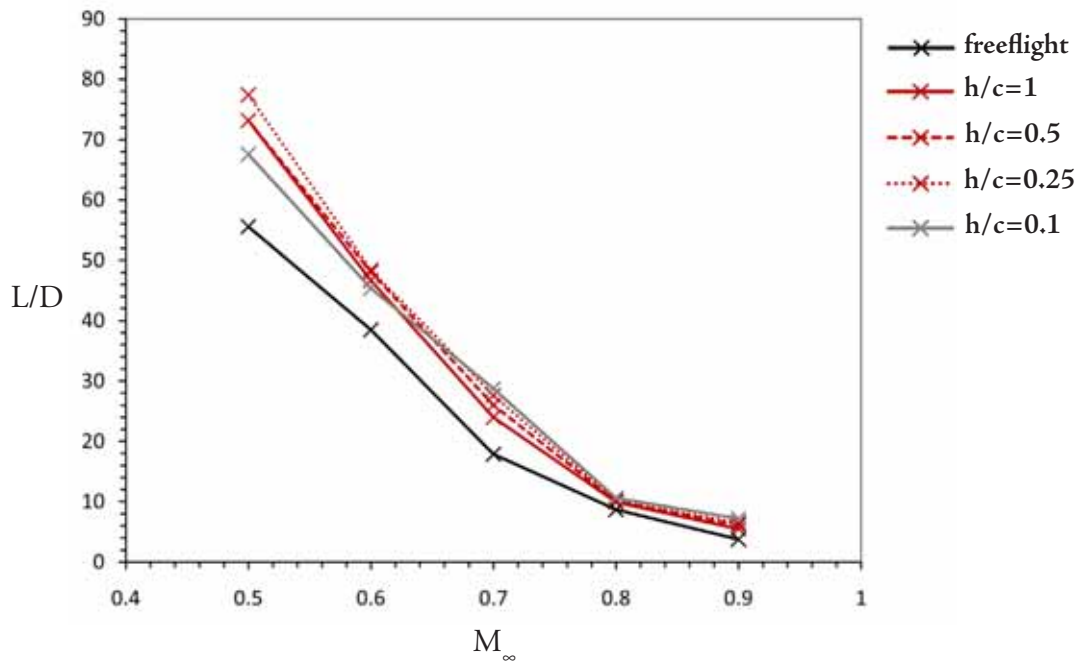
FIG



Aerodynamic efficiency,  $L/D$ , at  $2.79^\circ$  for different ground clearances as Mach number is increased.

7.16

FIG



Aerodynamic efficiency,  $L/D$ , at  $6^\circ$  for different ground clearances as Mach number is increased.

### 7.4.3 6° incidence

At the maximum incidence, the lift and drag behaviours are similar to those at 2.79°, with a peak in  $C_L$  occurring at  $M_\infty 0.7$  for all cases from freeflight to  $h/c=0.5$ . In freeflight the drop off in  $C_L$  is continuous thereafter, whereas at the higher ground clearances a partial recovery is made at  $M_\infty 0.9$  as the “ram” effect under the aerofoil continues and extensive separation on the upper surface of the wing is no longer possible with the shock waves now sitting at the trailing edge. The disappearance of the lower surface shock over these clearances as seen in figure 7.12 serves to aid greatly in the recovery of lift. At  $h/c=0.1$ , the drop in lift at  $M_\infty 0.8$  is mild, such is the increase to effective angle of attack at this clearance, and thus at this clearance the wing remains more efficient through the Mach range than in freeflight as shown in figure 7.15, although the large-scale separation it produces means that it is never more than a few percent more efficient than the lower-drag cases at higher ground clearances. The figure also highlights a clear trend towards decreasing efficiency with increasing Mach number (in ground effect as in freeflight), with the shock-separation induced drag the prime contributor to this.

## 7.5 Summary

The RAE 2822 section at Reynolds numbers approximating flight conditions was examined for several ground clearances (freeflight (no ground), and  $h/c=1, 0.5, 0.25$ , and  $0.1$ ), Mach numbers ( $0.5, 0.6, 0.7, 0.8, 0.9$ ) and angles of attack ( $0^\circ, 2.79^\circ$  and  $6^\circ$ ).

In general, the subsonic mechanisms that result in increased lift, and often enhanced efficiency, hold at high-subsonic Mach numbers. The high pressure increases underneath the aerofoil as more mass flow is directed over the upper surface, leading to an increase in effective angle of attack. This holds until very low clearances ( $h/c=0.1$ ), where the local curvature at the leading edge on the lower surface encourages the flow to accelerate and create low pressure over the middle portion of the wing, and this has a destructive effect on lift.

However, the introduction of shock waves into the flowfield has a disruptive effect on performance, particularly at the lowest clearances, where the early formation of a shock wave can lead to a sudden drop in the production of lift and an early transonic drag rise for the section. It can also lead to an early development of unsteady shock oscillations associated with buffet on the lower surface, and has a considerable effect on the pitching moment of the section, lending it a nose-up moment at low clearances where it would normally have a nose-down moment at higher clearances and in freeflight.

While an aerofoil could be optimised to delay or mitigate many of the undesirable effects described, it remains clear that sustained flight close to the ground at transonic Mach numbers would be particularly difficult without an advanced control system to account for very rapid changes to lift, drag and pitching moment caused by relatively small changes to ground clearance, incidence or Mach number. For instance, if flying close to the critical Mach number for the lower surface at  $h/c=0.1$ , even a sudden strong headwind gust could result in the abrupt formation of a shock wave between the aerofoil and ground causing a precipitous loss in lift and therefore altitude.

It is also worth noting that because increasing incidence is a factor in the onset of separation and oscillatory shock motion (Caruana *et al.*, 2003), the effective angle of attack is increased, the wing is likely to experience transonic buffet of the upper surface shock at Mach numbers lower than that at which the buffet boundary would exist for freeflight cases, although this effect was not pinpointed in the present study. The results indicate that without significant further research into appropriate aerofoil shapes and longitudinal control, a craft specifically designed to fly at high subsonic Mach numbers cannot be designed, and thus an “upper limit” to the cruising Mach number of such a craft would apply. The aerodynamic efficiency of the section at different ground clearances for increasing Mach number indicated that the onset of supersonic flow on the lower surface, achieved as early as  $M_{\infty} 0.5$  at  $h/c=0.1$ , means that flight in close ground proximity is no longer more efficient than freeflight. At the higher clearances, a peak in  $L/D$  occurs at  $M_{\infty} 0.7$ , beyond which there is little gain to be made by flying in ground effect, as increased separation and lower surface suction cancel out any enhanced effective angle of

attack. At  $M_\infty 0.9$ , shock reflection patterns emerge in the wake, forming a complex series of interactions.

Some of the results presented here are highly-influenced by the two-dimensionality of the flowfield, such as the very early onset of unsteady shock motion and the shock reflection patterns observed at  $M_\infty 0.9$ , and thus attention in the next chapter is turned to a three-dimensional wing.

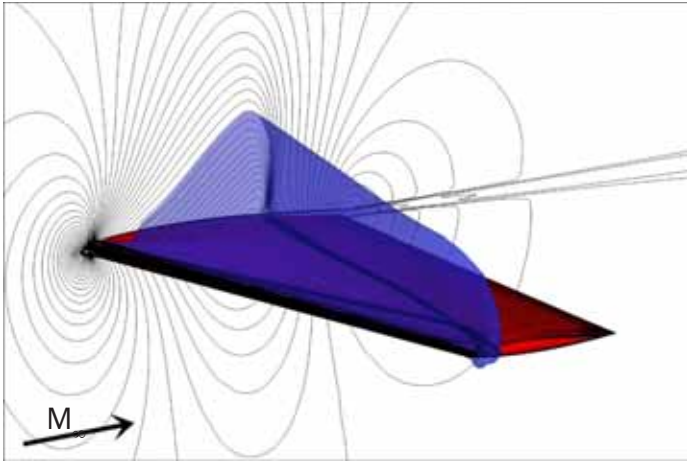
# Chapter: ONERA M6 Wing in Transonic Ground Effect



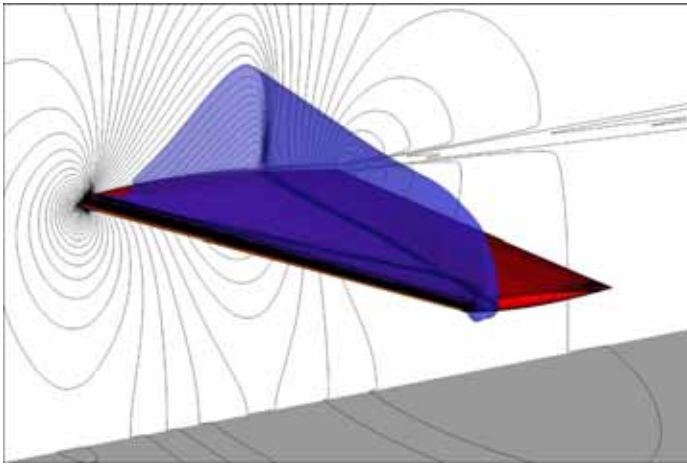
*The finite, swept ONERA M6 aerofoil at “Case 2308” conditions ( $M_\infty=0.8395$ ,  $\alpha=3.06^\circ$ ) is initially placed close to the ground with increasing proximity to provide an introductory determination of the ground’s influence on the wing’s aerodynamic characteristics, including the effect of the ground on the wing tip vortex path. As in chapter 7, a parametric study is presented, this time for four ground clearances, five freestream subsonic Mach numbers (from 0.5 to 0.9) and two angles of attack. Forces and pressure distributions are discussed, with further analysis of the complex three-dimensional wave structures.*

## 8.1 Introduction

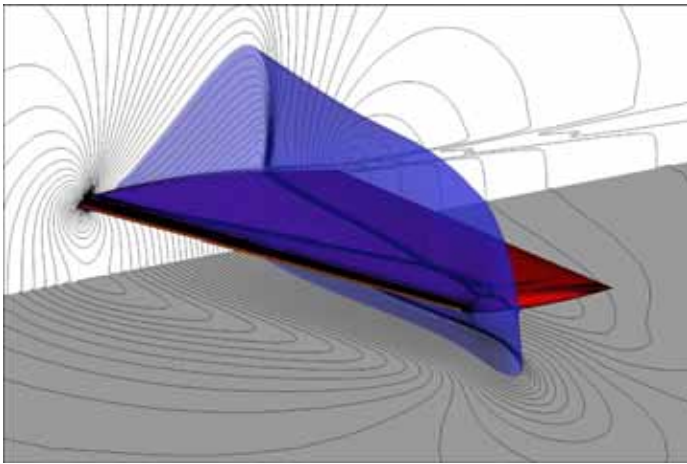
**W**ith the ONERA M6, an evaluation of the influence of the ground on a more complex flowfield is possible, including wing tip effects and vortex structures in the wake. It also provides a set of results more applicable to the real world for the highest freestream Mach numbers, as the flow is allowed to “relax” around the wing in a way in which it could not in two-dimensional simulations. The wing also features a thinner section than the RAE2822, and is symmetric, which allows a more straightforward examination of the ground effects when the incidence is  $0^\circ$ .



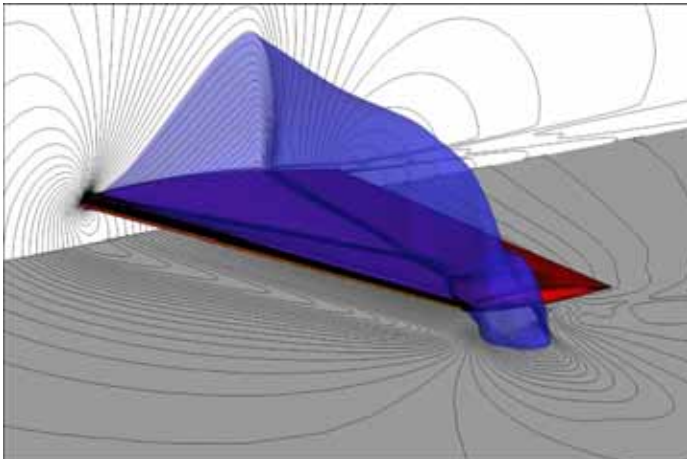
a)



b)

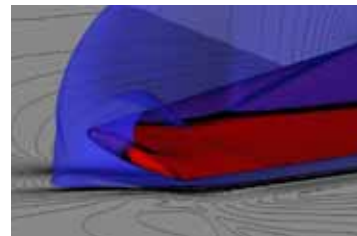


c)



d)

Contours of density on the wing (red), symmetry and ground planes, with regions of supersonic flow (blue) as indicated for ground clearances of a) freeflight (no ground), b)  $h/c=1$ , c)  $h/c=0.25$ , and d)  $h/c=0.1$ .



rear view at wingtip d)

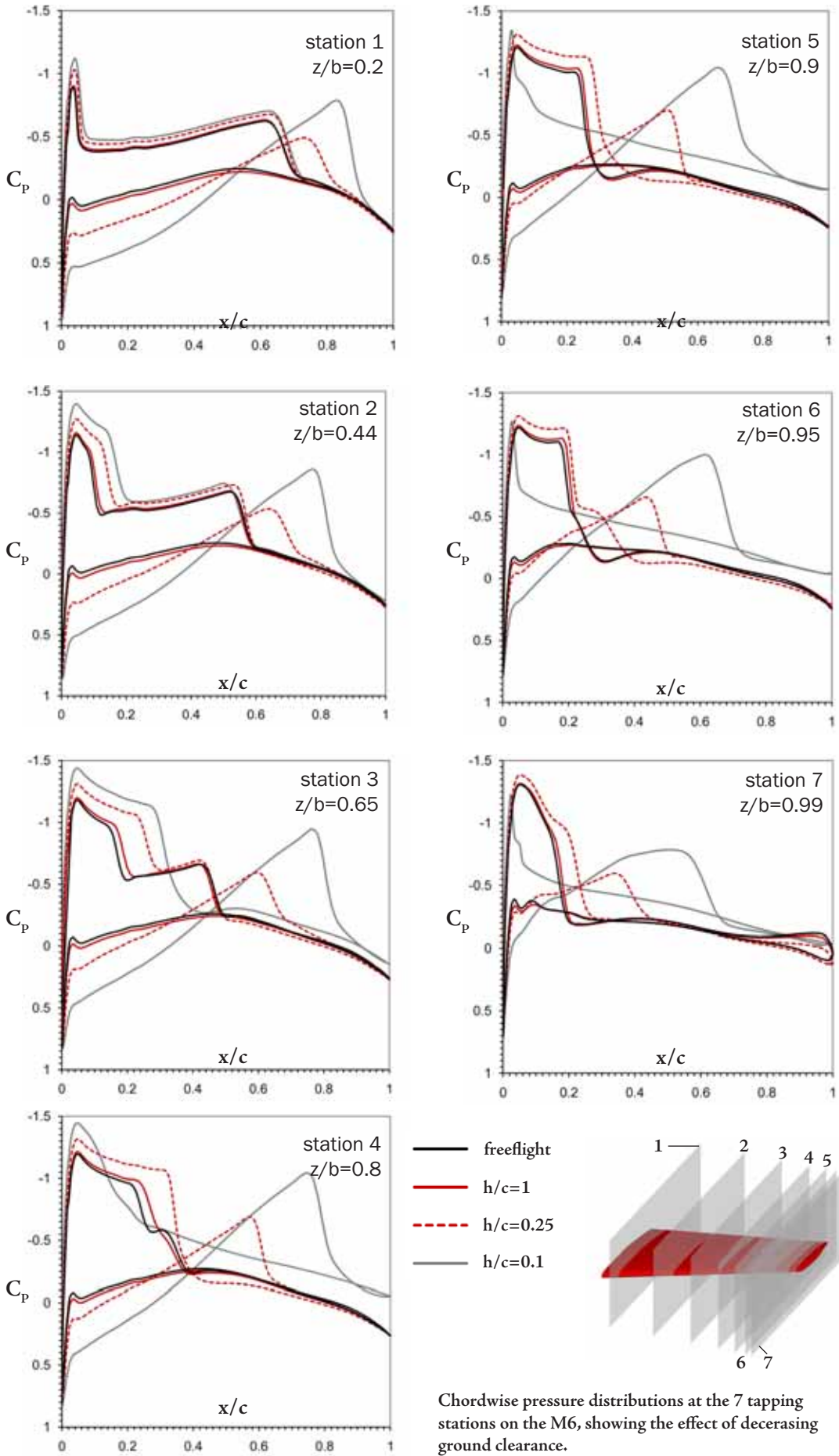
## 8.2 “Case 2308” with decreasing ground clearance

As with the example in section 7.2, the ground clearance is the only variable here, to provide a clear indication of the effect on aerodynamic performance of increasing ground proximity as compared to the familiar free-flight M6 “Case 2308” conditions as discussed in Chapter 4. The Reynolds number and scale remain the same;  $11.72 \times 10^6$  and a mean chord of 0.6461m, respectively. The freestream Mach number was 0.8395, with an angle of incidence of  $3.06^\circ$ .

Figure 8.1 shows density contours on the wing and symmetry plane as a means of visualisation, as well a Mach 1 iso-surface to illustrate the extent of supersonic flow in the three-dimensional flowfield. From freeflight conditions to a clearance of  $h/c=1$ , there are only minor observable changes, with an increase in the volume of the local supersonic flow region towards the tip. At  $h/c=0.25$  in figure 8.1c, a lower-surface shock has formed, and the upper surface terminating shock has been pushed back along the chord, accompanied by a notable expansion of the supersonic region along the chord to the tip. This suggests that the strength of the terminating shock on the upper surface is maintained across a greater proportion of the span, and thus the distribution of pressure on the upper surface is more even from root to tip. The supersonic region spills around the wing tip, indicating the merging of the upper and lower shocks, resulting in a portion of the strong normal wave sitting outboard of the tip.

The case at  $h/c=0.1$  in figure 8.1d proved to be transient in nature. Only small variations in lift and drag were obtained, and these have been time-averaged for subsequent plots. The reason for the unsteadiness in the flow stems from the detachment of flow at the wing tip close to its leading edge. This results in a conical region of subsonic flow which strongly influences the tip flow and the way in which the merged shock forms there.

The pressure distributions in figure 8.2 provide a clearer insight into the changes which occur with greater proximity to the ground plane. The seven pressure tapping stations described in figure 4.30 are used, for  $z/b$  locations of 0.2, 0.44, 0.65, 0.8, 0.9,



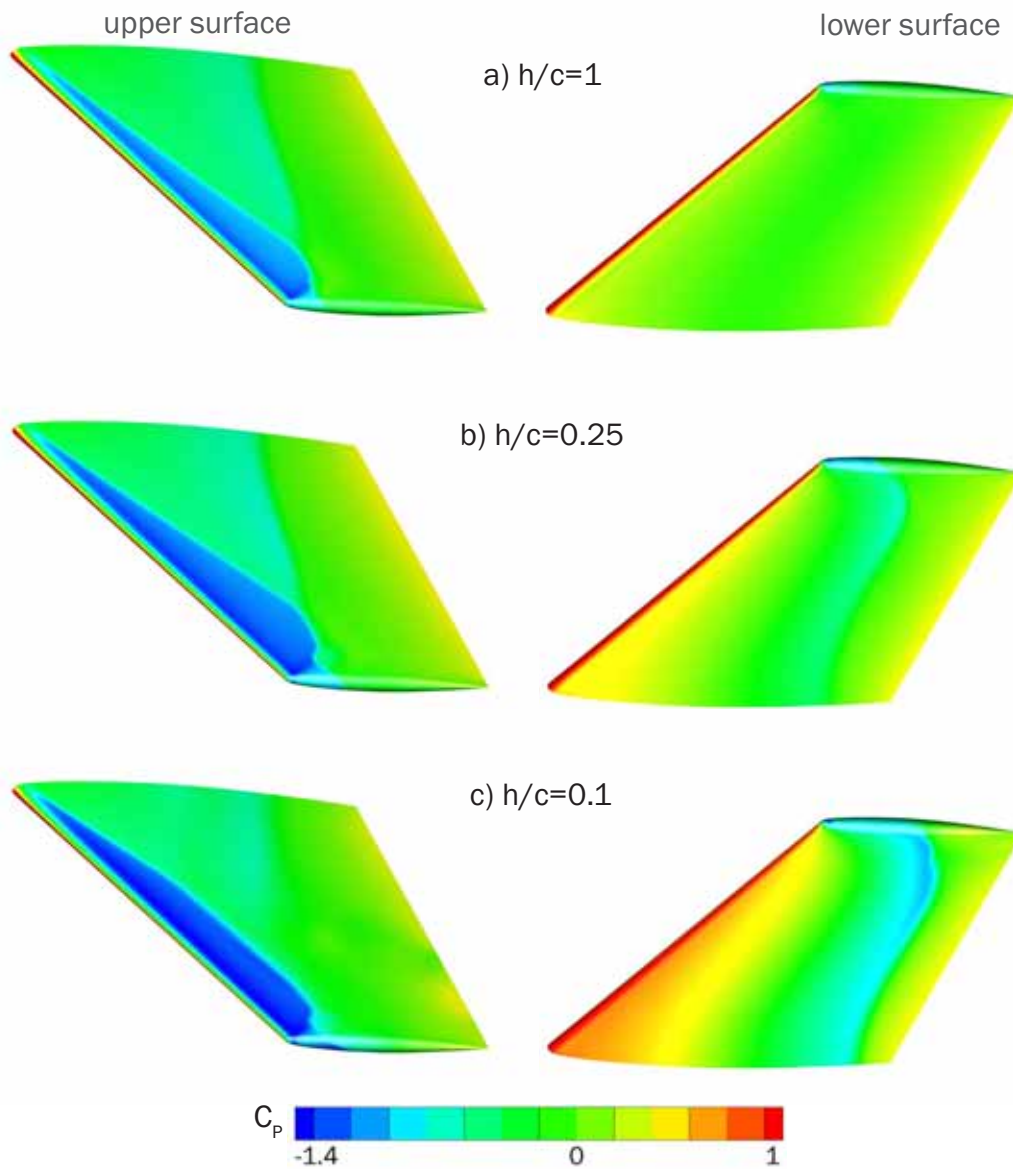
0.95 and 0.99.

The change in clearance from freeflight to  $h/c=1$  results in only minor changes to the distributions at each station, with shock locations moving back along the chord by approximately 1-2%. This is in contrast to the two-dimensional results of the last chapter which suggested that as the clearance was reduced, the effective angle of attack was increased and therefore the shock was drawn upstream, suggesting that three-dimensionality, particularly the effect of sweep, is a very strong influence on the flow. At station 4, the double-shock structure, commented upon in section 4.4.1 of Chapter 4 as being highly mesh-sensitive, has disappeared. The mesh resolution in the region is identical to that of the freeflight case, which suggests that a minor alteration to the spanwise flow has largely merged the double-shock system.

At  $h/c=0.25$ , the lower surface pressure distribution indicates the emergence of the shock at station 1, close to  $x/c=0.67$ . Upstream, the region of higher pressure caused by the decreased ground clearance is pronounced, as is the increase of the suction peak near the leading edge of the upper surface, indicating that as with the two-dimensional studies, the effective angle of attack has been augmented. While the wing now produces a greatly enhanced suction near the leading edge, the presence of the adverse gradient on the lower surface that terminates in the shock has a destructive influence on lift.

By station 4, the terminating shock on the upper surface has greater strength than at higher clearances, resulting in a much more pronounced pressure rise across it. At station 6 there is a double-shock system on the upper surface, which resembles the freeflight distribution at station 4, and is likewise a product of crossing of shocks as will shortly be seen in figure 9.3.

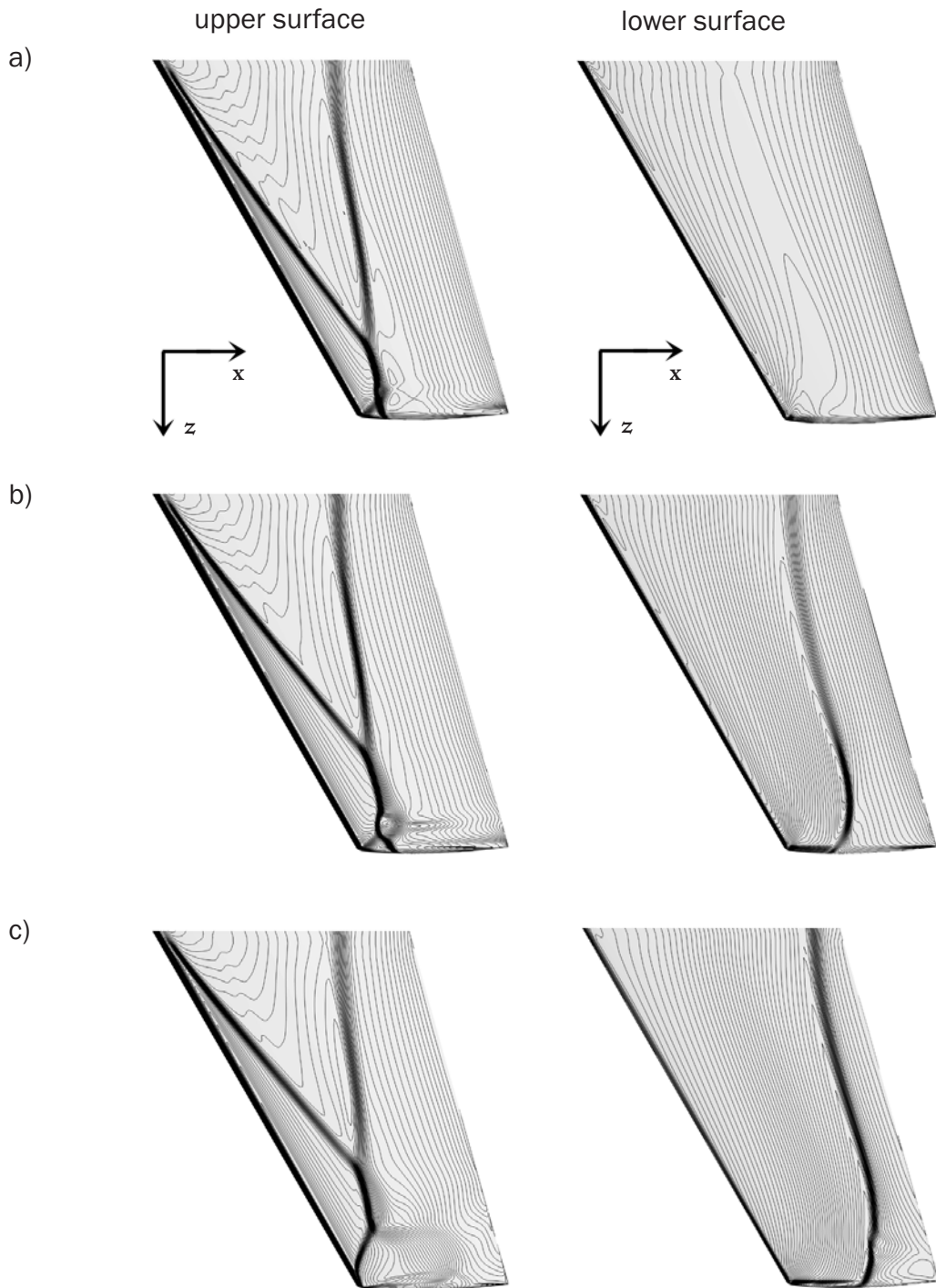
The pressure distributions for  $h/c=0.1$  are an amplification of the trends seen at  $h/c=0.25$ , as the flow is increasingly accelerated between the wing and ground and thus the lower shock sits further back along the chord ( $x/c=0.8$  at station 1) and has markedly increased in strength. The high pressure underneath the wing over the fore section is enhanced even further, meaning that the upwards suction on the wing is heightened further still. While the inboard stations 1-3 show markedly lower pressure



Contours of pressure coefficient with ground clearances of a)  $h/c=1$ , b)  $h/c=0.25$ , and c)  $h/c=0.1$ , at an incidence of  $3.06^\circ$  and  $M_\infty=0.7$ .

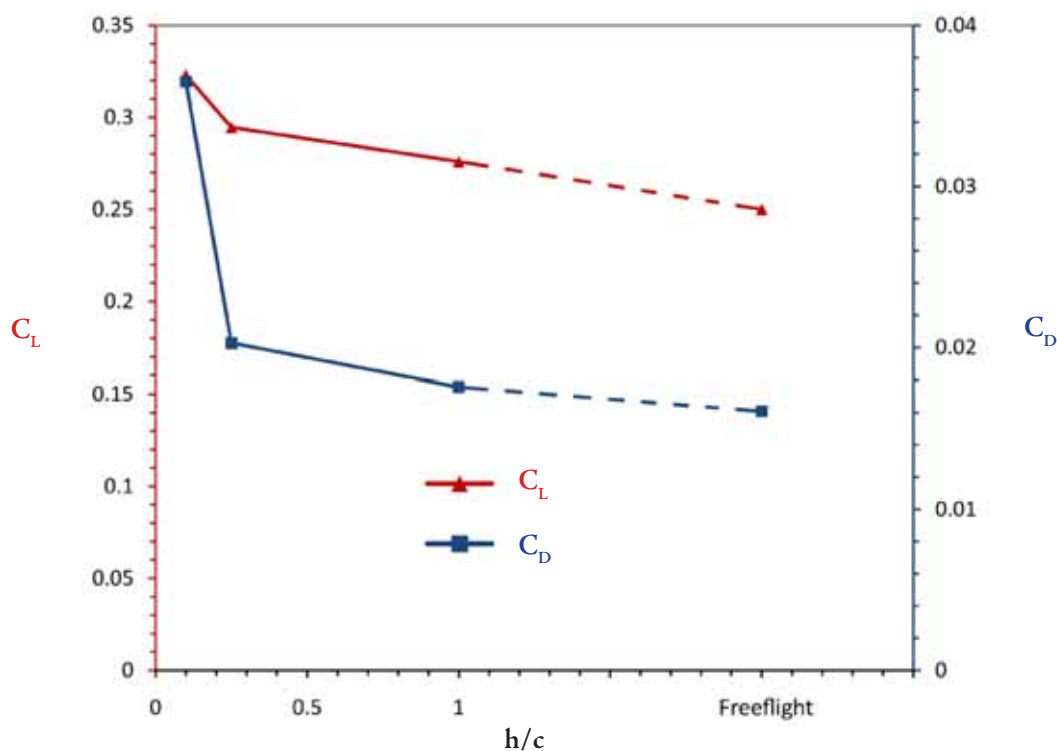
over the upper surface to the terminating shock, the “rooftop” distribution created begins to collapse by station 4, and the remaining stations coincide with the conical region of subsonic flow noted earlier, following the separation of flow close to the leading edge near the wing tip. The lower shock remains strong and continues to dominate the flowfield around the wing’s latter half at the outboard stations. The flow at the wingtip, further restricted by the presence of the ground, forms a more pronounced lateral “bulge” as seen in figure 8.1d, as represented by the significant mid-chord pressure drop at station 7.

Density contours over the upper and lower surfaces are more clearly presented in



Density contours over the upper (left) and lower (right) surfaces of the wing at a)  $h/c=1$ , b)  $h/c=0.25$ , and c)  $h/c=0.1$ .

figure 8.3. The changes to the upper surface distribution are clear; the “V” angle formed by the two shocks which merge towards the tip increases with decreasing clearance, as the terminating shock is pushed back, and the merging point is drawn inboard, such that at  $h/c=0.1$  the shock from the leading edge at the wing tip forms cleanly and becomes



Lift and drag coefficient distributions for “Case 2308” conditions with decreasing ground clearance.

part of the merging front without crossing the other shock system. The curvature and strength of the lower surface shock increases from  $h/c=0.25$  to  $0.1$ , and this shock too is pushed further back along the chord.

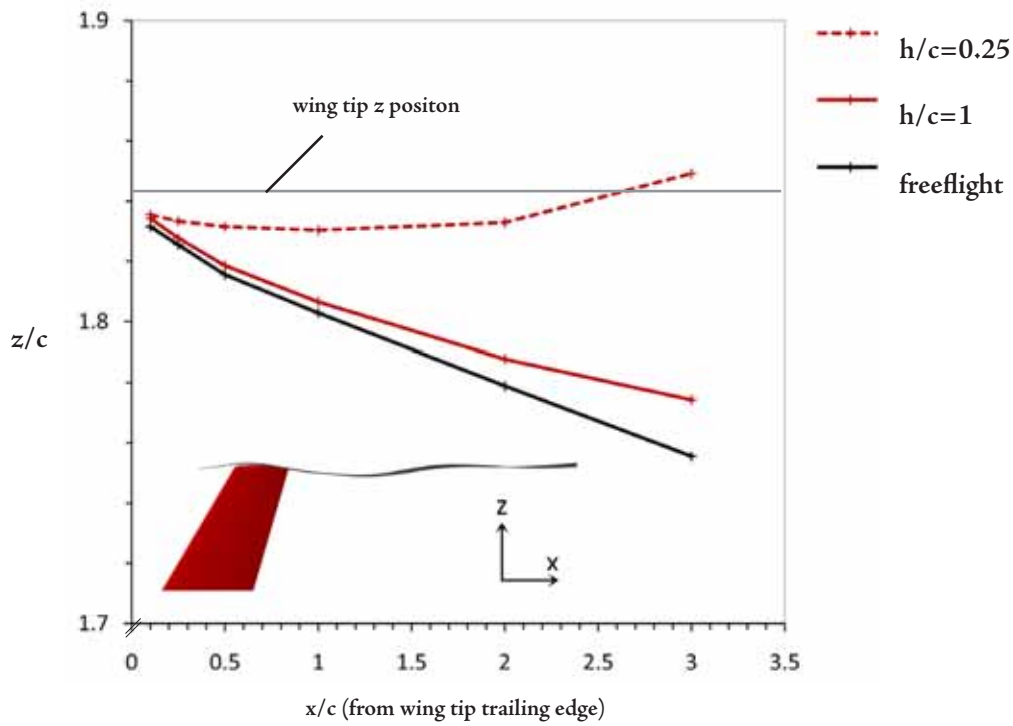
The effect which all of this has on the lift and drag coefficients is presented in figure 8.4. Despite the formation of the lower surface shock at  $h/c=0.1$  and  $0.25$ ,  $C_L$  continues to increase with decreasing ground clearance. The loading on the wing has changed significantly, however, as the majority of the lift is now generated over the inboard half of the wing, and the region close to the wing tip now generates very little positive suction.

Drag increases as the ground is approached and the shocks gain in intensity. At  $h/c=0.1$  the drag is approximately 80% higher than at  $h/c=0.25$ , due to the significant contribution in thickening the wake from the lower surface shock and the stronger upper surface terminating shock, as well as the separation which occurs close to the leading edge at the tip. The appearance of the lower shock at  $h/c=0.25$  results in an increase in

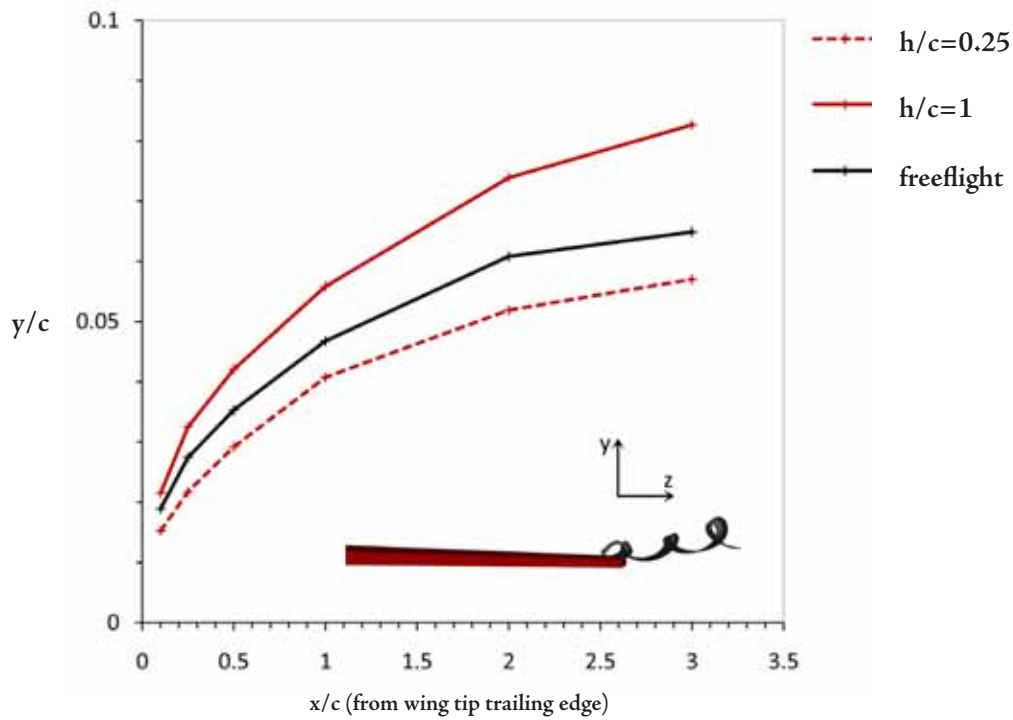
$C_D$  of 13% over the  $h/c=1$  case, which is a relatively modest increment considering that the increase from freeflight to  $h/c=1$ , where there is no lower surface shock, is 8.5%. To explain this, one must consider the contribution of induced drag made by the wingtip vortices.

Figures 8.6 and 8.7 show the vortex paths for freestream,  $h/c=1$  and  $h/c=0.25$  cases. At the two higher clearances, the vortex is drawn inboard from the tip in the  $z$ -direction. The movement into ground effect at  $h/c=1$  reduces this effect, but at  $h/c=0.25$  the vortex is observed to align almost parallel with the wing tip, and begins to travel outboard at the last measured point,  $3c$  downstream of the trailing edge at the wing tip, and thus does not interact directly with the wake from the main body of the wing as the vortices at higher clearances do. In the vertical sense in figure 8.6, the vortex deflects upwards from freeflight to  $h/c=1$ , but at  $h/c=0.25$ , this deflection is less than in freeflight, owing to the presence of the lower surface shock at the tip, which has a destructive effect on lift and thus induces a diminished upwash in that region.

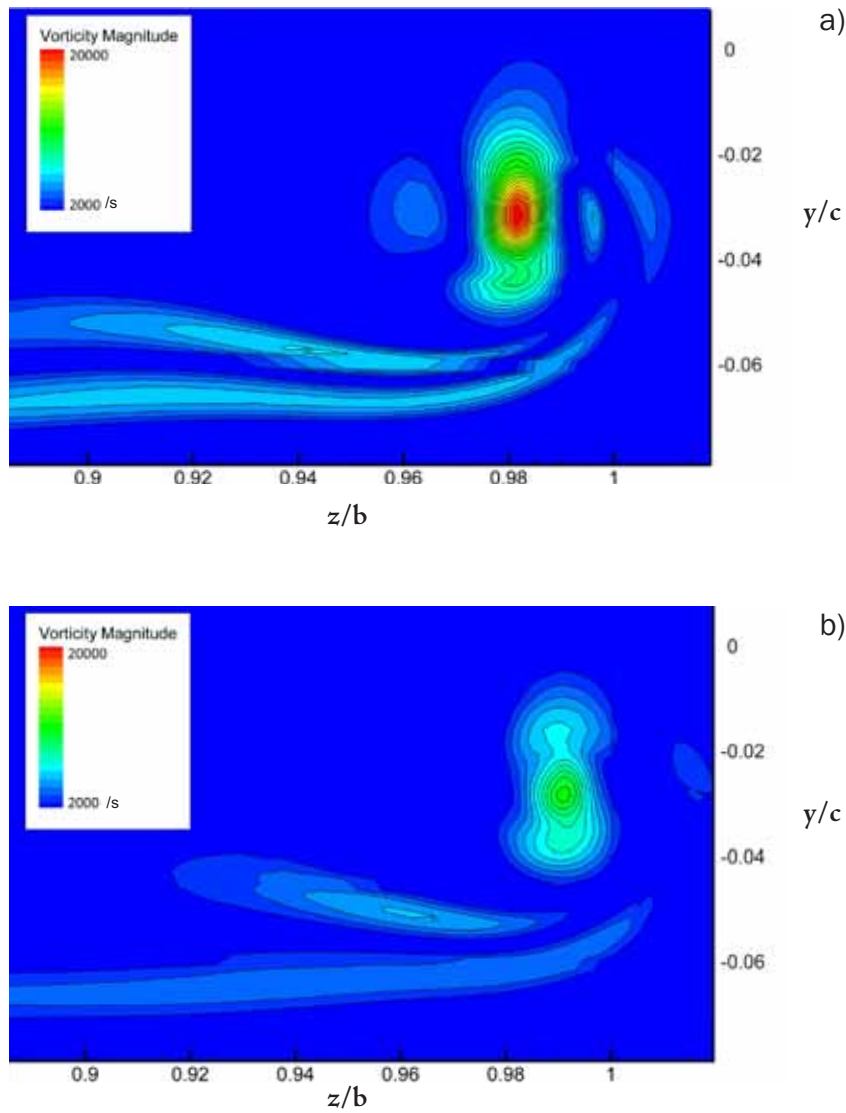
It seems logical that the strength of the vortex would increase with decreasing ground clearance. The higher pressure underneath the wing and the increase in lower pressure over the wing due to the increased effective angle of attack should result in a stronger vortex. However, the vorticity plots in figure 8.8 indicate that this is not the case at  $h/c=0.25$ . With the formation of the shockwave on the lower surface, and its accompanying low pressure region, the tendency of the flow to travel from lower to upper surface is curbed to an extent, reducing the intensity of the vortex. In addition, as ground clearance is reduced and the flow is increasingly constricted into a channel between the wing and ground, the flow acquires a stronger spanwise component. This observation agrees with the work of (Steinbach *et al.*, 1996), and is likely to be enhanced in the case of the M6 due to the sweep angle, which encourages flow to the wingtip. This enhanced velocity component, more exaggerated on the upper surface due to the higher local Mach numbers present there, counters the motion of the airflow from lower to upper surface and will be a contributing factor to the outwards lateral drift of the tip vortex downstream.



Wing tip vortex core paths in the z-direction (measured from the wing root), for freeflight,  $h/c=1$  and  $h/c=0.25$  cases.



Wing tip vortex core paths in the y-direction, for freeflight,  $h/c=1$  and  $h/c=0.25$  cases.



Contours of vorticity on a plane  $0.5c$  downstream of the wingtip for a)  $h/c=1$  and b)  $h/c=0.25$ .

### 8.3 Decreasing ground clearance for fixed Mach numbers

The remainder of this chapter describes results of a parametric study involving five Mach numbers (see table 8.1), four ground clearances and two angles of attack (see table 8.2). As in the similar table of the previous chapter, table 8.2 also highlights which simulations were run as transient cases, and those which featured any areas of local supersonic flow.

Table 8.1. List of Mach numbers and equivalent mean-chord-based Reynolds numbers

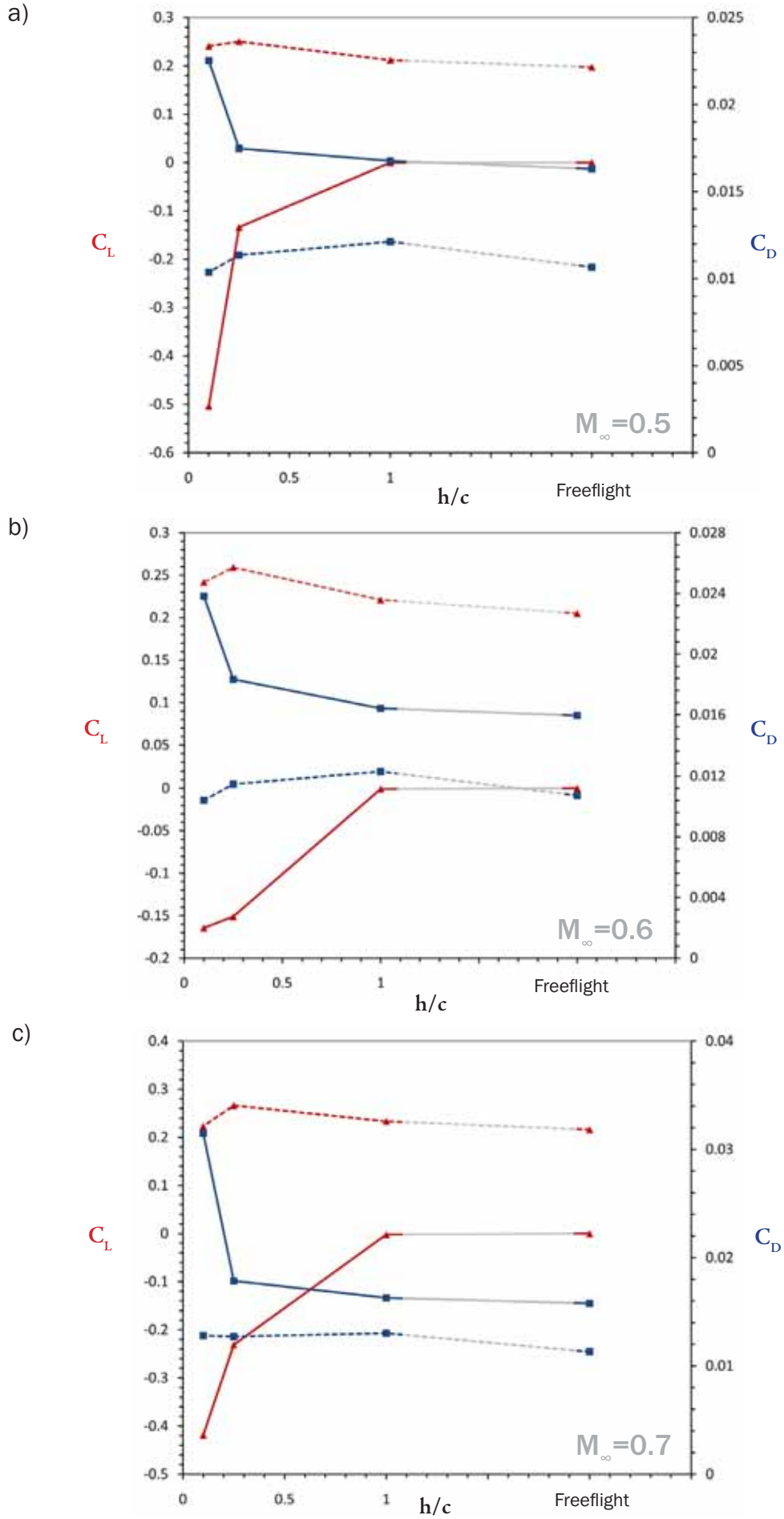
$M_\infty$	Reynolds Number
0.5	$7.46 \times 10^6$
0.6	$8.95 \times 10^6$
0.7	$10.45 \times 10^6$
0.8	$11.94 \times 10^6$
0.9	$13.43 \times 10^6$

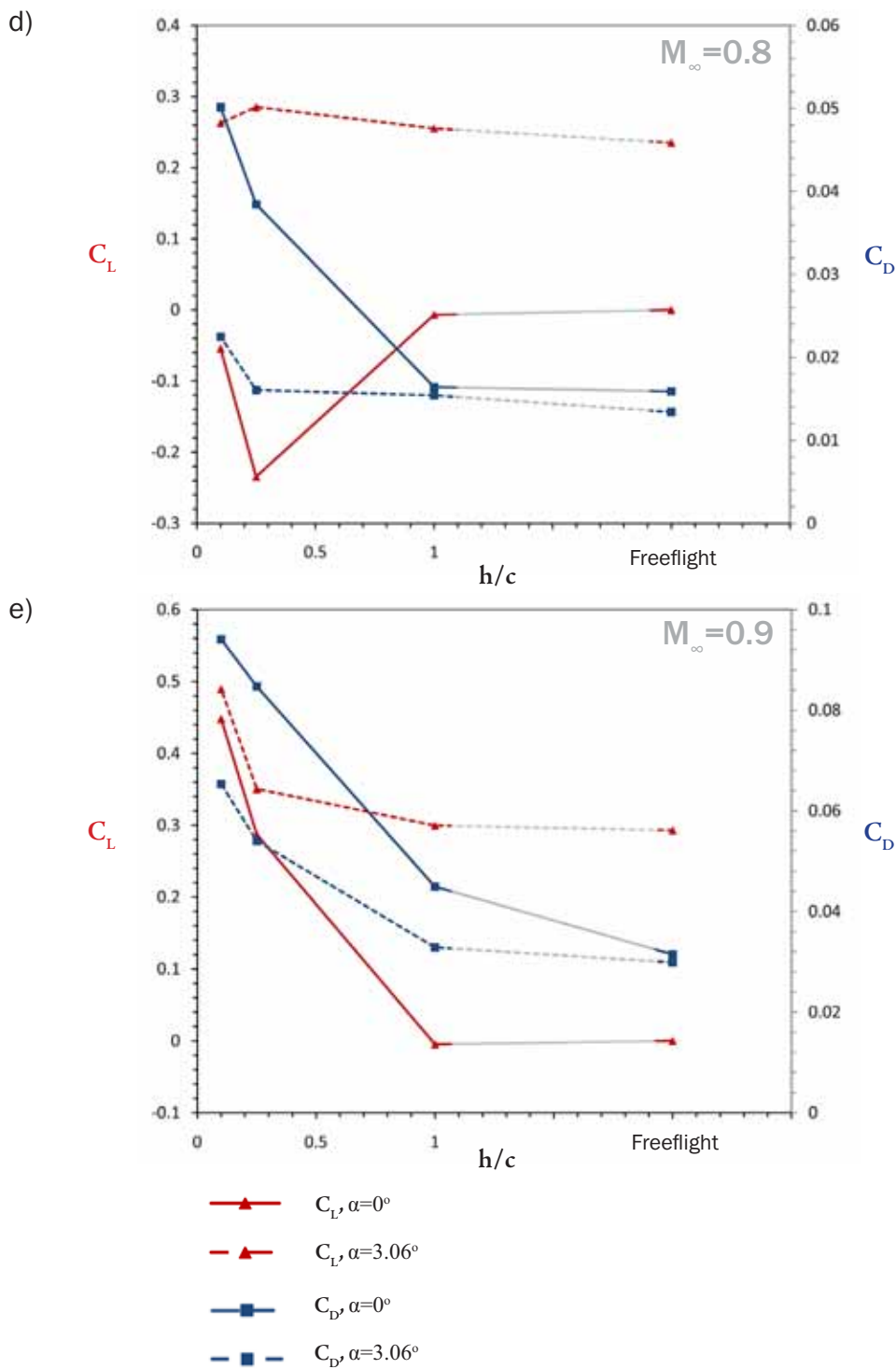
Table 8.2. List of simulations conducted, which cases were run as transient and which featured areas of supersonic flow around the wing.

$h/c = \infty$ (Freeflight)	$\alpha = 0^\circ$	$\alpha = 3.06^\circ$
$M_\infty = 0.5$		
0.6		
0.7		
0.8		
0.9		
$h/c = 1$	$\alpha = 0^\circ$	$\alpha = 3.06^\circ$
$M_\infty = 0.5$		
0.6		
0.7		
0.8		
0.9		
$h/c = 0.25$	$\alpha = 0^\circ$	$\alpha = 3.06^\circ$
$M_\infty = 0.5$		
0.6		
0.7		
0.8		
0.9		
$h/c = 0.1$	$\alpha = 0^\circ$	$\alpha = 3.06^\circ$
$M_\infty = 0.5$		
0.6		
0.7		
0.8		
0.9		

No supersonic flow	Areas of $M_t > 1$	Transient ~ steady state	Transient
--------------------	--------------------	--------------------------	-----------

8.9  
FIG

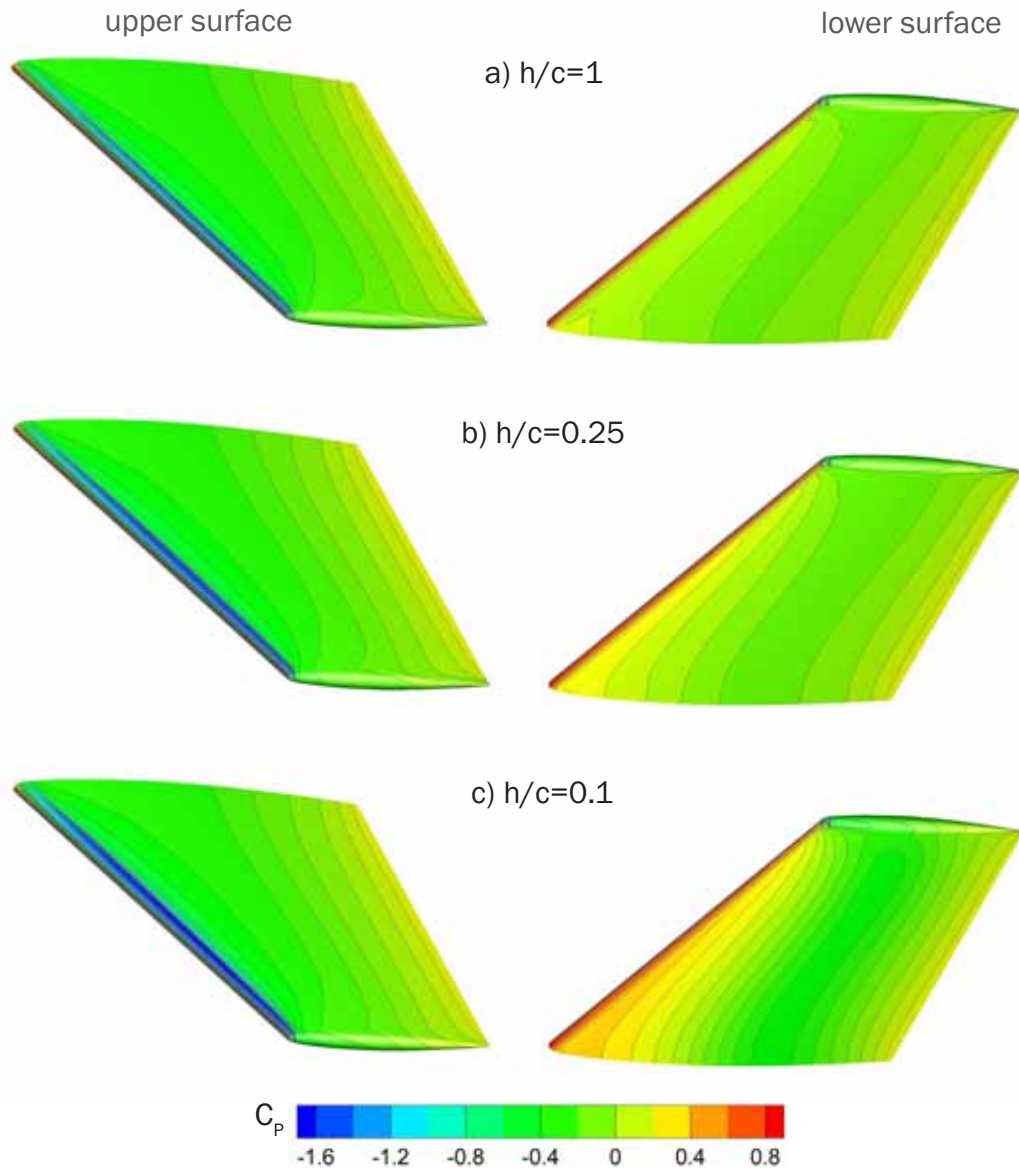




Lift and drag coefficients for  $0^\circ$ , and  $3.06^\circ$ , with decreasing ground clearance for a)  $M_\infty = 0.5$ , b) 0.6, c) 0.7, d) 0.8 and e) 0.9.

### 8.3.1 $3.06^\circ$ incidence

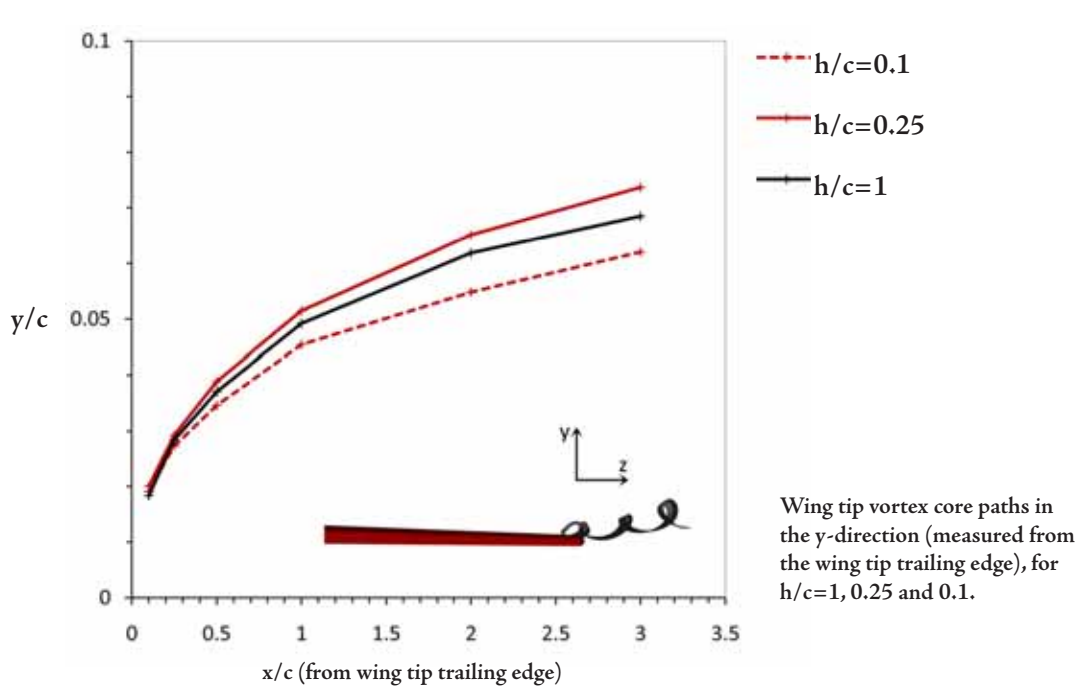
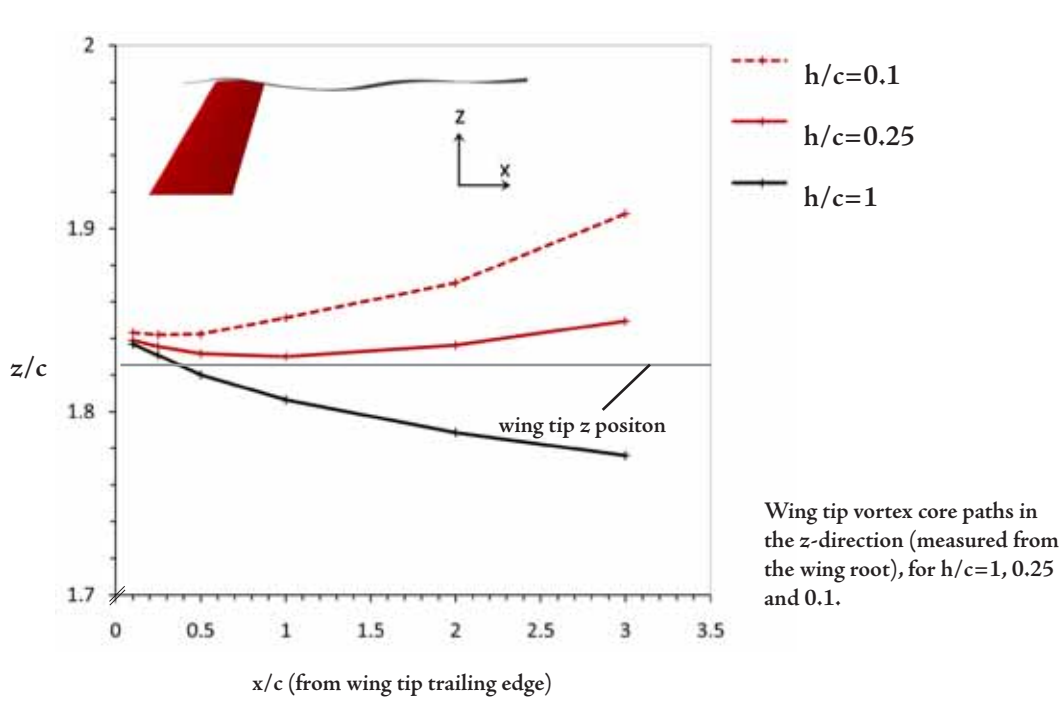
Figure 8.9 (pages 239-240) presents lift and drag coefficients for the wing as ground clearance is reduced for the five Mach numbers. From  $M_\infty = 0.5$  through  $M_\infty = 0.7$ , both



Contours of pressure coefficient with ground clearances of a)  $h/c=1$ , b)  $h/c=0.25$ , and c)  $h/c=0.1$ , at an incidence of  $3.06^\circ$  and  $M_\infty=0.7$ .

$C_L$  and  $C_D$  show very similar trends, albeit at different actual values (both increasing with Mach number); From freeflight to  $h/c=1$ , the lift and drag coefficients increase by approximately 7-8% and 12-13% respectively. From  $h/c=1$  to  $h/c=0.25$ , the lift coefficient in all three cases increases again by 13-15%, but  $C_D$  lowers by around 6-7% for  $M_\infty=0.5-0.6$ , and 3% for  $M_\infty=0.7$ . At  $M_\infty=0.7$ , where a significant shock wave has developed on the upper surface, the drag reduction is minimised as a result, and increases with ground proximity at higher Mach numbers.

From  $h/c=0.25$  to  $h/c=0.1$ , the lift coefficient drops by 5%, 7% and 13% for

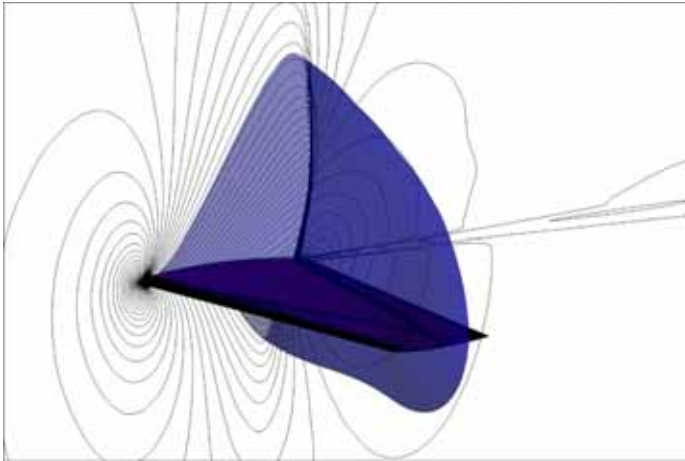


$M_\infty=0.5, 0.6$  and  $0.7$  respectively. At the same time,  $C_D$  drops by 9-10% for  $M_\infty=0.5-0.6$ , and is almost unchanged for the same cases at  $M_\infty=0.7$ . Therefore  $h/c=0.1$  and  $0.25$  emerge as a distinct peak in aerodynamic efficiency. At  $h/c=0.25$ , lift continues to rise even as there is a significant drop in drag, and at  $h/c=0.1$  the drop in lift is matched by reduced drag and a similar efficiency is retained. Therefore, only at the lower ground clearances is there an overall performance advantage over the freeflight case.

The increase in lift is caused by the factors already discussed in the previous section; the main contribution is from the marked augmentation of the high pressure under the wing towards the leading edge drawing the stagnation point downwards, increasing the effective angle of incidence of the wing and lending the pressure distribution a stronger front-loading of lift. The  $C_p$  contours in 8.10 illustrate this, and also show the way in which the pressure gradient on the lower surface becomes more pronounced at  $h/c=0.1$ . The drop-off in lift at this clearance comes as the flow which travels between the wing and ground is now sufficiently constricted as to experience a considerable acceleration. The accompanying pressure drop reduces the overall ability of the section to produce lift, and thus the wing, at this incidence, finds a peak  $C_L$  at  $h/c=0.25$ .

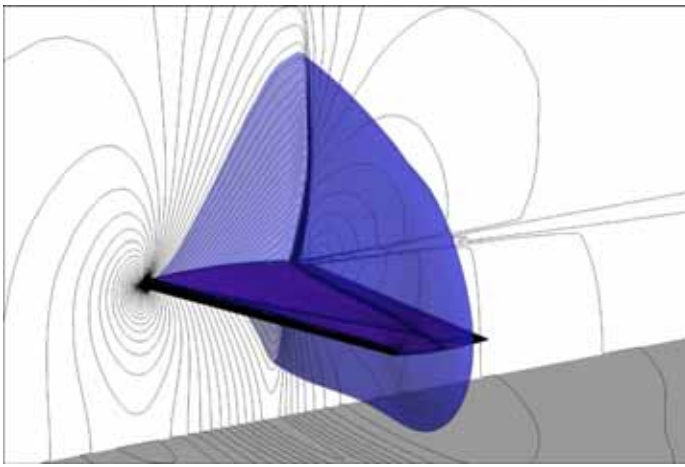
The reasons for the drop in  $C_D$  at  $h/c=0.25$  and  $0.1$  stem in part from the behaviour of the wing tip vortex. The strength of the vortex itself is reduced for the same reasons discussed in the previous section, and the changes to the path of the vortex core in ground effect are shown in figures 8.11 and 8.12. Here, it can be seen that at  $h/c=1$ , the vortex is still drawn markedly inboard from the tip, whereas at  $h/c=0.1$  it drifts outboard, and the flow near the wingtip is pushed out laterally due to the constraint of the ground. At  $h/c=0.25$ , however, the vortex remains largely parallel with the wing tip until 3 chord lengths downstream. Without any significant adverse increase in drag caused by the strengthening of shock waves in the  $M_\infty=0.5$  to  $0.7$  range, the drag reduction is significant. While this beneficial feature remains at higher Mach numbers, it becomes overwhelmed by the contribution to drag of the shock waves which form for cases beyond this freestream Mach number.

At  $M_\infty=0.8$ , in figure 8.9d, lift follows the same trend as the lower Mach numbers for decreased ground clearance, but  $C_D$  now increases with ground proximity across all cases due to an increase in shock strength. A lower surface shock is present at the two lower clearances, further contributing to the drag even though this is partially offset by the significant reduction in tip vortex strength. Nevertheless the increase in pressure difference between upper and lower surfaces, is enough to contribute sufficient extra suction to enhance the overall lift of the wing.

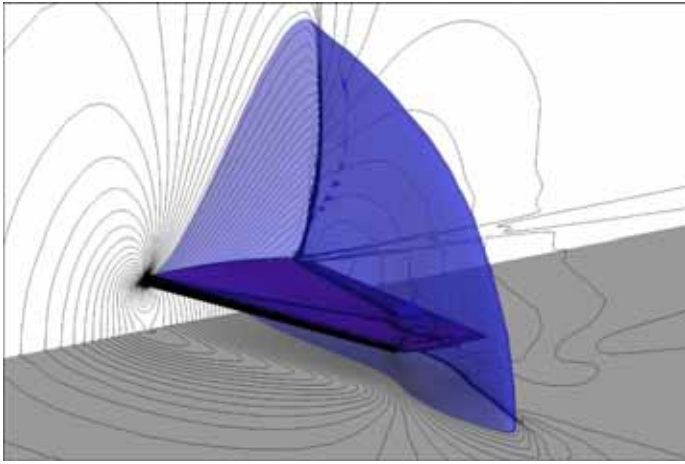


Contours of density on the wing, symmetry and ground planes, with regions of supersonic flow (blue) as indicated for  $M_\infty=0.8$  and ground clearances of a) freeflight (no ground, b)  $h/c=1$ , c)  $h/c=0.25$ , and d)  $h/c=0.1$ .

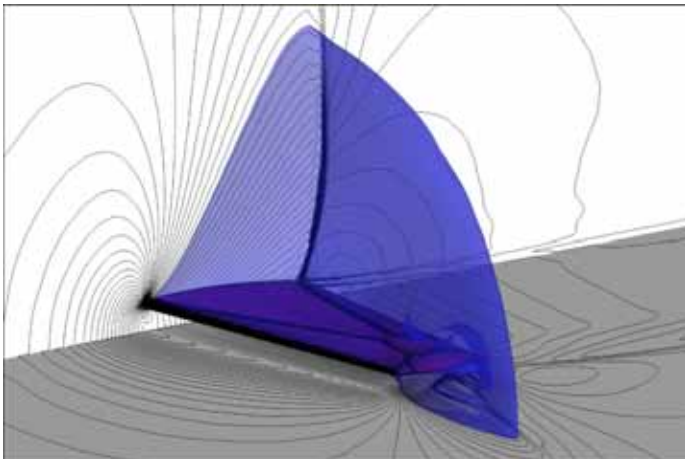
a)



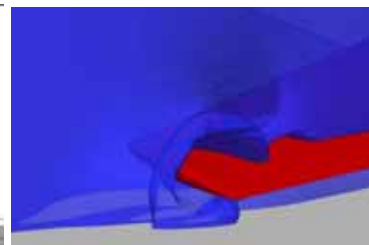
b)



c)



d)



rear view at wingtip d)

At  $M_\infty=0.9$ , figure 8.13 shows that the large-scale reflecting shock structures observed in the two-dimensional study are not present, confirming the opinion expressed in the previous chapter that the flowfields seen there at  $M_\infty=0.9$  were greatly exaggerated by the two-dimensional constraint on the flow. The flow is supersonic over a large proportion of the wing.

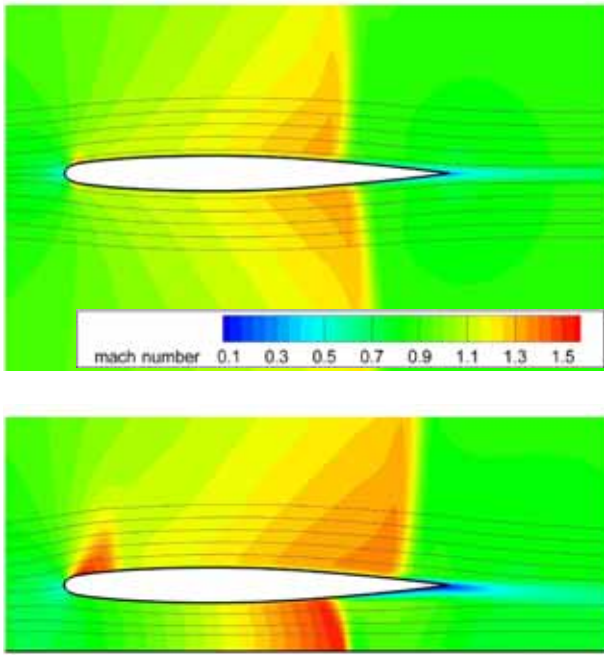
The drag increases sharply at  $h/c=0.1$  as the cone of subsonic flow initiated by wing tip separation at the leading edge is more exaggerated than at the Case 2308 conditions of section 8.1, as shown in figure 8.13. There is also separation at the foot of the merging shocks on the upper surface at  $h/c=0.25$ , and at  $h/c=0.1$  the two regions of separated flow are close together, leading to a very thick wake structure from the wing tip which further escalates the drag rise.

### 8.3.2 $0^\circ$ incidence

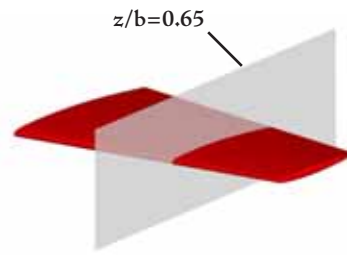
Returning to figure 8.9, at this incidence, the flow in freeflight is symmetrical (ignoring the effects of gravity) and therefore lift is zero. The ground has a marginal influence on the  $M_\infty=0.5$  flowfield at  $h/c=1$ , below which the acceleration of the flow between the wing and the ground, increasing the effective negative angle of incidence of the wing, produces a significant amount of downforce, particularly at  $h/c=0.1$  ( $C_L=-0.5$ ). At  $M_\infty=0.6$ , the  $h/c=0.25$  case behaves increasingly like the  $h/c=0.1$  case, with strong negative lift produced and a more marked increase in drag than at  $M_\infty=0.6$ . The  $h/c=0.1$  case produces less downforce than at  $M_\infty=0.5$ , however, as the flow under the wing becomes increasingly constrained by the ground and therefore a greater proportion of the mass flows around the upper surface or the side.

At  $M_\infty=0.7$ , a lower surface shock wave forms for the  $h/c=0.1$  and  $h/c=0.25$  cases, and this brings with it a 75% increase in drag at  $h/c=0.1$ , and an increase in downforce again, reversing the temporary trend seen at  $M_\infty=0.6$ . The shock on the  $h/c=0.25$  wing is small and does not interact with the ground.

At  $M_\infty=0.8$ , the drag rise is now significant at  $h/c=0.25$  as the strong shock meets the ground plane, although at  $h/c=0.1$  the downforce reduces. This returns the wing at



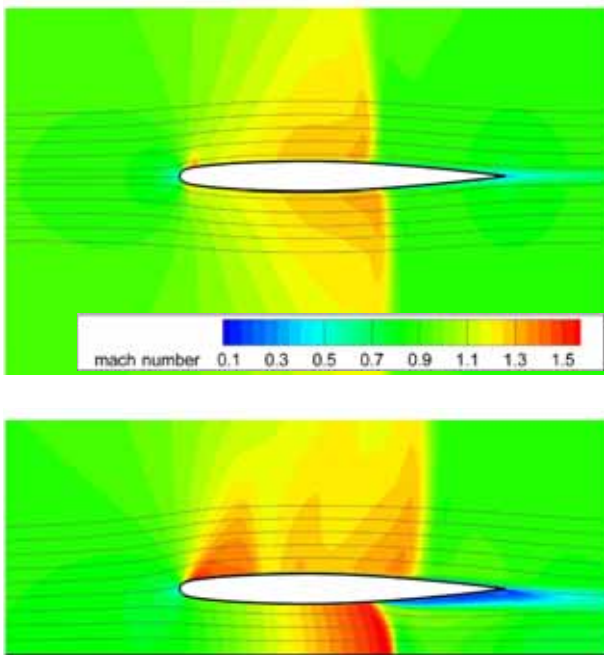
a)



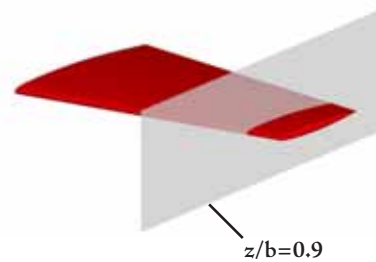
b)

Contours of Mach number and streamlines at  $z/b=0.65$  (station 3) for a)  $h/c=1$  and b)  $h/c=0.1$  at  $M_\infty=0.9$ .

8.14  
FIG



a)



b)

Contours of Mach number and streamlines at  $z/b=0.9$  (station 5) for a)  $h/c=1$  and b)  $h/c=0.1$  at  $M_\infty=0.9$ .

8.15  
FIG

this clearance to the effect seen in milder form at  $M_\infty=0.6$ ; with the shock spanning the wing on the undersurface, increasing freestream Mach number can push it back along the chord but flow increasingly diverts over the upper surface, reducing the effective negative angle of attack that the wing has acquired.

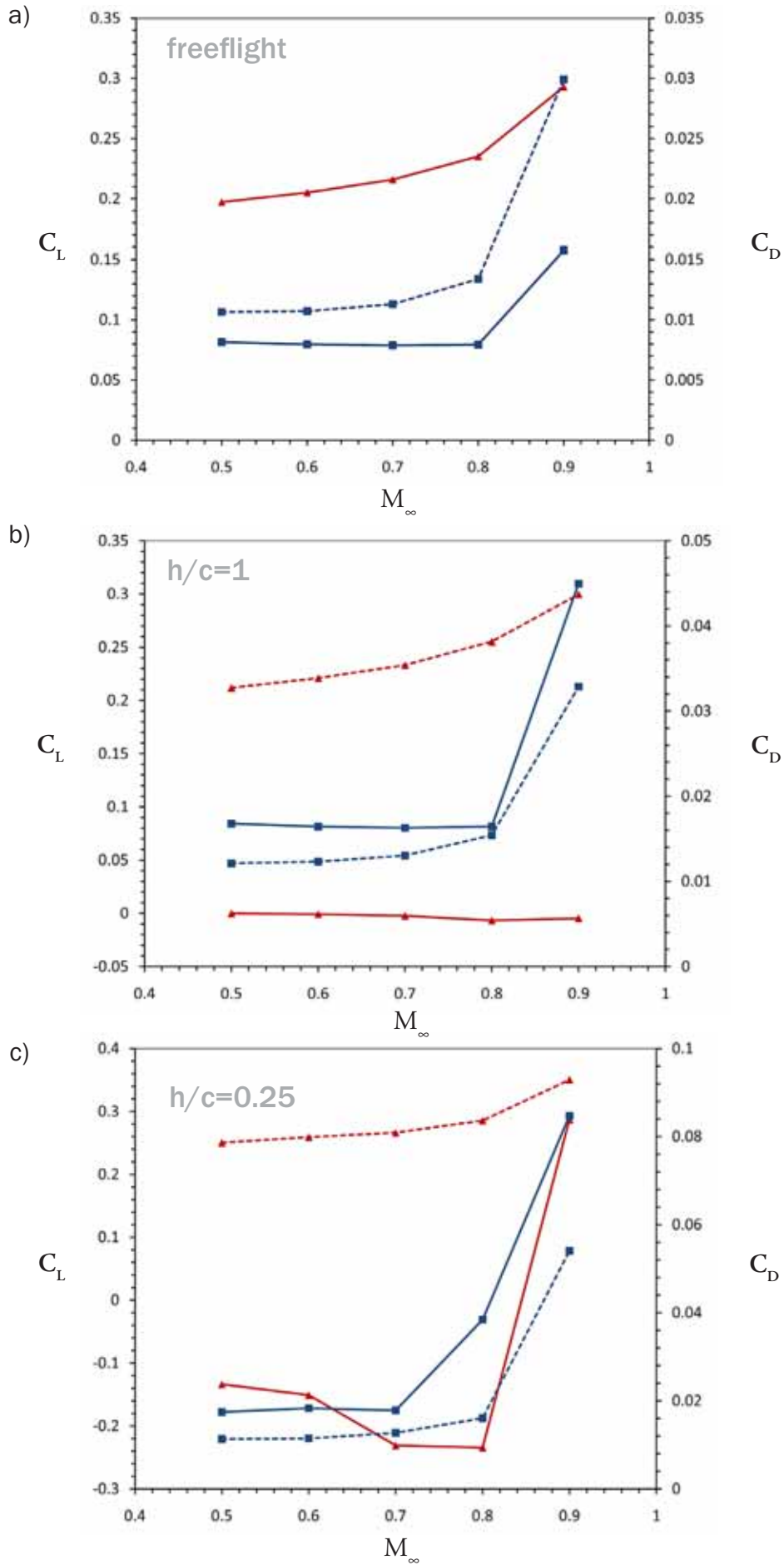
At  $M_\infty=0.9$ , the ground at  $h/c=1$  still has almost negligible influence on lift, but at all ground clearances drag increases with each increment to ground proximity, and the cases at  $h/c=0.25$  and  $0.1$  now produce levels of lift which are close to those produced by the wing at an incidence of  $3.06^\circ$ , marking a sudden and complete force reversal from the  $M_\infty=0.8$  cases at the same clearances. This is an extension of the trend seen previously, as the flow chooses to travel over the upper surface and around the side of the wing. This is illustrated in the streamlines and  $y$ -velocity contours shown in figure 8.14 and 8.15, which also highlights the markedly different shock formations on both surfaces between  $h/c=1$  and  $h/c=0.1$ .

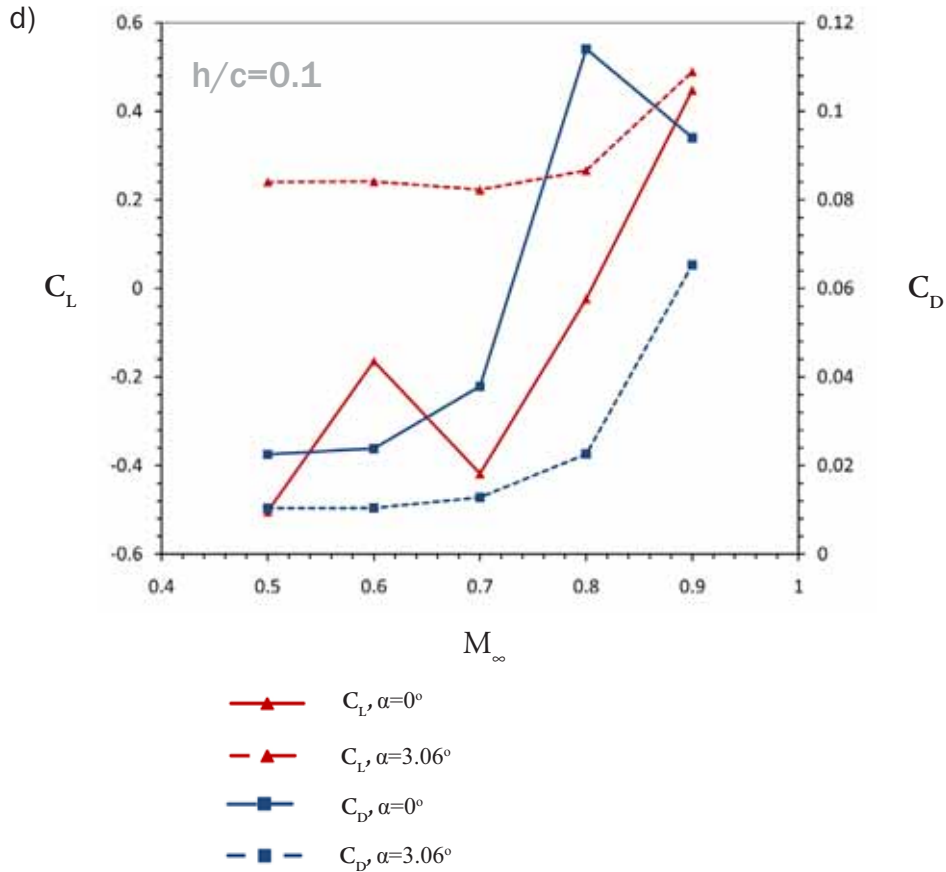
## 8.4 Increasing Mach numbers for fixed ground clearances

### 8.4.1 $3.06^\circ$ incidence

Looking briefly at the trends of  $C_L$  and  $C_D$  with increasing Mach number, the trends for lift and drag are very predictable at this incidence: lift coefficient generally increases non-linearly up to Mach 0.9 at all clearances, as does drag. The exception is the  $h/c=0.1$  case, where  $C_L$  actually falls slightly before improving at  $M_\infty=0.9$ , indicating that the increased tendency for separation and flow acceleration between the wing and ground at the point of maximum constriction is not balanced out by the greater levels of high pressure created on the forebody. The drag rise at this height as the wing moves from  $M_\infty=0.7$  to  $M_\infty=0.9$  is markedly more pronounced than at other clearances, and indicates an earlier onset of the transonic drag rise.

The most important conclusion to be drawn from these plots is that at  $M_\infty=0.8$  and  $0.9$ , it is not more efficient for the M6 to fly in close ground proximity than in freeflight, as confirmed by the  $L/D$  graph in figure 8.18. In Chapter 7 the  $h/c=0.1$  case for the two-dimensional aerofoil exhibited this trend at  $M_\infty=0.6$  onwards for a  $2.79^\circ$  incidence, and the other ground clearances generally retained an efficiency advantage until





Lift and drag coefficients for 0°, 3.06°, with increasing Mach number, for a) freeflight, b)  $h/c=1$ , c)  $h/c=0.25$ , and d)  $h/c=0.1$ .

$M_{\infty}=0.9$ . Here, at  $h/c=1$  the efficiency is less than in freeflight, due to the relatively larger increase to drag than lift. As has already been mentioned earlier in the chapter,  $h/c=0.25$  presents a fortuitous set of circumstances which produce favourable vortex behaviour while avoiding the more severe drag rises caused at  $h/c=0.1$  by more exaggerated shock strength, and thus retains an efficiency advantage until  $M_{\infty}=0.8$ . The formation of the lower surface shock at  $h/c=0.1$  for  $M_{\infty}=0.7$  immediately reduces the efficiency of the wing and it does not recover with increasing Mach number.

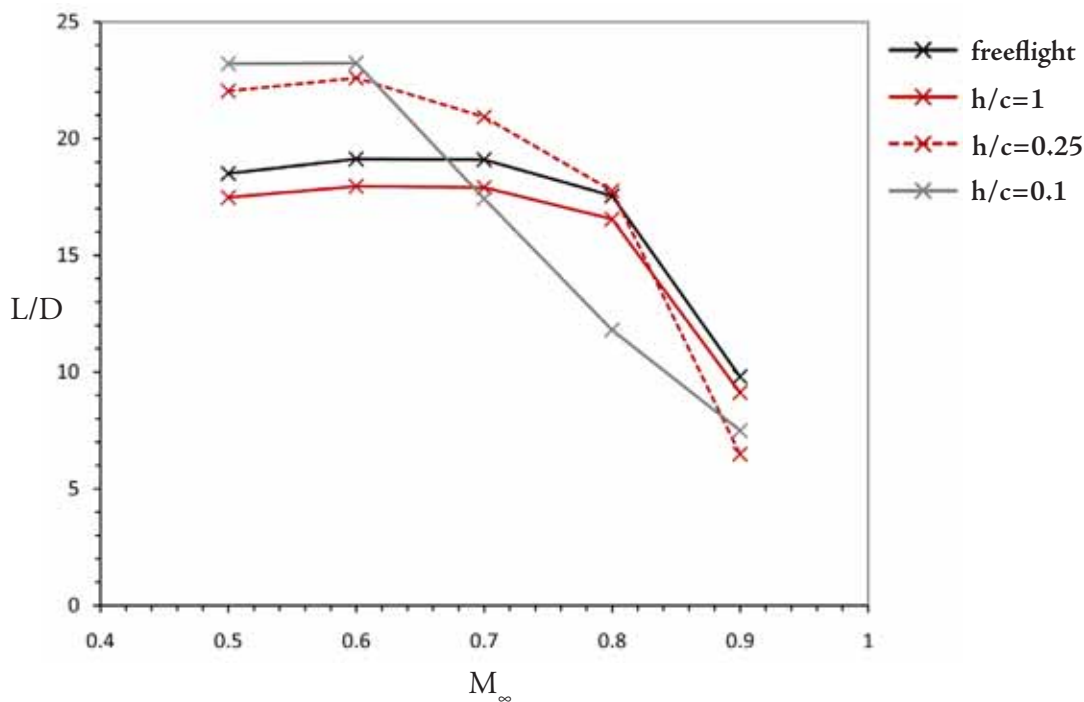
#### 8.4.2 0° incidence

At this incidence the trends with increasing Mach number are not as predictable. At  $M_{\infty}=0.8$  for freeflight conditions, the drag increases sharply due to the formation of upper and lower shock waves. This effect is exaggerated at  $h/c=1$ , but is most notable

at  $h/c=0.25$ , at which clearance  $C_D$  increases markedly at an earlier stage, between  $M_\infty=0.7$  and  $0.8$ , due to the lower critical Mach number of the section at that clearance. This effect is enhanced further still and occurs between  $M_\infty=0.6$  and  $0.7$  for the lowest ground clearance. Interestingly, at  $h/c=0.1$  the drag coefficient decreases from  $M_\infty=0.8$  to  $0.9$ . The reason for this is the force reversal occurring on the section; at  $M_\infty=0.8$  it still produces considerable downforce, and the flow under the wing is highly separated at the shock foot, particularly towards the wing tip. At  $M_\infty=0.9$  the section produces lift, and this provides something of a counterbalance for the separation on the underside, as proportionally more flow is directed over the wing and remains largely attached on the upper surface.

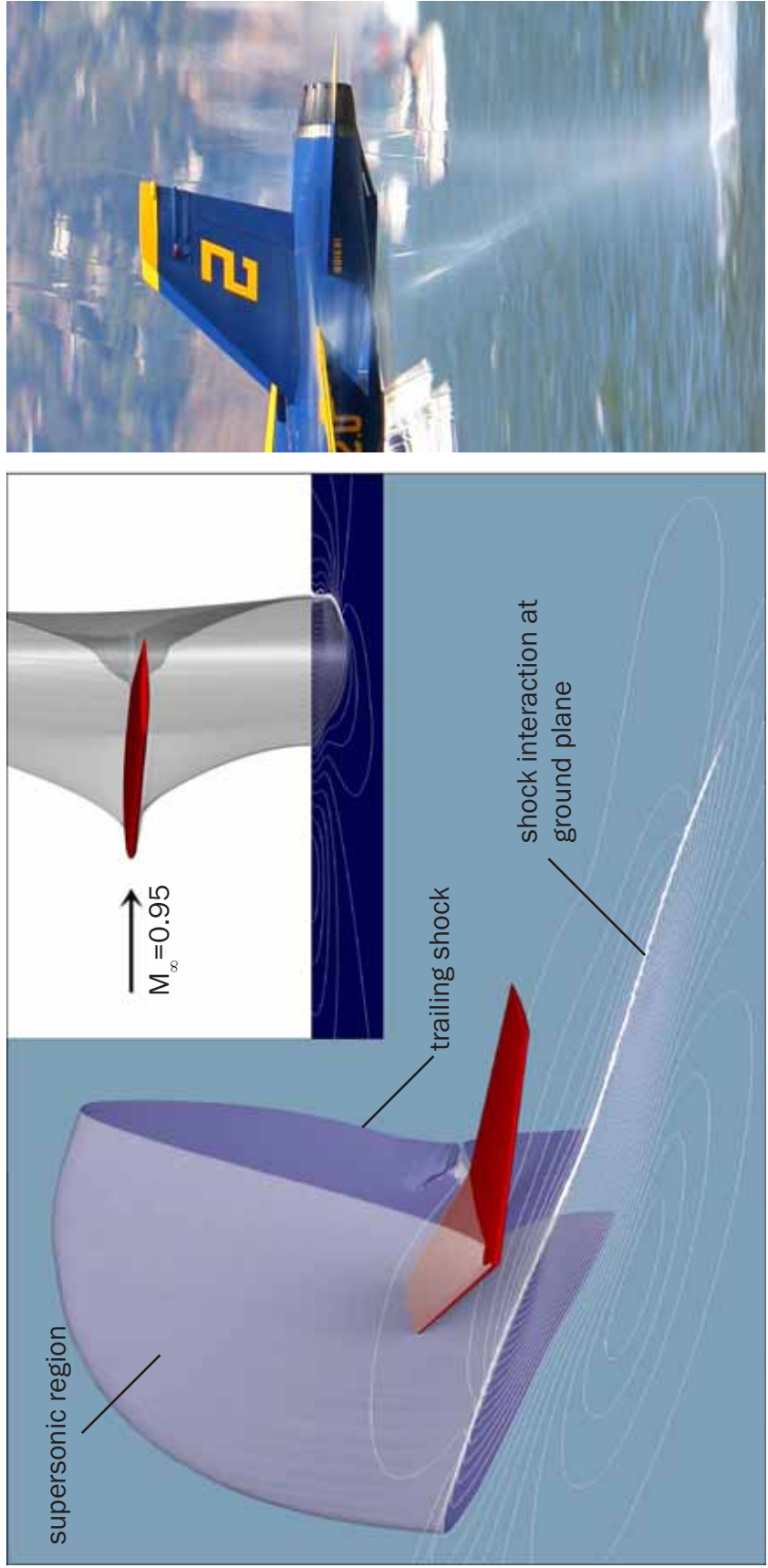
### 8.5 Isolated case at $M_\infty=0.95$

A final case was run for the wing at the  $0^\circ$  incidence for a brief comparison off freeflight and  $h/c=1$  conditions to loosely approximate the conditions of an extremely low-flying military jet performing a manoeuvre such as the “sneak pass” undertaken by the US



Aerodynamic efficiency,  $L/D$ , at  $3.06^\circ$  for different ground clearances as Mach number is increased.

8.17  
FIG



A qualitative comparison between shock structures at  $M_\infty = 0.95$  for CFD of the M6 wing ( $h/c=1$ , symmetry zone also shown) and an F/A-18 Hornet at approximately  $h/c=2$  and  $M_\infty = 0.93$  (photo: Matt Niesen).

Navy's Blue Angles display team, a photograph of which was first shown in figure 1.1. The comparison is qualitative, as the aircraft wing is more complex and the influence of the fuselage cannot be ignored, and furthermore the solid ground plane modelled in the CFD may not be a suitable proxy of the water surface which the aircraft flies over (though little observable deflection of the free surface can be seen in the image). Nevertheless, the shock structures which can be seen in figure 8.18 are very similar to those which can be discerned from an enlargement of the photograph in that region. The shock from the lower trailing edge interacts strongly with the ground, producing an inverted triangle pattern closed out by the reflected shock which is a strong normal recompression trailing the body. This trailing shock/ground interaction spreads laterally over a chord length from the wing tip, presenting a shock front which is considerably greater than at  $M_\infty=0.9$ . At that latter case, the graph in figure indicates that the wing is producing negligible lift, whereas at  $M_\infty=0.95$  it has a  $C_L$  of 0.495. We have already explored in the previous section the way in which at the lower ground clearances, for the highest Mach numbers, the  $0^\circ$  wing suddenly produces significant lift, and this is clearly true at higher clearances with continued increase in freestream Mach number. In practical terms, the results imply that if the aircraft were gently descending to this clearance for a pass at  $M_\infty>0.9$ , the ground effect is likely to provide a considerable increase in lift that would serve to push the aircraft upwards again. A sudden deceleration at a incidence could result in a sharp reduction in  $C_L$ .

## 8.6 Summary

Many of the trends observed for the two-dimensional study were also observed for the swept three-dimensional M6. For instance, low clearances and low incidence was liable to lead to the early onset of supersonic flow, including the formation of a lower surface shock, compared to freeflight cases. This lead to a sharp reduction in lift (or downforce at  $0^\circ$  incidence), and a significant increase in drag.

The increase to high pressure under the wing tended to be considerable close to the leading edge and inboard of the tip, and this coupled with the increased tendency of

flow to pass over or around the wing with the increasing constriction of greater ground proximity caused significant increases in lift. Shock-induced separation at the leading edge of the wingtip was found to be a large contributor to the high levels of drag produced at  $M_\infty=0.8$  and  $0.9$  for  $h/c=0.25$  and  $0.1$ .

At zero incidence the wing was found to produce downforce up until  $M_\infty=0.9$ , at which point  $C_L$  became positive as the flow increasingly diverted over the upper surface, as a culmination of a trend which began at the downforce peak at  $M_\infty=0.7$ .

At  $3.06\alpha$  incidence,  $C_L$  reached a peak at  $h/c=0.25$ , after which the lift dropped off as the acceleration of flow under the wing at the point of minimum clearance proved destructive to lift, and an increased tendency for separation at the shock feet was observed. Taking this incidence to be representative of a flight condition, it was shown that it was not more efficient to fly in ground effect at any clearance than in free unbounded flight for Mach numbers greater than  $0.8$ , as the increases to drag were not offset by continued gains in lift production.

It was also shown that the wing tip vortices, which travelled inboard to interfere with the wake at freeflight and  $h/c=1$  conditions, tended to be pushed increasingly outboard of the wing with decreasing ground clearance. They were also observed to decrease in strength with ground proximity, as an increase in spanwise flow to the tip of the air which was being increasingly accelerated over the upper surface countered the flow from lower to upper surface, and the acceleration of flow under the wing created greater low pressure there which led to a weaker tendency of the flow to be drawn to the upper surface at the tip.

Although changes to lift and drag were less sudden than with the two-dimensional RAE2822, it is difficult to discern the influence of the wing sweep and curvature of the wing section from this study alone. However, one can make a similar conclusion that it would be impractical to fly in sustained ground effect at transonic speeds, and at the least a sophisticated control system would be required to account for the large-scale changes to lift and drag which can occur with minor changes to altitude and attitude. The decreased efficiency in ground effect at such Mach numbers would invalidate the reason

for attempting to fly in ground proximity in the first place, although with optimised wing design (use of an endplate, flatter lower surface, less curvature at the leading edge and a sweep and taper appropriate for the design conditions) the critical effects may well be delayed until much higher  $M_\infty$  than in the present study.

# Chapter: A Supersonic Projectile in Ground Effect

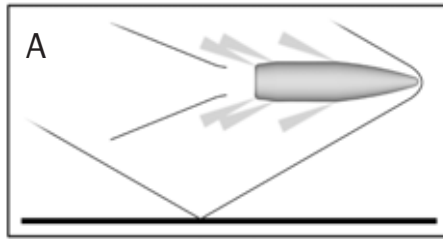


*Flow around a Mach 2.4 NATO 5.56mm projectile fired in close proximity to a ground plane was investigated, as a direct numerical reproduction of the live-range experiments described in Chapter 3. A non-spinning half-model and a full, spinning projectile were examined to clarify the influence of rotation. Multiple ground clearances were tested to obtain clear trends in changes to the aerodynamic coefficients, and the three-dimensional propagation and reflection of the shock waves is considered in detail here. The behaviour of the flow in the near wake was also studied as ground clearance was reduced.*

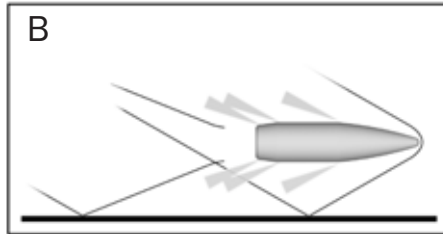
## 9.1 Introduction

Shock reflections from the ground plane visibly affect the flowfield around the projectile as was seen in chapters 4 and 5; this degree of influence is dependent on the ground clearance. The problem is unusual in that it involves a near-inviscid initial regular shock reflection at the ground plane, followed by both strong and weak shock/boundary layer interactions in a strongly three-dimensional flowfield.

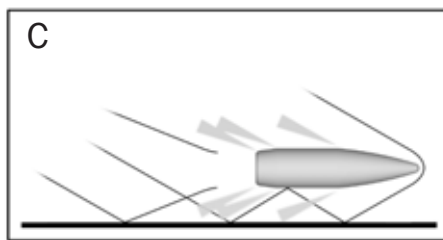
The types of ground effect flows which were observed from the schlieren of the live-range experiments described in Chapter 3, and three distinct categories have been proposed by the author, as shown in figure 9.1 and described in table 9.1.



**Type A** Shock reflection into far wake, negligible influence on projectile.



**Type B** Shock reflection into near wake, mild influence on wake, drag



**Type C** One or more shock reflections onto projectile and into wake, influences all aerodynamic characteristics

Interpretations of observed shock reflection interaction scenarios, as categorised into three types.

A Type A reflection interaction involves the reflection of the bow shock into the far wake, and the recompression wave trailing the projectile reflecting into the wake further still downstream. Although the wake thickens slightly and thus the drag on the projectile is not completely unaffected, the overall influence on the aerodynamic forces and moments experienced by the projectile is negligible. A Type B case involves the bow wave reflection impinging on the near-wake of the projectile (defined in this case as less than 1 projectile diameter from the base, which was observed to be the approximate maximum extent of recirculating flow for a freeflight case). The wake experiences a deflection due to the magnified pressure difference between the region below the wake and that above, and consequently the drag and pitching characteristics of the projectile would be affected as the base pressure is reduced. In a Type C reflection interaction, the bow wave reflects to impinge on the projectile body one or more times, and the recompression shock reflects into the wake to produce its own strong interaction. All aerodynamic forces and moments acting on the projectile are affected to varying extents by this scenario.

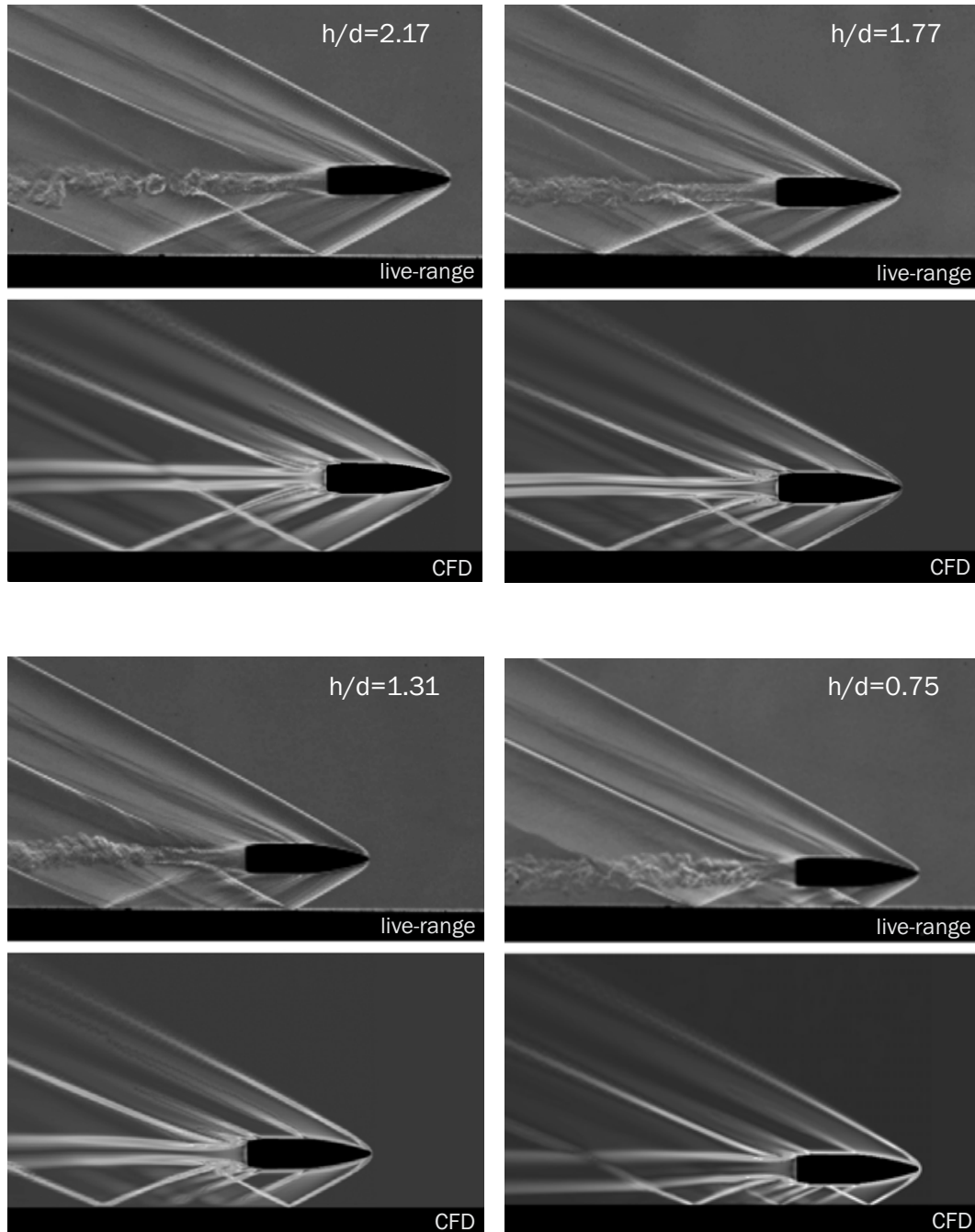
Table 9.1. CFD cases for live-range comparisons

h/d	Mesh Cells (after adaption)	Reflection Interaction Type
Freeflight	15.7x10 <sup>6</sup>	n/a
2.17	18.5x10 <sup>6</sup>	A
1.77	17.2x10 <sup>6</sup>	A
1.31	14.4x10 <sup>6</sup>	B
1	13.8x10 <sup>6</sup>	B
0.75	13.2x10 <sup>6</sup>	C
0.5	12.6x10 <sup>6</sup>	C
0.42	12.2x10 <sup>6</sup>	C
0.365	12.1x10 <sup>6</sup>	C
0.2	11.8x10 <sup>6</sup>	C

Observations from experimental schlieren video (as described in Chapter 3) of a Type C case showed that the flowfield around the projectile as it moved over the leading edge of the ground plane was complex and highly transient. Although it has not been modelled in the present CFD, it is worth describing; a series of reflections of shock and expansion waves occur, with the strong bow shock reflection re-impinging on the projectile body, and the lower recompression wave similarly reflects back into the wake further downstream. The wake itself adjusts over time to the changed flowfield and although the waves from the upper portion of the projectile remain essentially unchanged from freeflight conditions, the altered wake state affects the angle of the recompression shock. A thin boundary layer forms on the ground, though there is no evidence of any strong shock interactions due to its presence, and the reflection patterns remain highly regular, indicating a very small degree of influence.

Once the full flowfield has adjusted to the new conditions produced by close ground proximity, the shocks and their reflections are highly consistent in location and behaviour. Only the turbulent wake continues to develop over time, along with mild wave interferences, produced by the knurled strip, which are not thought to affect the aerodynamic performance of the projectile in any irregular fashion.

Given the limited imaging field (105mm x 87mm), changes to the projectile trajectory or incidence were not readily discernable from the video, apart from a small



Instantaneous schlieren images from time-resolved live-range footage with numerical schlieren comparisons showing good agreement with regards to shock angles and wake disturbances.

movement towards the ground. As far as could be ascertained given the resolution of the still images, this deviation was consistent in both freeflight and ground effect cases and thus can be wholly attributed to gravity, assuming a consistent firing angle (as confirmed from the schlieren).

## 9.2. Results and Discussion

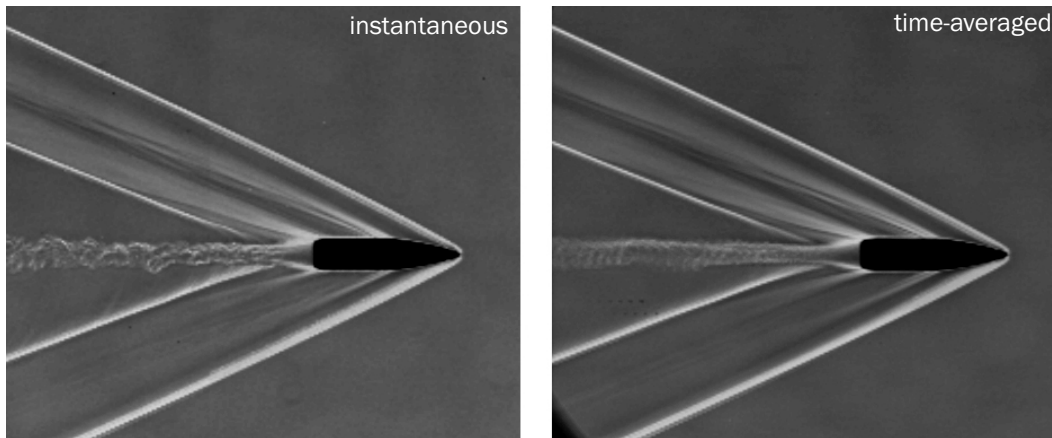
### 9.2.1 Comparisons to live-range experiments

Table 9.1 outlines the CFD cases for simulations of the projectile under the live-range conditions. All ground clearances were examined for both a spinning and non-spinning (half-model) projectile.

Ground clearances of  $h/d=2.17, 1.77, 1.31$  and  $0.75$  equate directly to experiments, for which numerical schlieren comparisons to instantaneous stills from the experimental video are presented in figure 9.2. Qualitatively, the images show good agreement for the shock locations and behaviour in reflecting from the ground plane. At  $h/d=2.17$  and  $1.77$ , which represent type A reflection interaction cases, the bow wave reflecting from the ground plane passes relatively unaffected through the recompression shock and interacts with the wake several projectile diameters downstream of the projectile base. The wake itself thickens slightly but the wave itself passes largely unaffected through it, interacting with the recompression shock in the farfield.

At  $h/d=1.31$ , which is of type B, the bow wave reflection interacts strongly with the near wake and does not reach the farfield with any significant strength. The wake itself is deflected upwards and the formation of the recompression shock is affected, resulting in a slightly adjusted shock angle as viewed on this plane. The reflection of the recompression wave itself causes a noticeable downwards deflection in the wake far downstream of the projectile base.

At  $h/d=0.75$ , a type C reflection interaction occurs, with the bow shock reflecting onto the projectile, impinging on the main body to the rear of the c.g., resulting in a subsequent secondary reflection from the projectile to the ground, which itself reflects into the wake region. At this point it largely dissipates, and the wake is drawn markedly towards the ground. As the pressure distribution changes over the projectile itself, the recompression shock is altered, with the region of the wave in closest proximity to the ground turned towards the ground plane, and reflecting into the wake to thicken it further while at the same time turning it back towards a streamwise alignment.



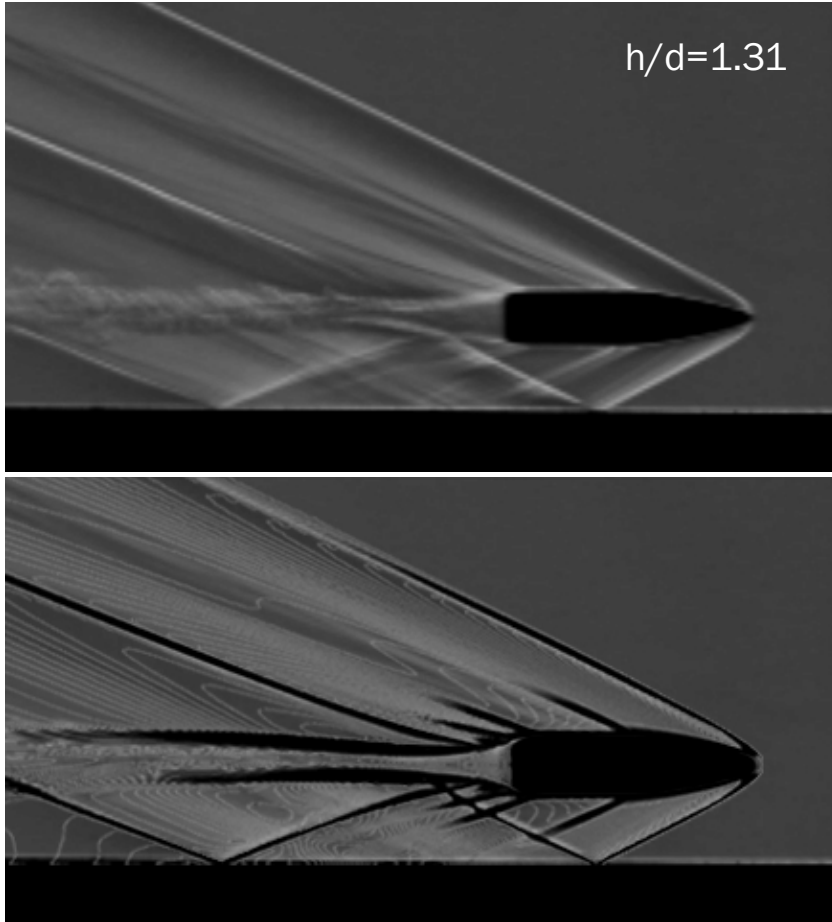
Instantaneous vs. time-averaged schlieren images from the live-range experiments.

In all cases, the angle of the recompression shock is also strongly influenced by the way in which the shear layer leaves the base of the projectile and forms the general outline of the wake region - the disintegration of the shear layer into a turbulent tumble at approximately  $1d$  from the base is a purely transient phenomenon not well represented in the steady-state CFD. However, when approximately 30 still images from the experiments are manually overlaid, frame by frame, a pseudo-steady flowfield more akin to the CFD begins to emerge, further highlighting the steady nature of the shock waves around the projectile. Here, in figure 9.3, the extent of the shear layer and wake is considerably clearer than in the instantaneous still, and thus a more appropriate comparison to the CFD is possible; this technique has been used to create the comparisons between CFD and experiment in figures 9.4 and 9.5, where excellent agreement between shock angles and locations is shown. Again, these figures contrast a type B and type C interaction, whereby the wake of the  $h/d=1.31$  case is observed to experience a slight upwards deflection as the first reflection of the bow shock interacts with the flow behind the projectile base. At  $h/d=0.75$ , the wake features a noticeable downwards deflection. We will return to consideration of the wake in section 9.2.5, where the mechanisms at work are discussed in detail.

The lowest ground clearance observed in the experiments was  $h/d=0.75$ , and for closer ground proximity, CFD provides the only results. Figure 9.6 shows contours of density for some of the clearances below  $h/d=0.75$ , in contrast to those matching

9.4

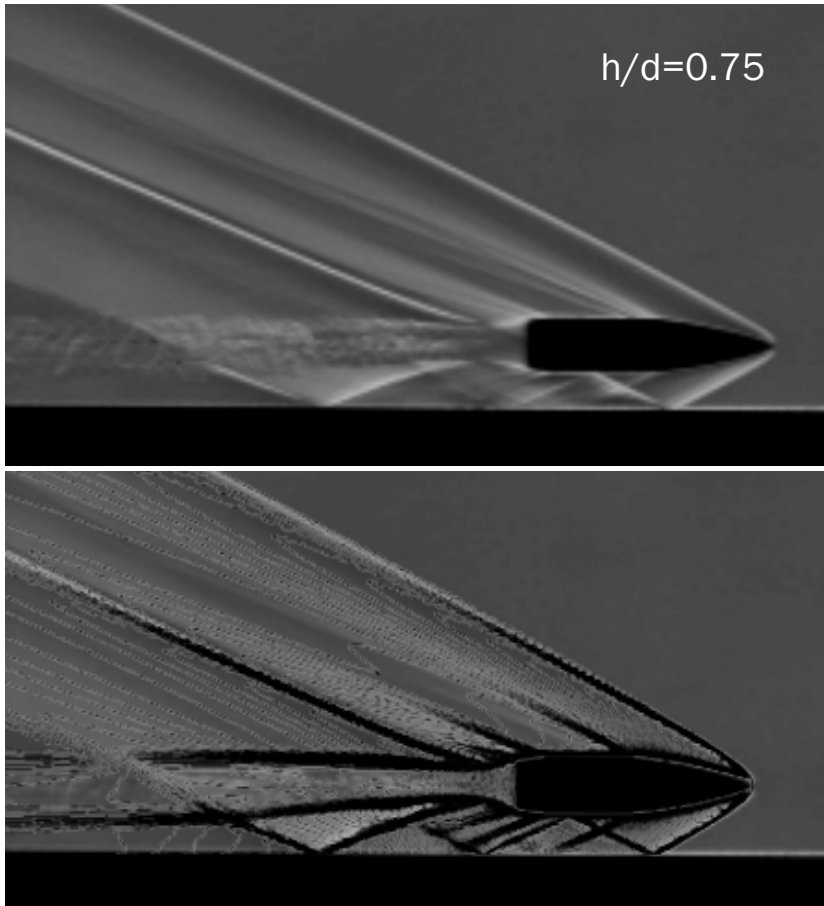
FIG



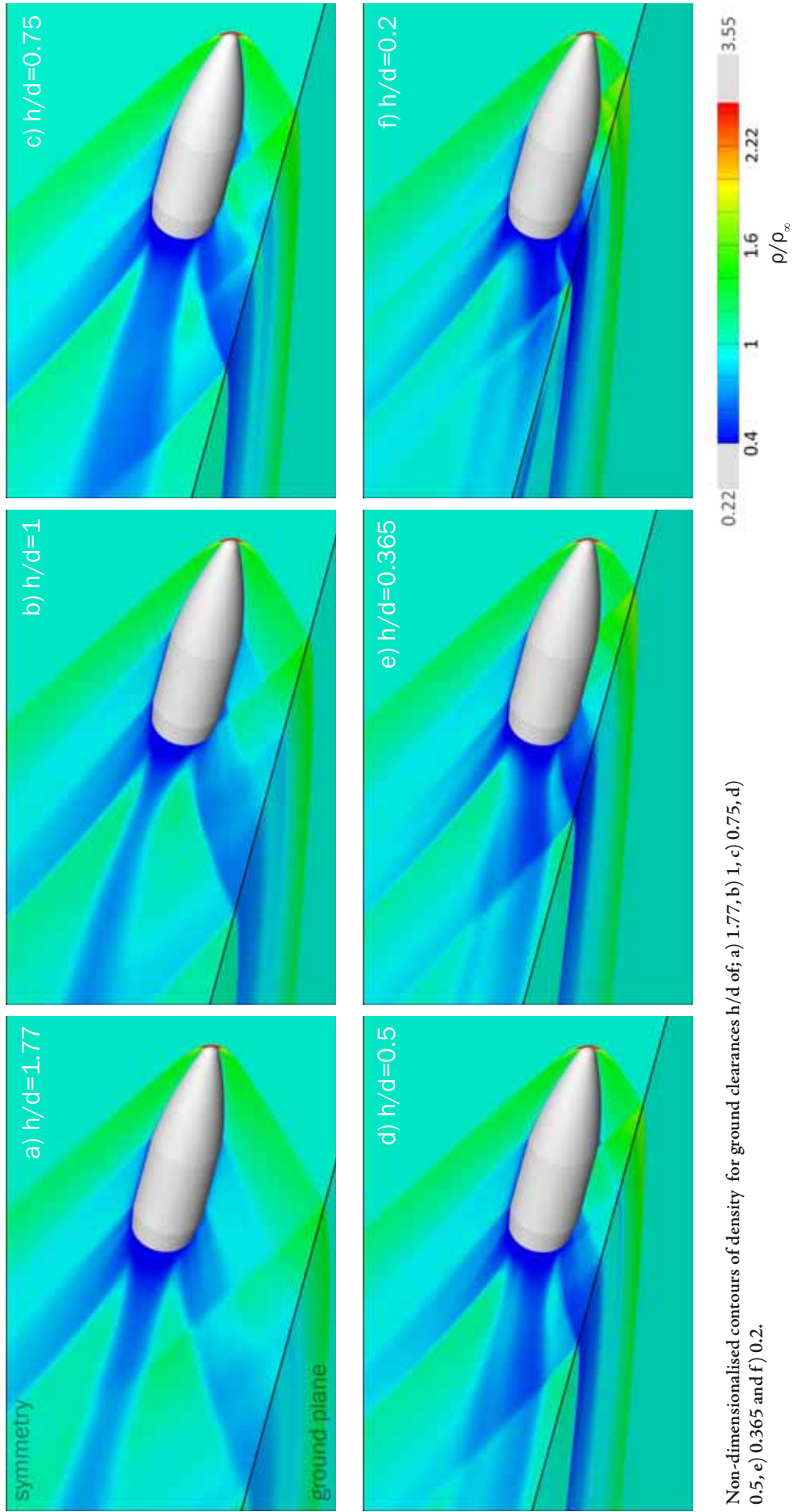
Time-averaged (over  $5 \times 10^{-5}$ s) schlieren images from the live-range video footage (top) for  $h/d=1.31$  with CFD contours of density overlaid (bottom).

9.5

FIG



Time-averaged (over  $5 \times 10^{-5}$ s) schlieren images from the live-range video footage (top) for  $h/d=0.75$ , with CFD contours of density overlaid (bottom).



Non-dimensionalised contours of density for ground clearances  $h/d$  of: a) 1.77, b) 1, c) 0.75, d) 0.5, e) 0.365 and f) 0.2.

experiments. The contours have been clipped to provide better resolution of the shock waves and their reflections.

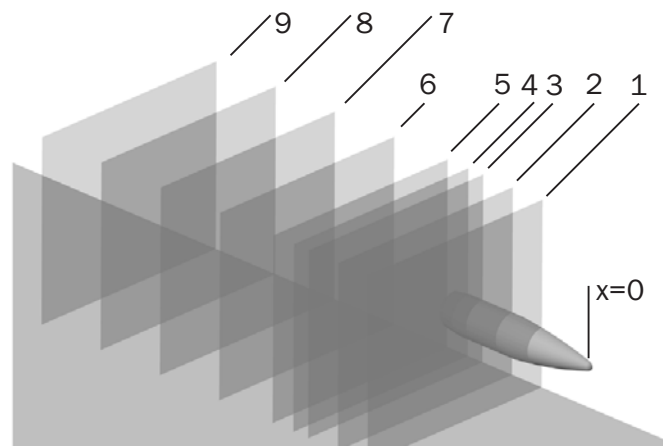
### 9.2.2 The three-dimensional flowfield

In the images presented to this point, the flow has largely been examined on a plane perpendicular to our viewpoint and the ground plane. For these ground effect cases, however, it can be highly misleading to ignore the strongly three-dimensional effects of the shock reflections. The waves which reflect from the ground and impinge upon the projectile do not simply reflect at an angle consistent with oblique shock/boundary layer interaction theory: this only holds for the wave as it exists purely on the  $0^\circ/180^\circ$  ( $z=0$ ) plane, or the symmetry plane for the half-model simulations.

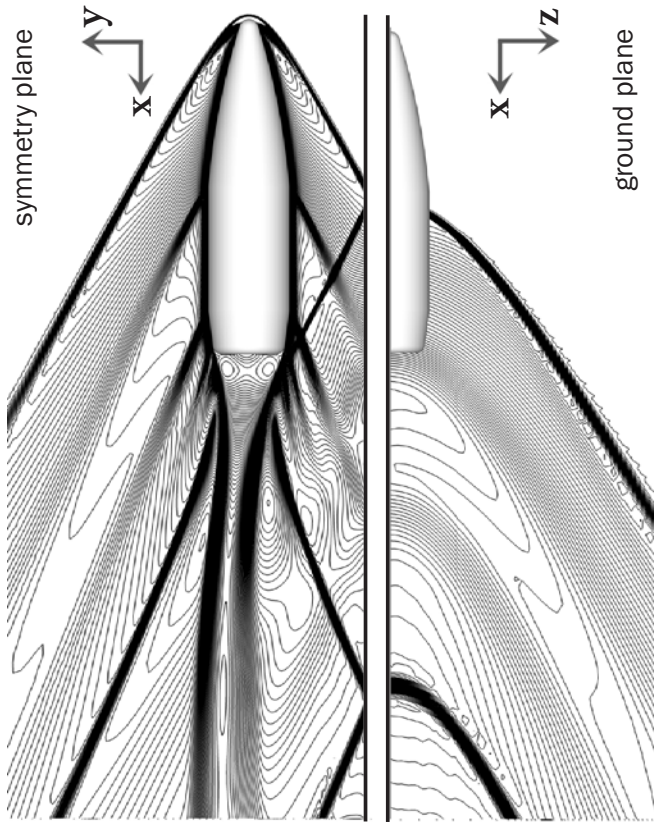
Figure 9.7 shows slice locations chosen to analyse the three-dimensional flowfield for shock propagation and other flow features. Figure 9.8 presents density contours on the symmetry and ground plane around the non-spinning projectile at an example ground clearance of  $h/d=1$ . To better understand these images we must consider the flowfield in a three-dimensional way. Figure 9.9 presents numerical schlieren on 8 slices taken through the flowfield at various positions of interest.

Slice 2 (2.37d from the nose of the projectile) presents the initial reflection of the bow wave from the ground plane as the rest of the wave propagates conically outwards. At this point an extremely thin boundary layer begins to form on the ground due to the

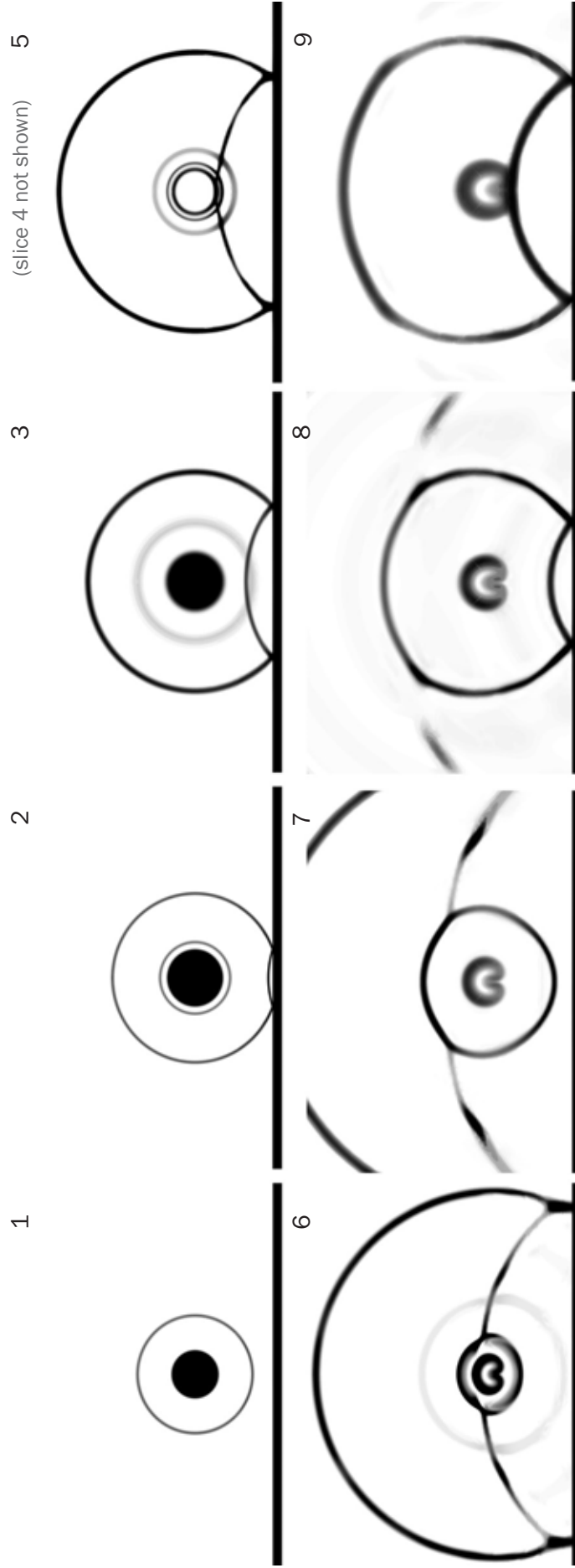
9.7  
FIG



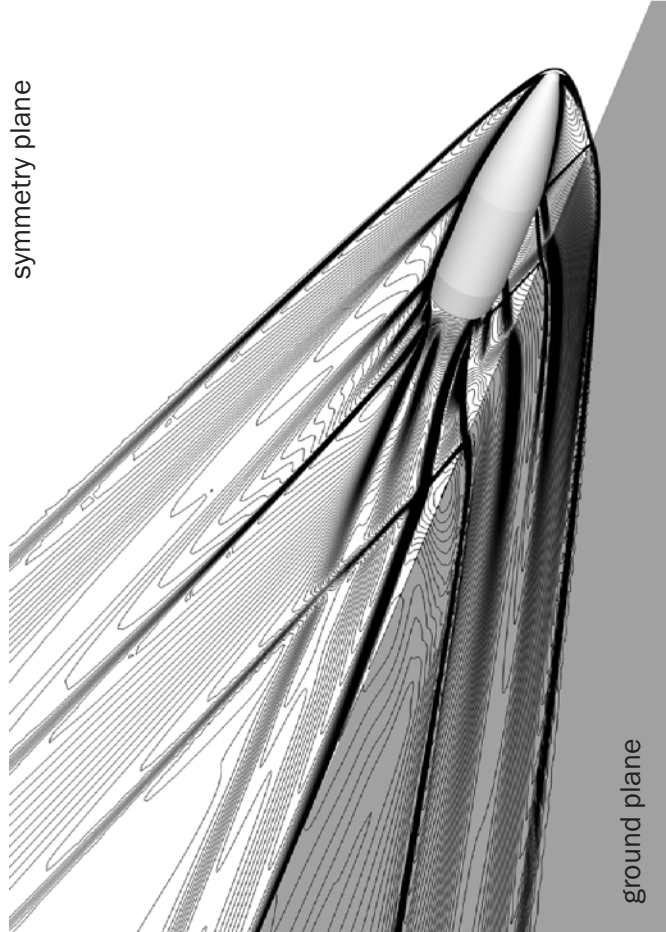
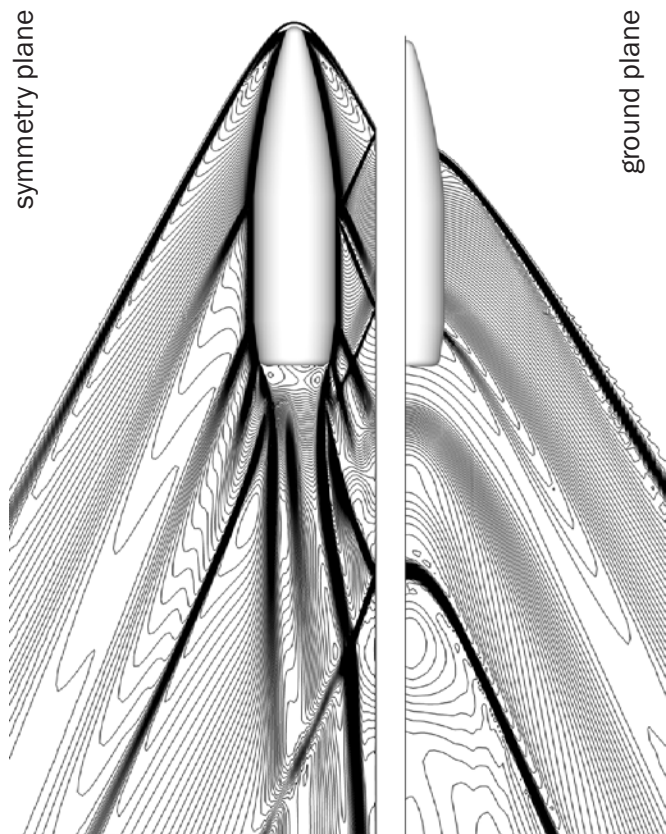
Slice locations from projectile nose; 1) 1.49d, 2) 2.37d, 3) 3.25d, 4) 3.68d (1mm downstream of the base)  
5) 4.30d, 6) 5.88d, 7) 7.63d, 8) 9.39d, 9) 11.14d.



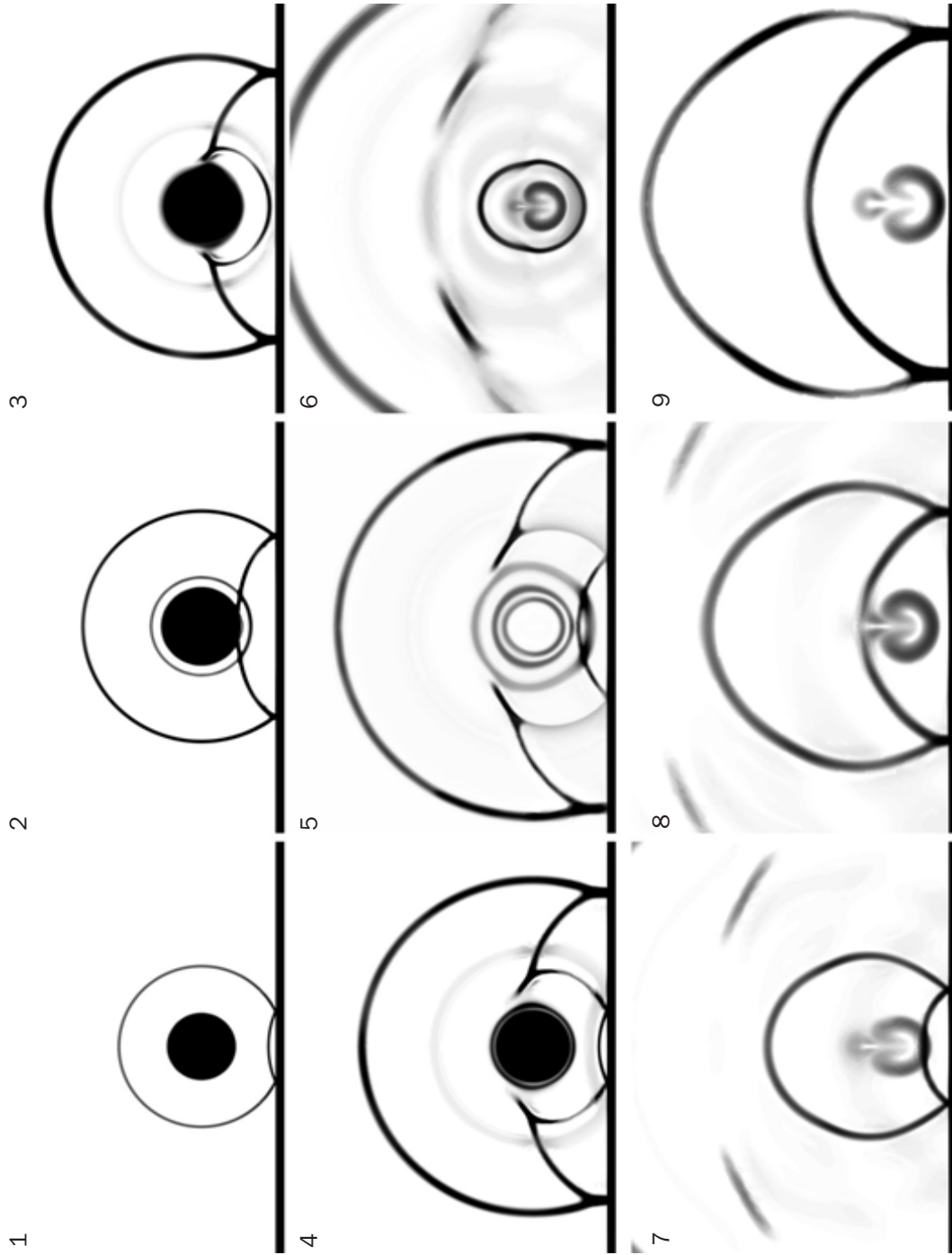
Density contours on the symmetry and ground planes for live-range projectile at  $h/d=1$



Contours of density to illustrate three-dimensional propagation and interactions of shock and expansion waves around the projectile at  $h/d=0.5$ , for slice locations described in figure 9.7 (not slice 4).



Density contours on the symmetry and ground planes for live-range projectile at  $h/d=0.5$



Contours of density to illustrate three-dimensional propagation and interactions of shock and expansion waves around the projectile at  $h/d=0.5$ , for slice locations from figure 9.7: from projectile nose; 1) 1.49d, 2) 2.37d, 3) 3.25d, 4) 3.68d, 5) 4.30d, 6) 5.88d, 7) 7.63d, 8) 9.39d, 9) 11.14d

velocity difference across the shock resulting in the flow no longer having an identical velocity to the ground plane as is the case upstream of the projectile.

Slice 3 (3.25d) shows the reflected bow wave passing through the expansion from the blend onto the main body. Slice 4 has been omitted here as it does not present any significant new flow features (but is used to discuss items relating to the clearance of  $h/d=0.5$  in figure 9.11)

Slice 5 (4.30d) shows the reflected bow wave interacting with the near wake, 1mm behind the projectile base, as the trailing expansion wave fans out. Also of note is the triple-point structure which the front of the bow wave now forms close to the ground. As it propagates into the far-field, the wavefront now incorporates a clear Mach stem at the ground, which increases in extent as the structure evolves downstream.

The shock interaction with the wake where the flow is recirculating involves the wave being rather weakly reflected in coincidence with the emerging recompression shock, rather than simply passing through the wake region. The remainder of the wave refracts around the wake core as shown in slice 6, with the pressure difference below and above the wake being great enough to draw flow upwards, resulting in the deflection of the wake seen previously in images of type B cases. The wake is also clearly distorted by the shock interaction, such that the shape of the recompression shock is highly asymmetric above and below the core of the wake. The remainder of the bow reflection circumnavigates the perimeter of the recompression shock into slice 7, continually weakened by the expansions stemming from the boat tail.

In slice 8, 9.39d downstream from the nose of the projectile, the recompression shock has experienced its own reflection from the ground plane, and since there now exists a very thin boundary layer there, a weak viscous interaction takes place. The wake vortices have reached their maximum height from the ground, though in slice 9 the reflected recompression shock begins its wake interaction.

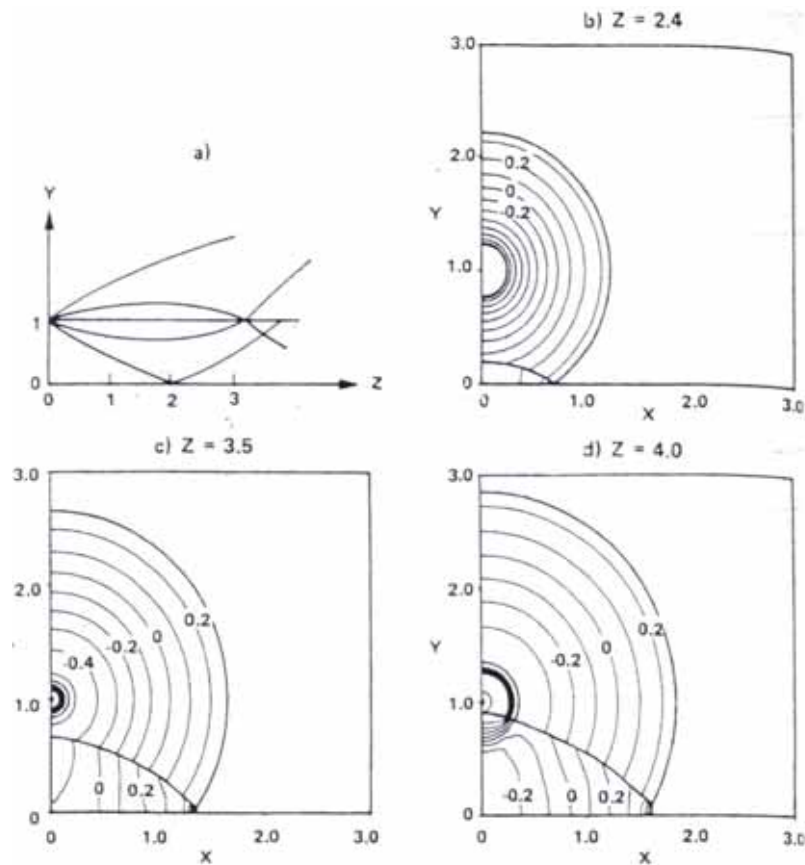
In contrast to the type B flowfield at  $h/d=1$ , slices for a type C  $h/d=0.5$  are presented in figures 9.10 and 9.11. At this lower clearance, the bow wave reflects from the ground in slice 1, and the reflection impinges on the projectile in slice 2 slightly

downstream from the blend from the ogive section to the main body which produces the expansion wave. In slice 3 the reflection propagates around the projectile circumference, resulting in a strong crossing boundary layer interaction that features a distinct triple point. The front of the wave is perturbed by the projectile body, giving it a significant component in the  $z$  plane. The boundary layer itself is somewhat dragged along by the perpendicular Mach stem at the body formed from the initial reflection, drawing fluid upwards around the projectile and causing a flow asymmetry between the upper and lower halves of the body which is more clearly seen in slice 4.

Slice 4 also shows the front of the reflected bow wave beginning to propagate away from the surface of the projectile, no longer able to follow the curvature of the body. This is accompanied by the expansion waves from the transition to the boat-tail region, and slice 5, 1mm behind the base of the projectile, indicates that these expansions and the last vestiges of the original reflection accompany each other into the farfield. The secondary reflection of the bow wave from the ground now impinges upon the free shear layer, but interacts strongly with the expansions from the base region and is significantly weakened before any meaningful wake interaction can occur.

In slice 6, the effect of the asymmetric pressure distribution and boundary layer thickness around the projectile clearly manifests itself in the formation of the recompression shock, which is distinctly asymmetric, and a strong downwards suction of flow in the centre of the wake is observed. Thus the wake is drawn towards the ground in the subsequent slices, initially elongating vertically in slice 7, then fattening again as the reflection of the recompression wave passes through it. By slice 9, the wake vortices are beginning to interact with the ground plane itself, and will continue to expand laterally in the presence of this boundary.

The flow patterns and images obtained are reminiscent of those produced by Marconi (1983) for an inviscid simulation (validated against experimental results) of a store/plate interaction, The present viscous Navier-Stokes simulations feature additional complexities, but transition of the propagating bow wave reflection at the ground plane from regular to Mach reflection, noted Marconi's work and reproduced in figure 9.12,



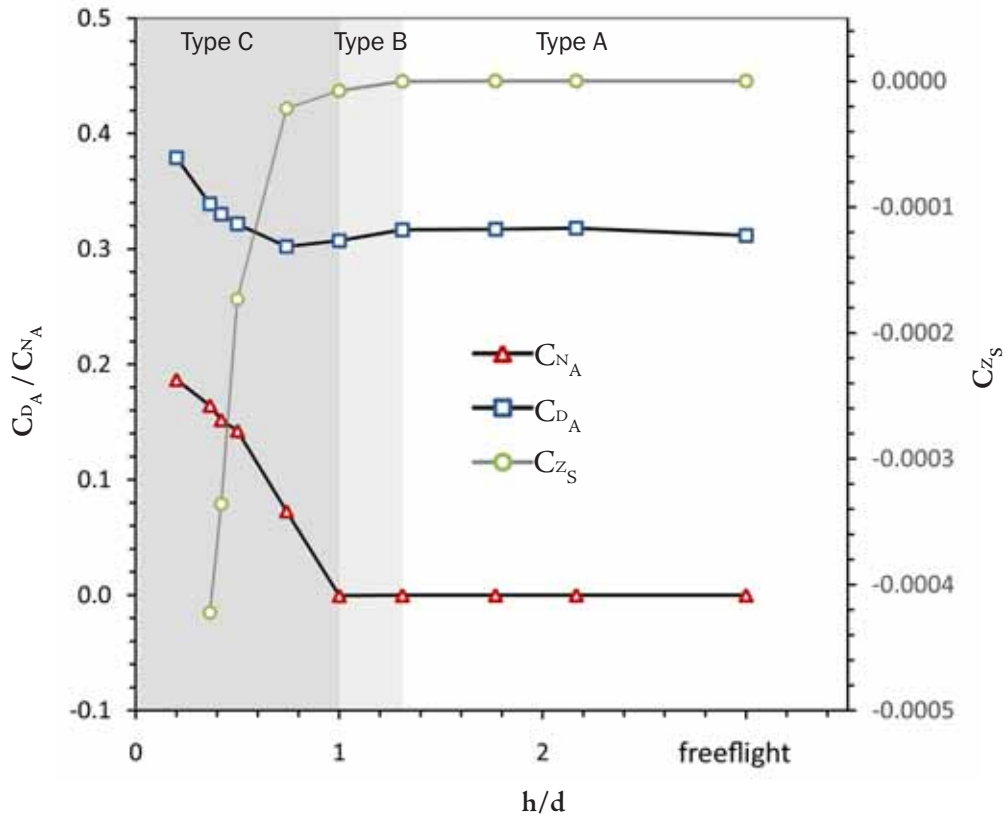
Cross-sectional shock shape and isobars for a Sears-Haak body,  $M_\infty=3$  (Marconi, 1983)

has been observed in figures 9.9 and 9.11, and thus is physically reasonable and not dependent on the moving ground.

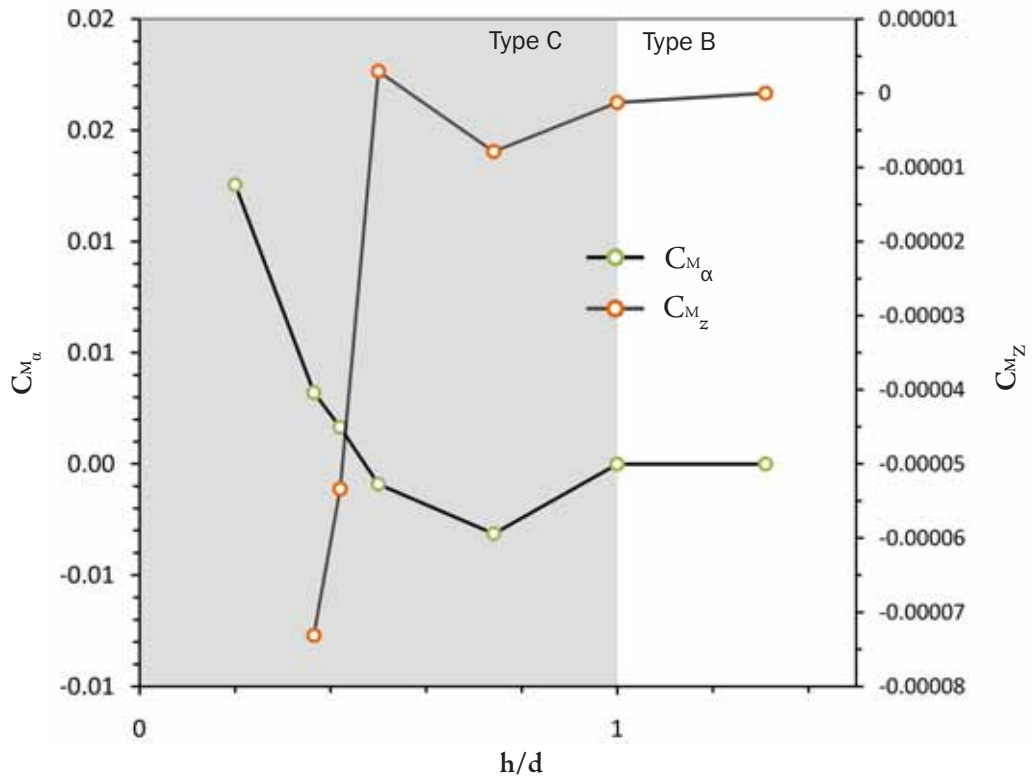
### 9.2.3 Forces and moments

Figures 9.13 and 9.14 present predicted aerodynamic force and moment coefficients for the full spinning projectile. The drag coefficient is largely unchanging for the type C reflection interactions, and dips slightly in the region of type B cases. This seems to indicate that the influence of the strong reflection of the bow wave on the near-wake region reduces the extent or strength of the wake and recompression shock.

At clearances lower than  $h/d=0.75$ , the drag increases markedly. Despite the shock impingements on the projectile, the viscous drag on the body does not change by anything more than a few percent; the main driver for the increased total drag is the effect the reflections have on the wake.



Changes to force coefficients for spinning live-range projectile as ground clearance is reduced



Changes to moment coefficients for spinning live-range projectile as ground clearance is reduced

The normal force acting on the projectile remains negligible until a type B reflection interaction occurs. However, an increase of several orders of magnitude is observed for type C cases, in which the pressure distribution around the projectile is directly affected. Given that the pressure downstream of a shock is higher than that ahead of it, the normal force increases in direct relation to the amount of high pressure produced on the lower half of the body surface. As the projectile is spinning, this normal force would not produce lift directly, but rather result in a perpendicular precession.

To place the increase in normal force (positive  $y$  direction) in perspective, consider that while the projectile itself has a mass equivalent to approximately 0.039N, the normal force acting on it at the most extreme  $h/d$  examined, 0.2, is 1.956N. In this respect, the  $z$  force of -0.0189N is also a significant contribution. This force may result in a tendency for movement away from the wall due to precession, albeit one which would not be great enough to defy the gravitational force (approximately 0.185N). As we are treating the ground as an infinite plane, it is likely that the projectile would move to one side ( $z$  direction) while the  $y$ -vector forces causing it to do so would simultaneously continue to increase non-linearly as ground clearance is reduced due to gravity. In the case of the finite ground plane of the original experiment, such marked deviation would not be observed, as the influence of the ground would be short-lived.

Recontextualising the problem in terms of a projectile fired in proximity to a vertical wall rather than a horizontal ground plane, the direction of spin of the projectile would determine any downwards or upwards deflection, exaggerated or tempered by gravity.

The motion of the projectile would not simply be a result of the normal,  $z$  and drag forces, however. The pitching tendency of the body is affected by the shock reflections as shown in figure 24, as referenced to the projectile's centre of gravity (estimated to be at  $x/l=0.7$  from the nose of the projectile (Purdon, 2006)). When the shock reflection impinges on the body behind the centre of gravity ( $h/d=0.75, 0.5$ ), the high-to-low pressure distribution around the boat-tail section results in a nose-down moment. The opposite is true at  $h/d < 0.5$ , where the reflected bow shock impinges

on the body upstream of the centre of gravity, resulting in a nose-up moment which increases significantly in magnitude with decreasing clearance.

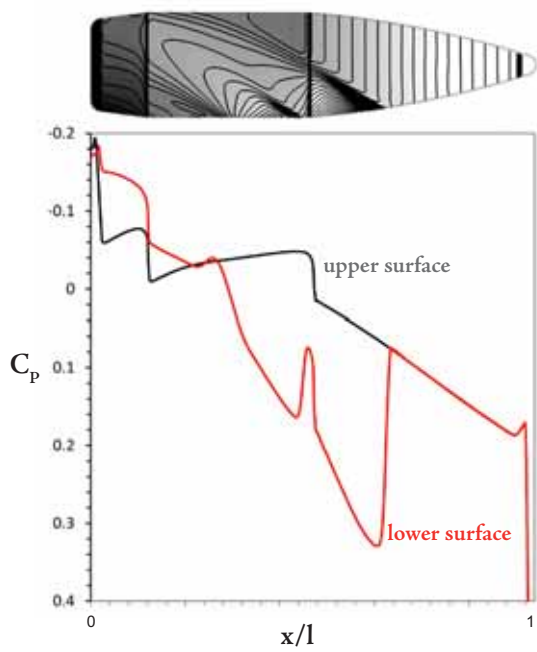
The  $z$ -moment acts on the projectile even in freeflight, due to the influence of spin. It is exaggerated by decreasing ground clearance, which would increase the tendency for the body to yaw, although the magnitude of the moment is small considering that the projectile is axially aligned with the freestream in all cases.

The coupling of a pitching moment, a mild yaw moment, a mild  $z$  force and a strong normal force would lead to a complex motion. Although we do not make any estimates as to changes in trajectory here, it can be deduced that the deviation of the projectile from its path if the ground plane were infinite would be significant, and the dynamic stability of the body could be critically affected. However, over any reasonably realistic ground or wall plane distance the influence on its final destination may well prove to be minimal.

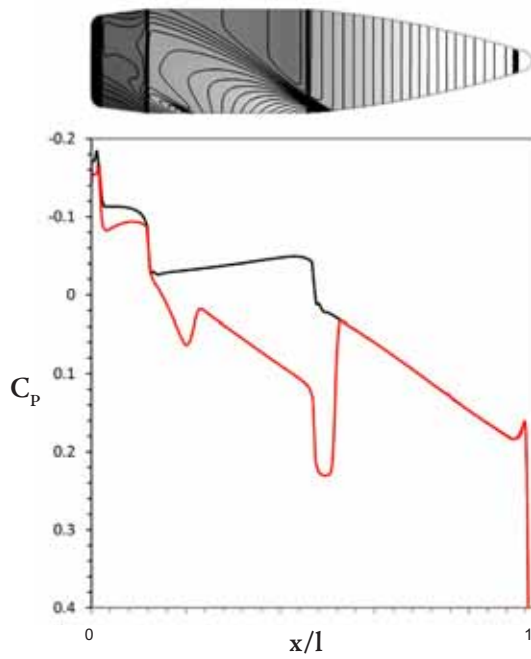
#### 9.2.4 Projectile and ground pressure distributions

In order to better understand the forces which act on the projectile in ground effect, the pressure distributions for various clearances are presented as contours in figures 9.15 to 9.18, as axial coefficients on the  $z=0$  ( $0^\circ/180^\circ$  plane) plane.

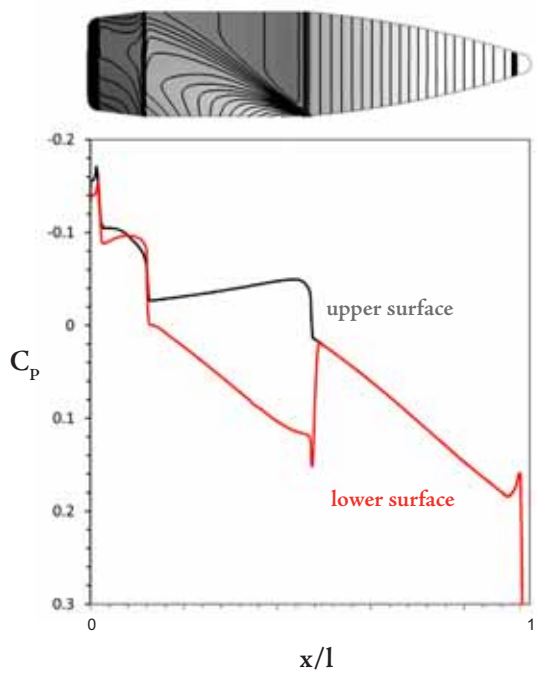
The contours serve to highlight the points of reflection impingement on the body, and also the way in which the reflected shocks wrap around the body. At clearances of  $h/d=0.365$  and  $0.2$ , the bow shock reflection interacts with the ogive forebody, where the pressure is already higher than over the rest of the body, and therefore the high pressure spike created by the shock is of considerably greater magnitude. At higher clearances the bow shock reflection is not only naturally weaker but has been influenced by the expansions around the forebody and thus the pressure increase across the shocks is not as great. The high pressure created behind the reflection impingement for  $h/d=0.75$  and  $0.5$  creates a centre of lift that is behind the centre of gravity, causing the nose-down pitching moment reported in figure 9.14. This tendency is reversed at lower clearances when one or more shock interactions cause increasing high pressure on the lower side of



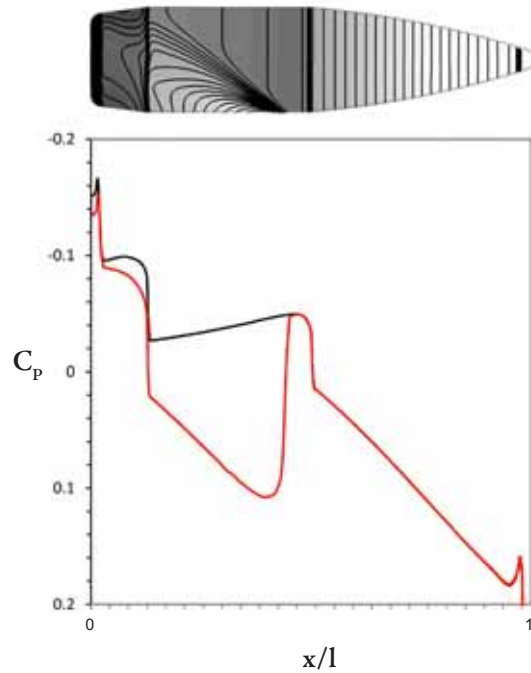
Projectile pressure distribution on the  $0^\circ/180^\circ$  (symmetry) plane for a ground clearance of  $h/d=0.2$ .



Projectile pressure distribution on the  $0^\circ/180^\circ$  (symmetry) plane for a ground clearance of  $h/d=0.365$ .



Projectile pressure distribution on the  $0^\circ/180^\circ$  (symmetry) plane for a ground clearance of  $h/d=0.42$ .



Projectile pressure distribution on the  $0^\circ/180^\circ$  (symmetry) plane for a ground clearance of  $h/d=0.5$ .

9.15

FIG

9.16

FIG

9.17

FIG

9.18

FIG

the body ahead of the c.g.

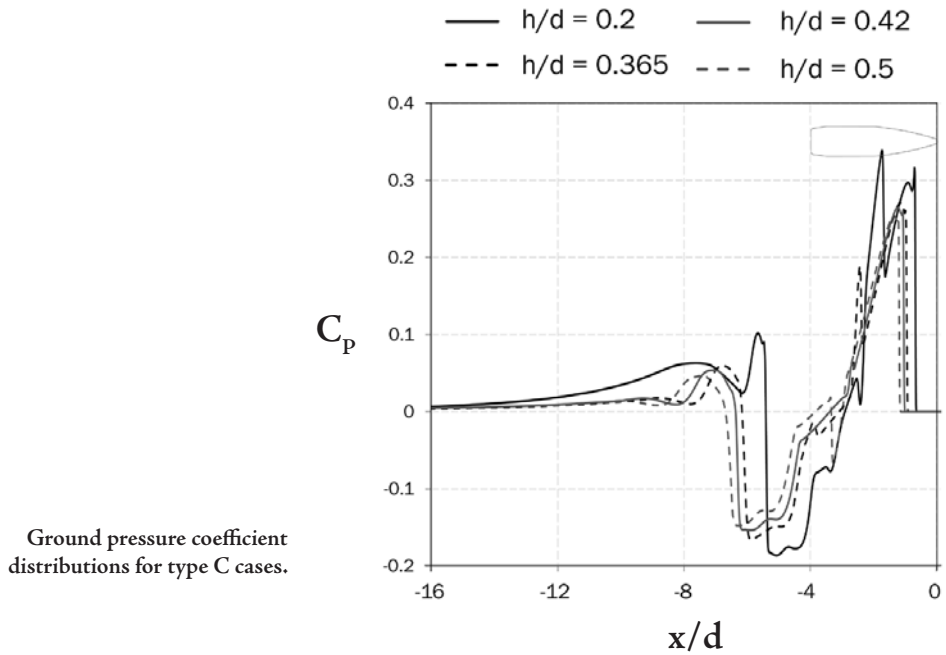
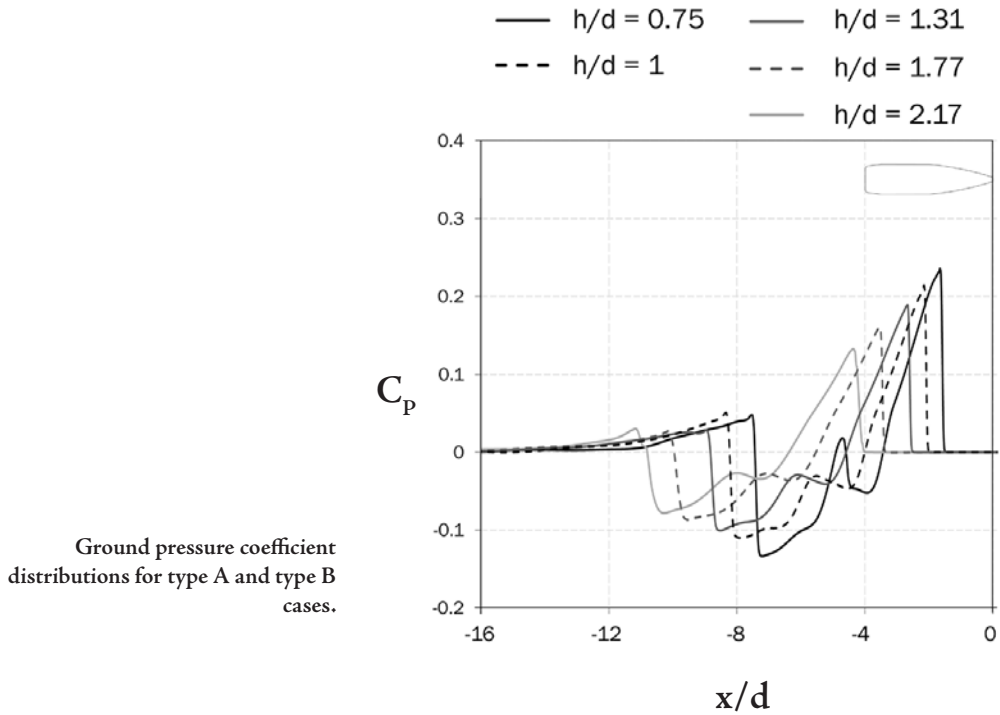
As ground clearance is reduced, pressure drops over the rear of the projectile. This is due to the reflection of expansion waves (which at higher clearances simply diffuse into the farfield) interacting with the rearward portion of the body. This concentration of low pressure, due to a constriction of the propagation of the expansion waves between the projectile and the ground, is the prime contributing factor to the wake deflections observed earlier in Section 9.2.1.

Figures 9.19 and 9.20 show the pressure distributions along the ground plane at  $z=0$  for all the ground clearances examined. Figure 9.18, presenting type A and B cases up to the type C  $h/d=0.75$  case, shows a fairly linear increase to the pressure rise across both the initial bow shock reflection and the recompression shock reflection further downstream, with decreasing ground clearance. The decrease in pressure caused by the series of expansions is similarly predictable with decreasing clearance. At  $h/d=0.75$ , the second reflection of the bow wave from the projectile registers at approximately  $5d$  from the nose, but its presence does not markedly affect the flow downstream which is still dominated by the expansion waves from the boat tail and the recompression shock.

In figure 9.20, the lowest clearance of  $h/d=0.2$  shows the impact of the second reflection of the bow wave at the ground plane on the high pressure flowfield around the ogive section. The shear layers from the base and the wake inside them interact strongly with the ground at this lowest clearance, as evidenced by the rise in pressure  $8d$  from the nose and the strong reflection signal from the recompression shock at  $x/d=5.5$ . In these respects, the lowest clearances stands in contrast to the relatively gradual changes observed for increasing ground proximity for the higher clearances, indicating that many additional flow features may present themselves at even lower ground clearances.

### 9.2.5 Flow in the wake

Having seen the way in which the projectile's proximity to the ground affects the pressure distribution around the projectile and on the ground, we may now examine directly the mechanisms at work in the wake which contribute to the deflections noted in section

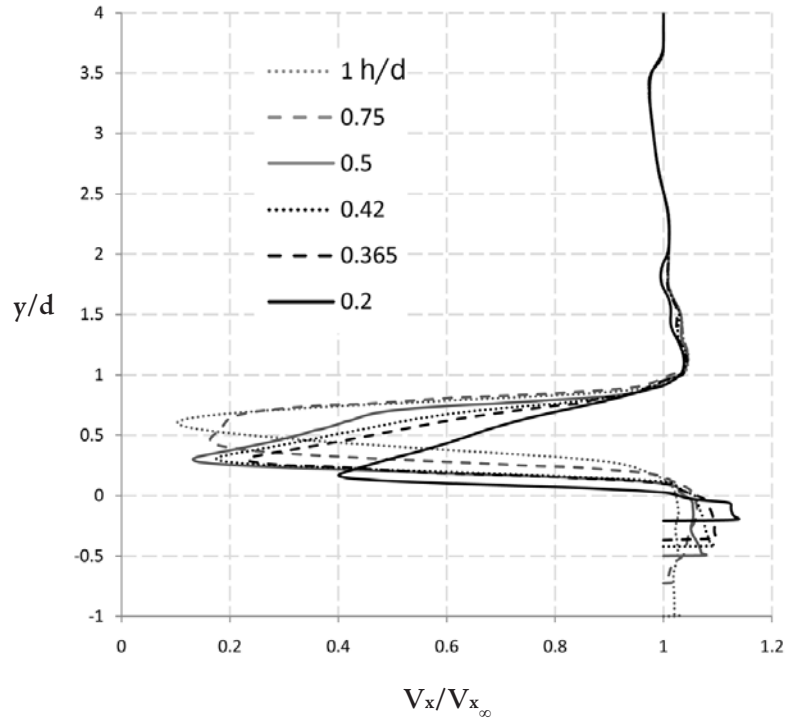


9.2.1, and thus the changes to the drag observed in section 9.2.3.

We saw previously in figures 9.4 and 9.5 that the wake can be observed as changing from an initial upward deflection for a type B reflection interaction, to a distinct downwards deflection for a type C case. This is caused by the pressure difference across the area between the projectile and the ground and that above it; pressure rises across

9.21

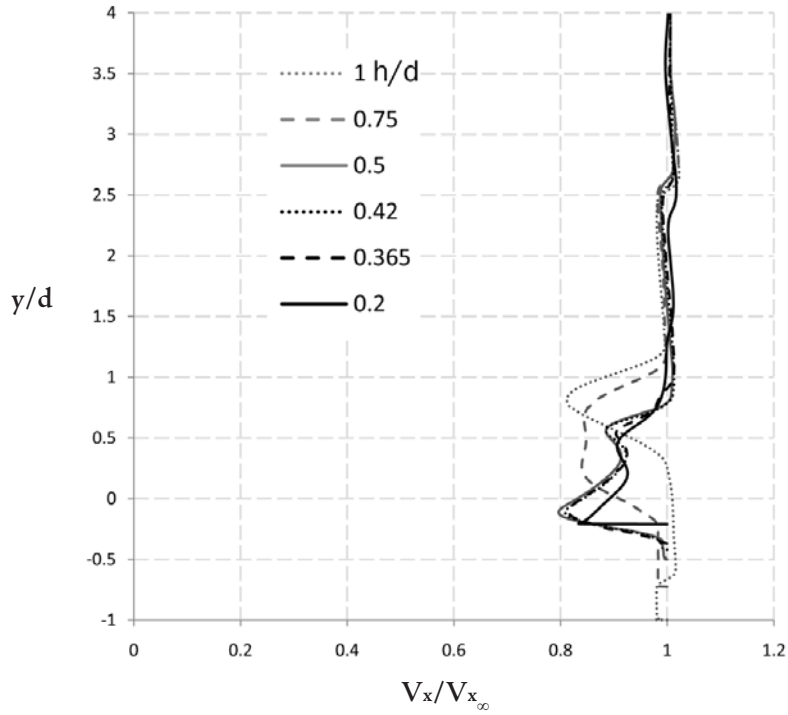
FIG



Wake profiles at  $x/d=1$  (from base)

9.22

FIG



Wake profiles at  $x/d=5$  (from base)

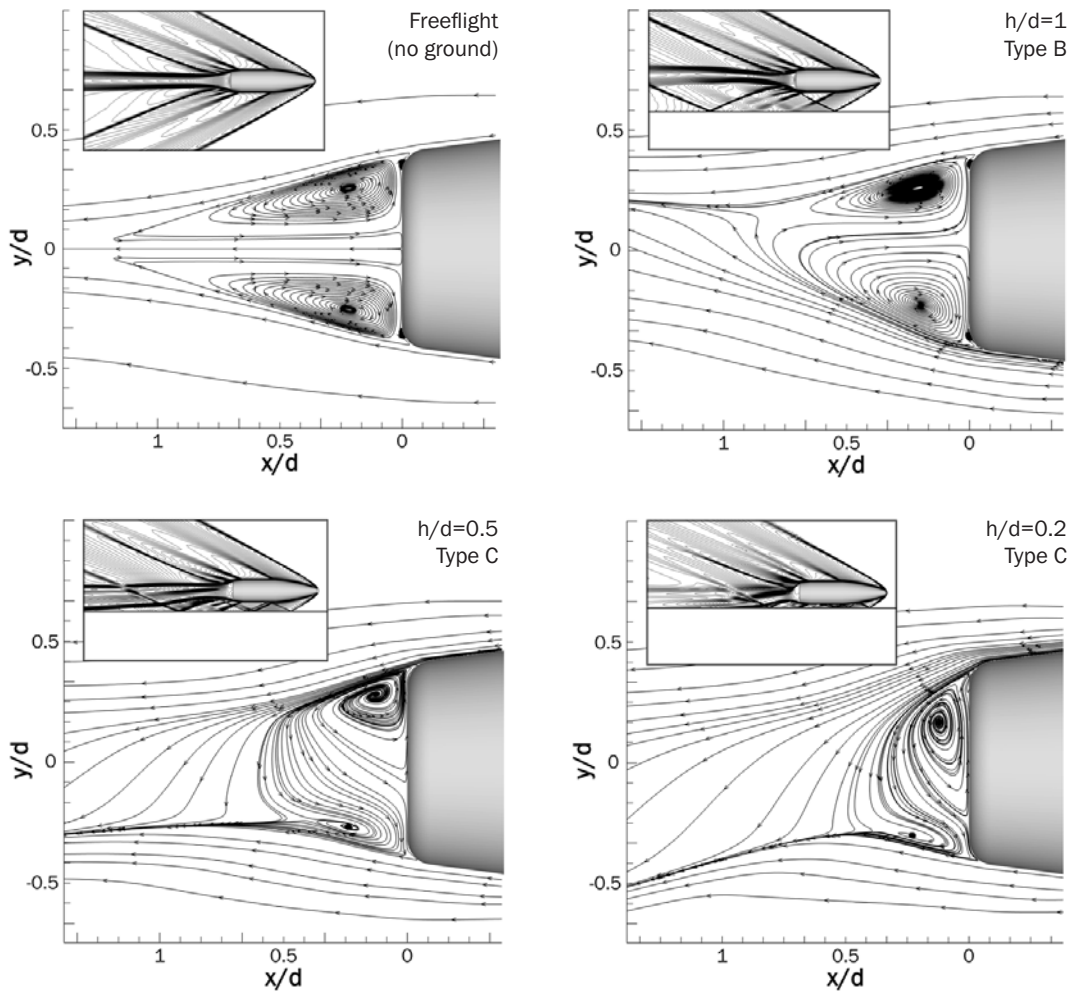
the reflected shocks, so the natural tendency of the flow in a type B scenario is to move upwards from the high pressure region to where it is lower, in the expansions above the wake. With closer proximity to the ground comes the concentration of the low pressure caused by the constrained, reflecting expansion waves, such that the area immediately below the wake draws air downwards.

Normalized streamwise velocity profiles are presented in figures 9.21 and 9.22, taken on the  $z=0$  plane. At  $h/d=1$ , the near-wake profile (1d from the base, beyond recirculation areas) is largely undisturbed by the pressure influence of the shock reflections upstream. As was seen in figure 9.6, the reflected bow shock has already interacted with the wake at this point, but no great distortion in streamwise velocity is present. At clearances less than 1d, the wake profile becomes increasingly asymmetric, with a bias towards the lower portion as the wake is pulled downwards. At 3d downstream from the base, in figure 33, the velocity deficit has recovered to about 0.7 of the freestream. The wakes of the projectiles at  $h/d < 0.5$  are still being drawn towards the ground plane, whereas the ones further from the ground have stabilised in an approximately horizontal inclination. The wake for the  $h/d=0.2$  case is interacting strongly with the ground plane, forming a thin boundary layer there.

5d from the base of the projectile, in figure 9.22, the shear layers in the wakes for the cases of  $h/d < 0.5$  are now beginning to interact with the ground, with the  $h/d=0.2$  wake forming a highly prominent interference which spreads laterally in the fashion of a subsonic vortex in ground effect.

The flow structures in the near wake and inside the primary recirculation region are strongly influenced by the changes in pressure distribution in the flowfield around the projectile. Figure 9.23 presents streamlines on the  $0^\circ/180^\circ$  plane at  $z=0$  in the base region for various ground clearances. In freeflight there are two distinct recirculation cells, perfectly axisymmetric. Also of note are small but distinct separated zones on the blend from the boat-tail to the base.

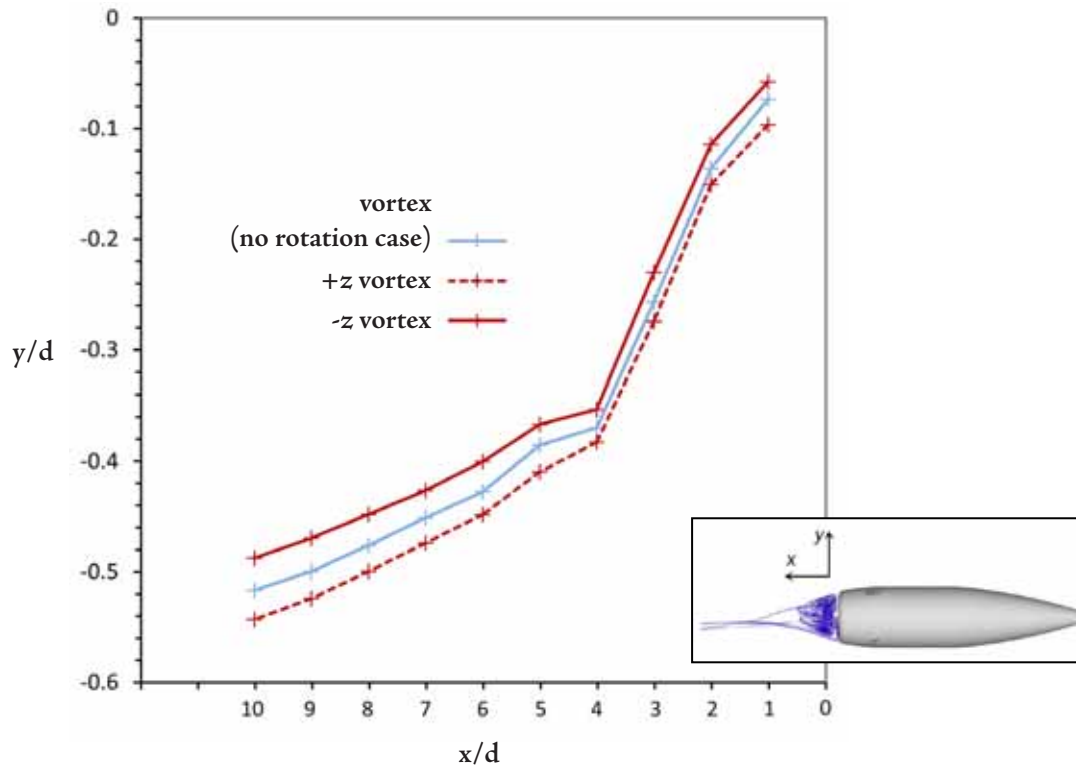
At  $h/d=1$ , the bow shock reflection interacting with the wake results in the upwards deflection previously discussed, and the upper recirculation cell becomes



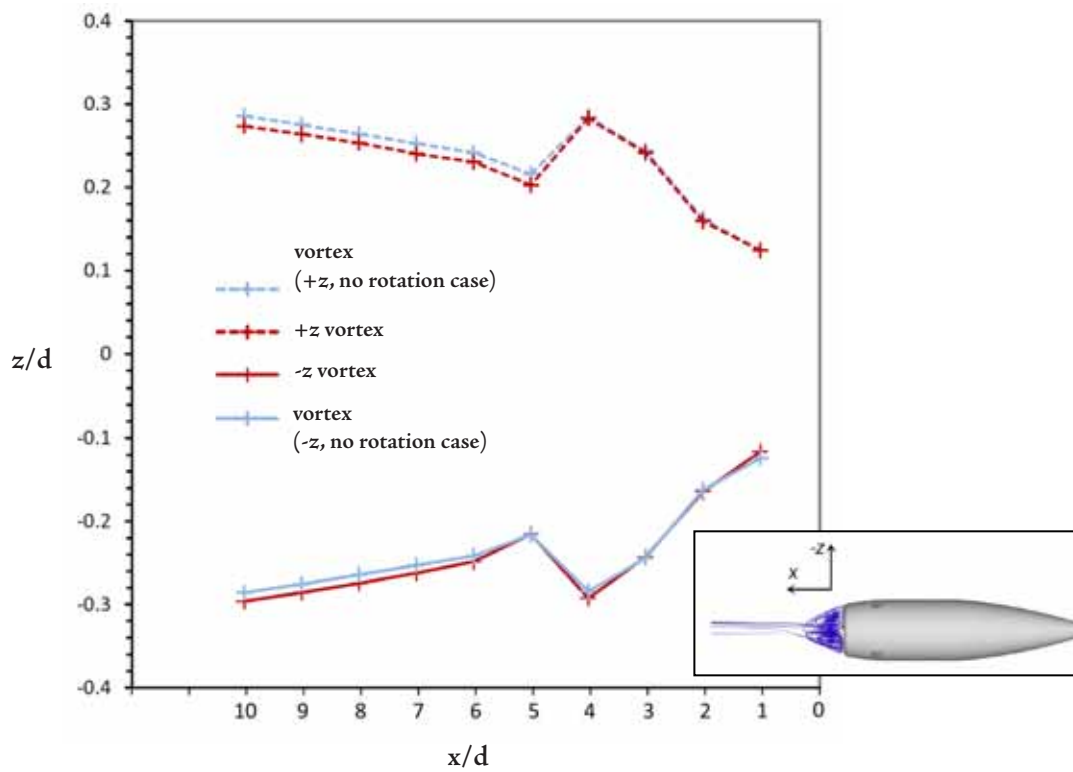
Streamlines in the near wake region highlighting the influence of ground clearance on recirculation cells.

compressed, as is consistent with the images presented in slices 5 and 6 of figure 9.9 as the wake distorts on all planes. The direction of flow is from the lower cell to the upper one. At  $h/d=0.5$ , this trend is reversed, again consistent with the deflections noted earlier, as flow now proceeds from the upper cell to the lower one, although both are now highly distorted from the regularity of the freestream case. All recirculation is confined to a region within  $0.5d$  of the base.

This trend continues at  $h/d=0.2$  where the downwash is at its most extreme, and the recirculation is confined to within  $0.3d$  of the base and is made up of a large upper cell and a weak lower one. The vertical extent of the recirculation has also diminished, and the lower cell has almost ceased to exist. The shear layer on the lower side angles downwards from  $0.5d$  of the base, such that it soon interacts with the ground as was



Paths of the two trailing vortices from the spinning projectile at  $h/d=0.5$ , in the  $xy$  plane, as compared to the path of vortices from the non-spinning projectile.



Paths of the two trailing vortices from the spinning projectile at  $h/d=0.5$ , in the  $xz$  plane, as compared to the path of vortices from the non-spinning projectile.

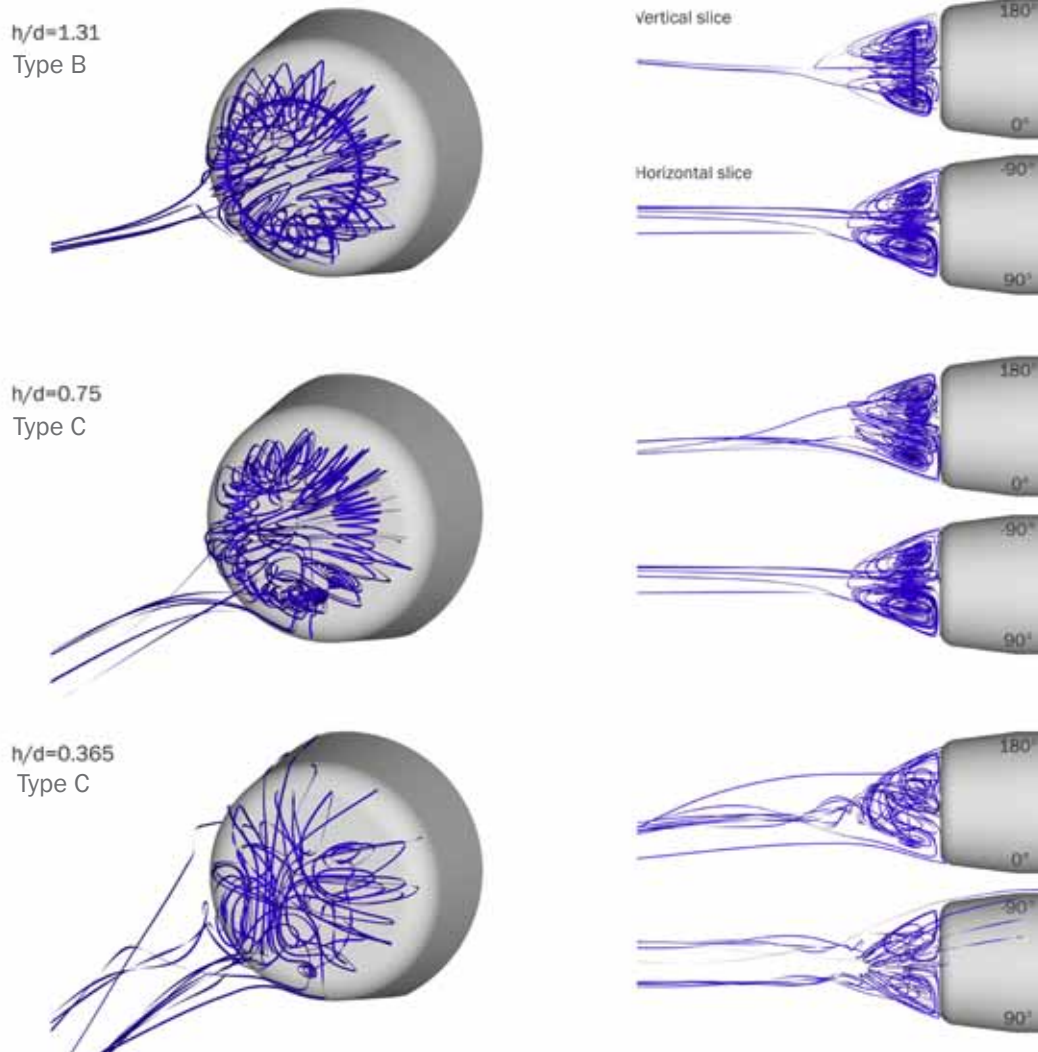
observed in figures 9.6. and 9.14.

Although the wake is structurally similar for the no-spin and spinning projectile, the rotational component introduces an axial twist, as shown in figures 9.24 and 9.25 for the case of  $h/d=0.5$ ; the vortices become increasingly misaligned downstream of the base. The jet-like feature previously noted in slices 6-9 of figure 9.11 is present in both spinning and non-spinning projectile wakes, as fluid from above is entrained into the counter-rotating cells which make up the vortex cores of the wake. This accounts for the thickening of the wake even in the absence of disruptive wave interactions, as the wake expands and increases in mass.

It is interesting to note that these wake patterns and the more general deflections discussed throughout the text are reminiscent of the results of base flow studies in literature on military projectiles at angles of incidence from  $2^\circ$  to  $5^\circ$  (Silton, 2005; Sahu, 1990; Sahu, 1989). This implies that a strong analogy can be drawn with the transonic wing work of chapters 7 and 8, whereby ground proximity and shock/ground interactions were observed to change the effective angle of attack of the section. While in the case of the projectile, this effect happens in stages across shock reflections rather than to the flowfield around the body as a whole, the analogy is an interesting common thread linking transonic and supersonic ground effect.

Looking again at the recirculation region behind the full spinning projectile, now in a three dimensional context, the effect of ground proximity on the near-wake region reveals additional flow structures not apparent from the planes already examined. Figure 9.27 presents streamlines, released from 5 points, 1mm from the base; 4 spaced equally at a radial distance of 2mm from the projectile axis of revolution, and one on the axis itself.

The way in which the recirculation structures break down is well illustrated in the three dimensional representation. At  $h/c=1.31$  the immediate wake is well structured, with a strong rotating vortex central to the recirculations observed on the planer diagrams. At  $h/c=0.75$ , the structures begin to break down - the circular vortex has distorted and forms a much looser helix. It also appears to feature a cyclonic component



Streamlines released from a plane 1mm from the base of the spinning projectile.

in the lower right quadrant. This feature is also present at  $h/c=0.365$ , although by now the streamlines indicate a severe breakdown of the regimented recirculation structures in the vertical plane, completing a trend of transition from a largely-symmetric, ordered structure to a highly asymmetric, more incoherent flow. The wake deflections observed earlier can also be noted in the streamlines, with the type B case exhibiting a strong upwards deflection following the shock interaction, while the streamlines for the type C cases increasingly deflect downwards with closer ground proximity.

## 9.3 Summary

A wide range of ground clearances were investigated for both spinning and non-spinning projectiles to establish changes to the flowfield around the projectile, and to determine both their causes and effects.

Three types of shock reflection interactions with the projectile in ground effect were identified based on this study - a Type A interaction ( $h/d > 1.31$ ) whereby the reflection of the projectile bow shock from the ground plane impinged only on the far wake, and was found to exert little influence on the aerodynamic forces and moments of the body. A Type B case ( $1 \leq h/d \leq 1.31$ ) was defined as featuring a strong interaction between the reflected bow wave and the near wake of the projectile, at which point the aerodynamic forces and moments were found to experience a change from freestream conditions, with drag decreasing. A Type C case ( $h/d \leq 0.75$ ) produced a strong normal force acting on the projectile, which, due to the body's rate of spin, would produce a lateral precession. Drag increased significantly as the wake was thickened and drawn towards the ground, and a weak lateral force was also discovered.

The projectile was also discovered to experience a marked pitching moment, initially nose-downwards at the high end of type C reflection interactions, then more strongly nose-up with continued decreasing ground clearance.

Reflections downstream of the projectile interacted heavily on the wake, distorting its structure and drawing it initially up (Type A and B cases), then strongly downwards to interact with the ground in the far-field (lower Type C cases), in a manner related to a change in effective angle of attack. These interactions were shown to be complex and highly three-dimensional, and CFD provided a wealth of information that was not gleaned from the original live-range or wind tunnel experiments: the detailed wake profiles, wake flow structures and the reason for their deflections, the ground pressure distributions describing the "footprint" of the shocks there, visualisation of the propagation of the shocks and their reflections in three dimensions, and force and moment data.

# Chapter: Conclusions

# 10

## 10.1 Conclusions

The effects of close ground proximity on compressible aerodynamic flows have been investigated numerically and experimentally. Such flows have relevance for a variety of applications such as high speed trains, vertical take-off jets, rocket-sled testing, proposed maglev-assisted launch vehicles, land speed record and high-performance vehicles, future high-speed wing-in-ground-effect aircraft, and military projectiles. Compressibility effects change, often substantially, the aerodynamic characteristics of a body. This occurs in particular when a shock wave reflects from the ground plane to interact again with the body or its wake. A study of existing literature indicated that the topic had been addressed sporadically in various contexts, without being researched in any comprehensive detail. One of the reasons for this is the difficulty involved in performing experiments which accurately simulate the flows in question with regards to ground boundary conditions.

Reynolds-averaged Navier-Stokes (RANS) modelling was used to generate all numerical results, with hexahedral meshes constructed for four bodies operating within their appropriate flow regimes: an inverted T026 high-lift wing (at  $M_\infty < 0.4$ ) akin to that which might be found on an open-wheel racing car; an RAE2822 sub-critical wing for both two-dimensional studies and three-dimensional comparisons to wind tunnel experiments (at  $1 > M_\infty > 0.5$ ); an ONERA M6 three-dimensional swept, tapered, axisymmetrical wing (also at  $1 > M_\infty > 0.5$ ), and a NATO

5.56mm small-arms projectile at Mach 2.4. The one-equation turbulence model of Spalart and Allmaras was found to perform to a high standard for all cases across the Mach numbers tested, and was used for all work bar the inverted wing, where a two-equation realizable  $k-\varepsilon$  model provided a slight advantage. The validation studies showed that there is still considerable work to be done in the field of turbulence modelling before RANS is a fully suitable tool for flows involving multiple shock reflections and interactions or, more pressingly, shock-separated or shock-oscillating flows.

Apart from turbulence model studies, the numerical approach was extensively verified and validated, including mesh convergence, domain size and inlet flow condition studies, against existing and new experimental data. Most notably, a series of experiments was conducted with an RAE 2822 wing at the U.S. Naval Academy's Transonic Blowdown Wind Tunnel, ostensibly to generate transonic ground effect data with which to compare the CFD, but also to examine means of performing tests in the absence of a moving ground. One important conclusion to draw here is that there is still a lack of good public-domain transonic experimental data, even without the complication of a ground plane. Generally experiments are presented with incomplete information about flow conditions or tunnel geometry, and the most commonly referenced experiments from the AGARD validation report of 1979 made extensive use of porous or slotted walls, which are not easily reproduced in CFD. Clear and comprehensive data regarding an aerofoil or wing in the transonic range in experiments featuring solid closed walls, despite being of little practical use on their own, would be the most beneficial for CFD validation purposes.

Construction of a transonic or supersonic moving ground is unfeasible and other means of accurately reproducing correct ground boundary conditions for controlled tests are complicated and expensive. Simple techniques used to simulate compressible ground effect problems in blowdown wind tunnels were therefore developed and evaluated: a symmetry (mirror-image) method, and an elevated ground plane. Both these methods were assessed for the projectile at Mach 2.4 and the RAE 2822 in the US Naval Academy wind tunnel in the Mach 0.5 to 0.75 range. In all cases, the symmetry method was found to be the most effective.

In supersonic flow, the elevated ground provides a reasonable approximation of moving ground conditions as the boundary layer there is small, but would not be adequate for tests

at extremely low clearances. Additionally, disturbances at the leading edge of the apparatus are difficult to avoid. This is even more important at transonic Mach numbers, where the leading edge disturbance is considerable, and even a carefully designed contour to maintain fully-attached flow would eventually create a shock wave at subsonic freestream Mach numbers, greatly disrupting the flow at the ground plane. The symmetry method, which produces a scenario akin to an inviscid interaction at the ground plane, features none of these problems, though it does increase the blockage in the test section. Issues of scale with regards to Reynolds number persist in the transonic regime, but with careful use of CFD as a complement to experiments, discrepancies can be quantified with confidence. Indeed, there is a clear need in the field of transonic and supersonic ground effect for reliable and detailed experimental data against which code can be validated, as well as a broader need for a greater understanding of the flow physics of shock/moving ground interactions.

Across low-subsonic Mach numbers ( $M_\infty < 0.4$ ) for a range of ground clearances, the inverted TO26 wing was used to study compressibility effects with an additional emphasis on wind tunnel/CFD correlation concerns. It was found that compressible effects are prevalent even at  $M_\infty < 0.1$ , where aerodynamic force coefficients can be mis-predicted by several percent by an incompressible simulation. These effects become significant at  $M_\infty > 0.15$ , particularly at lower ground clearances, though the behaviour of the lower endplate vortex was found to be barely affected by the density changes around the wing. Incompressible simulations were found to consistently underpredict the compressible force coefficients, and the critical Mach number of the wing was found to be less than  $M_\infty = 0.4$  at the lowest ground clearances, due to the high local Mach numbers produced by the venturi-effect the wing creates at close ground proximity.

Using this wing geometry, the practice of matching incompressible full-scale CFD to a half or quarter scale model in flows with identical Reynolds number but higher Mach number was found to be significantly flawed; it was determined that Mach scaling can be just as important, if not more so, than Reynolds scaling in such a scenario.

Having taken the subsonic study to the critical Mach number for that wing, subsequent investigation explored the mid-to-high Mach subsonic regime in more detail. The lifting RAE 2822 aerofoil and ONERA M6 wing were investigated over a range of Mach numbers

( $0.9 > M_\infty > 0.5$ ), ground clearances and angles of attack. The presence of the ground was found to affect the critical Mach number, and at low angles of attack and low ground clearances, a shock wave was prone to form on the lower surface prior to that on the upper surface, causing a significant drop-off in lift (and in some cases the production of downforce), and an accompanying increase in drag. The aerodynamic characteristics across all Mach numbers and clearances proved to be highly sensitive to ground proximity, with a step change in any variable often causing a considerable change in lift, drag or moment coefficient. At low angles of incidence, significant lift-loss or even downforce occurs when the lower shock forms prior to the upper surface shock. For the RAE 2822, this happened as early as  $M_\infty = 0.5$ . For the three-dimensional M6, the tip vortex was observed to reduce in strength with decreasing ground clearance, and was additionally found to travel increasingly outboard with ground proximity, as opposed to the inboard motion observed in freeflight, which served to lessen the induced drag contribution of the vortices. More complicated shock/boundary layer interactions occurred at the lowest clearances causing separation and accompanying large-scale drag rises as well as fluctuations in lift.

As a result of these factors, sustained transonic flight in ground effect would require a complex, rapid-response control system, and the wing section used would have to be carefully optimised to provide acceptable lift and handling characteristics while avoiding the formation of a lower surface shock. With the M6 at  $3.06^\circ$  incidence, it was shown that for  $M_\infty > 0.7$ , flight in close ground proximity was not more efficient than that of unbounded freeflight, annulling the primary advantage of ground effect aviation.

The lifting wing and aerofoil used at subsonic Mach numbers are not typical of the type appropriate for fully-supersonic flight, and thus to explore that end of the Mach scale, where shocks tend to be steady and oblique, a supersonic spinning NATO projectile travelling at  $M_\infty = 2.4$  was simulated at several ground clearances. The waves produced by the body reflected from the ground plane and interacted with the far wake, the near wake, and/or the body itself depending on the ground clearance. A categorisation system was therefore devised based on ground clearance as non-dimensionalised by the projectile diameter: A Type A interaction ( $h/d > 1.31$ ) whereby the reflection of the projectile bow shock from the ground plane impinged only on the far wake, and was found to exert little influence on the aerodynamic forces and moments

of the body. A Type B case ( $1 \leq h/d \leq 1.31$ ) was defined as featuring a strong interaction between the reflected bow wave and the near wake of the projectile, at which point the aerodynamic forces and moments were found to experience a change from freestream conditions, with drag decreasing. A Type C case ( $h/d \leq 0.75$ ) produced a strong normal force acting on the projectile, which, due to the body's rate of spin, would produce a lateral precession.

The influence of these wave reflections on the three-dimensional flowfield, the wake characteristics, and projectile pressure distribution was analysed, and their resultant effects on the aerodynamic coefficients were determined. Unlike in the near-sonic wing/aerofoil cases, the trends observed were reasonably consistent and predictable with decreasing ground clearance; the normal and drag forces acting on the projectile increased in exponential fashion once the reflections impinged on the projectile body again one or more times (at a height/diameter ground clearance  $h/d < 1$ ). Type A and B interactions resulted in upwards deflection of the wake, whereas a Type C case resulted in a significant downwards deflection, accompanied by a considerable thickening of the wake, producing the increased drag mentioned. Complicated flow structures were observed in the wake, and were determined to be highly sensitive to direct shock interaction or the altering of the pressure distribution around the projectile due to shock reflections re-impinging on the body upstream of the base region.

Given that the projectile was spinning, the increased normal force as the ground plane was approached would likely result in a lateral precession. Furthermore, the pitching moment of the projectile changed sign as ground clearance was reduced, adding to the complexity of the motion which would ensue.

## 10.2 Recommendations for future work

With regards to the experimental methods, a more detailed study of the limitations of the symmetry method would be useful, as extremely small ground clearances ( $h/c < 0.05$ ) are likely to feature inaccurate modelling when compared to an ideal moving ground. The nature of the

crossing shocks would also require more detailed study in order to definitively quantify any unwanted effects due to the lack of an actual ground plane, such as Mach reflection when regular reflection would be expected, and vice-versa. The use of high aspect-ratio wings and other apparatus which induces minimal spanwise flow disturbance, unlike that used in the present work, would provide results which could be used to provide a better quality of two-dimensional flow with which CFD can be more easily compared.

The subsonic inverted wing investigation indicated that compressibility effects could be significant even at low Mach numbers due to the presence of the ground. In order to better determine the influence of this in a more industrially-relevant way, other components of a racing car could be investigated, as areas such as the wheel/ground contact patch and the underbody/diffuser section will experience increased flow compressibility, and possibly to a greater extent than that of a stand-alone wing. Since the performance of all components are linked, a full-car evaluation may produce results which are markedly different when the air is treated as compressible as compared to an incompressible simulation, particularly at the higher end of the speed range of such vehicles.

At higher Mach numbers and for the lifting wing, it is clear that even if such flight were to become feasible by means of an adequately responsive flight control system, such speeds at the ground clearances typical of a large “WIG” aircraft could only be achieved over water. The interaction of a shock wave with water for an aeronautical application is thus an area which would benefit from greater study. It would also be useful to characterise a wing section which would avoid any lower-surface shock wave in the transonic operating range, whilst still providing acceptable lift and handling qualities.

As for the supersonic projectile, it is clear that changes to the body’s trajectory due to the presence of a ground or wall would be complex, given the coupling of changes to pitch and force and the influence of the magnus effect. More detailed experimental work would need to precede further computational study to determine path changes with reliable accuracy. A more bluff projectile at Mach 1.2 was also examined during the live range tests which originated the present computational study; the body was observed to move in the schlieren video, suggesting a greater ground influence at a transonic speed. This could be similarly investigated computationally using

the method described in this thesis.

More generally, a thorough investigation of the physical mechanical aspects of shock/moving ground interaction, including Mach reflection and transition to that condition, is required in order to characterise differences between that situation and established inviscid shock interaction/reflection theory, and a more detailed investigation of the influence of the moving ground on the oscillatory properties of transonic shocks would be of interest.

## References

- Ackroyd J. (1985) Thrust 2 – Design of the World Land Speed Record Car. *Proc. Instn. Mech. Engrs.* 199, pp. 239-264
- Aeschliman, D.P., Oberkampf, W.L. (1998) Experimental methodology for computational fluid dynamics code validation, *AIAA J.*, 36 (5), pp. 733–741
- Agathangelou, B., Gascoyne, M. (1998) Aerodynamic considerations of a formula 1 racing car, SAE Technical Report 980399
- Ahmed, M.R., Sharma, S.D. (2005) An investigation on the aerodynamics of a symmetrical airfoil in ground effect. *Experimental Thermal and Fluid Science*, 29, pp. 633–647
- Ahmed, M.R., Takasaki, T. & Kohama, Y. (2007) Aerodynamics of a NACA4412 Airfoil in Ground Effect, *AIAA Journal*, (45) 1, pp. 37-47.
- AIAA, (1998) Guide for the Verification and Validation of Computational Fluid Dynamics Simulations, AIAA, G-077-1998
- American Institute of Aeronautics and Astronautics (1998) Guide for the Verification and Validation of Computational Fluid Dynamics Simulations. AIAA G-077-1998.
- Anderson, D. (2001) *Fundamentals of Aerodynamics* (text). McGraw-Hill, USA.
- Appleby, E.M. (2006) Pressure effects on supersonic projectiles in close proximity to a wall. BE thesis, UNSW@ADFA
- Ayres R. (1996) Thrust SSC Environmental Testing. *Environmental Engineering*, 9 (2), pp. 28-30
- Baker, C.J., Humphreys, N.D. (1996) Assessment of the adequacy of various wind tunnel technique to obtain aerodynamic data for ground vehicles in cross winds. *J. Wind Eng. Ind. Aerodyn.* 60, pp. 49–68
- Baker, M.D., Mathias, D.L., Roth, K.R., Cummings, R.M. (2002) Numerical Investigation of Slat and Compressibility Effects for a High-Lift Wing, *Journal of Aircraft*, 39 (5) pp. 876-884
- Barber T.J., Leonardi E., Archer R.D. (2002) Causes for Discrepancies in Ground Effect Analyses. *The Aeronautical Journal*, 106 (1066), 653-657
- Barber, T.J. (2000) "A Study of a Lifting Wing in Ground Effect," PhD thesis, University of New South Wales
- Bartels, R.E. (1998) Flow and turbulence modeling and computation of shock buffet onset for conventional and supercritical airfoils NASA TP-1998-206908, NASA Langley, USA.
- Bartels, R.E. (1998) Flow and Turbulence Modeling and Computation of Shock Buffet Onset

for Conventional and Supercritical Airfoils, NASA / TP-1998-206908

Bearman, P.W., De Beer, D., Hamidy, E. and Harvey, J.K. (1998) The Effect of a Moving Floor on Wind Tunnel Simulation of Road Vehicles, SAE 880245, 1988

Ben-Dor, G. (2006) A State-of-the-Knowledge Review on Pseudo-Steady Shock-Wave Reflections and their Transition Criteria, *Shock Waves*, 15 (3-4), pp. 277-294

Boussinesq, J., (1877) "Thorie de Lcoulement Tourbillant," Mem. Prsents par Divers Savant Acad. Sci. Inst. Fr.

Brandt, A. (1979) Multi-level Adaptive Computations in Fluid Dynamics. Technical Report AIAA-79-1455, AIAA, Williamsburg, USA.

Caruana, D., Mignosi, A., Robitaille, C., Correge, M. (2003) Separated Flow and Buffeting Control. *Flow, turbulence and combustion*, 71(1-4).

Catalano, G.D., Sturek, W.B. (2001) A numerical investigation of subsonic and supersonic flow around axisymmetric bodies, , Army Research Laboratory report ARL-TR-2595

Chin-Hsen, L. (2000) Modelling and Numerical Simulation of low Mach-number compressible flows, CSIRO Division of Mathematics and Statistics, Australia.

Cook, P.H., M.A. McDonald, M.C.P. Firmin (1979) Aerofoil RAE 2822 - Pressure Distributions, and Boundary Layer and Wake Measurements. Experimental Data Base for Computer Program Assessment, AGARD Report AR 138, 1979.

Cuthill, E., McKee, J. (1969) Reducing the bandwidth of sparse symmetric matrices. *Proc. 24th Nat. Conf. ACM*, pp. 157-172

Dacles-Mariani, J., Zilliac, G. G. , Chow, J. S. , and Bradshaw, P. (1995) Numerical/Experimental Study of a Wingtip Vortex in the Near Field. *AIAA Journal*, 33(9), pp.1561-1568

Dam, C.P. (1999) Recent experience with different methods of drag prediction. *Progress in Aerospace Sciences*, 35 (8), pp. 751-798

Delery, J.M. (1985) Shock Wave/Turbulent Boundary Layer Interaction and its Control. *Progress in Aerospace Sciences*, 22, 209-280

Doig, G., A.J. Neely, T.J. Barber, E. Leonardi (2006) The Use of Thermochromic Liquid Crystals to Investigate Flow Field Interactions with the Ground around a Supersonic Land Speed Record Vehicle. *Proceedings of the 13 International Heat Transfer Conference*, Sydney,

Doig, G., Barber, T.J., Leonardi E., Neely, A.J. (2007) The Onset of Compressibility Effects for an Inverted Aerofoil in Ground Effect, *The Aeronautical Journal*, 111 (1126), pp. 797-806

Doig, G., Barber, T.J., Leonardi E., Neely, A.J., Kleine, H. (2008) Methods for Investigating Supersonic Ground Effect in a Blowdown Wind Tunnel, *Shock Waves*, 18 (2), pp. 155-159

Doig, G., H. Kleine, A.J. Neely, T.J. Barber, J.P. Purdon, E.M. Appleby, N.R. Mudford, E. Leonardi

(2007) The Aerodynamics of a Supersonic Projectile in Ground Effect Proceedings of the 26th International Symposium on Shock Waves, Göttingen, Germany

Dominy, R. G. (1992) Aerodynamics of Grand Prix Car, Proceedings of the Institution of Mechanical Engineers, (206), pp. 267-274

Dragos, L. (1990) Numerical solutions of the equation for a thin airfoil in ground effect, AIAA J. 28(12), pp. 2132-2134.

Dragos, L., Dinu, A. (1995) A direct boundary integral equations method to subsonic flow with circulation past thin airfoils in ground effect. Comput. Methods Appl. Mech. Eng., 121, pp.163-176

Dumbser, M., Moschetta, JM., Gressie, J. (2004) A matrix stability analysis of the carbuncle phenomenon, Journal of Computational Physics, 197 (2), pp. 647 - 670

Elkhoury, M (2007) Assessment and Modification of One-Equation Models of Turbulence for Wall-Bounded Flows, Transactions of the ASME (129)

Fago B., Lindner H., Mahrenholtz O. (1991) The effect of ground simulation on the flow around vehicles in wind tunnel testing. Journal of Wind Engineering and Industrial Aerodynamics, 38, pp. 47-57

Fink, M.P, Lastinger, J.L. (1961) Aerodynamic characteristics of low-aspect-ratio wings in close proximity to the ground, NASA Technical Note D-926

FLUENT (2006) "Fluent User Guide," FLUENT Inc.

Garbaruk, A., Shur, M., Strelets, M., Spalart, P.R. (2003) Numerical Study of Wind-Tunnel Walls Effects on Transonic Airfoil Flow, AIAA Journal 2003, 41 (6) pp. 1046-1054

Goethert, B. (1961) Transonic Wind Tunnel Testing (text), Dover Publications, New York (reprinted 2007)

Goldberg, U., Akdag, V., Palaniswamy, S., Oberoi, R., Bachchan, N., Glessner, P., Fredrick, W. (2006) CFD Analysis of the American Challenger Rocket Car. SAE 2006 World Congress & Exhibition (Vehicle Aerodynamics), pp. 251-258

Han, C., Cho, J., Moon, Y., Yoon, Y., Song, Y. (2005) Design of an Aerolevitation Electric Vehicle for High-Speed Ground Transportation System. Journal of Aircraft, 42 (1)

Henderson, L.F. (1967) The reflexion of a shock wave at a rigid wall in the presence of a boundary layer. Journal of Fluid Mechanics, 30(4), pp. 699-722

Kalitzin, G. (1998) An implementation of the v2-f model with application to transonic flows, Center for Turbulence Research, Annual Research Briefs (171)

Katz, J. (1985) Calculation of the Aerodynamic Forces on Automotive Lifting Surfaces. Journal of Fluids Engineering 107. pp.438-443.

- Katz, J. (2006) Aerodynamics of Race Cars. *Annual Review of Fluid Mechanics*, 38, pp. 27-63
- Keshtiban, I.J., Belblidia, F., Webster M.F. (2004) Compressible flow solvers for low Mach number flows - a review. *International Journal for Numerical Methods in Fluids*, 23, pp 77-103.
- Kohama, Y., Watanabe, H. (1998) Wind tunnel study of the new concept low-emission high-speed ground transport system. *Proc. of 4th KSMEJSME Fluids Eng. Conf.*
- Kral, L.D., (1998) Recent experience with different turbulence models applied to the calculation of drag over aircraft components. *Progress in Aerospace Sciences* (34)
- Krige, D.G. (1951) A statistical approach to some mine valuations and allied problems at the Witwatersrand, Master's thesis of the University of Witwatersrand, South Africa.
- Kubota, H., Stollery, J.L. (1982) An experimental study of the interaction between a glancing shock wave and a turbulent boundary layer. *J. Fluid Mech.*, 116, pp. 431-458
- Lamb, J.L. (2001) Critical Velocities for Rocket Sled Excitation for Rail Resonance. *Johns Hopkins APL Technical Digest*, 21 (3), 448-458
- Langlois, M., Masson, C., Paraschivoiu, I. (1998) Fully Three-Dimensional Transition Prediction on Swept Wings in Transonic Flows. *Journal of Aircraft*, 35 (2) pp. 254-259
- Launder, B.E., Spalding, D.B (1974) *The Numerical Computation of Turbulent Flows*. *Computer Methods in Applied Mechanics and Engineering*, 3, pp. 269-289
- Lee, H-W., Kim, K-C., Lee, J. (2006) Review of Maglev Train Technologies, *IEEE Transactions on Magnetics*, 42 (7).
- Mach E, Wosyka J (1875) Über einige mechanische Wirkungen des elektrischen Funkens. *Sitzungsber Akad Wiss Wien (II. Abth.)* 72:44–52
- Mahon, S. and Zhang, X. (2006) Computational Analysis of Pressure and Wake Characteristics on an Aerofoil in Ground Effect," *ASME J. Fluids Eng.*, Vol. 127, pp. 290-298
- Marconi, F. (1983) Shock reflection transition in 3-dimensional steady flow about interfering bodies. *AIAA Journal*, 21(5) pp.707-713
- Maskalik, A.I.; Rozhdestvensky, K. V. (1998) A View of the Present State of Research in Aero- and Hydrodynamics of Ekranoplans. *RTO AVT Symposium on "Fluid Dynamics Problems of Vehicles Operating near or in the Air-Sea Interface"*, Amsterdam, 5-8 October 1998.
- Matschke, G., Schulte-Werning, B., Gregoire, R., Beremnger T, Malfatti A, Mancini G. (1999) *TRANSAERO: Results of a European research project in railway aerodynamics*. *Proc. World Congr. Railw. Res.*, Tokyo.
- McBeath, S. "Slippery Customer" *Racecar Engineering* (Dec), 2006
- Menter, F. R. (1994) Two-Equation Eddy-Viscosity Turbulence Models for Engineering Applications, *AIAA Journal*, Vol. 32, No. 8 pp. 269-289

Menter, F. R. (1994), "Two-Equation Eddy-Viscosity Turbulence Models for Engineering Applications", *AIAA Journal*, 32, pp. 269-289.

Noble R., Tremayne D. (2002) *Thrust* (text), Partridge Press, ISBN 1-8522-5268-5

Oberoi, R., Chakravarthy, S., Fredrick, W., Glessner, P.T. (2006) Using CFD to design the American Challenger Rocket Car, SAE 206-013660,

Oberoi, R., S. Chakravarthy, O. Peroomian, Fredrick, W., Glessner, P.T, V. Akdag (2007) CFD Analysis of Directional Stability for the American Challenger Rocket Car, SAE 2007-01-3857

Pope, C.W. (1991) The simulation of flows in railway tunnels using 1/25th scale moving model facility. *Aerodynamics and Ventilation of Vehicle Tunnels*, ed. A. Haerter, pp. 48–56. New York: Elsevier

Powell, J; Maise, G; Paniagua, J; Rather, J (2008) Maglev Launch and the Next Race to Space, IEEE Aerospace Conference Proceedings 2008, Big Sky, USA

Purdon JP (2006) Supersonic projectiles in the vicinity of solid obstacles. Undergraduate Thesis submitted to the University of New South Wales at the Australian Defence Force Academy.

Purdon, J.P., Mudford, N.R., Kleine. H. (2007) Supersonic projectiles in the vicinity of solid obstacles. *Proc. 27th Int. Congr. High-Speed Photography and Photonics*, SPIE, Bellingham, vol. 6279

Raghunathana, R.S., Kimb, H-D., Setoguchi, T. (2002) Aerodynamics of high-speed railway trains, *Progress in Aerospace Sciences*, 38, pp.469–514

Rankine, W. J. M. (1870) On the thermodynamic theory of waves of finite longitudinal disturbances, *Phil. Trans. Roy. Soc. London*, 160, (1870), p. 277.

Ranzenbach, R. (1995) Cambered Airfoil in Ground Effect – Wind Tunnel and Road Conditions, 13th AIAA Applied Aerodynamics Conference, San Diego, USA, pp. 1208-1215.

Ranzenbach, R. and Barlow, J. (1994) Two Dimensional Aerofoil in Ground Effect, Experimental and Computational Study, SAE 942509

Ranzenbach, R. and Barlow, J. (1995) Cambered Airfoil in Ground Effect - Wind Tunnel and Road Conditions, AIAA 95-1909-CP

Ranzenbach, R. and Barlow, J. (1996) Cambered Airofoil in Ground Effect - An Experimental and Computational Study, SAE 960909

Ranzenbach, R. and Barlow, J. (1997) Multielement Aerofoil in Ground Effect, Experimental and Computational Study, AIAA 97-2238

Raymond, A. (1921) Ground Influence on Aerofoils. NACA TN-67

Reid, E. (1928) A Full-Scale Investigation of Ground Effect. NACA TR 265.

- Roohani, H.; Skews, B.W. (2008) Unsteady aerodynamic effects experienced by aerofoils during acceleration and retardation. Proceedings of the Institution of Mechanical Engineers, Journal of Aerospace Engineering, 222 (5), pp. 631-636.
- Rozhdestvensky, K. V. (2000) Aerodynamics of a Lifting System in Extreme Ground Effect (text) 1st ed., Springer-Verlag, New York, 2000.
- Rusanov, V.V. (1976) A blunt body in a supersonic stream, Annu. Rev. Fluid Mech., 8, pp. 377-404
- Sahu, J. (1994) Numerical computations of supersonic base flow with special emphasis on turbulence modeling, , AIAA Journal, 32 (7), pp. 1547-1549
- Sahu, J. (1990) Numerical computations of transonic critical aerodynamic behaviour, , AIAA Journal, 28 (5), pp.807-816
- Sahu, J. (1994) Three-dimensional flow calculation for a projectile with standard and dome bases, , Nietubicz, C., J. Spacecraft and Rockets, 31 (1), pp. 106-112
- Sardou, M. (1986) Reynolds effect and "moving ground effect" tested in a quarter scale wind tunnel over a high speed moving belt. Journal of Wind Engineering and Industrial Aerodynamics, 22 (2-3), pp. 245-270
- Sardou, M. (1986) Reynolds Effect and Moving Ground Effect Tested in a Quarter Scale Wind Tunnel Over a High Speed Moving Belt, J. of Wind Eng. & Industrial Aero., (22), pp.345-370
- Schetz, J. (2001) Aerodynamics of High Speed Trains. Annual Review of Fluid Mechanics, 33, pp.371-414
- Schetz, J. A. (2001) Aerodynamics of High Speed Trains, Annual Review of Fluid Mechanics, 33, pp. 371-414.
- Schmisser, J. D.; Gaitonde, Datta V. (2001) Numerical Investigation of Strong Crossing Shock-Wave/Turbulent Boundary-Layer Interactions. AIAA Journal, 39 (9), pp. 1742-1749
- Schmitt, V. and F. Charpin (1979) Pressure Distributions on the ONERA-M6-Wing at Transonic Mach Numbers. Experimental Data Base for Computer Program Assessment. Report of the Fluid Dynamics Panel Working Group 04, AGARD AR 138, May 1979.
- Shih T.H., Liou, W.W., Shabir, A., Yang, Z. and Zhu, J. (1995) A New k- $\epsilon$  Eddy Viscosity Model for High Reynolds Number Turbulent Flows," Computers Fluids, 24(3):227-238
- Shih, T.H., Liou, W. W., Shabbir, A., Yang, Z. and Zhu, J. (1995) A New k- $\epsilon$  Eddy-Viscosity Model for High Reynolds Number Turbulent Flows - Model Development and Validation, Computers & Fluids, 24, (3), pp 227-238
- Silton, S.I. (2005) Navier-Stokes computations for a spinning projectile from subsonic to supersonic speeds, J. Spacecraft and Rockets, 42 (2), pp. 223-231
- Singhn J. P. (2001), An improved Navier-Stokes flow computation of AGARD Case-10 flow

over RAE2822 airfoil using Baldwin-Lomax model, *Acta Mechanica* 151, pp 255-263

Skews, B.W. (2000) Three-dimensional effects in wind tunnel studies of shock wave reflection. *J. Fluid Mech.*, 407, pp. 85-104

Skews, B.W. (2000) Three-dimensional effects in wind tunnel studies of shock wave reflection. *Journal of Fluid Mechanics*, 407, pp. 85-104

Sowdon, A. and Hori, T. (1996) An Experimental Technique for Accurate Simulation of the Flowfield for Wing In Surface Effect Craft. *The Aeronautical Journal* June/July, pp. 215-222.

Spalart, P. and Allmaras, S. (1992) A one-equation turbulence model for aerodynamic flows, *AIAA Paper* 92-0439

Strike, W.T., Lucas, E.J. (1968) "Evaluation of Wind Tunnel Tests on AFMDC Monorail cone and spike nose sled configurations at Mach numbers from 2.0 to 5.0, *AEDC-TR-68-198* (AD679206)

Sturek, W.B., Nietubicz, C.J., Sahu, J., Weinacht, P., J. (1994) Applications of Computational Fluid Dynamics to the Aerodynamics of Army Projectiles, Spacecraft and Rockets, 31 (2), 186-199

Sturek, W.B., Schiff (1980) Computations of the Magnus effect for slender bodies in supersonic flight, , L.B., *AIAA paper* 80-1586-CP

Sudani, N., Sato, M., Kanda, H., Matsuno, K. (1994) Flow visualization studies on sidewall effects in two-dimensional transonic airfoil testing. *Journal of Aircraft* , 31 (6), pp. 1233-1239

Suzuki, M. (2004) An aerodynamic design of high-speed train for reducing flow-induced vibration in tunnel. *European Congress on Computational Methods in Applied Sciences and Engineering*, Jyväskylä

Torda T.P., and Uzgiris S.C. (1970) Blue Flame – A Land Speed Record Vehicle. *Mechanical Engineering*, 92(7), pp.9-18

Torda T.P., Morel T.A. (1971) Aerodynamic Design of a Land Speed Record Car, *Journal of Aircraft*, 8 (12), pp1029-1033

Tyll, J.S., Liu, D., Schetz, J.A., Marchman, J.F. (1996) Experimental studies of magnetic levitation train aerodynamics, *AIAA journal*, (34) 12, pp. 2465-2470

Weinacht, P. (2003) Prediction of projectile performance, stability, and free-flight motion using computational fluid dynamics, , *Army Research Laboratory report* ARL-TR-3015

Weinacht, P., Sturek, W.B., Schiff, L.B. (1997) Navier-Stokes predictions of pitch damping for axisymmetric projectiles, , *J. Spacecraft and Rockets*, 34 (6), 753-761

Weiselsberger, C. (1922) Wing resistance near the ground. *NACA TM-77*

Wilcox, D.C. (2004), *Turbulence Modeling for CFD*, ISBN 1-928729-10-X, 2nd Ed., DCW

Industries, Inc..

Zerihan, J. (2001) An Investigation into the Aerodynamics of Wings in Ground Effect, Ph.D. Thesis, University of Southampton, School of Engineering Sciences.

Zerihan, J. and Zhang, X. (2000) Force Enhancement of Gurney Flaps on a Wing in Ground Effect, AIAA 2000-2241

Zerihan, J. and Zhang, X., (2001) Aerodynamics of Gurney Flaps on a Wing in Ground Effect, AIAA Journal Vol. 39, no. 5, pp. 772-780

Zerihan, J., and Zhang, X. (2000) Aerodynamics of a Single Element Wing in Ground Effect, Journal of Aircraft, 37, (6), pp 1058-1064

Zhang, X. & Zerihan, J. (2003) Off-Surface Aerodynamic Measurements of a Wing in Ground Effect, Journal of Aircraft, Vol. 40, No. 4, July-August 2003, pp. 716-725

Zhang, X. and Zerihan, J. (2002) Aerodynamics of a Double Element Wing in Ground Effect, AIAA 2002-0834

Zhang, X. and Zerihan, J. (2003) Off Surface Aerodynamic Measurements of a Wing in Ground Effect, J. of Aircraft, Vol. 40, No. 4, pp. 716-725

Zhang, X. and Zerihan, J. (2004) Edge Vortices of a Double Element Wing in Ground Effect, J. of Aircraft, Vol. 41, No. 5, pp. 1127-1137

Zhang, X., Toet, W., Zerihan, J. (2006) Ground Effect Aerodynamics of Race Cars. Applied Mechanics Reviews, 59, pp. 33-49